

Lecture Notes in Mechanical Engineering

Zamberi Jamaludin  
Mohd Najib Ali Mokhtar *Editors*

# Intelligent Manufacturing and Mechatronics

Proceedings of the 2nd Symposium  
on Intelligent Manufacturing and  
Mechatronics – SympoSIMM 2019,  
8 July 2019, Melaka, Malaysia

 Springer

# **Lecture Notes in Mechanical Engineering**



**Lecture Notes in Mechanical Engineering (LNME)** publishes the latest developments in Mechanical Engineering - quickly, informally and with high quality. Original research reported in proceedings and post-proceedings represents the core of LNME. Volumes published in LNME embrace all aspects, subfields and new challenges of mechanical engineering. Topics in the series include:

- Engineering Design
- Machinery and Machine Elements
- Mechanical Structures and Stress Analysis
- Automotive Engineering
- Engine Technology
- Aerospace Technology and Astronautics
- Nanotechnology and Microengineering
- Control, Robotics, Mechatronics
- MEMS
- Theoretical and Applied Mechanics
- Dynamical Systems, Control
- Fluid Mechanics
- Engineering Thermodynamics, Heat and Mass Transfer
- Manufacturing
- Precision Engineering, Instrumentation, Measurement
- Materials Engineering
- Tribology and Surface Technology

To submit a proposal or request further information, please contact the Springer Editor in your country:

**China:** Li Shen at [li.shen@springer.com](mailto:li.shen@springer.com)

**India:** Dr. Akash Chakraborty at [akash.chakraborty@springernature.com](mailto:akash.chakraborty@springernature.com)

**Rest of Asia, Australia, New Zealand:** Swati Meherishi at [swati.meherishi@springer.com](mailto:swati.meherishi@springer.com)

**All other countries:** Dr. Leontina Di Cecco at [Leontina.dicecco@springer.com](mailto:Leontina.dicecco@springer.com)

To submit a proposal for a monograph, please check our Springer Tracts in Mechanical Engineering at <http://www.springer.com/series/11693> or contact [Leontina.dicecco@springer.com](mailto:Leontina.dicecco@springer.com)

**Indexed by SCOPUS. The books of the series are submitted for indexing to Web of Science.**

More information about this series at <http://www.springer.com/series/11236>

Zamberi Jamaludin · Mohd Najib Ali Mokhtar  
Editors

# Intelligent Manufacturing and Mechatronics

Proceedings of the 2nd Symposium  
on Intelligent Manufacturing  
and Mechatronics – SympoSIMM 2019,  
8 July 2019, Melaka, Malaysia

 Springer

*Editors*

Zamberi Jamaludin  
Fakulti Kejuruteraan Pembuatan  
Universiti Teknikal Malaysia Melaka  
Durian Tunggal, Melaka, Malaysia

Mohd Najib Ali Mokhtar  
Fakulti Kejuruteraan Pembuatan  
Universiti Teknikal Malaysia Melaka  
Durian Tunggal, Melaka, Malaysia

ISSN 2195-4356

ISSN 2195-4364 (electronic)

Lecture Notes in Mechanical Engineering

ISBN 978-981-13-9538-3

ISBN 978-981-13-9539-0 (eBook)

<https://doi.org/10.1007/978-981-13-9539-0>

© Springer Nature Singapore Pte Ltd. 2020, corrected publication 2021

This work is subject to copyright. All rights are reserved by the Publisher, whether the whole or part of the material is concerned, specifically the rights of translation, reprinting, reuse of illustrations, recitation, broadcasting, reproduction on microfilms or in any other physical way, and transmission or information storage and retrieval, electronic adaptation, computer software, or by similar or dissimilar methodology now known or hereafter developed.

The use of general descriptive names, registered names, trademarks, service marks, etc. in this publication does not imply, even in the absence of a specific statement, that such names are exempt from the relevant protective laws and regulations and therefore free for general use.

The publisher, the authors and the editors are safe to assume that the advice and information in this book are believed to be true and accurate at the date of publication. Neither the publisher nor the authors or the editors give a warranty, expressed or implied, with respect to the material contained herein or for any errors or omissions that may have been made. The publisher remains neutral with regard to jurisdictional claims in published maps and institutional affiliations.

This Springer imprint is published by the registered company Springer Nature Singapore Pte Ltd. The registered company address is: 152 Beach Road, #21-01/04 Gateway East, Singapore 189721, Singapore

# Preface

The 2nd Symposium on Intelligent Manufacturing and Mechatronics was organized by the Faculty of Manufacturing Engineering, Universiti Teknikal Malaysia Melaka (UTeM), on 8th of July 2019, at the Laman Hikmah Library, UTeM. This symposium was a manifestation of the commitment and strong belief of all who have contributed to its success, on the needs of embracing Industrial Revolution 4.0 as the way forward for manufacturing entities especially those in Malaysia. The relevance of this symposium was evidence from its successful inauguration on 29 January 2018 at the then Faculty of Manufacturing Engineering, Universiti Malaysia Pahang (UMP). This year's event has attracted a significant number of postgraduates and researchers in the field of manufacturing and mechatronics engineering, providing opportunities for intellectual discourse on recent topics related to the subject matters.

This symposium has enticed 83 submissions from authors nationwide. Each submission has undergone a rigorous peer-review process according to the selected tracks. Reviews were based on the manuscript's relevance to the tracks, novelty of the findings and the relevance of the topics to the themes of the symposium that are Intelligent Manufacturing and Mechatronics. Following the review process, 55 submissions were accepted while three submissions were withdrawn, and 25 submissions were rejected due to various reasons. The accepted papers were divided into five tracks covering various scopes of manufacturing and mechatronics engineering, namely Artificial Intelligence, Instrumentation and Controls, Intelligent Manufacturing, Modelling and Simulation, and Robotics. This book is organized into five parts based on the aforementioned tracks.

We would like to express our gratitude to all members of the Organizing Committee, without whom the organization of this symposium would be impossible. Special thanks go to the management of the Faculty of Manufacturing Engineering, UTeM, the management of Laman Hikmah Library, UTeM, the Faculty of Mechanical and Manufacturing Engineering, UMP, and all the sponsors who have been kind in their support towards the successful organization of this symposium. In addition, we would like to extend our thanks to all authors for their

participation and contributions towards the success of this symposium, without whom this symposium will not be a reality.

We sincerely hope that the contents of this book will benefit all readers in embracing the new era of Industrial Revolution 4.0 in the field of manufacturing and mechatronics engineering.

July 2019

Zamberi Jamaludin  
Mohd Najib Ali Mokhtar  
Mohd Nazrin Muhammad  
Silah Hayati Kamsani

# **Organizing Committee**

## **Patron**

Shahrin b. Sahib@Sahibuddin

## **Advisors**

Abu b. Abdullah  
Mohd Razali b. Muhamad

## **Chairman of the Organizing Committee**

Zamperi b. Jamaludin

## **Deputy Chairman**

Mohd Asyadi Azam b. Mohd Abid

## **Vice Chairmen of the Organizing Committee**

Mohd Najib b. Ali Mokhtar  
Mohd Hasnun Arif b. Hassan

## **Secretaries**

Silah Hayati bt. Kamsani  
Norazah bt. Mohamed Yazid

**Treasurers**

Khairul Faiz b. Zainal  
Siti Suhailin bt. Mohd Sidek

**Registration and Technical Committee**

Mohd Nazrin b. Muhammad  
Muhammad Hafidz Fazli b. Md. Fauadi  
Rahimah bt. Abdul Hamid  
Nik Syahrim b. Nik Anwar

**Promotion and ICT Committee**

Mohd Nazmin b. Maslan  
Nur Aidawaty bt. Rafan  
Syamimi bt. Shamsuddin  
Zaleha bt. Mustafa  
Mariam bt. Md. Ghazaly  
Chong Shin Horng

**Logistic Committee**

Lokman b. Abdullah  
Shariman b. Abdullah  
Azrul Azwan b. Abdul Rahman

**Sponsorship Committee**

Mahasan b. Mat Ali

**Banquet, Souvenirs and Certificate Committee**

Noor Asyikin bt. Sulaiman  
Masuriya Hani bt. Ab. Wahid  
Fadzly b. Nordin  
Amiza bt. Hj. Talib  
Siti Rohani bt. Manan  
Mohd Remy b. Ab. Karim  
Abdul Rahman Rosli b. Mahmood

## **Floor Manager**

Ruzaidi b. Zamri  
Fatimah bt. Md. Radzai  
Siti Rahmah bt. Shamsuri

## **IEEE UTeM Student Branch**

Liew Siaw Hong  
Sara Ragab Mahmoud  
Wong Rui Zhen



# Contents

## Artificial Intelligence

<b>Niblack Algorithm Modification Using Maximum-Minimum (Max-Min) Intensity Approaches on Low Contrast Document Images</b> . . . . .	3
Wan Azani Mustafa, Wan Khairunizam, A. S. Mat Yusoff, Syed Zulkarnain Syed Idrus, and Mohamad Nur Khairul Hafizi Rohani	
<b>Predicting Outcomes in Patients with Traumatic Brain Injury Using Machine Learning Models</b> . . . . .	12
Nor Safira Elaina Mohd Noor and Haidi Ibrahim	
<b>Blood Vessel Detection Monitoring System and Mobile Notification for Diabetic Retinopathy Diagnosis</b> . . . . .	21
Ahmad Syauqi Mahmud, Wan Azani Mustafa, Mohd Aminudin Jamlos, Syed Zulkarnain Syed Idrus, Wan Khairunizam, and Mohd Al Hafiz Mohd Naw	
<b>Reduction of Salt-and-Pepper Noise from Digital Grayscale Image by Using Recursive Switching Adaptive Median Filter</b> . . . . .	32
Aina Qistina Md. Taha and Haidi Ibrahim	
<b>Parameter Tuning in the Single-Solution Simulated Kalman Filter Optimizer</b> . . . . .	48
Nor Hidayati Abdul Aziz, Zuwairie Ibrahim, Nor Azlina Ab Aziz, Badaruddin Muhammad, Tasiransurini Ab Rahman, Mohd Saberi Mohamad, and Suhazri Amrin Rahmad	
<b>Path Tracking Simulation of the Buggy Car by Using Fuzzy Information of the Steering Wheel</b> . . . . .	57
Hafiz Halin, Wan Khairunizam, Hasri Haris, I. Zunaidi, Shahrman Abu Bakar, Z. M. Razlan, and Wan Azani Mustafa	

<b>The Classification of Skateboarding Trick Manoeuvres Through the Integration of IMU and Machine Learning</b> .....	67
Muhammad Amirul Abdullah, Muhammad Ar Rahim Ibrahim, Muhammad Nur Aiman Bin Shapiee, Mohd Azraai Mohd Razman, Rabiul Muazu Musa, and Anwar P. P. Abdul Majeed	
<b>Predicting Serious Injuries Due to Road Traffic Accidents in Malaysia by Means of Artificial Neural Network</b> .....	75
Nurul Qastalani Radzuan, Mohd Hasnun Arif Hassan, Anwar P. P. Abdul Majeed, Rabiul Muazu Musa, Mohd Azraai Mohd Razman, and Khairil Anwar Abu Kassim	
<b>Instrumentation and Controls</b>	
<b>Welding Quality Assessment Using Waveform Signal Analysis of Vibration</b> .....	83
A. M. Najib, E. R. Imam Fauzi, F. F. Kamarul Bahrin, and N. D. Zainudin	
<b>Arm Games for Virtual Reality Based Post-stroke Rehabilitation</b> .....	91
C. Basri Noor, Wan Khairunizam, S. Diny Syarifah, I. Zunaidi, Lee Hui Ling, A. B. Shahrman, M. R. Zuradzman, and Wan Azani Mustafa	
<b>Design of Sliding Mode Controller Using Smoothing Method for Chattering Suppression in Machine Tools</b> .....	102
Weng Sun Tong, Tsung Heng Chiew, Zamberi Jamaludin, Ahmad Yusairi Bani Hashim, Lokman Abdullah, and Nur Aidawaty Rafan	
<b>A New Approach of Finding Transfer Function of Piezoelectric Actuator Using Finite Element Modelling</b> .....	112
A. M. Najib, M. N. Muhammad, M. N. Maslan, A. Y. Bani Hashim, and A. J. Fairul	
<b>Mechanomyography: An Insight to Muscle Physiology</b> .....	129
Irsa Talib, Kenneth Sundaraj, Chee Kiang Lam, Md. Asraf Ali, and Jawad Hussain	
<b>Identification of a Piezoelectric Compact Actuator</b> .....	138
Mohd Nazmin Maslan, Mohd Syafiq Syed Mohamed, Ruzaidi Zamri, Lokman Abdullah, Mahasan Mat Ali, Mohd Zamzuri Ab Rashid, and Mohd Samsuddin Noorazizi	
<b>Seismic Control of a Building Structure Equip with Hybrid Mass Damper Using Sliding Mode Control</b> .....	146
Normaisharah Mamat, Fitri Yakub, Sheikh Ahmad Zaki Shaikh Salim, Mohd Zamzuri Ab Rashid, Sharifah Munawarah, and Shairatul Akma Roslan	

**Enhanced Time Synchronization Protocol for Wireless Sensor and Actuator Network** ..... 157  
 Yeong Chin Koo and Muhammad Nasiruddin Mahyuddin

**An Innovative Anti-theft System for Automotive** ..... 167  
 Firdaus Zainun, Samson Chan Kit Hwa, Nor Amylia Mohd Halmy, Choong Chia How, and Muhammad Nasiruddin Mahyuddin

**Intelligent Control of CNC System Based on IEC 61499 Function Block Technology** ..... 176  
 Muhammad Azri Othman, Zamberi Jamaludin, and Mohamad Minhat

**Analysis of Interpreted CAD/CAM Trajectory as Alternative Input Reference for Control System** ..... 186  
 Norhidayah Mat Seman, Zamberi Jamaludin, and Mohamad Minhat

**Effect of Cutting Forces on Surface Roughness for Varying Depth of Cut and Feed Rates in Milling Machining Process** ..... 195  
 Zamberi Jamaludin, Nur Ayunni Shamshol Ali, Nur Aidawaty Rafan, and Lokman Abdullah

**Intelligent Manufacturing**

**Mechanical Behaviour of Banana Fibre Reinforced Concrete with Kenaf Fibre as an Additive** ..... 207  
 Nurul Akmam Naaamandadin, Ahmad Izdihar Saharudin, Wan Azani Mustafa, and Ragunathan Santiago

**Characterization and Properties of Oil Palm Empty Fruit Bunch Reinforced Polyvinyl Alcohol Thin Films** ..... 214  
 Nurul Syazwani Othman, Ragunathan Santiagoo, Wan Azani Mustafa, Mustaffa Zainal, Azlinda Abdul Ghani, and Nurul Akmam Naaamandadin

**Mechanical Properties of the Utilisation Glass Powder as Partial Replacement of Cement in Concrete** ..... 221  
 Nurul Akmam Naaamandadin, Izzad Shafiq Abdul Aziz, Wan Azani Mustafa, and Ragunathan Santiago

**Optimization on Surface Roughness of Fused Deposition Modelling (FDM) 3D Printed Parts Using Taguchi Approach** ..... 230  
 Mohd Nazri Ahmad, Mohd Hidayat Ab Rahman, Nurul Ain Maidin, Mohd Hairizal Osman, Mohammad Khalid Wahid, Hussin Mohamed Saiful Firdaus, and Nur Afifah Abd Aziz

**Factors that Entrapped the Malaysian Mobile Provider in the Red Ocean Traps** ..... 244  
 M. F. M. Sam, H. Hafizuddin, B. C. Chew, and Y. F. Yusof

<b>Multi Response Optimisation of Injection Moulding Process Parameter Using Taguchi and Desirability Function</b> .....	252
Vivekanandan Panneerselvam and Faiz Mohd Turan	
<b>Utilization of Analytical Hierarchy Process (AHP) for Selecting the Best Design Concept of Conveyor System</b> .....	265
K. N. Kamaludin, L. Abdullah, M. N. Maslan, R. Zamri, M. Mat Ali, M. S. Syed Mohamed, and M. S. Noorazizi	
<b>Fabrication of Polypropylene/Acrylonitrile Butadiene Rubber/Kenaf Core Composites: Effect of Polypropylene Maleic Anhydride as Compatibilizer</b> .....	280
Nurul Syazwani Othman, Raguathan Santiago, Wan Azani Mustafa, Nur Liyana Othman, and Mohd Al Hafiz Mohd Nawawi	
<b>Pollutant Emission in Diesel Engine</b> .....	288
Mohd Al Hafiz Mohd Nawawi, Mohd Hazwan Mohd Hanid, Wan Azani Mustafa, Mohd Shahrir Kasim, and Raja Izamshah Raja Abdullah	
<b>A Bottle Neck Simulation System for a Generic Production Process</b> .....	299
Azrul Haniedy Jamil, Muhammad Nasiruddin Mahyuddin, Ahmad Rafeek Ibrahim, and Timothy Tong	
<b>Study of Sawing Performance of Band Saw Machine on Honeycomb Structure Material</b> .....	308
Chun-An Cheng and Chin-Chung Wei	
<b>Improvement of Material Removal Rate (MRR) Through Ultrasonic Vibration Frequency in Machining Hardened Material</b> ....	321
Azlan Ramli, R. Izamshah, and M. Akmal	
<b>The Effect of Carbon Fiber Reinforced Polymer (CFRP) Micro Drilling Parameter on Hole Accuracy</b> .....	333
N. Syuhada Nasir, N. Ab Wahab, and H. Sasahara	
<b>Hardness and Water Absorption Properties of Silicone Rubber Based Composites for High Voltage Insulator Applications</b> .....	343
Najwa Kamarudin, Jeefferie Abd Razak, Nurbahirah Norddin, Noraiham Mohamad, Lau Kok Tee, Tony Chew, and Nurzallia Mohd Saad	
<b>Mechanical Properties and Fracture Morphological Observation of Recycled Polypropylene (rPP) Filled Dried Banana Leaves Fibre (DBLF) Composites: Effects of Sodium Hydroxide (NaOH) Surface Treatment</b> .....	353
Thinakaran Narayanan, Jeefferie Abd Razak, Intan Sharida Othman, Noraiham Mohamad, Mohd Muzafar Ismail, and Ramli Junid	

**Surface Roughness Analysis of Zirconia Dental Restoration Manufactured Through CNC Milling Machine** ..... 361  
 Rahimah Abdul Hamid, Wan Nur Amirah Wan Muhamad, Raja Izamshah, and Mohd. Shahir Kasim

**Design and Analyses of Semi-automated Portable Oil Spill Skimmer for Water Treatment Application** ..... 372  
 L. Abdullah, K. Santuso, Z. Jamaludin, R. Zamri, and M. N. Maslan

**Modelling and Simulation**

**Flow Analysis of Three Plate Family Injection Mould Using Moldflow Software Analysis** ..... 387  
 Noorfa Idayu, Mohd Amran Md Ali, Mohd Shahir Kasim, Mohd Sanusi Abdul Aziz, Raja Izamshah Raja Abdullah, and Mohd Amri Sulaiman

**Optimization Process Parameters of Flat Plastic Part Having Side Gate System Using Flow Analysis Software** ..... 399  
 Mohd Amran Md Ali, Noorfa Idayu, Mohd Shukor Salleh, Mohd Najib Ali Mokhtar, Zulkeflee Abdullah, and Sivaraos

**Conceptual Framework for Lean Manufacturing Implementation in SMEs with PDCA Approach** ..... 410  
 Jia Yuik Chong and Puvanasvaran A. Perumal

**Comparisons in L32 2k-Factorial and L25 Taguchi for the 16 nm FinFET Statistical Optimization Applications** ..... 419  
 Ameer Farhan Roslan, Fauziyah Salehuddin, Anis Suhaila Mohd Zain, Khairil Ezwan Kaharudin, Abdul Razak Hanim, Haroon Hazura, and Siti Khadijah Idris

**Energy Consumption Clustering Analysis in Residential Building** ..... 436  
 Muhammad Aiman Razak, Fitri Yakub, Nur Najwa Izzati Sulaiman, Mohd Zamzuri Ab. Rashid, Sheikh Ahmad Zaki Shaikh Salim, Zainudin A. Rasid, and Aminudin Abu

**The Power Level Control of a Pressurised Water Reactor Nuclear Power Plant** ..... 451  
 Jothi Letchumy Mahendra Kumar, Anwar P. P. Abdul Majeed, Muhammad Aizzat Zakaria, Mohd Azraai Mohd Razman, and Mohd Ismail Khairuddin

**Mesh WSN in Midstream and Downstream of Oil and Gas Industry** ..... 456  
 A. S. Azman, M. Y. Lee, S. K. Subramaniam, and F. S. Feroz

**Wireless Sensor Networks in Midstream and Downstream in Oil and Gas Industry** ..... 466  
 M. Y. Lee, A. S. Azman, S. K. Subramaniam, and F. S. Feroz

**Performance Analysis of n-Channel VDG-MOSFET with High Dielectric Permittivity** . . . . . 475  
Ameer F. Roslan, K. E. Kaharudin, F. Salehuddin, A. S. M. Zain, A. R. Hanim, H. Hazura, S. K. Idris, and Z. A. M. Napiah

**Study of Gauss–Newton and Total Variation Image Reconstruction Approach in Imaging the Phantom in Concrete Using Electrical Resistance Tomography** . . . . . 487  
Vernoon Ang, M. H. F. Rahiman, and R. A. Rahim

**Temperatures Distribution and Contact Area of the Peaks of Three-Dimensional Rough Surfaces** . . . . . 497  
Shin-Yuh Chern, Wei-Lun Liu, Jeng-Haur Horng, Qiong-Mao Jiang, and Jin-Long Lin

**The Study of Light Effect on Surface Roughness of Metallic Surface by Using Vision System Technique** . . . . . 503  
R. Zamri, M. N. Maslan, M. S. Syed Mohamed, L. Abdullah, M. Mat Ali, and M. S. Noorazizi

**Robotics**

**The Design and Development of an Interactive Teaching Tool for Robotics and Control System Course Using Rapid Control Prototyping Solution** . . . . . 515  
Richard Lee Jiang Hong, Muhammad Nasiruddin Mahyuddin, Mohd Rizal Arshad, and Yeong Chin Koo

**Emotional States Analyze from Scaling Properties of EEG Signals Using Hurst Exponent for Stroke and Normal Groups** . . . . . 526  
Choong Wen Yean, Wan Khairunizam, Mohammad Iqbal Omar, Murugappan Murugappan, Zunaidi Ibrahim, Bong Siao Zheng, Shahriman Abu Bakar, Zuradzman Mohamad Razlan, and Wan Azani Mustafa

**Rover Car Outdoor Localization for Navigation Tracking Using Differential Global Positioning System Estimation** . . . . . 535  
Wi Kang Chew and Muhammad Aizzat Zakaria

**Dynamic Compensation Controller with Feedback Linearization Technique of 3 Degree of Freedom Exoskeleton Robotic Arm for Upper Limb Rehabilitation Purpose** . . . . . 557  
Muhammad Taha Ansari, Nur Fasihah Mohd Sobri, and Muhammad Nasiruddin Mahyuddin

**PLC Based Automated Coolant Supply System for Machining  
AISI 304L in CNC Milling** ..... 569  
Farizan Md Nor, Fairul Azni Jafar, Aisyah Jamri,  
Wan Nur Izzati Wan Md Hatta, and Mohd Hadzley Abu Bakar

**Non-static Vision Guided Pneumatic Pick and Place Robotic  
System with Shared Supervisory Control** ..... 580  
Ahmad Anas Yusof, Shakti Kumaran Asohkumaran,  
and Muhammad Arif Aiman Ramli

**Correction to: A Bottle Neck Simulation System for a Generic  
Production Process** ..... C1  
Azrul Haniedy Jamil, Muhammad Nasiruddin Mahyuddin,  
Ahmad Rafeek Ibrahim, and Timothy Tong

**Author Index** ..... 599

# **Artificial Intelligence**





# Niblack Algorithm Modification Using Maximum-Minimum (Max-Min) Intensity Approaches on Low Contrast Document Images

Wan Azani Mustafa<sup>1(✉)</sup>, Wan Khairunizam<sup>2</sup>, A. S. Mat Yusoff<sup>3</sup>,  
Syed Zulkarnain Syed Idrus<sup>4</sup>,  
and Mohamad Nur Khairul Hafizi Rohani<sup>5</sup>

<sup>1</sup> Faculty of Engineering Technology, Kampus Sg. Chuchuh,  
Universiti Malaysia Perlis, 02100 Padang Besar, Perlis, Malaysia  
wanazani@unimap.edu.my

<sup>2</sup> School of Mechatronic Engineering, Universiti Malaysia Perlis,  
Pauh Putra Campus, 02600 Arau, Perlis, Malaysia

<sup>3</sup> Institut Pendidikan Guru Kampus Sultan Mizan,  
22200 Besut, Terengganu, Malaysia

<sup>4</sup> School of Electrical System Engineering, Universiti Malaysia Perlis,  
Pauh Putra Main Campus, 02600 Arau, Perlis, Malaysia

<sup>5</sup> Center of Excellence Geopolymer and Green Technology,  
Universiti Malaysia Perlis, 01000 Kangar, Perlis, Malaysia

**Abstract.** In recent decades, detection or segmentation has been one of the major interesting research subjects due to the analysis of the information. However, most of the historical document has degraded and low contrast problem. Recently, many binarization methods were proposed in order to segment the text region from the background region in the low-quality image. In this paper, an improved binarization method was inspired by Niblack method was presented. The modification focuses to find the optimum threshold value by using the Maximum-Minimum intensity technique. The main target is to reduce the unwanted detection image and increase the resultant performance compared to the original Niblack method. The proposed method was applied to the document images from H-DIBCO 2012 and H-DIBCO 2014 dataset. The results of the numerical simulation indicate that the target was achieved by the F-Measure by F-measure (58.706), PSNR (10.778) and Accuracy (86.876). This finding will give a new benchmark to other researchers to propose an advance binarization method.

**Keywords:** Niblack · Max-Min · Document · Image

## 1 Introduction

Recently, researchers have shown an increased interest in document binarization approaches [1–3]. Binarization is the process to detect the text from the background which normally tests represent as ‘1’ (black) and background as ‘0’ (white) [4, 5].

Lately, many researchers suggest a binarization method based on structural symmetry [6], statistical information [7] and hierarchical deep supervised network [8]. Indeed, most of the approaches evaluated try to pool as much as useful information coming from different sources. That is the case of [9], following their previous work in [10].

They compare the various outputs from different methods. The pixels that are not unanimous in all the methods are marked as uncertain and then reclassified by using contrast information and the surrounding neighborhood. Arruda and Mello [11] compute weak and strong bi-level images by combining the structural contrast images with two different parametrizations of Niblack method. In a different study, Badekas and Papamarkos [12] use self-organization maps for combining of a few binarization approaches Otsu's, Bernsen's, Niblack's, Sauvola's and others.

In contrast, Khankasikam [13] states that there is not an optimal binarization technique suitable for all documents. Hence, they propose a selection algorithm where an MLP is trained to choose the best binarization method in each case from Niblack's, Bernsen's, Kapur's, Kittler's and Sauvola's. As the features, they use histograms, mean and standard deviation. The main drawback is that the selection is made instead of pixels or patches. Other approaches, like the one presented in [14] applies different methods with different parameters, and validate with a set of representative lines and apply the best method to the full document (or collections of documents).

An extreme approach is a work of [15], where an ANN for pixel classification is used but using several higher order features as input. The idea is to extract some features from other methods, for example, the Otsu's and Sauvola's thresholds. A novel approach is to treat the problem as 2D sequences and apply RNNs to classify the elements of the sequence. Besides, Afzal et al. [16] applied MDLSTM trained with Backpropagation Through - Time (BTT) on image patches. In some other examples of ML, for instance, Hedjam et al. [17] propose a maximum likelihood optimization using a high recall map by Sauvola. Besides, they restore the lost strokes combining the maximum likelihood with prior information. A Bayesian model using Hidden Markov Models (HMMs) is proposed by Su and Djafari [18] for removing bleed-through degradation. In other research, Su et al. [10] pixels are classified into three classes: background, foreground and uncertain pixel; the uncertain pixel is re-classified following an unsupervised k-means based procedure.

In this paper, a new document binarization based on the Max-Min average was proposed. The proposed method came from a modification of Niblack algorithm. The primary goal of this study was to determine the maximum threshold value in order to solve the noise problem from the Niblack method. In order to prove the effectiveness of the proposed method, three image quality assessment (IQA) which are Accuracy, F-measure and Peak Signal Noise Ratio (PSNR) have been calculated. This paper is organized into four sections. Section 2 explains the Max-Mean method, Sect. 3 shows the results performance in terms of the IQA. Section 4 describes the summary of the work.

## 2 Maximum-Minimum (Max-Min)

The Max-Min technique basically came from Niblack Method [19]. Niblack method is the most popular local thresholding algorithm because it is simple, easy to implement and performs on local thresholding of a two-dimensional for each pixel, Niblack takes a rectangular pixel-centered window and adapts the local threshold using the mean ( $m$ ) and standard deviation ( $s$ ) of this region. The equation of Niblack as follows [20];

$$T = m + ks \quad (1)$$

The threshold value is computed as: where  $k$  is the influence of the region deviation in the local threshold. This method requires to tune  $k$  and the input region size. The default windowing size and  $k$  is a  $3 \times 3$  and  $-0.2$ . The advantage of Niblack is that it always identifies the text regions correctly as a foreground. However, a major drawback of Niblack method is its dependence on the scale. The method will not work properly if the object size is varied and furthermore, if the image suffers from non-uniform illumination its effectiveness will decrease. The aim of the proposed method is to find the optimum threshold value in order to eliminate artefact detection. The lower threshold value will be able to detect the object (text region) and at the same time will reduce the unwanted image detection. However, if the threshold value is too low it will affect the detection, as well as the only darkest intensity, was successfully detected. In this study, assuming a text region darkest (low intensity) compared to the background (high intensity). Our proposed method involved two steps which are; (1) obtains the minimum intensity value on  $3 \times 3$  windowing size and (2) finds the maximum intensity value of the whole image. The proposed optimum threshold as follows;

$$A_v = [\max(\min(x, y))] \quad (2)$$

where,  $\min(x, y)$  is the minimum intensity of the image and  $\max$  is the maximum intensity for the image based on the minimum value on  $3 \times 3$  windowing size process. The final proposed algorithm is;

$$T = A_v + ks \quad (3)$$

Based on this algorithm, the unwanted detection image can be solved and automatically increased the binarization result. In order to evaluate the proposed method and compare the results with a few local methods, 2 dataset images were tested and the results are given in the following section.

### 3 Result and Discussion

In this experiment, two datasets from H-DIBCO 2012 (download at <http://utopia.duth.gr/~ipratika/HDIBCO2012/benchmark>) and H-DIBCO 2014 (download at <http://users.iit.demokritos.gr/~bgat/HDIBCO2014/benchmark>) are tested. The H-DIBCO 2012 contains a 14 image and H-DIBCO 2014 is 10 image, respectively. The input document image involved a few problems such as ink stains, blur, and low contrast effect.

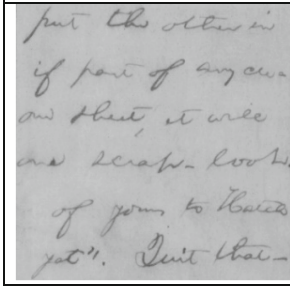
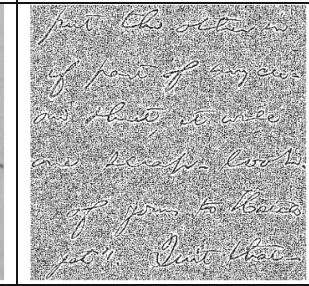
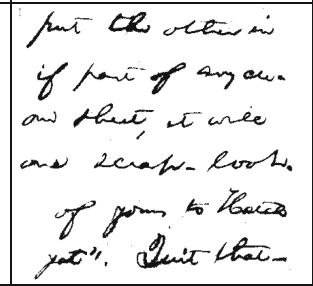
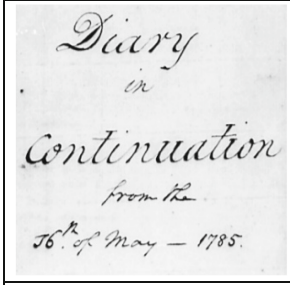
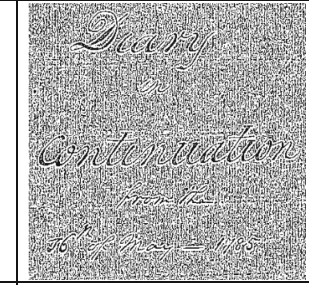
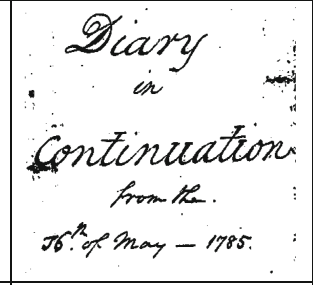
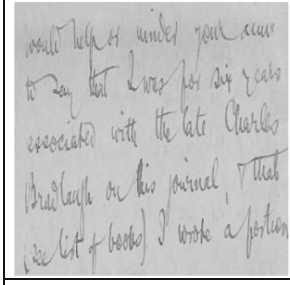
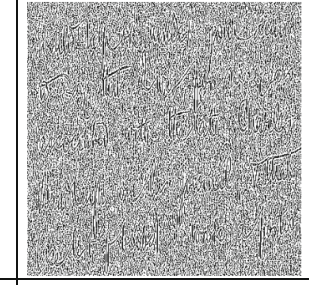
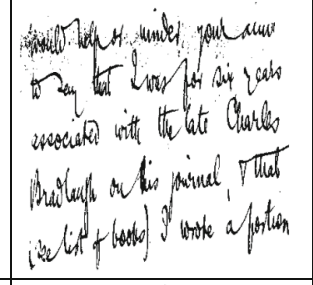
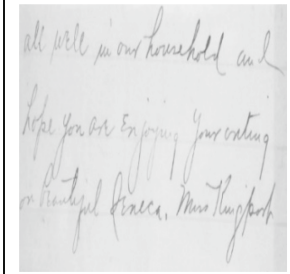
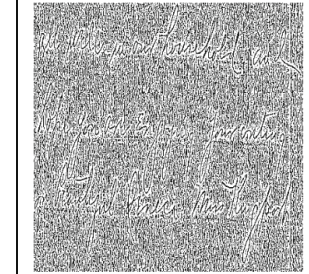
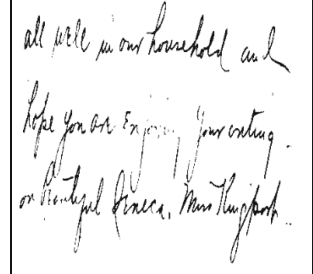
Original	Niblack	Max-Min
		
		
		
		

Fig. 1. Comparison resulting images based on H-DIBCO 2012 dataset

Many researchers agree that it is very difficult and challenge to segment or detect the text region in the degraded input image [21–24]. In this research, all coding was written using Matlab 2016 with a Toshiba L50-A laptop. The Niblack algorithm coding can be referred to [25]. Figure 1 presents the comparison result between the Niblack method and Max-Min method on H-DIBCO 2012 document images. Based on the result, the Niblack method failed to segment the text region, especially in non-uniform background images. The original Niblack algorithm produces a lower threshold value, so many unwanted regions also detected as the foreground (text) region. After applying the proposed method, the result was successful to separate text region and background region as shown in Table 1. The Max-Min method effective and properly working with low contrast document images.

In terms of numerical analysis, a few IQA such as F-measure, Accuracy and PSNR was obtained in order to compare the performance of Niblack method and Max-Min method. The good detection should be achieved highest F-measure, Accuracy and PSNR, respectively [26–29]. The comparison result is indicated in Table 1. Based on Table 1, all the three indications (F-measure, Accuracy and PSNR) show the improvement and automatically represent the high-quality detection images. The average result achieved the higher increment (%) which is an F-measure (160.63%), Accuracy (37.18%) and PSNR (140.58%) compared to the Niblack method.

**Table 1.** Comparison of IQA on H-DIBCO 2012 dataset

Image	F-Measure		Accuracy (%)		PSNR (dB)	
	Niblack	Max-Min	Niblack	Max-Min	Niblack	Max-Min
1	22.228	60.454	67.269	92.569	4.850	11.289
2	25.296	72.679	64.470	93.847	4.494	12.109
3	21.484	81.845	64.734	97.264	4.526	15.629
4	17.354	74.831	63.539	96.749	4.382	14.879
5	21.563	44.075	64.874	85.481	4.544	8.381
6	22.388	66.970	64.701	93.958	4.522	12.188
7	20.601	53.331	63.719	88.594	4.403	9.429
8	25.034	32.019	66.918	69.884	4.804	5.212
9	30.925	89.565	63.801	97.497	4.413	16.015
10	28.134	72.363	63.233	93.521	4.345	11.885
11	25.527	49.893	63.394	84.494	4.364	8.095
12	19.706	83.783	63.588	98.101	4.387	17.215
13	16.696	22.893	61.649	68.546	4.162	5.023
14	18.412	17.184	64.726	55.763	4.525	3.542
<b>Average</b>	<b>22.525</b>	<b>58.706</b>	<b>64.330</b>	<b>86.876</b>	<b>4.480</b>	<b>10.778</b>

Then, the proposed method also tested on H-DIBCO 2014 document dataset. The main problem of these images is low contrast background and non-uniform condition. According to Wang and Cui [30] is very difficult and impossible to obtain the absolute threshold value in the non-uniform image. This is supported by Liu et al. [31] study



which impossible to propose a perfect mathematical model for uneven illumination and low contrast image. However, the resulting images from the proposed method are quite good compared to the Niblack method as shown in Fig. 2. Although, with only small modifications to the Niblack algorithm, however, the results are very impressive. Based on Table 2, the Max-Min give a gorgeous image with reducing the noise and unwanted image.

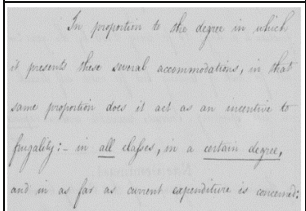
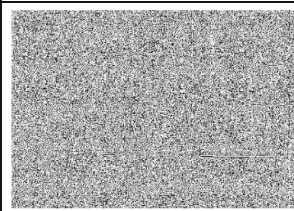
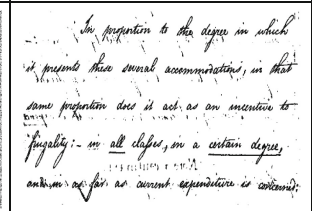
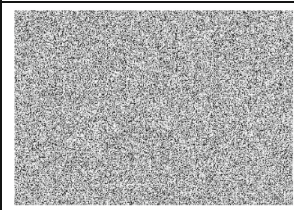
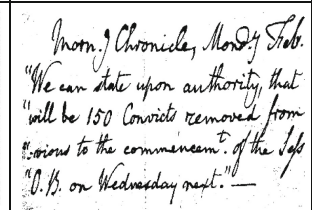
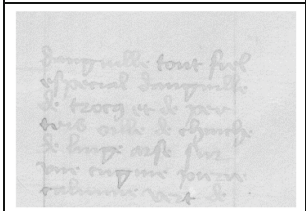
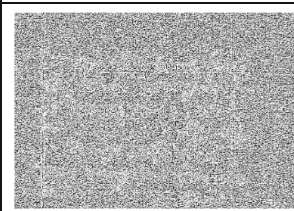
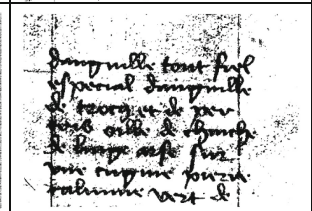
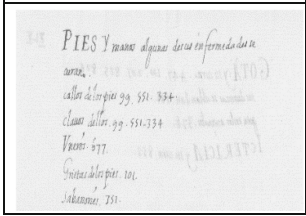
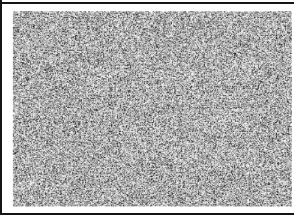
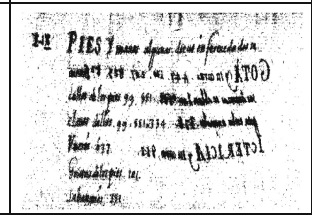
Original	Niblack	Max-Min
		
		
		
		

Fig. 2. Comparison resulting images based on H-DIBCO 2014 dataset

In the same evaluation, three indication performances which are F-measure, Accuracy and PSNR was calculated. The comparison result was present in Table 2. H-DIBCO 2014 dataset contains 10 images with low contrast. The average performance of the Max-Min technique is (F-measure = 53.162), (Accuracy = 76.889) and (PSNR = 8.276). All the three parameters show the higher result and it proves that the proposed method is more efficient in order to detect text region in the non-uniform image compared to the Niblack method.

**Table 2.** Comparison of IQA on H-DIBCO 2014 dataset

Image	F-Measure		Accuracy (%)		PSNR (dB)	
	Niblack	Max-Min	Niblack	Max-Min	Niblack	Max-Min
1	16.141	78.997	61.299	96.991	4.123	15.215
2	21.438	25.881	63.356	52.888	4.360	3.269
3	22.153	91.590	61.864	98.091	4.187	17.192
4	23.179	65.247	59.234	84.138	3.897	7.996
5	27.692	44.569	60.507	59.605	4.035	3.937
6	23.456	79.329	57.974	92.268	3.765	11.117
7	22.930	46.365	63.568	79.598	4.385	6.903
8	8.699	33.675	60.944	88.052	4.083	9.227
9	25.830	27.846	63.980	49.113	4.435	2.934
10	24.968	38.123	63.690	68.149	4.400	4.969
<b>Average</b>	<b>21.649</b>	<b>53.162</b>	<b>61.642</b>	<b>76.889</b>	<b>4.167</b>	<b>8.276</b>

## 4 Conclusion

Most libraries and archives are scanning the documents and publishing the resulting images without their corresponding transcriptions. This seriously limits the possibilities of document exploitation. Document Image Analysis aims to analyze and extract useful information from scanned documents. It involves all of the techniques and algorithms that are applied to these document images to obtain digital information related to them. In this study, a new binarization technique was proposed in order to detect the thin text region on non-uniform document images. This method inspired by the Niblack method with slight modification on a mathematical algorithm. The main target of this experiment is to improve the detection result compared to the original Niblack method. The proposed method was tested on two document dataset which is H-DIBCO 2012 and H-DIBCO 2014. Based on numerical analysis, the proposed method shows the good performance (example H-DIBCO 2012: F-measure = 58.706, Accuracy = 86.876 and PSNR = 10.778). The main performance can be summarized in Tables 1 and 2. Future research should be concentrate on the investigation of binarization on color document images.

## References

1. Kavitha, A.S., Shivakumara, P., Kumar, G.H., Lu, T.: Text segmentation in degraded historical document images. *Egypt Inform. J.* **17**, 189–197 (2016). <https://doi.org/10.1016/j.eij.2015.11.003>
2. Mustafa, W.A., Yazid, H.: Illumination and contrast correction strategy using bilateral filtering and binarization comparison. *J. Telecommun. Electron. Comput. Eng.* **8**, 67–73 (2016)
3. Mustafa, W.A., Yazid, H.: Background correction using average filtering and gradient based thresholding. *J. Telecommun. Electron. Comput. Eng.* **8**, 81–88 (2016)

4. Lelore, T., Bouchara, F.: Document image binarisation using Markov field model. In: 2009 10th International Conference Document Analysis and Recognition, pp. 551–555 (2009). <https://doi.org/10.1109/ICDAR.2009.117>
5. Mustafa, W.A., Yazid, H., Jaafar, M.: An improved sauvola approach on document images binarization. *J. Telecommun. Electron. Comput. Eng.* **10**, 43–50 (2018)
6. Jia, F., Shi, C., He, K., et al.: Degraded document image binarization using structural symmetry of strokes. *Pattern Recogn.* **74**, 225–240 (2018). <https://doi.org/10.1016/j.patcog.2017.09.032>
7. Ismail, S.M., Abdullah, S.N.H.S., Fauzi, F.: Statistical binarization techniques for document image analysis. *J. Comput. Sci.* **14**, 23–36 (2018)
8. Vo, Q.N., Kim, S.H., Yang, H.J., Lee, G.: Binarization of degraded document images based on hierarchical deep supervised network. *Pattern Recogn.* **74**, 568–586 (2018). <https://doi.org/10.1016/j.patcog.2017.08.025>
9. Su, B., Lu, S., Tan, C.L.: Combination of document image binarization techniques. In: Proceedings of the International Conference on Document Analysis and Recognition, ICDAR, pp. 22–26 (2011)
10. Su, B., Lu, S., Lim, T.C.: A self-training learning document binarization framework. In: Proceedings of International Conference on Pattern Recognition, pp. 3187–3190 (2010)
11. Arruda, A.W.A., Mello, C.A.B.: Binarization of degraded document images based on combination of contrast images. In: Proceedings of International Conference on Frontiers in Handwriting Recognition, ICFHR, pp. 615–620 (2014)
12. Badekas, E., Papamarkos, N.: Optimal combination of document binarization techniques using a self-organizing map neural network. *Eng. Appl. Artif. Intell.* **20**, 11–24 (2007)
13. Khankasikam, K.: The automatic binarization techniques selection: an artificial neural network approach. *Int. J. Digit. Content Technol. Appl.* **7**, 468 (2013)
14. Rangoni, Y., Shafait, F., Breuel, T.: OCR based thresholding. In: 11th IAPR Conference on Machine Vision Applications Vision Applications, pp. 3–6 (2009)
15. Wu, Y., Rawls, S., AbdAlmageed, W., Natarajan, P.: Learning document image binarization from data. In: IEEE International Conference on Image Process, pp. 3763–3767 (2016)
16. Afzal, M.Z., Pastor-pellicer, J., Shafait, F., et al.: Document image binarization using LSTM: a sequence learning approach. In: Third International Workshop on Historical Document Imaging and Processing, pp. 79–84 (2015). <https://doi.org/10.1145/2809544.2809561>
17. Hedjam, R., Moghaddam, R.F., Cheriet, M.: A spatially adaptive statistical method for the binarization of historical manuscripts and degraded document images. In: *Pattern Recognition*, pp. 2184–2196 (2011)
18. Su, F., Mohammad-Djafari, A.: Bayesian separation of document images with hidden Markov model. In: International Conference on Computer Vision Theory and Applications, pp. 1–6 (2007)
19. Niblack, W.: An introduction to digital image processing. Prentice-Hall, Englewood Cliffs (1986)
20. Khurshid, K., Siddiqi, I., Faure, C., Vincent, N.: Comparison of Niblack inspired binarization methods for ancient documents. In: Proceedings of SPIE-IS&T Electronic Imaging, vol. 7247, pp. 1–9 (2009). <https://doi.org/10.1117/12.805827>
21. Ntirogiannis, K., Gatos, B., Pratikakis, I.: A combined approach for the binarization of handwritten document images. *Pattern Recogn. Lett.* **35**, 3–15 (2014). <https://doi.org/10.1016/j.patrec.2012.09.026>
22. Singh, B.M., Sharma, R., Ghosh, D., Mittal, A.: Adaptive binarization of severely degraded and non-uniformly illuminated documents. *Int. J. Doc. Anal. Recognit.* **17**, 393–412 (2014). <https://doi.org/10.1007/s10032-014-0219-6>



23. Howe, N.R.: A Laplacian energy for document binarization. In: Proceedings of the International Conference on Document Analysis and Recognition, ICDAR, pp. 6–10 (2011)
24. Mustafa, W.A.: A proposed optimum threshold level for document image binarization. *J. Adv. Res. Comput. Appl.* **7**, 8–14 (2017)
25. Motl, J.: Niblack local thresholding. In: MATLAB Cent. File Exch (2013). <https://www.mathworks.com/matlabcentral/fileexchange/40849>. Accessed 2 May 2018
26. Mustafa, W.A., Yazid, H.: Image enhancement technique on contrast variation: a comprehensive review. *J. Telecommun. Electron. Comput. Eng.* **9**, 199–204 (2017)
27. Mustafa, W.A., Yazid, H., Kamaruddin, W.: Combination of gray-level and moment invariant for automatic blood vessel detection on retinal image. *J. Biomim. Biomater. Biomed. Eng.* **34**, 10–19 (2017). <https://doi.org/10.4028/www.scientific.net/JBBBE.34.10>
28. Mustafa, W.A., Kader, M.M.M.A.: A comparative study of automated segmentation methods for cell nucleus detection. *Malays. Appl. Biol.* **47**, 125–129 (2018)
29. Mustafa, W.A., Yazid, H.: Conversion of the retinal image using gray world technique. *J. Biomim. Biomater. Biomed. Eng.* **36**, 70–77 (2018). <https://doi.org/10.4028/www.scientific.net/JBBBE.36.70>
30. Wang, W., Cui, X.: A background correction method for particle image under non-uniform illumination conditions. In: International Conference on Signal Processing Systems (ICSPS), pp. 695–699 (2010)
31. Liu, J., Wang, X., Chen, M., et al.: Illumination and contrast balancing for remote sensing images. *Remote Sens.* **6**, 1102–1123 (2014). <https://doi.org/10.3390/rs6021102>



# Predicting Outcomes in Patients with Traumatic Brain Injury Using Machine Learning Models

Nor Safira Elaina Mohd Noor and Haidi Ibrahim<sup>(✉)</sup>

School of Electrical and Electronic Engineering, Universiti Sains Malaysia,  
Engineering Campus, 14300 Nibong Tebal, Penang, Malaysia  
haidi\_ibrahim@ieee.org

**Abstract.** Traumatic brain injury (TBI) is defined as blunt and penetrating injury to the head and/or brain caused by an external force that leads to temporary or permanent impairments to the brain function. Accurate measurement of prediction for the outcomes of affected individual is highly desirable to plan and optimize treatment decision. The clinical experts predict the outcomes of brain injury patients with a high degree of accuracy based on their experience and the standardized Glasgow Outcome Scale (GOS). The GOS has been used over the past 40 years and it plays an important role in developing the understanding of brain injury. Recent developments in Artificial Intelligence (AI) have heightened the need for developing predictive models using machine learning (ML) methods especially for TBI patients who require life-saving interventions. ML is a subfield of AI which allows the computer algorithms to learn patterns by studying data directly without being explicitly programmed. This paper compares the different ways in which predictive models evaluate the potential of ML for TBI outcome prediction. A literature survey of latest articles from 2016 to 2018 reveals that the predictions of existing predictive models compute different prediction performances in terms of accuracy, sensitivity, specificity and area under receiving operator characteristic (ROC) curve (AUC). Depending on the specific prediction task evaluated and the type of input features included, Artificial Neural Network (ANN) creates a powerful model to predict outcomes of TBI with profound accuracy compared to other ML models. Although ANNs are considered as “black-box” in computational models, their benefits in clinical medicine have infinite potentials in evidence-based medicine practice because ANNs can be trained on new patient information. Moreover, the existing predictive models show that ML can be leveraged to more accurately predict the outcomes of TBI patients. Most importantly, predictive models can provide real-time clinical utilization that leads to greater accuracy and higher predictive value for patients suffered from traumatic brain injury.

**Keywords:** Traumatic brain injury · Glasgow Outcome Scale · Artificial intelligence · Machine learning · Prediction outcome

## 1 Introduction

Traumatic brain injury (TBI) refers to severe head and/or brain injury resulting from a unique combination of mechanical forces with temporary or permanent impairments to each individual distinctive neuroanatomy. TBI can be classified based on severity (e.g., mild, moderate and severe), mechanism of closed or penetrating head injury or other features (e.g., specific location of brain injury or over a widespread area). Glasgow Coma Scale (GCS) is specifically used in clinical scoring system to classify the severity of TBI patients based on three categories; mild (GCS 13–15), moderate (GCS 9–12) and severe (GCS < 9) [1–3]. In addition to the head damage, TBI causes changes on pressure inside the skull and cerebral blood flow involving a complex cascade of metabolic events that influence ionic fluxes, neurotransmitter concentrations, edema and neuro-inflammatory response [4, 5].

TBI is considered as critical worldwide problem and challenge in healthcare and a major cause of morbidity and mortality especially in children and young adults [5–7]. In Malaysia, TBI due to road traffic accidents are the main reason of death especially for people who are below 45 years [8, 9] in which injury-related disability leads to long-lasting impact on behavioral, cognitive and physical impairments. These impacts, in turn, influence employment, economic and social consequences that significantly alter their life and productivity. In the United State of America (USA), TBI has also been classified as a critical health problem as it occurs at every 23 s [10]. Besides the fatal TBI, more than half million of Americans experience non-fatal TBIs every year which do not necessitate hospitalization but ultimately end up with permanent disability [10]. Meanwhile in Germany, TBI is the second most common cause of death among children aged from 0 (neonatal) to 15 years old [11].

Eventually, predicting the long-term functional recovery of patients suffering TBI becomes a crucial task to ensure that the patients with extreme brain damaged would be able to survive with early necessary interventions. Because TBI could lead to multiple organ dysfunction, the development of prediction models is particularly complex when evaluating the interaction between numerous clinical attributes to describe a long-lasting outcome for an individual patient after TBI. Prediction plays a vital role in evaluating the patient's outcomes. Therefore, an accurate predictive model is compulsory for therapeutic decision making. Many prognostic factors are needed for predicting fatality and functional outcomes after TBI but the Glasgow Outcome Scale (GOS) is typically used to determine the functional recovery of TBI patients by rating them based on the degree of residual disability namely dead, vegetative state, severe disability, moderate disability and good recovery (see Table 1) [11–13]. The GOS score was collected by an emergency medicine physician or neurosurgeon upon admission [14].

In recent years, there has been growing interest in developing machine learning (ML) models especially for clinical settings and neurosurgical application to imitate the performance of clinical experts [15–17]. ML models have been successfully applied as tools to assist in clinical diagnosis and neurosurgical outcome prediction across a wide range of fields including epilepsy, brain tumor, spine, neurovascular, Parkinson disease, TBI and hydrocephalus [16]. The ML algorithms have potentially driven more accurate

**Table 1.** Original descriptions of Glasgow Outcome Scale (GOS) categories by Jennet and Bond [13]

GOS	GOS category	Description of category
1	Death	Death due to original brain damage
2	Vegetative state	Unresponsive and unable to interact with environment for weeks or months after acute brain damage
3	Severe disability	Conscious but disabled. Dependent on daily support because of physical and/or mental causes
4	Moderate disability	Able to live independently in daily life but may rely on a special equipment for aiding in everyday activities. Unable to go to work or school
5	Good recovery	Resumption of normal life, although there may be minor neurological and physiological deficits. Able to return to work or school

and useful predictive models to estimate neurological recovery especially for TBI compared to conventional programming methods and clinical expert interpretations [16, 18]. The predictive models are practically useful for clinical practice and easy to evaluate, therefore integrating clinical decision-making with the computational approaches are crucial [16, 19].

The primary aim of this paper is to do a literature survey on the existing predictive models of TBI, by comparing the performance of ML models and putting emphasis on the development of a novel ML model to provide accurate predictions and improve clinical decision making. This paper is organized as follows. Section 2 introduces the basic knowledge about ML and important goals of using ML methods (e.g., classification and prediction). The performances of the existing TBI predictive models are compared and discussed briefly in Sect. 3. This is followed by the conclusion that is presented in Sect. 4.

## 2 Machine Learning

Artificial intelligence (AI) is a branch of computer science and engineering field and the domain of AI is ML [16, 17]. In ML, the computer systems work as a machine which can analyze data and learn the information from that data. The “learned” information is then used to explain processes by achieving additional knowledge from data (e.g., prediction of outcomes) [20]. In addition to that, ML allows the computer algorithms to facilitate the data extraction, enables the algorithms to execute the repeated analysis procedure and learn from experience, without explicitly being programmed [15, 20, 21].

Generally, ML has three types of algorithms; supervised, unsupervised and reinforcement learning. Each of the algorithms works on its particular mathematical structure [15]. The supervised learning algorithms learn from “labeled” training data to generate a model that can make predictions on previously unseen data [16, 17]. The

examples of ML models are the ANN, Support Vector Machine (SVM), Decision Tree (DT), Random Forest (RF), Naïve Bayes (NB), K-Nearest Neighbors (KNN) and Fuzzy C-Means [16].

The important goal for using ML methods is to calculate the classification or prediction of each model. Classification and prediction can be used in model extraction in order to obtain and describe the important classes of data or to predict future data trends [22]. Classification or prediction is capable to identify new outcomes from prior dataset and both are useful for handling the missing attributes values or at prediction time [7, 23, 24]. The existing predictive models of TBI are explained in Sect. 3.

### 3 A Literature Survey on the Existing Predictive Models of TBI

Historically, in 1993, McGonigal et al. were the first group of researchers who employed ML model to predict probability of survival (Ps) in patients with penetrating trauma [25]. A literature survey on the latest existing predictive models of TBI is conducted on journal articles from Science Direct, PubMed, Elsevier, Springer Link and some other publishers to identify all potentially relevant studies from 2016 to 2018 and we found only six articles which are specifically related to the prediction outcomes of TBI. Comparison of the existing predictive models of TBI is presented in Table 2. The predictive performance values are shown in Table 2 to compare and determine whether the model can achieve the highest accuracy of prediction performance.

The main purpose of predictive model is to build a model that is capable to perform the predictions. From Table 2, Pourahmad et al. [26] have confirmed the effectiveness of combining DT and ANN in order to improve the prediction performance in four hundred and ten TBI patients admitted into intensive care unit (ICU) in 2011–2012. DT worked by making a prediction or classification based on various input features with the use of bifurcating the feature space [16]. In the hybrid method, the ANN was mapped from the primary DT to help improve the modeling process. The hybrid method computed the highest area under receiving operating characteristic (ROC) curve (AUC) 0.705 than AUC of DT alone (0.695). The hybrid method had higher accuracy rate (*Acc*: 86.3% vs 82.2%), sensitivity (*Se*: 55.1% vs 47.6%) and specificity value (*Sp*: 93.6% vs 91.9%) than DT.

Previous study by Shafiei et al. [27] has compared the prediction performance between ANN and Logistic Regression (LR), in which the ANN models were the best prediction models for predicting psychological symptoms in 6 months after mild traumatic brain injury (mTBI). The architectures of ANN models were made up of an input layer, a hidden layer and output layer [31]. Shafiei et al. [27] built six models of ANN according to these configurations (input layer/hidden layer/output layer): Model 1 (14/7/2), Model 2 (14/8/2), Model 3 (14/9/2), Model 4 (14/10/2), Model 5 (14/11/2), Model 6 (14/12/2). The output layer provided two output variables, which were “Yes” denoting as having psychological symptom and “No” showing as no psychological symptom, discovered 6-month after mild injury. Shafiei et al. [27] demonstrated that the most accurate ANN architecture after training the network was the Model 3 (14/9/2) with root mean square, RMS 0.1029, AUC 0.869 and percentage of inaccurate

**Table 2.** Comparison prediction performance of the existing predictive models

References	Data	Input features	Output	Train set	Test set	Machine learning model	Prediction performance measures			
							Acc (%)	Se (%)	Sp (%)	AUC
Pourahmad et al. [26]	TBI	Clinical	Extended GOS favorable outcome GOS $\geq 5$ Un-favorable outcome GOS $\leq 4$	-	-	DT	82.20	47.60	91.10	0.695
Shafiei et al. [27]	TBI	Clinical	Psycho-logical symptoms (Yes/No)	50	50	ANN +DT ANN LR	86.30	55.1	93.6	0.705
Alanazi et al. [28]	TBI	Clinical	Comparing among predictive models	-	-	APM ANN FZ EM NB DA NF DT Affinity KNN Multi SVM LR	90.65	-	-	0.869
Hale et al. [14]	TBI	Clinical, CT	Favorable outcome GOS $\geq 4,5$ Un-favorable outcome GOS $\leq 3$	9032	3870	ANN	92.00	85.00	96.00	-
Hale et al. [29]	TBI	Clinical, CT	Clinically Relevant TBI	395	85	ANN	91.00	83.0	95.00	-
Rau et al. [30]	TBI	Clinical, CT	Mortality	1734	325	LR SVM DT NB ANN	81.00	69.00	90.00	-
							90.00	81.00	95.00	-
							74.00	58.00	85.00	-
							85.00	75.00	92.00	-
							85.00	74.00	92.00	-
							90.00	83.00	95.00	-
							83.00	72.00	0.91	-
							89.00	81.00	94.00	-
							80.00	66.00	89.00	-
							33.00	20.00	50.00	-
							97.98	99.73	60.47	0.990
							-	-	-	0.977
							93.54	59.38	93.54	0.942
							92.50	65.63	95.22	0.935
							92.92	43.75	98.29	0.872
							86.15	59.38	89.08	0.908
							92.00	84.3	92.83	0.968

CT, Computed Tomography images; TBI, Traumatic Brain Injury; GOS, Glasgow Outcome Scale; GOSE, Extended GOS; ANN, Artificial Neural Network; SVM, Support Vector Machine; DT, Decision Tree; NB, Naïve Bayes; APM, Accurate and Dynamic Predictive Model; LR, Logistic Regression; KNN, K-Nearest Neighbor; FZ, Fuzzy Model; EM, Ensemble Model; DA, Discriminant Analysis; NF, Neuro Fuzzy; Acc, Accuracy; Se, Sensitivity; Sp, Specificity; AUC, Area Under Receiving Operator Characteristic (ROC) Curve

prediction was the highest (9.35%) compared to the other ANN models. Overall, the authors concluded that ANN was the best choice for the prediction because the model had more stability in simulating complicated patterns than LR.

Alanazi et al. [28] evaluated the proposed prediction model named as Accurate and Dynamic Predictive Model (APM) which combined 11 predictive models, as shown in Table 2, to predict the TBI outcomes with 10-fold cross validation. The authors proposed a new TBI predictive model to obtain a better prediction which was based on GOS. Using the proposed model, the APM achieved the highest prediction performance in terms of accuracy, sensitivity and specificity. Although this approach was interesting, it failed to take into account the computational time consuming which required high-speed computers for validation of the model [7, 28].

To date, several studies have confirmed the effectiveness of ANN for predicting the outcomes of patients suffered with head injury. In recent studies, there was a model that combined clinical and radiological-interpreted computed tomography (CT) data to predict the outcomes of pediatric TBI patients whether the patients will survive throughout clinically relevant TBI (CRTBI) procedures [29]. Among 12,902 patients, the data were randomly partitioned into 3 groups (70% for training the ANN; 15% for validating the ANN; 15% for final testing the ANN) with two-layer feed-forward ANN. The results showed that the ANN had  $Se$  of 99.73%,  $Sp$  of 91.23% and the AUC was 0.9790 for the entire data set [29].

In another studies, Hale et al. [14] found that ANN has also provided the highest prediction performance than the traditional statistical model and initial computerized tomography (CT) classification systems (Helsinki, Rotterdam and Marshall) for predicting 6-month post-TBI outcomes in pediatric patients. The prediction outcome was determined to be favorable if patient had a GOS score of 4 or 5 ( $GOS \geq 4@5$ ) and the unfavorable outcome was defined as  $GOS \leq 3$  or death. ANN outperformed higher prediction performance with the AUC of  $0.9462 \pm 0.0422$  compared to AUC of predicting survival in Helsinki (0.814), Rotterdam (0.838) and Marshall (0.781).

Many experts now believe that rather than using the conventional statistical technique exclusively, it might be useful to develop ML models with more sophisticated data models using advanced mathematical approaches. This is because ML has the ability to execute multifaceted data sets and perform well on nonlinear data especially on missing data [6, 21, 32, 33]. Using this approach, Rau et al. [30] have been able to evaluate the prediction performance of TBI patients with high risk of mortality. In the analysis of mortality prediction, Rau et al. [28] found that ANN model worked as the superior prediction model compared to LR, SVM, NB and DT with high prediction performance AUC (0.968) followed by the LR (0.942), SVM (0.935), NB (0.908) and DT (0.872). ANN got the highest sensitivity,  $Se$  (84.38%) than the other four ML models when predicting the mortality of patients with isolated moderate and severe TBI.

## 4 Conclusion

In conclusion, the studies presented thus far offer evidence that ML algorithms can produce powerful prediction model and are increasingly being evaluated as prediction models for TBI. ANN can potentially create a powerful model to predict outcomes of TBI with profound accuracy compared to other ML models. The ANN is able to handle large numbers of clinical attributes allowing for greater discrimination and resolution of outcome prediction compared to other ML models. Furthermore, prediction produced by ML models is increasing in accuracy and can be personalized to individual patients due to the expandability of data collected on each patient. The predictive models have emerged as powerful platforms for doctors and medical staff in making decision for better treatments or therapies for patients.

**Acknowledgement.** This research is supported by the Ministry of Higher Education (MoHE) Malaysia, under Trans-disciplinary Research Grant Scheme (TRGS) with grant number 203\PELECT\6768002.

## References

1. Knaus, W.A., Draper, E.A., Wagner, D.P., Zimmerman, J.E.: APACHE II: a severity of disease classification system. *Crit. Care Med.* **13**, 818–829 (1985). <https://doi.org/10.1097/00003246-198510000-00009>
2. MRC CRASH Trial Collaborators: Predicting outcome after traumatic brain injury: practical prognostic models based on large cohort of international patients. *BMJ* **336**(7641), 425–429 (2008). <https://doi.org/10.1136/bmj.39461.643438.25>
3. Rimel, R.W., Jane, J.A., Edlich, R.F.: An injury severity scale for comprehensive management of central nervous system trauma. *J. Am. Coll. Emerg. Physicians* **8**, 64–67 (1979). [https://doi.org/10.1016/S0361-1124\(79\)80039-8](https://doi.org/10.1016/S0361-1124(79)80039-8)
4. Mitra, J., Shen, K.K., Ghose, S., Bourgeat, P., Fripp, J., Salvado, O., Pannek, K., Taylor, D.J., Mathias, J.L., Rose, S.: Statistical machine learning to identify traumatic brain injury (TBI) from structural disconnections of white matter networks. *NeuroImage* **129**, 247–259 (2016). <https://doi.org/10.1016/j.neuroimage.2016.01.056>
5. Alanazi, H.O., Abdullah, A.H., Al Juma, M.: A critical review for an accurate and dynamic prediction for the outcomes of traumatic brain injury based on Glasgow Outcome Scale. *J. Med. Sci.* **13**(4), 244–252 (2013). <https://doi.org/10.3923/jms.2013.244.252>
6. Alanazi, H.O., Abdullah, A.H., Qureshi, K.N., Larbani, M., Al Jumah, M.: Predicting the outcomes of traumatic brain injury using accurate and dynamic predictive model. *J. Theor. Appl. Inf. Technol.* **93**(2), 561–570 (2016)
7. Alanazi, H.O., Abdullah, A.H., Qureshi, K.N.: A critical review for developing accurate and dynamic predictive models using machine learning methods in medicine and health care. *J. Med. Syst.* **41**(4), 69 (2017). <https://doi.org/10.1007/s10916-017-0715-6>. (in Eng)
8. Moppett, I.K.: Traumatic brain injury: assessment, resuscitation and early management. *Br. J. Anaesth.* **99**(1), 18–31 (2007). <https://doi.org/10.1093/bja/aem128>
9. You, X., Liew, B.S., Rosman, A.K., Musa, K.I., Idris, Z.: The estimated cost of surgically managed isolated traumatic head injury secondary to road traffic accidents. *Neurosurg. Focus* **44**(5), E7 (2018). <https://doi.org/10.3171/2018.1.FOCUS17796>



10. Goffus, A.M., Anderson, G.D., Hoane, M.R.: Sustained delivery of nicotinamide limits cortical injury and improves functional recovery following traumatic brain injury. *J. Oxidative Med. Cell. Longev.* **3**(2), 145–152 (2010). <https://doi.org/10.4161/oxim.3.2.11315>
11. Emami, P., Czorlich, P., Fritzsche, F.S., Westphal, M., Rueger, J.M., Lefering, R., Hoffmann, M.: Impact of Glasgow Coma Scale score and pupil parameters on mortality rate and outcome in pediatric and adult severe traumatic brain injury: a retrospective, multicenter cohort study. *J. Neurosurg.* **126**(3), 760–767 (2017). <https://doi.org/10.3171/2016.1.JNS152385>
12. McMillan, T., Wilson, L., Ponsford, J., Levin, H., Teasdale, G., Bond, M.: The Glasgow Outcome Scale—40 years of application and refinement. *Nat. Rev. Neurol.* **12**(8), 477 (2016). <https://doi.org/10.1038/nrneurol.2016.89>
13. Jennett, B., Bond, M.: Assessment of outcome after severe brain damage: a practical scale. *Lancet* **305**(7905), 480–484 (1975). [https://doi.org/10.1016/S0140-6736\(75\)92830-5](https://doi.org/10.1016/S0140-6736(75)92830-5)
14. Hale, A.T., Stonko, D.P., Brown, A., Lim, J., Voce, D.J., Gannon, S.R., Le, T.M., Shannon, C.N.: Machine-learning analysis outperforms conventional statistical models and CT classification systems in predicting 6-month outcomes in pediatric patients sustaining traumatic brain injury. *Neurosurg. Focus* **45**(November), 1–7 (2018). <https://doi.org/10.3171/2018.8.FOCUS17773>
15. Senders, J.T., Arnaout, O., Karhade, A.V., Dasenbrock, H.H., Gormley, W.B., Broekman, M. L., Smith, T.R.: Natural and artificial intelligence in neurosurgery: a systematic review. *Neurosurgery* **83**(2), 181–192 (2017). <https://doi.org/10.1093/neuros/nyx384>
16. Senders, J.T., Staples, P.C., Karhade, A.V., Zaki, M.M., Gormley, W.B., Broekman, M.L.D., Smith, T.R., Arnaout, O.: Machine learning and neurosurgical outcome prediction: a systematic review. *World Neurosurg.* **109**(MI), 476.e471–486.e471 (2018). <https://doi.org/10.1016/j.wneu.2017.09.149>
17. Senders, J.T., Zaki, M.M., Karhade, A.V., Chang, B., Gormley, W.B., Broekman, M.L., Smith, T.R., Arnaout, O.: An introduction and overview of machine learning in neurosurgical care. *Acta Neurochir.* **160**(1), 29–38 (2018). <https://doi.org/10.1007/s00701-017-3385-8>
18. Lu, H.-Y., Li, T.-C., Tu, Y.-K., Tsai, J.-C., Lai, H.-S., Kuo, L.-T.: Predicting long-term outcome after traumatic brain injury using repeated measurements of Glasgow Coma Scale and data mining methods. *J. Med. Syst.* **39**(2), 14 (2015). <https://doi.org/10.1007/s10916-014-0187-x>
19. Gholipour, C., Rahim, F., Fakhree, A., Ziapour, B.: Using an artificial neural networks (ANNs) model for prediction of intensive care unit (ICU) outcome and length of stay at hospital in traumatic patients. *J. Clin. Diagn. Res.* **9**(4), 19–23 (2015). <https://doi.org/10.7860/JCDR/2015/9467.5828>
20. Liu, N.T., Salinas, J.: Machine learning for predicting outcomes in trauma. *Shock* **48**(5), 504–510 (2017). <https://doi.org/10.1097/SHK.0000000000000898>. (in Eng)
21. Kamal, H., Lopez, V., Sheth, S.A.: Machine learning in acute ischemic stroke neuroimaging. *Front. Neurol.* **9**(7–12), 2018 (2018). <https://doi.org/10.3389/fneur.2018.00945>
22. Kotsiantis, S.B., Zaharakis, I.D., Pintelas, P.E.: Machine learning: a review of classification and combining techniques. *Artif. Intell. Rev.* **26**(3), 159–190 (2006). <https://doi.org/10.1007/s10462-007-9052-3>
23. Juhola, M., Laurikkala, J.: Missing values: how many can they be to preserve classification reliability? *Artif. Intell. Rev.* **40**(3), 231–245 (2013). <https://doi.org/10.1007/s10462-011-9282-2>
24. Saar-Tsechansky, M., Provost, F.: Handling missing values when applying classification models. *J. Mach. Learn. Res.* **8**, 1623–1657 (2007)

25. McGonigal, M.D., Cole, J., Schwab, C.W., Kauder, D.R., Rotondo, M.F., Angood, P.B.: A new approach to probability of survival scoring for trauma quality assurance. *J. Trauma* **34** (6), 863–868 (1993)
26. Pourahmad, S., Hafizi-Rastani, I., Khalili, H., Paydar, S.: Identifying important attributes for prognostic prediction in traumatic brain injury patients. *Methods Inf. Med.* **55**(05), 440–449 (2016). <https://doi.org/10.3414/ME15-01-0080>
27. Shafiei, E., Fakharian, E., Omidi, A., Akbari, H., Delpisheh, A., Nademi, A.: Comparison of artificial neural network and logistic regression models for prediction of psychological symptom six months after mild traumatic brain injury. *Iran. J. Psychiatry Behav. Sci.* **11**(3), e5849 (2017). <https://doi.org/10.17795/ijpbs-5849>
28. Alanazi, H.O., Abdullah, A.H., Qureshi, K.N., Ismail, A.S.: Accurate and dynamic predictive model for better prediction in medicine and healthcare. *Ir. J. Med. Sci.* **128**(2), 1–13 (2018). <https://doi.org/10.1007/s11845-017-1655-3>
29. Hale, A.T., Stonko, D.P., Lim, J., Guillaumondegui, O.D., Shannon, C.N., Patel, M.B.: Using an artificial neural network to predict traumatic brain injury. *J. Neurosurg. Pediatr.* **1**, 1–8 (2018). <https://doi.org/10.3171/2018.8.PEDS18370>
30. Rau, C.-S., Kuo, P.-J., Chien, P.-C., Huang, C.-Y., Hsieh, H.-Y., Hsieh, C.-H.: Mortality prediction in patients with isolated moderate and severe traumatic brain injury using machine learning models. *PLoS ONE* **13**(11), 1–12 (2018). <https://doi.org/10.1371/journal.pone.0207192>
31. Kabir, G., Ahsan Akhtar Hasin, M.: Comparative analysis of artificial neural networks and neuro-fuzzy models for multicriteria demand forecasting. *Int. J. Fuzzy Syst. Appl.: IJFSA* **3**, 1–24 (2013). <https://doi.org/10.4018/ijfsa.2013010101>
32. Agoston, D.V., Langford, D.: Big data in traumatic brain injury: promise and challenges. *Concussion* **2**, 45 (2017). <https://doi.org/10.2217/cnc-2016-0013>
33. Johannesen, J.K., Bi, J., Jiang, R., Kenney, J.G., Chen, C.-M.A.: Machine learning identification of EEG features predicting working memory performance in schizophrenia and healthy adults. *Neuropsychiatr. Electrophysiol.* **2**(1), 3 (2016). <https://doi.org/10.1186/s40810-016-0017-0>



# Blood Vessel Detection Monitoring System and Mobile Notification for Diabetic Retinopathy Diagnosis

Ahmad Syauqi Mahmud<sup>1</sup>(✉), Wan Azani Mustafa<sup>1</sup>,  
Mohd Aminudin Jamlos<sup>1</sup>, Syed Zulkarnain Syed Idrus<sup>2</sup>,  
Wan Khairunizam<sup>3</sup>, and Mohd Al Hafiz Mohd Nawi<sup>1</sup>

<sup>1</sup> Faculty of Engineering Technology, Kampus Sg. Chuchuh,  
Universiti Malaysia Perlis, 02100 Padang Besar, Perlis, Malaysia  
syauqi9401@gmail.com

<sup>2</sup> Center of Excellence Geopolymer and Green Technology,  
Universiti Malaysia Perlis, 01000 Kangar, Perlis, Malaysia

<sup>3</sup> School of Mechatronic Engineering, Universiti Malaysia Perlis,  
Pauh Putra Campus, 02600 Arau, Perlis, Malaysia

**Abstract.** Disease diagnosis based on retinal image analysis is very popular in order to detect a few critical diseases such as diabetic retinopathy, high blood pressure, cancer and glaucoma. The important part of the retinal is a blood vessel. Besides, the blood vessel study plays an important part in different medical areas such as ophthalmology, oncology, and neurosurgery. The significance of the vessel analysis was helped by the continuous overview in clinical studies of new medical technologies intended for improving the visualization of vessels. In this paper, a new blood vessel detection based on a combination of Kirsch's templates and Fuzzy C-Means (FCM) was proposed. The main objective of this study is to improve the detection result of FCM and achieved more effective performance compared to the Kirsch's templates result. The proposed method experimented on 20 images is utilized namely from Digital Retina Images for Vessel Extraction (DRIVE) dataset. The resulting images are compared with the benchmark images based on a few image quality assessment (IQA) such as accuracy, sensitivity and specificity. The total average of accuracy is 92.64%, while sensitivity and specificity obtained was 95.73% and 60.45% respectively. The three parameters of the IQA will then be displayed in a column on the GUI. The second part of the system is for the mobile notification system to send SMS to a mobile phone. In order for the user to obtain the image analysis results, there must be a notification system on the mobile phone. By using the GSM module integrated with Arduino Uno, notification regarding image analysis will be sent to the mobile phone.

**Keywords:** Blood vessel · Monitoring · Mobile notification · Diabetic retinopathy

## 1 Introduction

The retinal blood vessel is recognized as a crucial part in both cardiovascular disease diagnosis and ophthalmological such as diabetic retinopathy and glaucoma [1, 2]. Diabetic retinopathy is a diabetes complication that affects the eyes [3–5]. The statistic of this disease increases in community health and it's also the reason for the loss of sight. Hence, the precise recognition of retinal blood vessel is vital. Manual diagnosis is usually performed by analyzing the images from a patient, as not all images show signs of diabetic retinopathy [6].

It raises the time and tips to an incorrect diagnostic decision for ophthalmologists. Hence, automatic segmentation of the vasculature might preserve the work of the ophthalmologists and will support in portraying spotted injuries. The characteristics of retinal vasculature together with tortuosity, width, length, angles, and branching pattern can play a part in the diagnostic result. Nevertheless, even though promising, manual segmentation of retinal blood vessels is repetitive work and time consuming, and it involves specialized expertise for even though the finest vessel could contribute to the differential diagnosis list [7]. The demand for faster and automatic study of the retinal vessel images must upraise for supporting ophthalmologists with this unpredictable and monotonous work.

## 2 Literature Review

In the retinal image, the blood vessel is one vital part and it acts as milestones for registration of retinal images of the similar patient collected from dissimilar sources. Over the previous era, blood vessel studies enable to determine several eye diseases. The extraction of blood vessels and vascular intersections in retinal images may assist physicians to diagnose eye disease on behalf of patient screening and clinical study [8–11]. The presence of a blood vessel may deliver data about the pathology of diseases, including diabetes and high blood. In recent developments, many approaches to automated retinal blood vessel segmentation were suggested.

In the previous era, blood vessel studies enable to determine several eye diseases. The extraction of blood vessels and vascular intersections in retinal images may assist physicians to diagnose eye disease on behalf of clinical study and patient screening. The presence of a blood vessel may deliver data about the pathology of diseases, including diabetes and high blood. In recent developments, many methods for retinal blood vessel segmentation was proposed [12–14]. Mendonça *et al.* [15] suggested an algorithm started on the extraction of vessel centerlines, which act as a reference for the subsequent vessel filling phase. The outputs of four directional differential operators are processed in order to select connected sets of candidate points to be further classified as centerline pixels using vessel derived features. Another study by Chaudhuri *et al.* [16] suggests a 2-D matched filtering applied by which vessel is figured out from the Gaussian kernel. To load into a vessel with a different structure, the kernel, then rotated at many different angles. Next, the threshold process is made in the image from the background to differentiate the vessel's silhouette. Besides, at the final stage, the process of post-processing would be completed as this filter detection method is obtainable to use in stationary processes.

### 3 Research Methodology

The proposed system consists of three stages, in the pre-processing part, the aim is to covert the retinal color image to the grayscale image and the second stage is the feature extraction of the image. Next, the third stage is a blood vessel segmentation using Fuzzy C-Means.

#### 3.1 Combination of Kirsch's Templates and Fuzzy C-Means (FCM)

Kirsch's template is one of the discrete versions of the first order derivatives used for edge enhancement and detection. It is used for detecting the blood vessels. For detecting the edges, the operator uses eight templates, which are consecutively rotated by  $45^\circ$ . By convolving the image Kirsch's template is one of the discrete versions of the first order derivatives used for edge enhancement and detection. It is used for detecting the blood vessels. For detecting the edges, the operator uses eight templates, which are consecutively rotated by  $45^\circ$ . By convolving the image with eight template impulse response arrays in each and every pixel, the gradient is then computed. Therefore, the gradient of different directions is achieved. From the several templates, the larger one is considered for the output value and later the edges are extracted. Kirsch template can set and reset the threshold values to obtain the most suitable edge of the images. Kirsch template works well for images having a clear distinction between the foreground and background [17, 18].

Fuzzy C-Means (FCM) is widely used in pattern recognition as a clustering method. FCM based segmentation is a fuzzy pixel classification. FCM allows data points or pixels to belong to multiple classes with varying degree of membership function between 0 to 1. FCM possesses the precious advantage of grading linguistic variables to fit for appropriate analysis in the discrete domain on a pro-rata basis. FCM computes cluster centers by minimizing the dissimilarity function using an iterative approach. By updating the cluster centers and the membership grades for each unique pixel, FCM shifts the cluster centers to the "true" location within a set of pixels [19–21]. To accommodate the introduction of fuzzy partitioning, the membership matrix  $(U) = [u_{ij}]$  is randomly initialized according to Eq. 1, where  $u_{ij}$  being the degree of membership function of the data point of  $i^{th}$  cluster  $x_i$ .

$$\sum_{i=1}^c u_{ij} = 1, \quad \forall j = 1, \dots, n \quad (1)$$

The performance index for membership matrix  $U$  and  $c_i$ 's used in FCM is given by Eq. 2.

$$J(U, c_1, c_2, \dots, c_c) = \sum_{i=1}^c J_i = \sum_{i=1}^c \sum_{j=1}^n u_{ij}^m d_{ij}^2 \quad (2)$$

$u_{ij}$  is between 0 and 1.  $c_i$  is the center of cluster  $i$ .  $d_{ij}$  is the Euclidian distance between  $i^{th}$  center ( $c_i$ ) and  $j^{th}$  data point.  $m \in [1, \infty]$  is a weighting exponent. To reach a minimum of dissimilarity function there are two conditions. These are given in Eqs. 3 and 4.

$$ci = \frac{\sum_{j=1}^n u_{ij}^m x_j}{\sum_{j=1}^n u_{ij}^m} \tag{3}$$

$$u_{ij} = \frac{1}{\sum_{k=1}^c \left(\frac{d_{ij}}{d_{kj}}\right)^{2/(m-1)}} \tag{4}$$

### 3.2 Mobile Notification System

The Graphical User interface (GUI) is built to link together with the hardware-based that contain Arduino board and Global System for Mobile communication (GSM). GSM uses a variation of time division multiple access (TDMA) and is the most widely used of the three digital wireless telephony technologies: TDMA, GSM and code-division multiple access (CDMA). GSM digitizes and compresses data, then sends it down a channel with two other streams of user data, each in its own time slot. It operates at either the 900 MHz or 1,800 MHz frequency band. With this product, it can

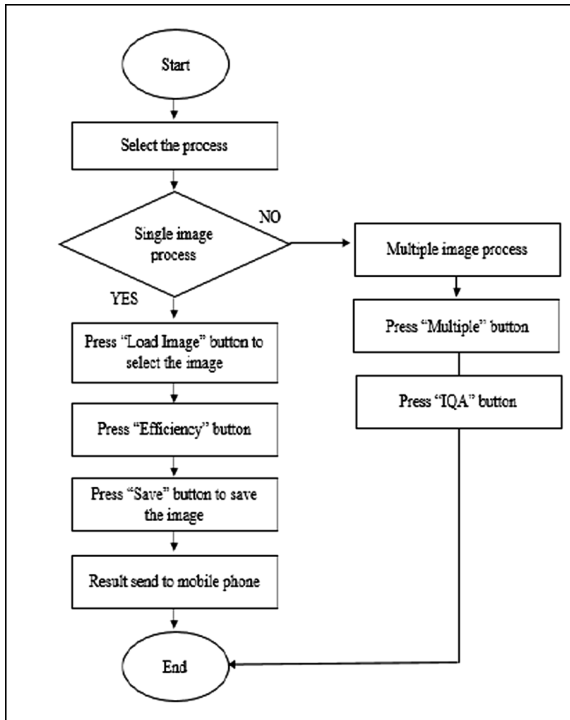


Fig. 1. The flowchart of GUI workflow

make communication between systems in the laptop with any target cell phone. The type of Arduino used is Arduino Uno while SIM900A is the name of the GSM that is used for this project.

First of all, a flowchart of GUI workflow is shown in Fig. 1 to conduct the segmentation process. There will be three buttons for single image segmentation with evaluation of image and two buttons for multiple images together with the evaluation of images. After the result come out, the Arduino will receive the result and activate the GSM signal to send the data towards the designated mobile phone and firstly notify the doctor about the result. The design of GUI development is shown in Fig. 2.

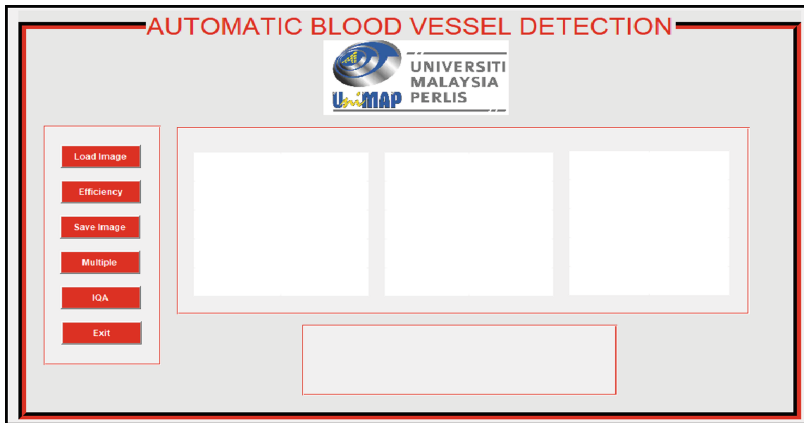


Fig. 2. Mobile notification system GUI design

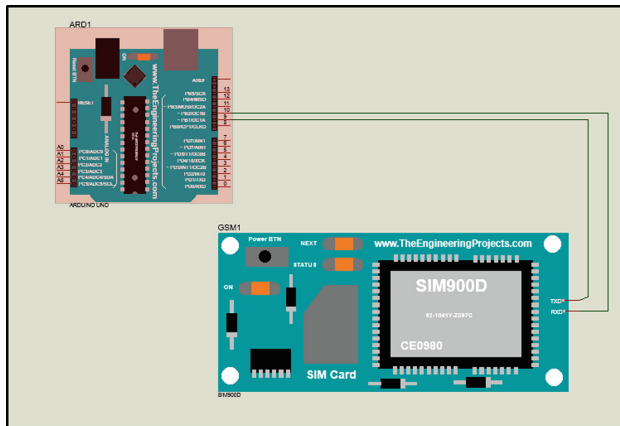


Fig. 3. Arduino Uno and GSM SIM900A module circuit connection

GSM module can be used to either sending or receiving both calls and SMS. The GSM module used in this paper is SIM900A, it is connected to the Arduino Uno board to enable the text message sending the process to the mobile phone. The SMS send contained efficiency results. Figure 3 illustrated the connection between the GSM and the Arduino Uno board. The completed GUI application is shown in Fig. 4.

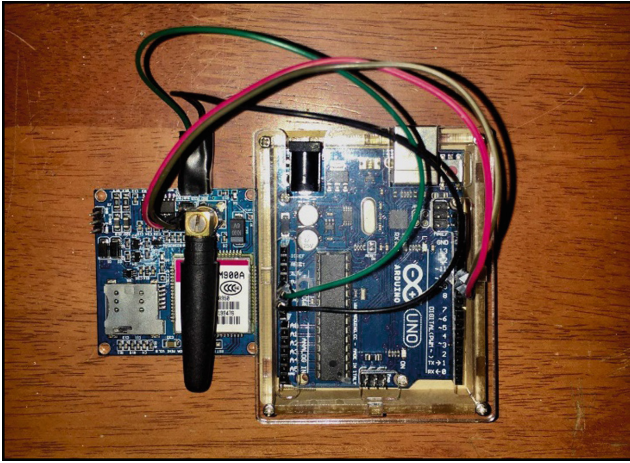


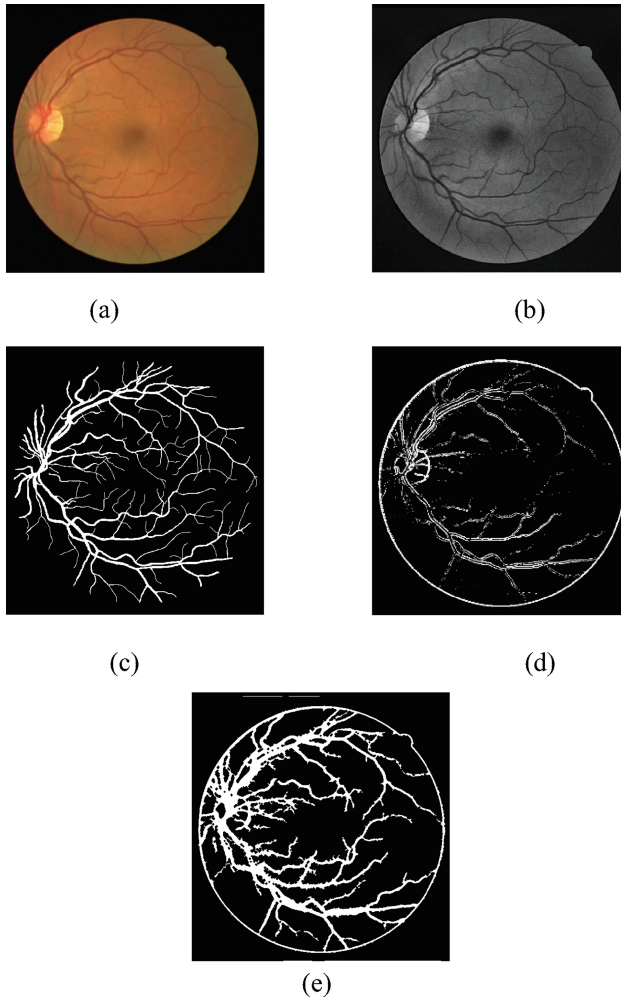
Fig. 4. Arduino Uno GSM and SIM900A module hardware

## 4 Results and Discussion

In this research, the programs were run in MATLAB R2017b from an HP laptop with Intel® Core™ i7-4500 CPU @2.40 GHz and 8.00 GB RAM. The method experimented with the 20 retinal images from DRIVE online database and can be download at <https://www.isi.uu.nl/Research/Databases/DRIVE/>. A DRIVE image is an established database and specific for blood vessel detection. The size image of each is  $565 \times 584$  pixels with 24-bit depth and 96 dpi. The original image is shown in Fig. 5(a). Different channels namely red, green and blue will be extracted. The vessels are visible in the red channel. In the pre-processing stage, the input image is resized and the green channel image is separate because the blood vessel appears brighter in the green channel image will be employed as shown in Fig. 5(b). In this paper, a comparison between ground truths vessel extractions from DRIVE Database as a benchmark is compared with the Kirsch Template method and is shown in Fig. 5(c) and (d). Then, a comparison is made between ground truths with our proposed method as shown in Fig. 5(e). Table 1 shows the result in term of accuracy, sensitivity and specificity between the two methods and the benchmark images.

In order to demonstrate the effectiveness, three parameters are used namely the accuracy, sensitivity and specificity. The equation for accuracy, sensitivity and specificity can refer to [22, 23]. Accuracy reflects the number of pixels that are correctly classified as vessel or non-vessel. Sensitivity (true positive rate) and specificity





**Fig. 5.** Resulting of the retinal image; (a) original image, (b) image after applying pre-processing, (c) ground truth image, (d) image after applying the Kirsch's technique and (e) image after applying the proposed method

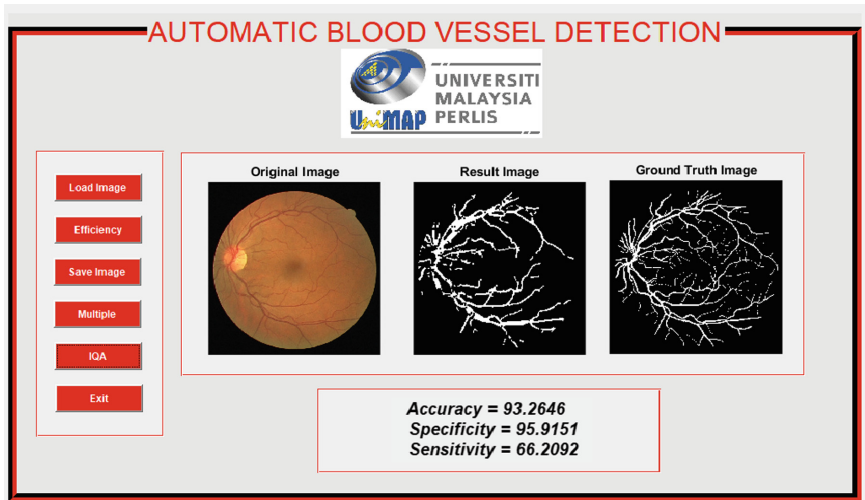
(true negative rate) are statistical measures of the performance of a binary classification test, where sensitivity reflects the ability of the algorithm to detect the vessel pixels while specificity is the ability to detect non-vessel pixels (or the ability to avoid noise pixels) [24]. In this work, the proposed method is compared with Kirsch Templates method in term of accuracy, sensitivity and specificity. Based on the result, a proposed method obtained slightly higher in term of accuracy which is 92.64% compare than 90.59%. The specificity result also shown improvement from 24.53% to 60.45%. Lastly, performance based on sensitivity gives the highest result which is 97.73% compare than 96.93%.

**Table 1.** Comparison between Kirsch Templates method and the proposed method based on ground truth

Image	Ground truth vs Kirsch templates			Ground truth vs proposed method		
	Accuracy %	Sensitivity %	Specificity %	Accuracy %	Sensitivity %	Specificity %
1	90.25	96.35	28.04	92.08	94.25	69.96
2	90.13	96.83	31.41	93.02	94.52	79.87
3	89.36	97.59	14.91	91.69	96.80	45.49
4	90.92	96.66	34.26	93.48	96.33	65.44
5	90.28	97.52	20.25	93.23	96.80	58.64
6	89.68	97.31	18.84	92.29	96.81	50.33
7	90.97	97.11	29.96	92.74	95.76	62.63
8	90.21	96.97	18.41	92.32	96.79	44.80
9	90.77	97.33	16.35	93.00	96.83	49.59
10	91.10	97.34	21.62	93.28	96.46	57.88
11	91.27	96.53	37.76	92.17	93.92	74.33
12	90.53	96.99	22.13	92.32	95.61	57.48
13	90.07	96.97	26.35	92.60	96.14	59.95
14	91.15	96.85	26.37	93.06	95.28	67.90
15	92.69	97.08	35.82	93.76	95.37	72.98
16	90.49	96.56	29.36	92.23	95.95	64.85
17	90.09	96.48	20.93	92.06	95.75	52.10
18	90.10	96.33	17.68	91.65	94.61	57.28
19	90.75	96.77	24.19	92.96	96.37	66.37
20	91.04	97.00	15.89	92.92	96.24	51.07
Avg.	90.59%	96.93%	24.53%	92.64%	97.73%	60.45%

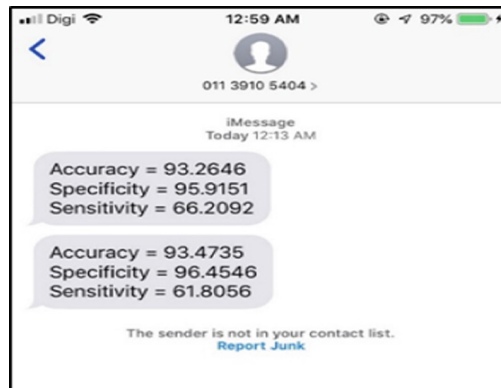
The GUI is created so that the system for blood vessel detection is easier for the user especially the doctor to conduct the segmentation process. Figure 6, 'Load Image' button function is to upload a retinal image into the system and then it will automatically proceed with the segmentation process and then the final image will be shown. Next, the evaluation of image will present when the 'Efficiency' button is pressed and the data will be shown below the image. The doctor can also save the result of the segmentation image with 'Save Image' button. In addition, there is also the 'Multiple' button for segmentation of multiple images and it will be saved automatically in a specific folder. Lastly, for the 'IQA' button the purpose is to evaluate the efficiency of the multiple images. After the button is pressed, it will take the multiple images and compared it with the reference image which is stored in another specific folder. After the evaluation is done the data will be automatically stored in the Excel file.

The SMS mobile notification is used for the IQA results delivery medium, as it is more convenient and simple. To receive an SMS, one does not need to have internet connections, as SMS only requires the doctor to have one SIM card for them to receive and send an SMS.



**Fig. 6.** Completed GUI application

After the “Efficiency” button on GUI is clicked, a mobile notification in form of SMS will be sent to the dedicated phone number. The SMS received such as shown in Fig. 7 consists of three different efficiency parameters which are Accuracy, Specificity, and Sensitivity. From the SMS, the receiver can compare the effectiveness of the proposed method applied to their document image.



**Fig. 7.** Efficiency analysis results via SMS

## 5 Conclusion

Segmentation algorithms form the core of medical image applications such as radiological diagnostic systems, multimodal image registration, creating anatomical atlases, visualization, and computer-aided surgery. It is still an open area for more exploration, though many capable methods and algorithms have been established. In this paper, new approaches based on a combination of Kirsch Templates and FCM were proposed. The aim is to improve the detection technique of Kirsch Templates. Based on the result, the proposed method successful to overcome the Kirsch Templates performance shown by Accuracy = 92.64%, Sensitivity = 97.73% and Specificity = 60.45. Although our proposed method can detect blood vessel effectively but still fail to detect small vessels. The future way of segmentation research will be to develop quicker and more accurate more automated methods. Then, GUI is integrated with GSM SIM900A module and Arduino Uno to send a mobile notification to the doctor mobile phone. Thus, the doctor can review the segmentation method efficiency.

## References

1. Adalarasan, R., Malathi, R.: Automatic detection of blood vessels in digital retinal images using soft computing technique. *Mater. Today Proc.* **5**, 1950–1959 (2018). <https://doi.org/10.1016/j.matpr.2017.11.298>
2. Mustafa, W.A., Yazid, H., Yaacob, S.: A review : comparison between different type of filtering methods on the contrast variation retinal images. In: *IEEE International Conference on Control System, Computing and Engineering*, pp. 542–546 (2014)
3. Gardner, T.W.: Diabetic retinopathy: a position statement by the American Diabetes Association. *Diab. Care* **40**, 412–418 (2017). <https://doi.org/10.2337/dc16-2641>
4. Antonetti, D.A., Klein, R., Gardner, T.W.: Diabetic retinopathy. *N. Engl. J. Med.* **366**, 1227–1239 (2012). <https://doi.org/10.1056/NEJMra1005073>
5. Mustafa, W.A., Abdul-nasir, A.S., Yazid, H.: Diabetic retinopathy (DR) on retinal image: a pilot study. *J. Phys. Conf. Ser. Pap.* **1019**, 1–6 (2018). <https://doi.org/10.1088/1742-6596/1019/1/012021>
6. Rodrigues, L.C., Marengoni, M.: Segmentation of optic disc and blood vessels in retinal images using wavelets, mathematical morphology and Hessian-based multi-scale filtering. *Biomed. Signal Process. Control* **36**, 39–49 (2017). <https://doi.org/10.1016/j.bspc.2017.03.014>
7. Singh, D., Singh, D., Singh, B.: A new morphology based approach for blood vessel segmentation in retinal images. In: *11th IEEE India Conference: Emerging Trends and Innovation in Technology, INDICON 2014* (2015). <https://doi.org/10.1109/INDICON.2014.7030686>
8. Xu, L., Luo, S.: A novel method for blood vessel detection from retinal images. *Biomed. Eng. Online* **9**, 14 (2010)
9. Mustafa, W.A., Kader, M.M.M.A.: Automatic blood vessel detection on retinal image using hybrid combination techniques. *Malays. Appl. Biol.* **47**, 47–52 (2018)
10. Mustafa, W.A., Yazid, H., Kamaruddin, W.: Combination of gray-level and moment invariant for automatic blood vessel detection on retinal image. *J. Biomimetics Biomater. Biomed. Eng.* **34**, 10–19 (2017). <https://doi.org/10.4028/www.scientific.net/JBBBE.34.10>

11. Mustafa, W.A., Yazid, H., Yaacob, S., Basah, S.: Blood vessel extraction using morphological operation for diabetic retinopathy. In: IEEE Region 10 Symposium, pp. 208–212 (2014). <https://doi.org/10.1109/TENCONSpring.2014.6863027>
12. Elbalaoui, A., Fakir, M., Taifi, K., Merbouha, A.: Automatic detection of blood vessel in retinal images. In: Proceedings - Computer Graphics, Imaging Visualization New Technology Trends, CGiV 2016, pp. 324–332 (2016). <https://doi.org/10.1109/CGiV.2016.69>
13. Yavuz, Z., Kose, C.: Blood vessel segmentation from retinal images based on enhancement methods. In: 2014 22nd Signal Processing and Communications Applications Conference, SIU 2014 - Proceedings (2014)
14. Roychowdhury, S., Koozekanani, D.D., Parhi, K.K.: Blood vessel segmentation of fundus images by major vessel extraction and subimage classification. *IEEE J. Biomed. Health Inform.* **19**, 1118–1128 (2015). <https://doi.org/10.1109/JBHI.2014.2335617>
15. Mendonça, A.M., Campilho, A.: Segmentation of retinal blood vessels by combining the detection of centerlines and morphological reconstruction. *IEEE Trans. Med. Imaging* **25**, 1200–1213 (2006). <https://doi.org/10.1109/TMI.2006.879955>
16. Chaudhuri, S., Chatterjee, S., Katz, N., et al.: Detection of blood vessels in retinal images using two-dimensional matched filters. *IEEE Trans. Med. Imaging* **8**, 263–269 (1989)
17. Bhadauria, H.S.: Vessels extraction from retinal images. *IOSR J. Electron. Commun. Eng.* **6**, 79–82 (2013)
18. Sivakamasundari, J., Kavitha, G., Natarajan, V., Ramakrishnan, S.: Proposal of a content based retinal image retrieval system using Kirsch template based edge detection. In: 2014 International Conference on Informatics, Electronics and Vision, ICIEV 2014 (2014)
19. Akhavan, R., Faez, K.: A novel retinal blood vessel segmentation algorithm using fuzzy segmentation. *Int. J. Electr. Comput. Eng.* **4**, 561–572 (2014)
20. Mustafa, W.A., Aziz, H., Khairunizam, W., et al.: Review of different binarization approaches on degraded document images. In: IEEE International Conference on Computational Approach in Smart Systems Design and Applications (ICASSDA), pp 1–8. IEEE (2018)
21. Mustafa, W.A., Jamaluddin, I., Khairunizam, W., et al.: Comparison of detection method on malaria cell images. In: IEEE International Conference on Computational Approach in Smart Systems Design and Applications (ICASSDA), pp 1–6. IEEE (2018)
22. Mustafa, W.A., Abdul-Nasir, A.S., Mohamed, Z.: Malaria parasites segmentation based on Sauvola algorithm modification. *Malays. Appl. Biol.* **47**, 71–76 (2018)
23. Mustafa, W.A., Abdul-nasir, A.S., Mohamed, Z., Yazid, H.: Segmentation based on morphological approach for enhanced malaria parasites detection. *J. Telecommun. Electron. Comput. Eng. Segm.* **10**, 15–20 (2018)
24. Fan, Z., Lu, J., Li, W., et al.: A hierarchical image matting model for blood vessel segmentation in fundus images. *Comput. Vis. Pattern Recognit.* 1–10 (2017). <https://arxiv.org/abs/1701.00892>



# Reduction of Salt-and-Pepper Noise from Digital Grayscale Image by Using Recursive Switching Adaptive Median Filter

Aina Qistina Md. Taha and Haidi Ibrahim<sup>(✉)</sup>

School of Electrical and Electronic Engineering, Engineering Campus,  
Universiti Sains Malaysia,  
14300 Nibong Tebal, Seberang Perai, Pulau Pinang, Malaysia  
haidi\_ibrahim@ieee.org

**Abstract.** Digital images may suffer from impulse noise, including salt-and-pepper noise. One of the common methods to deal with this noise is by using median filter, which is a type of non-linear filter. Standard median filter includes noisy pixels in calculating the median value for the restoration process. However, this will lead to an inaccurate result, where the noisy pixel values may be selected for the restoration. Another approach is by using recursive median filter, where the calculation for the median value is also based on the previous outputs. Therefore, in this paper, we investigate the feasibility of improving the performance of recursive median filter, by adapting it to switching and adaptive approaches. This scheme is called as Recursive Switching Adaptive Median Filter. As the switching median filter is used, the method is divided into two stages, which are noise detection and noise restoration stages. In the noise detection stage, salt-and-pepper pixel candidates are identified. Then, in the restoration stage, an adaptive method is used for the restoration. The size of the filter is expanding until there are at least eight noise-free pixel candidates defined by the window. As the recursive method is used, the noise mask is updated every time the restoration is done. The experimental results show that this scheme has good performance in terms of mean square error and structural similarity index measure, as compared to six other median filtering approaches. However, the scheme does not perform well at high level of corruption, especially when the level of corruption is more than 80%.

**Keywords:** Image processing · Noise reduction · Impulse noise · Salt-and-pepper noise · Recursive filter · Adaptive filter · Switching filter

## 1 Introduction

Digital image has been long used since 1957 in various fields of technology, such as satellite television, computer-tomography and magnetic resonance imaging as well as areas of research and technology of geographical information systems and in astronomy. However, digital image may suffer from noise, which can significantly deteriorate the quality of the image. With poor image quality, the information from the image may

be translated wrongly by the human, or by the subsequence process. Impulse noise is one of the noises that normally degraded the image, due to its high contrast [1].

There are many types of impulse noise, and one of them is the salt-and-pepper noise [1]. Salt-and-pepper noise is also called as the fixed valued impulse noise. In this noise model, the corrupted pixels are randomly distributed to two intensity levels (i.e., intensity levels of 0 or 255, for an eight-bit-per-pixel grayscale image). The noise intensities with maximum value of 255 appears as a white dot on the image (i.e. salt-like), where the noise of minimum value of 0 appears as a black dot (i.e. pepper) [2–4]. The “noisy” pixels are highly contrasted towards the neighboring pixels, which shows that even if the impulse noise level is low, it will also dramatically change the appearance of the digital image [5, 6]. Hence, a noise reduction technique is needed to eliminate noisy pixels and improve the quality of the digital image.

Usually, for impulse noise infested digital images, median filtering framework is popularly used. Median filter has a fairly well performance history in nonlinear processing. The earliest median filter was first introduced by Tukey [7], which is the Standard Median Filter (SMF). Basically, median filter or SMF replaces the center value of a filtering window with the median value of all the pixels values within the filtering window. The filtering window slides through the pixels of the digital image [4, 5]. However, the drawbacks of SMF is that it processes all of the image’s pixels and so the filter does not differentiate between the “noisy” pixels and “noise-free” pixels. Therefore, SMF removes fine details of the input image causing blurring, excessive smoothing and affecting the texture of the image [4, 5]. This also occurs at low noise level image [4, 5]. Due to these drawbacks, many researchers have proposed various improvements to SMF.

Weighted median filter assigns weights to each of its filter elements, representing the repetition of sample for the calculation of the median value. Center weighted median filter (CWMF) [8] is a special weighted median filter, where only the center kernel of the filter has a weight greater than 1. By doing so, the probability of selecting the center value as the restorative value is higher as compared with other pixels. This is useful especially when the center pixel is surrounded by many noisy pixels.

One of the branches for the improvement of median filter is based on switching approach. Switching median filter (SWMF), also known as decision based median filter has two stages in its overall process [9–11]. The two stages are the noise detection stage and the noise removal stage. In the noise detection stage is to differentiate between corrupted and non-corrupted pixels. These corrupted pixels are then moved to the noise removal stage where the corrupted pixels are then filtered whilst the non-corrupted pixel are left unchanged. In the survey done by George et al. [12], it is stated that SWMF is effective and successfully eliminates highly noised dense images (i.e. 5% to 70%) while preserving the details of the image. SWMF is also used to speed up the process of filtering corrupted image. But SWMF alone still cannot recover a highly corrupted image of more than 70% noise density.

Other improvement of the SMF is the implementation of Adaptive Median Filter (AMF). The advantage of it compared to SMF is its computational efficiency [11, 12]. AMF performs much better in retaining “noise-free” pixels by changing the size of the window depending on the noise density level in the window. However, AMF only performs well at low noise densities. At high noise densities the increasing window

sizes causes blurring to the de-noised image [10, 12, 13]. Therefore, some of AMF methods such as Dual Window Selective Median Filter (DWSMF) [14] and Extended Median Filter (EMF) [15] only consider filtering windows  $3 \times 3$  pixels and  $5 \times 5$  pixels in their algorithms.

Many of previous researchers proposed to combine both SWMF and AMF to overcome the drawbacks of both methods. One of them is the Simple Adaptive Median Filter (SAMF) [11]. This method consists of two main processing blocks, where the first block identifies the “noisy” pixels and “noise-free” pixel candidates. The second block filter the remaining “noisy” pixels from the first processing block. It will expand the local window to get at least eight “noise-free” pixels within the local filtering window.

Another approach is by using recursive median filter [16] and its variations, such as Enhanced Recursive Median Filter (ERMF) [17]. In this approach, the restoration value is obtained not only from the input, but also from the previously obtained output. In this approach, for every calculated new restoration value, this value is updated in both output and input image. This approach considers that the restored pixel is already a clean pixel, and thus can be included for the calculation of the median value. However, recursive median filter tends to propagate the wrongly calculated value in the image.

This paper is aimed to propose a recursive based method, by applying recursive approach to SAMF [10]. Therefore, three approaches will be combined in this method, which are recursive, switching, and adaptive filtering. The organization of this paper is as follows. Our methodology will be given in Sect. 2. Section 3 will present our experimental results and discussions. Section 4 will conclude our finding.

## 2 Methodology

As the proposed method, Recursive Adaptive Switching Median Filter (RASMF) is from switching filtering framework, the method has two stages. The first stage is the noise detection stage, whereas the second stage is the noise cancellation stage. These stages will be described in the following subsections.

### 2.1 Noise Detection Stage

Following the noise detection scheme of simple adaptive based filters [4, 5, 10], given an input image  $\mathbf{f}$ , this stage will produce mask  $\alpha$  to indicate the noisy pixel candidates. Noisy pixel candidate is assigned value 1. On the other hand, noise free pixel candidate is assigned value 0. The following formula is used in this noise detection stage:

$$\alpha(x, y) = \begin{cases} 1 & : f(x, y) = L - 1 \\ 1 & : f(x, y) = 0 \\ 0 & : \text{otherwise} \end{cases} \quad (1)$$

where  $(x, y)$  are the spatial coordinates, in horizontal and vertical, respectively, and  $L$  is the grayscale level of the image. For an eight-bit-per-pixel grayscale image,  $L$  is equal to 256. Using this noise detection scheme, all pixels, whether at maximum or minimum values, are considered as noise pixel candidate.



## 2.2 Noise Cancellation Stage

Similar to SAMF [10], RASMF only process noisy pixel candidates in this stage, which are pixels with  $\alpha(x, y)$  equal to 1. For noise-free candidates (i.e., pixels with  $\alpha(x, y) = 0$ ), the output pixel  $g(x, y)$  copies the value from the input pixel  $f(x, y)$  directly (i.e.,  $g(x, y) = f(x, y)$ ). On the other hand, for the noisy pixel candidates, the filter is made adaptive towards local noise content by counting the number of noise-free candidates.

Starting by using a window of size  $3 \times 3$  pixels, the window size is expanding until the number of noise-free candidates is equal or more than eight pixels. This can be found by  $\beta$ , which is defined as:

$$\beta = \sum_{i=x-r}^{x+r} \sum_{j=y-r}^{y+r} (1 - \alpha(i, j)) \quad (2)$$

where  $r$  is the radius of the filter, which is defined as:

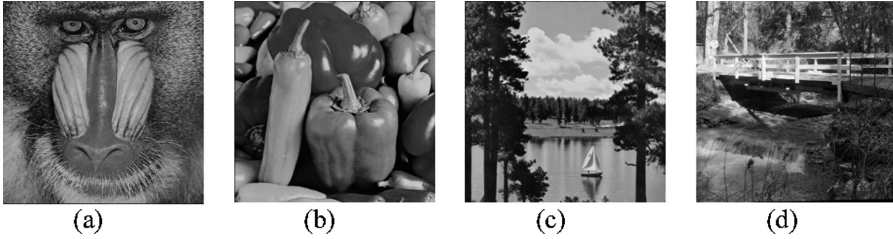
$$r = \text{floor}(w/2) \quad (3)$$

for a window of size  $w \times w$  pixels. Function  $\text{floor}()$  gives the floor value of the number, for example  $\text{floor}(2.9975)$  is equal to 2. The window will stop expanding when the value of  $\beta$  is equal or more than eight. When this condition is reached, then the corresponding output value  $\mathbf{g}$  is defined as the median value of the noise-free candidates (i.e., based on pixels  $f(x, y)$  with  $\alpha(x, y) = 0$ ).

However, as this is a recursive filter, after the value of the output pixel  $g(x, y)$  is obtained, two updates need to be carried out. First, the corresponding input is updated to be the same as the output (i.e.,  $f(x, y) = g(x, y)$ ). Second, as this pixel is now can be taken for the median calculation after the window moved to the next location, the corresponding noise mask need to be updated as a noise-free pixel (i.e., update  $\alpha(x, y) = 1$  to become  $\alpha(x, y) = 0$ ). The window is then reset to size  $3 \times 3$  pixels, and the process repeated for noisy pixel candidates. The window slides from left to right, top to bottom.

## 3 Experimental Results and Discussions

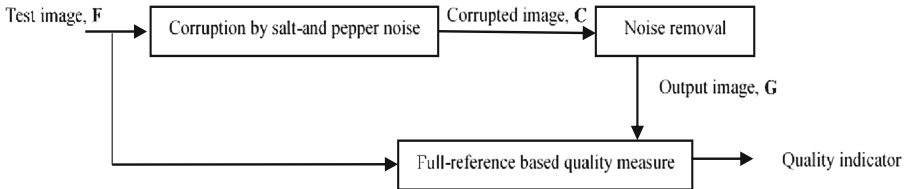
We have used four standard images, obtained from <http://sipi.usc.edu/database/database.php> as our test images  $\mathbf{F}$  in this experiment. These images are *Baboon*, *Peppers*, *SailboatOnLake* and *StreamAndBridge*. These images are shown in Fig. 1. All images have the same spatial resolutions, which is  $512 \times 512$  pixels (i.e., around 0.3 Mpixels). As our research only deals with grayscale digital image, *Baboon* and *Peppers* have been converted from 24-bit-per-pixel colour images into 8-bit-per-pixel grayscale images.



**Fig. 1.** Test images (a) Baboon (b) Peppers (c) SailboatOnLake (d) StreamAndBridge.

Image *Baboon* and *StreamAndBrige* are selected as they contain significantly large areas of small details. For example, the fur on the *Baboon*, and bushes and water stream on *StreamAndBridge*. *Peppers* and *SailboatOnLake* are selected as they have relatively large areas with almost the same intensity levels. Examples of this area are the bell peppers' surface on *Peppers*, and sky and water areas on *SailboatOnLake*.

The experimental setup used in this work is shown in Fig. 2. As shown by this figure, the image is corrupted by salt-and-pepper noise, to create the corrupted image *C*. Corruption level of  $n\%$  means that  $n\%$  from the image area is corrupted by salt-and-pepper noise. The noisy pixels are located randomly on the image.



**Fig. 2.** Experimental setup

In this work, we consider an equal number of salt noise pixels (i.e., noise with intensity level 255) and pepper noise pixels (i.e., noise with intensity level 0), which is  $0.5n\%$  for salt noise, and  $0.5n\%$  for pepper noise. For example, at 20% noise corruption level, for an image with dimensions  $512 \times 512$  pixels (i.e., 262,144 pixels), 52,428 pixels are noisy pixels, with 26,214 pixels are salt noise and 26,214 pixels are pepper noise. These noisy pixels are located randomly on the test image.

The corrupted images are then filtered by noise reduction algorithms to get the output image *G*. In addition to our proposed method that is RASMF, we also implemented six other median based methods for the evaluation purpose. These methods are the Standard Median Filter (SMF) of size  $3 \times 3$  pixels [7], Recursive Median Filter (RMF) of size  $3 \times 3$  pixels [16], Center Weighted Median Filter (CWMF) [8], Enhanced Recursive Median Filter (ERMF) [17], Dual Window Selective Median Filter (DWSMF) [14], and Extended Median Filter (EMF) [15]. RMF and ERMF are recursive based median filtering method. CWMF is based on weighted median filter. DWSMF and EMF are based on adaptive median filter.

To measure the performance of the methods, two full-reference based image quality measures are used. These measures are the mean square error (MSE) and structural similarity index measure (SSIM). MSE is given as [11]:

$$\text{MSE} = \frac{\sum_{y=1}^M \sum_{x=1}^N |G(y, x) - F(x, y)|^2}{M \times N} \quad (4)$$

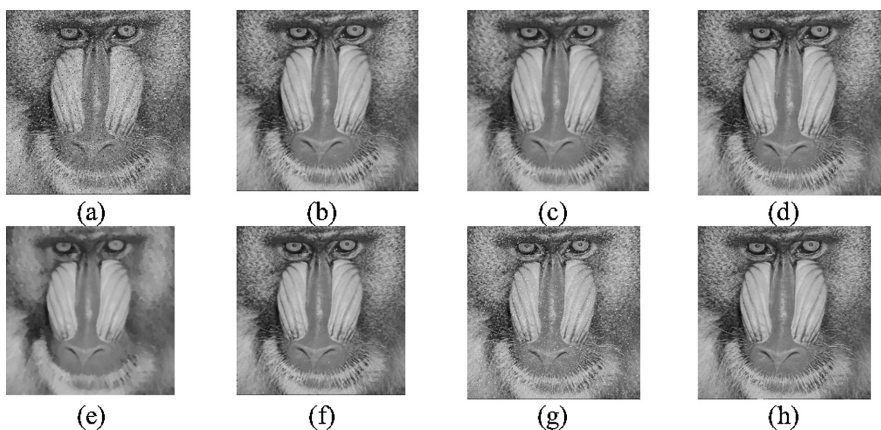
where  $G(y, x)$  and  $F(x, y)$  are the intensity levels at coordinates  $(y, x)$  from the output image  $\mathbf{G}$  and test image  $\mathbf{F}$  respectively. In this equation,  $M$  and  $N$  are the dimensions of the image, which is in this work, both  $M$  and  $N$  are equal to 512. A good noise reduction method will produce lower value of MSE.

The second measure is SSIM. This measure is defined as [18]:

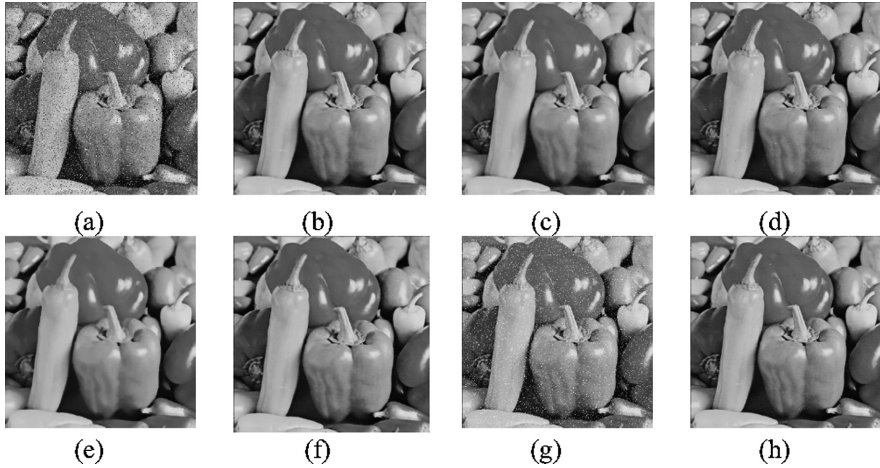
$$\text{SSIM} = \frac{(2\mu_F\mu_G + c_1) + (2\sigma_{FG} + c_2)}{(\mu_F^2 + \mu_G^2 + c_1) + (\sigma_F^2 + \sigma_G^2 + c_2)} \quad (5)$$

where  $c_1$  is equal to  $(0.01 \times 255)^2$  and  $c_2$  is  $(0.03 \times 255)^2$ . In this equation,  $\mu_F$ ,  $\mu_G$ ,  $\sigma_F$ ,  $\sigma_G$ , and  $\sigma_{FG}$  are the average intensity values, standard deviation values and cross-covariance values for image  $\mathbf{F}$  and image  $\mathbf{G}$ , respectively. A good method will produce a higher value of SSIM.

Figure 3(a) shows *Baboon* image been corrupted by 10% of salt-and-pepper noise. As shown by Fig. 3, most of the methods successfully eliminate salt-and-pepper noise from Baboon image at this noise level. SMF able to remove this noise as shown by Fig. 3(b). RMF, as shown in Fig. 3(c), also able to remove the noise, but the image looks smeared, especially at the fur regions and whiskers. Results from CWMF, DWSMF, and RASMF, as shown in Fig. 3(d), (f) and (h), respectively, are having almost the same quality with SMF. Some salt-and-pepper noise are still observable in



**Fig. 3.** (a) *Baboon* corrupted by 10% of salt-and-pepper noise. (b) Output from SMF [7]. (c) Output from RMF [16]. (d) Output from CWMF [8]. (e) Output from ERMF [17]. (f) Output from DWSMF [14]. (g) Output from EMF [15]. (h) Output from RASMF (the proposed method)



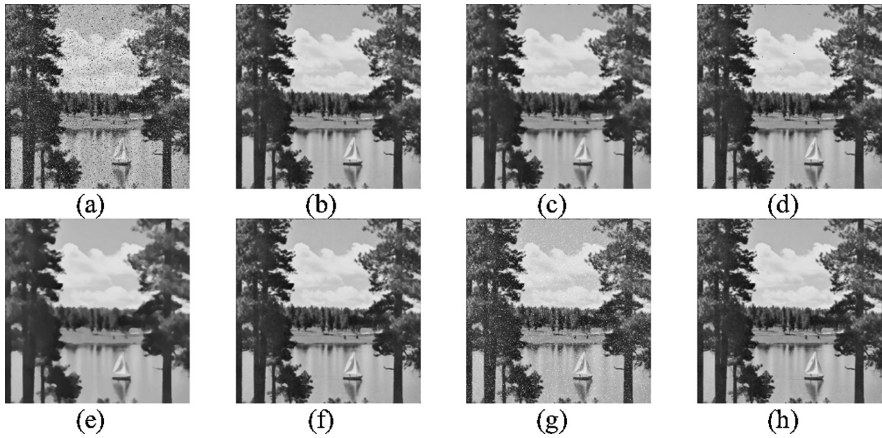
**Fig. 4.** (a) *Peppers* corrupted by 10% of salt-and-pepper noise. (b) Output from SMF [7]. (c) Output from RMF [16]. (d) Output from CWMF [8]. (e) Output from ERMF [17]. (f) Output from DWSMF [14]. (g) Output from EMF [15]. (h) Output from RASMF (the proposed method)

the output from EMF, as shown in Fig. 3(g). Result from ERMF, as shown in Fig. 3(e), although successfully remove the noise, the method tends to remove small details, including edges. In this figure, fine details of the fur are lost.

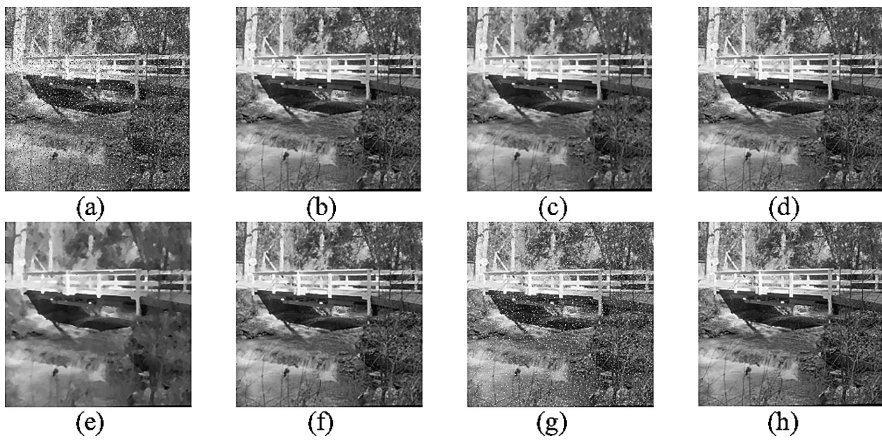
Figure 4 shows the outputs from the methods, when the input is *Peppers* with 10% salt-and-pepper noise. From this figure, we can see that all methods tested, except EMF, successfully remove the salt-and-pepper noise. In Fig. 4(g), some salt-and-pepper noise are still noticeable. The outputs from SMF, CWMF, DWSMF, and RASMF, as shown in Fig. 4(b), (d), (f) and (h), respectively, are almost identical with the input image, shown in Fig. 1(b). However, unlike the case of *Baboon* in Fig. 3, it is difficult to see the smear artefact in the output by RMF, as shown in Fig. 4(c). Result from ERMF, as shown in Fig. 4(e), shows that this method removes fine details, and smoothen the edges. However, as the *Peppers* image does not have much fine details, the effect is not as severe as compared to corresponding *Baboon* image, shown in Fig. 3(e).

Figure 5 presents the restored images when the input is *SailboatOnLake* that has been corrupted with 10% salt-and-pepper noise. In this figure, we can see that EMF was unsuccessful to remove salt-and-pepper noise, as in Fig. 5(g). White dots are still visible in this figure. SMF, RMF, CWMF, DWSMF, and RASMF methods, as shown in Fig. 5(b), (c), (d), (f) and (h), respectively, able to produce similar image to the original. Results from ERMF, as shown in Fig. 5(e) is smoother as compared to other results as this method removes fine details.

Figure 6 shows the results when the input is *StreamAndBridge*, with 10% salt-and-pepper noise. This figure shows that SMF, CWMF, DWSMF and RASMF, as shown in Fig. 6(b), (d), (f), and (h), can produce outputs similar to its original image shown in Fig. 1(d). Result from RMF method as shown by Fig. 6(c), has been smoothen by the method. Results from ERMF, as shown in Fig. 6(e) has been smeared by the method.



**Fig. 5.** (a) *SailboatOnLake* corrupted by 10% of salt-and-pepper noise. (b) Output from SMF [7]. (c) Output from RMF [16]. (d) Output from CWMF [8]. (e) Output from ERMF [17]. (f) Output from DWSMF [14]. (g) Output from EMF [15]. (h) Output from RASMF (the proposed method)

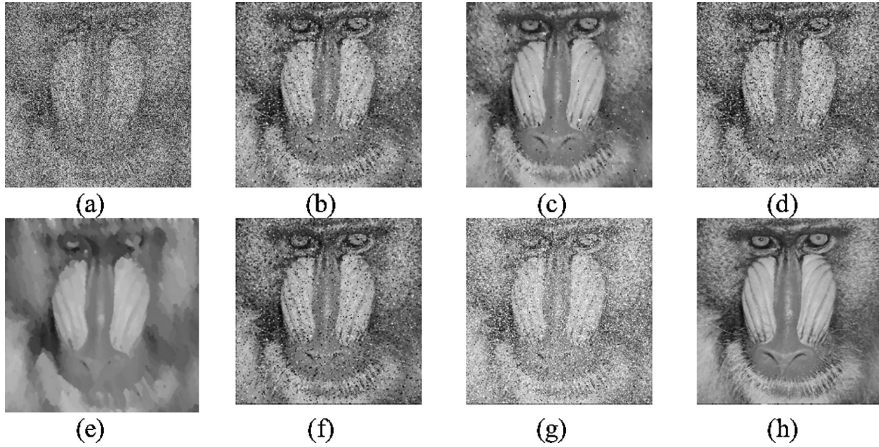


**Fig. 6.** (a) *StreamAndBridge* corrupted by 10% of salt-and-pepper noise. (b) Output from SMF [7]. (c) Output from RMF [16]. (d) Output from CWMF [8]. (e) Output from ERMF [17]. (f) Output from DWSMF [14]. (g) Output from EMF [15]. (h) Output from RASMF (the proposed method)

Figures 3, 4, 5 and 6 show the performance of the methods when the input image is being corrupted by 10% of salt-and-pepper noise. This can be considered as a low noise corruption level. From this visual inspection, it is shown that most of the methods tested in this work are able to remove the noise. EMF, although at this low noise level, is not able to remove the noise completely. RMF slightly reduce the sharpness of the object in the image, whereas ERMF makes the output images look smeared.



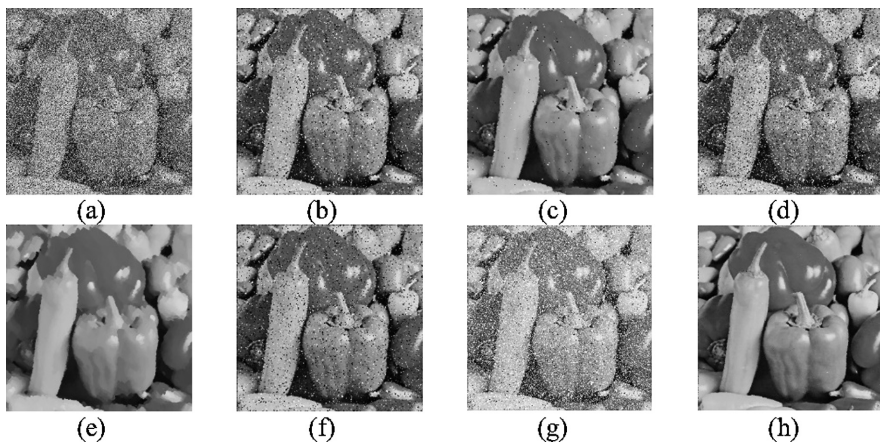
Figure 7 shows the outputs from the tested methods when the input is *Baboon* with 50% salt-and-pepper noise. As shown in Fig. 7(b), (d), (f), and (g), SMF, CWMF, DWMF and EMF have failed to remove the salt-and-pepper noise completely. Black and white dots are still visible in these images. Not much noise observed from the result from RMF, as shown in Fig. 7(c). ERMF significantly degrades the image appearance, as shown in Fig. 7(e). Figure 7(h) shows that our proposed method, which is RASMF, is still able to produce output image similar to the corresponding original image shown in Fig. 1(a).



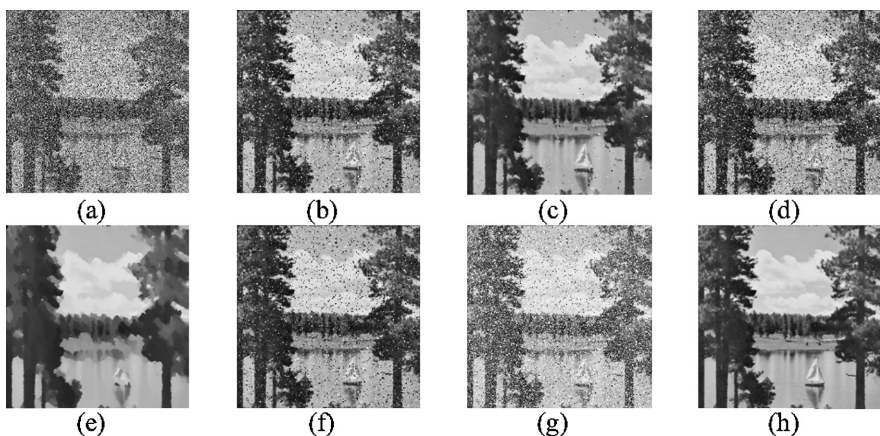
**Fig. 7.** (a) *Baboon* corrupted by 50% of salt-and-pepper noise. (b) Output from SMF [7]. (c) Output from RMF [16]. (d) Output from CWMF [8]. (e) Output from ERMF [17]. (f) Output from DWSMF [14]. (g) Output from EMF [15]. (h) Output from RASMF (the proposed method)

Figure 8 presents the results when the input is *Peppers* that has been corrupted by 50% of salt-and-pepper noise. As shown by this figure, salt-and-pepper noise are still visible on the outputs from SMF, RMF, CWMF, DWSMF and EMF, as shown by Fig. 8(b), (c), (d), (f), and (g), respectively. ERMF and our proposed method (RASMF), as shown in Fig. 8(e) and (h) respectively, successfully remove the salt-and-pepper noise. However, some information is lost by ERMF as compared to RASMF. The output by ERMF appears smoother than the output by RASMF.

The results when the input is *SailboatOnLake* corrupted by 50% of salt-and-pepper noise are shown in Fig. 9. As shown in Fig. 9(b), SMF failed to remove the noise. The result from RMF, as shown in Fig. 9(c), is better than SMF, with not many noisy pixels remained. Figure 9(d) indicates that CWMF is not able to perform well at this noise corruption level. Figure 9(e) shows that ERMF able to remove noise, but smears the image. The tree areas are degraded significantly by this method. From Fig. 9(f), it is shown that DWSMF is not capable to remove some of salt-and-pepper noisy pixels. EMF is also not performing well for this input image, as shown in Fig. 9(g). Our proposed method, which is RASMF, produces the best result, as shown in Fig. 9(h).

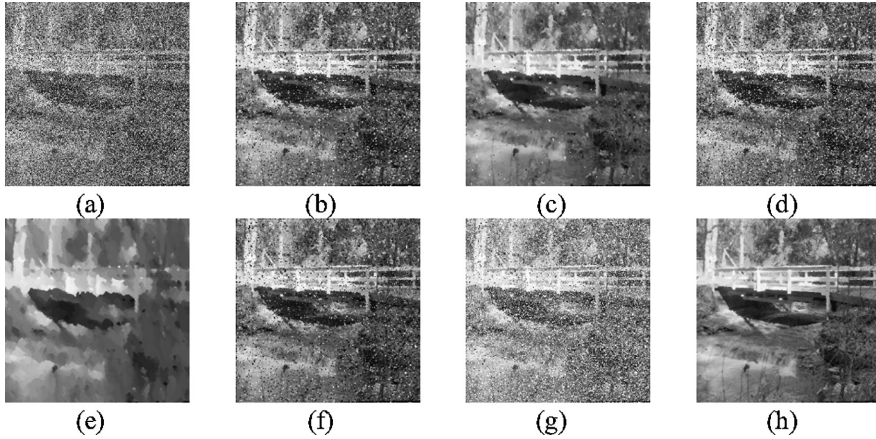


**Fig. 8.** (a) *Peppers* corrupted by 50% of salt-and-pepper noise. (b) Output from SMF [7]. (c) Output from RMF [16]. (d) Output from CWMF [8]. (e) Output from ERMF [17]. (f) Output from DWSMF [14]. (g) Output from EMF [15]. (h) Output from RASMF (the proposed method)



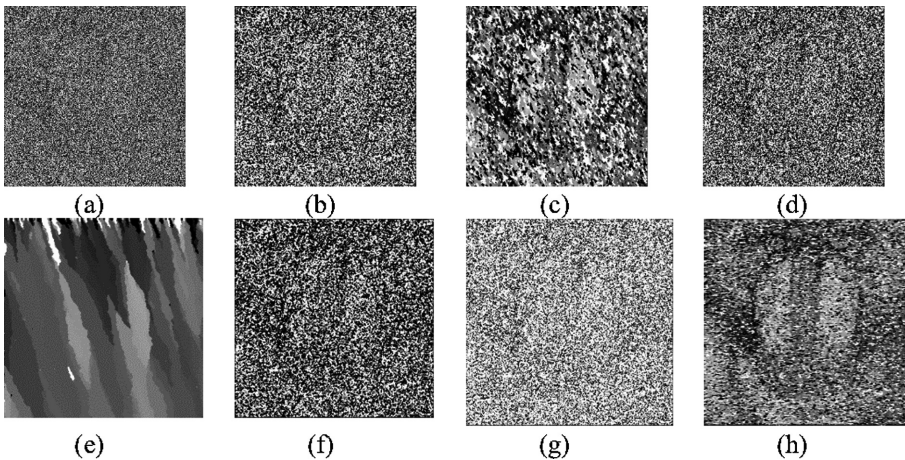
**Fig. 9.** (a) *SailboatOnLake* corrupted by 50% of salt-and-pepper noise. (b) Output from SMF [7]. (c) Output from RMF [16]. (d) Output from CWMF [8]. (e) Output from ERMF [17]. (f) Output from DWSMF [14]. (g) Output from EMF [15]. (h) Output from RASMF (the proposed method)

Figure 10 presents the results when the input is *StreamAndBridge* corrupted by 50% salt-and-pepper noise. As shown by this figure, white and black dots are still visible on the outputs from SMF, RMF, CWMF, DWSMF and EMF, as shown by Fig. 10(b), (c), (d), (f), and (g), respectively. ERMF, as shown in Fig. 10(e), degrades the appearance of the image significantly. Our proposed method, as shown in Fig. 10(h), produces the best result.



**Fig. 10.** (a) *StreamAndBridge* corrupted by 50% of salt-and-pepper noise. (b) Output from SMF [7]. (c) Output from RMF [16]. (d) Output from CWMF [8]. (e) Output from ERMF [17]. (f) Output from DWSMF [14]. (g) Output from EMF [15]. (h) Output from RASMF (the proposed method)

Figures 7, 8, 9 and 10 show the performance of the tested methods when the input image is being corrupted by 50% of salt-and-pepper noise. This can be considered as a medium noise corruption level. From this visual inspection, it is shown that most of the methods tested in this work are not able to remove the noise completely. Some salt-and-pepper noisy pixels are still visible from the outputs of RMF. ERMF, although can remove salt-and-pepper noise, degrades the image significantly as this technique smears the image. Our proposed method, which is RASMF, produce the best results for these four input images.

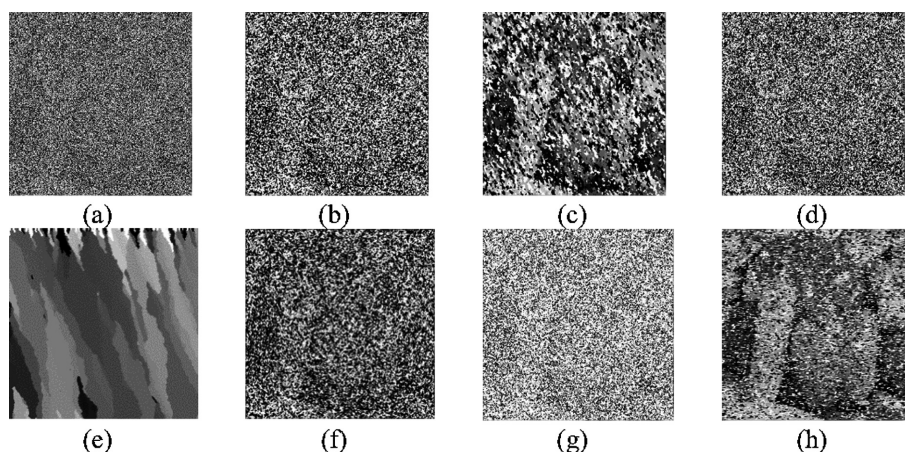


**Fig. 11.** (a) *Baboon* corrupted by 90% of salt-and-pepper noise. (b) Output from SMF [7]. (c) Output from RMF [16]. (d) Output from CWMF [8]. (e) Output from ERMF [17]. (f) Output from DWSMF [14]. (g) Output from EMF [15]. (h) Output from RASMF (the proposed method)



Figure 11 shows the results when the input is *Baboon* corrupted with 90% of salt-and-pepper noise. As shown by this figure, all methods have failed to remove noise at this corruption level. However, rough shape of the baboon's face can be observed in Fig. 11(c) and (h), which are the output from RMF and our proposed method (RASMF).

Figure 12 presents the outputs for *Peppers* corrupted with 90% of salt-and-pepper noise. As shown by this figure, all methods are not able to remove noise at this corruption level. However, rough shape of the peppers can be seen in Fig. 12(h), which is the output our proposed method (RASMF).



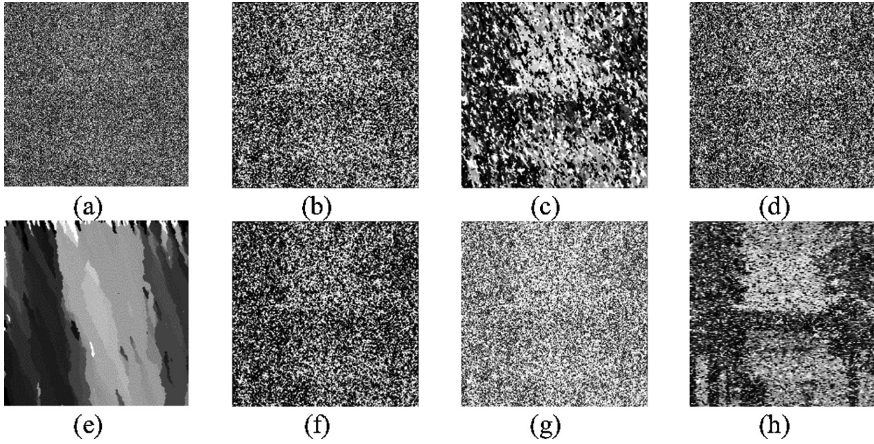
**Fig. 12.** (a) *Peppers* corrupted by 90% of salt-and-pepper noise. (b) Output from SMF [7]. (c) Output from RMF [16]. (d) Output from CWMF [8]. (e) Output from ERMF [17]. (f) Output from DWSMF [14]. (g) Output from EMF [15]. (h) Output from RASMF (the proposed method)

Figure 13 gives the outputs from *SailboatOnLake* corrupted with 90% of salt-and-pepper noise. This figure shows that all tested method failed to recover the original image content. Result from ERMF shown in Fig. 13(d), although does not contains black and white dots, is not resemble the original image, as shown in Fig. 1(c). However, a rough structure of the image can be seen in the output of our proposed method, as shown in Fig. 13(h).

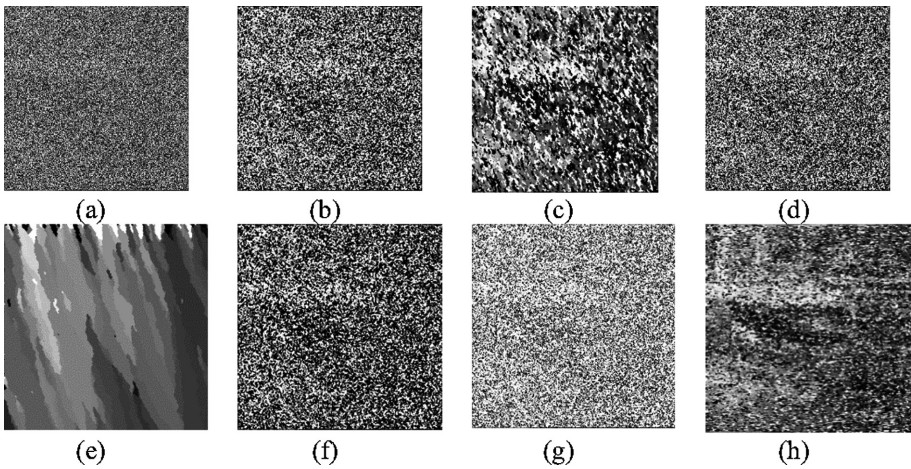
Similar observation can be seen in Fig. 14, where the input image is *StreamAnd-Bridge*. All of the tested methods failed to restore the image at this salt-and-pepper corruption level. However, a rough structure of the bridge can be observed in Fig. 14 (h), which is the output from our proposed method.

Figures 11, 12, 13 and 14 show the performance of the tested methods when the input image is being corrupted by 90% of salt-and-pepper noise. This can be considered as a high noise corruption level. From this visual inspection, it is shown that all of the tested methods are not able to restore the image. In all results, except the result from ERMF, the image still contains black and white dots, correspond to salt-and-pepper noise. As the restoration errors propagate in RMF method, larger dots are observed in

RMF results. Results from ERMF, although does not contain noisy dots, the contents of the image have been changed significantly. Rough structures, similar to the original image, can be observed in outputs from our proposed method, which is RASMF.

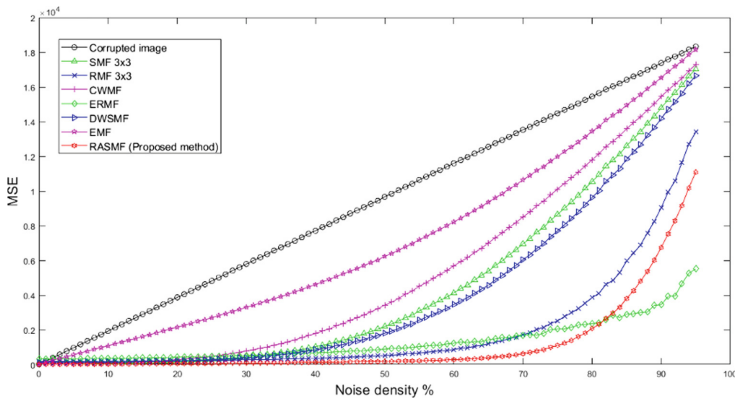


**Fig. 13.** (a) *SailboatOnLake* corrupted by 90% of salt-and-pepper noise. (b) Output from SMF [7]. (c) Output from RMF [16]. (d) Output from CWMF [8]. (e) Output from ERMF [17]. (f) Output from DWSMF [14]. (g) Output from EMF [15]. (h) Output from RASMF (the proposed method)



**Fig. 14.** (a) *StreamAndBridge* corrupted by 90% of salt-and-pepper noise. (b) Output from SMF [7]. (c) Output from RMF [16]. (d) Output from CWMF [8]. (e) Output from ERMF [17]. (f) Output from DWSMF [14]. (g) Output from EMF [15]. (h) Output from RASMF (the proposed method).

Therefore, based on the visual inspection from Figs. 3, 4, 5, 6, 7, 8, 9, 10, 11, 12, 13 and 14, we can see that most of the methods can perform well for low level of corruption. At medium corruption level, while other methods failed to remove the noise completely, our proposed method produces outputs similar to their corresponding clean input. At high corruption level, all method failed to remove the noise, but rough structure on the images can be seen on the outputs by our proposed method. Thus, in terms of visual appearance, our proposed method produces the best result.



**Fig. 15.** Plot of average MSE from four test images versus noise density

Figures 15 and 16 show the result in terms of average MSE and average SSIM, computed from four test images. Figure 15 shows the performance in terms of average MSE, for noise level from 0% to 95%, with step size of 1%. As shown by this figure, all methods successfully reduce the MSE value of the image, which is their MSE values are lower than the corrupted image, indicated by the black line. It is also shown that our proposed method, which is RSMF, indicated by the red line, has the lowest MSE values, until noise level 81%. After that noise level, ERMF shows the lowest MSE value.

Figure 16 shows the performance in terms of average SSIM, for noise level from 0% to 95%, with step size of 1%. Most of the methods have lower value of SSIM as compared to the SSIM value of the corrupted image indicated by the black line. However, as shown by this figure, our proposed method, RSMF, gives the best performance in terms of SSIM for noise density 0% to 79%. It is interesting to see the performance of ERMF, where its SSIM value is the lowest at low noise level, but the highest at high noise level.

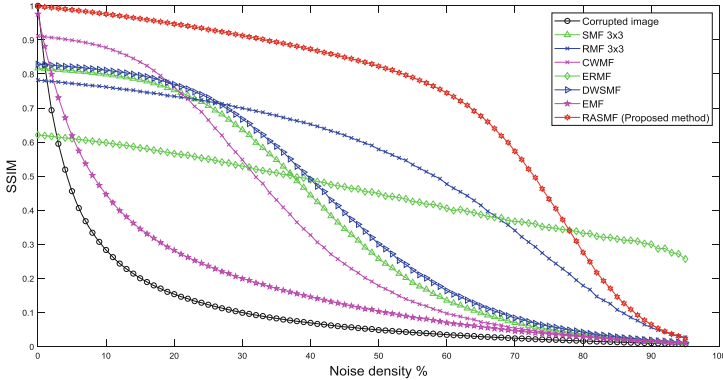


Fig. 16. Plot of average MSE from four test images versus noise density

## 4 Conclusion

This research has proposed a new noise reduction method, which is RASMF. As compared to the standard median filters and the recursive median filters, the proposed method shows the best performance, in terms of visual inspection, MSE and SSIM values. However, the proposed methods still need improvements for high level of noise. Based on the average MSE and SSIM values, we can say that RASMF is the best method until the corruption level is around 80%. Further investigation on improving this type of filter should be done in future.

**Acknowledgments.** This work was supported in part by the Universiti Sains Malaysia: Research University Grant 1001/PELECT/8014052.

## References

1. Teoh, S.H., Ibrahim, H.: Variations on impulse noise model in digital image processing field: a survey on current research inclination. *Int. J. Innov. Manag. Technol.* **4**(4), 393–396 (2013). <https://doi.org/10.7763/ijmt.2013.v4.428>
2. Kunsoth, R., Biswas, M.: Modified decision based median filter for impulse noise removal. In: 2016 International Conference on Wireless Communications, Signal Processing and Networking (WiSPNET), Chennai, India, pp. 1316–1319 (2016)
3. Pang, J., Zhang, S., Zhang, S.: A median filter based on the proportion of the image variance. In: 2016 IEEE Information Technology, Networking, Electronic and Automation Control Conference, Chongqing, China, pp. 123–127 (2016)
4. Boo, S.T., Ibrahim, H., Toh, K.K.V.: An improved progressive switching median filter. In: 2009 International Conference on Future Computer and Communication, Kuala Lumpur, Malaysia, pp. 136–139 (2009)
5. Ibrahim, H., Abdalameer, A.K.: Improvement of quantized adaptive switching median filter for impulse noise reduction in gray-scale digital images. *Turk. J. Electr. Eng. Comput. Sci.* **27**(1), 580–594 (2019). <https://doi.org/10.3906/elk-1709-139>

6. Teoh, H., Ibrahim, H.: Robust algorithm for broad impulse noise removal utilizing intensity distance and intensity height methodologies. *SIViP* **8**(2), 223–242 (2012). <https://doi.org/10.1007/s11760-013-0538-y>
7. Tukey, J.W.: *Exploratory Data Analysis*. Preliminary Edition. Addison-Wesley, Reading (1971)
8. Sun, T.: Center weighted median filters: some properties and their applications in image processing. *Signal Process.* **35**(3), 213–229 (1994). [https://doi.org/10.1016/0165-1684\(94\)90212-7](https://doi.org/10.1016/0165-1684(94)90212-7)
9. Teoh, S.H., Koik, B.T., Ibrahim, H.: Exploration of current trend on median filtering methods utilized in digital grayscale image processing. *Int. J. Mater. Mech. Manuf.* **1**(1), 50–54 (2013). <https://doi.org/10.7763/ijmmm.2013.v1.11>
10. Sharma, A., Chaurasia, V.: Removal of high density salt-and-pepper noise by recursive enhanced median filtering. In: 2014 2nd International Conference on Emerging Technology Trends in Electronics, Communication & Networking, Surat, India, pp. 1–4 (2014)
11. Ibrahim, H., Kong, N.S., Ng, T.F.: Simple adaptive median filter for the removal of impulse noise from highly corrupted images. *IEEE Trans. Consum. Electron.* **54**(4), 1920–1927 (2008). <https://doi.org/10.1109/tce.2008.4711254>
12. George, G., Oommen, R.M., Shelly, S., Philipose, S.S., Varghese, A.M.: A survey on various median filtering techniques for removal of impulse noise from digital image. In: 2018 Conference on Emerging Devices and Smart Systems (ICEDSS), Tamilnadu, India, pp. 235–238 (2018)
13. Lu, C.T., Chen, Y.Y., Wang, L.L., Chang, C.F.: Removal of salt-and-pepper noise in corrupted image using three-values-weighted approach with variable-size window. *Pattern Recogn. Lett.* **80**, 188–199 (2016). <https://doi.org/10.1016/j.patrec.2016.06.026>
14. Zhang, M.M., Kouri, D.J., Zhang, D.S.: Dual window selective median switching filter. In: 2017 11th International Conference on Signal Processing and Communication Systems (ICSPCS), Gold Coast, QLD, Australia, pp. 1–3 (2017)
15. Charmouti, B., Junoh, A.K., Wan Muhamad, W.Z.A., Mansor, M.N., Hasan, M.Z., Mashor, M.Y.: Extended median filter for salt and pepper noise in image. *Int. J. Appl. Eng. Res.* **12**(22), 12914–12918 (2017)
16. Nodes, T.A., Gallagher Jr., N.C.: Median filters: some modifications and their properties. *IEEE Trans. Acoust. Speech Signal Process.* **30**(5), 739–746 (1982). <https://doi.org/10.1109/tassp.1982.1163951>
17. Varshey, P., Tyagi, A.: An enhanced recursive median filter for noise reduction based on randomness in pixel values of an image. *Int. J. Comput. Appl.* **113**(8), 8–10 (2015). <https://doi.org/10.5120/19845-1706>
18. Zhou, W., Bovik, A.C., Sheikh, H.R., Simoncelli, E.P.: Image quality assessment: from error visibility to structural similarity. *IEEE Trans. Image Process.* **13**(4), 600–612 (2004). <https://doi.org/10.1109/tip.2003.819861>





# Parameter Tuning in the Single-Solution Simulated Kalman Filter Optimizer

Nor Hidayati Abdul Aziz<sup>1,2</sup>, Zuwairie Ibrahim<sup>2,3(✉)</sup>,  
Nor Azlina Ab Aziz<sup>1</sup>, Badaruddin Muhammad<sup>2</sup>,  
Tasiransurini Ab Rahman<sup>2</sup>, Mohd Saberi Mohamad<sup>4</sup>,  
and Suhazri Amrin Rahmad<sup>3</sup>

<sup>1</sup> Faculty of Engineering and Technology,  
Multimedia University, Melaka, Malaysia

<sup>2</sup> Faculty of Electrical and Electronics Engineering,  
Universiti Malaysia Pahang, Melaka, Malaysia  
zuwairie@ump.edu.my

<sup>3</sup> Faculty of Manufacturing, Universiti Malaysia Pahang, Melaka, Malaysia

<sup>4</sup> Faculty of Creative Technology and Heritage,  
Universiti Malaysia Kelantan, Melaka, Malaysia

**Abstract.** Single-solution simulated Kalman filter (ssSKF) is a variant of simulated Kalman filter (SKF) algorithm. Both algorithms employ the well-known Kalman filtering mechanism in an optimization process. Unlike the population-based SKF, the ssSKF operates using one agent. In this paper, parameter tuning of the ssSKF algorithm is presented.

**Keywords:** Optimization · Simulated Kalman filter

## 1 Introduction

An optimization algorithm called simulated Kalman filter (SKF) is a population-based optimizer inspired by the Kalman filtering process [1, 2]. Recently, a variant of SKF optimizer that operates using only an agent, which is called as single-solution SKF (ssSKF) [3], has been introduced. At present, the ssSKF algorithm is employed in solving a routing problem in hole drilling process [4] and no fundamental study and improvement to the ssSKF is reported.

The ssSKF offers a slight advantage over the SKF counterpart in terms of the number of parameters in the algorithm. The ssSKF requires the tuning of  $\alpha$  value to ensure good performance. The  $\alpha$  is a parameter in step-size  $\delta$ , which is important in the transition from the exploration to exploitation during an optimization process. Hence, in this paper, parameter tuning of  $\alpha$  value is studied. To generalize the finding, CEC2014 benchmark suite [5], which consists of 30 test functions of function minimization problem, is solved using ssSKF with different  $\alpha$  values. Then, a statistical analysis is performed to confirm the relation between the  $\alpha$  value and the performance of ssSKF.

## 2 Single-Solution Simulated Kalman Filter Algorithm (ssSKF)

The flowchart of ssSKF algorithm is shown in Fig. 1. The algorithm begins with random initial solution,  $X(0)$ . Initial error covariance,  $P(0)$ , is set to a normally distributed random number. Then, fitness is calculated. After that, according to the type of problem, the best-so-far solution,  $X_{\text{best}}$ , is updated. The  $X_{\text{best}}$  is updated only if the solution at current iteration,  $X(t)$ , is better. For minimization problem,  $X_{\text{best}}$  is updated if the fitness of  $X(t)$  is less than the fitness of  $X_{\text{best}}$ . On the other hand, for maximization problem,  $X_{\text{best}}$  is updated if the fitness of  $X(t)$  is greater than the fitness of  $X_{\text{best}}$ .

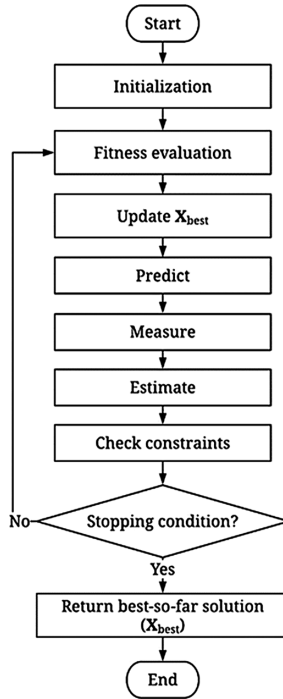


Fig. 1. The flowchart of the ssSKF algorithm

During prediction, the following equations are used to predict the optimum solution:

$$\mathbf{X}^d(t|t+1) \sim U[\mathbf{X}_{\text{best}}^d - \delta, \mathbf{X}_{\text{best}}^d + \delta] \quad (1)$$

$$P^d(t|t+1) = P^d(t) + \text{randn}^d \quad (2)$$

where  $\text{randn}^d$  is a normally distributed random number and is used whenever the parameter value is needed for each dimension in every iteration. The ssSKF makes a

prediction that resides in a confined neighborhood of  $[\mathbf{X}_{best}^d - \delta, \mathbf{X}_{best}^d + \delta]$  in every dimension, with the  $\mathbf{X}_{best}$  to be the center of the neighborhood. The size of the local neighbourhood is determined by the adaptively decreasing step-size  $\delta$ .

$$\delta = e^{-\frac{\alpha t}{tMax}} \times \delta_0 \quad (3)$$

where  $tMax$  is the maximum number of iteration. The initial neighbourhood limit,  $\delta_0$ , determined using  $\delta_0 = \max(|lowerlimit|, |upperlimit|)$  to ensure maximum coverage of the search space during the first iteration.

The next step is measurement. In this step, the best-so-far solution,  $\mathbf{X}_{best}^d$  steered the agent's simulated measurement value,  $\mathbf{Z}^d(t)$ , as follows:

$$\mathbf{Z}^d(t) = \mathbf{X}^d(t|t+1) + \Delta \quad (4)$$

$$\Delta = \sin(rand^d \times 2\pi) \times |\mathbf{X}^d(t|t+1) - \mathbf{X}_{best}^d| \quad (5)$$

The purpose of the measurement is to give feedback to the estimation process. The measurement is simulated in such a way that the measured value of the agent may take any random value surrounding the predicted value,  $\mathbf{X}^d(t|t+1)$ , either approaching to or moving away from the best-so-far solution,  $\mathbf{X}_{best}^d$ , balancing between exploration and exploitation. The exploration and exploitation mechanisms are further compromised as the distance between the predicted value and the best-so-far solution decreases with the increase of the number of iterations.

Finally, during the estimation step, the solution and error covariance estimates for the next iteration are calculated using the estimate equations right after the calculation of the Kalman gain.

$$K^d(t) = \frac{P^d(t|t+1)}{P^d(t|t+1) + rand^d} \quad (6)$$

$$\mathbf{X}^d(t+1) = \mathbf{X}^d(t|t+1) + K^d(t) \times (\mathbf{Z}^d(t) - \mathbf{X}^d(t|t+1)) \quad (7)$$

$$P^d(t+1) = (1 - K^d(t)) \times P^d(t|t+1) \quad (8)$$

At the end of the estimation step, a better solution for the next iteration that lies between the predicted and the measured value is produced. This process continues until the maximum number of iterations.

The performance of the ssSKF algorithm depends on the selection of  $\alpha$ . In (3), it can be observed that the  $\alpha$  regulates the value of the step-size,  $\delta$ , that determines the size of the local neighbourhood during prediction. This fact might affect the convergence behaviour of the algorithm. Thus, an analysis of the effects of different  $\alpha$  values to the overall performance of the ssSKF algorithm is needed.



### 3 Experiment, Result, and Discussion

The CEC 2014 benchmark suite [5] is chosen to evaluate the performance of the ssSKF algorithm with different  $\alpha$  values ( $\alpha = 1, 2, 3, 4, 5, 6, 7, 8, 9, 10$ ). This test suite consists of four groups of functions; unimodal functions, simple multimodal functions, hybrid functions, and composition functions, which can be used to represent the real numerical optimization problems. As listed in Table 1, there are 30 functions in this test suite. Each function corresponds to one optimization problem and has their own ideal fitness value represents the global or optimal solution. The stopping condition is set to 1000000 number of function evaluations. The complexity of the benchmark functions is set at 50 dimensions and the experiments are carried out for 50 times.

A Friedman statistical test is then carried out to test for differences in performance between the results at 5% significance level. To control the familywise error rate, the Holm procedure is chosen. These analyses are performed by using the KEEL software which can be downloaded via <http://www.keel.es>.

The experimental results are shown in Tables 1 and 2. The Friedman test analysis is presented in Table 3. The statistical analysis shows that the performance of the ssSKF algorithm is improving as the  $\alpha$  value increases. The Friedman statistic was carried out considering reduction performance distributed according to chi-square value of 190.205455 with 9 degrees of freedom. The results of post hoc Holm's analysis as in Table 4 shows that the ssSKF algorithm performs significantly better when  $\alpha = 10$  compared to  $\alpha = 5$  and lesser, as the Holm's test reject those hypotheses that have a p-value  $\leq 0.0125$ .

To further investigate if a higher value of the adaptive coefficient,  $\alpha$ , still gives any positive impact on the ssSKF performance, the adaptive coefficient value,  $\alpha$ , are increased from 11 to 20 under the same experimental parameter settings. The results are shown in Table 5.

Then, the ssSKF performance with  $\alpha = 10$  was compared to the ssSKF performance with  $\alpha = 11$  to 20 using the  $1 \times N$  Friedman test with significance level of 0.05. The data for the analysis is provided in Table 5. The Friedman test statistics of 49.306061 with 10 degrees of freedom as shown in Tables 6 and 7 yields that ssSKF algorithm with  $\alpha = 10$  is performing the best in solving CEC 2014 benchmark problems. When the adaptive coefficient value,  $\alpha$ , is further increased, reflecting a fast increase in the rate of reduction of the step-size,  $\delta$ , the performance of the ssSKF algorithm in solving the CEC 2014 benchmark problems decreased. Although the decrement of the performance is not in the sequence of the increment of the adaptive coefficient value,  $\alpha$ , it is observed that any further increase in  $\alpha$  from 11 to 20 does not give any positive impact on the algorithm's performance.

**Table 1.** The CEC 2014 benchmark test suite.

	No.	Functions	Ideal fitness
Unimodal functions	1	Rotated High Conditioned Elliptic function	100
	2	Rotated Bent Cigar function	200
	3	Rotated Discus function	300
Simple Multimodal functions	4	Shifted and Rotated Rosenbrock's function	400
	5	Shifted and Rotated Ackley's function	500
	6	Shifted and Rotated Weierstrass function	600
	7	Shifted and Rotated Griewank's function	700
	8	Shifted Rastrigin's function	800
	9	Shifted and Rotated Rastrigin's function	900
	10	Shifted Schwefel's function	1000
	11	Shifted and Rotated Schwefel's function	1100
	12	Shifted and Rotated Katsura function	1200
	13	Shifted and Rotated HappyCat function	1300
	14	Shifted and Rotated HGBat function	1400
	15	Shifted and Rotated Expanded Griewank's plus Rosenbrock's function	1500
	16	Shifted and Rotated Expanded Scaffer's F6 function	1600
	Hybrid functions	17	Hybrid function 1 (N = 3)
18		Hybrid function 2 (N = 3)	1800
19		Hybrid function 3 (N = 4)	1900
20		Hybrid function 4 (N = 4)	2000
21		Hybrid function 5 (N = 5)	2100
22		Hybrid function 6 (N = 5)	2200
Composition functions	23	Composition function 1 (N = 5)	2300
	24	Composition function 2 (N = 3)	2400
	25	Composition function 3 (N = 3)	2500
	26	Composition function 4 (N = 5)	2600
	27	Composition function 5 (N = 5)	2700
	28	Composition function 6 (N = 5)	2800
	29	Composition function 7 (N = 3)	2900
	30	Composition function 8 (N = 3)	3000

**Table 2.** Results ( $\alpha = 1, 2, 3, 4, 5, 6, 7, 8, 9, 10$ )

No.	$\alpha = 1$	$\alpha = 2$	$\alpha = 3$	$\alpha = 4$	$\alpha = 5$	$\alpha = 6$	$\alpha = 7$	$\alpha = 8$	$\alpha = 9$	$\alpha = 10$
1	4.79E +08	1.06E +08	2.45E +07	1.09E +07	5.19E +06	2.74E +06	1.87E +06	1.05E +06	6.66E +05	3.89E +05
2	2.79E +10	4.60E +09	6.43E +08	9.28E +07	1.27E +07	1.83E +06	2.64E +05	42016	10240	8210
3	72761	16707	3125.6	721.87	365.42	309.93	301.31	300.21	300.03	300
4	3809.3	939.55	582.62	515.08	501.79	498.37	492.22	493.65	495.16	489.53
5	521.1	521.11	521.12	521.12	521.11	520.93	520.25	520.04	520.01	520
6	661.09	645.37	631.07	623.39	618.42	617.47	615.68	615.06	614.98	616.11
7	981.28	745.24	707.5	701.9	701.13	700.95	700.33	700.06	700.02	700.01
8	1287.5	1233.2	1149.5	997.77	971.94	969	978.16	970.27	970.8	975.99
9	1430.4	1364.8	1282.4	1119.6	1076.3	1070.1	1078.7	1079.4	1078.3	1081.3
10	13750	12753	9662.3	6432.8	5855.4	5802.7	5657.6	5602.4	5731.6	5738.3
11	14234	13822	11480	7222.5	6215.5	6328.7	6227.6	6082.4	6033.8	6267.5
12	1203.2	1203.1	1203.1	1202.3	1201.1	1200.4	1200.2	1200.1	1200.1	1200.1
13	1303.4	1300.8	1300.6	1300.6	1300.6	1300.6	1300.6	1300.6	1300.6	1300.6
14	1478.5	1405.4	1400.5	1400.4	1400.4	1400.5	1400.4	1400.5	1400.5	1400.4
15	47468	1614.1	1542.2	1535.9	1532.7	1524.3	1514	1512.5	1511	1511.1
16	1622.2	1621.7	1621.4	1621.1	1620.6	1620.4	1620.2	1620.2	1620.2	1620.2
17	2.08E +07	5.25E +06	1.35E +06	7.17E +05	3.48E +05	1.64E +05	99576	61071	41329	28454
18	7.76E +08	1.22E +08	1.79E +07	2.51E +06	3.51E +05	51577	10416	5506	4292.2	3534.5
19	2093	1973	1934.9	1923.7	1920.3	1921.3	1919	1919.4	1919.4	1919.4
20	19185	4275.3	2777.6	2593.6	2486.2	2456.9	2439.6	2452.4	2451.2	2444.2
21	7.06E +06	1.89E +06	5.70E +05	4.03E +05	2.25E +05	1.51E +05	96244	74640	53495	38048
22	4187.2	3643.1	3101.5	2908.5	2792.2	2861.4	2837.5	2887.4	2861.2	2919.6
23	2891.8	2709.2	2666.6	2653.5	2647.8	2645.7	2644.9	2644.6	2644.5	2644.5
24	2799.6	2723.9	2694.8	2679.8	2676.2	2675.1	2675.9	2674.9	2676.2	2674.7
25	2779.9	2734.7	2718.3	2712.6	2711.5	2710.9	2710.6	2711.5	2711.1	2711.7
26	2703.2	2705.2	2702.6	2710.7	2704.6	2708.5	2712.5	2708.5	2710.5	2706.5
27	4556.3	4147.5	3794.3	3642.5	3545.7	3463.1	3460.4	3447.2	3465.3	3457.9
28	7938.9	6189.4	5281.1	4681.6	4638.7	4680.1	4732.6	4623.1	4790.1	4644
29	8.83E +07	1.49E +07	2.26E +06	3.44E +05	84923	38905	33639	37481	34281	30535
30	9.20E +05	2.39E +05	1.01E +05	61588	50361	41010	37900	35764	36826	35905

**Table 3.** Friedman average rankings based on different  $\alpha$  values ( $\alpha = 1, 2, 3, 4, 5, 6, 7, 8, 9, 10$ )

The $\alpha$ value	Ranking
1	9.6000
2	8.7667
3	7.6667
4	6.8167
5	5.0833
6	4.6167
7	3.6167
8	3.0833
9	3.0833
10	2.6667

**Table 4.** Post hoc Holm analysis for different  $\alpha$  values ( $\alpha = 1, 2, 3, 4, 5, 6, 7, 8, 9, 10$ )

i	Comparison	$z = (R_0 - R_i)SE$	p	Holm
9	$\alpha = 10$ vs $\alpha = 1$	8.86915	0	0.005556
8	$\alpha = 10$ vs $\alpha = 2$	7.803146	0	0.00625
7	$\alpha = 10$ vs 3	6.396021	0	0.007143
6	$\alpha = 10$ vs 4	5.308698	0	0.008333
5	$\alpha = 10$ vs $\alpha = 5$	3.091410	0.001992	0.01
4	$\alpha = 10$ vs $\alpha = 6$	2.494448	0.012615	0.0125
3	$\alpha = 10$ vs $\alpha = 7$	1.215244	0.224273	0.016667
2	$\alpha = 10$ vs $\alpha = 8$	0.533002	0.594032	0.025
1	$\alpha = 10$ vs $\alpha = 9$	0.533002	0.594032	0.05

**Table 5.** Results ( $\alpha = 11, 12, 13, 14, 15, 16, 17, 18, 19, 20$ )

No.	$\alpha = 11$	$\alpha = 12$	$\alpha = 13$	$\alpha = 14$	$\alpha = 15$	$\alpha = 16$	$\alpha = 17$	$\alpha = 18$	$\alpha = 19$	$\alpha = 20$
1	3.03E +05	2.70E +05	2.70E +05	2.98E +05	3.21E +05	3.21E +05	3.52E +05	3.81E +05	3.45E +05	4.28E +05
2	6305.1	7066.9	6307.6	5360.9	7275.8	6704	7852.4	8025.6	6297.6	8471.3
3	300	300	300	300	300	300	300	300	300	300
4	489.22	487.46	486.9	496.81	495.61	481.63	484.56	493.81	484.87	496.34
5	520	520	520	520	520	520	520	520	520	520
6	615.06	616.56	616.52	616.57	617.26	616.42	616.97	616.83	618.44	618.61
7	700.01	700.01	700.01	700.01	700.01	700.01	700.01	700.01	700.01	700.01
8	976.43	976.31	986.45	994.16	982.41	982.1	983.05	983.99	989.44	986.87
9	1089.8	1091.7	1091.8	1096.7	1084.5	1092.1	1094.1	1096	1091.6	1096.6
10	5588.2	5996.1	5963.8	6008	5744.6	6249.5	6039.9	6164	5866	6022.5
11	6136.6	6239.5	6509	6423.3	6335.2	6369.1	6407.6	6470.5	6292	6195.6
12	1200.1	1200.1	1200.1	1200.1	1200.1	1200.1	1200.1	1200.1	1200.1	1200.1

(continued)

**Table 5.** (continued)

No.	$\alpha = 11$	$\alpha = 12$	$\alpha = 13$	$\alpha = 14$	$\alpha = 15$	$\alpha = 16$	$\alpha = 17$	$\alpha = 18$	$\alpha = 19$	$\alpha = 20$
13	1300.6	1300.6	1300.6	1300.6	1300.6	1300.6	1300.6	1300.6	1300.6	1300.7
14	1400.6	1400.5	1400.5	1400.6	1400.4	1400.5	1400.4	1400.4	1400.5	1400.5
15	1510.4	1510.8	1510.9	1509.9	1510.8	1511.1	1511.3	1511.3	1510.7	1511.2
16	1620.5	1620.5	1620.6	1620.5	1620.4	1620.6	1620.6	1620.7	1620.6	1620.8
17	23028	18217	16970	18279	16973	18185	22142	23395	25205	21330
18	3975	3889.6	3914.6	3756.1	4662.4	4073.6	4021	4016.9	3946.7	3759.4
19	1923.2	1923.1	1921.5	1923.4	1923	1924	1920.4	1919.2	1920	1923.4
20	2464.3	2462.8	2466.8	2467.8	2461	2464.5	2486.3	2454.3	2491.6	2491.1
21	31534	28239	28653	32479	30888	37004	34334	36400	41070	48419
22	2791.9	2915.4	2892	2977.2	3023.5	2934.5	2944.5	2944	2902.7	2995.5
23	2644.5	2644.6	2644.6	2644.7	2644.7	2644.7	2644.8	2644.8	2644.9	2645
24	2677.6	2677.6	2677.6	2676.7	2677.7	2677.5	2678.2	2678.6	2678.3	2678.3
25	2712.2	2711.9	2712.2	2712.7	2711.8	2713.3	2713.1	2712.5	2713.5	2712.5
26	2712.5	2704.6	2716.5	2710.5	2706.6	2718.5	2718.5	2726.4	2720.5	2720.5
27	3441.5	3455.2	3455.5	3449.2	3490.7	3463.9	3490.1	3485.8	3506.8	3508.7
28	4679.7	4892.8	4767	4821.2	4885.2	4857.5	4991	4910.8	4917.5	4974.5
29	24783	27910	24358	25852	25595	25018	23674	26155	24765	23944
30	39301	37288	37876	38167	37539	37863	39310	37848	39996	38492

**Table 6.** Friedman average rankings based on different  $\alpha$  values ( $\alpha = 10, 11, 12, 13, 14, 15, 16, 17, 18, 19, 20$ )

The $\alpha$ value	Ranking
10	4.3333
11	4.4667
12	4.5667
13	5.0167
14	6.1167
15	5.4667
16	6.2500
17	7.1000
18	7.3500
19	6.9667
20	8.3667

**Table 7.** Post hoc Holm analysis for different  $\alpha$  values ( $\alpha = 11, 12, 13, 14, 15, 16, 17, 18, 19, 20$ )

i	Comparison	$z = (R_0 - R_i)SE$	$p$	Holm
10	$\alpha = 10$ vs $\alpha = 20$	4.709919	0.000002	0.005
9	$\alpha = 10$ vs $\alpha = 19$	3.522708	0.000427	0.005556
8	$\alpha = 10$ vs 18	3.230771	0.001235	0.00625
7	$\alpha = 10$ vs 17	3.075071	0.002105	0.007143
6	$\alpha = 10$ vs $\alpha = 16$	2.238184	0.025209	0.008333
5	$\alpha = 10$ vs $\alpha = 15$	2.082485	0.037298	0.01
4	$\alpha = 10$ vs $\alpha = 14$	1.323448	0.185686	0.0125
3	$\alpha = 10$ vs $\alpha = 13$	0.797961	0.424893	0.016667
2	$\alpha = 10$ vs $\alpha = 12$	0.272475	0.785257	0.025
1	$\alpha = 10$ vs $\alpha = 11$	0.155700	0.876270	0.05

## 4 Conclusion

The ssSKF is a new metaheuristic which operates using one agent. In ssSKF,  $\alpha$  is the only parameter that requires proper tuning to obtain a good optimization process. The  $\alpha$  value regulates the value of the step-size,  $\delta$ , that determines the size of the local neighbourhood during prediction. It can be concluded that the  $\alpha$  value effect the performance of ssSKF algorithm. Different  $\alpha$  values have been tested in solving 30 function minimization problems in CEC 2014 benchmark suite. Based on Friedman test and post hoc Holm analysis, it can be concluded that, in general,  $\alpha = 10$  could be good in solving most of optimization problems using ssSKF.

**Acknowledgments.** This research is supported by the Fundamental Research Grant Scheme awarded by the Ministry of Higher Education Malaysia to Universiti Malaysia Pahang (RDU170106).

## References

1. Ibrahim, Z., Abdul Aziz, N.H., Ab Aziz, N.A., Razali, S., Shapiai, M.I.: A Kalman filter approach for solving unimodal optimization problem. *ICIC Express Lett.* **9**, 3415–3422 (2015)
2. Ibrahim, Z., Abdul Aziz, N.H., Ab Aziz, N.A., Razali, S., Mohamad, M.S.: Simulated Kalman filter: a novel estimation-based metaheuristic optimization algorithm. *Adv. Sci. Lett.* **22**, 2941–2946 (2016)
3. Abdul Aziz, N.H., Ibrahim, Z., Ab Aziz, N.A., Mohamad, M.S., Watada, J.: Single-solution simulated Kalman filter algorithm for global optimisation problems. *Sadhana* **43** (2018)
4. Abdul Aziz, N.H., Ibrahim, Z., Ab Aziz, N.A., Yusof, Z.M., Mohamad, M.S.: Single-solution simulated Kalman filter algorithm for routing in printed circuit board drilling process. *Lecture Notes in Mechanical Engineering (Intelligent Manufacturing & Mechatronics)*, pp. 649–655 (2018)
5. Liang, J.J., Qu, B.Y., Suganthan, P.N.: Problem definitions and evaluation criteria for the CEC 2014 special session and competition on single objective real-parameter numerical optimization. Technical report 201311, Computational Intelligence Laboratory, Zhengzhou University, Zhengzhou, China and Nanyang Technological University, Singapore (2013)



# Path Tracking Simulation of the Buggy Car by Using Fuzzy Information of the Steering Wheel

Hafiz Halin<sup>1</sup>, Wan Khairunizam<sup>2</sup>(✉), Hasri Haris<sup>3</sup>, I. Zunaidi<sup>4</sup>,  
Shahriman Abu Bakar<sup>2</sup>, Z. M. Razlan<sup>2</sup>, and Wan Azani Mustafa<sup>5</sup>

- <sup>1</sup> Advanced Intelligent Computing and Sustainable Research Group (AICOS),  
Universiti Malaysia Perlis (UniMAP), Kampung Kubang,  
02600 Arau, Perlis, Malaysia  
abdhafiz.halin@gmail.com
- <sup>2</sup> School of Mechatronic Engineering,  
University Malaysia Perlis (UniMAP), Arau, Malaysia  
khairunizam@unimap.edu.my
- <sup>3</sup> Kolej Kemahiran Tinggi MARA Balik Pulau,  
Balik Pulau, Pulau Pinang, Malaysia
- <sup>4</sup> University of Sunderland, Sunderland, UK
- <sup>5</sup> Faculty of Engineering Technology, Universiti Malaysia Perlis (UniMAP),  
Kampung Kubang, 02600 Arau, Perlis, Malaysia

**Abstract.** The steering wheel control is the method used for the navigation of an autonomous vehicle. In order to control the autonomous vehicle, the steering wheel controller must be able to adapt as the road condition and surrounding environment can change abruptly. The existed autonomous system currently in the testing phase. The system still needs to improve because there is some report regarding an accident caused by the test autonomous vehicles. The aim of this research is to implement the human driving capability into the Fuzzy controller. One of the human capabilities is the ability to make a decision based on the current situation. The fuzzy system is developed based on human driving data while controlling a buggy car. The experiments used to collect data such as position, speed, heading and steering wheel angle. Data then use to develop the membership function for the fuzzy inputs and output. The simulation is performed in order to study the performance of the Fuzzy controller. The performance of the Fuzzy controller is satisfactory and can be improved. The maximum path tracking error recorded is 9 m and 7.5 m for right and left turn simulations.

**Keywords:** Path tracking · Fuzzy · Buggy car · Steering wheel · Simulation · Controller

## 1 Introduction

The autonomous vehicles firstly develop for the Moon exploration mission [1]. The Stanford cart can navigate 1 m path in 15 min. The development of the autonomous vehicle is advancing since then. The hype for the autonomous system is higher because of the introduction of the Industrial Revolution 4.0 (IR 4.0) [2]. One of the elements in IR 4.0 is the automation system. The aim of IR 4.0 is to develop a fully automated system. This situation coincides with the nature of the autonomous vehicle. The autonomous vehicle also develops in order to increase passengers' safety and comfort [3]. The advanced programmable system in the autonomous vehicle can reduce the risk for the traffic accident [4] as the number of vehicles on the road is increasing.

The development of the autonomous vehicles is actively running either by the researcher or by the automotive company [5]. Currently, an organization like Program on Advanced Technology for the Highway (PATH) [6], Intelligent Transportation Systems (ITS) [7], and Automated Highway Systems (AHS) [8] are actively developing new technology for the autonomous vehicle. Whereas, companies such as Uber [9], Waymo [10], Toyota [11], GM, Volkswagen, nuTonomy [12], and Tesla [13] are some examples that currently develop their autonomous vehicles. Some of them currently test the autonomous vehicle around the United States. Nevada, California, and Florida allow the autonomous vehicle testing in the city but with certain requirements.

The development of the Fuzzy controller starts by defining the parameter values for the inputs and output membership function. The membership function is developed based on data from the human navigation experiments [14]. The human navigation experiments are the experiments use to gather data for the human characters while driving a buggy car. There are two sub-controllers develop for the Fuzzy steering wheel control, which is the Fuzzy controller 1 (FZ1) and Fuzzy controller 2 (FZ2). The output for both controllers will be used to control the path tracking of the autonomous vehicle [15]. The path tracking errors are recorded during the simulation of the Fuzzy controller. This paper consists of experiments and simulation studies in order to develop the Fuzzy controller for the steering wheel control.

This paper consists of an abstract, introduction, methodology, result and discussion, and a conclusion. Abstract explains the brief description of the overall paper content. The introduction consists of related past research. The methodology explains the method of experiments. The methodologies section is divided into 4 subsections, which is the development of the Fuzzy controller, vehicle mathematical model, Fuzzy simulation and path tracking error measurement. Result and discussion present experiments result for the simulation result for the Fuzzy path tracking simulation. Finally, the conclusion concludes the finding from the experiments.

## 2 Methodologies

### 2.1 The Development of the Fuzzy Controller

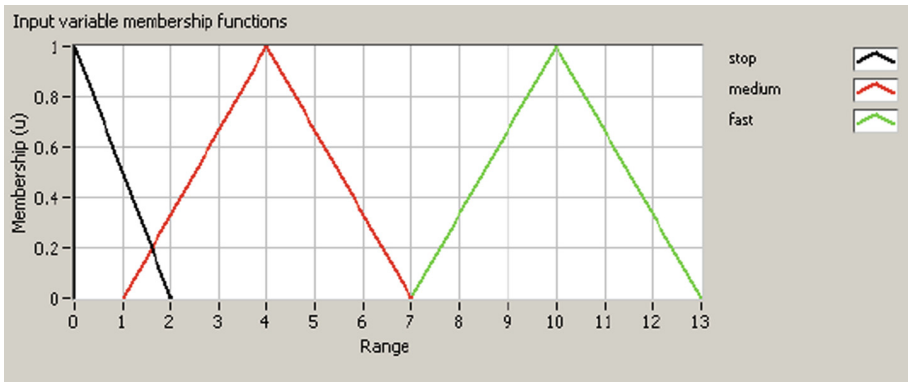
The development of the Fuzzy controller starts with data collection (human navigation experiments) from the subject while controlling the buggy car. The Human Navigation



Experiments were developed in order to gather data such as coordinate position, steering wheel angle, heading, and speed of the buggy car from each subjects while navigating through the same path. The path for the experiments consist of straight, left and right turn maneuver.

Data form Human Navigation Experiments then used for the development of the membership function for the inputs (heading, speed, steering angle, and steering wheel angle) and output (steering wheel turn angle) of the Fuzzy controller. The steering wheel turn angle is the angle used by the controller in order to correct the vehicle steering wheel angle for the path tracking. The average ( $\mu$ ) and standard deviation (std) values from the human navigation data were used for the variables development of the Fuzzy membership function. The performance of the developed Fuzzy controller was validated in the simulation.

Figure 1 shows the membership function for the speed input. There were three linguistic variables for the speed input, which is stop, medium and fast. The value for the standard deviation ( $\sigma$ ), mean ( $\mu$ ),  $\mu - \sigma$ , and  $\mu + \sigma$  values for each linguistic variable are shown in Table 1. In this paper, only one of the developed membership function is presented. Figure 2 shows the overall process for the development of the Fuzzy simulation.



**Fig. 1.** Membership function for the speed (input)

**Table 1.** The variable’s value for the speed membership function

Variables for the membership function	$\mu - \sigma$ (km/h)	$\mu + \sigma$ (km/h)	Mean, $\mu$	Std, $\sigma$
Stop	0	2	1	2
Medium	1	7	4	3
Fast	7	13	10	3

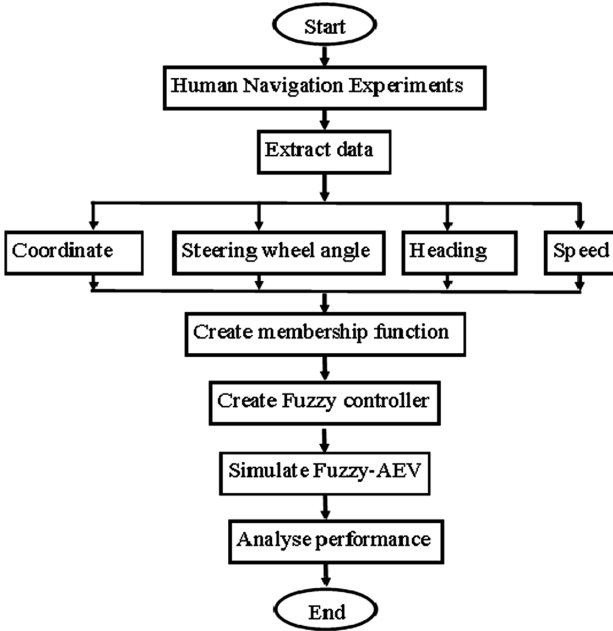


Fig. 2. Development of the Fuzzy controller

### 2.2 Mathematical Model of a Buggy Car

The two-wheel model used to visualize the force acting on a vehicle. The two-wheel model derives from Ackerman vehicle model. The two-wheel model was derived by assuming the 2 front wheels as 1 as shown in Fig. 3. It is defined as the rear wheel. The side force  $f_f$  and  $f_r$  are projected through the local coordinate (x, y), where it appears as forces  $f_x, f_y$  and the torque,  $m_z$  around the z-axis as in Eq. (1).

$$\begin{bmatrix} f_x \\ f_y \\ m_z \end{bmatrix} = \begin{bmatrix} -\sin \delta & 0 \\ \cos \delta & 1 \\ l_f \cos \delta & -l_r \end{bmatrix} \begin{bmatrix} f_f \\ f_r \end{bmatrix} \tag{1}$$

The variables  $\beta, V$ , and  $r$  caused by forces acting on the vehicle. Equations (2), (3), and (4) are the equations for vehicle three-degree of freedom in the horizontal plane shown below;

(1) Longitudinal motion

$$-mV(\dot{\beta} + r) \sin \beta + m\dot{V} \cos \beta = f_x \tag{2}$$

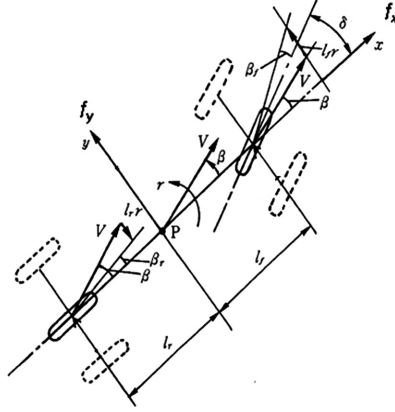


Fig. 3. Vehicular two-wheel model

(2) Lateral motion

$$mV(\dot{\beta} + r) \cos \beta + m\dot{V} \sin \beta = f_y \quad (3)$$

(3) Yaw motion

$$I\dot{r} = m_z \quad (4)$$

Equation (5) obtained from Eqs. (2) to (4)

$$\begin{bmatrix} mV(\dot{\beta} + r) \\ m\dot{V} \\ I\dot{r} \end{bmatrix} = \begin{bmatrix} -\sin \beta & \cos \beta & 0 \\ (\dot{\beta} + r) \cos \beta & \sin \beta & 0 \\ 0 & 0 & 1 \end{bmatrix} \begin{bmatrix} f_x \\ f_y \\ m_z \end{bmatrix} \quad (5)$$

The side force  $f_y$  (Eq. (6)) is known to be a nonlinear function of the tire sideslip angles  $\beta_f, \beta_r$ , in other words:

$$f_y = f_f(\beta_f) + f_r(\beta_r) \quad (6)$$

The Eqs. (5) and (6) known as a two-wheel model (Fig. 3).

### 2.3 Fuzzy Simulation

The triangle membership function is chosen for AEV fuzzy controller because of its performance [16]. The membership function for the fuzzy controller was developed as in [14] using human data while controlling the buggy car as a reference.

The "IF... THEN" rule used to develop rule-based for the Fuzzy controller. Then, the Mamdani inference systems were used to compute the output for the fuzzy controller. The value for membership functions were extracted from human navigation experiments [17].

The steering wheel angle value, coordinate, heading, and speed used as input for the Fuzzy controller. The output for the controller was steering wheel turn angle.

The Fuzzy membership function consists of four inputs with two different sets of the fuzzy controller. Fuzzy controller 1 (FZ1) used steering wheel angle and speed as the input while Fuzzy controller 2 (FZ2) used heading angle and wheel angle as input. The output for the FZ1 and FZ2 was steering wheel turn angle. The output from FZ1 and FZ2 have their own dedicated rule weights as shown in Fig. 4. The system chooses the highest rule weight among two Fuzzy controllers in order to get the suitable steering wheel turn angle.

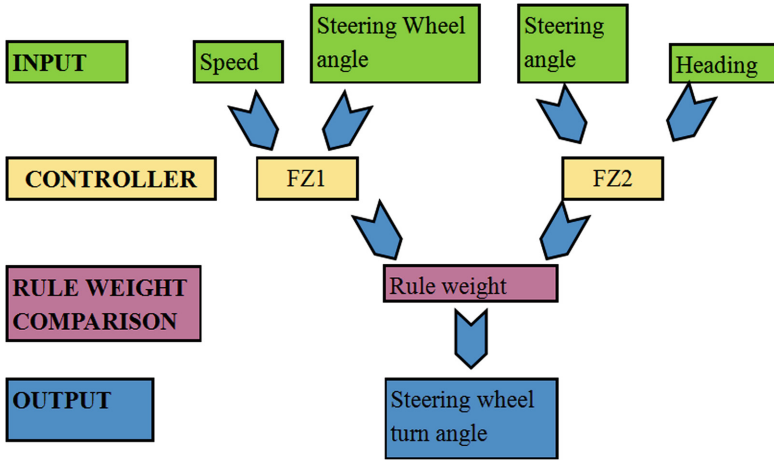


Fig. 4. The overall architecture of the developed Fuzzy controller

The performance of the Fuzzy controller was simulated in the LabVIEW program. The simulate AEV was set to follow the waypoints in two different paths, which were right and left turns. The path tracking errors were calculated during the simulation. The path tracking error was defined as the distance between the anchor points to the reference path. Figure 5 shows the five predetermined waypoints selected for



Fig. 5. Coordinate and positions for all waypoints

navigation which were Point 1 until Point 5 (P1 to P5). Each waypoint has its' dedicated longitude and latitude coordinate.

### 2.4 Path Tracking Error

The path tracking errors ( $d_p$ ) were measured from the center of gravity (CG) to the nearest reference anchor point on the path. During the simulation, path tracking error data will be recorded. The path tracking error distance calculated as in Eq. (7).

$$\text{Path tracking error, } d_p = (\text{EarthRadius}) \times \arccos \left[ \begin{array}{l} \cos(90 - \text{latitude2}) \times \cos(90 - \text{latitude1}) \\ + \sin(90 - \text{latitude2}) \times \sin(90 - \text{latitude1}) \\ \times \cos(\text{longitude2} - \text{longitude1}) \end{array} \right] \quad (7)$$

## 3 Result and Discussion

### 3.1 Steering Wheel Control Simulation

Figure 6 shows the comparison between the reference and simulation of the steering wheel control. The reference steering wheel angle is generated from the average values

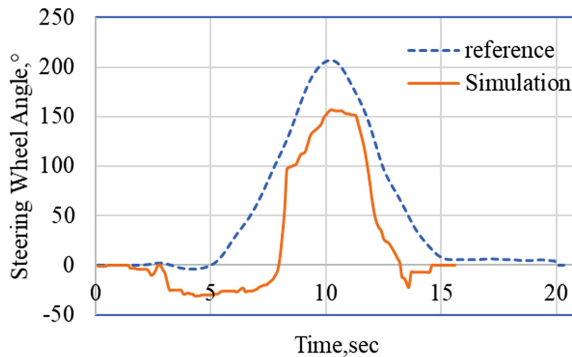


Fig. 6. Simulation versus reference steering wheel angle for right turn

of the steering wheel angle for right turn maneuver in human navigation experiments. The maximum steering wheel error between reference and simulation is 103°. The large steering wheel angle error can be reduced by improving the membership function and the rule-based in the Fuzzy controller.

Figure 7 shows the difference between reference steering wheel angles for left turn maneuver to the simulated result. The simulated steering wheel angle shows the ability of the Fuzzy controller in order to take the left turn. The angles transition is not as smooth as the reference angle, but the simulation result still manages to take the turn. The maximum steering wheel error between reference and reference is 79°.

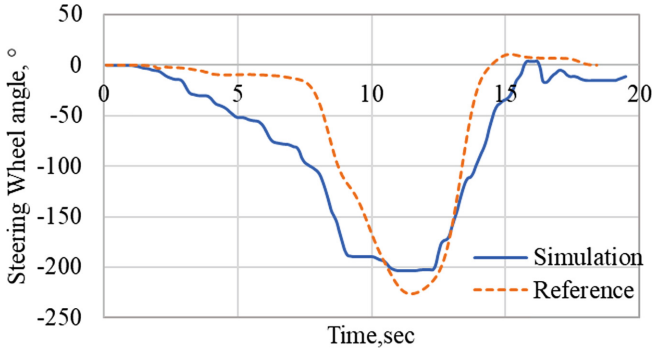


Fig. 7. Simulation versus reference steering wheel angle for left turn

### 3.2 Path Tracking Error Simulation

Figure 8 shows the simulation results of the path taken for the right turn maneuver. The maximum path tracking error for the right turn maneuver is 9 m. The simulate AEV shows high deviation at initial of the experiments but at the end of the path, the simulate AEV reach the final waypoint. Figure 9 shows the simulation results of the path taken for the left turn maneuver. The maximum recorded path tracking error for the left turn is 7.5 m. After the left turn, the simulate AEV produces high path tracking error as the vehicle try to navigate into the desired path.

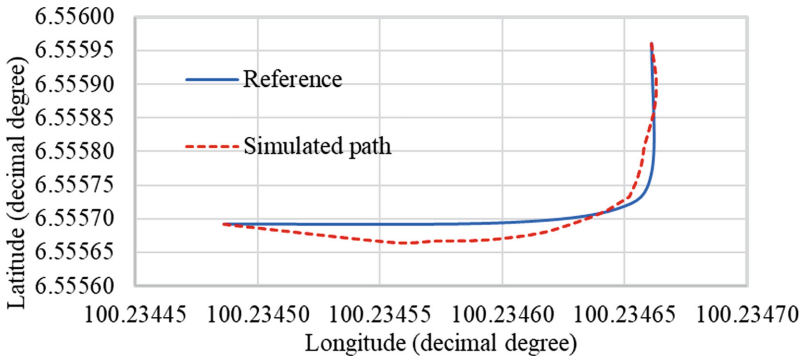
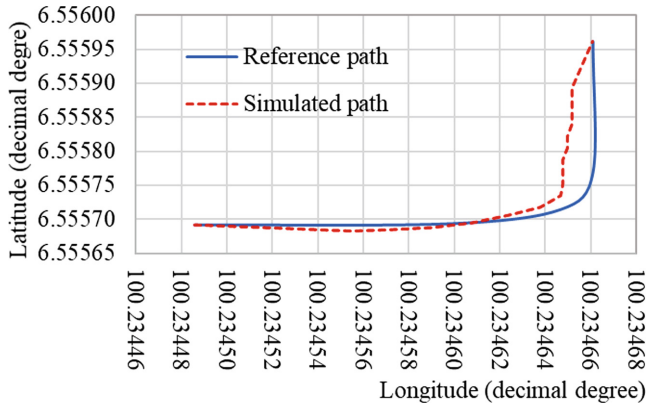


Fig. 8. Path tracking simulation for the right turn maneuver



**Fig. 9.** Path tracking simulation for the left tune maneuver

## 4 Conclusion

The performance of the developed Fuzzy controller needs to be improved. The path tracking error and steering wheel angle show a large deviation from the reference data. The path tracking error recorded the highest value in the right turn maneuver which is 9 m. The steering wheel angle error recorded the highest value during the right turn simulation which is  $103^\circ$ . The future plan is to improve the developed rule-based and collect more data from human driving experiments in order to improve the membership function.

**Acknowledgment.** Special gratitude to the members of the UniMAP Advanced Intelligent Computing and Sustainability Research Group (AICoS) and Intelligent Signal Processing (ISP). Thanks to Majlis Amanah Rakyat (MARA) and Universiti Malaysia Perlis (UniMAP) for their technical and financial support.

## References


1. Moravec, H.P.: The stanford cart and the CMU rover. *Proc. IEEE* **71**(7), 872–884 (1983)
2. Bahrin, M.A.K., Othman, M.F., Azli, N.H.N., Talib, M.F.: Industry 4.0: a review on industrial automation and robotic. *J. Teknol.* **78**(6–13), 137–143 (2016)
3. Ikram, K., et al.: Analysis of human behavior during braking for autonomous electric vehicles. In: *Advanced Structured Materials*, vol. 85, pp. 453–459 (2018)
4. Kritayakirana, K. (Mick): *Autonomous vehicle control at the limits of handling* (2012)
5. Recherches, A.D.D.E.S.: *Toward fully autonomous vehicle navigation using hybrid multi-controller architectures*, pp. 85–98 (2015)
6. Shladover, S.E., et al.: Automatic vehicle control developments in the PATH program. *IEEE Trans. Veh. Technol.* **40**(1), 114–130 (1991)
7. ITS Joint Program Office: *In: ITS Strategic Plan 2015–2019* (2015)
8. McMillin, B., Sanford, K.L.: *Automated highway systems*. In: *IEEE Potentials* (1998)

9. Florian Ranft, P.D., Martin Adler, E.G., Laza, M.: Freeing the road: shaping the future for autonomous vehicles (2016)
10. Lee, T.B.: Waymo makes history testing on public roads with no one at the wheel. In: *ars technica* (2017)
11. Kamiyama K.: Toyota. In: *The Hybrid Factory in Europe: The Japanese Management and Production System Transferred* (2004)
12. Ackerman, E: nuTonomy to Test World's First Fully Autonomous Taxi Service in Singapore This Year. In: *spectrum.ieee* (2016). [Online]. Available: <https://spectrum.ieee.org/cars-that-think/transportation/self-driving/nuTonomy-to-launch-worlds-first-fully-autonomous-taxi-service-in-singapore-this-year>. Accessed 12 Aug 2018
13. Endsley, M.R.: Autonomous driving systems: a preliminary naturalistic study of the tesla model S. *J. Cogn. Eng. Decis. Mak.* **11**(3), 225–238 (2017)
14. Halin, H., et al.: Investigation of steering wheel control of an electric buggy car for designing fuzzy controller. In: *Lecture Notes in Mechanical Engineering*, no. 9789811087875, pp. 459–468 (2018)
15. Halin, H., et al.: Simulation studies - path tracking of an autonomous electric vehicle (AEV) by using fuzzy information of speed and steering angle. In: *2018 International Conference on Computational Approach in Smart Systems Design and Applications (ICASSDA)*, pp. 1–4 (2018)
16. Zhao, J., Bose. B.K.: Evaluation of membership functions for fuzzy logic controlled induction motor drive. In: *IEEE 2002 28th Annual Conference of the Industrial Electronics Society*, pp. 229–234 (2002)
17. Halin, H., et al.: Design simulation of a fuzzy steering wheel controller for a buggy car. In: *2018 International Conference on Intelligent Informatics and Biomedical Sciences (ICIIBMS)*, vol. 3, pp. 85–89 (2018)





# The Classification of Skateboarding Trick Manoeuvres Through the Integration of IMU and Machine Learning

Muhammad Amirul Abdullah, Muhammad Ar Rahim Ibrahim,  
Muhammad Nur Aiman Bin Shapiee, Mohd Azraai Mohd Razman,  
Rabiu Muazu Musa, and Anwar P. P. Abdul Majeed 

Innovative Manufacturing, Mechatronics and Sports Laboratory,  
Universiti Malaysia Pahang, 26600 Pekan, Pahang Darul Makmur, Malaysia  
ama.jeed@ump.edu.my

**Abstract.** The evaluation of tricks executions in skateboarding is commonly carried out subjectively. The panels of judges rely on their prior experience in classifying the effectiveness of tricks performance during skateboarding competitions. This technique of classifying tricks often fell short in providing accurate evaluations during competition. Therefore, an objective and unbiased means of evaluating skateboarding tricks is non-trivial. This study aims at classifying flat ground tricks namely Ollie, Kickflip, Shove-it, Nollie and Frontside 180 through the use of inertial measurement unit (IMU) and machine learning models. An amateur skateboarder (23 years of age  $\pm$  5.0 years' experience) executed five tricks for each type of trick repeatedly on a customized ORY skateboard (IMU sensor fused) on a cemented ground. From the IMU data, a number of features were extracted and engineered. On the pretext of classification models, Support vector machine (SVM),  $k$ -NN, artificial neural networks (ANN), logistic regression (LR), random forest (RF) and Naïve Bayes (NB) was employed to identify the type of tricks performed. The results suggest that LR and NB have the highest classification accuracy with 95.0% followed by ANN and SVM together capped at 90.0% and RF and  $k$ -NN with 85.0% and 75.0%, respectively. It could be concluded that the proposed method is able to classify the skateboard tricks well. This will assist the judges in providing more accurate evaluations of trick performance as opposed to the subjective and conventional techniques currently applied.

**Keywords:** IMU sensor · Machine learning · Skateboard · Classification · Trick

## 1 Introduction

Skateboarding is an industry that is worth amounting USD 4.8 billion [1]. Moreover, in 2016, the sport was announced to debut in the 2020 Summer Olympic Games, Tokyo. Furthermore, with the recent introduction of the aforesaid sport in the 2018 Asian Games, suggests that this sport is increasingly popular and warrants the scouting of such talents at an early stage. Nonetheless, it is worth noting that the evaluation of the

tricks is often carried out subjectively by judges based on prior experience that in turn, often prone to biasness if not inaccurate evaluations.

To date, there exist limited literature with regards to the classification of the tricks Groh et al. [2] utilised five different machine learning algorithm namely k-Nearest Neighbor (kNN), Support Vector Machine with a radial-basis kernel (RBF-SVM), Linear Support Vector Machine (LSVM), Naïve Bayes (NB) and Random Forest (RF) to classify only one skateboarding trick i.e., Ollie via data obtained from both IMU sensors as well as motion capture system. Eleven skateboarders were recruited for the study (age:  $23 \pm 4$  years, height:  $179 \pm 5$  cm, stance types: 5 goofy; 6 regulars). It was shown from their investigation that the RBF-SVM yield the best classification accuracy of 89.1%.

In an earlier investigation, Groh et al. [3] carried out an investigation employing different machine learning models in classifying six tricks (Ollie, nollie, kickflip, heelflip, pop shove-it and 360-flip) through data acquired via IMU sensors as well as motion capture system. Seven experience male skateboarders (age:  $25 \pm 4$ , stand: 4 goofy, 3 regular) participated in the study. A number of time-series data features were extracted namely, mean, variance, skewness, kurtosis, dominant frequency, bandwidth, the correlation between x-y-axis, x-z-axis and y-z-axis. It was shown from the investigation that the NB and SVM obtained a relatively high classification accuracy of 97.8%.

A study was carried out by using IMU and machine learning in classifying snowboarding tricks [4], a sport which is similar in nature with skateboarding. The IMU was placed to the top right side of the snowboard using the attachment device and fit tightly with fast mounting. Eleven male snowboarders were recruited for data collection for part A (event) and B (tricks) to perform two tricks categories with three tricks classes. In the feature extraction, thresholds were defined from magnetometer signals. Nine gyroscopes signals extracted from the total rotation, rotation of half trick, rotation of s half trick. Four classifiers: NB, *k*-NN, SVM and C4.5 were compared. The Leave-One-Out cross-validation (LOOCV) technique was used to evaluate the recall and precision evaluation metrics. For event detection, recall and precision gained 99.0% and 36.8%, respectively. Conversely, for the trick category, grind obtained 96.6% and 88.5% for recall and precision, respectively. In addition, for airs trick, recall and precision gained 97.4% and 91.0%, respectively.

It is worth noting, although limited studies have been conducted with regards to skateboarding, nonetheless, other sporting activities that have used IMU sensors, as well as machine learning, has been well-documented [5–12]. This paper aims at evaluating a number of machine learning models based on selected IMU signals in classifying Ollie, Kickflip, Shove-it, Nollie and Frontside 180 tricks. This outcome of this investigation may serve useful to a more objective based evaluation by the judges as well as providing a means for skateboarders to further improve their performance.

## 2 Methodology

### 2.1 Instrumented IMU Device

Figure 1 depicts the design of the instrumented IMU device modelled using CATIA. The casing of the device is printed using a Zortrax M200 Plus 3D printer. The material selected for printing the instrumented IMU device is Acrylonitrile butadiene styrene (ABS) owing to its desirable mechanical properties, primarily high impact strength and good shock absorbing as the device will be prone to impacts and shocks from the tricks. The instrumented IMU consists of an IMU unit (MPU6050), a Bluetooth Module (HC-05), a microcontroller (Arduino Pro Mini) as well as a 3.7 V Lithium Polymer Battery. The tricks are detected based on the acceleration ( $m/s^2$ ) as well as the angular velocity ( $^\circ/s$ ) readings extracted from the accelerometer and the gyroscope, respectively. The signals captured (with a sampling time of 0.05 s) are then sent to a personal computer (PC) for further processing.

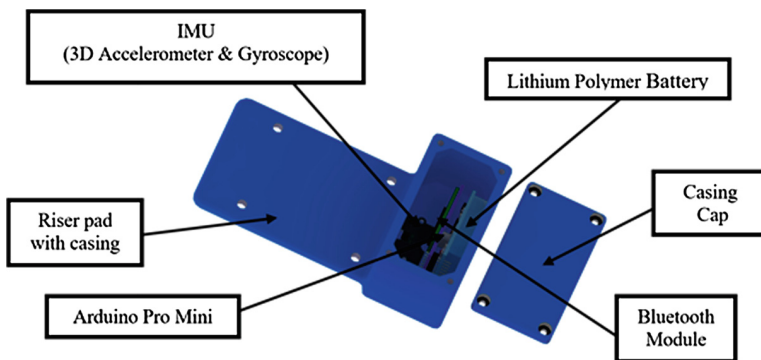


Fig. 1. Instrumented IMU device

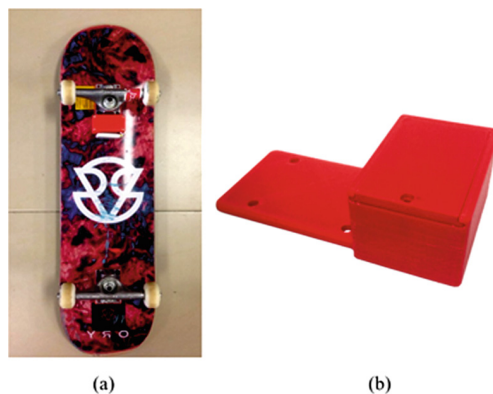


Fig. 2. The instrumented IMU attached at bottom front of the board (a) attachment of the IMU to the skateboard (b) The 3D printed IMU device

Figure 2 shows the placement of the instrumented IMU device on the skateboard. It is placed at the bottom front of the board, and the device specifically fixed behind the front truck. To ensure the stability of the device, fasteners are used to fixate the device on the board. The selection of the position of the device is non-trivial as it does not impair the movement of the skateboarders whilst performing a given trick. Moreover, the placement of the device at the location reduces the risk of the device to be damaged throughout the data collection process.

## 2.2 Data Collection

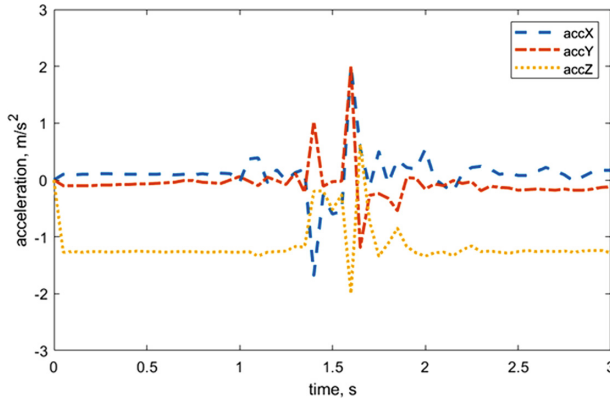
One skateboarder (23 years old, 170 cm and 54 kg) was recruited from the University Malaysia Pahang (UMP) skatepark. The skateboarder is required to perform five different tricks (as shown in Table 1) and to be repeated 5 times per trick. The tricks were chosen based on the experience of the skateboarder. The axis of the rotation is referring to the goofy stance direction. An example of the trick as well as its corresponding signals (acceleration and angular velocities) are depicted in Figs. 3, 4 and 5, respectively.

**Table 1.** List of the skateboarding tricks evaluated

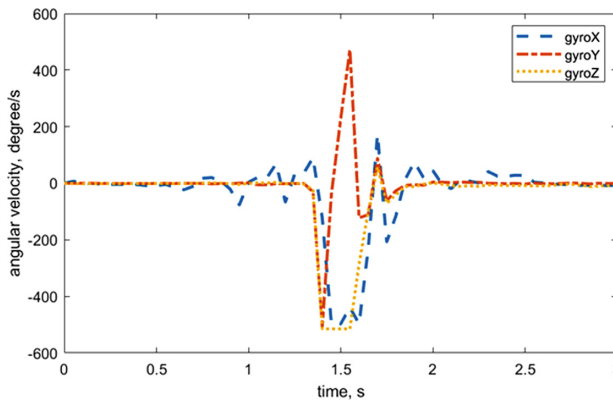
Name	Rotation (angle and axis)
Ollie (O)	Board incline about the x-axis (Approximately $45^\circ+y$ )
Nollie FS Shuvit (NFS)	Board incline about the z-axis (Approximately $180^\circ-z$ )
Frontside $180^\circ$ (FS180)	Clockwise about z-axis ( $180^\circ-z$ )
Pop Shove-it (PS)	Clockwise about z-axis ( $180^\circ+z$ )
Kickflip (K)	Clockwise about y-axis ( $360^\circ+x$ )



**Fig. 3.** An NFS trick executed



**Fig. 4.** Acceleration signals for NFS



**Fig. 5.** Gyro signals for NFS

### 2.3 Machine Learning

**Feature Selection.** The raw signals extracted from the IMU are then processed by using MATLAB 2016b in order to obtain the following statistical features, namely mean, skewness, kurtosis, peak to peak, root mean square as well as the standard deviation for all the readings (all six degrees of freedom). Once the features have been selected, further investigation on the sensitivity of the features was carried out by evaluating the information gain of the features via Orange Data Mining software V3.11.

**Classifiers.** A number of classifiers were used to investigate its effectiveness in classifying the skateboarding tricks, namely Support Vector Machine (SVM),  $k$ -Nearest Neighbour ( $k$ -Nearest Neighbour), Artificial Neural Network (ANN), Logistic Regression (LR), Random Forest (RF) and Naïve Bayes (NB). It is worth noting that

the settings of the classifiers are taken as default from the Orange platform. The classifiers were evaluated based on its classification accuracy (CA), the area under the curve (AUC), specificity, sensitivity, recall, precision as well as the F1-score which are derived from the confusion matrix. A detailed treatment of the evaluation metrics is reported in [13]. The leave-one-out cross-validation technique was employed in the present investigation.

### 3 Results and Discussion

A total of 40 trick events were carried out by the skateboarder, and the success rate of the landings was recorded. From the 40 tricks, only 20 tricks were found to be successful and the data obtained were used to develop the machine learning models. The features that were finally used upon taking into consideration of the sensitivity test via the information gain are all the six original signals as well as the inclusion of the kurtosis, mean, root mean square, peak to peak, and skewness of the x-axis acceleration readings.

It could be observed from Table 2, that the LR and the NB model yielded a classification accuracy (CA) of 95% each, followed by ANN and SVM that yielded a CA of 90.0% whilst RF and  $k$ -NN models obtained a CA of 85.0% and 75.0%, respectively. Further inspection on the confusion matrix of both the LR and NB models (Figs. 6 and 7, respectively), revealed that the misclassification (highlighted in red) recorded by the LR model came from the Ollie trick that was misclassified as Frontside 180° (FS180), whilst the misclassification recorded by the NB model was the Kickflip (K) trick that was misclassified as Pop Shove-it (PS). It could be concluded from this preliminary investigation that the combination of the selected features with different machine learning models is able to provide a reasonable classification accuracy of the performed skateboarding tricks.

**Table 2.** Evaluation of the developed classifiers

Method	AUC	CA	F1	Precision	Recall
LR	1.000	0.950	0.949	0.960	0.950
NB	1.000	0.950	0.949	0.960	0.950
ANN	1.000	0.900	0.899	0.910	0.900
SVM	1.000	0.900	0.893	0.933	0.900
RF	1.000	0.850	0.838	0.880	0.850
$k$ -NN	1.000	0.750	0.752	0.833	0.750

		Predicted					$\Sigma$
		FS180	K	NFS	O	PS	
Actual	FS180	4	0	0	0	0	4
	K	0	4	0	0	0	4
	NFS	0	0	4	0	0	4
	O	1	0	0	3	0	4
	PS	0	0	0	0	4	4
$\Sigma$		4	3	4	4	5	20

Fig. 6. Confusion matrix of the Logistic Regression model developed

		Predicted					$\Sigma$
		FS180	K	NFS	O	PS	
Actual	FS180	4	0	0	0	0	4
	K	0	3	0	0	1	4
	NFS	0	0	4	0	0	4
	O	0	0	0	4	0	4
	PS	0	0	0	0	4	4
$\Sigma$		4	3	4	4	5	20

Fig. 7. Confusion matrix of the Naïve Bayes model developed

## 4 Conclusion

In this preliminary investigation, an offline skateboarding tricks classification system was developed. It was shown from the investigation that the selection of the features is non-trivial in providing a reasonably accuracy classification of the evaluated skateboarding tricks. It was also demonstrated that both the LR as well as the NB model yielded a high CA of 95%. Future study will be carried out by including more subjects, engineering different features, as well as performing hyperparameter optimisation on different machine learning models. The preliminary results further suggest the applicability of the proposed system in providing an objective based judgement on skateboarding tricks. This will assist the judges in providing a more accurate evaluation of trick performance as opposed to the subjective and conventional techniques currently applied in this sport.

## References

1. Corrêa, N.K., de Lima, J.C.M., Russomano, T., dos Santos, M.A.: Development of a skateboarding trick classifier using accelerometry and machine learning. *Res. Biomed. Eng.* **33**, 362–369 (2017)
2. Groh, B.H., Fleckenstein, M., Kautz, T., Eskofier, B.M.: Classification and visualization of skateboard tricks using wearable sensors. *Pervasive Mob. Comput.* **40**, 42–55 (2017)
3. Groh, B.H., Kautz, T., Schuldhuis, D., Eskofier, B.M.: IMU-based trick classification in skateboarding. In: *KDD Workshop on Large-Scale Sports Analytics*, p 17 (2015)
4. Groh, B.H., Fleckenstein, M., Eskofier, B.M.: Wearable trick classification in freestyle snowboarding. In: *2016 IEEE 13th International Conference on Wearable and Implantable Body Sensor Networks (BSN)*, pp 89–93. IEEE (2016)
5. Brock, H., Ohgi, Y.: Assessing motion style errors in Ski jumping using inertial sensor devices. *IEEE Sens. J.* **17**, 3794–3804 (2017). <https://doi.org/10.1109/jsen.2017.2699162>
6. Wang, Y., Chen, M., Wang, X., Chan, R.H.M., Li, W.J.: IoT for next-generation racket sports training. *IEEE Internet Things J.* **5**, 4558–4566 (2018)
7. Gellaerts, J., Bogdanov, E., Dadashi, F., Mariani, B.: In-field validation of an inertial sensor-based system for movement analysis and classification in ski mountaineering. *Sensors* **18**, 885 (2018)
8. Kos, M., Kramberger, I.: Tennis stroke consistency analysis using miniature wearable IMU. In: *2018 25th International Conference on Systems, Signals and Image Processing (IWSSIP)*, pp. 1–4. IEEE (2018)
9. McGrath, J.W., Neville, J., Stewart, T., Cronin, J.: Cricket fast bowling detection in a training setting using an inertial measurement unit and machine learning. *J. Sports Sci.* **37**, pp. 1–7 (2018)
10. Ahamed, N.U., Kobsar, D., Benson, L., Clermont, C., Kohrs, R., Osis, S.T., Ferber, R.: Using wearable sensors to classify subject-specific running biomechanical gait patterns based on changes in environmental weather conditions. *PLoS ONE* **13**, e0203839 (2018)
11. Worsey, M.T.O., Espinosa, H.G., Shepherd, J.B., Thiel, D.V.: Inertial sensors for performance analysis in combat sports: a systematic review. *Sports* **7**, 28 (2019)
12. Musa, R.M., Majeed, A.P.P.A., Taha, Z., Chang, S.W., Nasir, A.F.A., Abdullah, M.R.: A machine learning approach of predicting high potential archers by means of physical fitness indicators. *PLoS ONE* **14**, e0209638 (2019)
13. Taha, Z., Musa, R.M., Abdul Majeed, A.P.P., Alim, M.M., Abdullah, M.R.: The identification of high potential archers based on fitness and motor ability variables: a support vector machine approach. *Hum. Mov. Sci.* **57**, 184–193 (2018). <https://doi.org/10.1016/j.humov.2017.12.008>





# Predicting Serious Injuries Due to Road Traffic Accidents in Malaysia by Means of Artificial Neural Network

Nurul Qastalani Radzuan<sup>1</sup>, Mohd Hasnun Arif Hassan<sup>1</sup>(✉),  
Anwar P. P. Abdul Majeed<sup>1</sup>, Rabiuh Muazu Musa<sup>1</sup>,  
Mohd Azraai Mohd Razman<sup>1</sup>, and Khairil Anwar Abu Kassim<sup>2</sup>

<sup>1</sup> Innovative Manufacturing, Mechatronics and Sports Laboratory (iMAMS),  
Faculty of Mechanical and Manufacturing Engineering, Universiti Malaysia  
Pahang, 26600 Pekan, Pahang, Malaysia

mh.asnun@ump.edu.my

<sup>2</sup> Malaysian Institute of Road Safety Research (MIROS), Lot 125-135,  
Jalan TKS 1, Taman Kajang Sentral, 43000 Kajang, Selangor, Malaysia

**Abstract.** Malaysia has recorded a steady increase in the number of road traffic accidents from year to year at an alarming rate of 5%. Serious injuries due to the accidents, which could lead to permanent disability, might cause a long-term problem to the nation economy-wise. Predicting the number of serious injury cases in the future is important in understanding the trend of road traffic accidents to help policymakers in proposing a countermeasure. Time-series model has been employed to predict the occurrence of road traffic crashes including fatalities. Nonetheless, the prediction of serious injury cases, which should not be taken lightly due to its potential impact, has not been proposed especially with regards to Malaysian road traffic accident data. This study attempts to employ artificial neural networks (ANN), a machine learning algorithm, to predict the number of serious injury cases in Malaysia based on the road traffic accident data of the past 20 years. Machine learning has increasingly been adopted in recent years owing to its ability to predict as well as catering for the non-linear behaviour of the data examined. A single-hidden ANN model was developed based on seven features, namely the number of registered vehicles, population, length of federal road, length of FELDA road, length of federal institutional road, length of federal territory road, and length of the expressway in order to predict the number of serious injuries. It was established from the present investigation that the developed ANN model is capable to predict the number of serious injuries from 1997 until 2017 with a mean absolute percentage error of only 3%. This demonstrates the capability of the developed machine learning in road traffic accident prediction, and it could be useful in outlining an action plan to mitigate the number of serious injuries in Malaysia.

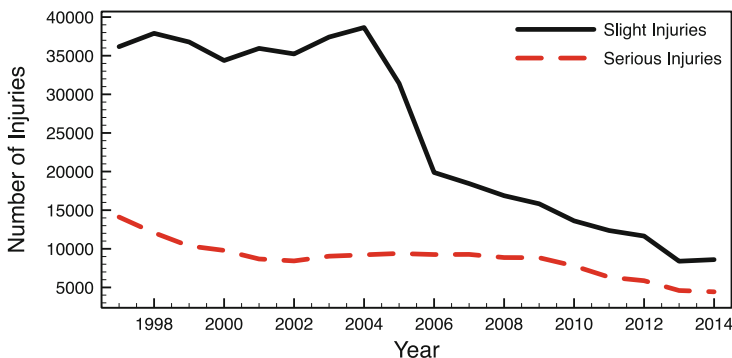
**Keywords:** Road traffic accident · Prediction · Serious injuries · Machine learning · Artificial neural network

## 1 Introduction

The number of registered vehicles in Malaysia shows an increasing trend every year. A published data reveals that since 1997, there is a steady increase of the number of registered vehicles in Malaysia at an annual rate of 7% [1]. This is in tandem with the increase of population in Malaysia, which also shows a steady increasing trend at 2% each year since 1997. With the increase of vehicles on Malaysian road, the number of road traffic accidents demonstrates a steady increase as well. At an average rate of 5% per year, more than 500,000 road crashes were recorded in 2017 on Malaysian road [1]. This is an alarming statistic that warrants an appropriate action plan.

There is a total of 380,700.83 km of road network in Malaysia as of 2017 [2] and the road length could increase due to the ongoing road construction in several states. The road network includes federal road (FedR), Federal Land Development Authority (FELDA) road (FELR), federal institutional road (FIR), industrial road (IR), federal territory road (FTR), and expressway (Ex). Each type of road has its own attributes and level of safety features to reduce road conflict and further reducing accident risk. For instance, on the expressway, the speed limit is 110 km/h and vehicles are prohibited from making a U-turn in the middle of the road. Meanwhile, the federal institutional road is commonly seen at institutional facilities such as universities, military bases, and airports which has a low-speed limit and almost no access control.

Injuries due to road traffic crashes vary from slight injuries, serious injuries, and the worst of all, deaths. Figure 1 depicts the trend of slight injuries and serious injuries due to road traffic accidents in Malaysia from 1997 until 2014 [1]. It is observed that slight injury cases demonstrate a relatively substantial decrease as compared to serious injury cases. This indicates that the number of less dangerous crashes has decreased, which might be attributed to the increase of driving skills among Malaysians, or to the road safety campaigns conducted by the government agencies. Nonetheless, the number of serious injury cases, although reducing every year, is not at a healthy rate. Although this is not fatal, serious injuries due to road traffic accidents should not be taken lightly since these injuries might result in permanent disabilities, which in the end will affect the national economic growth [3].



**Fig. 1.** Slight and serious injury cases due to road crashes in Malaysia from 1997 until 2014 [1]

The future prediction of the number of serious injury cases could facilitate governmental agencies such as the Malaysian Institute of Road Safety Research (MIROS) to come up with an action plan to further reduce the number of serious injuries. Understanding how and by how many the serious injury cases will change and grow in the future is a crucial step before planning a countermeasure. Time-series model has been used in predicting road traffic accidents [4]. One of the most commonly used time-series models is the autoregressive integrated moving average (ARIMA). ARIMA model was employed by Radin Umar [5] to predict road deaths in Malaysia in the year 2000. This model was updated and further used by Sarani et al. [6] to predict Malaysian road deaths in 2020. Nonetheless, there has been no model developed to predict the number of serious injury cases due to road traffic accidents, especially in Malaysia.

Machine learning is a subset of artificial intelligence, whose application has become increasingly popular, primarily due to its ability to learn non-linear behaviour of data. Various machine learning algorithms have been applied in many fields such as in production, sports and even in engine performance [7–9]. Nonetheless, the application of machine learning in predicting road traffic accident is still in its infancy. Therefore, the objective of this study is to employ artificial neural networks (ANN) to predict the number of serious injury cases due to road traffic accidents on Malaysian road. Subsequent section details the development and validation of the model. This is followed by discussing the prediction of serious injury cases using the developed ANN model.

## 2 Methodology

This section discusses the general description of the methodology of the study and the data used. The analysis was conducted using MATLAB® 2016b. The following subsections cover the dataset used and the development of the ANN model.

### 2.1 Dataset

The road length, as well as the population and number of registered vehicles, were obtained from Malaysia Public Work Department (JKR) [6] and Road Safety Department of Malaysia (JKJR), respectively [1]. We attempted to develop an ANN model to predict the number of serious injuries based on Malaysian traffic accident scenario. Published data from 1997 to 2017 was used to perform the analysis in predicting the number of serious injuries (SeIn). The dataset from 1997 to 2014 was used as training data while the rest is used for validation. The SeIn model was developed based on seven independent variables while the number of serious injuries cases is the parameter to be predicted. Table 1 shows the correlation of the data with each other, where *Reg.Veh.* is the number of registered vehicles, *Pop.* is the number of population, *FedR* is the length of road network includes federal road, *FELR* is the length of the Federal Land Development Authority road, *FIR* is the length of the federal

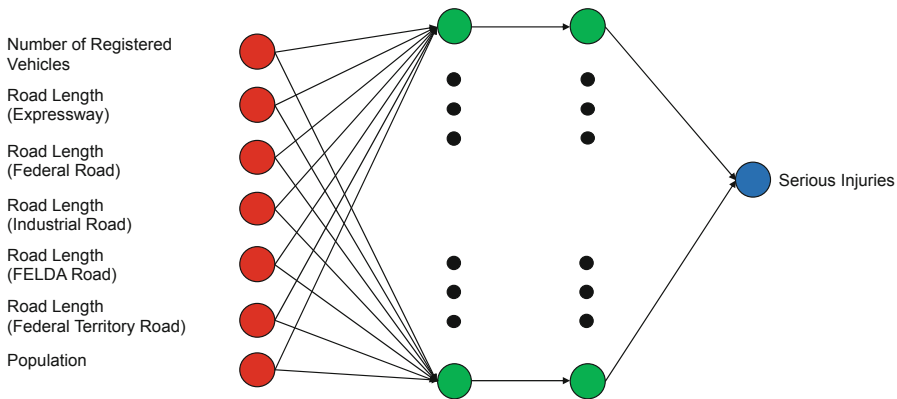
institutional road, *IR* is the length of the industrial road, *FTR* is the length of the federal territory road, *Ex* is the length of expressway, and *SeIN* is the number of serious injuries. There is a very low correlation between the federal institutional road (FIR) and the number of serious injuries. This is shown by the p-value of 0.5868 which is larger than 0.05 (p-value > 0.05). Hence, FIR was neglected in the development of the prediction model.

**Table 1.** Correlation of the features and the parameter of interest (SeIn)

Variable	Reg.veh.	Pop.	FedR	FELR	FIR	IR	FTR	Ex	SeIn
<i>Reg.veh.</i>	1.0000								
<i>Pop.</i>	0.9932	1.0000							
<i>FedR</i>	0.9638	0.9788	1.0000						
<i>FELR</i>	0.8618	0.8960	0.8782	1.0000					
<i>FIR</i>	0.2926	0.2442	0.1971	-0.1373	1.0000				
<i>IR</i>	0.7694	0.8102	0.8064	0.9248	-0.2585	1.0000			
<i>FTR</i>	0.9143	0.8752	0.8427	0.6890	0.3764	0.5661	1.0000		
<i>Ex</i>	0.9141	0.9130	0.8951	0.7911	0.3089	0.7432	0.7941	1.0000	
<i>SeIn</i>	-0.8795	-0.8860	-0.9108	-0.7968	-0.1373	-0.6417	-0.8015	-0.7857	1.0000
<i>p-value</i>	0.0000	0.0000	0.0000	0.0001	0.5868	0.0041	0.0001	0.0001	

### 2.2 ANN Model Development

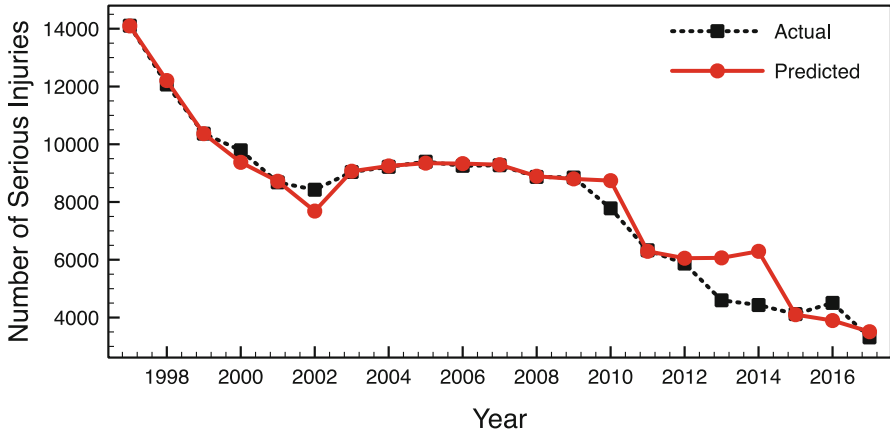
The present investigation employed a single hidden layer feed-forward ANN model. The network topology of the developed Multiple-Input Single-Output (MISO) ANN model is 7:10:1, in which ten hidden neurons was found to be suitable to provide a reasonably accurate model. The activation function and the learning algorithm utilised in the study are tangent-sigmoid and Levenberg–Marquardt, respectively. A leave-one-out cross-validation technique was employed owing to the number of data used. Figure 2 illustrates the topology of the ANN model developed.



**Fig. 2.** The topology of the developed ANN model

### 3 Results and Discussion

An ANN model was developed to predict serious injury cases in Malaysia using seven features: the number of registered vehicles, population, length of federal road, length of FELDA road, length of federal institutional road, length of federal territory road, and length of the expressway.



**Fig. 3.** Actual and predicted serious injury cases in Malaysia from 1997 until 2017

Figure 3 shows the comparison between the actual data of serious injury cases and the predicted number of serious injury cases from 1997 until 2017. The accuracy of the prediction was evaluated using the mean absolute error (MAE), mean absolute percentage error (MAPE), root mean square error (RMSE) and coefficient of determination (R-Squared) as shown in Table 2.

**Table 2.** Performance evaluation of the developed ANN model

Evaluation matrix	ANN model
MAE	291.62
MAPE	5%
RMSE	591
R-Squared	95%

It is evident from Fig. 3 and the performance evaluation (Table 2) that the developed model was able to predict the number of serious injuries due to road traffic accident with a reasonably high accuracy (R-Squared of 95%). We speculate that the accuracy could be further increased if more features such as types of vehicle, gender of the driver, among others, are included in the model. Future study will look into other features that might be contributed to the number of slight injury cases. In addition, the evaluation of different activation functions, as well as learning algorithms will be investigated towards improving the efficacy of the prediction.

## 4 Conclusion

Serious injuries due to road traffic accidents might result in permanent disabilities, which in turn could affect the economic growth of a country. In Malaysia, the trend of serious injury cases is declining, nonetheless at a slow rate. It is important to understand how the number of serious injuries changes over time to propose an action plan. This is where statistical prediction plays an important role. In this study, we implemented a machine learning technique known as Artificial Neural Networks to predict the number of serious injuries due to road traffic accident. Seven features were used in developing the model, with the number of serious injuries as the target parameter to be predicted. The model was found to be able to predict the number of serious injuries reasonably well, with 95% accuracy. This study demonstrates the capability of machine learning in predicting the occurrence of road traffic accident and the severity of the injury.

**Acknowledgements.** The authors would like to acknowledge ASEAN NCAP, FIA Foundation, Global NCAP, OEMs, Malaysian Institute of Road Safety Research (MIROS) and the Society of Automotive Engineers Malaysia (SAE Malaysia) for funding this study under the ASEAN NCAP Holistic Collaborative Research (ANCHOR II) grant. Also, the authors are thankful to the Universiti Malaysia Pahang for providing the facilities to conduct the study.

## References

1. Jabatan Keselamatan Jalan Raya Malaysia: Buku Statistik Keselamatan Jalan Raya (2018)
2. Jabatan Kerja Raya: Statistik Jalan Edisi 2016. Jabatan Kerja Raya, Kuala Lumpur (2016)
3. Olsson, M., Järbrink, K., Divakar, U., Bajpai, R., Upton, Z., Schmidtchen, A., Car, J.: The humanistic and economic burden of chronic wounds: a systematic review. *Wound Rep. Reg.* **27**(1), 114–125 (2019)
4. Mcleod, A.I., Vingilis, E.R.: Power computations in time series analysis for traffic safety interventions. *Accid. Anal. Prev.* **40**(3), 1244–1248 (2008)
5. Radin Umar, R.S.: Model kematian jalan raya di Malaysia: unjuran tahun 2000. *Pertanika J. Sci. Technol.* **6**(2), 107–119 (1998)
6. Sarani, R., Syed Mohamed Rahim, S.A., Mohd Marjan, J., Wong, S.V.: Predicting Malaysian Road Fatalities for year 2020, MRR 06/2012, Malaysian Institute of Road Safety Research, Kuala Lumpur (2012)
7. Musa, R.M., Majeed, A.P.P.A., Taha, Z., Siow, W.C., Ab Nasir, A.F., Abdullah, M.R.: A machine learning approach of predicting high potential archers by means of physical fitness indicators. *PLoS ONE* **14**(1), e0209638 (2019)
8. Taha, Z., Musa, R.M., Abdul Majeed, A.P.P., Abdullah, M.R., Ab Nasir, A.F., Hassan, M.H. A.: Classification of high performance archers by means of bio-physiological performance variables via k-nearest neighbour classification model. In: Hassan, M. (ed.) *Intelligent Manufacturing and Mechatronics. Lecture Notes in Mechanical Engineering*. Springer, Singapore (2018)
9. Yusri, I.M., Majeed, A.A., Mamat, R., Ghazali, M.F., Awad, O.I., Azmi, W.H.: A review on the application of response surface method and artificial neural network in engine performance and exhaust emissions characteristics in alternative fuel. *Renew. Sustain. Energ. Rev.* **90**, 665–686 (2018)

# **Instrumentation and Controls**



# Welding Quality Assessment Using Waveform Signal Analysis of Vibration

A. M. Najib<sup>1</sup>(✉), E. R. Imam Fauzi<sup>2</sup>, F. F. Kamarul Bahrin<sup>1</sup>,  
and N. D. Zainudin<sup>1</sup>

<sup>1</sup> Fakulti Kejuruteraan Pembuatan, Universiti Teknikal Malaysia Melaka (UTeM), Hang Tuah Jaya, 76100 Durian Tunggal, Malacca, Malaysia  
najibali@utem.edu.my

<sup>2</sup> Manufacturing Engineering Group, School of Mechanical Engineering, Universiti Sains Malaysia (USM), 14300 Nibong Tebal, Penang, Malaysia

**Abstract.** The present study aims to investigate the quality of welding coupons in terms of mechanical strength by using the waveform signal analysis of time domain. The custom designed mechanical vibrator system combined with two sensor array was served to perform the tests and visualizing their results. The obtained vibration waveform from the mechanical vibration test has been compared with tensile test results. From the vibration waveform, peak to peak value is chosen to represent the waveform size, while for the tensile test result, maximum force is used to represent the strength of welding structure. The vibration waveform value then is compared with maximum force to find the relationship. From the analysis, a correlation between vibration signal and tensile strength was developed. This result agreed well with the early hypothesis of that a higher vibration waveform signal indicates a poor weld quality while the lower vibration waveform signal represents a sound quality. However, a statistical analysis reveals that there is no strong correlation between the vibration signal and mechanical strength. Despite, the acquired waveform signal was not giving an obvious indication of the hidden defects as well as its location due to the high noise level. Contradiction in results may arise due to the unbalanced data treatment and insufficient number of specimens. This study of the signal analysis method as a pre-assessment technique to quantify a weld quality, is important in the attempt to create a system monitoring for welding structure with using non-destructive test with new approach.

**Keywords:** Signal waveform · Welding quality · Tensile strength · Non-destructive test

## 1 Introduction

In order to be kept in deterministic boundaries of production results, quality control and monitoring system is essential. The quality assessment can be done during the pre-process stage, in-process stage or post-process stage. Study of the quality control of structure system has been attracted many researchers to be active in this field due to our society often shocked by the violent failure of a structural system. For the past 10 years have seen a rapid increase in the amount of research related to structure study. The



increased interest in structure study and its relation to safety and economy that has motivated this study become essential in the industries.

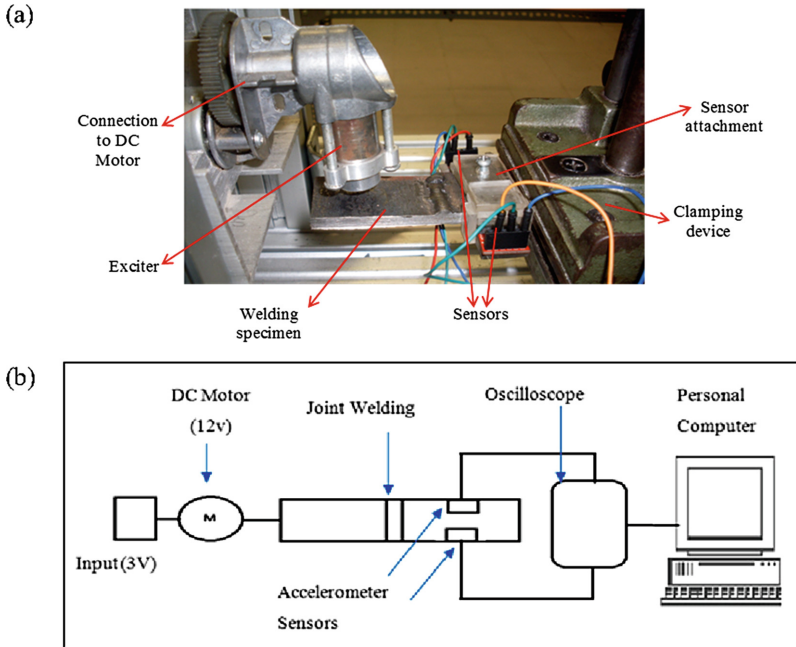
In monitoring the structural integrity of welding components, attempts have been made to find the potentially fast, accurate and robust method of detecting weld defects and assessing the overall weld joint quality. Direct quality assessment using non-destructive test such as radiographic testing, magnetic particle testing, liquid penetrant testing, and ultrasonic testing was widely used as conventional method in identifying both surface and sub-surface welding deficiencies. New approaches by using sound and vibration signal can be considered as unique and simple method in this field. In a study by [1], new approaches of weld quality assessment were developed by using the acceleration-time data obtained from the piezoelectric accelerometers. They introduced the used of arrangement of time series models and exponentially weighted moving average (EWMA) control charts to observe the variation of the selected features. In case of real-time monitoring system, an attempt has been made to develop weld quality inspection by using servo encoder in resistance spot welding [2]. The servo gun spot welding system has the advantages of precise control and feedback of electrode position and pressure. For that reason, it provides the possibility of controlling and inspecting weld quality online, thus it can accurately distinguish weld failures. Meanwhile, the applications of the wavelet signal information [3–5], acoustic emission technique [6–8] and vibration signal analysis [9] in detecting weld failures have shown great potential in promoting the non-contact measurement. In a work related to the online monitoring using sound signal [10], a discrete wavelet transformation was used to analyze the acquired sound during the welding process. Significant results were obtained in revealing the hidden information associated with the existence of weld defects and irregularities.

In this present work, the strength of welded coupons was determined by using the waveform signal analysis of time domain. A series of experimental analysis was successfully demonstrated to investigate the correlation between the vibration signal and mechanical strength of welded carbon steel specimens. This study of the signal analysis method as a pre-assessment technique to quantify a weld quality, is important in the attempt to create a system monitoring for welding structure with using non-destructive test with new approach.

## 2 Experimental Procedure

### 2.1 Designs for Experimental Setup

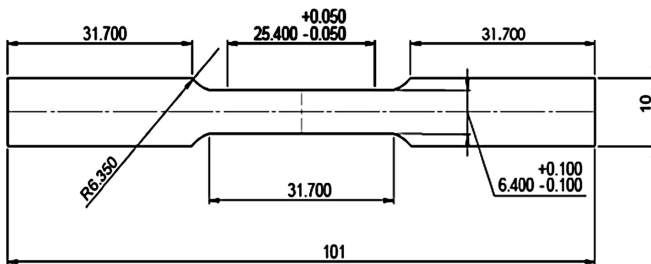
The mechanical vibration test system was designed to perform the vibration testing for the welding specimens. The system consists of 6 V DC motor and exciter that has been attach to the welding specimen for continuous vibration. Two-sensor array consisted of accelerometer (SN-ADXL335) with 3 V nominal power, was attached together on the plate to detect the vibration signal and sends the signal to the data acquisition system for analysis. Figure 1 shows the experimental setup for the vibration system.



**Fig. 1.** (a) Experimental setup (b) Schematic diagram for the mechanical vibration system

## 2.2 Uniaxial Tensile Test

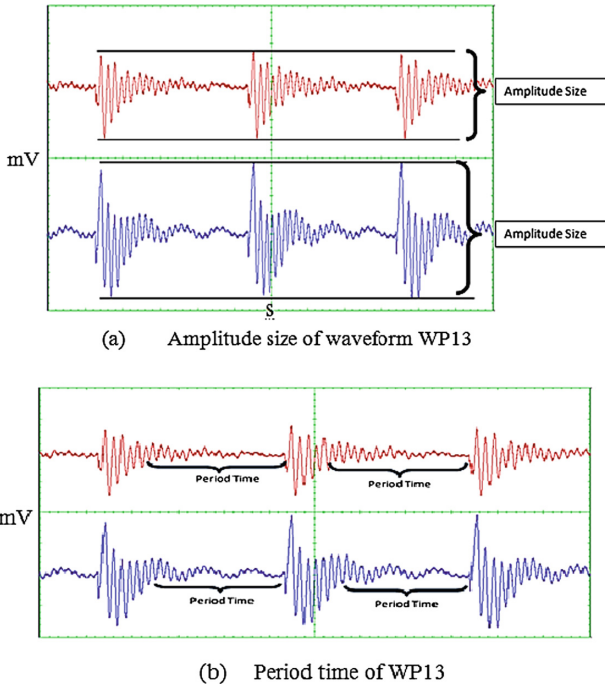
Static tensile tests of the components were conducted at ambient temperature using a UTM Shimadzu testing machine. The displacement rate was 10 mm/min for all samples, in accordance to the ASTM E8 standard recommendation. The elongation and displacement were recorded accordingly. Figure 2 shows the dimension of a dogbone specimen, which is in accordance to the ASTM E8 [11]. The welded structure specimens were cut perpendicular to the weld line so that the weld was centered in the section, and the loading was normal to the welding direction. Specimens were cut using wire electrical discharge machining (EDM). To avoid any influence of surface roughness on plastic behaviour, none of the samples were subjected to surface polishing.



**Fig. 2.** Dimension of dogbone specimen for tensile test

### 2.3 Data Analysis

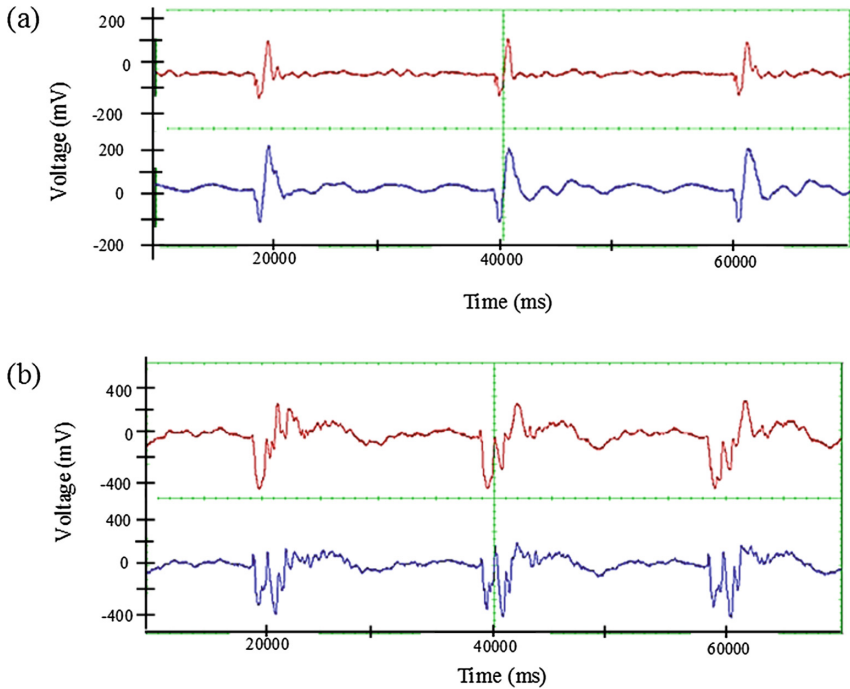
To ensure consistency and validity of data measurement, a specimen with sound weld quality and without any surface defect was obtained for a reference signal. Two vibration signals were detected from each specimen, due to the different location of sensor. Almost similar signals were produced from each channel, CH1 and CH2. The entire recorded signal was in time domain. The amplitude size was measured in terms of peak to peak amplitude in a particular period time as shown in Fig. 3.



**Fig. 3.** Obtained vibration signal from the experiment in terms of (a) amplitude size (b) period time

### 3 Results and Discussion

During the experiment, a total of 40 samples were taken for diagnosis. Most of them were in good conditions, while only several of them were in faulty condition. Figure 4 depicted the vibration signal obtained in both conditions, good and faulty. From the figure, it can be clearly seen that a high value of peak to peak amplitude was obtained from the specimen with faulty condition, while moderate amplitude was produced from the good condition specimen. This finding was in a good agreement with the early hypothesis.



**Fig. 4.** Vibration signal obtained from (a) good condition weld coupon (b) faulty condition weld coupon

However, out of 40 samples, only 15% of them were considered in faulty condition. The classification of the specimens was done taking into account of the reference sample, by assuming that the reference sample was in good condition. The reference sample has a maximum tensile force of 48.13 kN, which accounting for 2673.89 MPa of maximum tensile strength. This sample was considered as a sound welding coupon due to the maximum increase of strength value (safety factor,  $\gamma = 6.08$ ), which is higher than recommended value. In accordance to the Eurocode Standard [12], the minimum recommended safety factor for welded joint should be 1.25. Therefore, a welding specimen can be categorised as in a good condition when the safety factor is achieving 1.25 or higher, while a lower safety factor (lower than 1.25) can be considered as a defect specimen.

To evaluate the weld quality of the specimens, the vibration signal was compared to the maximum force obtained during tensile test. From a regression analysis, a relationship can be drawn as follows:

$$y = 370.2 + 0.971x \quad (1)$$

where  $y$  represents the vibration signal in unit mV and  $x$  is the maximum force in kN. Figure 5 depicted the fitted line plot of the vibration signal and maximum force. From the figure, no clear correlation can be seen. Additionally, the  $R^2$  value seems too small reflecting that the variability in the data can be explained partially. Clearly, the quoted level of significance here (95% Confidence Interval and 95% Prediction Interval) applies only for general contrast in the treatment without taking into account of variability in the entire model. The normal probability plot is shown in Fig. 6(a). The general impression of the error distribution is approximately normal with the probability plot to bend down slightly on the left side and upward slightly on the right side. This implies that the presence of outlier does not affect the analysis. However, the plot of residuals in Fig. 6(b) shows apparent pattern, indicating that the homogeneity of variances is violated. This may have attributed from the unbalanced design and unequal sample size.

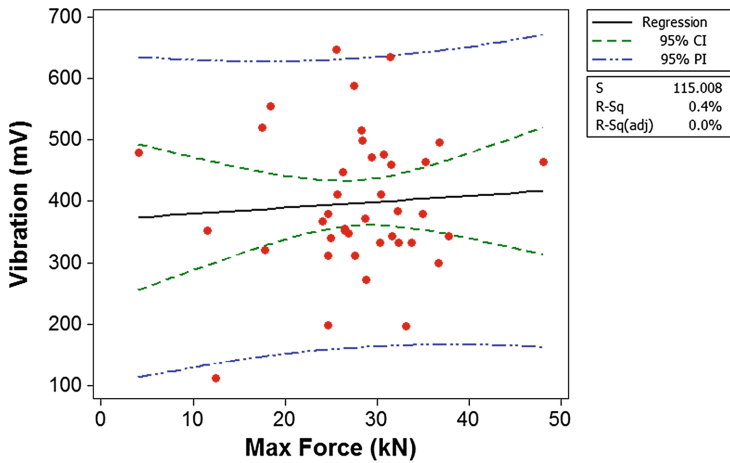


Fig. 5. Fitted line plot of vibration signal and maximum force

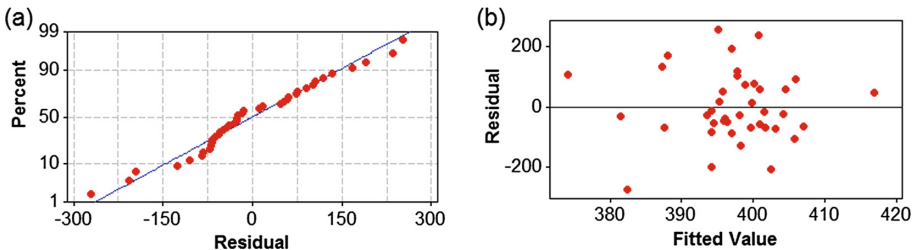


Fig. 6. (a) Normal probability plot of residuals (b) Plot of residuals versus fitted values

## 4 Conclusion

This study has demonstrated an attempt of using vibration signal to investigate the quality of welding coupons in terms of mechanical strength. Correlation between vibration signal wavelet and mechanical strength was analysed using ANOVA. Experimental results reveal that higher peak to peak amplitude of vibration signal was obtained from a good quality weld joint specimen. While a specimen with faulty condition produced lower amplitude value. This finding was in a good agreement with the early hypothesis. However, from the statistical analysis, no strong evidence of relationship can be drawn between the vibration signal and mechanical strength of welded coupons. This result may arise due to the unbalanced analysis design and insufficient sample size. Thus, further expansion of the design basis with more balanced data is essential to improve the analysis.

**Acknowledgements.** The authors are grateful to the Universiti Teknikal Malaysia Melaka (UTeM) for the technical support. This research was partially funded by UTeM through research grant PJP/2018/FKP(5A)9/S01585.

## References

1. Rao, P., Ratnam, C.H.: Damage identification of welded structures using time series models and exponentially weighted moving average control charts. *Jordan J. Mech. Ind. Eng.* **4**, 701–710 (2010)
2. Xinmin, L., Xiaoyun, Z., Yansong, Z., Guanlong, C.: Weld quality inspection based on online measured indentation from servo encoder in resistance spot welding. *IEEE Trans. Instrum. Meas.* **56**, 1501–1505 (2007)
3. Das, B., Pal, S., Bag, S.: Defect detection in friction stir welding process using signal information and fractal theory. *Procedia Eng.* **144**, 172–178 (2016). <https://doi.org/10.1016/j.proeng.2016.05.021>
4. Mariusz, Z., Bogdan, Z., Michal, L.: The use of modal analysis in the evaluation of welded steel. In: *Studies and Proceedings Polish Association for Knowledge Management, Poland* (2016)
5. Szeleziński, A., Muc, A., Murawski, L.: 2D and 3D time-frequency dynamic characteristics in the quality assessment of welded joints. *Sci. J. Marit. Univ. Szczec.* **56**(128), 41–46 (2018). <https://doi.org/10.17402/312>
6. Wuriti, G.S., Thomas, T., Chattopadhyaya, S.: Prediction of tensile failure load for maraging steel weldment by acoustic emission technique. In: *Advances in Manufacturing Engineering and Materials*. Springer, Cham (2019)
7. Droubi, M.G., Faisal, N.H., Orr, F., Steel, J.A., El-Shaib, M.: Acoustic emission method for defect detection and identification in carbon steel welded joints. *J. Constr. Steel Res.* **134**, 28–37 (2017). <https://doi.org/10.1016/j.jcsr.2017.03.012>
8. Chai, M., Qin, M., Zheng, Y., Hou, X., Zhang, Z., Cheng, G., Duan, Q.: Acoustic emission detection during welding residual stresses release in 2.25 Cr1Mo0.25V steel welds. *Mater. Today Proc.* **5**, 13759–13766 (2018). <https://doi.org/10.1016/j.matpr.2018.02.016>
9. Deac, S., Crăștiu, I., Vodă, M., Simoiu, D., Nyaguly, E., Bereteu, L.: Defects detection on the welded reinforcing steel with self-shielded wires by vibration tests. In: *MATEC Web of Conferences*, vol. 126, p. 01007 (2017). <https://doi.org/10.1051/mateconf/201712601007>

10. Yusof, M.F.M., Kamaruzaman, M.A., Zubair, M., Ishak, M.: Detection of defects on weld bead through the wavelet analysis of the acquired arc sound signal. *J. Mech. Eng. Sci.* **10**, 2031–2042 (2016). <https://doi.org/10.15282/jmes.10.2.2016.8.0192>
11. ASTM International: E8/E8 M standard test methods for tension testing of metallic materials. West Conshohocken, USA (2010). <https://doi.org/10.1520/e0008>
12. European Standard (CEN): Eurocode 3: design of steel structures—part 1–8: design of joints (2005). <https://doi.org/10.2514/2.2772>



# Arm Games for Virtual Reality Based Post-stroke Rehabilitation

C. Basri Noor<sup>1</sup>(✉), Wan Khairunizam<sup>1</sup>, S. Diny Syarifah<sup>2</sup>, I. Zunaidi<sup>3</sup>,  
Lee Hui Ling<sup>1</sup>, A. B. Shahrman<sup>1</sup>, M. R. Zuradzman<sup>1</sup>,  
and Wan Azani Mustafa<sup>1</sup>

<sup>1</sup> School of Mechatronic Engineering,  
University Malaysia Perlis (UniMAP) Perlis, Kangar, Malaysia  
basrinoorc@gmail.com, {khairunizam, shahrman,  
zuradzman, wanazani}@unimap.edu.my,  
huiling1018@hotmail.com

<sup>2</sup> Department of Informatics Engineering,  
University of Suryakencana Cianjur, Cianjur, Indonesia  
dsy.sany@gmail.com

<sup>3</sup> Sustainable Advanced Manufacturing,  
University of Sunderland, Sunderland, UK  
zunaidi@yahoo.com

**Abstract.** Stroke is a leading cause of serious long-term disability. World Health Organization (WHO) published that the second leading of death is stroke accident and every year, 15 million people worldwide suffer from stroke attack, two-thirds of them have a permanent disability. Muscle impairment can be treated by intensive movements involving repetitive task, task-oriented and task-variegated. Conventional stroke rehabilitation is expensive, less engaging and at the same time need more time for the rehabilitation process and need more energy and time for the therapist to guide the stroke-survivor. Modern stroke rehabilitation is more promising and more effective with modern rehabilitation aids allowing the rehabilitation process to be faster, however, this therapist method can be obtained in the big cities. To cover the lack of rehabilitation process in this research will develop and improve post-stroke rehabilitation using games. This research using electromyography (EMG) device to analyze the muscle contraction during the rehabilitation process and using Kinect XBOX to record trajectory hands movements. Five games from movements sequence have designed and will be examined in this research. This games obtained two results, the first is the EMG signal and the second is trajectory data. EMG signal can recognize muscle contractions during playing game and the trajectory data can save the pattern of movements and showed the pattern to the monitor. EMG signal processing using time or frequency feature extractions is a good idea to obtain more information from muscle contractions, also velocity, similarities and error movements can be obtained by study the possible approaches.

**Keywords:** Post-stroke rehabilitation · Electromyography (EMG) · Kinect XBOX · Movement sequence · Trajectory



## 1 Introduction

A Stroke is “a brain attack” and it occurs when the blood supply to the part of the brain is interrupted or reduced. This condition caused brain cells to lack oxygen and nutrition so brain cells will die. When stroke attacked, brain abilities controlled by that area such as memory and muscle control are lost. In Malaysia, stroke is the top five killers with 81.91/100,000 rate in a population [15]. In 2017 World Health Organization (WHO) published that the second leading of death is stroke accident where more than 15 million people have strokes every year and two-thirds of them have the permanent disability [1]. Usually, the side effects of stroke are hemiplegia and hemiparesis. Hemiplegia is the condition which one-side of the body becomes paralyzed, while hemiparesis is the condition of one sided weakness, hemiparesis attack roughly about 80% of stroke patient [16]. Losing muscle control will affect daily activity such as walking, drinking, eating, dressing and grabbing object and disabilities will reduce the quality of life [3]. Muscle disabilities can be treated with the right rehabilitation procedures. The rehabilitation must start as soon as after a stroke attack and after have a recommendation from hospital [2]. Motor Impairment and muscle control could be improved by intents use of activity movement involving repetitive task, task-orientated and task-variegated which will result in improving motor skills and muscular strength by preventing muscle spasticity, muscle atrophy and osteoporosis [3–5]. Previous researchers declare besides right rehabilitation procedure personal motivating and rehabilitation environment can influence the process of treatment. On the other hand coordination training between muscle control and visions its need in the process rehabilitation.

Virtual Reality (VR) game is technological developments in the game where a player will be connected with the virtual environment so can motivate the spirit’s player to complete a game. Rehabilitation based on VR has become a popular platform among researchers and rehabilitation specialist in replacing the conventional stroke rehabilitation which is repetitive and boring [6]. It is an effective way of establishing a variable and stimulating environment, allowing the patient to engage in meaningful and motivating therapeutic activities [7]. Despite the virtual rehabilitation, many have flaws but this method has shown advantages [8, 9]. On the other research has shown that rehabilitation using movement sequence is better than using random sequence even though this result is still in the research phase.

This paper organized as follows: Sect. 2 discusses the related works of the research. Section 3 describes the proposed methodologies used in the research. Section 4 presents the outcomes and discussions. Finally, conclusion and future works are described in Sect. 5.

## 2 Related Works

Muscle impairment can be restored by some hand movement exercises with organized, repetitive task and task-oriented, this exercise will result in improving motor skill and muscular strength, as in [17]. According to an investigation, daily activities movement such as eating and reaching object can be literature for designing arm movement

[10, 12, 23]. Arm movements which have sequence warming-up – moderate – difficult – cool-down movements are more effective than random or functional movement in stroke rehabilitation [11, 20, 21, 24]. Studies in post-stroke rehabilitation reported that the most important in process rehabilitation is the monitoring of muscle activity during recovery [19, 26, 27]. Performance assessment from measurement device including arm robotic, functional electrical stimulus and electromyography can help the therapist to evaluate a condition of stroke patient [13, 25]. Virtual reality in stroke rehabilitation can become patients more comfortable, satisfied and motivated patient to improve their quality of life [9, 12, 22, 28]. Rehabilitation using game can be motivated patients and made the rehabilitation process more attractive, engaging and not boring [6–8]. In other hands, process rehabilitation post-stroke must be done with a safe and effective to avoid muscle injury during rehabilitation, as in [18].

### 3 Methodologies

#### 3.1 Arm Movement for Post-stroke Rehabilitation

About 80 per cent of stroke patient suffers from hemiparesis where the condition of the one-sided body is a weakness. Muscle weakness and muscle control can be treated by repetitive movement. In traditional stroke rehabilitation, there are two basic movements, which are fundamental and functional movements. Arm fundamental movement is a basic movement which one movement direction such as flexion, extension, abduction and circumduction Fig. 1. Arm functional movement is a combination of movements from fundamental movement [14].

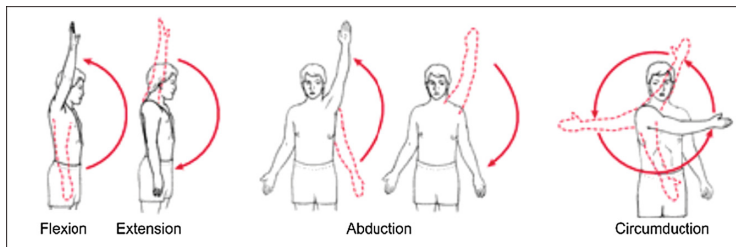


Fig. 1. Arm fundamental movements

#### 3.2 Virtual Environmental

Post-stroke rehabilitations virtual environmental was designed with area  $4\text{ m} \times 3\text{ m}$ . The system using DELSYS Bagnoli 8 channel for EMG signal acquisitions, Kinect XBOX one for the motion sensor, high-performance laptop for data collections and processing, projector and screen for games displaying. The players will be sat in front of a screen with a range of 1.5 meters (Fig. 2).

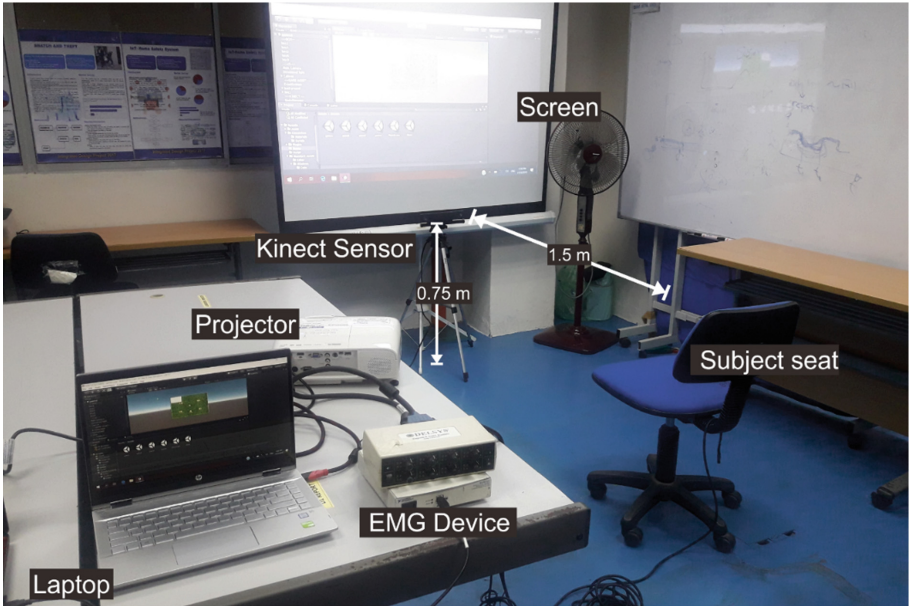


Fig. 2. Design of virtual environmental

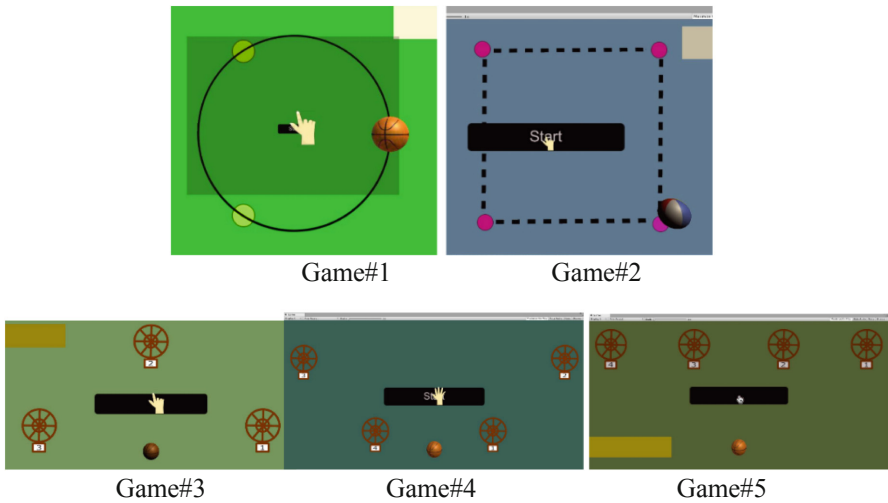
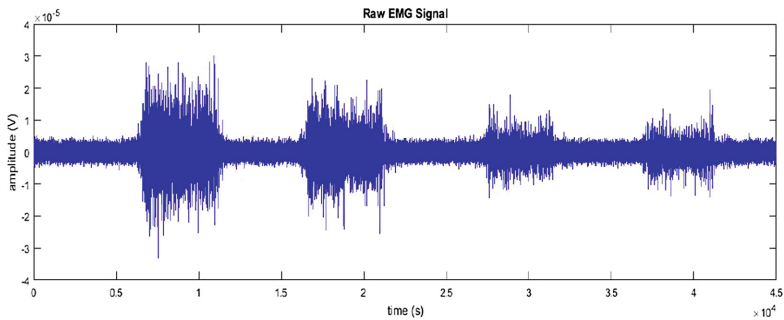


Fig. 3. Virtual environment game using Kinect

Virtual environment game design of post-stroke rehabilitation showed by Fig. 3. There are five games, game#1 and game#2 games subjects needed to grab the balls and move to follow the line until the finish. Game#3, game#4 and game#5, the subjects needed to grab the ball and move it to the bucket with sequence from bucket#1 until bucket#4.

## I. Electromyography (EMG) Device

EMG is an electrodiagnostic medicine technique for evaluating and recording the electrical activity produced by skeletal muscles. The electric potential generated by muscle cells when these cells are electrically or neurologically activated as shown in Fig. 4. Many information can be obtained from the EMG signal such as abnormalities, activation level and the biomechanics of human or animal movement [13].



**Fig. 4.** EMG signal during muscle contractions

## II. Kinect Sensor

Kinect XBOX is motions and sound sensors were to detect arm movement and to record trajectory data. In modern stroke rehabilitation, Kinect XBOX used to connect real reality to virtual reality, showed in Fig. 5.



**Fig. 5.** Kinect XBOX 360

### 3.3 Design Game of Arm Movement Sequence

Arm movement for post-stroke rehabilitation is designed based on daily activities and fundamental movements, moreover, arm games for rehabilitation have a goal target as performance evaluation. Five movement sequences have been made and are examined in this research. Two of them are sweep movements which make a circle and square patterns and the others are pick and place movements. The movement sequence is shown in Fig. 6.

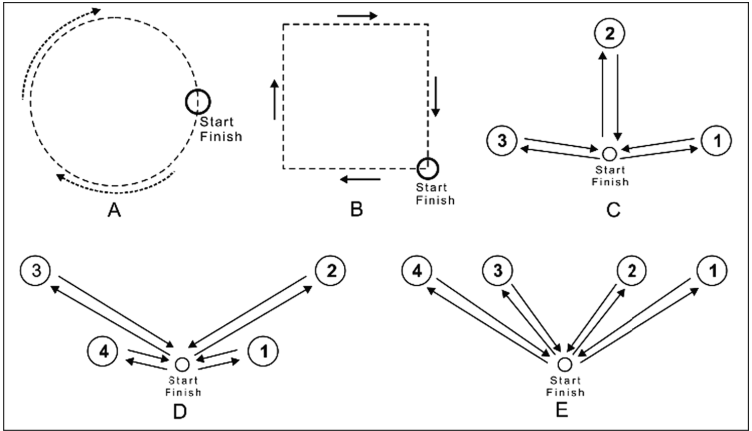


Fig. 6. Design of arm movement sequence

### 3.4 Data Collections

Five students between the ages of 23 and 30 years old include male and female in good conditions were prepared for this experiment. The participants were graduate or undergraduate students of University Malaysia Perlis. Before data collecting, every subject briefed on experimental procedures and their signature used as approval to be participants. Using healthy subjects caused this research is a laboratory prototype for EMG signal studying and movement sequence were used in this research is applicable for post-stroke patients. Deltoid muscle was chosen in this research to evaluate the arm movement sequence. Electrode placement skin preparation and fixation were accomplished according to guidelines of the surface electromyography for the non-invasive assessment of muscles (SENIAM) [29]. For deltoid muscle the electrode needs to be placed at one finger width distal and anterior to the acromion (Fig. 7).

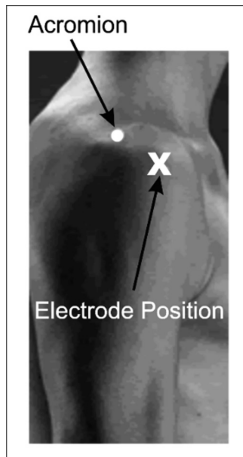


Fig. 7. Electrode placement at deltoid muscle

### 3.5 Signal Processing

To obtain the muscle activity envelopes, all the EMG signals were filtered using 5th order Butterworth digital filter of 10 Hz cut off frequency to remove high-frequency noises [14, 15]. Muscle activity envelopes were then used for further analysis.

The statistical information of EMG signal was extracted in MATLAB R2013b. Time domain feature extractions are usually used to detect the muscle contraction and muscle activity. In this research root mean square (RMS) from time domain feature extraction used for signal analysis in each movements.

RMS is defined as the square root of the mean over time of the square of the vertical distance of the graph from the rest state, related to constant force and non-fatigue contraction of the muscle. The formulation is shown in (1).

$$\text{RMS} = \text{SQRT} [1/N \times \text{SUM}(x^2(t))] \quad (1)$$

Where,

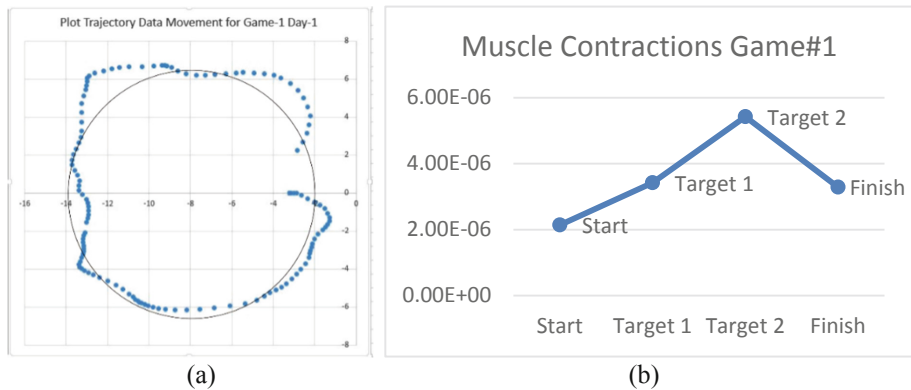
N = total number of sample

x = EMG data in time domain

t = the interval in second, and t ranging from 1 to N

## 4 Result and Discussion

Five movement sequences have been designed in this game. The rehabilitation progress is monitored through signals from EMG and the movement of virtual hand trajectory as shown in Figs. 8, 9, 10, 11, 12.



**Fig. 8.** Game #1: (a) Virtual hand position (b) EMG signal at deltoid

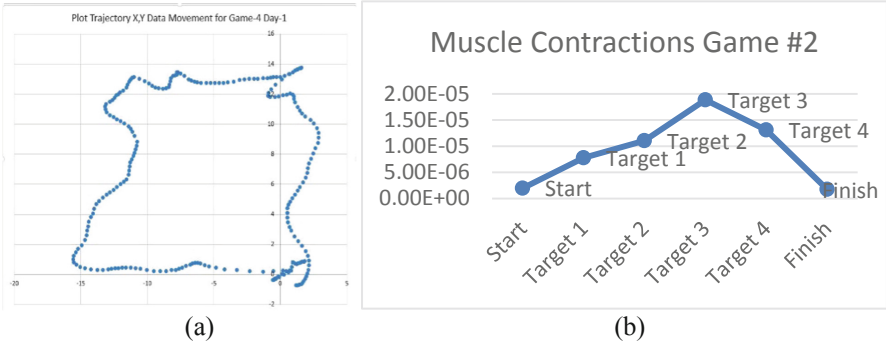


Fig. 9. Game #2: (a) Virtual hand position (b) EMG signal at deltoid

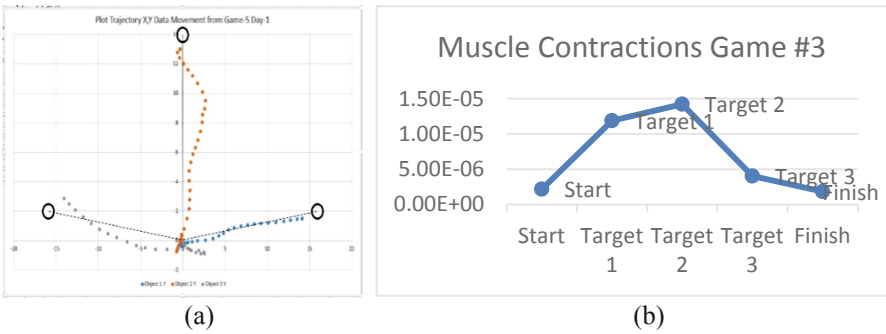


Fig. 10. Game #3: (a) Virtual hand position (b) EMG signal at deltoid

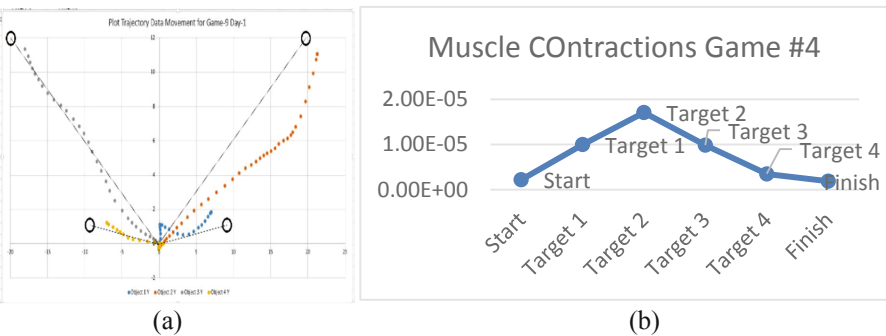
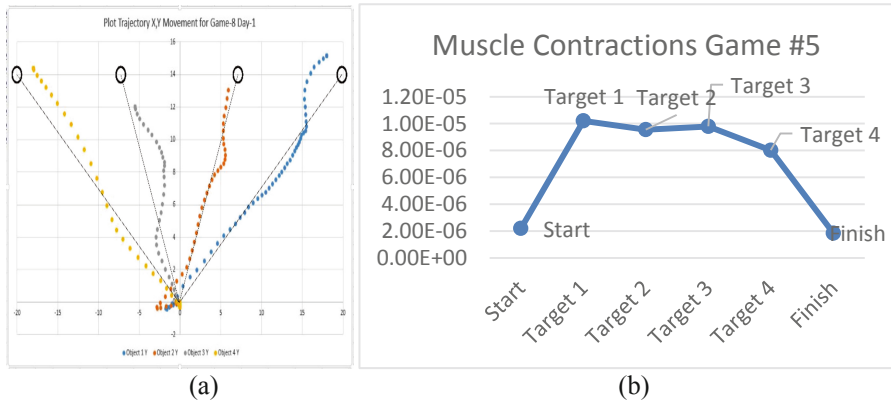


Fig. 11. Game #4: (a) Virtual hand position (b) EMG signal at deltoid



**Fig. 12.** Game #5: (a) Virtual hand position (b) EMG signal at deltoid

## 5 Conclusion

The aim of this research is to design the monitoring system based on arm games movements sequence for arm rehabilitation after-stroke using electromyography and hands trajectory. Arm games movements for post-stroke rehabilitation work well and can be applied in the modern post-stroke rehabilitation process. EMG signal and trajectory data from arm movements during playing a game can be used as a reference for performance evaluation. Arm movement pattern during rehabilitation can be seen from trajectory data processing, by doing further research make it possible to get more information such as similarities, acceleration, velocity and error movements. On the other hand, EMG signals have obtained from game playing can detect muscle contractions. EMG signal needs to be processed more deeply using signal processing and feature extraction methods to investigate more information from muscle contractions. Post-stroke rehabilitation using games can engage and motivate the patient during the rehabilitation process.

**Acknowledgements.** TUSB Research UniMAP supports this research under the research grant 2017/08/0006.

## References

1. Leading Cause of Death Malaysia: Stroke.: Retrieved from <http://www.worldlifeexpectancy.com/malaysia-stroke> (2017)
2. Mayo ayo Clinic Staff.: Stroke rehabilitation: what to expect as you recover. Retrieved from <http://www.mayoclinic.org/stroke-rehabilitation/art-20045172> (2017)
3. Dobkin, B.H.: Strategies for stroke rehabilitation. *Lancet Neurol.* **3**(9), 528–536 (2004)
4. Rienen, R., Frey, M., Bernhardt, M., Nef, T., Colombo, G.: Human-centered rehabilitation robotics. In: 9th International Conference on Rehabilitation Robotics, pp. 319–322 (2005)



5. Yeh, S., Lee, S., Wang, J., Chen, S., Chen, Y., Yang, Y., Hung, Y.: Virtual reality for post-stroke shoulder-arm motor rehabilitation : training system & assessment method. In: Paper Presented at 14th International Conference on e-Health Networking, Applications and Services, pp. 190–195. Beijing, China: IEEE (2012)
6. Yeh, S., Stewart, J., McLaughlin, M., Parsons, T., Winstein, C. J., Rizzo, A.: VR aided motor training for post-stroke rehabilitation: system design, clinical test, methodology for evaluation. In: Proceedings of the IEEE Virtual Reality Conference, pp. 299–300. Charlotte, USA (2007)
7. Prashun, P., Hadley, G., Gatzidis, C., Swain, I.: Investigating the trend of virtual reality-based stroke rehabilitation systems. In: Proceedings of the 14th International Conference Information Visualisation, pp. 641–647. London, UK (2010)
8. Trombetta, M., Henrique, M., Rogofski, B.: Motion Rehab AVE 3D: VR-based exergame for post stroke rehabilitation. *J. Comput. Methods Progr. Biomed.* **151**, 15–20 (2017). <https://doi.org/10.1016/j.cmpb.2017.08.008>
9. Esfahlani, S., Bogdan, M., Alireza, S., George, W.: Validity of the Kinect and Myo armband in serious game for assessing upper-limb movement. *J. Entertain. Comput.* **27**, 150–156 (2018). <https://doi.org/10.1016/j.entcom.2018.05.003>
10. Kutlu M., Freeman C., Ann-Marie H.: A home based FES system for upper-limb stroke rehabilitation with iterative learning control. *J. Int. Fed. Autom. Control. Papers on-line* **50**(1), 12089–12094 (2016)
11. Khairunizam, W., K., Suhaimi, R., Aswad, A.R.: Design of arm movement sequence for upper limb management after stroke. In: Proceedings of the International workshop on Nonlinier Circuits, Communications and Signal Processing. George Town, Malaysia (2015)
12. Sevgi, A., Ilkin, M., Oya, Umit Y., Sacide, S.: Virtual reality in upper extremity rehabilitation of stroke patients: a randomized controlled trial. *J. Stroke cerebrovasc. Dis.* **27**(2), 3473–3478 (2018). <https://doi.org/10.1016/j.jstrokecerebrovasdis.2018.08.007>
13. Rash, G.S., EdD.: Electromyography fundamentals. [https://www.researchgate.net/publication/265248133\\_Electromyography\\_Fundamentals](https://www.researchgate.net/publication/265248133_Electromyography_Fundamentals) (2002)
14. Kaewboon, W., Limsakul, C., Phukpattaranont, P.: Upper limbs rehabilitation system for stroke patient with biofeedback and force. In: Proceedings of the Biomedical Engineering International Conference. Amphur Muang, Thailand (2013)
15. Ritchie, H., Roser, M.: Causes of death. <https://ourworldindata.org/causes-of-death> (2017)
16. Stroke associations.: Physical effect of stroke. <https://www.stroke.org/we-can-help/survivors/stroke-recovery/post-stroke-conditions/physical/> (2013)
17. Riener, R., Frey, M., Bernhardt, M., Nef, T., Colombo, G.: Human centered rehabilitation robotics. In: Proceedings of the 9th International Conference Rehabilitation Robotics, pp. 319–322. Chicago, USA (2005)
18. Ivey, F.M., Hafer-Macko, C.E., Macko, R.F.: Exercise rehabilitation after stroke. *J. NeuroRx* **3**(4), 439–450 (2006). <https://doi.org/10.1016/j.nurx.2006.07.011>
19. Htoon, Z.L., Na'im, Sidek, S., Fatai, S.: Assessment of upper limb MUSCLE tone level based on estimated impedance parameters. In: Proceedings of the Conference on Biomedical Engineering and Sciences. Kuala Lumpur, Malaysia (2016)
20. Kleim, J.A., Jones, T.A.: Principles of experience-dependent neural plasticity: implications for rehabilitation after brain damage. *J. Speech Lang Hear Res.* **51**(1), 225–239 (2008). [https://doi.org/10.1044/1092-4388\(2008/018\)](https://doi.org/10.1044/1092-4388(2008/018))
21. Takeuchi, N., Izumi, S.I.: Rehabilitation with post-stroke motor recovery: a review with a focus on neural plasticity. *J. Stroke Res. Treat.* (2013). <https://doi.org/10.1155/2013/128641>
22. Sveistrup, H.: Motor rehabilitation using virtual reality. *J. NeuroEng. Rehabil.* (2004). <https://doi.org/10.1186/1743-0003-1-10>

23. Langhorne, P., Bernhardt, J., Kwakkel, G.: Stroke rehabilitation. *Lancet. J. Stroke Care* **377**(9778), 1693–1702 (2011). [https://doi.org/10.1016/S0140-6736\(11\)60325-5](https://doi.org/10.1016/S0140-6736(11)60325-5)
24. Suhaimi, R., Khairunizam, W., Ariffin, M.A.: Design of movement sequence for arm rehabilitation of post-stroke. In: Proceedings of the International Conference on Control System, Computing and Engineering. George Town, Malaysia (2015)
25. Suhaimi, R., Aswad, A.R., Adnan, N.H., Asyraf, F., Khairunizam, W., Hazry, D., Shahrman, A.B., Bakar, A., Razlan, Z.M.: Analysis of EMG-based muscles activity for stroke rehabilitation. In: Proceedings of the 2nd International Conference on Electronic Design (ICED), pp. 167–170. Penang, Malaysia (2014)
26. Basri, N.C., Khairunizam, W., Zunaidi, I., Bakar, S.A., Razlan, Z.M.: Investigation of upper limb movements for VR based post-stroke rehabilitation device. In: Proceedings of the 14th International Colloquium on signal processing and It's Applications (CSPA). Batu Feringghi, Malaysia (2018)
27. Majid, M.S.H., Khairunizam, W., Shahrman, A.B., Zunaidi, I.: EMG feature extraction for upper-limb functional movement during rehabilitation. In: Proceedings of the International Conference on Inteligent Informatics and Biomedical Science (ICIIMBS). Bangkok, Thailand (2018)
28. Majid, M.S., Khairunizam, W., Shahrman, A.B., Bakar, A.S., Zunaidi, I.: Performance evaluation of a VR-based arm rehabilitation using movements sequence pattern. In: Proceedings of the 14th International Colloquium on Signal Processing and It's Applications (CSPA). Batu Feringghi, Malaysia (2018)
29. Recommendation for sensor locations on individual muscles. Retrieved from [http://seniam.org/sensor\\_location.htm](http://seniam.org/sensor_location.htm)



# Design of Sliding Mode Controller Using Smoothing Method for Chattering Suppression in Machine Tools

Weng Sun Tong<sup>1</sup>, Tsung Heng Chiew<sup>1</sup>(✉), Zamberi Jamaludin<sup>2</sup>,  
Ahmad Yusairi Bani Hashim<sup>2</sup>, Lokman Abdullah<sup>2</sup>,  
and Nur Aidawaty Rafan<sup>2</sup>

<sup>1</sup> Department of Mechanical Engineering, Faculty of Engineering and Technology, Tunku Abdul Rahman University College, Jalan Genting Kelang, Setapak, 53300 Kuala Lumpur, Malaysia

chiewth@tarc.edu.my

<sup>2</sup> Faculty of Manufacturing Engineering, Universiti Teknikal Malaysia Melaka, Hang Tuah Jaya, Durian Tunggal, 76100 Melaka, Malaysia

**Abstract.** Sliding mode controller is a widely known robust controller, providing outstanding control performances especially in disturbance rejection. However, the chattering phenomenon that induced undesired vibration often constrained the applicability and control performance of sliding mode controller. This undesirable vibration is caused by high frequency switching, originating from signum function in mathematical formulation of the controller. This paper proposes a smoothing method in designing the sliding mode controller to reduce the chattering effect induced by the signum function. The proposed smoothing method modified and replaced the original signum function in control laws of sliding mode controller using three respective smoothing functions, namely; hyperbolic tangent function, Langevin function, and Gauss error function. The control performances of proposed algorithms in terms of tracking error reduction and chattering suppression were compared with original sliding mode controller and the popular pseudo-sliding mode controller. Simulated results showed that Langevin function is superior in both tracking error reduction and chattering suppression (94.3%). Both Gauss error function and hyperbolic tangent function able to compensate chattering but with tradeoff in tracking error reduction.

**Keywords:** Chattering · Machine tools · Simulation · Sliding mode controller · Smoothing function

## 1 Introduction

High performances of machine tools and technologies are the main aim of most of the engineers and scientists, especially in manufacturing field as these could affect the mass production and efficiency of operations in industry aligned with the current trend of industrial revolution 4.0. The major challenges put forward engineers to produce and maintain the high performance of machine tools including the time-varying parameters,

nonlinearities, dynamic factors, and other relevant uncertainties and disturbances. One of the solutions to these challenges is through the application of robust control system on machine tools. A robust controller becomes desirable as the classic proportional-integral-derivative (PID) controller and cascade controller, equipped on typical machine tools failed to cope with the presence of high nonlinearities and disturbances. Consequently, sliding mode controller (SMC), popularized by Utkin et al. [1] becomes one of the attractive solutions to these challenges due to its high robustness property.

SMC is one of the suitable solutions due to its insensitivity towards uncertainties, which able to compensate the typical internal and external disturbances such as friction and cutting forces in machine tools [2]. However, the applicability and control performances of SMC is often constrained by the chattering effect that induced undesired vibration on the system. This chattering phenomenon is inevitable due to the high frequency oscillation, originating from the signum function associated with mathematical formulation of control laws in SMC [3]. The chattering effect induced vibration causing high heat loss and low accuracy of the mechanical system. Based on the literature review performed, various methods and works has been implemented to reduce the chattering effect of SMC [4]. One of the common methods applied in literature is the modification of original SMC to form pseudo-SMC. In pseudo-SMC, the signum function is replaced by a sigmoid-like function [5] or saturation function [6, 7] to create a certain degree of smoothing effect during the transition at near zero state. Effect of pseudo-SMC able to attenuate the chattering effect to a certain degree as demonstrated by Maheswararao et al. [8] on speed control of DC motor. However, the common drawback is the additional parameter and trade-off in terms of tracking error reduction if improper parameter was used [9].

Other attractive method for chattering suppression is the second order sliding mode controller (SOSMC), introduced by Levant [10]. Recent works of Munoz et al. [11] on altitude tracking of quadrotor unmanned aerial system using SOSMC, and the works of Rubio et al. [12] on CNC milling demonstrated the effectiveness of SOSMC in chattering attenuation during trajectories tracking. A significant reduction of chattering effect was reported in the recent works of [2] where the arc-tangent function was applied to replace the signum function in SOSMC. However, great trade-off in tracking error reduction was recorded. This paper extends the idea of [2] and proposes three smoothing functions, namely; hyperbolic tangent function, Gauss error function, and Langevin function to replace the signum function in SMC for chattering attenuation. The proposed smoothing functions provided certain degree of smoothing that able to relieve the discontinuity exhibited in the original control law of SMC, therefore, reduced the chattering effect. The proposed functions were incorporated into the SMC and the control performances of the modified SMCs were compared and analysed numerically.

This paper is organised as follows. Section 2 presents the system modelling of the considered setup, a direct driven single axis positioning system. Section 3 shows the design of traditional SMC including formulae and control scheme involved while Sect. 4 presents the modification of SMC using the proposed smoothing functions. Section 5 presents and discusses the simulation results. Lastly, Sect. 6 concludes the results and provides future recommendations for the current work.

## 2 System Modelling

The considered system is a single axis positioning system driven by an ironless flat linear motor equipped with 4  $\mu\text{m}$ -resolution linear encoder as shown in Fig. 1. The system dynamics was described as a single-input-single-output (SISO) model through frequency domain identification method. The SISO frequency response function (FRF) was approximated using H1 estimator [13] based on measured input voltage,  $u(t)$  and output position,  $y(t)$  signals corresponding to the band-limited white noise excitation signal filtered at a frequency of 15 Hz. A sampling frequency of 5000 Hz and a total duration of 300 s was applied for the measurements. A parametric model was then fitted on the measured FRF using nonlinear least square frequency domain identification method [13], yielding a second order model with a time delay of 0.00045 s as shown in Eq. (1).

$$\ddot{y}(t) = -B\dot{y}(t) + Au(t) \quad (1)$$

where the model parameters  $A = 7.5\text{e}8 \mu\text{m}/\text{V}\cdot\text{s}^2$ , and  $B = 3622 \text{ s}^{-1}$ . Both  $\dot{y}(t)$  and  $\ddot{y}(t)$  are the first and second time derivatives of actual output position, respectively while  $u(t)$  represents the control input.

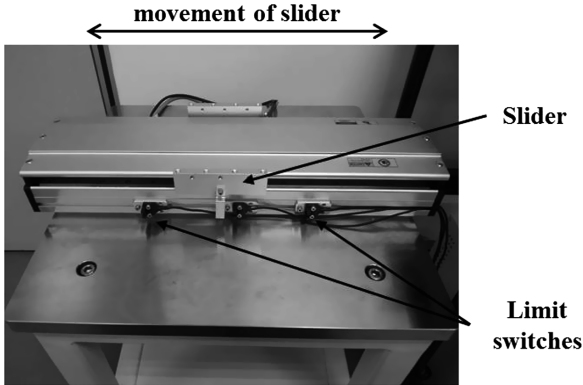


Fig. 1. Single axis positioning system driven by linear motor

## 3 Design of Sliding Mode Controller (SMC)

Figure 2 shows the general control scheme of SMC. Two design components are considered in designing SMC, namely; sliding surface, and control law [1]. Sliding surface,  $s(t)$  relates the tracking error,  $e(t)$  and the first derivative of tracking error,  $\dot{e}(t)$  as shown in Eq. (2).

$$s(t) = \lambda e + \dot{e}; \quad e(t) = y(t) - r(t), \tag{2}$$

where both  $y(t)$  and  $r(t)$  represents the desired input position and actual output position respectively while constant  $\lambda > 0$ . Equation 2 is further extended to form the first derivative of sliding surface,  $\dot{s}(t)$  and second derivative of tracking error,  $\ddot{e}(t)$  as shown in Eqs. (3) and (4). Equation (5) is generated based on the extension of Eq. (3) using Eq. (1).

$$\dot{s}(t) = \lambda \dot{e}(t) + \ddot{e}(t), \tag{3}$$

$$\ddot{e}(t) = \ddot{y}(t) - \ddot{r}(t), \tag{4}$$

$$\dot{s}(t) = \lambda \dot{e}(t) + Au(t) - B\dot{y}(t) - \ddot{r}(t). \tag{5}$$

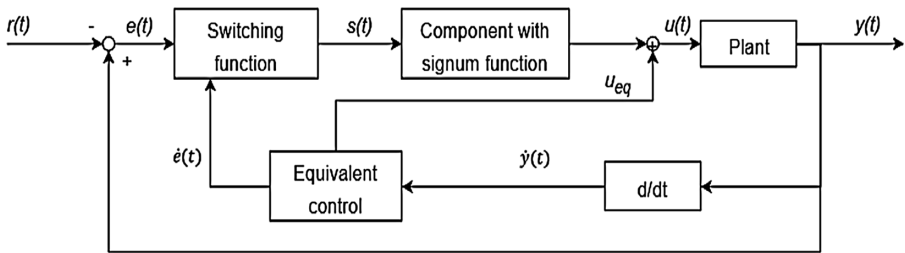


Fig. 2. The general control scheme of SMC

On the other hand, control law consists of equivalent control,  $u_{eq}(t)$  that relates a velocity feedforward and an acceleration feedforward with a positive constant,  $K$  as shown in Eq. (6). When  $s(t) = 0$  and  $\dot{s}(t) = 0$ , Eq. (5) is extended to generate the equivalent control equation as shown in Eq. (7).

$$u(t) = u_{eq}(t) - K \cdot \text{sign}(s(t)); \quad K = \frac{k}{A}, \quad \text{sign}(s(t)) = \begin{cases} 1, & s > 0 \\ 0, & s = 0 \\ -1, & s < 0 \end{cases} \tag{6}$$

$$u_{eq}(t) = \frac{1}{A}(Cy(t) + B\dot{y}(t) + \ddot{r}(t) - \lambda \dot{e}(t)), \tag{7}$$

where  $k$  is a positive constant while signum function is represented by  $\text{sign}$ . Figure 3 shows the characteristic of signum function in which a discontinuity is formed at the zero region of  $s$ -function. This discontinuity results in high frequency switching that leads to chattering phenomenon [3].

General practice in literature is the application of sigmoid-like function,  $V_\delta(s(t))$  as shown in Eq. (8) to replace the discontinuous signum function. However, additional variable, the degree of smoothing,  $\delta$  increases the complexity of the controller design [4].

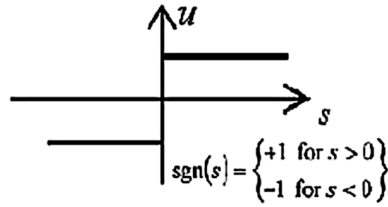


Fig. 3. Characteristics of signum function []

$$V_{\delta}(s(t)) = \frac{s(t)}{|s(t)| + \delta}. \tag{8}$$

### 4 Modification of SMC

Three alternative smoothing functions are proposed, namely; hyperbolic tangent function, Langevin function, and Gauss error function. These proposed functions exhibit similar properties of signum function but with smoother transition at near zero region of  $s$ -function. In addition, the proposed functions able to provide certain degree of smoothing without additional parameters. By replacing the signum function, the control law of original SMC (refer to Eq. (6)) was modified into (i) SMC with hyperbolic tangent function (H-SMC), (ii) SMC with Langevin function (L-SMC), and (iii) SMC with Gauss error function (Ge-SMC), as shown in Eqs. (9), (10), and (11) respectively.

$$u_{H-SMC}(t) = u_{eq}(t) - K \cdot \tanh (s(t)) , \tag{9}$$

$$u_{L-SMC}(t) = u_{eq}(t) - K \cdot \left( \coth (s(t)) - \frac{1}{s(t)} \right) , \tag{10}$$

$$u_{Ge-SMC}(t) = u_{eq}(t) - K \cdot erf (s(t)) , \tag{11}$$

Figure 4 compares the characteristic of smoothing functions: Gauss error function, hyperbolic tangent function, sigmoid-like function, and Langevin function. Results showed that all proposed functions and sigmoid-like function produced some degree of smoothing during transition at near zero region of  $s$ -function. Furthermore, Langevin function and sigmoid-like function also adjusted the gain  $K$  due to the nature of the mathematical formulation of the functions (refer to Eqs. (8) and (10)).

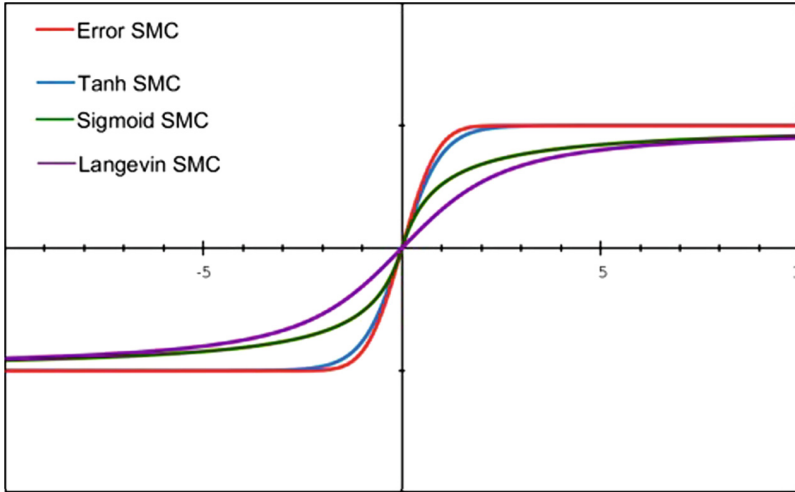


Fig. 4. Characteristics of proposed functions and sigmoid-like function

## 5 Results and Discussion

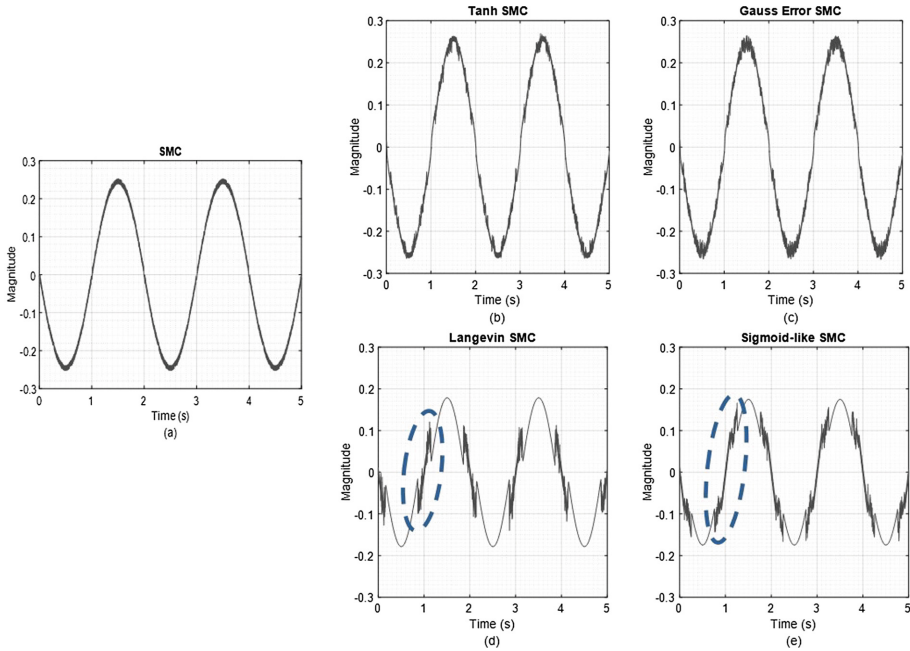
The control performances of all designed control algorithms were simulated based on system model shown in Eq. (1) and compared in terms of tracking error reduction, and chattering suppression ability. The parameters used for all control algorithms are  $\lambda = 302.1$  and  $K = 0.001$  while additional parameter  $\delta = 0.935$  for sigmoid-like function. A sinusoidal wave with amplitude of 20 mm and frequency of 0.5 Hz was used as excitation signal and the simulation was conducted based on control scheme shown in Fig. 2.

### 5.1 Tracking Error

Analysis on tracking error was extended into maximum tracking error and root mean square error (RMSE). Figure 5 shows the simulated tracking error,  $e(t)$  for all designed control algorithms while Table 1 presents the RMSE and maximum tracking error of respective control algorithms.

Based on Fig. 5 and Table 1, it was observed that L-SMC and pseudo-SMC produced much lower tracking error compared to other control algorithms while H-SMC and Ge-SMC produced similar outputs as original SMC. The high oscillation observed in Fig. 4d, e (refer to the dotted circle) is due to the trajectory transformation of the slider from acceleration to deceleration (constant velocity) as it prepared for motion reversal, consistent with the works presented in [2]. In addition, in reference to Figs. 3 and 4, the strength of switching for H-SMC and Ge-SMC became weaker at near zero region due to the imperfect switching and this leads to the deterioration in tracking performance compared to SMC. In contrast, the weak switching for both L-SMC and pseudo-SMC was compensated by the gain adjustment exhibited in the mathematical formulation of Langevin and sigmoid-like functions. A note to be highlighted is





**Fig. 5.** Simulated tracking error for **a** SMC, **b** H-SMC, **c** Ge-SMC, **d** L-SMC, and **e** pseudo-SMC

**Table 1.** RMSE and maximum tracking error of designed control algorithms

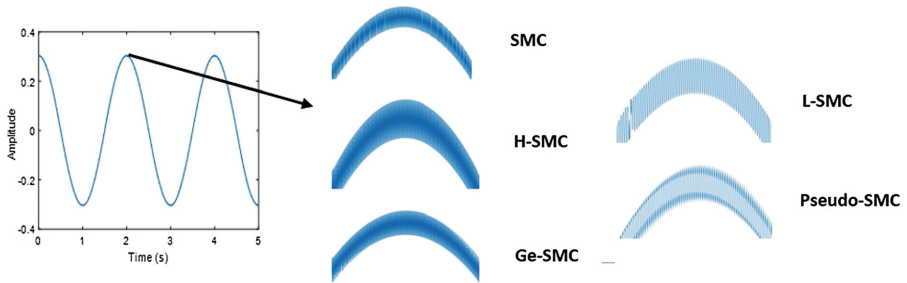
Controller	RMSE ( $\mu\text{m}$ )	Improvement (%)	Maximum tracking error ( $\mu\text{m}$ )	Improvement (%)
SMC	0.1773	Reference	0.2550	Reference
H-SMC	0.1805	-1.8	0.2687	-5.3
Ge-SMC	0.1784	-0.6	0.2638	-3.5
L-SMC	0.1159	34.6	0.1796	29.6
Pseudo-SMC	0.1210	31.8	0.1757	31.1

L-SMC able to produce comparable results to pseudo-SMC without introducing extra variables.

### 5.2 Chattering Suppression

Analysis on chattering suppression was conducted through spectral analysis where the time domain control command input,  $u(t)$  for each control algorithm was transformed into frequency domain through Fast Fourier Transformation (FFT) method. Figure 6 presents characteristics of control command input for different variation of SMC. Based on Fig. 6, it was observed that the L-SMC and pseudo-SMC have clearer signals

compared to SMC, H-SMC, and Ge-SMC. In addition, Fig. 7 shows the results of FFT performed on control command input of different variation of SMCs. Table 2 summarises quantitatively the results of Fig. 7. Four significant peaks were observed at frequencies of 1400 Hz, 1670 Hz, 2000 Hz, and 2200 Hz. These peaks implied the presence of chattering as oscillation occurred at high frequency [1, 3] was observed.

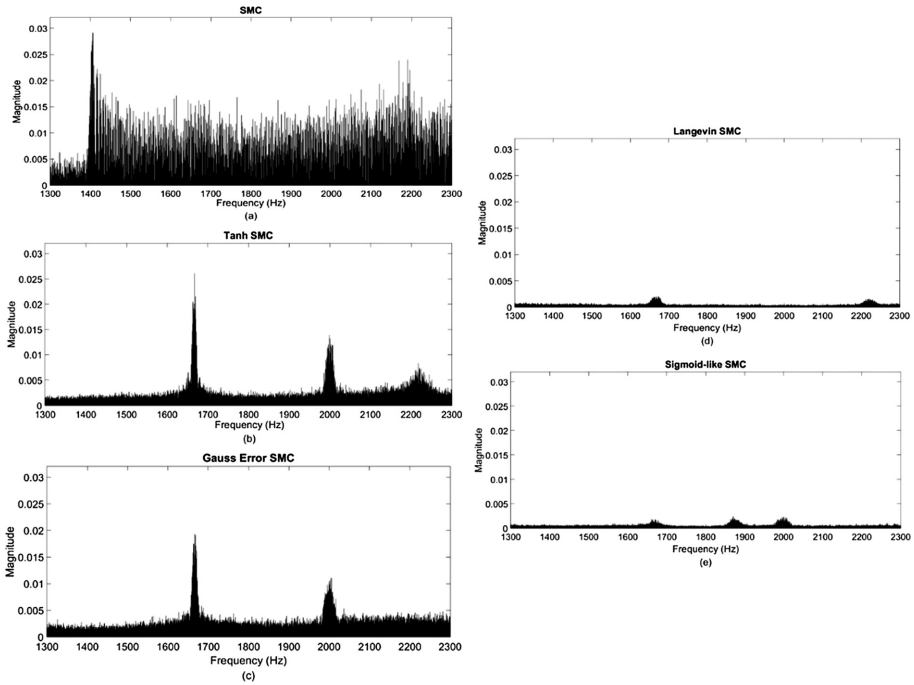


**Fig. 6.** Characteristics of control command input for SMC, H-SMC, Ge-SMC, L-SMC, and pseudo-SMC

The presence of peaks at high frequencies confirmed the findings by Utkin et al. [1] who stated that chattering is the product of high frequency oscillation. Thus, reduction in amplitude of FFT at value at these region represents the attenuation of chattering itself. Results from Table 2 showed that L-SMC is superior in chattering suppression, that is, 94.3% in average, almost 2 times better compared to SMC. Pseudo-SMC produced similar results which is 93.1% in chattering reduction. This is followed by Ge-SMC (50.9%) and H-SMC (33.4%).

Replacement of the signum function by hyperbolic tangent function, Gauss error function, Langevin function, and sigmoid-like function were able to reduce chattering to some extent as these functions smoothen the transition effect at near zero regions. However, the effect of hyperbolic tangent function and Gauss error function were only moderate when compared to the Langevin and sigmoid-like functions. The smoothening and gain adjustment of L-SMC and pseudo-SMC decreased the requirements on gain parameter  $K$ . Therefore, smaller gain value of  $K$  was possible, and this reduced chattering.

When observing simultaneously both tracking error (Table 1) and chattering attenuation (Table 2), it was observed that both H-SMC and Ge-SMC able to suppress the chattering effect but larger tracking error as a trade-off. Both L-SMC and pseudo-SMC performed excellent in tracking error reduction as well as chattering attenuation. L-SMC is considered better than pseudo-SMC as L-SMC does not required extra variable for the degree of smoothening.



**Fig. 7.** FFTs of control command input signals at high frequency regions for **a** SMC, **b** H-SMC, **c** Ge-SMC, **d** L-SMC, and **e** pseudo-SMC

**Table 2.** Respective peaks at high frequency regions for different variation of SMCs

Controller	Magnitude at Frequencies, $\times 10^{-3}$			
	1400 Hz	1670 Hz	2000 Hz	2200 Hz
SMC	29.06	17.51	18.27	24.01
H-SMC	1.98	26.07	13.87	8.33
Ge-SMC	2.21	19.16	11.01	4.57
L-SMC	0.56	2.05	0.49	1.56
Pseudo-SMC	0.62	2.16	1.73	0.84

## 6 Conclusion and Future Recommendations

In conclusion, this paper proposes smoothing method for the design of SMC. Three smoothing functions, namely; hyperbolic tangent function, Gauss error function, and Langevin function. Simulated control performances of proposed control algorithms on direct driven single axis positioning system were compared to SMC and pseudo-SMC in terms of tracking error reduction and chattering attenuation. L-SMC provides the best performance in terms of RMSE reduction (34.6%) and chattering reduction of 94.3% in average. Although pseudo-SMC has comparable performance as L-SMC,

it required an extra variable which increased the complexity of the control algorithm. Both H-SMC and Ge-SMC could partially suppress the chattering but weaker in tracking error reduction as a trade-off. L-SMC is recommended for system that required high precision but sensitive towards chattering effect. For future recommendations, the proposed control algorithms could be validated on real system and further analysed in terms of robustness and disturbance rejection.

**Acknowledgements.** The authors would like to thank Tunku Abdul Rahman University College for the research facilities and financial support. The authors also would like to thank Universiti Teknikal Malaysia Melaka for the equipment provided.

## References

1. Utkin, V., Guldner, J., Shi, J.: Sliding Mode Control in Electromechanical Systems, 2nd edn. CRC Press, Boca Raton (2009)
2. Chiew, T.H.: Super twisting sliding mode controllers and Kalman–Bucy filter for single axis positioning system. Ph.D. thesis, Universiti Teknikal Malaysia Melaka (2018)
3. Edwards, C., Spurgeon, S.K.: Sliding Mode Control: Theory and Applications, 1st edn. CRC Press, London (1998)
4. Jamaludin, Z., Brussel, H.V., Swevers, J.: Classical cascade and sliding mode control tracking performances for a XY feed table of a high-speed machine tool. *Int. J. Precis. Technol.* **1**, 65–74 (2007). <https://doi.org/10.1504/IJPTECH.2007.015345>
5. Lee, H., Utkin, V.: Chattering suppression methods in sliding mode control systems. *Annu. Rev. Control* **31**, 179–188 (2007). <https://doi.org/10.1016/j.arcontrol.2007.08.001>
6. Sahamijoo, A., Piltan, F., Mazloom, M.H., Avazpour, M.R., Ghiasi, H., Sulaiman, N.B.: Methodologies of chattering attenuation in sliding mode controller. *Int. J. Hybrid Inf. Technol.* **9**, 11–36 (2016). <https://doi.org/10.14257/ijhit.2016.9.2.02>
7. Wang, S., Gao, Y., Liu, J., Wu, L.: Saturated sliding mode control with limited magnitude and rate. *IET Control Theory Appl.* **12**, 1075–1085 (2018). <https://doi.org/10.1049/iet-cta.2017.1081>
8. Maheswararao, U., Babu, Y.S.K., Amaresh, K.: Sliding mode speed control of a DC motor. In: International Conference on Communication Systems and Network Technologies, India (2011)
9. Tiwari, P.M., Janardhanan, S., Nabi, M.U.: Attitude control using higher order sliding mode. *Aerosp. Sci. Technol.* **308**, 632–646 (2016). <https://doi.org/10.1016/j.ast.2016.04.012>
10. Levant, A.: Principles of 2-sliding mode design. *Automatica* **43**, 576–586 (2007). <https://doi.org/10.1016/j.automatica.2006.10.008>
11. Munoz, F., Hernandez, I.G., Salazar, S., Espinoza, E.S., Lozano, R.: Second order sliding mode controllers for altitude control of a quadrotor UAS: real-time implementation in outdoor environments. *Neurocomputing* **233**, 61–71 (2017). <https://doi.org/10.1016/j.neucom.2016.08.111>
12. Rubio, L., Ibeas, A., Luo, X.: P-PI and super twisting sliding mode control schemes comparison for high precision CNC machining. In: 24th Iranian Conference on Electrical Engineering (ICEE), Iran (2016)
13. Pintelon, R., Schoukens, J.: System Identification—A Frequency Domain Approach, 2nd edn. Wiley, New York (2012)



# A New Approach of Finding Transfer Function of Piezoelectric Actuator Using Finite Element Modelling

A. M. Najib (✉), M. N. Muhammad, M. N. Maslan,  
A. Y. Bani Hashim, and A. J. Fairul

Fakulti Kejuruteraan Pembuatan, Universiti Teknikal Malaysia Melaka (UTeM),  
Hang Tuah Jaya, Durian Tunggal, 76100 Melaka, Malaysia  
najibali@utem.edu.my

**Abstract.** The piezoelectric element can be used both as actuator and sensor. The control of the piezo element system requires knowledge of transfer functions between the input and the output of the system. The transfer function is complicated to be determined using an analytical approach, especially for a thin structure with embedded actuators and sensors. The goal of this paper is to present a new approach using a finite element formulation for the piezoelectric element as an aiding tool for an analytical approach to estimate the system transfer function. A 3D finite-element model is developed with piezoelectric patches, which are surface bonded on a thin quadrilateral plate and supported with spring damper elements. The results show that the behaviour of the piezoelectric element for various electric excitation and motor vibration depends on the different frequency range. The mode shapes and natural frequencies at specific frequency spectrum are also presented. It can be concluded that the finite element modelling can be used as a new tool for scientific investigation of this material in various form.

**Keywords:** Piezoelectric · Finite element · Transfer function

## 1 Introduction

There are numerous engineering applications that employ thin structure and are subjected to a variety of excitations and vibrations. Piezo-element on a thin structure has been studied by a number of researchers for vibration control [1–4] of the membrane as well as structure monitoring [5, 6], and energy harvesting [7]. Nowadays, piezo-element has emerged as a preferred vibration control mechanism.

The previous study by Halim [8] used various piezo-element configurations for controlling different modes shapes. In another study made by [9, 10], the effect of using the piezoelectric patch as an actuator in rectangular beams was investigated. Distinctive mode shapes of the thin structure at various operating frequencies with two piezo-patches configuration can be determined using computer simulation and sand forming on the plate [11]. In the application of the finite element method for piezoelectric elements, numerous development of FEM model has been established, with the aim to

study the piezoelectric structures ranging from the shell of three-dimensional and two-dimensional elements [12, 13].

Meanwhile, several analyses with various numbers of piezo-element configurations have been carried out. Yaman [14] analyzed 5-patch configuration of piezo-element for clamped square plate while other configurations such as 9-patch and 12-patch configurations were studied by [15, 16]. Recent advances in computer technology have given a capability for a practical solution in developing and analyzing a system with the help of finite-element software before a full-scale system is developed. The finite element method (FEM) using computer simulation was implemented by Nguyen et al. [17] to solve the piezoelectric problems, and its applications relate to the piezoelectric actuators. Rajan and Kamal [18] studied the technique for vibration control of smart plates using distributed piezoelectric sensors and actuators subjected to cyclic loads. The dynamic behaviour of the composite plate with piezoelectric patches under airflow was investigated by Chung et al. using the finite element method [19]. Up to the author knowledge, up to date, there is still a lack of publication relate to the transfer function of piezoelement with the aid of the finite element method.

This study presents a new approach to calculate transfer function with the aid of the finite element method. The finite-element analysis for thin plate structure excited by patches of piezoelectric transducer and force excitation from a vibration motor was presented. Electrical and mechanical characteristics of 2-patch configuration for a damped square plate at different excitations were investigated. This analysis will be used as an approximation model of the dynamic system for calculating the transfer function based on knowledge computed input and output data.

## 2 Methodology

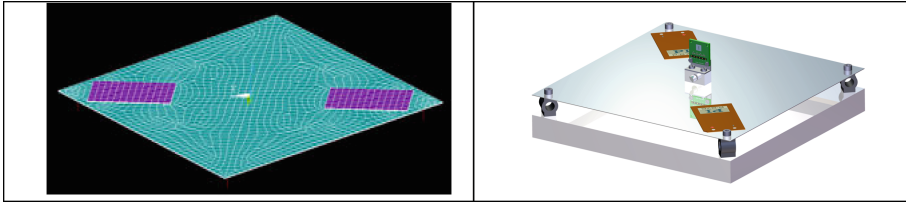
### 2.1 Finite Element Model

The FEM model is used as a tool to increase understanding of the behaviour of the system and to find the transfer function of the system at a particular frequency spectrum. In the modal analysis, the natural frequencies and corresponding mode shapes were presented. The results from modal analysis were compared to the experimental result. By numerical simulation in harmonic analysis, the effects of the system in actuator mode at appropriate electric excitation from piezoelectric actuator were investigated, and appropriate transfer functions were developed.

The finite element model consists of a spring-mass system. The spring-mass system contains a membrane made out of stainless steel, two piezoelectric bender elements and an acceleration sensor in the middle. The membrane with a thickness of 0.5 mm is fixed with 4 shock absorbers on a massive aluminium block (200 mm × 200 mm × 20 mm) to decouple any vibrations from the ground. The vibration motor and the piezoelectric element is used as the input of the system, and the output was measured in terms of the maximum deflection of the shell structure.

Figure 1 shows the specimen structure modelling by ANSYS. A 3D element 'SOLID45' with 3 degrees of freedom (DOF) and 8 nodes is used for modelling the plate structure and bonding layer. A 3D coupled field element 'SOLID5' with 8 nodes

is used for modelling piezoelectric actuators. This element allows the coupled DOF of displacement and voltage. The mass of mounting parts of the vibration motor and the sensors are considered as constant value acting at one node, and it is represented by structural point mass element ‘MASS21’ with 3 degrees of freedom ( $U_x, U_y, U_z$ ). The supports of the plate are modelled by combination element ‘COMBIN14’ with a DOF in longitudinal  $U_z$  direction and have 2 nodes. The constant value of spring constant and damping ratio are defined. The base plate and the air are not to be modelled.



**Fig. 1.** Thin plate structure, piezo-patches and vibration motor of the finite element model and 3D structures

## 2.2 Material Data for Modelling

The following equation describes the behaviour of the coupled electromechanical problem in the analysis. The value of stress and electric displacement depends on the stress and the electric field quantity in the system.

$$\begin{aligned} \{T\} &= [C^E]\{S\} - [e]\{E\} \\ \{D\} &= [e]^t\{S\} + [\varepsilon^s]\{E\} \end{aligned} \quad (1)$$

Where

- $\{T\}$  = Stress vector (six components  $x, y, z, xy, yz, xz$ )
- $\{S\}$  = Strain vector (six components  $x, y, z, xy, yz, xz$ )
- $\{D\}$  = Electric displacement vector (three components  $x, y, z$ )
- $\{E\}$  = Electric field vector (three components  $x, y, z$ )
- $[C^E]$  = Stiffness matrix evaluated at the constant electric field, i.e. short circuit.
- $[e]$  = Piezoelectric matrix related to stress over the electric field.
- $[e]^t$  = Piezoelectric matrix relating stress/electric field (transposed).
- $[\varepsilon^s]$  = Dielectric matrix evaluated at constant strain, i.e. mechanically clamped.

For the piezoelectric element, there are four essential parameters describing the physical behaviour; (i) density (ii) relative permittivity (iii) piezoelectric matrix (iv) stiffness matrix. The piezo-element used for this experiment is PIC252. For the purpose of simulation, the data was provided by the manufacturer. The stiffness matrix under a constant electric field is expressed as:

$$\text{Stiffness Matrix, } c = \begin{pmatrix} 123.00 & 76.70 & 70.25 & 0 & 0 & 0 \\ 0 & 123.00 & 70.25 & 0 & 0 & 0 \\ 0 & 0 & 97.11 & 0 & 0 & 0 \\ 0 & 0 & 0 & 23.11 & 0 & 0 \\ 0 & 0 & 0 & 0 & 22.26 & 0 \\ 0 & 0 & 0 & 0 & 0 & 22.26 \end{pmatrix}$$

The permittivity matrix at a constant strain can be written as:

$$\text{Permittivity Matrix, } \varepsilon = \begin{pmatrix} 930 & 0 & 0 \\ 0 & 930 & 0 \\ 0 & 0 & 857 \end{pmatrix}$$

The piezoelectric matrix is presented as:

$$\text{Piezoelectric Matrix, } e^t = \begin{pmatrix} 0 & 0 & -7.15 \\ 0 & 0 & -7.15 \\ 0 & 0 & 13.7 \\ 0 & 0 & 0 \\ 0 & 11.9 & 0 \\ 11.9 & 0 & 0 \end{pmatrix}$$

Table 1 presents the mechanical and electrical properties of piezoelectric element provided by manufacturer.

**Table 1.** Mechanical and electrical properties of the piezoelectric element

Properties	Value
Stiffness, $c_{11E}$	123.00 GPa
Stiffness, $c_{12E}$	76.70 GPa
Stiffness, $c_{13E}$	70.25 GPa
Stiffness, $c_{33E}$	97.11 GPa
Stiffness, $c_{44E}$	22.26 GPa
Stiffness, $c_{66E}$	23.15 GPa
Permittivity, $\varepsilon_{11Sr}$	930.00
Permittivity, $\varepsilon_{33Sr}$	857.00
Piezoelectric coefficient, $e_{31}$	-7.15 N/Vm
Piezoelectric coefficient, $e_{33}$	13.70 N/Vm
Piezoelectric coefficient, $e_{15}$	11.9 N/Vm
Density, $\rho$	7800 kg/m <sup>3</sup>

For a linear elastic calculation in ANSYS, E-modulus, density and Poisson’s ratio of the steel plate and glue are needed. Material properties for steel plate and the adhesive layer was presented in Table 2.



**Table 2.** Material properties for steel plate and Hysol bond

Material	E-Modulus ( $\times 10^9$ N/m <sup>2</sup> )	Density (kg/m <sup>3</sup> )	Poisson's ratio
Steel plate	210	8030	0.31
Glue (Hysol Bond)	1.7	3261	0.34

Due to the lack of information about the centre mass, which includes sensors and mounting plate, therefore an approximation of the stiffness and damping factor are necessary. The approximations were made by varying the value of stiffness. Increasing the stiffness of spring will also increase the natural frequency of the system and will change the mode shapes of the system. The value of maximum displacement and acceleration are compared with experimental results. From the analysis, it was found that the stiffness value for spring is 8 times larger than the experimental value. This is due to the fact that the line element 'COMBIN14' used in the model has been divided into 8 equal lengths through meshing. Table 3 shows the material data for the full model used for the analysis.

**Table 3.** Material data of centre mass and spring damper

Material	Mass (kg)	Stiffness (N/m)	Poisson's ratio
Sensor and mounting block	0.084	–	–
Spring and damping element	–	10000	0.01

### 2.3 Meshing and Unit System

Since the gradient of the thin plate in the thickness direction are high, therefore three elements of 3D solid were used in the thickness direction. To ensure appropriate meshing quality, the width of an element needs to be at least five times of the minimum thickness. Therefore, the global size is set to be 10 times of the minimum thickness, which is 1.6 mm. Sweep meshing method has been used for the 3D structure meshing, which is a combination of free and mapped meshing.

## 3 Results and Discussion

### 3.1 General Behavior of the System

The investigation of the piezoelectric element system was started with the static analysis. The static analysis was carried out in order to obtain the value of the maximum deformation of the plate at different voltage excitations. Figure 2 shows the result of the static analysis at voltage excitation of 50 V and -50 V, respectively. From the figure, it is evident that the piezoelectric expands laterally at the positive voltage excitement. This is due to the expansion at the upper plate and compression at the lower plate. The application of an electric field along the polarization direction make the patch expand in the perpendicular direction, thus producing a local strain on the

patch and forcing the plate to bend upwards. The local maximum occurs at the area where the piezoelectric patches are bonded with the plate. During the negative voltage excitement, the contraction was detected at the piezoelectric actuator. The application of electric field opposite to the polarization direction yields the contraction of the piezo actuator in the direction perpendicular to the electric field, thus in turns bend the plate downwards.

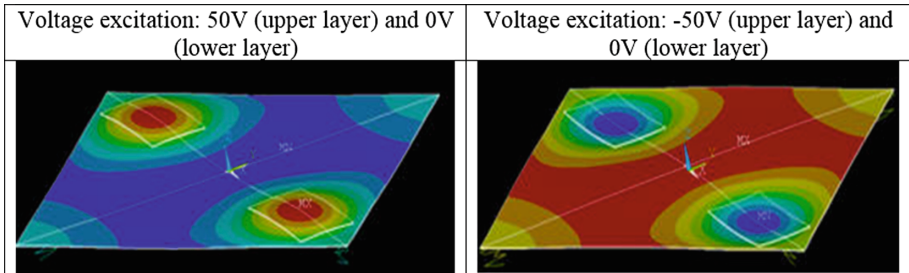


Fig. 2. Static analysis at different voltage excitations

### 3.2 Natural Frequency and Mode Shapes

Modal analysis based on the Lancosz method was performed to study the natural frequencies and mode shapes of all possible excitations. For the analysis, the frequency spectrum from 0 Hz to 500 Hz was selected, and the results were presented. The obtained mode shapes were then compared with the experimental results. The experiments were conducted using sand grain, which is placed on the vibration plate. The system is then excited at a particular frequency and the shape of the sand after a certain time is captured. Figure 3 until Fig. 7 illustrates the natural frequencies of the system and the corresponding mode shapes during simulation and experimental.

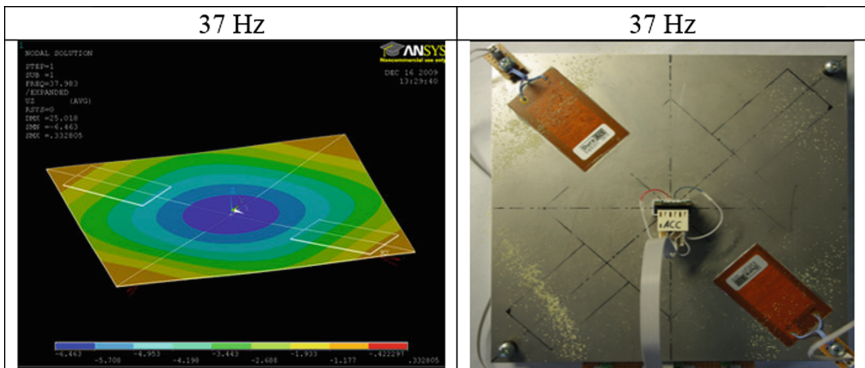


Fig. 3. Mode shape from simulation and experiment at 37 Hz

Figure 3 depicted the mode shape obtained at 37 Hz natural frequency from both simulation and experimental analysis. The corresponding figure shows that the centre of the plate moves downwards whereas the four edges were in phase and move upwards. Figure 4 illustrates the mode shape resulting from the force excitation from the vibration motor at 130 Hz. From the figure, it can be seen that the centre plate moves to maximum point (denotes by red area spectrum), while all four side edges tend to deform in upwards direction. The neutral line denotes by the green line (in left figure) was in circular mode and touching the upper side of the piezo patch.

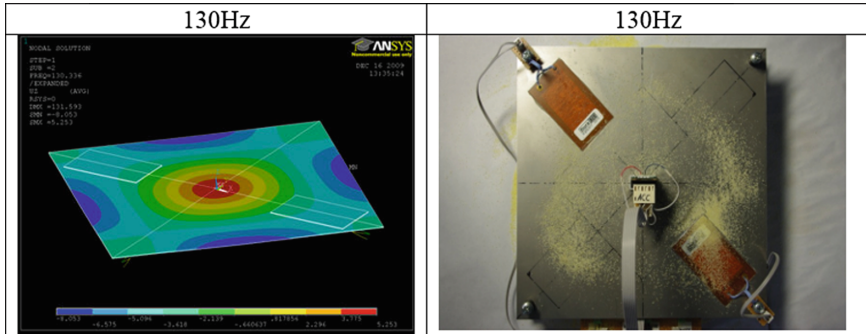


Fig. 4. Mode shape from simulation and experiment at 130 Hz

The third natural frequency was found when the piezo patch was supplied with 50 V at frequency 165 Hz. The sand grain shape depicted in Fig. 5, which was excited at frequency 165 Hz have a similar pattern with resulting neutral line (denotes by the green line) from simulation analysis. The mode shape shows that edges at piezo patch side move to minimum point (denotes by blue area), whereas the other two sides move to maximum points (denotes by red area).

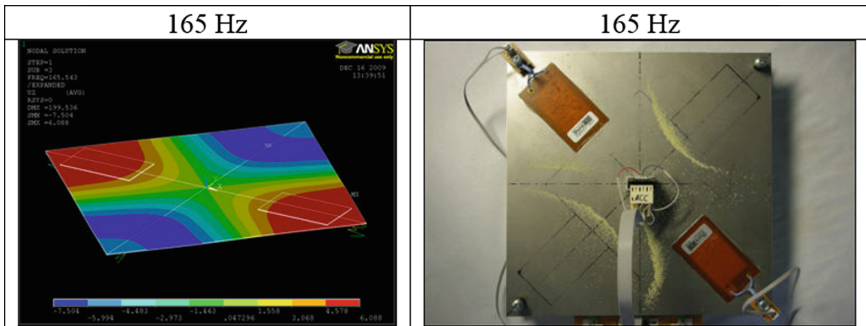


Fig. 5. Mode shape from simulation and experiment at 165 Hz

Figure 6 presents the mode shape obtained from simulation and experiment when the piezo patches were supplied with 50 V at frequency 357 Hz. The right figure shows a similar shape resulted from the experiment at an exciting frequency of 357 Hz. The neutral line, which was indicated by the sand grain, can be found at the sides and the centre of the plate. This experimental result agrees well with the simulation analysis, as illustrated in the left figure.

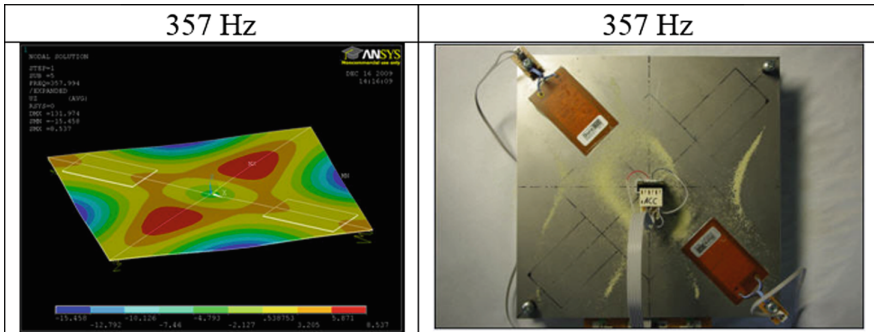


Fig. 6. Mode shape from simulation and experiment at 357 Hz

Figure 7 shows a random shape recorded from simulation in ANSYS and experiment at an exciting frequency of 500 Hz. The similar pattern of sand grain resulted from the experiments was observed, and thus validated the mode shape from the simulation.

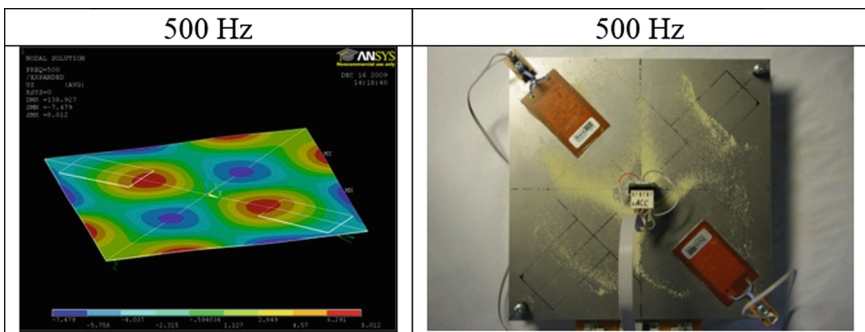


Fig. 7. Mode shape from simulation and experiment at 500 Hz

The results from modal analysis represent all possible mode shape and natural frequencies of the structure were presented in this study. However, only a quarter model was built for the analysis which means only the symmetry excitation was considered throughout the study. This includes the force excitation applied in the middle of the plate and voltage excitation applied on the piezo patches.

Figure 8 shows the plot of resonance-frequencies of the mechanical system obtained using the electrical excitation of the piezo actuators as well as the force excitation of the vibration motor from the experiment. The comparison of the normalized magnitude shows that the natural frequency can be achieved at 30 Hz and somewhere between 126 Hz and 147 Hz.

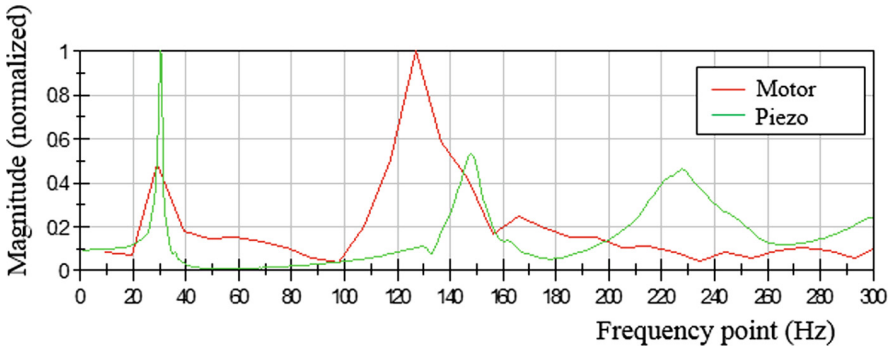


Fig. 8. Frequency response of system from an experiment using electrical- and force excitation

### 3.3 Transfer Function of the System

The transfer function of the system can be found by dividing the output signal over the input signal. In this system, the primary input of the system is the voltage excitation, and the output signal is presented by the acceleration. Figure 9 illustrates the definition of the transfer function in the system.

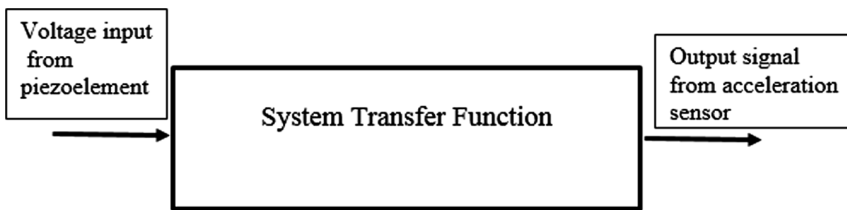
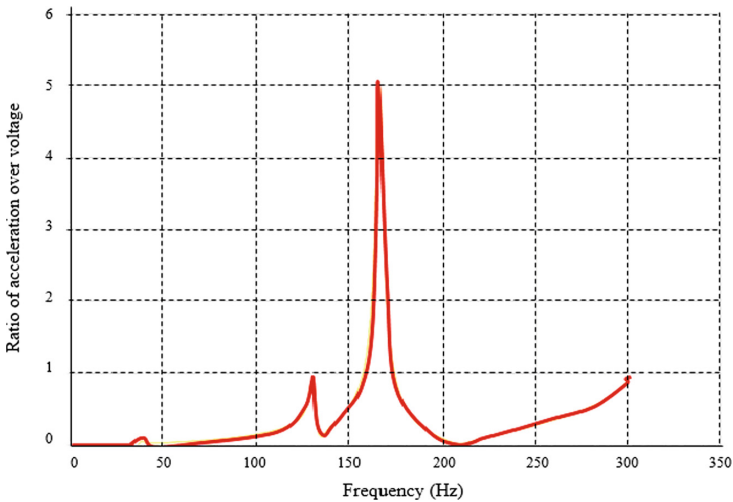


Fig. 9. Definition of the transfer function of the system

$T_{av}$  is the ratio describing the change in acceleration over the excitation voltage of piezo-element. The unit of  $T_{av}$  is  $\text{ms}^{-2}/\text{V}$ . Figure 10 depicts the relationship for defined frequency spectrum and Table 4 shows the constant value of  $T_{av}$  at around the natural frequency.

Meanwhile, the acceleration transfer function of the system can be found by dividing the output signal of frequency response over the input signal of the frequency response. Harmonic analyses in ANSYS are used to extract the frequency response of the signal. Figure 11 shows the definition of the transfer function of acceleration in the system.



**Fig. 10.** Ratio of acceleration and voltage at a frequency range of 0 Hz to 300 Hz

**Table 4.** Constant value of  $T_{av}$  at certain frequency range

Freq. (Hz)	$T_{av}$ ( $\text{ms}^{-2}/V$ )	Freq. (Hz)	$T_{av}$ ( $\text{ms}^{-2}/V$ )	Freq. (Hz)	$T_{av}$ ( $\text{ms}^{-2}/V$ )
24.0	0.00515	126.0	0.48575	204.0	0.04507
25.5	0.00569	127.5	0.60328	205.5	0.03310
27.0	0.00620	129.0	0.82463	207.0	0.02406
28.5	0.00662	130.5	0.89436	208.5	0.02038
30.0	0.00691	132.0	0.37792	210.0	0.02257
31.5	0.00691	133.5	0.14491	211.5	0.02972
33.0	0.00633	135.0	0.12056	213.0	0.03929
34.5	0.00443	136.5	0.16588	214.5	0.04961
36.0	0.00362	138.0	0.21225	216.0	0.06011
37.5	0.0477	139.5	0.25400	217.5	0.07059

The input signals were obtained from the centre of the piezo patch actuator. The selected points at node 21415 are the maximum deflection point from the static analysis. The output signal was measured at the centre of the plate where the measurement sensors are placed. The output signal of the system is measured at node 21463. Figure 12a gives an overview of the ratio of the output signal over the input signal. The most significant ratio of the output signal over input signal is 12.2, and it occurs at frequency 36 Hz, followed by a signal at frequency 133 Hz with the maximum ratio of 3.2. The last signal was observed at frequency 209 Hz with a ratio of 1.5. These signals can be transformed to a bode plot, as illustrated in Fig. 12b, which is more appropriate for formulating a transfer function.

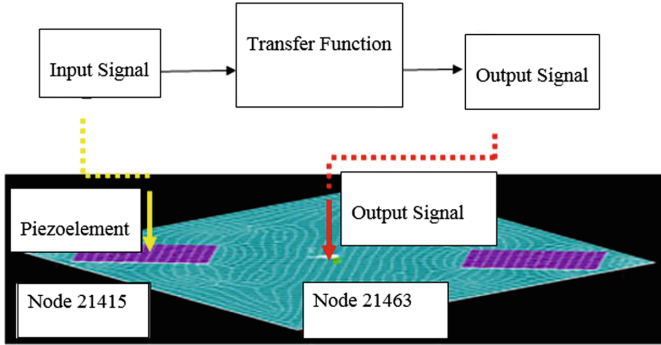


Fig. 11. The transfer function of acceleration in the system

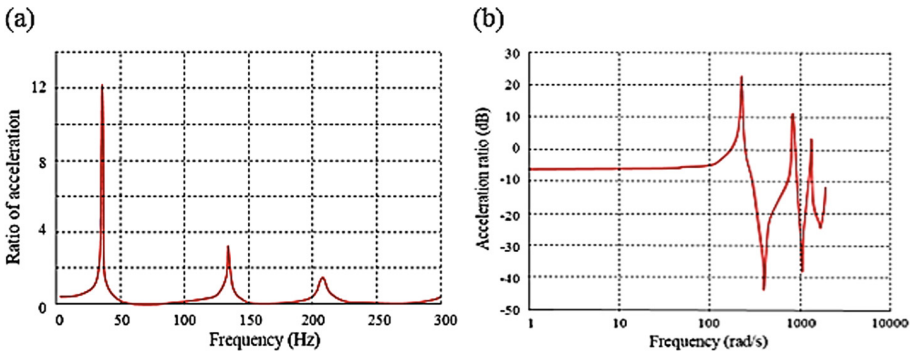


Fig. 12. (a) Signal ratio of the acceleration and (b) bode plot of acceleration

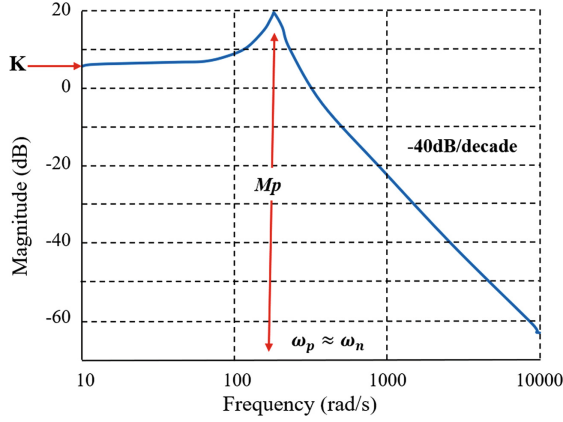
### 3.4 Mathematical Approach to Estimate the Transfer Function

The general equation represents by the bode plot in Fig. 13 is:

$$G(s) = \frac{K}{s^2 + aS + b} \tag{2}$$

where  $a = 2\xi\omega_n$  and  $b = \omega_n^2$ .  $\omega_n$  is the system's natural frequency and  $\xi$  is the system's damping ratio. Constant  $K$  is the initial gain of the transfer function and, it could be the DC gain of the system. At a very low frequency,  $s$  is set to be zero since  $s = j\omega$ . Therefore, the value of  $K$  can be expressed as:

$$\lim_{s \rightarrow 0} 20 \log|G(s)| = 20 \log \frac{1}{b} \tag{3}$$



**Fig. 13.** Bode plot of second-order system with damping

At a very high frequency, the value of  $s$  is set to infinity and the transfer function approaches negative infinity at  $-40$  dB/decade. Therefore, the value of  $K$  at high frequency can be written in the form of:

$$\lim_{s \rightarrow \infty} 20 \log |G(s)| = -20 \log \infty \quad (4)$$

To calculate the maximum value of the transfer function,  $M_p$ , the first derivative of the transfer was used. For local maximum, first derivative of transfer function  $G(s)$  is zero, therefore:

$$|G(j\omega_p)| = \frac{1}{\left| (b - \omega_p^2) + a\omega_p j \right|} \quad (5)$$

where  $\omega_p$  is the circular frequency at maximum point. Hence, at a maximum point,

$$\frac{d|G(j\omega_p)|}{d\omega_p} = 0 \quad (6)$$

If the value of  $a < b$ , hence

$$\omega_p = \sqrt{b - a^2/2} \quad (7)$$

However, if  $a^2/2 \ll b$ , then

$$\omega_p = \sqrt{b} \quad (8)$$



Therefore, the value of peak frequency is about the value of natural frequency,  $\omega_p \approx \omega_n$ . Based on this consideration, the transfer function can be expressed as:

$$|G(j\omega_n)| = \frac{1}{|(\omega_n^2 - \omega_n^2) + a\omega_n j|} = \frac{1}{a\sqrt{b}} \quad (9)$$

Therefore,

$$M_p = 20 \log \frac{1}{a\sqrt{b}} \quad (10)$$

The same equation can be used to estimate the local minimum of the transfer function. Using the derived equation, the transfer function can be estimated. The value is compared with the plotted data from ANSYS and needs to be adjusted with the help of the plotted function in MATLAB. Following function presented in Fig. 14 was used to adjust the equation and plot the estimated equation.

```
function [] = tf_acceleration ()
    G0=tf(125390,1);
    G1=tf([1 13 156689],[1 6 35530]);
    G2=tf([1 26 1094430],[1 19 703594]);
    G3=tf(1,[1 31 1716215]);
    Gs=G0*G1*G2*G3;

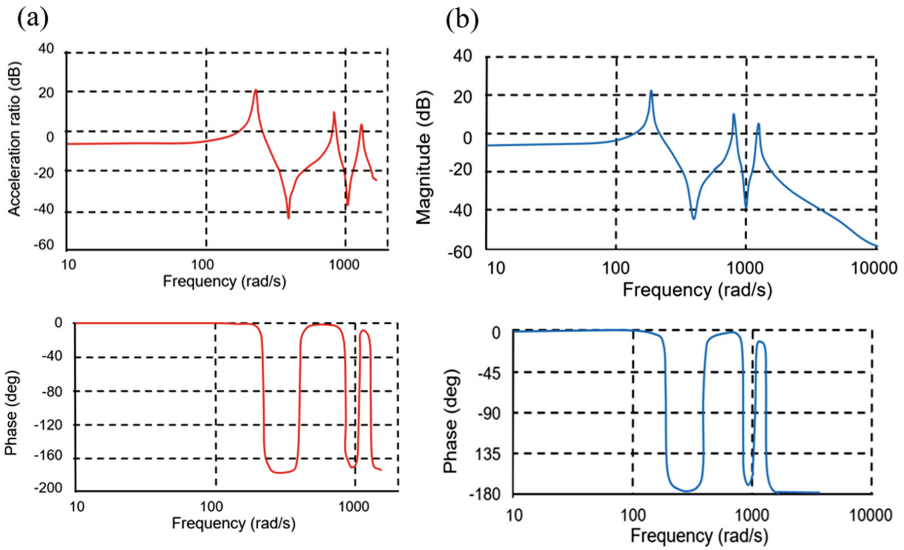
    P=bodeoptions;
    P.PhaseVisible = 'on';
    P.FreqUnits = 'rad/s';
    bodeplot(Gs,P)
    grid on
end
```

Middle term of polynomial coefficient is adjusted

**Fig. 14.** Function in MATLAB used to modify the equation

As depicted in Fig. 14, only the middle term of the polynomial coefficient is adjusted. Changing the polynomial coefficient will affect the position of zeroes and poles in the bode plot. Figure 15a illustrated the bode diagram of the transfer function from a simulation result using ANSYS. By using the diagram, the transfer function equation is estimated and plotted in MATLAB accordingly, as shown in Fig. 15b. The equation of the transfer function is estimated as:

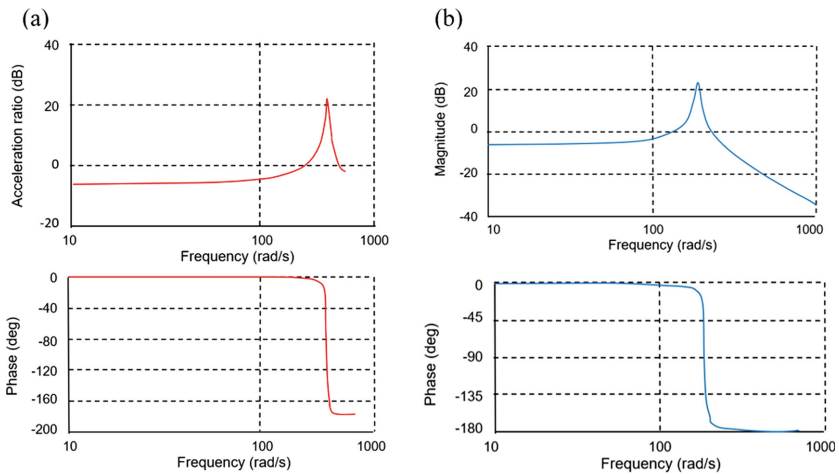
$$G(s) = \frac{125390(s^2 + 13s + 156689)(s^2 + 26s + 1094430)}{(s^2 + 6s + 35530)(s^2 + 17s + 703594)(s^2 + 31s + 1716215)} \quad (11)$$



**Fig. 15.** a. Bode plot of the transfer function from simulation b. Bode plot from estimated equation

### 3.5 Transfer Function Estimation

The transfer function will be used at selected operating frequencies ranging from 0 Hz to 140 Hz. At low-frequency range of 0–35 Hz, the estimated equation for the plot of the acceleration transfer function is expressed as:



**Fig. 16.** Bode plot of the frequency range 0–35 Hz a. obtained from simulation with ANSYS and b. obtained from estimation with MATLAB

$$G(s) = \frac{17807}{s^2 + 7S + 35530} \tag{12}$$

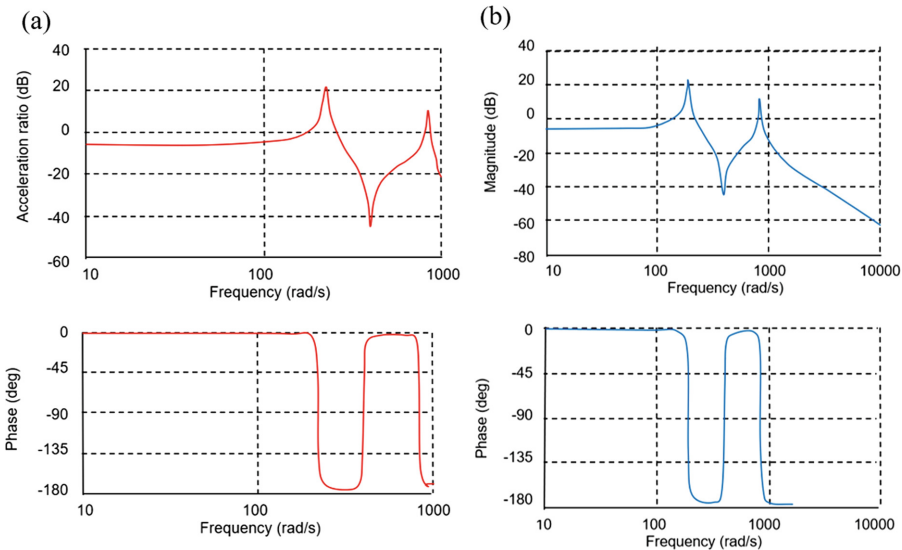
Figure 16 illustrates the bode plot created using ANSYS data and the estimated equation plotted using MATLAB software.

The bode plot from the estimated equation depicts a smoother curve compared to ANSYS data. An identical magnitude and phase plot were detected in both plots, indicating that the model is valid for real behaviour of the system. From both phase plots, the maximum phase shift in the acceleration transfer function is  $-180^\circ$ . The phase plots intersect at  $-90^\circ$  where the natural frequency occurred. In this case, the natural frequency is equivalent to 35530 rad/s or 30 Hz. Close analysis reveals that overshoot appeared in the gain plot, which represents the damping in the system. If the damping ratio is decreased, then the peak in the gain plot will be much higher. It is considered as a second order system due to the largest asymptote in the gain plot, which is decreasing at  $-40$  dB/decade.

For the defined frequency range of 0–140 Hz, the selected operating frequency is 133 Hz. The estimated equation of acceleration transfer function is:

$$G(s) = \frac{79962(s^2 + 13s + 156689)}{(s^2 + 6S + 35530)(s^2 + 19s + 703594)} \tag{13}$$

Figure 17 depicts the bode plot created using ANSYS data and the estimated equation plotted using MATLAB software. The obtained bode plot from the estimated equation and ANSYS data reveal a similar pattern in terms of gain plot and phase plot.



**Fig. 17.** Bode plot of the frequency range 0–140 Hz **a** obtained from simulation with ANSYS and **b** obtained from estimation with MATLAB

Hence, it is evident that the estimated equation is valid for modelling the real behaviour of the system. From both phase plots, the maximum phase shift in the acceleration transfer function is  $180^\circ$ . An intersection at  $-90^\circ$  was observed, where the maximum and minimum points are located in the system. In this case, the values are equivalent to 30 Hz, 63 Hz and 133 Hz. The overshoot appeared in the gain plot indicating the presence of the damping factor of the system. The gain plot shows that at increasing frequency, the magnitude of poles is decreasing from 21 dB to 10 dB. This plot was considered as a second order system because of the significant decrease of the largest asymptote at  $-40$  dB/decade.

## 4 Conclusion

A new approach of using a finite element formulation for a coupled mechanical-electrical structure starting from the constitutive equations for finding transfer function has been presented here. General multi-layered piezoelectric shell elements have been successfully developed and integrated into the commercial finite element package ANSYS. From the study, it can be concluded that the finite element model can be used to develop the transfer function and enhance the understanding of a system consist of piezo elements. By using numerical analysis, the natural frequencies of the system at low-frequency range are detected at 37 Hz, 130 Hz and 145 Hz. This result was in a good agreement with the experimental investigation. The mode shapes and natural frequencies from both numerical and experimental analysis provided similar results with a maximum of 3% deviation.

**Acknowledgements.** The authors acknowledge the support from Universiti Teknikal Malaysia Melaka (UTeM). This research was partially funded through research grants of PJP/2018/FKP (5A)9/S01585.

## References

1. Karagülle, H., Malgaca, L., Öktem, H.F.: Analysis of active vibration control in smart structures by ANSYS. *Smart Mater. Struct.* **13**, 661–667 (2004)
2. Al Hazmi, M.W.: Finite element analysis of cantilever structure excited by patches of piezoelectric actuators. In: 11th Intersociety Conference on Thermal and Thermomechanical Phenomena in Electronic Systems (ITHERM), Orlando, pp. 809–814 (2008)
3. Koziem, M.S., Koltowski, B.: Comparison of active and passive damping of plate vibration by piezoelectric actuators—FEM simulation. *Acta Phys. Pol. A* **119**(6A), 1005–1008 (2011)
4. Gosiewski, Z., Koszewnik, A.P.: Fast prototyping method for the active vibration damping system of mechanical structures. *Mech. Syst. Signal Process.* **36**(1), 136–151 (2012)
5. Chen, Y., Xue, X.: Advances in the structural health monitoring of bridges using piezoelectric transducers. *Sensors* **18**(12), 1–24 (2018)
6. Bilgunde, P.N., Bond, L.J.: In-situ health monitoring of piezoelectric sensors using electromechanical impedance: a numerical perspective. *AIP Conf. Proc.* **1949**, 1–8 (2018)
7. Gedeon, D., Rupitsch, S.J.: Finite element based system simulation for piezoelectric vibration energy harvesting devices. *J. Intell. Mater. Syst. Struct.* **29**(7), 1333–1347 (2018)

8. Halim, D., Moheimani, S.O.R.: An optimization approach to optimal placement of collocated piezoelectric actuators and sensors on a thin plate. *Mechatronics* **13**, 27–47 (2003)
9. Gibbs, G.P., Fuller, C.R.: Excitation of thin beams using asymmetric piezoelectric actuators. *J. Acoust. Soc. Am.* **92**(6), 3221–3227 (1992)
10. Fuller, C.R., Elliot, S.J., Nelson, P.A.: *Active Control of Vibration*, 1st edn. pp. 27–35. Academic Press, Cambridge (1996)
11. Najib, A.M., Muhammad, M.N., Fairul, A.J., Bani Hashim, A.Y., Hasib, H.: Analysis of unimorph piezoceramic patches on damped square shaped plate. *Appl. Mech. Mater.* **315**, 865–971 (2013)
12. Kpeky, F., Abed-Meraim, F., Daya, E.M.: New linear and quadratic prismatic piezoelectric solid-shell finite elements. *Appl. Math. Comput.* **319**, 355–368 (2018)
13. Carrera, E., Valvano, S., Kulikov, G.M.: Electro-mechanical analysis of composite and sandwich multilayered structures by shell elements with node-dependent kinematics. *Int. J. Smart Nano Mater.* **9**(1), 1–33 (2018)
14. Yaman, Y., Caliskan, T., Nalbantoglu, V., Prasad, E., Waechter, D.: Active vibration control of a smart plate. In: *ICAS 2002 Congress*, Toronto, Canada (2002)
15. Young-Hun, L.: Finite-element simulation of closed loop vibration control of a smart plate under transient loading. *Smart Mater. Struct.* **12**(2), 272–286 (2003)
16. Joshi, A., Khot, S.M.: Smart actuator effectiveness improvement through modal analysis. In: *VETOMAC-3 and ACSIM 2004 International Conference*, pp. 142–150 (2004)
17. Nguyen, V.T., Kumar, P., Leong, J.Y.C.: Finite element modelling and simulations of piezoelectric actuators responses with uncertainty quantification. *Computation* **6**(60), 1–20 (2018)
18. Rajan, L.W., Kamal, M.B.: Shape control and vibration analysis of piezolaminated plates subjected to electromechanical loading. *Open J. Civ. Eng.* **6**(3), 335–345 (2016)
19. Chung, N.T., Thuy, N.N., Thu, D.T.N., Chau, L.H.: Numerical and experimental analysis of the dynamic behavior of piezoelectric stiffened composite plates subjected to airflow. *Math. Probl. Eng.* **2019**, 1–10 (2019)



# Mechanomyography: An Insight to Muscle Physiology

Irsa Talib<sup>1</sup>(✉), Kenneth Sundaraj<sup>2</sup>, Chee Kiang Lam<sup>1</sup>,  
Md. Asraf Ali<sup>3</sup>, and Jawad Hussain<sup>2</sup>

<sup>1</sup> School of Mechatronic Engineering, Universiti Malaysia Perlis (UniMAP),  
02600 Arau, Perlis, Malaysia  
irsatalib@gmail.com

<sup>2</sup> Centre for Telecommunication Research and Innovation (CeTRI),  
Fakulti Kejuruteraan Elektronik & Kejuruteraan Komputer (FKEKK),  
Universiti Teknikal Malaysia Melaka (UTeM), Durian Tunggal, Malaysia

<sup>3</sup> Daffodil International University, Dhaka, Bangladesh

**Abstract.** The aim of this review article is to highlight an important application of mechanomyography as a tool to study muscle physiology related issues. Skeletal muscles are of vital significance in our body and contribute well towards all type of movements. Although, there are other techniques in vogue used for non-invasive assessment of muscle. But mechanomyography (MMG) do offer shear benefits for reliable muscle study. So, a substantial number of related articles were searched for this technical review from various databases including SCOPUS, PubMed, ScienceDirect, IEEE Xplore and springer link. Records were screened according to the selection criteria. The studies related to muscle physiology aspects analyzed using MMG were only selected for detailed analysis. During in depth analysis of records finally selected for this article, physiology aspects investigated via MMG were divided into seven sections including muscle stiffness, Parkinson disease, effect of dehydration, muscle contractile properties, muscle contraction mechanics, muscle temperature and muscle hypertrophy. The findings of this review suggest that MMG is a useful and reliable tool to investigate muscle physiology and it has significant applications in sports and medicine. Muscle contractile properties can be employed for future investigation on muscle fatigue, stiffness, atrophy and even functional mechanics of muscle. This review might fill the gap in knowledge in understanding of muscle physiology using MMG.

**Keywords:** Contractile properties · Electromyography · Mechanomyography · Muscle physiology

## 1 Introduction

### 1.1 What Are Skeletal Muscles?

Muscles form a major portion of body mass. Although, there are three major types of body muscles, but skeletal muscles are of vital importance due to their role in producing movement [9]. They are connected to bones through tendons. Hence, they

transmit body movements through their coordination with skeleton. Muscles are coordinated by the commands sent from central nervous system directly to motor units [12]. Thus, motor units are functional building blocks of muscle fibres. Attachment of motor unit with muscle fibre is shown in Fig. 1. Skeletal muscles possess significant importance due to their peculiar function in body movements.

## 1.2 Significance of Muscle Physiology

Understanding of muscle physiology is very important while studying muscles as a key player in human movement. Muscle physiology is important for many health-related areas including rehabilitation, prosthetic control and medicine [19]. It could be equally significant in sports, gymnastics and athletics as well.

## 1.3 MMG Versus Other Non-invasive Tools

There are four contemporary non-invasive tools used for muscle study including ultrasound, infra-red radiation, electromyography (EMG) [11] and mechanomyography (MMG) [10]. First two tools have disadvantages for being radiation techniques. Electromyography is the study of muscle through the measurement of electrical potential produced by muscle fibers during movement [23]. It has been a useful tool for muscle study since decades [2]. But its reliability is doubtful in some cases like in an environment with electrical noise [28]. Secondly, it needs skin preparations to be made, before experiment. There is another technique known as mechanomyography, which provides shear benefits in comparison to EMG [30]. Mechanomyography is a non-invasive tool which is used to study muscle function and mechanics through the measure of vibrations produced in skeletal muscles [15]. It is a reliable tool with higher signal to noise ratio than EMG [6]. There is no need of skin preparations as well. Light weight sensors can accurately measure muscle activity [31]. Various MMG signal parameters, including both time and frequency domain have been investigated in literature.

## 2 Muscle Physiology and MMG

Temporal and spectral features of MMG signal can be used for analysis of muscle physiology and mechanics even at the level of muscle functional unit [31]. Many of the physiology aspects related to muscle have been observed by MMG [18]. These physiology aspects could be in terms of both muscle condition and muscle contraction mechanics as well. In this review article we have summarized and critically analysed the physiology measures which have been contributed by MMG. The physiological aspects of muscle covered by MMG can be divided into seven sections including: muscle stiffness, muscle dehydration, muscle contractile properties, muscle contraction mechanics, muscle temperature and exercise hypertrophy as listed in Table 1. Hence, this article not only advocates for the reliability of MMG, but it also contributes to the knowledge in the field of muscle physiology.

## 2.1 Muscle Stiffness

Muscle condition could be changed due to some disease, exercise or accident. It is important to investigate muscle condition using some technique during any of the above situation. If there is some stiffness in muscle's natural condition, MMG can be used to observe muscle stiffness [9]. Muscle stiffness has been measured using piezoelectric contact sensors in [3]. It was tested using both isometric and isokinetic testing. Stiffness could be related to MMG amplitude and mean power frequency (MPF). Another study measured muscle stiffness using displacement sensor in terms of contractile properties of muscle [24]. Maximal displacement ( $D_m$ ) was observed to increase with decrease in muscle stiffness. This observation could be useful in stiffness monitoring in space flight and microgravity models. It could be applied to clinical research for rehabilitation purpose also.

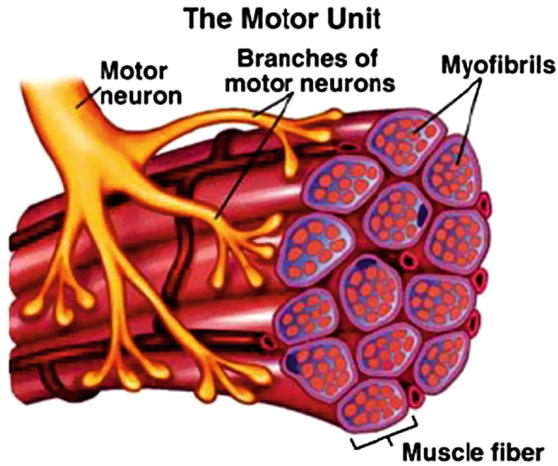
## 2.2 Parkinson Disease

MMG has been used to assess muscle condition in Parkinson disease (PD) patients for rehabilitation purpose. The authors in [21] used a hybrid probe for both MMG and EMG measurements in PD subjects. Neuromuscular activity was assessed in patients by evaluating their ability to carry load. MMG proved to assess neuromuscular activity in patients as compared to normal subjects much better than EMG. It is due to the reason that MMG remains less affected by tremor in subject posture [17]. The same authors further investigated tremor related changes in PD patients using MMG [20]. Unfortunately, no difference was detected between normal subjects and patients related to tremor effects. It was due to the reason that patients were analyzed in their medication on phase. Hence, fruitful results could not appear. But it opened a new area in MMG for the analysis of diseased muscle.

## 2.3 Effect of Dehydration on Muscle

Dehydration is a common phase in athletic and sports activity, which needs to be investigated in detail to know the risk at muscle level caused through dehydration. Hence, [8] observed the effect of dehydration in ten subjects belonging to both female and male genders using a piezoelectric contact sensor in MMG. The mechanomyogram showed no difference in MMG amplitude and frequency parameters in dehydrated muscle. This shows that moderate dehydration is safe for muscles. But there is a dire need to test this protocol on dehydration for severe situations. So that the results can be employed to field of sports and athletics.





**Fig. 1.** Attachment of motor unit on muscle fiber

## 2.4 Muscle Contractile Properties

Contractile properties of muscle infer to valuable information on muscle physiology. So, this area needs special attention of researchers using MMG as muscle function tool in future. Many records in literature including [24, 27–29, 32, 33], have used displacement sensor to study contractile properties of muscle. Contractile parameters including delay time ( $T_d$ ), contraction time ( $T_c$ ), half relaxation time ( $T_r$ ) and maximal amplitude ( $D_m$ ) carry useful information about muscle stiffness [24] and muscle deformation [27]. At the same time these contractile properties of muscle using MMG can indicate the approach of muscle fatigue [29] as well. In case of muscle damage, MMG has been used to monitor muscle condition during hypertrophy till rehabilitation completed [28].

## 2.5 Muscle Contraction Mechanics-MU Activation Pattern

To understand muscle physiology, one must know the muscle mechanics at functional level of muscle building blocks. Motor unit is a functional unit of muscle which transmit the order coming from central nervous system through motor neuron to muscle fibers. To have a deep look on muscle mechanics we need to know what is happening inside the skin when some physical activity is performed. MMG uncovers vital information about motor unit (MU) functional strategy. Piezoelectric contact sensor has been used in [26] and [4] to explain MU activation pattern under specific experiment protocol. With the increase in external load motor unit recruitment is the MU activation strategy which is obvious from both time and frequency domain parameters of MMG signal.

## 2.6 Muscle Temperature

Effect of muscle functioning on muscle temperature is another physical parameter which has been analyzed in [5] and [7]. Accelerometer has been employed in both the records. Male participants only took part in the experiment. [5] concluded that reduction in muscle temperature reduces sarcolemma propagation properties of muscle. While, [7] investigated the effect of fatigue on temperature and found no difference in temperature for fatigued muscle. The application of temperature effect for various other muscle test protocol opens new questions in sports and medicine research.

## 2.7 Exercise Hypertrophy and Atrophy

Muscle hypertrophy and atrophy has been diagnosed through MMG signal parameters in [28]. Change in contractile properties of hypertrophic muscle has been monitored using laser displacement sensor. This paves the path to advance use of MMG as rehabilitation tool in applied research.

## 3 Results and Discussion

MMG has been used for muscle function assessment since last two decades. This review article reveals the unique application of MMG as a tool to study muscle physiology. Various physiological attributes of muscle studied through MMG, including stiffness, disease, dehydration, temperature and hypertrophy have been summarized here. MMG can also be used for understanding of muscle mechanics and motor unit strategy information [22]. This information could be equally useful for muscle function study in the field of medicine as well as athletics [16]. Each of the physiological aspect studied through MMG opens several new questions which invite MMG to solve these myths of physiology. Moreover, most of the records support the application of MMG as a valid tool [14]. As there are many of EMG studies showing comparable results [1]. Even that MMG is better in some cases like when physiological tremor [25] and electrical noise are issues of concern. MMG along with vital benefits of ease and reliability proves to be a better tool to investigate muscle physiology. All combined advantages of MMG should be incorporated in advance muscle research for both applied and clinical prospects.

**Table 1.** Summary of articles analyzing muscle physiology using MMG

Sr. no.	Authors	Details of participants	MMG Transducer used in study	Muscle physiology attribute studied
1.	Beck et al. [3]	10 adult subjects including 5 males and 5 females	Piezoelectric crystal contact sensor	Muscle stiffness

**Remarks:** Muscle stiffness assessed by isometric and isokinetic testing

(continued)

**Table 1.** (continued)

Sr. no.	Authors	Details of participants	MMG Transducer used in study	Muscle physiology attribute studied
2.	Pisot et al. [24]	10 healthy male subjects	Displacement sensor	Muscle stiffness
<b>Remarks:</b> Use of contractile parameters of muscle to measure stiffness				
3.	Marusiak et al. [20]	15 female subjects including 9 Parkinson disease patients and 6 healthy women	Hybrid sensor for both EMG and MMG	Ability to carry load in PD patients
<b>Remarks:</b> Neuromuscular activity assessed in PD patients				
4.	Marusiak et al. [21]	20 female subjects including 10 Parkinson disease patients and 10 healthy women	Hybrid sensor for both EMG and MMG	Tremor related changes in PD patients
<b>Remarks:</b> No difference could be found among two subjects' groups because PD patients participated in experiment with medication ON state				
5.	Evetovich et al. [8]	10 subjects including 4 females and 6 males	Piezoelectric crystal contact sensor	Dehydration
<b>Remarks:</b> Moderate dehydration do not affect muscle function as assessed by MMG				
6.	Simunic et al. [27]	15 female subjects	Digital displacement sensor	Contractile properties of muscle
<b>Remarks:</b> Skeletal muscle deformation can be studied through various contractile parameters including delay time (Td), contraction time (Tc), half relaxation time (Tr) and maximal amplitude (Dm)				
7.	Pisot et al. [24]	10 healthy male subjects	Displacement sensor	Contractile properties of muscle
<b>Remarks:</b> Change in contractile parameters can be used to measure muscle stiffness				
8.	Than et al. [32]	19 subjects in total	Laser measurement device	Contractile properties of muscle
<b>Remarks:</b> Contractile parameters measured by MMG can be used for monitoring of muscle having hypertrophic state				
9.	Tosovic et al. [33]	11 subjects including both males and females	Laser displacement sensor	Contractile properties of muscle
<b>Remarks:</b> Contractile parameters can detect muscle fatigue				
10.	Qi et al. [26]	12 subjects including 6 females and 6 males	Piezoelectric transducer	Muscle contraction mechanics
<b>Remarks:</b> MMG total intensity was lower during concentric contraction than eccentric contraction which may be due to physiological tremor				

(continued)

**Table 1.** (continued)

Sr. no.	Authors	Details of participants	MMG Transducer used in study	Muscle physiology attribute studied
11.	Beck et al. [3]	12 adult subjects including 6 females and 6 males	Piezoelectric crystal contact sensor	Muscle contraction mechanics
<b>Remarks:</b> MMG time and frequency domain parameters can describe motor control strategy which depicts muscle contraction				
12.	Cè et al. [5]	15 physically active male subjects	Accelerometer	Muscle temperature
<b>Remarks:</b> Reduction in muscle temperature reduces sarcolemma propagation properties				
13.	Cè et al. [6]	15 physically active male subjects	Accelerometer	Muscle temperature
<b>Remarks:</b> Muscle temperature is not affected by fatigue				
14.	Than et al. [32]	19 subjects in total	Laser measurement device	Muscle hypertrophy and atrophy
<b>Remarks:</b> Muscle hypertrophy and atrophy can be diagnosed through MMG signal parameters				

## 4 Conclusion

Muscle physiology is of vital importance for progress in understanding and research for rehabilitation, sports, athletics and gymnastics [13]. MMG has shown its potential capability to analyze various physiological aspects related to muscle. This review article critically analyzed past studies dealing with MMG and physiology issues. It suggests further research on muscle stiffness, contractile properties and muscle hypertrophy along with clarity in muscle function. Muscle contraction mechanisms can be highlighted with support of physiology to get maximum advantage out of MMG as an insight to muscle physiology.

**Acknowledgements.** The authors would like to thank Universiti Teknikal Malaysia Melaka (UTeM) for providing a conducive platform to conduct the research.

## References

1. Ahamed, N.U., Sundaraj, K., Ahmad, B., et al.: Effects of anthropometric variables and electrode placement on the SEMG activity of the biceps brachii muscle during submaximal isometric contraction in arm wrestling. *Biomedizinische Technik/Biomed. Eng.* **58**(5), 475–488 (2013)
2. Ahamed, N.U., Sundaraj, K., Ahmad, R.B., et al.: Electromyographic responses during elbow movement at two angles with voluntary contraction: influences of muscle activity on upper arm biceps brachii. *Res. J. Appl. Sci. Eng. Technol.* **4**(22), 4591–4595 (2012)

3. Beck, T.W., Housh, T.J., Johnson, G.O., et al.: Mechanomyographic amplitude and mean power frequency versus torque relationships during isokinetic and isometric muscle actions of the biceps brachii. *J. Electromyogr. Kinesiol.* **14**(5), 555–564 (2004)
4. Beck, T.W., Housh, T.J., Johnson, G.O., et al.: Mechanomyographic and electromyographic time and frequency domain responses during submaximal to maximal isokinetic muscle actions of the biceps brachii. *Eur. J. Appl. Physiol.* **92**(3), 352–359 (2004)
5. Cè, E., Rampichini, S., Agnello, L., et al.: Effects of temperature and fatigue on the electromechanical delay components. *Muscle Nerve* **47**(4), 566–576 (2013)
6. Cè, E., Rampichini, S., Esposito, F.: Novel insights into skeletal muscle function by mechanomyography: from the laboratory to the field. *Sport Sci. Health* **11**(1), 1–28 (2015)
7. Cè, E., Rampichini, S., Venturelli, M., et al.: Electromechanical delay components during relaxation after voluntary contraction: reliability and effects of fatigue. *Muscle Nerve* **51**(6), 907–915 (2015)
8. Evetovich, T.K., Boyd, J.C., Drake, S.M., et al.: Effect of moderate dehydration on torque, electromyography, and mechanomyography. *Muscle Nerve* **26**(2), 225–231 (2002)
9. Han, H., Jo, S., Kim, J.: Comparative study of a muscle stiffness sensor and electromyography and mechanomyography under fatigue conditions. *Med. Biol. Eng. Comput.* **53**(7), 577–588 (2015)
10. Hill, E., Housh, T.J., Smith, C., et al.: Effect of sex on torque, recovery, EMG, and MMG responses to fatigue. *J. Musculoskelet. Neuronal Interact.* **16**(4), 310 (2016)
11. Hussain, J., Sundaraj, K., Low, Y., et al.: Electromyography—a reliable technique for muscle activity assessment. *J. Telecommun. Electron. Comput. Eng. JTEC* **10**(2–6), 155–159 (2018)
12. Hussain, J., Sundaraj, K., Low, Y.F., et al.: Fatigue assessment in the brachii muscles during dynamic contractions. *Int. J. Appl. Eng. Res.* **12**(22), 12403–12408 (2017)
13. Hussain, J., Sundaraj, K., Low, Y.F., et al.: A systematic review on fatigue analysis in triceps brachii using surface electromyography. *Biomed. Signal Process. Control* **40**, 396–414 (2018)
14. Ibitoye, M.O., Hamzaid, N.A., Zuniga, J.M., et al.: Mechanomyography and muscle function assessment: a review of current state and prospects. *Clin. Biomech.* **29**(6), 691–704 (2014)
15. Islam, A., Sundaraj, K., Ahmad, B., et al.: Mechanomyography sensors for muscle assessment: a brief review. *J. Phys. Therapy Sci.* **24**(12), 1359–1365 (2012)
16. Islam, M.A., Sundaraj, K., Ahmad, R.B., et al.: Mechanomyogram for muscle function assessment: a review. *PloS ONE* **8**(3), e58902 (2013)
17. Jotta, B., Garcia, M.A.C., Pino, A.V., et al.: Characterization of the mechanomyographic signal of three different muscles and at different levels of isometric contractions. *Acta Bioeng. Biomech.* **17**(4), 73–84 (2015)
18. Kimura, T., Fujibayashi, M., Tanaka, S., et al.: Mechanomyographic responses in quadriceps muscles during fatigue by continuous cycle exercise. *Eur. J. Appl. Physiol.* **104**(4), 651–656 (2008)
19. Krueger, E., Scheeren, E.M., Nogueira-Neto, G.N., et al.: Advances and perspectives of mechanomyography. *Revista Brasileira de Engenharia Biomédica* **30**(4), 384–401 (2014)
20. Marusiak, J., Jaskólska, A., Jarocka, E., et al.: Electromyography and mechanomyography of elbow agonists and antagonists in Parkinson disease. *Muscle Nerve* **40**(2), 240–248 (2009)
21. Marusiak, J., Jaskólska, A., Kisiel-Sajewicz, K., et al.: EMG and MMG activities of agonist and antagonist muscles in Parkinson's disease patients during absolute submaximal load holding. *J. Electromyogr. Kinesiol.* **19**(5), 903–914 (2009)
22. Okkesim, Ş., Coşkun, K.: Features for muscle fatigue computed from electromyogram and mechanomyogram: a new one. *Proc. Inst. Mech. Eng. Part H J. Eng. Med.* **230**(12), 1096–1105 (2016)

23. Paravlić, A., Zubac, D., Šimunič, B.: Reliability of the twitch evoked skeletal muscle electromechanical efficiency: a ratio between tensiomyogram and M-wave amplitudes. *J. Electromyogr. Kinesiol.* **37**, 108–116 (2017)
24. Pišot, R., Narici, M.V., Šimunič, B., et al.: Whole muscle contractile parameters and thickness loss during 35-day bed rest. *Eur. J. Appl. Physiol.* **104**(2), 409–414 (2008)
25. Posatskiy, A., Chau, T.: The effects of motion artifact on mechanomyography: a comparative study of microphones and accelerometers. *J. Electromyogr. Kinesiol.* **22**(2), 320–324 (2012)
26. Qi, L., Wakeling, J.M., Ferguson-Pell, M.: Spectral properties of electromyographic and mechanomyographic signals during dynamic concentric and eccentric contractions of the human biceps brachii muscle. *J. Electromyogr. Kinesiol.* **21**(6), 1056–1063 (2011)
27. Šimunič, B., Križaj, D., Narici, M., et al.: Twitch parameters in transversal and longitudinal biceps brachii response. *Annales Kinesiologiae* **1**(1), 61–80 (2010)
28. Talib, I., Sundaraj, K., Lam, C.: Choice of mechanomyography sensors for diverse types of muscle activities. *J. Telecommun. Electron. Comput. Eng. (JTEC)* **10**(1–13), 79–82 (2018)
29. Talib, I., Sundaraj, K., Lam, C., et al.: Development of a standalone application to measure crosstalk in MMG signals from forearm muscles during wrist postures. *J. Telecommun. Electron. Comput. Eng. (JTEC)* **10**(2–7), 103–106 (2018)
30. Talib, I., Sundaraj, K., Lam, C.K., et al.: A review on crosstalk in myographic signals. *Eur. J. Appl. Physiol.* **119**(1), 9–28 (2019)
31. Talib, I., Sundaraj, K., Lam, C.K., et al.: A systematic review of muscle activity assessment of the biceps brachii muscle using mechanomyography. *J. Musculoskelet. Neuronal Interact.* **18**(4), 446 (2018)
32. Than, C., Tosovic, D., Seidl, L., et al.: The effect of exercise hypertrophy and disuse atrophy on muscle contractile properties: a mechanomyographic analysis. *Eur. J. Appl. Physiol.* **116**(11–12), 2155–2165 (2016)
33. Tosovic, D., Than, C., Brown, J.: The effects of accumulated muscle fatigue on the mechanomyographic waveform: implications for injury prediction. *Eur. J. Appl. Physiol.* **116**, 1485–1494 (2016)



# Identification of a Piezoelectric Compact Actuator

Mohd Nazmin Maslan<sup>1</sup>(✉), Mohd Syafiq Syed Mohamed<sup>1</sup>,  
Ruzaidi Zamri<sup>1</sup>, Lokman Abdullah<sup>1</sup>, Mahasan Mat Ali<sup>1</sup>,  
Mohd Zamzuri Ab Rashid<sup>2</sup>, and Mohd Samsuddin Noorazizi<sup>3</sup>

<sup>1</sup> Faculty of Manufacturing Engineering, Universiti Teknikal Malaysia Melaka (UTeM), Hang Tuah Jaya, Durian Tunggal, 76100 Melaka, Malaysia  
nazmin@utem.edu.my

<sup>2</sup> Faculty of Electrical Engineering, Universiti Teknikal Malaysia Melaka (UTeM), Hang Tuah Jaya, Durian Tunggal, 76100 Melaka, Malaysia

<sup>3</sup> Department of Engineering, Razak Faculty of Technology and Informatics, UTM Kuala Lumpur, Level 6, Razak Tower, Jalan Sultan Yahya Petra, 54100 Kuala Lumpur, Malaysia

**Abstract.** This paper describes the identification of a highly nonlinear and hysteretic piezoelectric compact actuator. A system identification technique was used based on observed data from the actuator mounted on a base structure. The parameter estimation process was conducted using the recursive least squares algorithm. Once the transfer function model has been obtained, it is required to verify whether the model is good enough or it meets the necessary requirements to represent the system. The experimental results and the SI approach indicate the effectiveness of the proposed scheme.

**Keywords:** Piezoelectric · Compact actuator · Transfer function · System identification

## 1 Introduction

Piezoelectric actuators that are commonly classified as smart actuators find many useful applications in various disciplines, particularly related to robotics, biomedical tools plus actuation and control of mechanisms [1]. When voltage is applied to the actuators, they respond by changing their dimension (e.g., displacement). Due to the inherent hysteretic and nonlinear features of the piezoelectric actuators [2], it is very difficult to model their transfer functions that are particularly required in typical design and development process involving the modelling and control of these actuators so that their application in various systems is feasible and adequately justified [3, 4]. Constructing the dynamic models to predict their electromechanical behaviour precisely remains an ongoing area of research.

System identification (SI) is a method of measuring a system transfer function or some equivalent mathematical description from measurements of the system input and output. This method may provide a useful tool to study the behavior of piezoelectric actuators. There are numerous applications of SI techniques [5]. Well-developed techniques for parameters estimation of models such as least-square, instrumental

variable and maximum likelihood tend to fail in the search for the global optimum if the search space is nonlinear in the parameters [6]. In [7], a relay feedback identification was employed for actuators with hysteresis. Sung and Lee [8] had stated that nonlinear characteristic response of the piezoelectric actuator system can be linearized as second-order linear dynamic model whilst setting the PID controller to regulate the output displacement.

In this paper, the transfer function of a piezoelectric compact actuator is determined using the SI technique. The results involving selected practical model is then validated through comprehensive testing.

## 2 Piezoelectric Compact Actuator

The compact actuator based on stacked piezo actuator is selected. Figure 1 shows the P-840 and P-841 series piezo actuators. They are high-resolution linear actuators that provide sub-millisecond response and sub-nanometer resolution suitable for static and dynamic applications (Table 1).



**Fig. 1.** PI P-840, P-841 piezoelectric compact actuators [9]

These actuators are equipped with highly reliable multilayer piezo ceramic stacks protected by a non-magnetic stainless steel case with internal spring preload. The preload makes them ideal for dynamic applications and tensile loads, while the ceramic only insulation makes them resistant to ambient humidity and leakage-current failures.

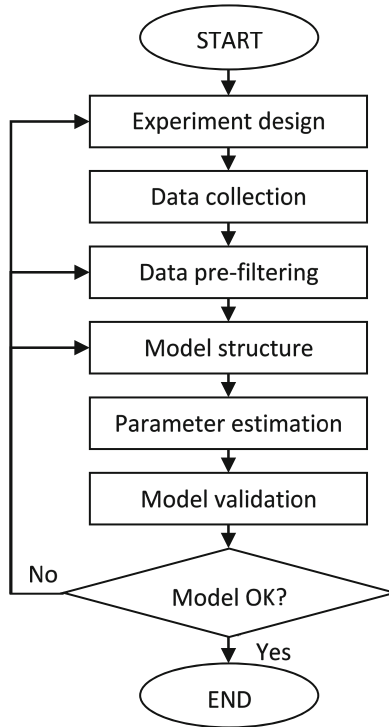
**Table 1.** Specifications for the P-841.20 piezoelectric compact actuator

Parameters	Value
Dimensions L × D	50.0 × Ø12.0 mm
Mass without cable	28 g
Operating voltage	0–100 V
Open-loop travel	30 μm ± 20%
Closed-loop travel	30 μm
Closed-loop/open-loop resolution	0.6/0.3 nm
Static large-signal stiffness	27 N/μm ± 20%
Push force capacity	1000 N



### 3 System Identification

Based on the input and output data gathered, the standard SI procedure shall be followed as shown in Fig. 2.



**Fig. 2.** Procedure of SI technique

First, the experimental setup is designed and developed. Then, the input and output data of the actuator are collected via a PC-based data acquisition system. Next, the data are pre-filtered by normalizing them and the model structure of the system is chosen. Subsequently, the parameter is estimated using the identification method. Lastly, the model validation is conducted. The main focus in SI is on the parameter estimation process in which the recursive least-squares (RLS) algorithm was used. The algorithm

can be used to estimate parameters of a transfer function where the estimated parameters are updated at every sampling interval [10]. Consider a discrete-time (D-T) system in the form:

$$y(k) = \frac{b_1 z^{-1} + b_2 z^{-2} + \dots + b_m z^{-m}}{1 + a_1 z^{-1} + a_2 z^{-2} + \dots + a_n z^{-n}} u(k) \quad (1)$$

which can also be written as:

$$\begin{aligned} y(k) + a_1 y(k-1) + a_2 y(k-2) + \dots + a_n y(k-n) \\ = b_1 u(k-1) + b_2 u(k-2) + \dots + b_m u(k-m) \end{aligned} \quad (2a)$$

Equation (1) is known as the D-T transfer function.  $b_1 \dots b_m$  and  $a_1 \dots a_n$  can be estimated using the RLS algorithm by first transforming Eq. (2a) into a regression equation.

$$y(k) = y(k-1) \dots y(k-n) \quad u(k) \dots u(k-m) \begin{bmatrix} a_1 \\ \vdots \\ a_n \\ b_1 \\ \vdots \\ b_m \end{bmatrix} \quad (2b)$$

The regression in Eq. (2b) is then used in the RLS algorithm.

## 4 Experimental Setup

Figure 3 shows the schematic diagram and photograph of the experimental setup. The displacement output of the actuator was captured using a laser displacement sensor. A personal computer (PC) via a 16-bit PCI data acquisition (DAQ) card obtains the displacement signals.

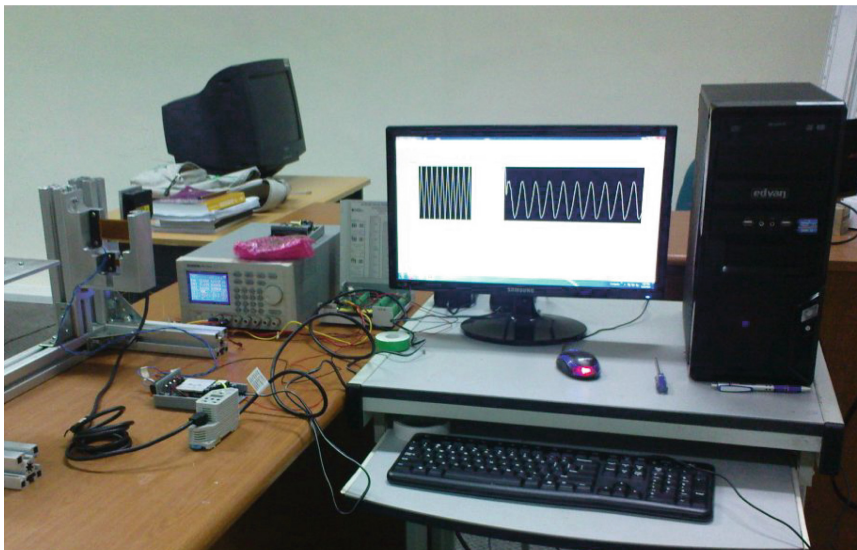
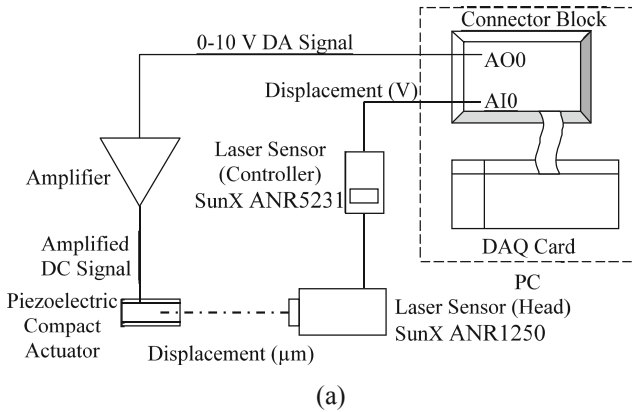
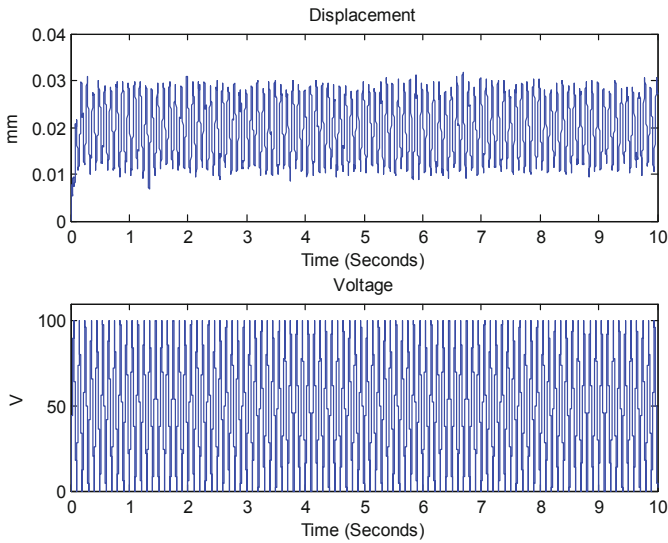


Fig. 3. Experimental setup

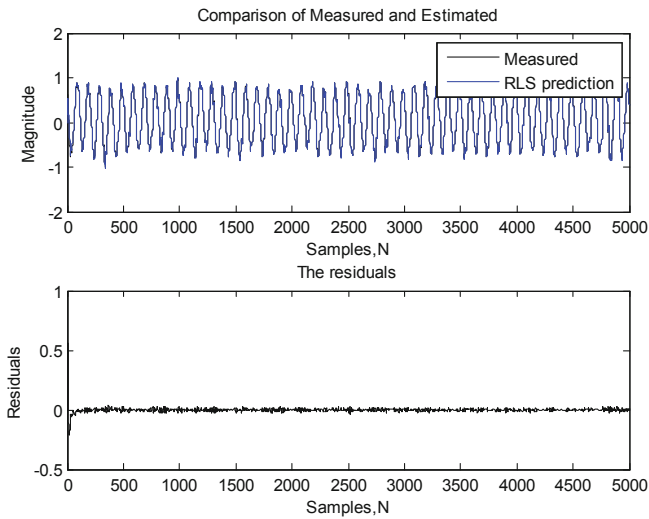
### 5 System Modelling

The software for data capturing were performed using LabVIEW. The period for the experiment was 10 s, and at a sampling rate of 1 kHz. A voltage input of 10 V 10 Hz triangle-wave is supplied via the DAQ. The actuator’s amplifier will amplify the voltage to 100 V. A low frequency (10 Hz) input waveform was used to reduce the dynamic effect of the actuator. Afterwards, a MATLAB program has been created based on the RLS using ARX model for executing the SI command lines. Once the transfer function model has been obtained, it is required to verify whether the model is good enough or it meets the necessary requirements to represent the system.

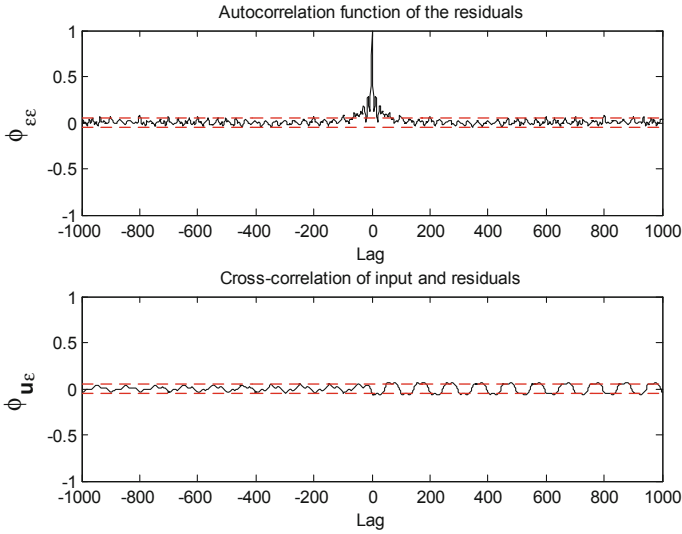
To identify the piezoelectric compact actuator model parameters, the model reduction is applied. The relationship between the input voltage and output displacement can be linearized as second order. This holds true according to the literature of piezoelectric actuators [7, 11].



**Fig. 4.** Endpoint displacement of piezoelectric compact actuator to a 100 V 10 Hz triangle-wave



**Fig. 5.** Model output and residuals of piezoelectric compact actuator using RLS



**Fig. 6.** Validation results of piezoelectric compact actuator using RLS

Figure 4 shows the endpoint displacement of piezoelectric compact actuator to a 100 V 10 Hz triangle-wave input voltage.

The top axes of Fig. 5 show the model output plot which is comparing between the measured output and model output for validating the model. A close agreement between the RLS prediction and the measured output proves the validity of the estimated parameters. The error signal or residuals at the bottom axes show that the prediction drops the error considerably.

Moreover, the behavior of its residuals is checked for validating the model, as shown in Fig. 6. The horizontal axis represents the number of lags when the correlation is estimated. The region inside the red lines are the 95% confidence intervals computed for these values. The top axes show the whiteness test that determines whether or not the error signal is a white noise. Referring to the top axes of Fig. 6, the residuals appear to be uncorrelated as the residual auto-correlation function is within the confidence intervals.

The bottom axes show the independence test that determines whether or not the residuals are uncorrelated with past inputs. Referring to the bottom axes of Fig. 6, there is no correlation between the residuals and the inputs and independent with each other.

The transfer function  $G$  for the piezoelectric compact actuator which is determined using the SI technique is given as (3).

$$G(s) = \frac{-0.06833s^2 + 0.09016s - 0.02183}{0.3548s^2 - 1.359s + 0.0044} \quad (3)$$

with a mean square error (mse) of  $2.7855 \times 10^{-4}$ .

## 6 Conclusion

An identification method has been proposed for the piezoelectric compact actuator using the RLS for parameter estimation. The whiteness test and independence test of the RLS prediction show that the residuals are uncorrelated and no correlation between the residuals and the inputs, respectively. Thus, the model produced by the RLS prediction is acceptable. Overall, the experimental results and the SI approach indicate the effectiveness of the proposed scheme.

**Acknowledgments.** The authors acknowledge the support from Universiti Teknikal Malaysia Melaka (UTeM). This research was partially funded through research grants of PJP/2018/FKP (7C)/S01588.

## References

1. Wu, Y., Culter, S., Zou, Q., Pannozzo, G., Leang, K.K., Devasia, S.: Modelling and control of smart actuators: integrating nano/bio technology into the ME curriculum. In: ASEE Annual Conference and Exposition. Pittsburgh, PA, USA (2008)
2. Valadkhan, S., Morris, K., Khajepour, A.: Robust control of smart material-based actuators. *Recent Adv. Learn. Control* **371**, 249–262 (2008). [https://doi.org/10.1007/978-1-84800-155-8\\_18](https://doi.org/10.1007/978-1-84800-155-8_18)
3. Banks, H.T., Kurdila, A.J., Webb, G.: Identification of hysteretic control influence operators representing smart actuators. Part I: Formulation. *Math. Probl. Eng.* **3**(4), 287–328 (1997). <https://doi.org/10.1155/S1024123X97000586>
4. Lien, J.P., York, A., Fang, T., Buckner, G.D.: Modeling piezoelectric actuators with hysteretic recurrent neural networks. *Sens. Actuators A Phys.* **163**(2), 516–525 (2010). <https://doi.org/10.1016/j.sna.2010.08.013>
5. Ljung, L.: *System Identification: Theory for the User*, 2nd edn. Prentice Hall PTR, Upper Saddle River (1999)
6. Hossain, M.A., Tokhi, M.O., Chipperfield, A.J., Baxter, M.J., Fonseca, C.M., Dakev, N.V.: Adaptive active vibration control using genetic algorithms. In: 1st International Conference on Genetic Algorithms in Engineering Systems: Innovations and Applications. Sheffield, UK (1995)
7. Cheng, Y.-C., Yu, C.-C.: Relay feedback identification for actuators with hysteresis. *Ind. Eng. Chem. Res.* **39**(11), 4239–4249 (2000). <https://doi.org/10.1021/ie000008h>
8. Sung, B.-J., Lee, E.-W., Kim, I.-S.: Displacement control of piezoelectric actuator using the PID controller and system identification method. In: Proceedings of International Conference on Power System Technology, New Delhi, India (2008)
9. PI (2018) Positioning with Piezo Systems. Physik Instrumente (PI) GmbH & Co. KG
10. Wellstead, P.E., Zarrop, M.B.: *Self-tuning Systems: Control and Signal Processing*, pp. 85–95. Wiley, West Sussex (1991)
11. Badr, B.M., Ali, W.G.: Identification and control for a single-axis PZT nanopositioner stage. In: Proceedings of International Conference on Modeling, Simulation and Applied Optimization (ICMSAO). Kuala Lumpur, Malaysia (2011)



# Seismic Control of a Building Structure Equip with Hybrid Mass Damper Using Sliding Mode Control

Normaisharah Mamat<sup>1</sup>, Fitri Yakub<sup>1(✉)</sup>,  
Sheikh Ahmad Zaki Shaikh Salim<sup>1</sup>, Mohd Zamzuri Ab Rashid<sup>1,2</sup>,  
Sharifah Munawarah<sup>1</sup>, and Shairatul Akma Roslan<sup>1</sup>

<sup>1</sup> Malaysia-Japan International Institute of Technology,  
Universiti Teknologi Malaysia,  
Jln Sultan Yahya Petra, 54100 Kuala Lumpur, Malaysia  
mftri.kl@utm.my

<sup>2</sup> Centre for Robotics and Industrial Automation, Fakulti Kejuruteraan Elektrik,  
Universiti Teknikal Malaysia Melaka, 76100 Durian Tunggal, Melaka, Malaysia

**Abstract.** This paper addresses the issue of the impact of controllers in suppressing the vibration of structural building during seismic. It is important to implement an appropriate controller to avoid a huge impact to the building structure from damage and collapse while earthquake occur. Sliding mode controller (SMC) and proportional-integral-derivative (PID) are proposed to alleviate the vibration. SMC is selected as control strategy because of its robust control technique that can reject the disturbances while PID is known as simple control design. The simulation for two storey building equipped with structural control device which known as hybrid mass damper placed at the top floor of the structure that represent by mass, spring and damper are constructed by using Matlab/Simulink. The input excitation to the structure is taken from El Centro earthquake with magnitude of 6.9 Mw. The output response for the system generates displacement, velocity, control input, and frequency response. Based from the result, SMC has better performance compared to PID and overall SMC is success to suppress the building vibration according to the displacement performance obtained.

**Keywords:** Vibration control · Seismic · Building · Sliding mode control

## 1 Introduction

Structural control plays an important role to prevent structural damages that cause by earthquake or strong winds. Various control devices have been implemented nowadays to guarantee the safety of the building structure such as passive, active, semi-active and hybrid device. Each of these types control devices has their own advantages and disadvantages. Passive device is simple design and can operate without using external power supply. However due to its behavior that does not add energy to the structure, therefore the structure become unstable because of most of them can be tunes based on particular structural frequency. In structural control, passive control device had proposed by Elias et al. and Kaveh et al. [1, 2] by using tuned mass damper.

Active device is then introduced in early 1970s to overcome the problems cause by passive control device. However, the usage of active control device using large power supplies to attenuate the building vibration. Paper proposed by Guclu [3] had implemented active device to the building structure to suppress the vibration and resulted the building vibration is reduced. Semi-active device cannot inject mechanical energy into controller but this type of control device has excellent behavior in using less power requirement and can using battery in case of the main power supply is fail. Hybrid device is quiet complicated design however it combines the advantages of passive and active control device and thus overcome the limitation that cause by the other control devices [4]. In structural control, hybrid control device had been implemented in paper presented by [5–7]. Most of the papers applied hybrid mass damper investigated the potential of this type of control device in improving the efficiency of the controlled structure.

In order to ensure the desired control signal to control the devices, it is essential to design the controller to suppress the vibration. Various types of controllers have been proposed to suppress building vibration such as PID, fuzzy logic control, linear-quadratic-regulator, etc. Sharma et al. [8] had proposed fuzzy logic controller on a single DOF system by design triangular membership functions of various numbers, shapes and sizes to evaluate the effect of controller to the system. Amini et al. [9] presented linear-quadratic regulator to find the optimal control forces to reduce vibration for 10-storey building. It is difficult to find appropriate weighting matrices for the optimal control system and a suitable systemic method.

This paper proposed SMC and PID in suppressing the building vibration. PID is chosen because of its simple design and only using tuning parameter for proportional, derivative and integral gain. While SMC is chosen due to its attractive characteristics that has fast response. SMC is one of the robust control techniques that was firstly introduces by Emelyanov in 1950. Moreover, it is able to reject external disturbances and meet satisfy matching conditions. Other than structural control, SMC also had been applied in robotics and actuating system. SMC is design using two main steps which is sliding surface design and control law design. The sliding surface design is by making the nonlinear plant's state trajectory is maintained on the sliding surface while control law design is to make the system to drive and maintain the system state within the boundary of switching function [10].

## 2 System Modelling

The system model is using two-degree-of-freedom mass spring damper as shown in Fig. 1 with implementation of hybrid mass damper at the second floor.  $m_1$ , and  $m_2$  are represented as mass at first and second floor,  $k_1$  and  $k_2$  are spring stiffness and  $c_1$  and  $c_2$  is damper for each floor.  $m_d$ ,  $k_d$  and  $c_d$  are represent as mass, spring stiffness and damper for hybrid mass damper. The mathematical model for the system and actuator is written as;



$$m_1\ddot{x}_1 + (c_1 + c_2)\dot{x}_1 - c_2\dot{x}_2 + (k_1 + k_2)x_1 - k_2x_2 = -m_1\ddot{x}_g \tag{1}$$

$$m_2\ddot{x}_2 + (c_2 + c_d)\dot{x}_2 - c_d\dot{x}_d + (k_2 + k_d)x_2 - k_dx_d = -m_2\ddot{x}_g - F_u \tag{2}$$

$$m_d\ddot{x}_d + c_d\dot{x}_d - c_d\dot{x}_2 + k_dx_d - k_dx_2 = -m_d\ddot{x}_g + F_u \tag{3}$$

$$Ri + K_e(\dot{x}_1 - \dot{x}_0) = u \tag{4}$$

$$F_u = K_t i \tag{5}$$

Where  $u$ ,  $I$ ,  $R$ ,  $K_t$  are control voltage to the system, armature coil current, resistance value, armature coil induced voltage and thrust constant [11].

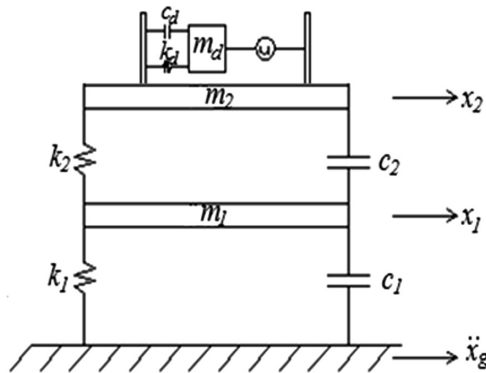


Fig. 1. Two storey building structure

Input excitation to the building structure taken from El Centro earthquake occur in 1940 is shown in Fig. 2 with the acceleration value is  $\pm 0.3$  g for 30 s.

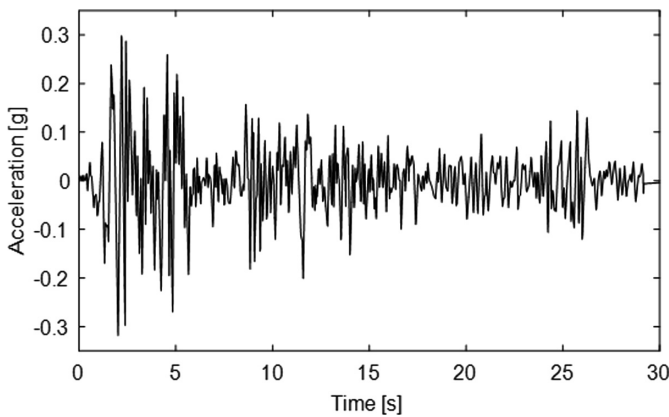


Fig. 2. El Centro earthquake ecelerogram

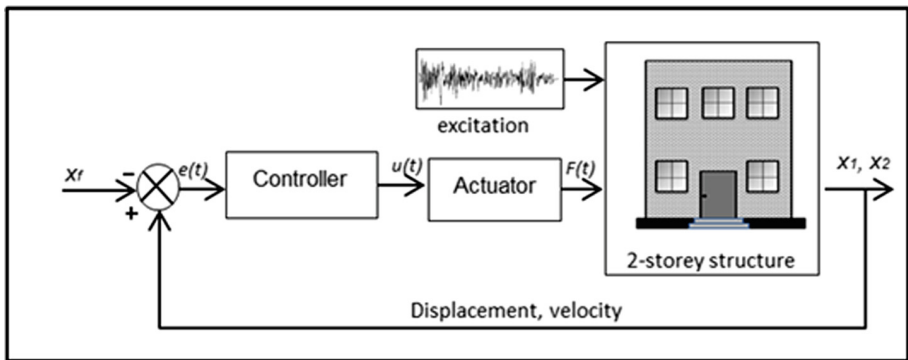
The parameter value for the system is tabulated in Table 1.

**Table 1.** System parameter

	Mass (kg)	Stiffness (10e5 N/m)	Damping (10e5 N.s/m)
Structure (1 <sup>st</sup> and 2 <sup>nd</sup> floor)	320000	930	15.69
Hybrid mass damper	44000	36.7	0.71

### 3 Controller Design

The controller plays an important role in giving the correct signal to reduce the building vibration. The implementation of controller with the structural building is illustrated in closed loop block diagram shown in Fig. 3 where  $x_f$  is the desired value,  $e(t)$  is error,  $u(t)$  is control signal, and  $F_u(t)$  is control force produce by actuator.



**Fig. 3.** Block diagram for the system, actuator and controller

#### 3.1 PID Controller

PID is well known controller as it was simple and easy implement method. The equation for PID is shown in (6) and is construct by using Simulink as shown in Fig. 4 where  $K_p$ ,  $K_i$  and  $K_d$  is non-negative coefficient for proportional, integral and derivative.

$$u(t) = K_p e(t) + K_i \int_0^t e(\tau) d\tau + K_d \frac{d}{dt} e(t) \quad (6)$$

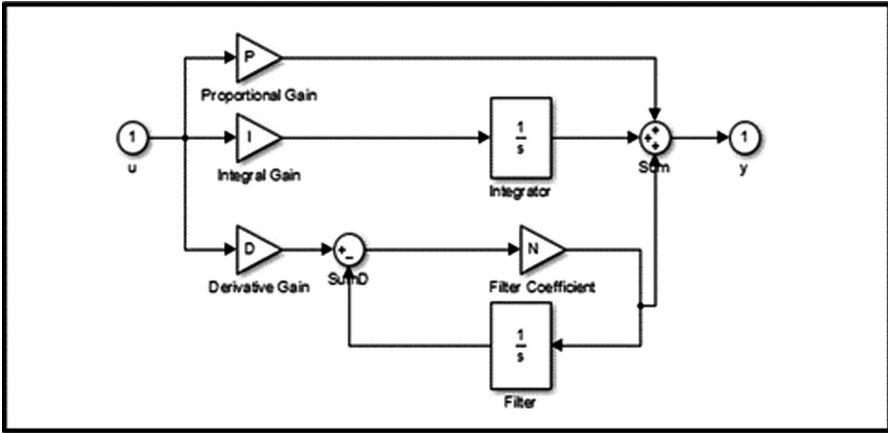


Fig. 4. PID controller

### 3.2 Sliding Mode Controller

SMC is the widely most accepted control algorithms especially in civil engineering structures because of its character of adaptiveness and robustness control methods. In SMC design, the sliding surface that defined in the state-space form conducts the state trajectory towards switching surface by nonlinear switched feedback control law. Using control law design, the system trajectory will stay on the switching surface [12]. The derivation of SMC has proposed by Tseng et al. [13] and [14]. Firstly, sliding surface is design by transform the system equation in (1), (2) and (3) into state space representation in (7) by neglecting ground motion written as in (8). Since the parameter value for  $k_1$  and  $k_2$ ,  $c_1$  and  $c_2$  and  $m_1$  and  $m_2$  are same, then only variable  $k$ ,  $c$ , and  $m$  are used as;

$$\dot{x} = Ax + Bu \tag{7}$$

$$\begin{bmatrix} \dot{x}_1 \\ \dot{x}_2 \\ \dot{x}_3 \\ \dot{x}_4 \\ \dot{x}_5 \\ \dot{x}_6 \end{bmatrix} = \begin{bmatrix} 0 & 1 & 0 & 0 & 0 & 0 \\ -2k/m & -2c/m & k/m & c/m & 0 & 0 \\ 0 & 0 & 0 & 1 & 0 & 0 \\ 0 & 0 & -(k+kd)/m & -(c+cd)/m & k/m & k/m \\ 0 & 0 & 0 & 0 & 0 & 1 \\ 0 & 0 & kd/m_d & cd/m_d & -kd/m_d & -cd/m_d \end{bmatrix} \begin{bmatrix} x_1 \\ x_2 \\ x_3 \\ x_4 \\ x_5 \\ x_6 \end{bmatrix} + \begin{bmatrix} 0 \\ 0 \\ 0 \\ -1 \\ 0 \\ 1 \end{bmatrix} u \tag{8}$$

$$T_r^{-1}\dot{Z} = A[T_r^{-1}Z] + Bu \tag{9}$$

$$\dot{Z} = A_T Z + B_T u \tag{10}$$

Where  $A_T = T_r A T_r^{-1}$  and  $B_T = T_r B$

$$T_r = \begin{bmatrix} I_n & -B_1 B_2 \\ I_n & B_2 \end{bmatrix} \quad (11)$$

$$A_T = \begin{bmatrix} A_{11} & A_{12} \\ A_{21} & A_{22} \end{bmatrix} \quad (12)$$

$$B_T = \begin{bmatrix} 0 \\ B_2 \end{bmatrix} \quad (13)$$

The system matrices obtained is then transform to  $z$ -coordinates written as

$$\dot{z}_1 = A_{11}z_1 + A_{12}z_2 \quad (14)$$

$$\dot{z}_2 = A_{21}z_1 + A_{22}z_2 + B_2 u \quad (15)$$

Since the switching function matrix partition is  $s = c_1 z_1 + c_2 z_2 = 0 = M z_1 + z_2 = 0$ , then,

$$\dot{z}_1 = (A_{11} - A_{12}M)z_1 \quad (16)$$

The weighting matrices of  $M$  are calculated by using quadratic optimization approach as below;

$$J = \frac{1}{2} \int_{t_0}^{\infty} z_1(t)^T Q_{11} z_1(t) + 2z_1(t)^T Q_{12} z_2(t) + z_2(t)^T Q_{22} z_2(t) dt \quad (17)$$

$$\hat{Q} = Q_{11} - Q_{12} Q_{22}^{-1} Q_{12}^T \quad (18)$$

$$\hat{A} = A_{11} - A_{12} Q_{22}^{-1} Q_{12}^T \quad (19)$$

Then the matrix  $M$  is calculated by

$$M = Q_{22}^{-1} Q_{12}^T + Q_{22}^{-1} A_{12}^T \hat{P} \quad (20)$$

Where  $\hat{P}$  is obtain by Ricatti equation. After some computation, the sliding surface matrix,  $S$  is given by

$$S = [M I_{m \times m}] \times T_r = c^T \quad (21)$$

$$c^T = 1e + 04 * [0.6725 \quad -3.2973 \quad 0.0001 \quad 0 \quad 0.001 \quad 3.2974] \quad (22)$$

After sliding surface is obtained, then the next step is to design control law. By using Gao's power rate law  $k|s|^{\alpha} \text{sgn}(s)$ , the sliding surface is written as in (23) and differentiating the sliding surface generate the equation as in (24).

$$s = c^T(x) \tag{23}$$

$$\dot{s} = c^T(\dot{x}) \tag{24}$$

$$c^T(Ax + Bu) = -k|s|^\alpha \text{sgn}(s) \tag{25}$$

Finally control design for SMC is obtained written as in (26) where  $k$  is switching gain,  $\alpha$  is tuning parameter in range 0 until 1.

$$u = -(C^T B)^{-1} (C^T Ax + k|s|^\alpha \text{sgn}(s)) \tag{26}$$

### 4 Result and Discussion

The simulation result is carried out by using Matlab/Simulink. The parameter used for PID is set up to  $P = 7$ ,  $I = 10/s$  and  $D = 1$  s while the parameter for SMC is  $\alpha = 0.9$  and  $k = 1$ . The result obtained for first and second storey for displacement and velocity performance as shown in Figs. 5 and 6. As shown, the implementations of controllers suppress the vibration amplitude of the building for both floors. The second storey result show that SMC reduced until 30% from uncontrolled system while PID reduced until 13% of uncontrolled structure. The same reduction obtains for the first floor. According to the result, it shown that SMC has superior performance compared to PID. The control voltage produced by SMC and PID in suppressed the building vibrations are shown in Fig. 7 where SMC generate higher voltage compared to PID.

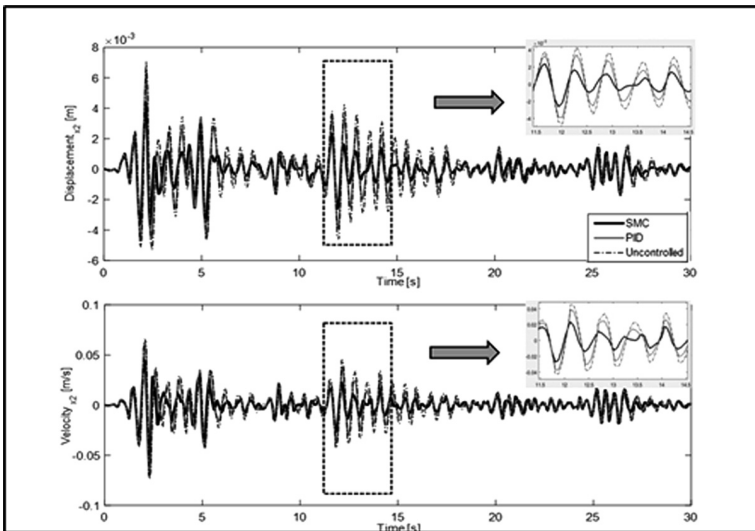


Fig. 5. Second storey displacement and velocity response

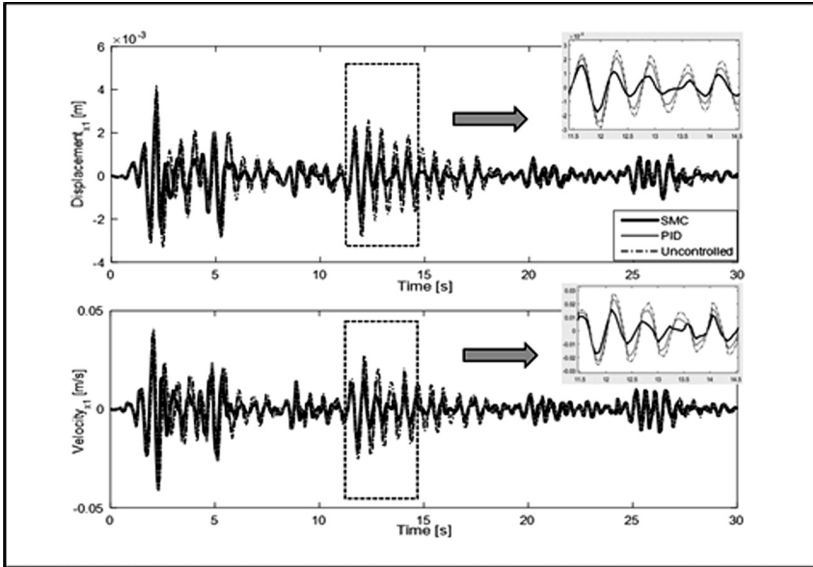


Fig. 6. First storey displacement and velocity response

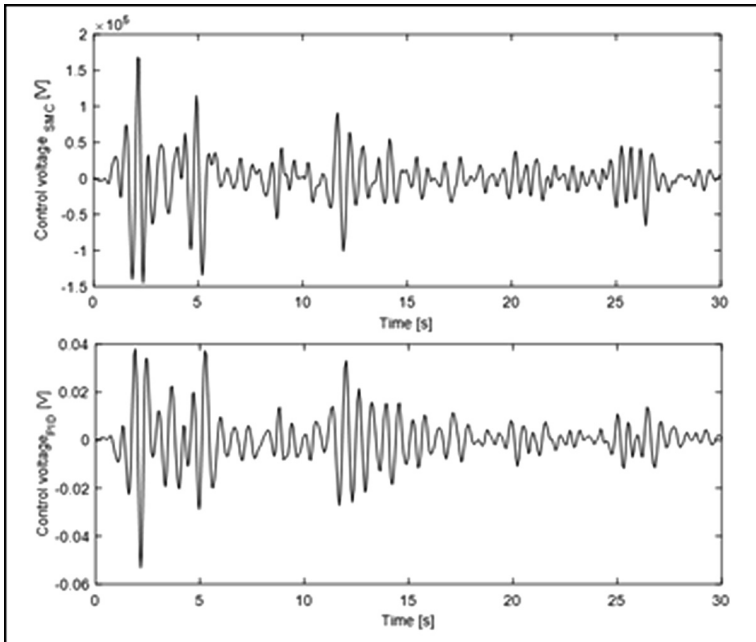


Fig. 7. Control input for PID and SMC

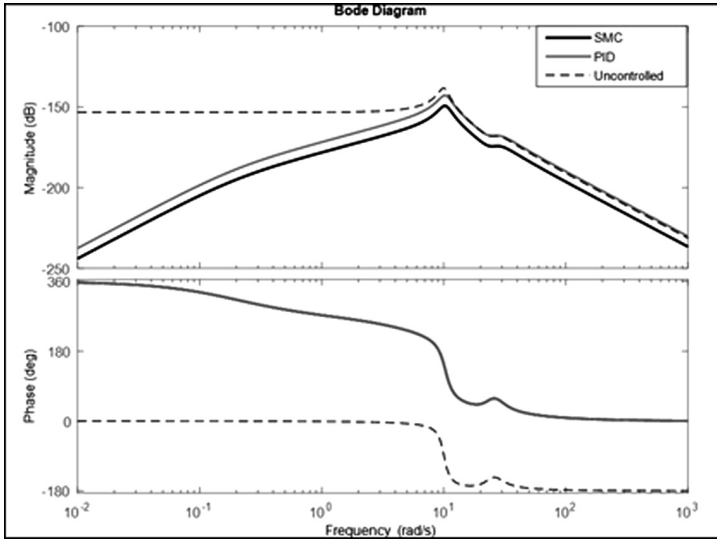


Fig. 8. Frequency response

The higher voltage is used by SMC compared to PID suitable with the reduction performance in reducing the vibration of the building.

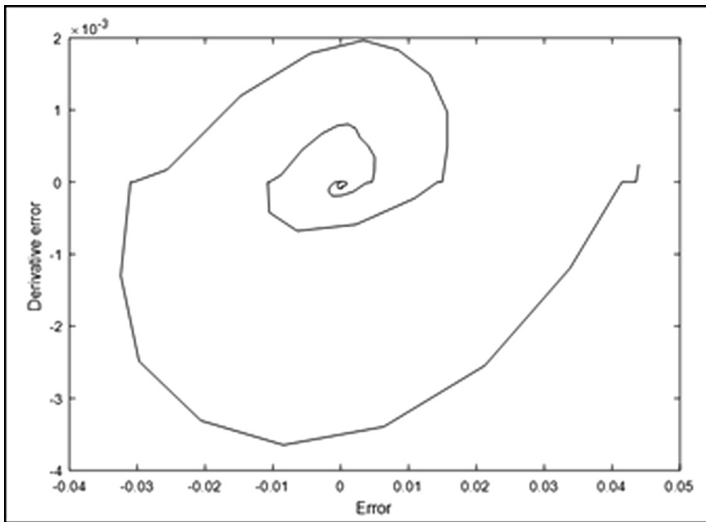


Fig. 9. Sliding surface response for SMC

The frequency response generate from the system with controllers are shown in Fig. 8. As expected, the implementation of SMC produced lowest frequency responses compared to PID and uncontrolled system. The sliding surface produced by SMC is shown in Fig. 9. Based from the sliding surface obtained, the state trajectory move toward the switching plane  $s(x) = 0$ .

## 5 Conclusion

In this study, two degree-of-freedom structure equipped with hybrid mass damper is proposed by implemented PID and SMC to suppress the vibration during seismic. The performance of controllers in reducing the building vibration is evaluated based on the displacement and velocity result. According to the result obtained, the proposed controllers are success to suppress the vibration. In this case, SMC have better performance in alleviate the vibration compared to PID.

**Acknowledgements.** Authors want to express gratitude to Wind Engineering for (Urban, Artificial, Man-made) Environment Laboratory, Malaysia – Japan International Institute of Technology (MJIT), University Teknologi Malaysia, Jalan Sultan Yahya Petra, 54100 Kuala Lumpur, Malaysia and Center for Robotics and Industrial Automation, Faculty of Electrical Engineering, Universiti Teknikal Malaysia Melaka, Hang Tuah Jaya, 76100 Durian Tunggal, Melaka for sponsoring this research.

## References

1. Elias, S., Matsagar, V.: Research developments in vibration control of structures using passive tuned mass dampers. *Annu. Rev. Control* **44**, 129–156 (2017)
2. Kaveh, A., Mohammadi, S., Khadem Hosseini, O., Keyhani, A., Kalatjari, V.R.: Optimum parameters of tuned mass dampers for seismic applications using charged system search. *Iran J. Sci. Technol. Trans. Civ. Eng.* **39**, 21–40 (2015)
3. Guclu, R.: Fuzzy logic control of vibrations of analytical multi-degree-of-freedom structural systems. *Turk. J. Eng. Environ. Sci.* **27**, 157–168 (2003)
4. Thenozhi, S., Yu, W.: Advances in modeling and vibration control of building structures. *Annu. Rev. Control* **37**, 346–364 (2013)
5. Pourzeynali, S., Lavasani, H.H., Modarayi, A.H.: Active control of high rise building structures using fuzzy logic and genetic algorithms. *Eng. Struct.* **29**, 346–357 (2006). <https://doi.org/10.1016/j.engstruct.04.015>
6. Shariatmadar, H., Meshkat Razavi, H.: Seismic control response of structures using an ATMD with fuzzy logic controller and PSO method. *Struct. Eng. Mech.* **51**, 547–564 (2014)
7. Guclu, R., Yazici, H.: Vibration control of a structure with ATMD against earthquake using fuzzy logic controllers. *J. Sound Vib.* **318**, 36–49 (2008)
8. Sharma, M., Singh, S.P.: Fuzzy logic based vibration control of a single degree of freedom system. In: *Recent Advance in Engineering and Computational Sciences (RAECS)*, pp. 1–6. IEEE (2014)
9. Amini, F., Hazaveh, N.K., Rad, A.A.: Wavelet PSO-based LQR algorithm for optimal structural control using active tuned mass dampers. *Comput. Civ. Infrastruct. Eng.* **28**, 542–557 (2013)



10. Liu, J., Wang, X.: *Advanced Sliding Mode Control for Mechanical Systems: Design, Analysis and MATLAB Simulation*. Springer, New York (2012)
11. Guclu, R.: Sliding mode and PID control of a structural system against earthquake. *Math. Comput. Model.* **44**, 210–217 (2006). <https://doi.org/10.1016/j.mcm.2006.01.014>
12. Alli, H., Yakut, O.: Fuzzy sliding-mode control of structures. *Eng. Struct.* **27**, 277–284 (2004). <https://doi.org/10.1016/j.engstruct.10.007>
13. Tseng, Y.-W., Wang, Y.-N.: Sliding mode control with state derivative output feedback in reciprocal state space form. In: *Abstract and Applied Analysis*, vol. 2013. Hindawi (2013)
14. Maria, G., Selvaganesan, N., Kumar, B.A., Kapoor, S.: Dynamic analysis and sliding mode vibration control for a two storeyed flexible building structure. In: *2015 International Conference on Control Communication and Computing India (ICCC)*, pp. 24–29. IEEE (2015)



# Enhanced Time Synchronization Protocol for Wireless Sensor and Actuator Network

Yeong Chin Koo and Muhammad Nasiruddin Mahyuddin<sup>(✉)</sup>

School of Electrical and Electronic Engineering, Universiti Sains Malaysia,  
14300 Nibong Tebal, Malaysia  
kooyeongchin@yahoo.com, nasiruddin@usm.my

**Abstract.** Time synchronization is one of the critical and elementary issues that need to be solved in a wireless sensor and actuator network so that all the nodes and actuators can share the same time notion and then cooperate seamlessly. In this paper, an enhanced control-theoretic distributed time synchronization protocol, which utilized sliding mode control and PID control to achieve the convergence is introduced, investigated and compared with existing protocols in literature. As a result, the introduced time synchronization protocol shows convincing results. The protocol can converge in finite time and has the lowest cumulative integral errors among the compared protocols.

**Keywords:** Distributed control · PID · Sliding mode control · Time synchronization · Wireless sensor and actuator network

## 1 Introduction

Nowadays, many wireless sensor and actuator networks (WSANs) have been developed to be applied in different areas of applications such as remote monitoring, target tracking, localization, health care support, agriculture, military and industrial applications [1]. Time synchronization is always one of the crucial and elementary issues to be addressed in a WSAN [2], especially those applications that require data fusion/aggregation and duty-cycling. For example, in a tracking application, the sensor nodes will first record the time when they detected the subject and then transmit the information to a base station, where all the different information from different nodes will be fused and aggregated to estimate the speed of the subject. Thus, in this situation, all the nodes should be synchronized to associate all the different reports. Through time synchronization, all the nodes and actuators in a WSAN will refer to a common notion of time [1], or synchronized within the range of given synchronization errors [3].

Every node in a WSAN has a clock module to record the timing of the events sensed and/or executed by the nodes. Every clock module has an oscillator of specified frequency, and a counter register. Nowadays, most of the electronic equipments available in the market use quartz crystal oscillators in their clock modules as quartz crystal oscillators are low cost yet still have acceptable precise and stable frequency [4]. WSANs are usually consist of low-cost materials and therefore low-end crystals are chosen as the oscillators for the clock modules in the nodes. This in turn causes the clock drift and jitter in the nodes. Therefore, time synchronization is needed to fix this issue.

To achieve time synchronization in a wired network, there are two widely used solutions: network time protocol (NTP) and global positioning system (GPS) [5]. Although these two solutions can provide a good time synchronization in wired network, both solutions are not suitable to be applied in WSN due to some issues [1]. NTP is computationally intensive and therefore requires a lot of energy but energy is scarce in a WSN as most of the nodes are powered up by a mobile power source. In the case of GPS, besides it also needs a lot of energy, the nodes might lose the GPS signals in a challenging wireless environment.

Since the introduction of WSN, many protocols and algorithms have been introduced in the literature to synchronize the time in a WSN. In general, based on the communication topology, the existing time synchronization protocols in the literature can be briefly categorized into two categories: centralized and distributed [6, 7].

The examples of centralized protocols are Reference Broadcast Synchronization protocol (RBS) [8], Timing-Sync protocol for Sensor Networks (TPSN) [9], and Flooding Time Synchronization Protocol (FTSP) [10]. In general, centralized protocols will initially choose a node as the global clock reference to other nodes in the network. Then, all the other nodes will be arranged in a spanning tree, rooted at that global reference node. Although the centralized protocols can provide fast convergence, the main drawback of this type of protocol is that it is easily affected by the topology changes. If any of the nodes fails to operate, the time synchronization will also fail.

To solve the issue, distributed protocols such as Average Time Synchronization (ATS) [11, 12], Consensus Clock Synchronization (CCS) [13], Time Synchronization using Distributed Observer algorithm with Sliding mode control element (TSDOS) [14], Time Synchronization using Max and Average consensus protocol (TSMA) [15], Maximum Time Synchronization (MTS) [16], Adaptive Proportional-Integral Synchronization (PISync) [17] have been proposed. Distributed protocols do not have the limitation of topology changes as they do not need any special node to be elected as the global reference node and all the nodes in the networks apply the same protocol. Therefore, distributed protocols are very robust toward topology changes.

As pointed in [17, 18], most of the time synchronization protocols made the assumption that the clock skews are remained constant throughout the time, which are impossible in real life applications, as the clock skew of a sensor node is easily affected by the environmental effects.

In this paper, we introduced a distributed time synchronization protocol which incorporates two control elements, sliding mode control and PID. The introduced protocol has the following characteristic: distributed, scalable, robust and finite-time convergence of time synchronization error. The rest of the paper is organized as follows. Section 2 describes the methodology of the introduced time synchronization protocol while Sect. 3 explains the experiment setup. The simulation results, which compared with time synchronization protocols from the literature are displayed and discussed in Sect. 4. Lastly, Sect. 5 concludes the paper.

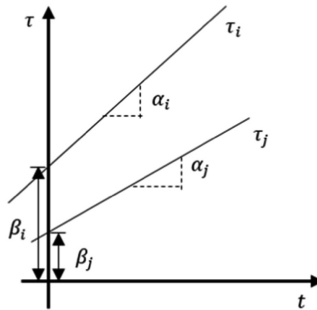
## 2 Methodology

### 2.1 Clock Modelling

As aforementioned, every node  $i$  in a WSAN has its own local clock. The local clock is a monotonically non-decreasing function of  $t$  and it can be modelled as a first order dynamic equation:

$$\tau_i(t) = \alpha_i t + \beta_i \tag{1}$$

where  $\tau_i$  is the clock reading,  $\alpha_i$  is the local clock skew (clock speed), and  $\beta_i$  is the local clock offset, which is the time difference at time instant  $t_0$ , between clock  $\tau_i$  and real time. Figure 1 visualizes the clock dynamics of two nodes, differentiated by their clock skews and clock offsets [11].



**Fig. 1.** The clock dynamic of node  $i$  and  $j$  compared in terms of their respective local clock skew and clock offset

As observable from Fig. 1, different nodes have different clock skews and clock offsets, this is due to limitation of the quartz crystal in the clock module as explained in previous section. Hence, the main objective of time synchronization is to synchronize the nodes so that all nodes will converge to a common relative clock dynamic.

However, the nodes cannot obtain the clock parameters  $\alpha_i$  and  $\beta_i$  directly as the absolute reference time  $t$  is inaccessible by the nodes [12]. Luckily, this issue can be solved by expressing  $t$  as a shared variable by rearrange the Eq. (1),

$$t = \frac{\tau_i - \beta_i}{\alpha_i} \tag{2}$$

And substitute Eqs. (2) into Eq. (1) for node  $j$ , we then obtain

$$\tau_j = \frac{\alpha_j}{\alpha_i} \tau_i + \beta_j - \frac{\alpha_j}{\alpha_i} \beta_i \tag{3}$$

It is observable from Eq. (3) that now the absolute reference time  $t$  has been removed from the equation. As suggested in [12], the clock skews and offsets of all the nodes in a network can be obtained in the end by estimating the relative magnitude

$\frac{\alpha_i}{\alpha_j}$  and the offset imposed  $\left(\beta_j - \frac{\alpha_j}{\alpha_i}\beta_i\right)$ . If these magnitudes are estimated finally, we can obtain the clock dynamics estimates  $\hat{\tau}_i$ , as expressed in the equation below,

$$\hat{\tau}_i = \hat{\alpha}_i\tau_i + \hat{o}_i \quad (4)$$

where  $\hat{\alpha}_i$  is the relative clock skew estimate and  $\hat{o}_i$  is the clock offset estimate. It is observable from Eq. (4) that each node will estimate its own virtual time  $\hat{\tau}_i$  before the estimates are sent to its connected neighbor node  $j$ . The final objective of the time synchronization is achieved when all the nodes synchronized and refer to a common virtual reference clock  $\tau_r$ ,

$$\tau_r(t) = \alpha_r t + o_r \quad (5)$$

$$\lim_{t \rightarrow \infty} \hat{\tau}_i = \tau_r, \quad \forall i \quad (6)$$

Equation (6) describes the consensus in achieving the common reference time, which is similar to the ATS algorithm [12]. Like ATS, the algorithm introduced in this paper also adopts a kind of low pass filter structure. On top of that, we enhance the algorithm by imposing a sliding-mode like term and PID element for fast convergence. The sliding-mode like term is applied in both relative skew estimates and clock skew estimates while the PID element is imposed in the clock offset estimates.

## 2.2 Time Synchronization Scheme

The time synchronization protocol introduced in this paper in an extended algorithm from the work TSDOS [14] by introducing PID control element in the clock offset estimates, which we called TSDOS\_PID. An assumption is made in this algorithm in which the communication between a pair of nodes is instantaneous, with the help of the MAC-layer time-stamping. Like TSDOS, the introduced algorithm has three main parts: the relative skew rate estimation, the skew rate estimation, and the offset estimation.

**Relative Skew Estimation.** Every node  $i$  tries to estimate the relative skew rate with respect to their neighbor node  $j$ . To enhance the relative skew estimation, a sliding plane  $\epsilon_i$  need to define first,

$$\epsilon_i = \frac{\tau_j(t_2) - \tau_j(t_1)}{\tau_i(t_2) - \tau_i(t_1)} \quad (7)$$

where  $\tau_{i,j}(t_1)$ ,  $\tau_{i,j}(t_2)$  are the clock readings, taken at time  $t_1$  and  $t_2$  for node  $i$  and node  $j$  respectively. Next, the relative comparative error is fed into a low-pass filter structure to calculate the relative skew estimation,  $\hat{\xi}_i$ ,

$$\hat{\xi}_i(t^+) = \rho_\xi \hat{\xi}_i(t) + (1 - \rho_\xi) \text{sign}(\epsilon_i) \quad (8)$$

where  $\rho_\xi \in \{0, 1\}$  is the relative skew tuning parameter. A signum function will push the comparative clock pairs to the plane defined in Eq. (7).

**Skew Estimation.** After the relative clock skew estimates is updated, the estimates will be used to estimate the clock skew  $\hat{\alpha}_i$ , with the help of sliding mode term in the filter,

$$\hat{\alpha}_i(t^+) = \rho_s \hat{\alpha}_i(t) + (1 - \rho_s) \hat{\xi}_i \text{sign}(\hat{\alpha}_j) \quad (9)$$

where  $\hat{\alpha}_j$  is the virtual clock skew estimate of the connected neighbour node  $j$  and  $\rho_s \in \{0, 1\}$  is the clock skew tuning parameter.

**Offset Estimation.** After update the clock skew, the offset can be estimated. Unlike the previous two estimations, offset estimation does not incorporate sliding mode term in the filter but instead a PID control term. To apply the PID control term, the error between two nodes' virtual clock estimates needs to be measured first,

$$\bar{\tau}_{ij} = \hat{\tau}_j - \hat{\tau}_i \quad (10)$$

The error is then subjected into a PID controller,

$$\bar{\tau}_i = k_p \bar{\tau}_{ij} + k_i \int \bar{\tau}_{ij} dt + k_d \frac{d\bar{\tau}_{ij}}{dt} \quad (11)$$

where  $k_p$ ,  $k_i$ ,  $k_d$  are the PID's proportional, integral, and derivative gain, respectively. After that, the clock offset can be estimated by,

$$\hat{\delta}_i(t^+) = \hat{\delta}_i(t) + (1 - \rho_o)(\bar{\tau}_i) \quad (12)$$

where  $\rho_o \in \{0, 1\}$  is the offset tuning parameter.

Finally, after all the estimates are updated, the virtual clock estimator can be obtained by substitute the newly updated estimates into Eq. (4). Algorithm 1 summarizes the protocol.

---

Algorithm 1: Pseudocode Overview of The Introduced Time Synchronization Protocol

---

**Initialization:**  $\hat{\alpha}_i \leftarrow 1$ ;  $\hat{\delta}_i \leftarrow 0$

**Step 1:** Define *Sliding Plane*,  $\epsilon_i = \frac{\tau_j(t_2) - \tau_j(t_1)}{\tau_i(t_2) - \tau_i(t_1)}$

**Step 2:** Estimate *Relative Skew Estimate*,  $\hat{\xi}_i(t^+) = \rho_\xi \hat{\xi}_i(t) + (1 - \rho_\xi) \text{sign}(\epsilon_i)$

**Step 3:** Update *Skew Estimate*,  $\hat{\alpha}_i(t^+) = \rho_s \hat{\alpha}_i(t) + (1 - \rho_s) \hat{\xi}_i \text{sign}(\hat{\alpha}_j)$

**Step 4:** Calculate *Offset Estimate*,

$$\hat{\delta}_i(t^+) = \hat{\delta}_i(t) + (1 - \rho_o)(\bar{\tau}_i)$$

where  $\bar{\tau}_i = k_p \bar{\tau}_{ij} + k_i \int \bar{\tau}_{ij} dt + k_d \frac{d\bar{\tau}_{ij}}{dt}$  and  $\bar{\tau}_{ij} = \hat{\tau}_j - \hat{\tau}_i$

**Output:** Obtain *Virtual Clock Estimate*,  $\hat{\tau}_i = \hat{\alpha}_i \tau_i + \hat{\delta}_i$

---

### 3 Simulation Setup

Two experimental simulation scenarios are designed in this paper to justify the introduced synchronization protocol. The experimental simulations are simulated using MATLAB<sup>TM</sup> Simulink<sup>TM</sup>. The synchronization period of these simulation scenarios is set to be 1 ms and is simulating for a total of 100 s. Figure 2 illustrates the connectivity among the 5 nodes simulated to represent the ad-hoc deployment in a network.

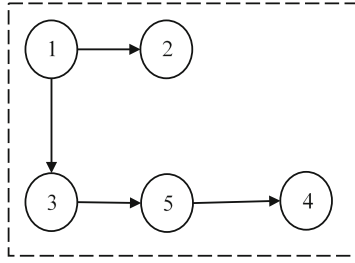


Fig. 2. The connectivity among the 5 nodes

#### 3.1 Ideal Scenario

The objective of first simulation scenario is simply to prove the convergence of TSDOS\_PID under ideal condition. In this first scenario, all 5 nodes in the network are required to synchronize to a same virtual clock estimate and have small convergence error.

#### 3.2 Time Varying Clock Skew Scenario

In the second scenario, we change the presumably static clock skew into time varying clock skew,

$$\tau_i(t) = \alpha_i(t)t + \beta_i \quad (13)$$

where  $\alpha_i$  in Eq. (1) is modified into  $\alpha_i(t)$  to represent the clock skew as a time-varying variable, instead of a static variable, so that the simulation will be more practical with real life applications. The clock skews are set to change every 10 s, which mean there will be a total 10 changing instances for all the 5 nodes in the network, throughout the 100 s of simulation time. In this second scenario, the synchronization result of TSDOS\_PID are compared with the three protocols from literature: ATS [12], PISync [17], TSDOS [14].

#### 3.3 Cumulative Integral Absolute Error, CIAE

In the time varying clock skew scenario, cumulative Integral Absolute Error (cIAE) is computed to measure the computational effort of the protocol,

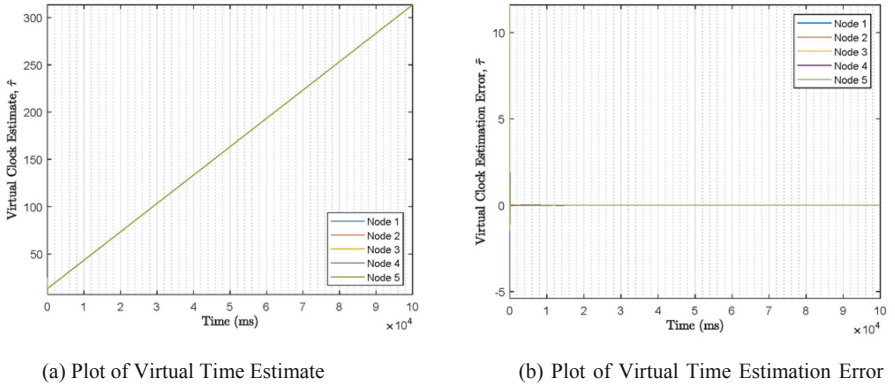
$$cIAE = \sum_{i=1}^{\mathcal{N}} \int_0^T |e_i| dt \quad (14)$$

where  $\mathcal{N}$  is the total number of nodes in the network and  $e_i$  is the convergence error.  $cIAE$  can be used as an indication of the energy consumption of the protocol, hence lesser value is preferable.

## 4 Results and Discussion

### 4.1 Ideal Scenario

Figure 3 represents the result plots of the introduced protocol in first scenario. In general, it is observable that TSDOS\_PID can synchronize all the nodes in the network. In Fig. 3(a), it shows the virtual time estimate of all 5 nodes follow a same monotonically non-decreasing function of time. Besides, Fig. 3(b) also proves that all the 5 nodes have a fixed value of virtual time estimation error, which is near to 0 after all the 5 nodes reach consensus.



**Fig. 3.** Result plots for TSDOS\_PID under ideal scenario

### 4.2 Time Varying Clock Skew Scenario

Figures 4 and 5 illustrate the virtual time estimate and the virtual time estimation error, respectively, for ATS, PISync, TSDOS, and TSDOS\_PID. From both result figures, it is noticeable that whenever the clock skew changed, ATS, TSDOS, and TSDOS\_PID will have a spike but these three protocols are able to find a new consensus very fast afterward and the error will converge to a constant value. In PISync, even though there is no spike whenever the clock skews changed, the synchronization error will change to a bigger range of bounded values.

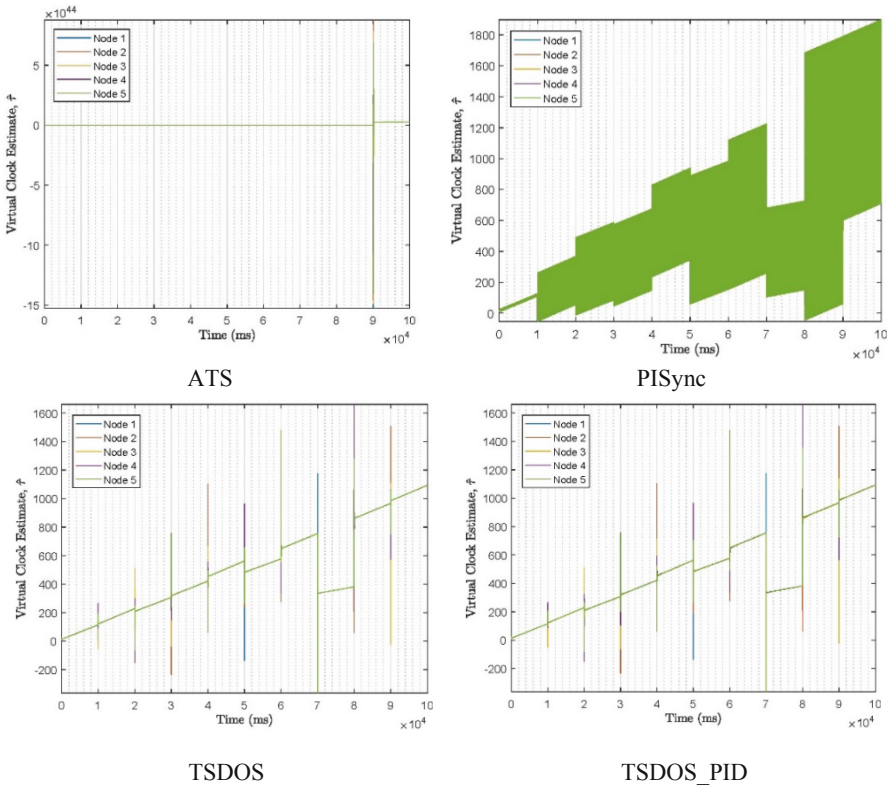
Table 1 tabularized the  $cIAE$  for the protocols in comparison. The ranking in the table in arrange from the highest value of  $cIAE$  (1st) to lowest value of  $cIAE$  (4th). It is



noticeable that when there are 10 changes in the clock skews, ATS has the highest value of cIAE, followed by PISync, then TSDOS and lastly TSDOS\_PID. This means ATS required the most computational energy when there are 10 changes while TSDOS\_PID requires the least energy. In other words, TSDOS\_PID has the best performance among the 4 compared protocols when the clock skews vary for 10 times during the 100 s of simulation.

**Table 1.** cIAE of ATS, PISync, TSDOS, and TSDOS\_PID

Protocol	cIAE	Ranking
ATS	$3.8376 \times 10^{136}$	1st
PISync	$1.0053 \times 10^{13}$	2nd
TSDOS	$8.4865 \times 10^9$	3rd
<b>TSDOS_PID</b>	<b><math>3.9195 \times 10^9</math></b>	<b>4th</b>



**Fig. 4.** Plot of virtual time estimate of ATS, PISync, TSDOS and TSDOS\_PID under time varying clock skew scenario

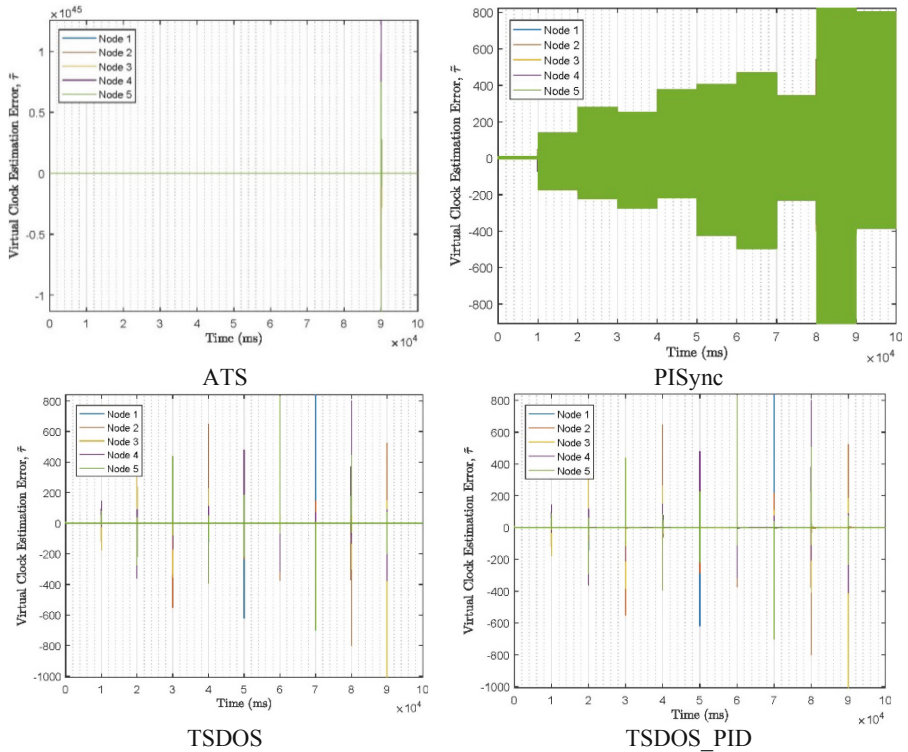


Fig. 5. Plot of virtual time estimation error of ATS, PISync, TSDOS and TSDOS\_PID under time varying clock skew scenario

## 5 Conclusion

An enhanced time synchronization protocol using two control elements, sliding mode control and PID control is introduced in this paper. The introduced protocol, TSDOS\_PID, is distributed, scalable and robust. TSDOS\_PID has the best performance when compared to another 3 protocols from literature where it has the lowest cIAE in the time varying clock skew scenario. Future work will involve more realistic scenario in the simulation such as introduce noise into the simulation.

**Acknowledgement.** This work was supported by a Research University (RUi) grant (1001/PELECT/8014029).

## References

1. Akyildiz, I.F., Vuran, M.C.: Wireless Sensor Networks, 1st edn. Wiley, Chichester (2010)
2. Djenouri, D., Bagaa, M.: Synchronization protocols and implementation issues in wireless sensor networks: a review. *IEEE Syst. J.* **10**(2), 617–627 (2016)

3. Chen, Z., Huang, Y., Wang, Z., Tao, F.: Time synchronization for long-chain-type wireless sensor networks. *Int. J. Distrib. Sens. Netw.* **14**(9), 1–11 (2018)
4. Lichtenauer, J., Shen, J., Valstar, M., Pantic, M.: Cost-effective solution to synchronised audio-visual data capture using multiple sensors. *Image Vis. Comput.* **29**(10), 666–680 (2011)
5. Chaudhary, M.H., Scheers, B.: Practical one-way time synchronization schemes with experimental evaluation. In: 2018 IEEE 19th International Workshop on Signal Processing Advances in Wireless Communications (SPAWC), pp. 1–5 (2018)
6. Chen, Z., Li, D., Huang, Y., Tang, C.: Event-triggered communication for time synchronization in WSNs. *Neurocomputing* **177**, 416–426 (2016)
7. Koo, Y.C., Mahyuddin, M.N.: Brief reviews: time synchronization protocols in wireless sensor network—centralized versus distributed. In: *Lecture Notes in Electrical Engineering*, vol. 398, pp. 435–441 (2017)
8. Elson, J., Girod, L., Estrin, D.: Fine-grained network time synchronization using reference broadcasts. In: *ACM SIGOPS Operating System Review*, vol. 36, no. SI, pp. 147–163 (2002)
9. Ganeriwal, S., Kumar, R., Srivastava, M.B.: Timing-sync protocol for sensor networks. In: *Proceedings of the 1st ACM Conference on Embedded Networked Sensor Systems (SenSys)*, pp. 138–149 (2003)
10. Maróti, M., Kusy, B., Simon, G., Lédeczi, Á.: The flooding time synchronization protocol. In: *Proceedings of the 2nd ACM International Conference on Embedded Networked Sensor Systems (SenSys 2004)*, pp. 39–49 (2004)
11. Schenato, L., Gamba, G.: A distributed consensus protocol for clock synchronization in wireless sensor network. In: 46th IEEE Conference on Decision and Control, pp. 2289–2294 (2007)
12. Schenato, L., Fiorentin, F.: Average TimeSynch: a consensus-based protocol for clock synchronization in wireless sensor networks. *Automatica* **47**(9), 1878–1886 (2011)
13. Maggs, M.K., O’Keefe, S.G., Thiel, D.V.: Consensus clock synchronization for wireless sensor networks. *IEEE Sens. J.* **12**(6), 2269–2277 (2012)
14. Koo, Y.C., Mahyuddin, M.N.: An enhanced distributed control-theoretic time synchronization protocol using sliding mode control for wireless sensor and actuator network. *Indones. J. Electr. Eng. Comput. Sci.* **14**(2), 688–695 (2019)
15. Dengchang, Z., Zhulin, A., Yongjun, X.: Time synchronization in wireless sensor networks using max and average consensus protocol. *Int. J. Distrib. Sens. Netw.* **9**(3), 10 (2013)
16. He, J., Cheng, P., Shi, L., Chen, J., Sun, Y.: Time synchronization in WSNs: a maximum-value-based consensus approach. *IEEE Trans. Autom. Control* **59**(3), 660–675 (2014)
17. Yıldırım, K.S., Carli, R., Schenato, L.: Adaptive proportional-integral clock synchronization in wireless sensor networks. *IEEE Trans. Control Syst. Technol.* **26**(2), 610–623 (2018)
18. Yang, W., Fu, M., Xing, H.: Clock synchronization over wireless sensor network via a filter-based approach. In: 2017 Chinese Automation Congress (CAC), pp. 2478–2483 (2017)



# An Innovative Anti-theft System for Automotive

Firdaus Zainun, Samson Chan Kit Hwa, Nor Amylia Mohd Halmy,  
Choong Chia How, and Muhammad Nasiruddin Mahyuddin<sup>(✉)</sup>

School of Electrical and Electronics Engineering, Universiti Sains Malaysia,  
Nibong Tebal, P.Pinang, Malaysia  
nasiruddin@usm.my

**Abstract.** An innovative anti-theft system for automotive is proposed to uphold the principle of improving and solving the problems related to vehicle burglaries in our community. Here, the system was introduced with its design specifically done in fulfilling several considerations such as able to detect the sound frequency produced when the burglar breaks the vehicle's mirror and also the motion of burglar in the vehicle. The system was designed using microphone and bandpass filter to detect the specific sound frequency of the vehicle's glass breakage. The motion of burglar in the vehicle will be detected by using PIR sensor in the system. Furthermore, Arduino Nano was used in the system to program the input signal from the sensors to the output such as buzzer which can produce a loud noise to attract the attention of the public and disturbs the decision making of the burglar. In order to improve the system, it was added with a function to be able to make a phone call to the user whenever the system is triggered whether by the glass breakage or the motion of burglar.

**Keywords:** Burglar alarm · Automotive application · Occupant hazard

## 1 Introduction

In recent years, the number of cars in China increased by tens of millions each year, and the increasing number of vehicles has brought the anti-theft or vehicles some challenges. For traditional alarm, in the event of car theft, the alarm installed in the car will make alarming sound immediately [1]. However, not all the cars on the road have such security feature.

In India, the total number of vehicles stands at around 100 million at present but it is expected to touch the million mark by the year 2020. Whereas in USA, which has the largest vehicles population in the world, the number of motor cars outnumber of licensed. With this rapidly increasing the number of vehicles on the road, there has been an increase in the road, so at the same time the number of crimes involving vehicles crimes also increase. In the capital city of Delhi alone there is a vehicle stolen every 36 min which amount to around 40 thefts per day [2]. Malaysia encountered with similar cases related to car burglaries. Statistics from Vehicle Theft Reduction Council of Malaysia (VTREC) Berhad stated that, 5073 units of cars were stolen in 2012 and in 2013, 4776 units of cars also went missing. Solutions to the theft problem are driven by

customer and police wants, primarily concerned with the loss of the vehicle, but also theft of contents and personal security, legal directives and insurance requirements. Many efforts on developing vehicle security systems have been reported [1–10]. The philosophy behind the design of the anti-theft system is that if the thief in question can be disturbed by some kind of sounds which hamper his judgement and consequently his action, theft can be prevented. The high frequency pitch is thought to draw other people attention to the crime scene thereby preventing the thief in question from committing the theft crime as he is reluctant to proceed the crime.

An anti-theft system which is small in size and yet reliable in terms of performance is to be designed, developed and field tested.

## 2 System Specification and Features

The proposed anti-theft system will be designed and developed based on the following requirement and design criteria.

### 2.1 Requirement Specification

- Able to sense specific sound frequency produced by glass breakage
- Able to detect the motion of burglar in the vehicle
- Able to sound loudly (15 dB above environment noise)
- Able to notify the user when glass breakage happened via phone app.

### 2.2 Design Criteria

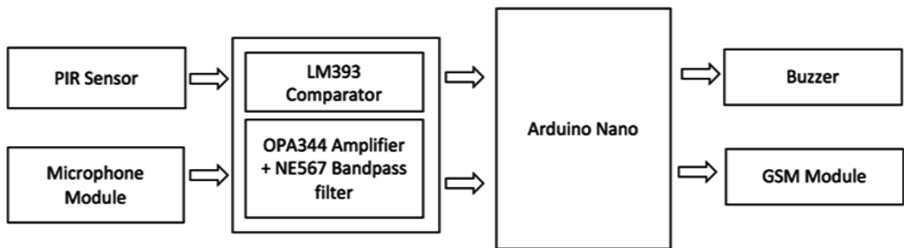
The proposed anti-theft system is expected to reduce the occurrence of burglary, in particular, involving automotive. The system not only has the ability to prevent the burglary but to protect the automotive's user safety and its associated belonging from being stolen or damaged. This project is able to sense specific sound frequency where the glass break and sound loudly (120 dB). This project also can notify the user when glass breakage happened via smartphone. This project consists of two parts which are hardware design and software development. This project used the PIR sensor to detect the motion in the entire car. The PIR sensor is chosen because it allow you to sense motion of human. Sparkfun Electret Microphone Module is integrated to detect the range of frequencies relating to glass breakage. The signal from the sensor will then pass to Arduino to be processed and turned them into useful information. A SIM 900A GSM Module is then used to notify the user through GSM when glass breakage is detected. By using this way, user can alert if there's a glass breakage occurred and user will receive phone call through their mobile phones. An alarm will be sounded with a purpose to alert to the passers-by of the burglary and indirectly disrupt the decision making of the burglar.

### 3 Design Methodology

This section involves the implementations of the proposed solution. The project development flow, system design specifications, system block diagram, system operational flow, hardware development, hardware components descriptions and software development.

#### 3.1 System Block Diagram

Figure 1 shows the system block diagram for this Responsive Anti-Theft System project. In this section, microphone module, PIR sensor, GSM module and buzzer will interface to Arduino Nano to complete the whole system.



**Fig. 1.** System block diagram

PIR sensor and microphone module are on the standby mode in picking up the stimulus signal. Once glass breakage occur, PIR sensor and microphone module will pick the sound signal and transmit it to the Arduino Uno for further analysis. If the picked sound falls within the intended breakage frequency range, then it will trigger the alarm. The user will be notified through a cell phone by the use of installed GSM module.

#### 3.2 Audio Signal Frequency Analysis

A normal microphone gives the analogue output with two characteristics: amplitude and frequency. To detect the audio amplitude, LM393 acts as a comparator to compare the threshold value of audio signal. Specific range of frequency of audio signal can be detected by using a bandpass filter built with NE 567 IC. Figure 2 below shows the configuration of a bandpass filter using NE567.

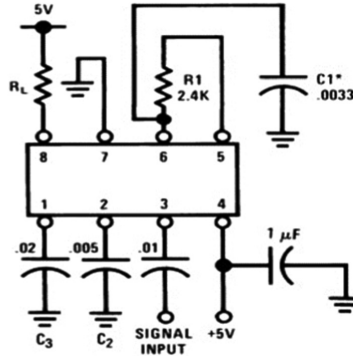


Fig. 2. Schematic used along with NE567

The bandpass filter’s frequency range is determined by the central frequency and bandwidth. The formulas below show the central frequency and bandwidth.

$$f_o \approx \frac{1.1}{R_1 C_1} \tag{1}$$

where  $R_1$  = Timing Resistor  
 $C_1$  = Timing Capacitor

$$BW = 1070 \sqrt{\frac{V_i}{f_o C_2}} \text{ in \% of } f_o \tag{2}$$

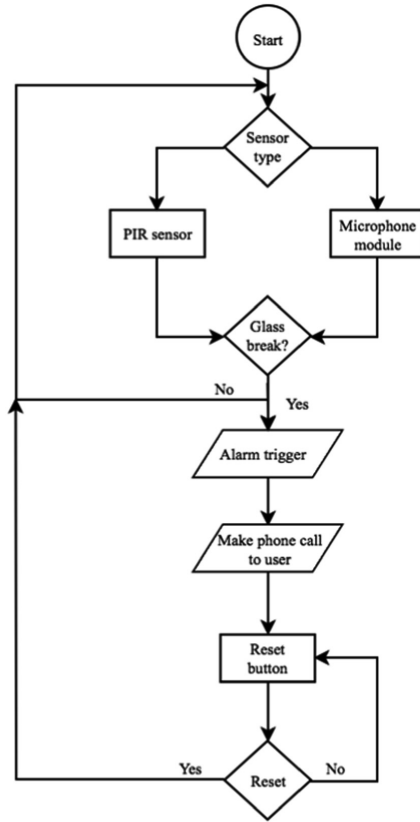
where  $V_i$  = Input voltage (volts rms),  $V_i \leq 200$  mV  
 $C_2$  = Capacitance at Pin 2( $\mu$ F)

When the input audio signals fall at the range of the bandpass filter ‘frequency, the pin 8 give a low output and load R receive power.

In this project, we use  $R_1 = 2.7$  k $\Omega$ ,  $C_1 = 0.05$   $\mu$ F and  $C_2 = 0.05$   $\mu$ F, central frequency is 8.15 kHz and Bandwidth is from 8.15 to 10 kHz since the maximum detectable audio frequency is 10 kHz for the microphone sensor that we have selected.

### 3.3 System Operational Flow

Figure 3 shows the system operational flow. At the beginning, the reading of PIR sensor and microphone will be monitored in a loop until glass breakage is found. Upon the glass breaking, the alarm will be triggered and it will also make phone call to user. The system is reset normal when reset function is triggered.



**Fig. 3.** System operational flow

### 3.4 Fabrication

The encapsulating casing for the prototype is designed by using SolidWorks and further exported and processed for 3D printing process. The circuit will be implemented and embedded together as a complete prototype. This prototype will be tested in the car. Endurance test for PLA cover will be tested in this stage.

### 3.5 Hardware Component Descriptions

The main hardware component that will be used in this project are stated in Table 1. The reason of selecting all of these components are also explained.



**Table 1.** Hardware components

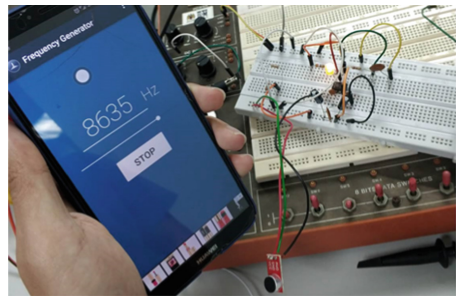
Hardware	Description
1. Arduino Nano	As a controller for R.A.T.S, Arduino Nano receive information from the sensors (mic and vibration sensor), it will analyze the data received, and sounds the alarms and alerting light if glass breakage is detected. It also sends signals to GSM module to notify the user
2. Sparkfun electret microphone breakout module	An Electret microphone (100 Hz–10 kHz) with a 60x mic preamplifier to amplify the sounds of voice, claps, door knocks or any sounds loud enough to be picked up by a microcontroller’s analog-to-digital converter. To detect certain frequencies produced during glass breakage and convert it into electrical signal
3. PIR sensor	To allow to sense motion, almost always used to detect whether a human has moved in or out of the sensors range
4. Buzzer	Receive signal from Arduino Nano, it will sound loudly (120 dB) if glass breakage happened or detect motion
6. SIM 900A GSM module	Receives signal from the Arduino to notify the user through GSM when glass breakage is detected
7. PLA	Type of printing materials to build up the prototype

### 4 Result and Discussion

In this project, Sparkfun Electret Microphone Breakout associated with a band pass filter using NE567 N was employed in the proposed design to detect the specific frequency produced by the glass breakage during the burglary. The minimum frequency produced is 8 kHz as calculated in the analysis. The bandwidth frequency is around 2 kHz.



**Fig. 4.** Frequency at 7570 Hz



**Fig. 5.** Frequency at 8635 Hz

In order to generate the specific frequency, a mobile phone application named “Frequency Generator” is used. LED lights up indicates that frequency is in range of bandwidth frequency. In Fig. 4, it is shown that 7570 Hz is produced but it is not in the

range. Hence, the LED is not light up. The LED is only light up as shown in Fig. 5 when the frequency is 8635 Hz.



**Fig. 6.** Frequency at 9798 Hz



**Fig. 7.** Frequency at 11475 Hz

Figure 6 shows frequency generated at 9798 Hz and the LED is light up. However, the LED will be off when the frequency continues to increase and exceed the frequency bandwidth as shown in Fig. 7 which has the frequency of 11475 Hz.

PIR sensor is the heart of the anti-theft system. It is motion detector which identifies any object that moves inside its range of view. The purpose of PIR is to detect the motion of theft or babies in the car and trigger the alarm. This PIR contains comparator and give digital output. Motion detected will produces a HIGH and no motion will be represented by a LOW signal. Figure 8 shows the PIR when it is not triggered and Fig. 9 shows the PIR when it is triggered.



**Fig. 8.** PIR in standby mode



**Fig. 9.** PIR in detection mode

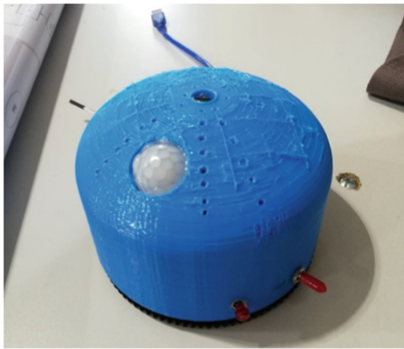
GSM enables the system to notify the user almost instantly when the burglar breaks into the vehicle. Both microphone module and PIR sensor will send a signal to GSM when the burglar is detected. GSM will directly make a phone call to the phone number set in the system. The program is set to call the phone number for 20 s. Blue light is

light up on GSM module to indicate that it is ready to make a phone call. Figure 10 shows an example when a phone call is made to the user by proposed system.

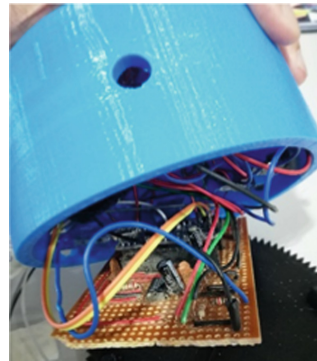


**Fig. 10.** Receiving call from the anti-theft system

A buzzer is connected in the proposed system. It is used to produce a loud noise to attract the attention of the surrounding and disturb the burglar. The buzzer is able to create a loud noise which is up to 120 dB.



**Fig. 11.** The prototype is 3D printed



**Fig. 12.** Circuit system

Figure 11 shows the final prototype of the system. The encapsulating body of the prototype is 3D printed using PLA material. All the components used are placed in the prototype. The circuit is soldered to Donut Board and placed inside the prototype (Fig. 12).

## 5 Conclusion

This innovative anti-theft portable system is designed for all the vehicle owner. It successfully detects the frequency where the glass happened to break. It also able to detect any motion that happened in the car with PIR sensor. Both sensors work

simultaneously provided a secure environment in the cars. When the glass is smashed during the burglary or motion is detected, the user will be notified through phone call from the system. This alarm will sound at 120 dB to interrupt the decision making of the thief whilst at the same time attracting attention from the neighboring passersby. Future improvement will be aimed at alerting parents in situations of potential physical danger, for example, on occasions of infants being left alone in closed apartments or vehicles.

## References

1. Hu, J., Li, J., Li, G.: Automobile anti-theft system based on GSM and GPS module. In: Proceeding of Fifth International Conference on Intelligent Networks and Intelligent Systems, Tianjin, 2012, pp. 199–201 (2012). <https://doi.org/10.1109/icinis.2012.86>
2. Sadagopan, V.K., Rajendran, U., Francis, A.J.: Anti-theft control system design using embedded system. In: Proceedings of 2011 IEEE International Conference on Vehicular Electronics and Safety, Beijing, 2011, pp. 1–5 (2011). <https://doi.org/10.1109/icves.2011.5983776>
3. Mukherjee, K.: Anti-theft vehicle tracking and immobilization system. In: Proceedings of 2014 International Conference on Power, Control and Embedded Systems (ICPCES), Allahabad, 2014, pp. 1–4 (2014). <https://doi.org/10.1109/icpces.2014.7062814>
4. Dey, M., Arif, M.A., Mahmud, M.A.: Anti-theft protection of vehicle by GSM & GPS with fingerprint verification. In: Proceedings of 2017 International Conference on Electrical, Computer and Communication Engineering (ECCE), Cox's Bazar, 2017, pp. 916–920 (2017). <https://doi.org/10.1109/ecace.2017.7913034>
5. Noman, A.T., Hossain, S., Islam, M.S., Islam, M.E., Ahmed, N., Chowdhury, M.A.M.: Design and implementation of microcontroller based anti-theft vehicle security system using GPS, GSM and RFID. In: Proceedings of 2018 4th International Conference on Electrical Engineering and Information & Communication Technology (iCEEICT), Dhaka, Bangladesh, 2018, pp. 97–101 (2018). <https://doi.org/10.1109/ceeict.2018.8628051>
6. Lili, W., Tiejun, C.: Automobile anti-theft system design based on GSM. In: proceedings of International Conference on Advanced Computer Control, Singapore, pp. 551–554 (2009). <https://doi.org/10.1109/icacc.2009.44>
7. Liu, Z., Zhang, A., Li, S.: Vehicle anti-theft tracking system based on Internet of things. In: Proceedings of 2013 IEEE International Conference on Vehicular Electronics and Safety, Dongguan, pp. 48–52 (2013). <https://doi.org/10.1109/icves.2013.6619601>
8. Sohail, O., Naqash, T.: Anti-theft cloud application for android operating system (Nougats). In: Proceedings of 2018 IEEE International Conference on Applied System Invention (ICASI), Chiba, pp. 321–324 (2018). <https://doi.org/10.1109/icasi.2018.8394598>
9. Mamun, K.A., Ashraf, Z.: Anti-theft vehicle security system with preventive action. In: Proceedings of 2015 2nd Asia-Pacific World Congress on Computer Science and Engineering (APWC on CSE), Nadi, 2015, pp. 1–6 (2015). <https://doi.org/10.1109/apwccse.2015.7476241>
10. Faridah, Y., Amir Asyraf, W.M., Rahman, W.A.: Car alarm detection device. In: Proceedings of 2016 IEEE Symposium on Computer Applications & Industrial Electronics (ISCAIE), Batu Feringghi, pp. 195–199 (2016). <https://doi.org/10.1109/iscaie.2016.7575062>



# Intelligent Control of CNC System Based on IEC 61499 Function Block Technology

Muhammad Azri Othman<sup>1,2</sup>, Zamberi Jamaludin<sup>1</sup>,  
and Mohamad Minhat<sup>1</sup>✉

<sup>1</sup> Faculty of Manufacturing Engineering, Universiti Teknikal Malaysia Melaka,  
Hang Tuah Jaya, 76100 Durian Tunggal, Malacca, Malaysia  
mohdm@utem.edu.my

<sup>2</sup> Centre for Diploma Studies, Universiti Tun Hussein Onn Malaysia,  
86400 Parit Raja, Batu Pahat, Johor, Malaysia

**Abstract.** For being more competitive, more productive and more cost effective, machining industry requires a numerous change that are not only involving implementation method but also technology improvements. The major challenge is to find new solution for synergize the computer numerical control (CNC) machine tool control system capability to be more flexible and adaptable towards intelligence of next generation CNC machine tool. Availability of high level and detailed information data interface in CNC machine tool system provides real opportunity and challenge to promote the improvement of CNC system intelligent capability. One of famous research recently was the development of ISO 14649 (STEP-NC) as a next generation of data model interface for CNC system. However, STEP/STEP-NC is a passive data interface model which not contain any intelligent functionality. Therefore, there are still a lot of works must be done and more dynamics approaches needed for enhancing intelligent functionality to the STEP-NC compliant CNC system. This will eventually make next generation CNC system can be fully developed. The aim of this paper is to analyse the potential of IEC 61499 function block as enabler technology in enhancing intelligent functionality for next generation CNC system.

**Keywords:** CNC · IEC 61499 · Function block · Intelligent

## 1 Introduction

In the highly competitive nature of today's world economies, shop floors are being forced to shift toward implementing new high technology methodologies and pushing the machine tools to its next transformation. Dealing with tight product quality requirement and frequent changes in customer demands are the modern trends for machining sector and manufacturing industry in general. Whereby, manufacturing environment on-going transform from mass production to mass customization production [1]. For being more competitive, more productive and more cost effective, the numerous changes are not merely involving implementation method but also technology improvements. The major challenge is to find a new solution for synergize the

computer numerical control (CNC) machine tool control system capability to more flexible and adaptable towards intelligently and openness system of next generation CNC machine tool.

Up to now, there are many researchers having done in promoting and development of ISO 14649 (STEP-NC) as a next generation of data model interface for CNC system. The variety of STEP-NC compliant controller prototypes have been developed to confirm the advantages of STEP-NC over the current G&M codes standard. The most latest STEP-NC compliant controller development has been reviewed by Othman et al. [2], author believe that STEP-NC will totally replacing G&M code as CNC data interface. However, STEP-NC is a passive data interface model which not contain any intelligent functionality. Therefore, there are still a lot of works must be done and more dynamics approaches needed for enhancing intelligent functionality to the STEP-NC compliant CNC system. Then, only the next generation CNC system can be fully developed.

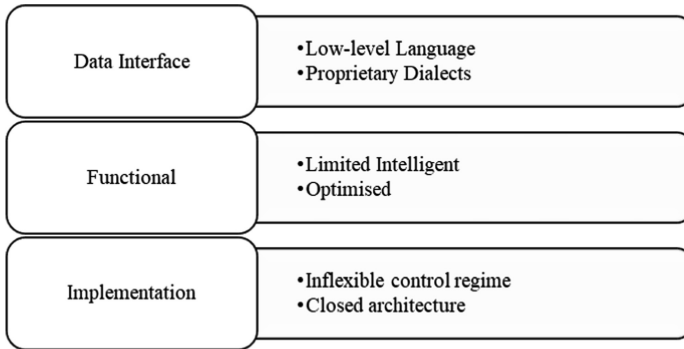
This manuscript addresses the need of intelligent CNC system based on a decentralized control systems (DCS) and distributed process planning (DPP) for improving the performance of CNC machines when dealing with dynamical manufacturing environment. The proposed architecture is intended for creating a last-minute machine code that could be used towards creating a dynamics approach in the creating of native machining programs. The modelling system is built by interconnect the IEC 61499 function blocks. These function blocks share information by event-based communication mechanisms and encapsulate their customized data and algorithms involving event and of event-driven invocation of software components, types and instances of function blocks, and interface of function blocks [3]. This paper is organised as following: in Sect. 2, impediment of existing CNC system is discussed. Then, in Sect. 3, IEC 61499 Function Block is introduced as enabler technology for enhancing intelligent functionality to CNC controller. Followed by Sect. 4, where all the research work related to function block application in manufacturing are reviewed. After that, the overview of the proposed system based on IEC61499 presented in Sect. 5. Finally, conclusion and future work in Sect. 6.

## 2 Impediments of Contemporary CNC System

The term CNC is a widely recognised and commonly being uses in the manufacturing industry. This technology has brought tremendous changes to the manufacturing industry especially metal working sector. However, despite progression towards the development of next generation CNC systems, there are multiple impediments are founded in the existing system in realising that aims (Fig. 1). These impediments can be categories into 3 different levels: (1) Data interface level; (2) Functional level; (3) Implementation level.

### 2.1 Data Interface Level

In data interface level, G&M codes (ISO 6983) that have been extensively used by the most existing CNC machine tools nowadays are considered as an outdated and



**Fig. 1.** Limitation of existing CNC machine tool system

bottleneck for developing next generation CNC machine tools. In reality, G&M codes provide only low-level information that is expressed the simple cutting tool motion commands and its auxiliary switching functions. Due to this fact, CNC manufacturers have been adding their own dialect to the standard [4]. Consequently, program file exchangeable or reuse is highly difficult if not impossible. Moreover, any changes made at machine level cannot be directly feedback to designer and process planner since the data uses at each stage of product developed, starting from design to machining are noncompliance to each others. Hence, on site knowledge is wasted and buried on the shop-floor [5].

## 2.2 Functional Level

In functional level, no access to high-level information on the machine level make intelligent functionality is still limited. With limited information availability, CNC machine tools are not able to react adaptively to any unpredicted events or uncertainties due to unexpected change/failure. Thus, automatic modification and adjustment of machining condition respecting actual machine status cannot be realised. As a result, machining condition and tool paths are hardly optimized. In most cases, resulting in useless effort spent in the process planning and NC code generation in advance.

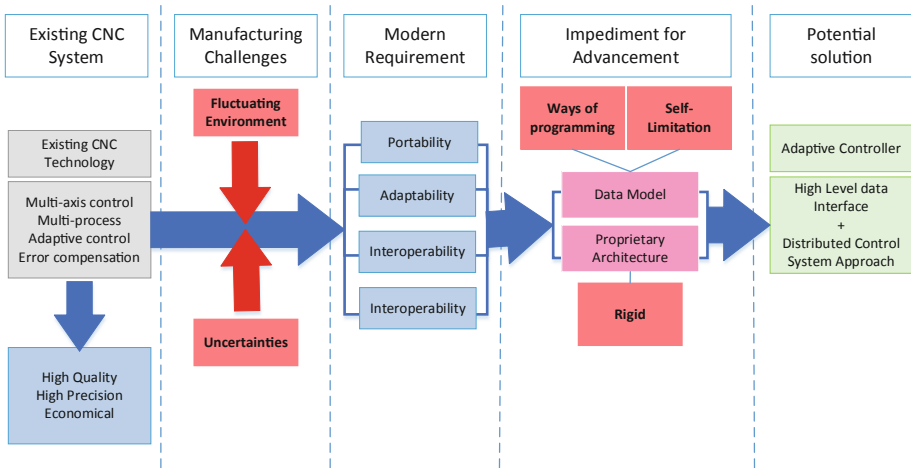
## 2.3 Implementation Level

As a termination mechanism, CNC machine tool is responding to convert inputs into semi-finished or finished outputs based on customer requirement. Even CNC machine already passed several revolution stages, the way it being programmed are remain almost unchanged. Traditionally, machining operations are fully executed referring to predefined NC program that is generated beforehand. Mostly, created program is rigid in such ways any cutting conditions and machining sequences modification during machining operations are nearly impossible. Simply said, CNC machines are 'blind slave' that only followed the input program without fail and regardless whether the



input program would lead to unsuitable or inappropriate tools movements, which may result of less productivity or low-quality product.

Based on the modern manufacturing scenario illustrated in Fig. 2, in order to cope with requirements for modern CNC manufacturing environment, the development a new CNC controller with the ability to have autonomous process planning and adaptive control system are really demanding. One of the establish methodology is by merging STEP-NC and IEC 61499 function block as two enabler technology. Combination of both technologies was proven in creating and establish interoperable CNC machining system. The introduction of the IEC61499 function block and the implementation of IEC 61499 function block technology in manufacturing application are discussed in the following sections.



**Fig. 2.** Modern CNC manufacturing scenario and future potential enhancement

### 3 IEC 61499 Function Blocks

IEC 61499 was first introduced in 2005. With the aims to addressing most of ambiguities in first edition, second edition was established in 2012. This standard is developed by International Electrotechnical Commission with the aims to create open, component-oriented building blocks and platform-independent framework to improve re-usability, re-configurability, interoperability, and portability of future automation and control system. Moreover, it allowed real time changes or faulty machinery could potentially be handled directly without taking the control system to offline mode [6].

IEC 61499 is extends the programmable function Block notion from the IEC 61131-3 standard based on an explicit event-driven model. Each FB is functional as a software unit that encapsulates local data, state transitions and algorithms within a well-defined event data interface. FBs can be designed to behave in a similar way as an electronic device or a circuit and this function block can represent a small task in a control plan or can be encapsulate with multiple control unit [7]. The execution of an



individual FB in the network is triggered by the event it received, if not, FB will keep remaining in idle condition for the rest of time.

## **4 An Overview of IEC 61499 Function Block Application in Manufacturing**

Studies over the past decade have provided important information and confirmed the benefits of IEC 61499 function block over the mainstream PLC technology derives from IEC 61131-3 standard with regard to efficiency of design and redesign process, and better reusability and interoperability [8]. Since that, a number of studies was reported in multiple areas of project such migration of IEC 61131-3 PLC to IEC 61499 FBs, mechatronic, material handling system, smart grid, manufacturing systems, process planning, machining, process control and optimization and energy sustainability. It shows that IEC 61499 has received high attention among the researcher, academician and industry players. However, in this paper only summaries the research work related to machining, process planning, process control and optimization, and sustainable machinery system (Table 1).

Basically, IEC 61499 FBs offers good concepts for the design and the implementation of a distributed control systems (DCS) [7]. For that reason, FBs are for modelling of distributed systems that can be implemented by means of any software and hardware available simultaneously. By taking the advantages of IEC 61499 FBs, the proposed system is uses IEC 61499 FBs as the interface between the input data model with the controller. Ideally, the proposed system will receive a generic STEP/STEP-NC program file as input and machine-specific decisions including cutting tool selection, machining parameter determination and tool path generation are designate later by the controller. For that purpose, a set of new intelligent functionalities algorithms are created and be embedded inside each dedicated FBs.

## **5 Overview of the Proposed System**

Ultimately, the main goal for this research projects was to develop an adaptive controller based on combination of STEP/STEP NC and IEC 61499 technologies. The goal is to establish open CNC system that provides vendor-neutral, tool-neutral and controller-neutral architecture of CNC. With the availability of a complete and structured data model at machine level, gives new controller to have more intelligent functionalities and interoperable characteristics to better meet the modern machining environment.

This research involved working with generic and native program, in order to ensure the controller to have the desired adaptivity and interoperability. ISO 10303 (STEP standard) and ISO 14649 (STEP-NC standard) are use as a data model for the system. Basically, there are four phases involving: (1) analyzing and interpreting a STEP and/or STEP-NC file into an internal data; (2) transferring the interpreted data to the underlying function blocks; (3) generate machine specific data required for machining process; (4) finally generating command data for executed machining task.

**Table 1.** IEC 61499 research work related to machining systems

Authors	Year	Description
<b>i. Process planning application</b>		
Liu et al. [9]	2016	Proposed a dynamic features modelling using FBs. In this concept, features interpretation is associated with the capabilities of selected machine, cutter and cutting parameters
Ji et al. [10]	2016	Proposed cloud DPP concept and adaptive machining feature (MF) sequence for selection and rescheduled cutting tools and setup merging against unexpected events
Wang [11]	2015	Proposed an adaptive process planning (APP) using enriched m-features and IEC 61499 FBs. Based on machine availability monitoring information, APP done setup merging and job dispatching to reach best utilisation of machines and their capabilities
Liu and Wang [12]	2007	Based on manufacturing constraints and datum references, Authors proposed a sequence generator module for distributed process planning system
Wang et al. [13]	2003	Proposed a new distributed process planning (DPP) methodology that uses two-layer hierarchy decision making strategy- Supervisory Planning (shop-floor level) and Operation Planning (machine level)
<b>ii. Machining application</b>		
Minhat et al. [14]	2009	Proposed a layered STEP-NC/FB CNC controller architecture as simplifying the design of CNC machine controller. This prototype interprets STEP-NC directly into machine understandable code. It is G&M code free system
Wang et al. [15]	2007	Develop a STEP compliant CNC system based on function blocks to translate STEP-NC data into G&M code
<b>iii. Process control and optimisation application</b>		
Nikoloas et al. [16]	2014	Proposed optimization model for machining parameter selection based on real time machine monitoring for cloud manufacturing environment
<b>iv. Sustainable machining system application</b>		
Peng and Xu [17]	2017	Propose interoperable energy consumption analysis system based on IEC 61499 FBs and STEP-NC data models
Peng et al. [18]	2014	Present a novel energy demand modeling approach based on IEC61499 FBs using on-machine optimisation analysis

At the design phase, the computer aided design (CAD) file is saved in the format STEP AP203 and/or AP-214. Both of these formats are well recognised to provides the neutral data format for exchanging design data between different parts of the CAx chain. After that, this file is then interpreted to form feature information that conforms to AP-224. All of these features are used as inputs for generic process plans and native process plans. Some general information regarding selected manufacturing resources done during generic process plans before, machining strategy and production

requirements is then defined for each feature to form a native data for the selected CNC machine tool (see Fig. 3).

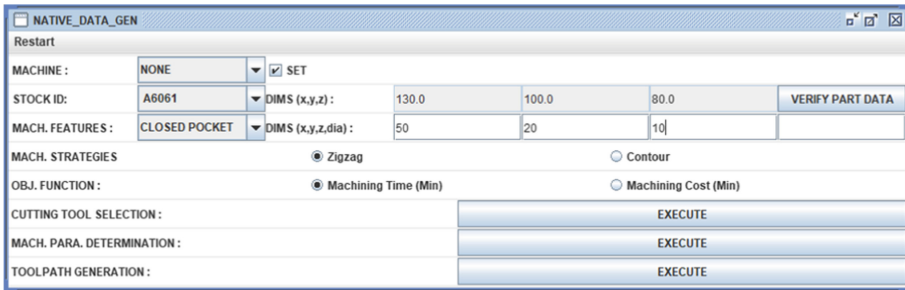


Fig. 3. GUI for native data generator module

Referring to Fig. 4, the native data generation tasks was starts with the activity where all the information form the generic STEP-NC file is transferred to IEC61499 FB structure. The process is start with execution of cutting tool algorithm to choose the reasonable cutting tool for each feature based on list of cutting tool available on the selected machine. After that, machining parameter such as cutting speed, feed rate and depth of cut is determined by the machining parameter generation module. Finally, the tool path generation module interprets that native program to generate machining tool path. The detail of each modules in this system are not discussed detail in this paper.

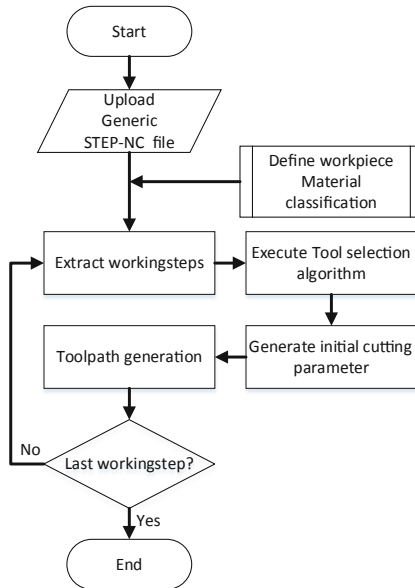


Fig. 4. Process flow for generation of machine specific data

In this research work, 3-axis open architecture PC based CNC machine will be for performing actual machining process. The toolpath data and others required machining data generated before is send to MATLAB SIMULINK platform and then, will be execute via the control scheme that was developed by a group of researchers from control and instrumentation laboratory, Universiti Teknikal Malaysia Melaka. The overall configuration for the proposed system is illustrated in Fig. 5.

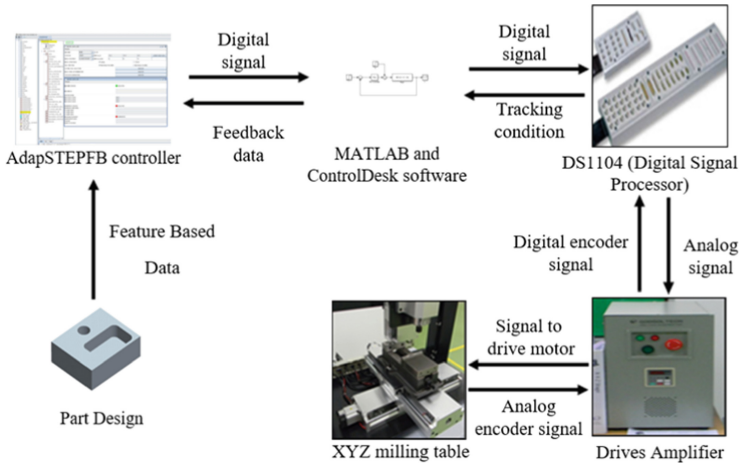


Fig. 5. Overall configuration of the proposed system

## 6 Conclusion

To make up for the deficiency in current CNC machining control structure, CNC controller modules must be capable to react adaptively to a dynamic machining. Previous feasibilities studies have proven that IEC 61499 FBs can be uses in designing next generation intelligent CNC system. These papers presented one of research work to develop IEC 61499 based controller. Based on the developed prototype and previous research done, author belief by applying FB to the control of CNC machines means giving them extra intelligence and autonomy to better handle and adapts to changes, for a more successful fulfillment of their manufacturing objectives. For the future work, the final tuning of the prototype and the actual machining be performed, after that, the overall performance of the developed prototype will be discussed in detail on other research paper.

**Acknowledgements.** The authors would like to appreciate Ministry of Higher Education, Universiti Tun Hussein Onn Malaysia (UTHM), and Universiti Teknikal Malaysia Melaka (UTeM) for the financial support and facilities provided.

## References

1. Klocke, F., Spöcker, G., Huwer, T., Bobek, T., Arntz, K.: Reducing data loss within adaptive process chains in the context of commonly-used CAx systems. *Prod. Eng.* **9**, 307–316 (2015). <https://doi.org/10.1007/s11740-015-0616-9>
2. Othman, M.A., Minhath, M., Jamaludin, Z.: An overview on STEP-NC compliant controller development. In: *IOP Conference Series: Materials Science and Engineering*, vol. 257, pp. 41–51 (2017)
3. Minhath, M., Xu, X.: Feature-based machining using function block technology. In: *Proceedings of 2009 IEEE International Conference on Control and Automation*. Christchurch, New Zealand, pp. 2398–2403 (2009)
4. Xu, X.W., Newman, S.T.: Making CNC machine tools more open, interoperable and intelligent—a review of the technologies. *Comput. Ind.* **57**, 141–152 (2006). <https://doi.org/10.1016/j.compind.2005.06.002>
5. Zhang, X., Afsharizand, B., Essink, W., Newman, S.T., Nassehi, A.: A STEP-compliant method for manufacturing knowledge capture. *Proc. CIRP* **20**, 103–108 (2014). <https://doi.org/10.1016/j.procir.2014.05.038>
6. Yan, J., Vyatkin, V.: Extension of reconfigurability provisions in IEC 61499. In: *Proceedings of 18th IEEE Conference on Emerging Technologies & Factory Automation (ETFA)*. Cagliari, Italy, pp. 1–7 (2013)
7. Minhath, M., Xu, X., Vyatkin, V.: STEPNCMillUoA: a CNC system based on STEP-NC and function block architecture. *Int. J. Mechatron. Manuf. Syst.* **2**, 3–19 (2009). <https://doi.org/10.1504/IJMMS.2009.024345>
8. Pang, C., Patil, S., Yang, C.W., Vyatkin, V., Shalyto, A.: A portability study of IEC 61499: semantics and tools. In: *Proceedings of 12th IEEE International Conference on Industrial Informatics (INDIN)*, Porto Alegre, Brazil, pp. 440–445 (2014)
9. Liu, X., Li, Y., Wang, L.: Combining dynamic machining feature with function blocks for adaptive machining. *IEEE Trans. Autom. Sci. Eng.* **13**, 828–841 (2016). <https://doi.org/10.1109/TASE.2015.2409294>
10. Ji, W., Wang, L., Haghghi, A., Givehchi, M., Liu, X.: A reachability based approach for machining feature sequencing. *J. Manuf. Syst.* **40**, 96–104 (2015). <https://doi.org/10.1016/j.jmsy.2016.06.006>
11. Wang, L.: An overview of function block enabled adaptive process planning for machining. *J. Manuf. Syst.* **35**, 10–25 (2015). <https://doi.org/10.1016/j.jmsy.2014.11.013>
12. Liu, Z., Wang, L.: Sequencing of interacting prismatic machining features for process planning. *Comput. Ind.* **58**, 295–303 (2007). <https://doi.org/10.1016/j.compind.2006.07.003>
13. Wang, L., Feng, H.Y., Cai, N.: Architecture design for distributed process planning. *J. Manuf. Syst.* **22**, 99 (2013). [https://doi.org/10.1016/S0278-6125\(03\)90008-2](https://doi.org/10.1016/S0278-6125(03)90008-2)
14. Minhath, M., Vyatkin, V., Xu, X., Wong, S., Al-Bayaa, Z.: A novel open CNC architecture based on STEP-NC data model and IEC 61499 function blocks. *Robot. Comput. Integr. Manuf.* **25**, 560–569 (2009). <https://doi.org/10.1016/j.rcim.2008.03.021>
15. Wang, H., Xu, X., Des Tedford, J.: An adaptable CNC system based on STEP-NC and function blocks. *Int. J. Prod. Res.* **45**, 3809–3829 (2007). <https://doi.org/10.1080/00207540600774075>
16. Nikolaos, T., Jörn, M., Michael, D., Dimitris, M.: Optimal machining parameter selection based on real-time machine monitoring using IEC61499 function blocks for use in a cloud manufacturing environment: a case study for face milling. In: *Proceedings of the ASME 2014 International Manufacturing Science and Engineering Conference*, MI, USA, pp. 1–9 (2014)

17. Peng, T., Xu, X.: An interoperable energy consumption analysis system for CNC machining. *J. Clean. Prod.* **140**, 1828–1841 (2017). <https://doi.org/10.1016/j.jclepro.2016.07.083>
18. Peng, T., Xu, X., Wang, L.: A novel energy demand modelling approach for CNC machining based on function blocks. *J. Manuf. Syst.* **33**, 196–208 (2014). <https://doi.org/10.1016/j.jmsy.2013.12.004>



# Analysis of Interpreted CAD/CAM Trajectory as Alternative Input Reference for Control System

Norhidayah Mat Seman, Zamberi Jamaludin<sup>(✉)</sup>,  
and Mohamad Minhat

Faculty of Manufacturing Engineering, Universiti Teknikal Malaysia Melaka,  
Hang Tuah Jaya, 76100 Durian Tunggal, Malacca, Malaysia  
zamberi@utem.edu.my

**Abstract.** A novel CAD/CAM-control system (CADCAMConSys) interpreter functions to communicate data seamlessly between CAD/CAM and control system of a machine tool. It was developed using MATLAB graphical user interface that serves as an alternative graphical input interface for position controller. The developed interpreter is capable to interpret CAD/CAM data to be utilized as an alternative reference input for position control scheme designed in MATLAB/Simulink environment. The interpreter aims to further enhance the flexibility and capability of a prototype XYZ milling machine that integrates CAD/CAM data with position control schemes and algorithms designed in MATLAB/Simulink platform. This paper focuses on the analysis of the compatibility of the interpreted CAD/CAM data as the input reference for the controller. This research is expected to produce a control system with versatility in input signal forms.

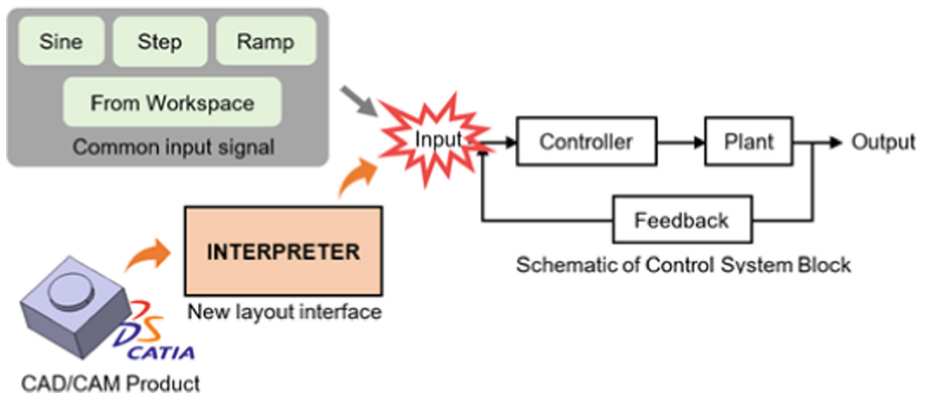
**Keywords:** Interpreter · MATLAB GUI · CAD/CAM · Control systems

## 1 Introduction

The milling Computer Numerical Control (CNC) machine tool is a well-known manufacturing process embedded in a machine tool which plays an important role in the manufacturing industry. To-date, commercial CNC machine uses ready-made and standard machine control unit for the selected machine tool. This means that the commercial product has a limitation which its controller is only compatible with its machine tool. Hence, the need for the customized system comes into an attraction in this research. However, the customized system is rarely adaptable to a new application. Open architecture system can overcome the adaptability issue [1]. An interpreter is one of the modules in an open architecture-controlled system. The interpreter encourages the adaptability, openness, and compatibility of the non-real-time software as utilization in flexible control systems in machine tools. Yadav and Ramesh [2] described the function of an interpreter as to translate source codes line by line and then execute the source codes immediately. [3] designated an interpreter by using software engineering

concepts and experienced the challenges thus proposed the utilization of graphical user interface (GUI) to have a more interactive interpreter.

Modern control systems apply the concept of data integration. This research uses an interactive interpreter to bridge the CAD/CAM data and control system. The interpreter is defined as a software application that is used to directly execute program tasks written using the programming languages into the desired output. The formulation of a CAD/CAM-control system (CADCAMConSys) interpreter brings the functionality to execute NC codes data into lists of positions of data for an advanced control system in machine tool application. Currently, a prototype XYZ milling table positioning system is controlled using an in-house designed advanced position controller using predefined reference trajectory as its reference input signal. It can effectively control the positions of the XY milling table based on the input reference points. However, [4] had discovered that the controllers usually utilized waveform signal as the input reference such as step, ramp, and sinusoidal signals which are currently applied in the library of the Simulink software. Thus, [5] had proposed an interpreter to introduce the utilization of CAD/CAM data as an alternative input for the position controller. Figure 1 visualizes the idea of a new layout interface of an interpreter for having CAD/CAM product as an alternative input reference for the control system.



**Fig. 1.** An idea of new layout interface as input for control system

The integration between CAD/CAM and the position control system has been clarified using the interpreter designed in various interactive software such as Java IDE [6], Python [7], NI LabVIEW [8], Visual C++ [9], and Visual Basic [10]. Since there was no developed interpreter using MATLAB platform for this particular aim, [11] had designed the graphical user interface (GUI) of the interpreter in MATLAB GUI platform since the position controller was previously designed in MATLAB/Simulink software. A system that effectively combined both the controller and the CAD design software would add flexibility to the overall control system thus expanding the quality of parts and products that are produced.



Figure 2 depicts the architectural framework design of CADCAMConSys interpreter which consists of the integration of multiple software includes CATIA, MATLAB, Simulink, and ControlDesk. The desired CAD/CAM geometrical input is designed in CATIA software and later generated the NC codes. The NC codes file needs to be in \*.txt format to be the input for the interpreter. The developed interpreter has several functions which includes: (i) load file, (ii) extract data, (iii) convert data, (iv) execute data, and (v) simulate data. The executed data which is the output of the interpreter becomes the input reference data positions of  $x$  and  $y$  axes for the position controller. This research implements the interpreted data positions of  $x$  and  $y$  axes for cascade P/PI controller for the XY positioning table of the milling machine. In order to operate the XY positioning table, a ControlDesk human-machine interface (HMI) for the controller is utilized. The ControlDesk HMI is interfaced with Simulink controller scheme where the user can control the machine tool with the aid of the interactive HMI.

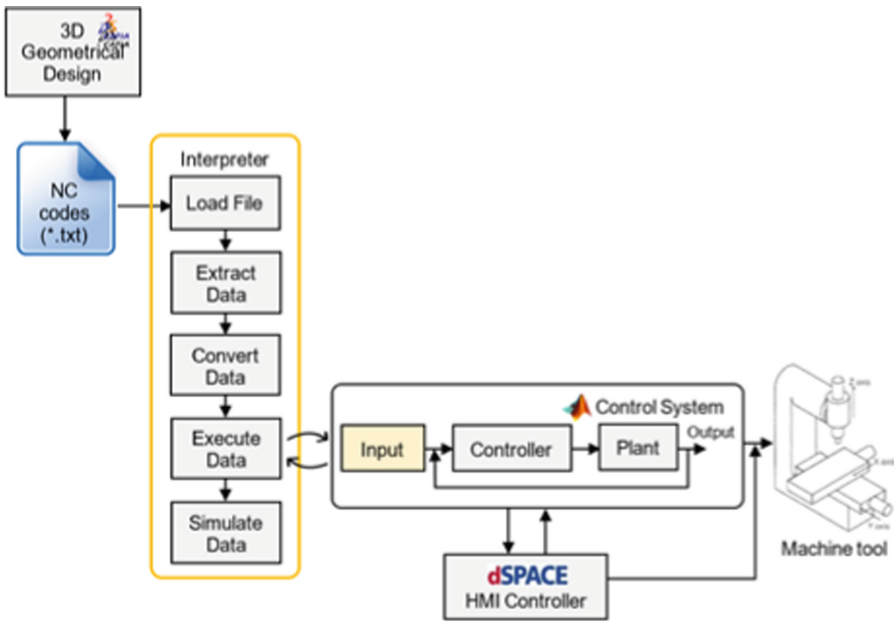
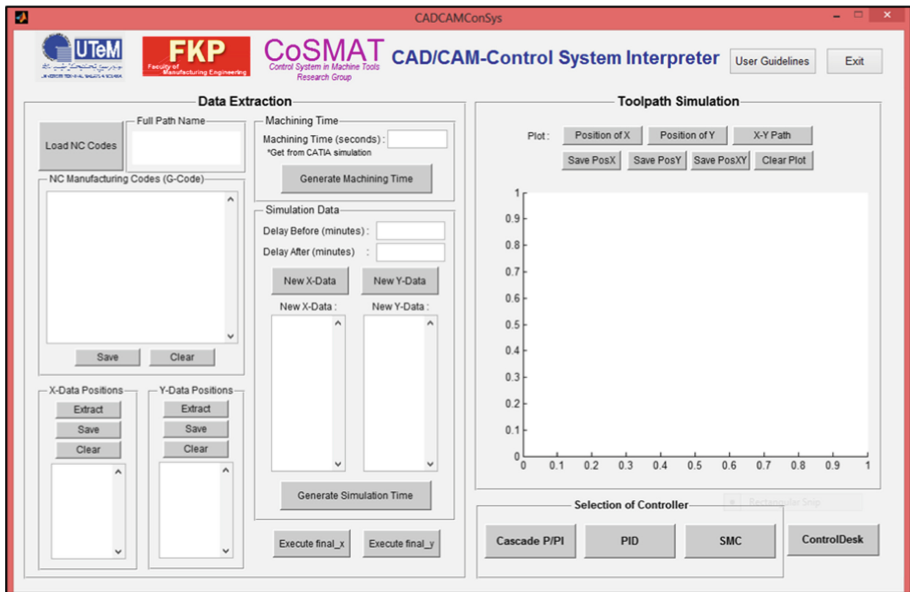


Fig. 2. Architectural framework design of CADCAMConSys interpreter

Section 2 explains the design of the GUI of the CAD/CAM-control system (CADCAMConSys) interpreter. Section 3 describes the experimental setup with the implementation of interpreted data. Section 4 presents the validation results and discusses the compatibility of the interpreted data as alternative input reference for the controller. Lastly, Sect. 5 concludes the research and recommends future work.

## 2 CAD/CAM-Control System GUI Design

In this research, an interpreter namely CADCAMConSys interpreter was designed and implemented for seamless data communication between CAD/CAM drawing in CATIA software and technology with a machine tool position controller of choice designed in MATLAB/Simulink environment. Figure 3 presents the interface of CADCAMConSys interpreter which was designed in MATLAB GUI environment. By using the interpreter, the user has the advantage of having NC codes data as input reference for the controller. Besides, this interpreter gives the user the choices of the controller as for the interpreted data to be implemented with.



**Fig. 3.** Graphical user interface of CADCAMConSys interpreter designed in MATLAB

Firstly, the user needed to upload the NC codes file in \*.txt format. The interface displayed the contents of the NC codes. Next, the user needed to push the Extract button for data positions of  $x$  and  $y$  and the interpreter will extract the selected values, convert them into numerical values, and display in the text boxes as well as save the values in the MATLAB Workspace. In order to execute the positions of data which consisted of the position value and time value, this interpreter came with the timing functions. The user needed to manually enter the Machining Time which generated by CATIA simulation. The machining time was the results of feedrate and spindle speeds determined by the user during the CAM strategies in CATIA. In the interface of CADCAMConSys interpreter, delay time (before) and delay time (after) can be manually added by the user for several minutes. The delay time were utilized for experimental validation. However, the delay time were optional for the user. With the

additional delay time, the user had enough time to set up the configuration of the ControlDesk HMI for the experimental purpose. *NewXdata* and *NewYdata* were then updated which included with the delay time before and after.

A position controller for XY positioning table utilized input reference of positions data. These positions of data consisted of position values and sampling time values. Thus, after having the updated data for  $x$ -axis and  $y$ -axis, the Generate Simulation Time was clicked and then the generation of the time taken for real experiment work was executed and saved in MATLAB Workspace. Last but not least, the saved data for positions of  $x$  and  $y$  axes and also the time were executed into *final\_x* and *final\_y* that were saved in MATLAB Workspace. These *final\_x* and *final\_y* were the input reference for a controller for  $x$ -axis and  $y$ -axis of the positioning table. Later, the *final\_x* and *final\_y* data were simulated to ensure the correct positions or path that generated from CATIA.

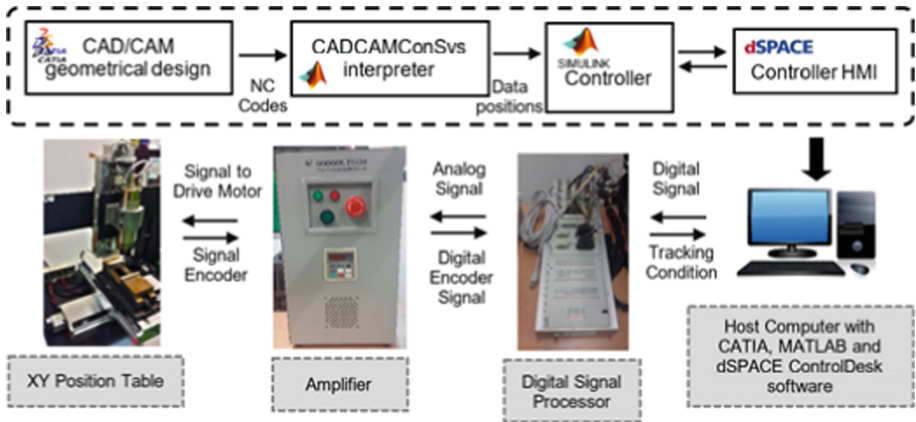
This CADCAMConSys interpreter also occupied with buttons that interfaced and linked the interpreter with Simulink controller scheme and ControlDesk HMI. The user had several choices to select for the controller scheme such as cascade P/PI controller, PID controller, and a sliding mode controller. This research only validated the utilization of the interpreted CAD/CAM data on the cascade P/PI controller.

### 3 Experimental Setup

The efficiency of the system interpreter is evaluated on a real experimental setup consisting of a Googol Tech XYZ-Stage milling machine driven by a ball-screw servo drive system. The complete description of the experimental setup is based on [12]. Figure 4 depicts a schematic diagram of an experimental setup which embedded with the integration of multiple software. In this research, the host computer is equipped with CATIA, MATLAB/Simulink, and dSPACE ControlDesk software. The software integration is capable to control the motions of  $x$ -axis and  $y$ -axis of the XYZ-Stage as well as monitor the position of the milling table. The CATIA software is utilized to design the 3D geometrical drawing and then generate the NC codes. The CAD-CAMConSys interpreter is developed using MATLAB GUI platform. Using the interpreter, the NC codes are generated into data positions of  $x$ -axis and  $y$ -axis. These data positions (readable by Simulink) are then inputted as a reference to the cascade P/PI position controller designed by Rafan [13]. The controller is interfaced with ControlDesk software because this experimental setup is equipped with dSPACE DS1104 digital signal processor controller board.

### 4 Results and Discussions

The performance of the interpreted CAD/CAM data by the CADCAMConSys interpreter was validated. The interpreted CAD/CAM data was implemented as data positions for  $x$ -axis and  $y$ -axis. The data was implemented as an input reference for cascade



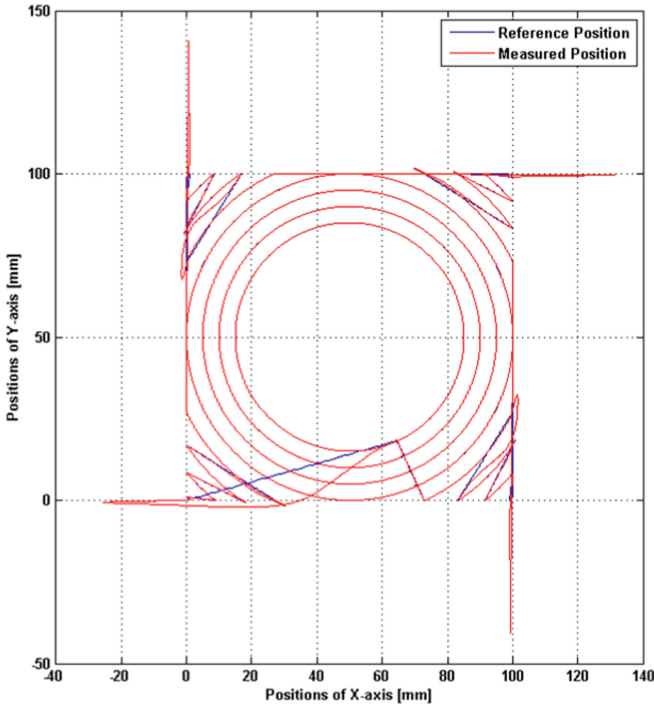
**Fig. 4.** Schematic diagram of experimental setup embedded with software integration

P/PI position controller of the XY positioning table. The actual position, desired position, and the tracking errors were recorded and presented. Figure 5 shows the successful result of an experiment. The blue line is the reference positions that represent the desired positions while the red line is the measured positions that represent the actual captured positions of data. The graph demonstrates near perfect similarities between the desired and actual positions of data with the aid of the cascade P/PI controller.

From the figure, the positioning of data began with the elimination of the four edges; edge 1, edge 2, edge 3, and edge 4 consecutively, and continued with tracking of the circle until the circle reached the diameter of 60 mm. During the elimination of data at the four edges, the high overshoots happened because of the limitation of the machine whereby the controller only covered the compensation of the tracking error, not the positioning error. Hence, the controller was designed by raising the speed to achieve superiority in compensating the tracking error.

The system utilized the interpreted CAD/CAM data as the input reference signal of amplitude 0.1 mm at a frequency of 18.85 Hz with controller parameters of proportional gain,  $K_p$  and integral gain,  $K_i$  at 0.007 Vs/mm and 0.008 Vs<sup>2</sup>/mm respectively for speed loop and velocity gain,  $K_v$  at 50 s<sup>-1</sup> for position loop. In the analysis, Fig. 6 records the tracking errors for the final circle with a diameter of 60 mm and analyses in the time domain. The control performance analyses were performed based on root mean square error (RMSE). The RMSE was performed in MATLAB by using the Eq. (1). The RMSE value for the tracking error was too small, at 0.0033 mm for both  $x$ -axis and  $y$ -axis.

$$RMSE = \sqrt{\text{mean}(\text{Error}^2)} \quad (1)$$



**Fig. 5.** Experimental result of interpreted CAD/CAM data as input reference for cascade P/PI position controller

Results obtained indicated that the interpreted  $x$  and  $y$  data positions are able to adapt as the reference input signal for cascade P/PI controller for XY positioning table of the milling machine. The interpreted CAD/CAM data in forms of data positions are also compatible with the From Workspace source block from Simulink library in designing the controller. From the findings, the CAD/CAMConSys interpreter is forecasted to contribute in term of facilitating the utilization of more advanced position controller as a preferred controller for CNC machine builders. The interpreter has presented a preference for easier and seamless integration between the CAD data and CAM machining details with enormous choices for the suitable position controllers of the drives systems. This would bring advantages to the manufacturing industry in terms of rising accuracy, machinability, and robustness.

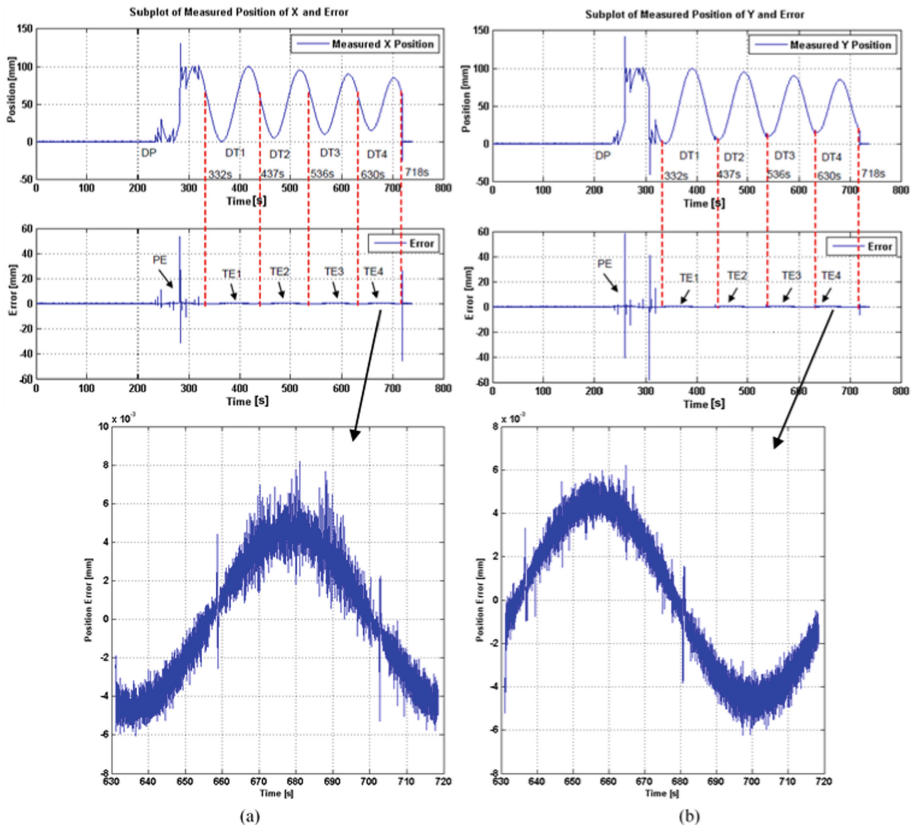


Fig. 6. Tracking errors for (a) x-axis and (b) y-axis

## 5 Conclusions

As a conclusion, the CADCAMConSys interpreter was successfully designed and validated using experimental data. The interpreter acts as the communication bridge between a CAD/CAM system and control system. The interpreted NC codes data was tested using the simulation in the CADCAMConSys interpreter and physical machining using cascade P/PI controller in the XY positioning table. It was proven that the interpreted data can adapt and compatible as the input reference of the cascade P/PI controller. For future study, issue related to the execution of positioning time needs to be addressed as this characteristic also contributes to the performance of the CAD-CAMConSys interpreter.

**Acknowledgments.** This research work is supported by the Malaysia Ministry of Higher Education (MoHE) through research grant FRGS/1/2015/TK03/FKP/02/F00281. The authors would also like to acknowledge the Faculty of Manufacturing Engineering, Universiti Teknikal Malaysia Melaka (UTeM) for the facilities and support provided.

## References

1. Ford, W.E.: What is an open architecture robot controller. In: Proceedings of 1994 9th IEEE International Symposium on Intelligent Control, Columbus (2002)
2. Yadav, A., Ramesh, M.: Fundamentals of Computers: For Undergraduate Courses in Commerce and Management. Pearson Education India, New Delhi (2011)
3. Wu, F., Narang, H., Cabral, M.: Design and implementation of an interpreter using software engineering concepts. *Int. J. Adv. Comput. Sci. Appl.* **5**(7), 170–177 (2014). <https://doi.org/10.14569/IJACSA.2014.050726>
4. Mat Seman, N., Jamaludin, Z., Minhat, M.: A conceptual design of an interpreter for an open architecture control system. In: Proceedings of Innovative Research and Industrial Dialogue 2016, Melaka (2016)
5. Mat Seman, N., Jamaludin, Z., Minhat, M.: Design of CAD/CAM-simulink data exchange system for machine tool application. *J. Adv. Manuf. Technol.* **12**(1(2)), 1–14 (2018)
6. Elias, D.M., Yusof, Y., Minhat, M.: Design and machining control via interoperable function blocks and STEP-NC data model. In: International Conference on Flexible Automation and Intelligent Manufacturing, Helsinki (2012)
7. Yaman, U., Dolen, M.: A novel command generation paradigm for production machine systems. *Robot. Comput. Int. Manuf.* **51**, 25–36 (2018). <https://doi.org/10.1016/j.rcim.2017.11.016>
8. Yusof, Y., Latif, K.: New interpretation module for open architecture control based CNC systems. *Proc. CIRP* **26**, 729–734 (2015). <https://doi.org/10.1016/j.procir.2014.07.051>
9. Qin, Y., Xiao, J., Wang, G.: The open architecture CNC system based on 6-axis flame pipe cutting machine. In: Proceedings—3rd International Conference on Measuring Technology and Mechatronics Automation, Shanghai (2011)
10. Rafan, N.C.: A study on the performance of an XY table for laser spot welding. Meng. Dissertation, UM (2008)
11. Mat Seman, N., Jamaludin, Z., Minhat, M.: System interface design for CAD/CAM-Simulink data exchange system using MATLAB ®. In: Hassan, M.H.A. (ed.) Intelligent Manufacturing and Mechatronics. Lecture Notes in Mechanical Engineering, Pekan, Pahang, pp 639–647 (2018)
12. Chiew, T.H.: N-PID controller with feedforward of generalized maxwell-slip and static friction model for friction compensation in machine tools. MSc Thesis, UTeM (2014)
13. Rafan, N.A.: Stick slip friction models control design approach for friction compensation in machine tools drive system. Ph.D. Thesis, UTeM (2017)



# Effect of Cutting Forces on Surface Roughness for Varying Depth of Cut and Feed Rates in Milling Machining Process

Zamberi Jamaludin<sup>(✉)</sup>, Nur Ayunni Shamshol Ali,  
Nur Aidawaty Rafan, and Lokman Abdullah

Fakulti Kejuruteraan Pembuatan, Universiti Teknikal Malaysia Melaka,  
Hang Tuah Jaya, Durian Tunggal, 76100 Melaka, Malaysia  
zamberi@utem.edu.my

**Abstract.** The aim of this study is to evaluate characteristics of cutting force at varying cutting conditions during milling machining process. Firstly, material selected as the work piece to be machined was aluminium whereby the cutting forces during actual milling process at varying cutting conditions were measured using a Kistler dynamometer. The milling process consisted of circular shaped aluminium product of 60 mm diameter. The cutting parameters that were varied consist of cutting speed, spindle speed, feed rate and depth of cut. Depth of cuts of 1 mm, 2 mm and 2.5 mm along with the spindle speeds of 500 rpm, 1000 rpm and 1500 rpm were selected for this study. Next, the cutting forces characteristics were will be analysed by using a Fast Fourier Transform methods through the MATLAB software. Analyses of the cutting forces showed harmonics frequencies of varying amplitudes. Next, the surface roughness and roundness of the cut materials were analysed. These analyses provide insight into factors that give most influence on the quality of the cut materials for varying characteristics of cutting forces, thus enabling effective strategies to be implemented for damping of the high frequencies cutting forces. Results obtained showed that higher magnitude components of the cutting forces were produced at greater spindle speed and depth of cut. Meanwhile, improvement in quality of surface roughness were measured at higher spindle speed.

**Keywords:** Cutting force · FFT analysis · Compensation · Precision

## 1 Introduction

Machining is defined as a process whereby raw material known as work piece is shaped into desired dimensions and surface finish conditions through systematic materials removal process. According to Singh et al. (2014), machining is an important activity in manufacturing of metal-based parts and products and milling is one amongst the most common method used.

In precision machining (Ramesh and Srinivasulu 2016) every process need to be stringently control to avoid deviation from the desired process parameters. Precision of the final parts and products depend on many factors. These factors include machine structural integrity, servo drive mechanism, position control of the guideways, and



process planning parameters. Among these factors, controlling the machining process parameters create the best practical solution due to the ease of application. In machining, the properties of the finish part are influenced by the magnitude and profiles of the cutting force and these could be verified based on the surface roughness measurement. Cutting forces cannot be avoided as it is the outcome from the necessary interaction between the tool part and the work piece. However, cutting force exerts unnecessary force onto the drives system of the positioning table and if not well damped the cutting force will cause machine vibration, which then reduces machine accuracy, efficiency and reliability (Jamaludin 2008).

A work piece machinability is mainly determined by cutting conditions set upon by the selection of the cutting parameters such as the feed rate, depth of cut, spindle speed, cutting speed, coolant and tool geometry. The quality of machined surface is characterized by the accuracy of its manufacture with relevance to the dimension that has been fixed by the designer. Variations in the cutting parameters have great impact on the cutting force profile generated. Each sort of cutting implementations leaves its own individual pattern. This pattern is known as surface finish or surface roughness (Imhade and Ugochukwu 2015). For example, as the spindle speed (rpm) increases, the build-up edge vanishes, chip fracture decreases, and hence, the roughness decreases. Therefore, the understanding of these different cutting force profiles is essential for efficient cutting process. According to Indexed et al. (2018), the spindle speed, the radial depth of cut, axial depth of cut and feed rate affect the shapes and the surface roughness of the work-piece materials. For example, feed rate selection has a strong impact on the tool life, machine wear and tear, surface finish and part quality. It has been established that (Latif et al. 2017) cutting speed, feed rate and depth of cut have impacted the surface roughness such that the surface roughness increases with increases in both the feed rate and depth of cut. Furthermore, Ibrahim et al. (2017) have investigated the impact of feed rate and depth of cut on cutting forces and surface roughness in end milling process of mild steel. It was stated that the feed rate increase which resulted in increases in cutting forces for the  $x$  and  $y$  orientation and improves the surface roughness. Mehdi and Zghal (2012) have modeled the cutting force that included thrust and tangential damping in peripheral milling process with observation that increasing feed rate, axial and radial depth of cut, and tool diameter increased the amplitude of the cutting force but these values decreased with increasing cutting speed. Also, according to Abdullah et al. (2008), surface finish can be improved by increasing the cutting speed. It was explained that in machining of multiphase materials at lower cutting speeds, the occurrence of built-up edge produced substantial burr quantity on the machined surface and consequently deteriorated the surface finish quality. This phenomenon has resulted in dynamic instability of the cutting process with increment in the magnitude of the cutting forces. It was stated that increases in the depth of cut increases the surface roughness values. Meanwhile, Miyaguchi et al. (2001) have showed that in ultra-high speed face milling, increasing cutting speed causes a decrease in the magnitude of the cutting forces. According to Ibrahim et al. (2017), the roughness profile for cutter shows distinct pattern at variety depth of cut that is the roughness profile increases as result of increases in the depth of cut. Furthermore, it was reported by Anil et al. (2017) that increased in feed rates and depth of cuts generated additional cutting force and

produced poor surface quality while higher cutting speed with lower depth of cut and lower feed rates created good surface finish.

This paper analysed and characterized cutting forces of varying cutting conditions and parameters, measured using a Kistler dynamometer unit. Series of experiments were conducted and the measured cutting forces were analysed and characterised so that the knowledge gained could be applied as future reference in the development of robust positioning controller for CNC machines. The content of this paper is organized as follows; section two describes the experimental setup and the research methodology, while section three lists the results obtained followed by a critical discussion. This paper ends with a conclusion based on the results obtained with relevant future recommendations.

## 2 Experimental Setup and Research Methodology

### 2.1 Experimental Setup

This paper presents data analyses and characterizations of cutting forces for varying cutting conditions, namely depth of cut and spindle speed. The overall research framework is presented in the following Fig. 1.

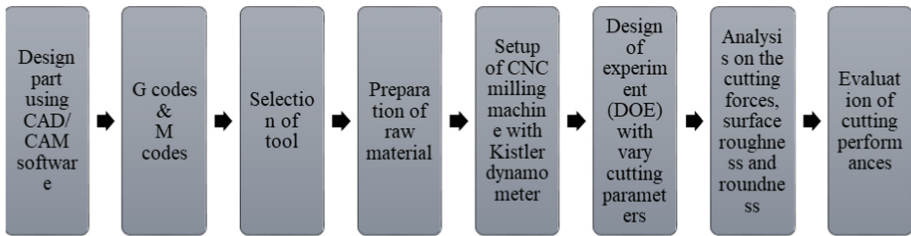


Fig. 1. Overall research framework

Cutting processes were performed on aluminium bar of dimension 10 cm × 4 cm using a HAAS VOP-C 3-axis CNC milling machine. The three orthogonal elements of the cutting forces were measured using a Kistler dynamometer. The aluminium work piece was mounted on the jig and connected to dynamometer over a fixture. The dynamometer was linked to a multi-channel charge amplifier to acquire the output signal. Also, a high-speed data acquisition (DAQ) card was applied for data gathering purposes, as shown in Fig. 2.

A Mitutoyo SJ-301 Portable Surface Roughness Tester with a resolution of 1 μm was used to measure the surface roughness of the aluminium. A Mahr surface roundness tester was applied for analyse of the surface roundness error of the machined part.

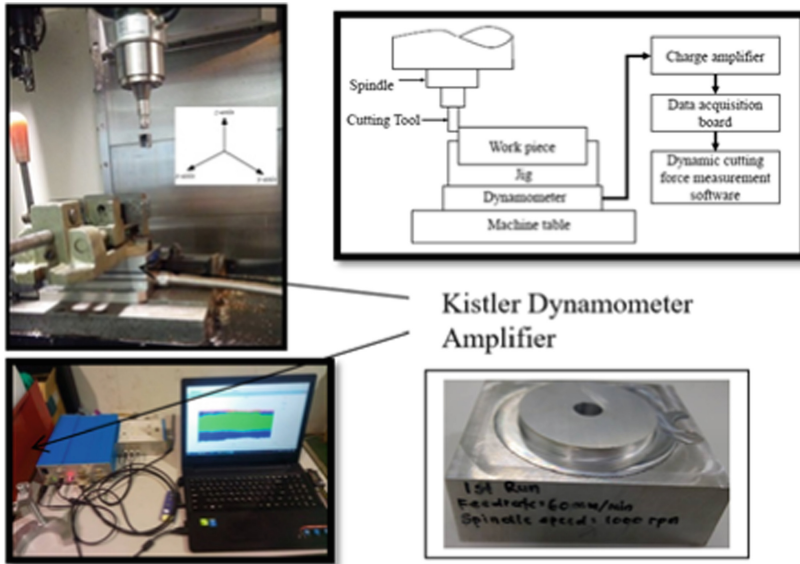


Fig. 2. Experimental setup

## 2.2 Experimental Design

The analyses on cutting force for the CNC milling process focusses on two parameters, namely the depth of cut and the spindle rotations. Circular contour machining of 60 mm diameter was performed for each of the cutting parameter variation using a 10 mm diameter HSS coating carbide end mill cutting tool. In the machining processes, the controlled parameters were the depth of cut ( $d$ ), feed rate ( $f$ ), spindle speed ( $S$ ) and cutting speed ( $V_c$ ) (Table 1).

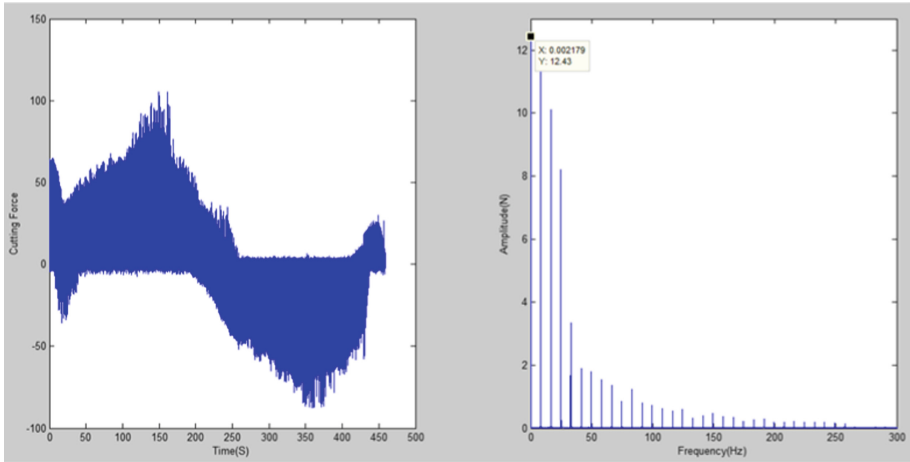
Table 1. Contour machining parameters

Cutting parameters	1	2	3
Feed rate (mm/min)	30	60	90
Spindle speed (rpm)	500	1000	1500
Depth of cut	(1 mm, 2 mm, 2.5 mm)		

## 3 Results and Discussion

### 3.1 Cutting Forces

Analyses of the measured cutting force obtained by the Kistler Dynamometer were made using a MATLAB R2012b software. Figure 3 shows example of a Fast Fourier



**Fig. 3.** Cutting force and FFT result for 1 mm depth of cut and 500 RPM

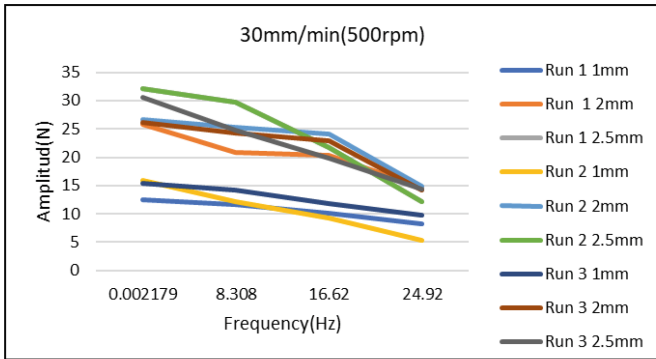
Transform (FFT) analysis on the measured cutting forces for a depth of cut of 1 mm and a spindle speed of 500 rpm.

Here, the FFT results clearly identify the harmonics frequencies associated with the spindle speed value of 500 RPM where the fundamental frequency equals 8.3 Hz. The harmonics frequencies vary with changes in the spindle speed rotations (Chiew et al. 2017). The following Figs. 4, 5 and 6 illustrates the maximum peaks of the FFT results for different depth of cuts and feed rates. Table 2 summarizes these peak values of the cutting force harmonics. Results presented showed that the harmonics frequencies vary with the spindle speed applied. Highest peaks were observed for the first harmonics in all the different cases.

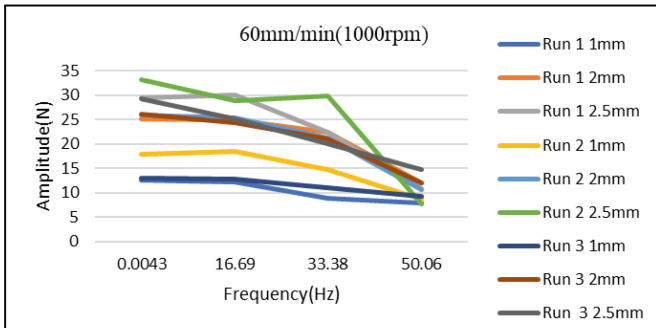
Table 2 on the other hand summarizes the maximum peak values of the cutting forces, increasing due to the increasing of the spindle speed and the feed rate. General observation showed that the maximum peaks recorded increased with increasing spindle speed and depth of cut. For example, the maximum peak value was doubled as the depth of cut was doubled from 1 mm to 2 mm. Meanwhile, from the 2 mm to 2.5 mm increase in the depth of cut, the increase in the peak amplitude ranges from 9% to 22%. Figure 5 shows the maximum peak values for different depth of cut and spindle speed rotations. The magnitude of the cutting forces increased with increasing depth of cut. At 2 mm and 2.5 mm depths of cut, the value of cutting force increased dramatically for 1500 rpm spindle speed compared to the 500 rpm and 1000 rpm. Lastly, the higher the spindle speed and deeper depth of cut, higher cutting forces were observed as reflected from higher magnitude of the first harmonic frequency (Sparham et al. 2016).

### 3.2 Surface Roughness

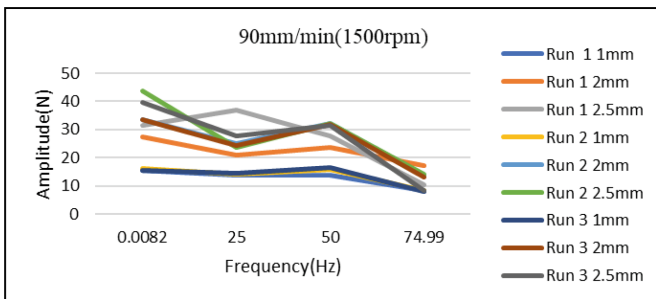
The second part of this work centres on the impact of depth of cut and spindle speed rotations on surface roughness value of the finish product. Table 3 lists decreasing



(a)



(b)



(c)

Fig. 4. Peak amplitudes of FFT for different feed rates and depth of cuts

surface roughness values for increasing spindle speed and feed rate. Surface roughness values decrease in the range of 22% to 24% for every increase in 500 rpm. Meanwhile for 1000 rpm increase, the surface roughness decreased within the range of 33% to 35%. This shows that surface quality improved with greater spindle speed and feed rate. Similar observations were recorded by Imhade and Ugochukwu (2015) and Balic et al. (2016). Figure 6 shows sample of surface roughness measurement results using the 10-point based approach. This data have been proven by the research study.

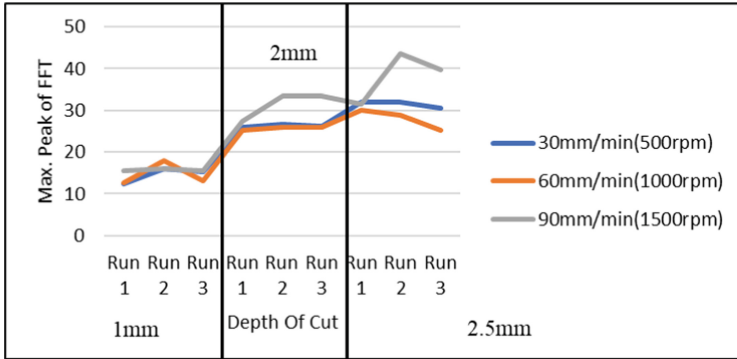


Fig. 5. Maximum peaks of FFT for different depth of cuts and spindle speed

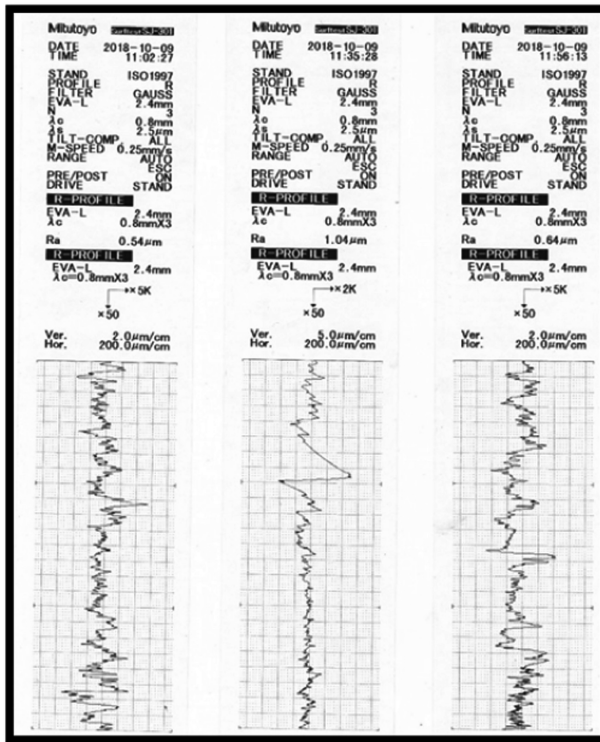


Fig. 6. Surface roughness measurement based on 10-point analysis

**Table 2.** Maximum peaks for different depths of cut and feed rates

Feed rates\depth of cuts	1 mm			2 mm			2.5 mm		
	Run 1	Run 2	Run 3	Run 1	Run 2	Run 3	Run 1	Run 2	Run 3
30 mm/min (500 rpm)	12.43	15.93	15.39	25.86	26.72	26.09	32.08	32.08	30.55
60 mm/min (1500 rpm)	12.61	17.92	13.04	25.14	25.85	26.04	29.99	28.76	25.18
90 mm/min (1500 rpm)	15.55	16.15	15.54	27.3	33.53	33.49	31.54	43.61	39.68

**Table 3.** Surface roughness values based on 10-point locations

(30 mm/min, 500 rpm)	(60 mm/min, 1000 rpm)	(90 mm/min, 1500 rpm)
0.64	0.57	0.44
0.86	0.6	0.48
0.64	0.58	0.5
0.76	0.54	0.46
0.74	0.6	0.43
0.72	0.49	0.51
0.75	0.47	0.47
0.65	0.56	0.43
0.64	0.59	0.49
0.65	0.47	0.47

## 4 Conclusions

The present study was carried out to as a mean to characterize and analyse cutting force profile for varying cutting conditions in milling machining process. Several types of analysis were performed including FFT analyses using MATLAB software and surface roughness testing and measurements. Two factors that were varied were depths of cut and the spindle speed. Results showed that greater spindle speed and larger depths of cut produced higher magnitude cutting force as translated by the highest point on the first harmonics frequency of the cutting force spectrum. Patterns that were observed in the form of these harmonics analyses served as great tool and knowledge for future development of effective and smart milling machining process that eliminate potential vibration and chattering issues during machining. An intelligent controller approach could then be develop utilizing knowledge of these cutting force profiles as a method to ensure effective and efficient milling machining process thus eliminating waste by eliminating rejects through precise positioning with reduced vibrating effect.

**Acknowledgments.** The authors would like to extend our gratitude to Universiti Teknikal Malaysia Melaka and the Fakulti Kejuruteraan Pembuatan for the support and facilities provided in the undertaking of this project.

## References

- Abdullah, A.B., Chia, L.Y., Samad, Z.: The effect of feed rate and cutting speed to surface roughness. *Asian J. Sci. Res.* **1**(1), 12–21 (2008)
- Anil, K.C., Vikas, M.G., Shanmukha Teja, B., Sreenivas Rao, K.V.: Effect of cutting parameters on surface finish and machinability of graphite reinforced Al-8011 matrix composite. In: IOP Conference Series: Materials Science and Engineering, vol. 191 (2017)
- Balic, J., Kovacic, M., Vaupotic, B.: Intelligent programming of CNC turning operations using genetic algorithm. *J. Intell. Manuf.* **17**(3), 331–340 (2016). <https://doi.org/10.1007/s10845-005-0001-1>
- Chiew, T.H., Jamaludin, Z., Bani Hashim, A.Y., Abdullah, L., Rafan, N.A.: Design of super twisting algorithm for chattering suppression in machine tools. *Int. J. Control Autom. Syst.* **15** (3), 1260–1266 (2017)
- Ibrahim, M.R., Latif, A.A., Rahim, E.A., Amran, A.Z., Peter, C.P.E.: Effect of feed rate and depth of cut on cutting forces and surface roughness in end milling of mild steel with noviano cutting tool (2017)
- Imhade, P.O., Ugochukwu, C.O.: Effects of cutting parameters on surface roughness during end milling of aluminium under minimum quantity lubrication (MQL). *Int. J. Sci. Res. (IJSR)* **4** (5), 2937–2942 (2015). <https://doi.org/10.5923/j.jmea.20150501.01>
- Indexed, S., Okokpujie, I.P., Ajayi, O.O., Afolalu, S.A., Abioye, A.A., Salawu, E.Y., Udo, M.: Modeling and optimization of surface roughness in end milling of aluminium using least square approximation method and response. *Int. J. Mech. Eng. Technol.* **9**(1), 587–600 (2018)
- Jamaludin, Z.: Disturbance compensation for machine tools with linear motor drives. Ph.D. thesis, Faculty of Engineering, Department of Mechanical Engineering, Div. of Production, Machine Design, and Automation (P.M.A), Katholieke Universiteit Leuven (2008)
- Latif, A.A., Ibrahim, M.R., Amran, A.Z., Rahim, E.A.: A study on the effect of feed rate and cutting speed on surface roughness and material removal rate of mild steel. *IOP Conf. Ser. Mater. Sci. Eng.* **257**(1), 012025 (2017)
- Mehdi, K., Zghal, A.: Modelling cutting force including thrust and tangential damping in peripheral milling process. *Int. J. Mach. Mach. Mater.* **12**(3), 236–251 (2012)
- Miyaguchi, T., Masuda, M., Takeoka, E., Iwabe, H.: Effect of tool stiffness upon tool wear in high spindle speed milling using small ball end mill. *Precis. Eng.* **25**(2), 145–154 (2001)
- Ramesh, V., Srinivasulu, M.: Study on computer numerical control (CNC) machines. *Int. J. Adv. Sci. Res.* **1**, 20–25 (2016)
- Singh, E.M., Sanjeevverma, E., Jain, S.K.: A literature review on machining of different materials with CNC. *Int. J. Emerg. Res. Manag. Technol.* **9359**(8), 50–53 (2014)
- Sparham, M., Sarhan, A.A.D., Mardi, N.A., Dahari, M., Hamdi, M.: Cutting force analysis to estimate the friction force in linear guideways of CNC machine. *Measurement* **85**, 65–79 (2016). *Journal of the International Measurement Confederation*



# **Intelligent Manufacturing**



# Mechanical Behaviour of Banana Fibre Reinforced Concrete with Kenaf Fibre as an Additive

Nurul Akmam Naaamandadin<sup>1</sup>(✉), Ahmad Izdihar Saharudin<sup>1</sup>,  
Wan Azani Mustafa<sup>1</sup>, and Ragunathan Santiago<sup>2</sup>

<sup>1</sup> Faculty of Engineering Technology, Kampus Sg. Chuchuh,  
Universiti Malaysia Perlis, 02100 Padang Besar, Perlis, Malaysia  
nurulakmam@unimap.edu.my

<sup>2</sup> School of Environmental Engineering, Universiti Malaysia Perlis,  
PusatJewawi 3, 02600 Arau, Perlis, Malaysia

**Abstract.** The aim of this study is to investigate the effect of various kenaf fibre (KF) ratio as an additive: banana fibre (BF) reinforced concrete compared to normal concrete (NC) on the mechanical properties of the reinforced concrete. Thus, this paper will discuss the effect of fibres as the additives to reinforced concrete mixed. The properties included compressive strength and splitting tensile strength. The different ratio of KF1.4%: BF1.5%, KF1.6%: BF1.5% and KF1.8%: BF1.5% were used in this study. The results show that the strength was increased with the increasing of fibre additives, but they were not stiff compared to the normal concrete. While the splitting tensile strength increased when the content of fibre increased. The test data indicates that the addition of fibre will increase the mechanical properties of the concrete.

**Keywords:** Kenaf fibre · Banana fibre · Mechanical properties of concrete

## 1 Introduction

Concrete is widely used in the construction industry as it is a low-cost material, long lasting and can withstand with high temperatures. A combination of cementations materials is mixed with either water or some other liquid or both with the course (crushed stone) and fine aggregate (sand) to form concrete [1, 2]. However, the production of Portland cement requires an immense amount of energy, and the by-product is greenhouse gases. Even though it can be made up locally, it is durable, can be left unpainted, stable, does not release any harmful chemicals and it is also virtually maintenance free. Agriculture waste such as banana and kenaf trees which fall on the ground need to be disposed of or otherwise, the disease will be spread out to the nearby area. As for example, high fever which causes by the mosquito breeding at the unconventional dispose area will pass through all the residential area.

## 2 Literature Review

In 1999, GreenTech Malaysia had implemented the Malaysia Industrial Energy Efficiency Improvement Project (MIEEIP) [3]. The project aims to remove barriers and encourage implementation of EE improvements in eight energy-intensive manufacturing industries such as cement, ceramic, iron and steel, food, glass, wood, pulp and paper, rubber and oleo chemical, plastics and textile [4].

In accordance with that, standards had been developed for the green products to ensure the market confidence in the green products and seep for the non-genuine products from entering or misleading the market. As result, the green products had been labeled to assist the public, especially for the non-technical citizens to choose the products those have minimum impact on the environment and safe for health. In cooperating with the green concrete, fibre from agriculture waste can be considered as green material by way of reducing the process of extraction, manufacturing, and transportation steps required to process the concrete or cement. Sustainable construction can be achieved with eco-friendly cement with approved industrial by-products with the replacement of 10%–20% of Ordinary Portland Cement (OPC) by mass for concrete production of structural building elements [5].

### 2.1 Banana Fibre

According to Awang, Ahmad and Al-Mulali [6] banana fibre helps in increasing of flexural strength of concrete as it has a good mechanical strength [7, 8]. After harvesting the fruits and banana leaf, banana fibre can be extracted from the stem [9, 10]. Consequently, it can reduce the demand pressure on global natural resources [11] and solve the issue of limited area to the disposed waste material [12, 13].

### 2.2 Kenaf Fibre

Kenaf can be planted in various types of soils and it requires minimum chemical treatment to grow up effectively [14]. Besides that, between the duration of 4 to 5 months, kenaf tree can raise up until 3.5–4.5 m of height [15]. The fast growth of kenaf can solve the deficiency of fibres from the forest trees [16].

The previous researcher [17] states that in order to carry out the best achievement of the essential fibre and to increase the chemistry of the mixture in the concrete, it needs chemical pre-treatment. There are many trial mixtures had been processed in order to get the best mix proportions and create relevant mixing process for kenaf fibre reinforced concrete [18]. The results show that the volume contents of fibre that appropriate is 1.2% and 2.4%.

## 3 Sampling Preparation and Experimental Procedure

The mixture proportion of fresh concrete and fibre produced in the laboratory are shown in Table 1. Mix design for this study was using concrete Grade 30 for all samples including normal samples and fibre concretes samples. Then, a total of the

cement was used are 50.76 kg, fine aggregates 98.28 kg, coarse aggregates 86.40 kg and water 25.92 kg. Total of 24 samples concrete mixtures were prepared for banana fibre mixed, the slurry was added in a ratio of 1.4%, 1.6% and 1.8% with a constant of 1.5% of banana fibre. The banana fibre was added by percentage of coarse aggregates volume.

**Table 1.** Mix proportion of concrete

Mix	w/c ratio	Cement (kg)	Fine aggregate (kg)	Coarse aggregate (kg)	Water (kg)
NC	0.5	4.23	8.19	7.20	2.16
KF1.4%: BF1.5%	0.5	4.23	8.19	7.20	2.16
KF1.6%: BF1.5%	0.5	4.23	8.19	7.20	2.16
KF1.8%: BF1.5%	0.5	4.23	8.19	7.20	2.16

The concrete test carried out by using ASTM - C 39: Compressive Strength of Cylindrical Concrete Specimens. There is a total of 24 samples used in which consists of 12 cube samples for compression testing and 12 cylinder samples for splitting tensile testing. Splitting tensile strength determined by following to ASTM - C 293 (center point loading). The compression and splitting tensile strength test were done 28 days after curing.

## 4 Result

### 4.1 Compressive Strength

The compressive strength of concrete samples with the inclusion of kenaf fibre and banana fibre are shown in Table 2.

The result shows that when additive of fibre increase, the strength of the concrete increase but it is not stiff compared to NC. The maximum compressive strength of 35.0 MPa and 33.6 MPa was recorded by NC for 28 days with the mean reading of 33.8 MPa. While for KF1.4%:BF1.5% the result shows the reading 24.2 MPa, 23.9 MPa and 24.7 MPa with mean reading 24.3 MPa and 71.89% of reduction. KF1.6%:BF1.5% compressive strength were slightly increased. The results show that the strength was 26.7 MPa, 25.4 MPa and 23.2 MPa with mean reading 25.1 MPa and 74.26 percentage of reduction. Lastly, KF1.8%:BF1.5% shows the result of compressive strength 29.8 MPa, 32.0 MPa and 30.1 MPa with mean reading 30.6 MPa and 90.53% of reduction.

**Table 2.** Result of compressive strength

Mix	Compressive strength (N/mm <sup>2</sup> )				
	28 days				
	Reading 1	Reading 2	Reading 3	Mean reading	Percentage of reduction (%)
NC	33.6 MPa	35.0 MPa	32.8 MPa	33.8 MPa	100
KF1.4%: BF1.5%	24.2 MPa	23.9 MPa	24.7 MPa	24.3 MPa	71.89
KF1.6%: BF1.5%	26.7 MPa	25.4 MPa	23.2 MPa	25.1 MPa	74.26
KF1.8%: BF1.5%	30.1 MPa	32.0 MPa	29.8 MPa	30.6 MPa	90.53

## 4.2 Splitting Tensile Strength

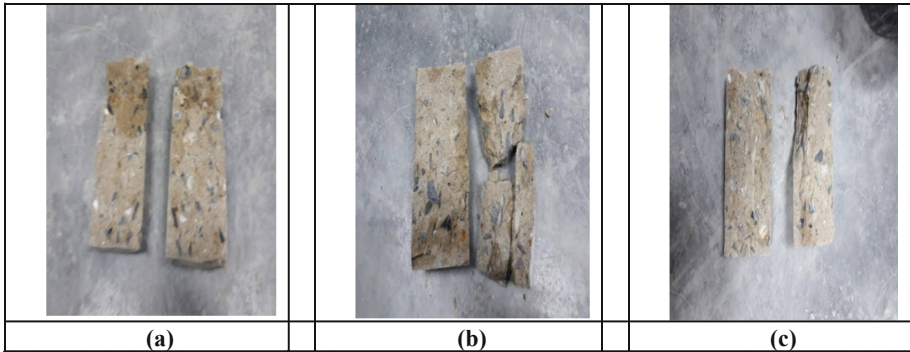
Splitting Tensile Strength of concrete samples with the inclusion of kenaf fibre and banana fibre are shown in Table 3.

**Table 3.** Result of splitting tensile strength

Mix	Tensile strength (N/mm <sup>2</sup> )				
	28 days				
	Reading 1	Reading 2	Reading 3	Mean reading	Percentage of reduction (%)
NC	3.7 N/mm <sup>2</sup>	3.4 N/mm <sup>2</sup>	3.6 N/mm <sup>2</sup>	3.57 N/mm <sup>2</sup>	100
KF1.4%: BF1.5%	7.8 N/mm <sup>2</sup>	7.5 N/mm <sup>2</sup>	7.6 N/mm <sup>2</sup>	7.63 N/mm <sup>2</sup>	213.7
KF1.6%: BF1.5%	8.9 N/mm <sup>2</sup>	8.7 N/mm <sup>2</sup>	9.0 N/mm <sup>2</sup>	8.87 N/mm <sup>2</sup>	248.5
KF1.8%: BF1.5%	9.2 N/mm <sup>2</sup>	9.6 N/mm <sup>2</sup>	9.4 N/mm <sup>2</sup>	9.4 N/mm <sup>2</sup>	263.3

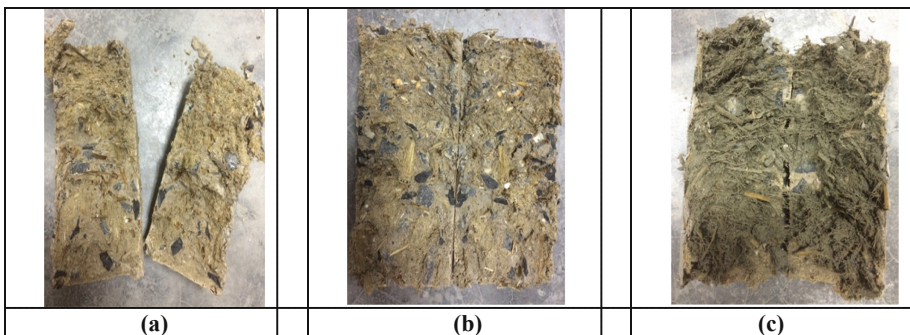
The result from the above table shows that the highest reading of splitting tensile strength is 9.4 N/mm<sup>2</sup> with 263.3 percentage of reduction for KF1.8%:BF1.5% sample. The trend shows that the splitting tensile strength is increasing with the increasing of kenaf fibre as an additive. The mean reading of KF1.6%:BF1.5% is 8.87 N/mm<sup>2</sup> and KF1.4%:BF1.5% is 7.63 N/mm<sup>2</sup>. NC had the lowest splitting tensile strength among of all four mixes which are 3.57 N/mm<sup>2</sup> in average.

Table 2 and Fig. 1(a)–(c) shows the result of splitting tensile strength test with the failure rate of 50%. It demonstrates that materials such as coarse aggregate, sand, and cement do not help to increase the mechanical properties of the concrete. The large size of coarse aggregates also caused low tensile strength in which the aggregates had to stand with the tension forced until they produced cracks in the surface of the samples.



**Fig. 1.** (a) The result of splitting tensile strength for normal concrete (b) The result of splitting tensile strength for normal concrete (c) The result of splitting tensile strength for normal concrete

Figure 2(a)–(c) shows that kenaf fibre and banana fibre bonding to each other. As a result, it proved that the combination of kenaf fibre and banana fibre into a mix of concrete increased the splitting tensile strength. Accordingly, it can be concluded that the addition of fibre will gain the splitting tensile strength of the concrete. The high content of kenaf fibre plays an important role as to make the concrete bonding become closely. Meanwhile, the samples were mixed with the curtain of the water–cement ratio.



**Fig. 2.** (a) The result of splitting tensile strength for KF1.4%:BF1.5% (b) The result of splitting tensile strength for KF1.6%:BF1.5% (c) The result of splitting tensile strength for KF1.8%:BF1.5%

## 5 Conclusions

This study highlights the influence of kenaf fibre range from 1.4% to 1.8% in 1.5% of banana fibre concrete for a period of 28 days. The following conclusion is presumed.

- (a) First, the compression strength of the banana fibre reinforced concretes were increased with the increase of the proportional to the percentage additional of kenaf fibre. However, the strength is lower than the normal concretes.
- (b) Secondly, normal concretes were weaker compared to the banana fibre reinforced concrete with kenaf fibre as an additive.

The findings show that, KF1.8%:BF1.5% is suitable for structural parts of the building. Thus, it can be concluded that, agriculture waste can be used as part of the building structure and at the same time it can solve the issue of limited area to the disposed agriculture waste. It also can reduce air pollution if the agriculture waste gone through the burning process.

## References

1. Kubba, S.: Handbook of Green Building Design, and Construction. Elsevier, Amsterdam (2012)
2. Freed, E.C.: Green Building & Remodeling for Dummies. Wiley, Indianapolis (2008)
3. Ahmad, A., Ernest, K., Ibrahim, K., Razak, A.K.: The Malaysian industrial energy efficiency improvement project—energy audit program. *Adv. Malays. Energy Res.* **1999**, 129–136 (1999)
4. Sustainable Development Initiatives in Malaysia (2010)
5. BCA: BCA green mark for new buildings (2015)
6. Awang, H., Ahmad, M.H., Al-Mulali, M.Z.: Influence of kenaf and polypropylene fibres on mechanical and durability properties of fibre reinforced lightweight foamed concrete. *J. Eng. Sci. Technol.* **10**, 496–508 (2015)
7. Mukhopadhyay, S., Fanguero, R., et al.: Banana fibers: variability and fracture behaviour. *J. Eng. Fibers Fabr.* **3**, 1–7 (2008)
8. Mustafa, W.A., Saidi, S.A., Zainal, M., Santiagoo, R.: A proposed compatibilizer materials on banana skin powder (BSP) composites using different temperature. *J. Adv. Res. Fluid Mech. Therm. Sci.* **43**, 121–127 (2018)
9. Santhosh, J., Balanarasimman, N., Chandrasekar, R., Raja, S.: Study of properties of banana fiber reinforced composites. *Int. J. Res. Eng. Technol.* **3**, 144–150 (2014)
10. Ghani, A.A., Mustafa, W.A., Rohani, M.N.K.H., et al.: Material treatment of polypropylene (PP)/recycle acrylonitrile butadiene rubber (NBrr) and banana skin powder (BSP) using thermal mixing techniques. *J. Adv. Res. Fluid Mech. Therm. Sci.* **52**, 1–11 (2018)
11. Akinwumi, I.I., Olatunbosun, O.M., Olofinnade, O.M., Awoyera, P.O.: Structural evaluation of lightweight concrete produced using waste newspaper and office paper. *Civ. Environ. Res.* (2014). <https://doi.org/10.1134/S0040601513020018>
12. Foti, D.: Use of recycled waste pet bottles fibers for the reinforcement of concrete. *Compos. Struct.* (2013). <https://doi.org/10.1016/j.compstruct.2012.09.019>

13. Mustafa, W.A., Zainal, M., Santiago, R., et al.: Structure analysis on polypropylene maleic anhydride (PPMAH)/polypropylene(PP)/recycled acrylonitrile butadiene rubber (NBRr)/banana skin powder (BSP) composites treatment. *J. Adv. Res. Fluid Mech. Therm. Sci.* **50**, 40–46 (2018)
14. Mustafa, Z., Ragunathan, S., Othman, N.S., et al: Fabrication and properties of polypropylene and kenaf fiber composite. In: IOP Conference Series Materials Science Engineering, vol. 429, p. 012016 (2018). <https://doi.org/10.1088/1757-899X/429/1/012016>
15. Zaveri, M.: Absorbency Characteristics of Kenaf Core Particles. North Carolina State University, Raleigh (2004)
16. Mustafa, Z., Ragunathan, S., Othman, N.S., et al: Thermoplastic elastomer composite using benzyl chloride treatment on kenaf core powder mixing with polypropylene and virgin acrylonitrile butadiene rubber. In: IOP Conference Sereries Materials Science and Engineering, vol. 429, p. 012013 (2018). <https://doi.org/10.1088/1757-899X/429/1/012013>
17. Elsaid, A., Dawood, M., Seracino, R., Bobko, C.: Mechanical properties of kenaf fiber reinforced concrete. *Constr. Build. Mater.* (2011). <https://doi.org/10.1016/j.conbuildmat.2010.11.052>
18. Mostafa, M., Uddin, N.: Experimental analysis of compressed earth block (CEB) with banana fibers resisting flexural and compression forces. *Case Stud. Constr. Mater.* (2016). <https://doi.org/10.1016/j.cscm.2016.07.001>





# Characterization and Properties of Oil Palm Empty Fruit Bunch Reinforced Polyvinyl Alcohol Thin Films

Nurul Syazwani Othman<sup>1</sup>(✉), Ragunathan Santiago<sup>1</sup>,  
Wan Azani Mustafa<sup>2</sup>, Mustaffa Zainal<sup>1</sup>, Azlinda Abdul Ghani<sup>2</sup>,  
and Nurul Akmam Naaamandadin<sup>2</sup>

<sup>1</sup> School of Environmental Engineering, Universiti Malaysia Perlis,  
PusatJejawi 3, 02600 Arau, Perlis, Malaysia  
wanienuro191@yahoo.com

<sup>2</sup> Faculty of Engineering Technology, Universiti Malaysia Perlis,  
Kampus Sg. Chuchuh, 02100 Padang Besar, Perlis, Malaysia

**Abstract.** This paper focuses on the mechanical and morphological properties of oil palm empty fruit bunch (OPEFB) fibre reinforced in polyvinyl alcohol (PVOH). Samples were prepared via solution casting method with different loading of OPEFB fibre range from 5 wt% to 30 wt%. To improve the performance of thin films, tapioca starch (TS) was added into the formulation. From the result obtained, the tensile strength of PVOH/OPEFB thin films decreases as fibre loading increases. This might due to the weak interfacial adhesion between OPEFB fibre and PVOH matrix and also the tendency of fibres agglomeration to form the non-homogeneous compound. However, interestingly to observe that tapioca starch addition has increased the tensile strength and Young's modulus of the thin films. From scanning electron microscopy analysis, the presence of tapioca starch has enhanced the adhesion of PVOH matrix and OPEFB fibre.

**Keywords:** Polyvinyl alcohol · Oil palm empty fruit bunch · Solution casting · Tapioca starch · Thin films

## 1 Introduction

Generally, petrochemical-based polymers have been utilized mainly in packaging industries such as foods, cosmetics, chemicals, and pharmaceuticals. The widespread plastics uses have attracted worldwide due to their durability, stable and favorable in mechanical and thermal properties [1]. However, this rapid plastics material evolution has created genuine environmental issues since they cannot be degraded or decomposed easily in nature [2, 3]. Thus, many researchers from academic and industries have raised their concern to modify the current products become degradable in any mechanisms [4]. The use of natural fibers in polymer composites is important in terms to lessen the waste disposal issues. Natural fibres such as rice husk, flax, hemp, sugarcane bagasse, kenaf, banana skin [5], oil palm fibre [6] have been utilized as a filler in the fabrication of natural polymer composites. The huge loads of wastes can be converted into affordable value-added products which then allow them to be applied in

varied applications. Natural fibres are renewable sources, low in cost, completely or partially recyclable, and able to degrade [7].

Polyvinyl alcohol (PVOH) is a synthetic polymer that can naturally degrade and dissolve in water. It has good physical properties, better chemical barrier, water dissolvable and totally biodegrades [8]. It has been widely used in the packaging industry. The incorporation of OPEFB fibre in PVOH is preferable in order to produce eco-sustainable products. It is not only produced biodegradable materials but also can reduce the problem of biomass waste leftover at the oil palm plantation. There are some disadvantages using this natural fiber such as incompatibility with hydrophobic polymer matrices, low degradation temperature and high tendency towards agglomeration during processing. Therefore, tapioca starch is used to promote the adhesion properties between the OPEFB fibre and PVOH matrix. This research is to study the production of PVOH thin film reinforced OPEFB fibre with the addition of tapioca starch (TS) to enhance the thin film performance.

## 2 Methodology

### 2.1 Samples Preparation

Oil palm empty fruit bunch (OPEFB) was collected from United Oil Palm Industries Sdn. Bhd. at Nibong Tebal, Pulau Pinang. OPEFB fibre was dried in an oven with temperature 90 °C for 24 h to remove moisture content. Then, OPEFB fibre was ground and sieved into powder form with a particle size less than 150 µm. It was dried again to remove excessive moisture. Polyvinyl alcohol (PVOH) was obtained from Sigma-Aldrich Chemical with Mw 89,000 to 98,000 and 99% hydrolyzed. Tapioca starch was purchase from Thye Huat Chan Sdn Bhd. Table 1 shows the formulations of PVOH/OPEFB thin films.

**Table 1.** Formulation of PVOH/OPEFB and PVOH/OPEFB/TS thin films.

Materials	Amount ratio					
	100	95	90	85	80	70
PVOH	100	95	90	85	80	70
OPEFB*	0	5	10	15	20	30
TS**	5	5	5	5	5	5

\*Based on the weight percent of PVOH

\*\*weight, wt% of PVOH

### 2.2 Preparation of Thin Films

PVOH/OPEFB thin films were prepared by the solution casting method. Firstly, PVOH was dissolved in 100 ml of distilled water. Then, OPEFB fibre was added to the solution. The mixture continuously stirred for almost 60 min at 80 °C. For PVOH/EFB/TS thin film, tapioca starch was added and stirred for another 30 min without heating. Then, the solution was poured into the glass petri dish and dried in an

oven for 24 h at 50 °C. After the drying process, the thin films were peeled off and cut into dumbbell specimens by using Wallace die cutter model S6/1/6.A.

### 2.3 Mechanical and Morphological Tests

The mechanical properties of thin films were analyzed to identify the tensile strength, Young's modulus, and elongation at break. The test was conducted followed the ASTM D 882-00 using Instron Universal testing machine. The initial jaw separation distance was set to 50 mm and the crosshead speed of 20 mm/min. Five repetitions from each thin films formulation were evaluated.

The surface morphology of thin films was observed by using a scanning electron microscope (SEM). The cross-section of fracture thin films surface morphology was sputter-coated with a thin platinum layer using JFC-1600 auto fine coater to avoid electrostatic charging and poor image resolution during the examination.

## 3 Result and Discussion

### 3.1 Mechanical Properties

The tensile strength of PVOH/OPEFB and PVOH/OPEFB/TS thin films is presented in Fig. 1. The tensile strength decreased with increasing OPEFB fibre loading. Commonly, the presence of hydroxyl groups (-OH) groups in natural fibre make it compatible with PVOH matrix since fibre are hydrophilic in nature. However, due to the direct incorporation of OPEFB fibre, the chemical components on the fibre surfaces, such as lignin, amorphous cellulose, and impurities, might interrupt the interactions between cellulose crystallinity of OPEFB with PVOH matrix [9, 10]. Besides, filler-filler interaction becomes inevitable as more OPEFB fibre added. The same observation has been reported by previous researchers [11, 12], noticed that the reduction of tensile

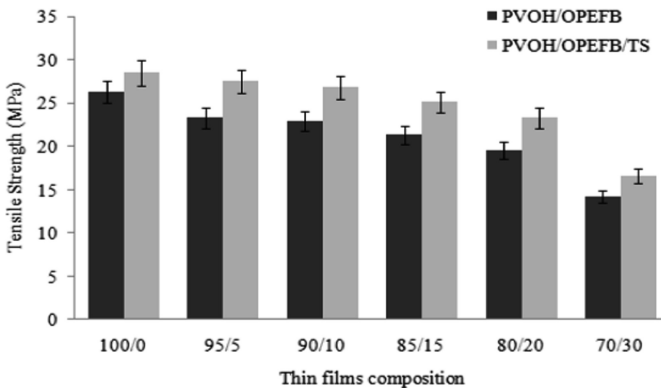


Fig. 1. Tensile strength of PVOH/OPEFB and PVOH/OPEFB/TS thin films

strength was due to the insufficient of the matrix to encapsulate the fibres and less ability to transfer stress to the fibres. Thus, OPEFB strands have a prominent tendency to agglomerate among themselves into bundles and consequently lower the contact area with the matrix.

With the addition of tapioca starch, the better tensile strength of PVOH/OPEFB thin film has resulted. Tapioca starch with PVOH eventually has an identical chemical in nature. PVOH has excellent compatibility with starch and thus, a good affinity could serve between them. The high tensile strength indicates that better interfacial adhesion could observe between OPEFB fibre and PVOH matrix with the addition of tapioca starch which also acts as cross-linking agents. According to Azmi et al. [13], good dispersion of starch can improve the tensile strength of the composite film.

Figure 2 shows the effect of the addition of tapioca starch on Young's modulus PVOH/OPEFB thin films with various OPEFB fibre contents. A further increase in Young's modulus was observed along with increasing OPEFB fibre content. It explained the stiffness of the thin films was increases as more OPEFB fibre added into the composites. Significant improvement in Young's modulus resulted with addition tapioca starch. This was due to the high modulus of starch which can increase the stiffness of thin films. The inherent chains stiffness and rigidity of starch resulted in the restriction of movement fibre in the PVOH matrices. Similar research has been reported previously by using different methods and matrices [14, 15].

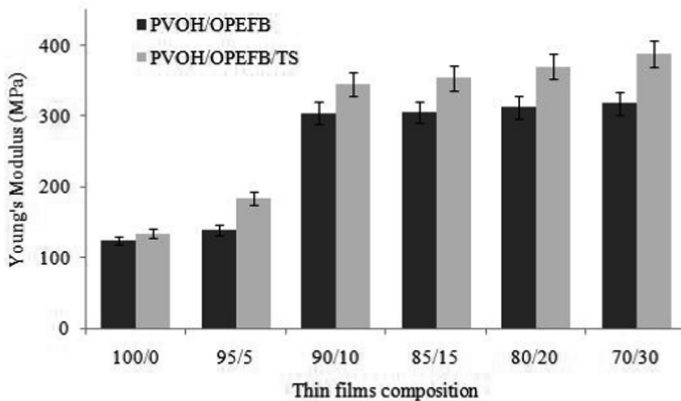
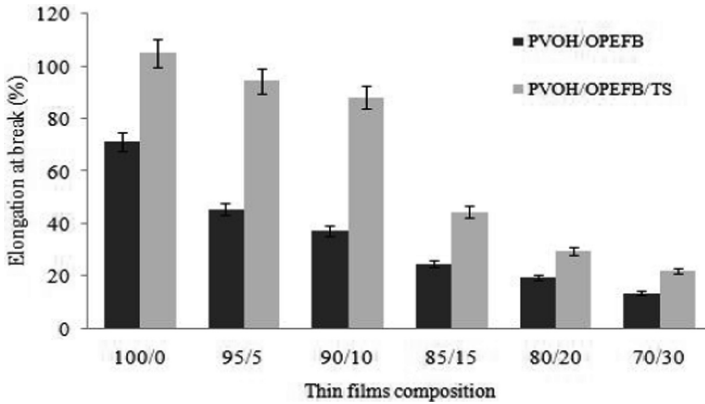


Fig. 2. Young's modulus of PVOH/OPEFB and PVOH/OPEFB/TS thin films

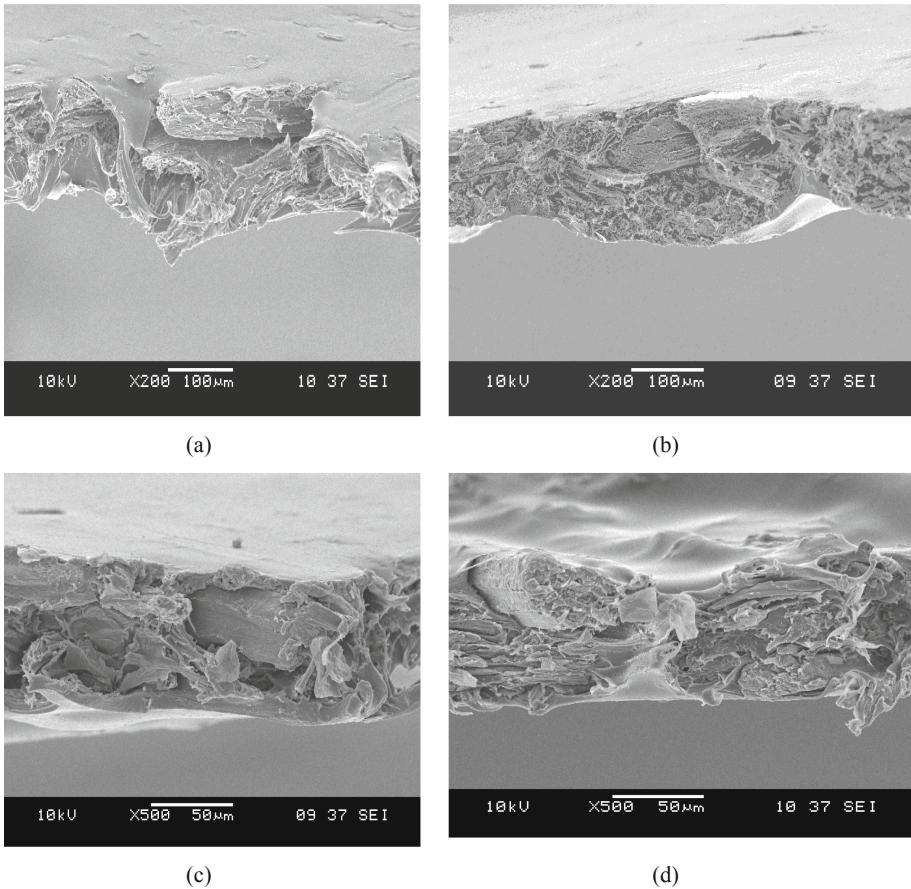
Figure 3 shows the elongation at break of both types of thin films. The percentage of elongation was continuously decreased as the amount of OPEFB fibre increased. However, elongation at break for PVOH/OPEFB/TS thin film has significantly higher compared to thin films without starch. This behavior was due to more intra and intermolecular interactions of hydrogen bonds between PVOH/OPEFB and tapioca starch. According to Behera et al. [16], the high percentage of filler in the composite thin film contribute to easily crack along with fibre end propagate. The trends are almost similar to the previous reports [15, 17].



**Fig. 3.** Elongation at break of PVOH/OPEFB and PVOH/OPEFB/TS thin films

### 3.2 Morphological Study

The fracture tensile surface of 5 wt% of fibre loading in PVOH/OPEFB thin film is shown in Fig. 4(a). Based on the observations, some holes and the detachable gap was observed at the PVOH surface. This indication showed the weak interfacial adhesion between PVOH matrix and OPEFB fibres. This might due to the insufficient wetting of OPEFB fibre with the matrix. Figure 4(b) shows the fracture tensile surface of 5 wt% of PVOH/OPEFB thin film with tapioca starch. The attachment of EFB fibre with PVOH matrix is better, showing that, an improvement of interfacial adhesion resulted with adhesion of tapioca starch. Figure 4(c) and (d) shows the micrographs with 30wt % of OPEFB fibre loading. It can be seen the composite thin films became more brittle due to the high rigidity. Besides, poor adhesion of OPEFB fibre with PVOH matrix was observed due to the non-homogeneous dispersion of fibres. Thin films with tapioca starch as shown in Fig. 4(d) shows hairy-like matrices which indicate the films surfaces resulted to be more ductile which lead to have higher elongation at break. With tapioca starch, the composite film has improved the adhesion of OPEFB fibre and PVOH matrix. Some previous research has supported the composites outcome [18].



**Fig. 4.** The tensile fracture surface of; (a) 95/5 PVOH/OPEFB thin film at magnification X200; (b) 95/5/5 PVOH/OPEFB/TS thin film at magnification X200; (c) 70/30 PVOH/OPEFB thin film at magnification X500 and; (d) 70/30/5 PVOH/OPEFB/TS thin film at magnification X500

## 4 Conclusion

Incorporation of tapioca starch has improved the tensile strength and Young's modulus of PVOH/OPEFB thin film. From the morphological study, better interfacial adhesion between PVOH and OPEFB has shown as a good encapsulation of OPEFB fibre in the presence of tapioca starch.

## References

1. Rivard, C., Moens, L., Roberts, K., et al.: Starch esters as biodegradable plastics: effects of ester group chain length and degree of substitution on anaerobic biodegradation. *Enzyme Microb. Technol.* **17**, 848–852 (1995)

2. Shah, A.A., Hasan, F., Hameed, A., Ahmed, S.: Biological degradation of plastics: a comprehensive review biological degradation of plastics: a comprehensive review. *Biotechnol. Adv.* **26**, 246–265 (2008). <https://doi.org/10.1016/j.biotechadv.2007.12.005>
3. Mustafa, W.A., Saidi, S.A., Zainal, M., Santiago, R.: Experimental study of composites material based on thermal analysis. *J. Adv. Res. Fluid Mech. Therm. Sci.* **43**, 37–44 (2018)
4. Kawai, F.: Breakdown of plastics and polymers by microorganisms. In: *Advances in Biochemical Engineering/Biotechnology*, pp. 151–194. Springer, Berlin, Heidelberg (1995)
5. Ghani, A.A., Mustafa, W.A., Hafizi, M.N.K.R., et al.: Material treatment of polypropylene/recycle acrylonitrile butadiene rubber/banana skin powder using thermal mixing technique. *J. Adv. Res. Fluid Mech. Therm. Sci.* **52**, 1–11 (2018)
6. Othman, N.S., Santiago, R., Mustaffa, Z., et al.: Studies on water absorption of polypropylene/recycled acrylonitrile butadiene rubber/empty fruit bunch composites. *IOP Conf. Ser. Mater. Sci. Eng.* **429**, 012091 (2018). <https://doi.org/10.1088/1757-899X/429/1/012091>
7. Sanjay, M.R., Arpitha, G.R., Naik, L.L., et al.: Applications of natural fibers and its composites: an overview. *Nat. Resour.* **07**, 108–114 (2016). <https://doi.org/10.4236/nr.2016.73011>
8. Ateva, P., Levapren, L.: Polyvinyls and acrylics. In: *Film Properties of Plastics and Elastomers*, pp. 219–254 (2012)
9. Tan, B.K., Ching, Y.C., Poh, S.C., Abdullah, L.C.: A review of natural fiber reinforced poly (vinyl alcohol) based composites: application and opportunity. *Polymers* **7**, 2205–2222 (2015). <https://doi.org/10.3390/polym7111509>
10. Panaitescu, D.M., Frone, A.N., Ghiurea, M., et al.: Properties of polymer composites with cellulose microfibrils. In: *Advances in Composite Materials: Ecodesign and Analysis*, pp. 103–124. In Tech (2010)
11. Othman, N.S., Santiago, R., Zainal, M., et al.: Tensile and morphological studies of polypropylene/empty fruit bunch composite: effect of maleic anhydride-grafted polypropylene. In: *Material Science and Engineering* (2018)
12. Zainal, M., Aihsan, M.Z., Mustafa, W.A., Santiago, R.: Experimental study on thermal and tensile properties on polypropylene maleic Akademia Baru experimental study on thermal and tensile properties on polypropylene maleic anhydride as a compatibilizer in polypropylene/sugarcane bagasse composite. *J. Adv. Res. Fluid Mech. Therm. Sci.* **43**, 141–148 (2018)
13. Azmi, N., Bakar, A.A., Samsudin, S.A., Aziz, N.A.A.: Preparation and characterization of tapioca starch filled polycaprolactone composite films. *Malays. J. Anal. Sci.* **18**, 612–617 (2014)
14. Yavuz, H., Babaç, C.: Preparation and biodegradation of starch/polycaprolactone films. *J. Polym. Environ.* **11**, 107–108 (2003)
15. Chee, C.Y., Rahman, A., Sukiman, N.L., Chuah, C.H.: Preparation and characterization of polyvinyl alcohol-based composite reinforced with nanocellulose and nanosilica. *BioResources* **10**, 3364–3377 (2015). <https://doi.org/10.15376/biores.10.2.3364-3377>
16. Behera, A.K., Avancha, S., Basak, R.K., et al.: Fabrication and characterizations of biodegradable jute reinforced soy based green composites. *Carbohydr. Polym.* **88**, 329–335 (2012)
17. Nuradibah, M.A., Yusoff, N.A., Sam, S.T.: Effect of adipic acid as crosslinking agent in polyvinyl alcohol/nanocellulose from rice straw biocomposites. *JERE* **10**, 79–84 (2018)
18. Kim, E.G., Kim, B.S., Kim, D.S.: Physical properties and morphology of polycaprolactone/starch/pine-leaf composites. *J. Appl. Polym. Sci.* **103**, 928–934 (2007). <https://doi.org/10.1002/app>





# Mechanical Properties of the Utilisation Glass Powder as Partial Replacement of Cement in Concrete

Nurul Akmam Naaamandadin<sup>1</sup>(✉), Izzad Shafiq Abdul Aziz<sup>1</sup>,  
Wan Azani Mustafa<sup>1</sup>, and Ragunathan Santiago<sup>2</sup>

<sup>1</sup> Faculty of Engineering Technology, Universiti Malaysia Perlis, Kampus Sg. Chuchuh, 02100 Padang Besar, Perlis, Malaysia  
nurulakmam@unimap.edu.my

<sup>2</sup> School of Environmental Engineering, Universiti Malaysia Perlis, Pusat Jejawi 3, 02600 Arau, Perlis, Malaysia

**Abstract.** Waste glass as a partial replacement of the cement can contribute to the sustainable development, environmentally friendly, energy-efficiency and economical in the construction industry. Thus, this paper will discuss the effect of glass powder when partially replaced the cement as 4%, 8%, and 12%. They have been tested for its compressive strength and split tensile up to 28 days of curing. It was expected to undergo pozzolanic reactions with cement hydrates, forming secondary Calcium Silicate Hydrate (C–S–H) once waste glass was milled down to the micro size particles. The results showed that the compressive strength of 4% replacement of glass powder concrete is 40.8 MPa at 28 days of testing which can be classified achieving the objective because higher than conventional concrete. The results indicate that the concrete with waste glass powder was able to increase the workability of concrete and also the compressive strength.

**Keywords:** Glass powder · Partial replacement of cement · Mechanical properties

## 1 Introduction

The utilisation of waste materials or mechanical by-items as a partial replacement for mixture in concrete is a feasible technique for lessening the utilisation of Ordinary Portland Cement (OPC), and therefore diminishing the natural and vitality effects of concrete creation. Waste glass powder used in concrete as a partial replacement of cement could be an important step toward the development of sustainable environmentally friendly, energy-efficient and economical infrastructure systems [1]. The waste glass powder offers sought concoction structure and reactivity for use as a supplementary cement material which can be a beneficial point to the substance of solidness, dampness resistance and sturdiness of cement.

Replaced with waste glass powder provides compressive strengths exceeding those of control concrete [2]. At that point, utilization of waste glass powder in concrete will



produce a valuable outcome and has a huge possibility to raise the concrete strength when lowering the utilization of Portland cement.

The glass powder could bring about the alkali-silica reaction (ASR) in cement, yet the glass powder could stifle their ASR propensity, an impact like supplementary cementitious materials (SCMs) [3]. A glass was idle that might be reused without changing its invention property. The properties influence the pozzolanic behavior of waste glass and most pozzolans in concrete, are fineness, chemical composition, and the pore solution present for a reaction. The basic conduct of concrete depends on blending extents and material properties of the composite framework and these components do not change in the wake of solidifying [4]. Exact concrete blend configuration may change the properties of cement yet by including distinctive materials as one of the components of the impact of the concrete properties.

## 2 Experimental Procedure

### 2.1 Raw Material

The process was started by obtaining waste glasses from the waste disposal area. Waste glasses collected were in the range of small to medium-sized. Large size would be complicated to destruct. After that, the glasses went through the cleaning and drying process. This process was to make them easy to be crushed and the glass powder would not be mixed with other agents. Through the wrecking process, the glasses were impinged by using the impact testing machine. Rate lacing performed was 5 times. Then, the outcome of the impingement of the glasses went through the sieving process by using the sieve shaker. The sieve sizes used were in the range of 0.003–0.060 mm.

### 2.2 Mix Design and Process

The mixture proportion of fresh concrete and waste materials produced in the laboratory is shown in Tables 1 and 2. A total of 36 samples concrete mixtures were produced, divided into different sizes of moulds such as cube concrete and cylinder concrete. The types of the mixture produced, which were the addition of samples concrete, thus the waste materials were added by volume in concrete. The ranging of glass powder was from 4% to 12%. The fine aggregate (sand), and coarse aggregate were used in this research as well.

**Table 1.** Mix proportion of cube concrete

	w/c ratio %	Glass powder (kg)	Cement (kg)	Fine aggregate (kg)	Coarse aggregate (kg)	Water (kg)
NC	0.5	0	1.410	2.730	2.325	0.710
GC4%	0.5	0.057	1.353	2.730	2.325	0.710
GC8%	0.5	0.114	1.296	2.730	2.325	0.710
GC12%	0.5	0.168	1.242	2.730	2.325	0.710

**Table 2.** Mix proportion of cylinder concrete

	w/c ratio %	Glass powder (kg)	Cement (kg)	Fine aggregate (kg)	Coarse aggregate (kg)	Water (kg)
NC	0.5	0	2.820	5.460	4.650	1.410
GC4%	0.5	0.113	2.707	5.460	4.650	1.410
GC8%	0.5	0.226	2.594	5.460	4.650	1.410
GC12%	0.5	0.338	2.482	5.460	4.650	1.410

During the concrete mixing process; the moulds should be laminated with a thin layer of oil before they could be used in order to prohibit adherence of concrete. The fine aggregate, cement, water and glass powder were added when mixer running. The concrete was placed in the moulds by using a concrete scoop and shovel. Mix the concrete in the mixing pan with a shovel or trowel to avoid segregation when moulding of the sample. Concrete scoop or blunted trowel were used to tap around the top surface edge of the mould in order to assure symmetrical conveyance of the concrete and to diminish coarse aggregate segregation inside the mould. The method of making and placing concrete must meet the ASTM C192 [5].

The implicate air was issued with compaction method by using vibration strategies. Therefore, concrete must be compacted properly in the cube mould until the entrapped air was less than 2%. If the compaction was not done properly, the entrapped air remained within the concrete mass. As a result, in every 1% entrapped air there would be around 5% to 6% drop in strength [6]. Concrete was poured into the mould layer by layer approximately in balanced volume. Each layer was compacted either using hand or by vibrator. The compaction by hand was using the tamping steel bar of 16 mm diameter, 60 cm long and bullet-pointed at the lower end specified in [5]. While compacting by hand, the number of strokes for each layer should be at least 20. The stroke should be infiltrated in the gap space in each layer of the concrete. After the last layer has compacted, the surface of the concrete must be leveled using a trowel and covered with a metal plate to avert vanishing of the concrete.

### 2.3 Testing and Analysing

The standard slump test was used according to ASTM C143 [7]. The compressive strength of cube concrete shapes would give the data of the concrete potential strength mixture from which it was tested. The compressive strength of concrete was carried out according to ASTM C109 [8]. If the concrete feeble in strain, even a little unconvencionality of load, it will actuate consolidated bending and axial force condition. As a result, the concrete will turn up to failure at the apparent tensile stress other than the rigidity. Therefore, in designing these structures, tensile strength is a major element and crucial than compressive strength. Consequently, in this study, the test was conducted according to ASTM C496 [9], in which, samples had undergone the curing process for 28 days.

### 3 Results and Discussion

#### 3.1 Test of Glass Powder Concrete

The slumps of glass powder concrete are shown in Table 3. The value of normal concrete was stated 60 mm. The range of the designated slumps was 60–180 mm. All the mixed proportion achieved low workability. This result occurred caused by the glass powder added. It was clearly provided with the absorption water in concrete. Thus, the workability of all the glass concrete (GC) was compatible to be used as the sampling due to low of workability. Despite the fact, it was not very low in which it hard to handle (Fig. 1).

**Table 3.** Slump test result of cube concrete and cylinder concrete

Type of mixtures	w/c ratio %	Slump test (mm)	Type of slump	Percentage of reduction (%)
NC	0.5	60	True	100
GC4%	0.5	25	True	36
GC8%	0.5	30	True	49
GC12%	0.5	38	True	54



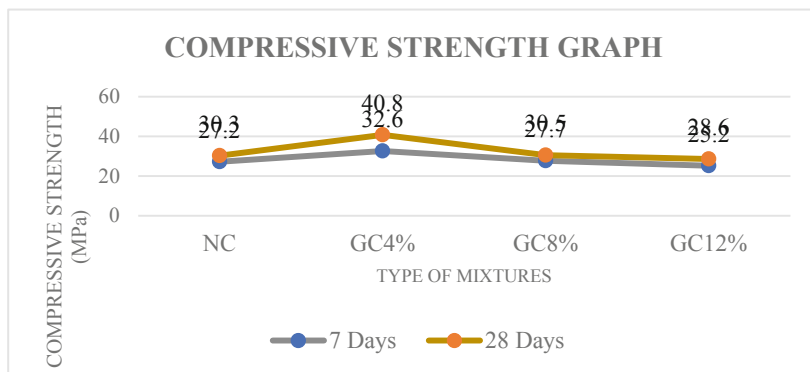
**Fig. 1.** Slump result (1) NC, (2) GC4%, (3) GC8% and (4) GC12%

#### 3.2 Compressive Strength of Glass Powder Concrete

The compressive strength of the cubes was evaluated by non-destructive testing methods. The result of compressive strength tested at 7 and 28 days are presented in Table 4. However, the trend of all compressive result clearly shown the tendency of the small decrease in the strength in the concretes containing higher utilisation of the glass powder as shown in Fig. 2 at 7 and 28 days. The data for normal concrete at 7 days of compressive strength which is 27.2 MPa where 72.8% of strength reduction which is acceptable in term of 7 days of curing. Then, the value of 28 days of normal concrete indicates an increasing value which is 30.3 MPa if compared with 7 days concrete result of the required value is 27.2 MPa. Thus, the strength of normal concrete has increase directly proportional to 7 and 28 days. According to Sharifi Y., Houshiar M. and Aghebati B. (2013) [10], normally, the concrete strength was increased because of

**Table 4.** Result of compressive strength

Type of mixtures	Compressive strength (N/mm <sup>2</sup> )		
	7 days (MPa)	28 days (MPa)	Percentage of reduction 28 days (%)
NC	27.2	30.3	100
GC4%	32.6	40.8	134
GC8%	27.7	30.5	101
GC12%	25.2	28.6	95

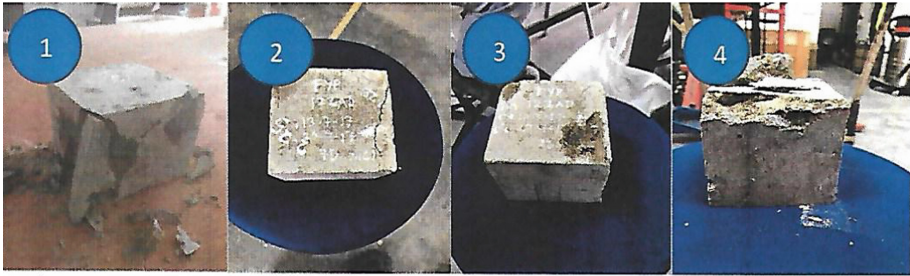


**Fig. 2.** Compressive strength graph of concrete

the maturity at the curing periods. In the arrangement of concrete, the cement deed as a glue which binds together the aggregates to attain the final cast product. The test was conduct based on ASTM C109 for this study [8].

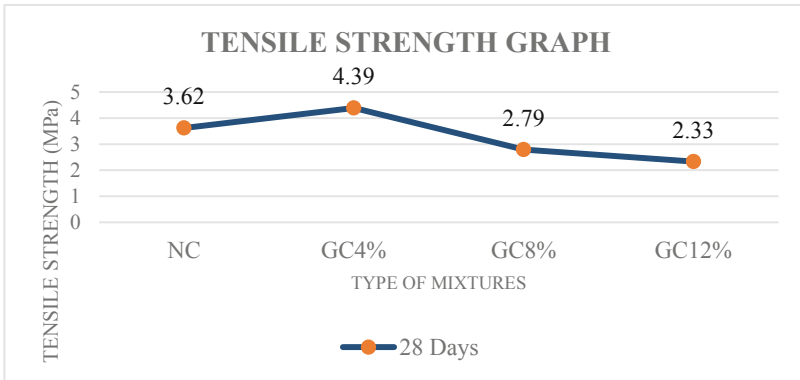
Refer to Fig. 2, it is shown that, 4% of utilisation of glass powder is more effective compared to 8% and 12% of glass powder used. This may cause to the lower content of Portland cement at higher glass powder replacement level [11]. This shows that using 8% of glass powder can achieve maximum compressive strength that can be retained by the normal concrete. As a result, this shows that glass powder has an influence on the strength of concrete. It proves that these phases include evaluation of the pozzolanic effect of glass powder itself where the second phase involves studying the properties of glass powder blended cement [11]. The pozzolanic response is the chemical responses that happen in Portland concrete within a mixture of glass powder to increase the strength properties of concrete upon the expansion of pozzolans. This is shown GC4% sample has a high wide spectrum of mechanical properties and durability properties to stick close to the design specification of the construction.

Figure 3 explained the types of fracture of cubes samples after tested, the samples produce various types of fracture. The NC, GC8%, and GC12%, showing a semi-explosive failure of fracture, while GC4% shows non-explosive failure. This proved that GC4% has high durability properties compared than the other sample. This is indicating that excessive usage of glass powder may increase the pace of water



**Fig. 3.** Fracture Cube (1) NC, (2) GC4%, (3) GC8% and (4) GC12%

absorption in concrete. This excess water also greatly lower the concrete strength. Based on the high rate of water absorption from the glass powder it can lead to shrinkage of the concrete (Fig. 4).



**Fig. 4.** Tensile strength graph of concrete

Drying shrinkage of ordinary strength/performance concrete is mainly due to the moisture loss to the atmosphere. Thus, resulting in drying shrinkage stress development in concrete structures when it is internally or externally restrained [12]. Shrinkage is a major caused to lower the strength of concrete and happened to cause the concrete less durable. As a result, concrete solidifies and dries it shrinks. It was acknowledged not only caused thermal stress but also drying shrinkage stress affects the cracking potential of cast-in-place concrete structures at early ages [12].

### 3.3 Split Tensile Strength Test of Glass Powder Concrete

Based on Table 5, GC4% has the highest reading of tensile strength of concrete with 4.39 MPa compared to normal concrete which has 3.62 MPa and other mixture concrete sample. This shown that GC8% and GC12% concrete is very weak in tension.

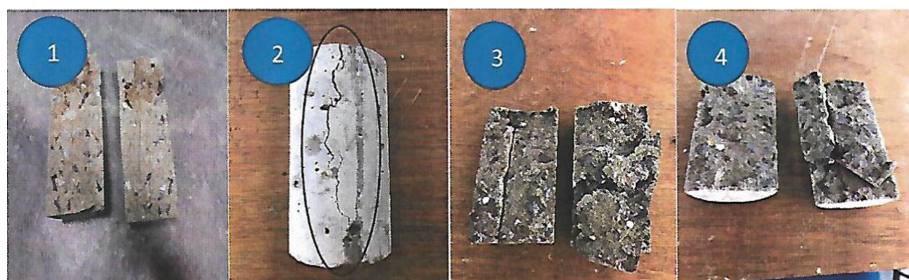
**Table 5.** Result of tensile strength

Type of mixtures	Tensile strength (N/mm <sup>2</sup> )	
	28 days (MPa)	Percentage of reduction 28 days (%)
NC	3.62	100
GC4%	4.39	121
GC8%	2.79	77
GC12%	2.33	64

The sample not expected can resist the direct tension that applied. It is proved that utilisation of 4% and 12% of glass powder is not effective because they cannot achieve the maximum tensile of the normal concrete. It is due to the sample brittle nature which is preventing the sample to resist an applied tensile force. With 2.79 MPa and 2.33 MPa, sample GC8% and GC12% still have lower tensile strength compared to normal concrete so that not effectively to be used regarding the same grade of concrete which is grade-30.

As refer to Vishaliny et al. [4], they have used 10% augmentation of glass powder utilisation with concrete G30 but they used 28 and 60 days of curing. In every samples case, when the percentage of glass powder increased, the crack form quickly in areas affected by load. The shrinkage condition against concrete and affects the strength of materials. This reduction is related to the variations of the water content of the mortar, which leads to the development of tensile stresses at the concrete [13]. Aggregates confine free shrinkage of the mix and crack are created in their proximity.

As shown in Fig. 5, GC4% concrete just having a little crack at the concrete compared to the other sample. The higher constraint on strength, growth and the high water content in GC8% and GC12% sample with more porous aggregates likely to be the major sense of this tendency. Normal concrete, GC8%, and GC12% show that they were receiving more shrinkage that lowering the tensile strength properties of the sample to overcome the shear stress that been receive to the concrete. At this point, the sample cannot prevent the semi-explosive failure of the concrete. In point of this, if the stiffness of concrete is low, the greater the elastic compatibility between aggregates and mortar, which reduces stress concentration and the advancement of micro-cracking.

**Fig. 5.** Fracture Cylinder (1) NC, (2) GC4%, (3) GC8% and (4) GC12%

## 4 Conclusion

All the objectives of this study were obtained which is the concrete that utilises waste glass powder has a very high compressive and tensile strength of normal concrete. The result that attains from the slump test of waste glass powder seems have increased the strength properties of the concrete. In term of strength, concrete that utilizes waste glass powder abundantly have higher strength when using 4% of glass powder as replacement of the cement in concrete and provide a high value of the grade 30 compared to normal concrete with the same grade. According to Panchangam [14], the density of glass powder concrete is less compared to that of normal concrete. Therefore, glass powder concrete can be used as lightweight concrete. Concrete noticeably lighter when mix with waste glass powder. Furthermore, environmental effects can be minimised and the use of cement can be minimized through this research. In concrete research have shown that it is conceivable to facilitate these two developments, in the way of limiting the requirement for the huge demand of cement production capacity and generate adjustment of practical improvement on a worldwide scale.

## 5 Recommendation

The present research provides the effectiveness of concrete that utilising waste glass powder. Suggestions for further research from this study to be enhanced, to be developed and to be inspected are:

1. Adding a chemical activator in the mix of glass powder concrete, determine the similarity of concrete compressive strength or better.
2. Making specimens of concrete, which utilising a diverse degrees of waste glass powder in the production of concrete.
3. Deciding the reasonable level of utilisation of glass powder to accomplish the ideal compressive strength
4. Determining the effectiveness of concrete that utilising waste glass powder in construction the building structures.

## References

1. Vasudevan, G., Ganis, S., Pillay, K.: Performance of using waste glass powder in concrete as replacement of cement. *Am. J. Eng. Res.* **2**, 2320–2847 (2013)
2. Islam, G.M.S., Rahman, M.H., Kazi, N.: Waste glass powder as partial replacement of cement for sustainable concrete practice. *Int. J. Sustain. Built Environ.* (2017). <https://doi.org/10.1016/j.ijsbe.2016.10.005>
3. Shinde, R.: Utilization of glass powder and fly ash in concrete production. *Int. J. Sci. Res. Dev.* **2**, 1063–1066 (2014)
4. Vishaliny, H., Govindarajulu, D., Vijayakumar, G., et al.: Studies on glass powder as partial replacement of cement in concrete production. *Int. J. Emerg. Technol. Adv. Eng.* **3**, 153–157 (2013)



5. ASTM: ASTM C192/C192M-02 Standard Practice for Making and Curing Concrete Test Specimens in the Laboratory. ASTM International (2002). <https://doi.org/10.1520/C0192>
6. Malu, S.S.: Compression test on concrete. *Civ. Eng.* **1** (2013)
7. ASTM: Standard Test Method for Slump of Hydraulic-Cement Concrete (2015)
8. ASTM: Standard Test Method for Compressive Strength of Hydraulic Cement Mortars (Using 2-in or [50-mm] Cube Specimens) (2012)
9. ASTM C496/C496M-17: Standard Test Method for Splitting Tensile Strength of Cylindrical Concrete Specimens ASTM C-496. ASTM International (2011). [https://doi.org/10.1520/C0496\\_C0496M-11](https://doi.org/10.1520/C0496_C0496M-11)
10. Sharifi, Y., Houshiar, M., Aghebati, B.: Recycled glass replacement as fine aggregate in self-compacting concrete. *Front. Struct. Civ. Eng.* (2013). <https://doi.org/10.1007/s11709-013-0224-8>
11. Aliabdo, A.A., Abd Elmoaty, A.E.M., Aboshama, A.Y.: Utilization of waste glass powder in the production of cement and concrete. *Constr. Build. Mater.* (2016). <https://doi.org/10.1016/j.conbuildmat.2016.08.016>
12. Choi, S.: Experimental characterization of age-dependency of shrinkage coefficient of hardening concrete. *KSCE J. Civ. Eng.* (2016). <https://doi.org/10.1007/s12205-015-0460-7>
13. Bogas, J.A., Nogueira, R.: Tensile strength of structural expanded clay lightweight concrete subjected to different curing conditions. *KSCE J. Civ. Eng.* (2014). <https://doi.org/10.1007/s12205-014-0061-x>
14. Chandrakala, K., Srichandana, D.P.: Experimental study on effects of glass powder in concrete. *Int. J. Mag. Eng. Technol. Manag. Res.* **2**, 383–387 (2015)





# Optimization on Surface Roughness of Fused Deposition Modelling (FDM) 3D Printed Parts Using Taguchi Approach

Mohd Nazri Ahmad<sup>(✉)</sup>, Mohd Hidayat Ab Rahman,  
Nurul Ain Maidin, Mohd Hairizal Osman, Mohammad Khalid Wahid,  
Hussin Mohamed Saiful Firdaus, and Nur Afifah Abd Aziz

Faculty of Mechanical and Manufacturing Engineering Technology,  
Universiti Teknikal Malaysia Melaka, Hang Tuah Jaya,  
76100 Durian Tunggal, Malacca, Malaysia  
mohdnazri.ahmad@utem.edu.my

**Abstract.** Taguchi Method is an effective tool introduced for the optimization of the product or process quality. In order to achieve the optimum performance of the 3D printed parts, the Taguchi method was employed because it is a simplified yet powerful method for experimental design using the orthogonal array method. In this research, an orthogonal array of  $L_9 (3^4)$  was used to determine four parameters with three levels each. The samples with ASTM D638 type IV standard ware fabricated by 3D Printer type FDM. The results were obtained and data was analysed. Thus, the result shows the optimum parameters are print pattern (cross), orientation on Y-axis ( $0^\circ$ ), support angle ( $0^\circ$ ) and side walk (0.15 mm). The study demonstrates that the better surface roughness (Ra) of printed parts by Fused Deposition Modelling (FDM) machine that can be optimized by using Taguchi method and the outcomes of this study might be used as reference for other researchers.

**Keywords:** Taguchi method · FDM · Orthogonal array · Surface roughness · Additive manufacturing

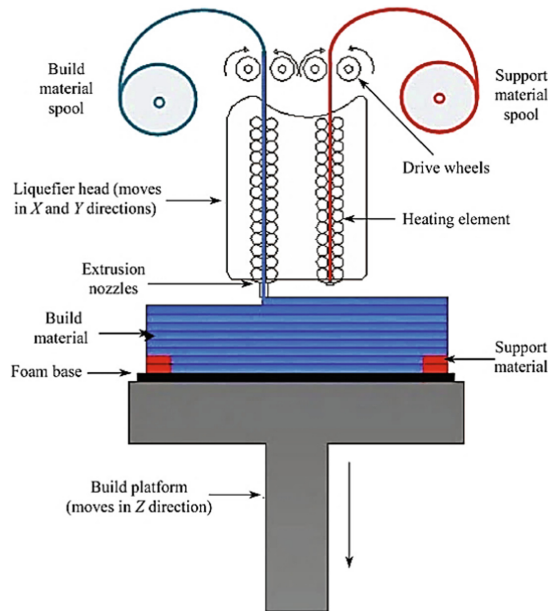
## 1 Introduction

Rapid prototyping (RP) is basically an additive manufacturing process used to rapidly fabricate a model of a part using 3D CAD data. In spite of the fact that RP technology has demonstrated its potency in industries, some possible materials are not good to RP technologies. It can be solved by either improving the materials or altering the procedure parameters amid manufacture stage to show signs of improved mechanical properties. Consequently, it is compulsory to upgrade the task parameters to improve the exactness, quality, and properties of the part that delivered from RP system [1]. Additive manufacturing technology is broadly utilized as a part of building for redid items, utilitarian models and reasonable models. Additive manufacturing process offers an effective strategy of building difficult geometry to reduce the pattern and creation process duration at least cost because of the nonattendance of any tooling needs [2].

Furthermore, Kumar et al. [3] states rapid prototyping (RP) is a manufacturing technology that creates 3D physical models specifically from 2D CAD data utilizing a layered assembling (LM) process that stacks and bonds thin layers in a single heading. Ever since the stereolithography exists, the concept has been experimented and numerous new process are introduced, patented and commercialized which some have been dropping out and disappeared [4]. Fusion Deposition Manufacturing (FDM) technology is perfect for manufacturing useful models, models or part of from thermoplastic materials, with great mechanical, thermal and chemical resistance.

Fused Deposition Modelling (FDM) uses a thermoplastic filament which is heated to its melting point and then extruded layer by layer to fabricate a three dimensional parts.

In another study, FDM was broadly used as part of additive manufacturing technology that gives utilitarian models in different thermoplastics because of its capacity to deliver complex geometrical parts accurately and securely in an office-accommodating condition. As shown in Fig. 1, in this procedure, the material is melted into fluid state in a liquefier head and after that specifically saved through a nozzle that follows the parts cross sectional geometry to construct 3D sections straightforwardly from a CAD shown in a layer by layer way [5].



**Fig. 1.** Principle of FDM process [5]

The surface finish based on various process parameters of the FDM machine. With appropriate modification of the build parameters, quality can be essentially enhanced without bringing extra costs. Bual [6] established the FDM method gives some impact of slice layer and backing structure thickness on the surface roughness of

part. Estimation of finished was done on both side of the example in perpendicular to the direction of a build layer. Besides, the part surface nearby the best layer of the help has a smoother structure when compared with alternate surfaces. Surface roughness is smoothness of the surface measurement of a product and it is a factor that impacts the manufacturing cost. The surface finish also affects the life of any product [7].

A Taguchi method is a descriptive analysis that appoints a product or process so works all the more reliably in the working condition. Taguchi strategy is received for improving procedure factors, as it is straightforward and simple. The strategy is prevalently known as the factorial outline of tests. This strategy utilizes an exceptional arrangement of exhibits called orthogonal arrays. The orthogonal arrays technique lies in picking the level mixes of the information plan factors for each trial [8]. Ahmad et al. [9] reports the better dimensional accuracy of vacuum casting process can be optimized by implementing Taguchi method. The Orthogonal Array gives much decreased ‘deviation’ to explore different avenues regarding ‘ideal setting’ of control parameters. By utilizing Minitab17 programming, we can execute a Taguchi Design [10]. The key process in Taguchi method is to optimize the process parameter to accomplish best quality. On the off chance that the quantity of process parameter increments, there are many analyses must be done to get the optimized parameter. To make it simple, Taguchi method utilizes the outline of orthogonal arrays (OA) to contemplate the procedure parameter with the modest number of tests. An ideal combination of parameters that causes minimal defects can be discovered using Taguchi’s orthogonal array and ANOVA strategy [11].

The experimental observations are future transformed into signal-to-noise (S/N) ratios. Signal-to-noise (S/N) ratio was used by Taguchi as the quality characteristics of choice and here are several S/N ratios available depending on the type of performance characteristics [12]. The S/N ratio can be characterized into three categories when the characteristics are continuous as in Eq. (1), (2) and (3):

Nominal is the best characteristic:

$$\frac{S}{N} = -10\log \bar{y}s_y^2 \quad (1)$$

Smaller the better characteristics:

$$\frac{S}{N} = -10\log 1n \sum y^2 \quad (2)$$

Larger the better characteristics:

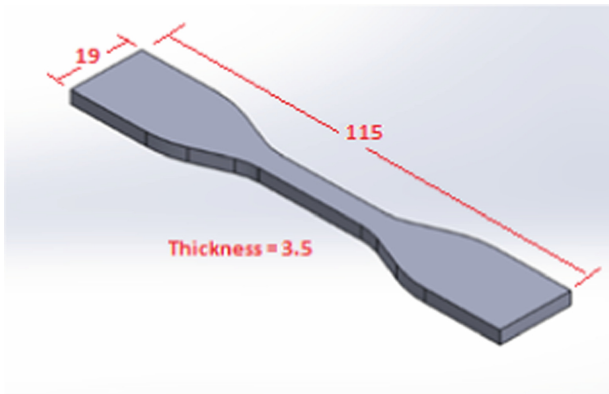
$$\frac{S}{N} = -10\log 1n \sum 1y^2 \quad (3)$$

where ‘ $\bar{y}$ ’ is the average observed data, ‘ $s_y^2$ ’ the variance of ‘ $y$ ’, ‘ $n$ ’ the number of observations, and ‘ $y$ ’ the observed data. For each type of characteristics, with the above S/N ratio transformation, the higher the S/N ratio the better is the result [13].

Taguchi parameter design requires the identification of factors affecting targeted quality characteristics, relevant literature must be reviewed to screen the most important among a number of factors or conditions affecting surface roughness of milled surface. As a multi-point machining process, more potential variability makes it even harder to obtain a surface roughness model in milling operations compared with single point machining [14]. An orthogonal array of  $L_9(3^4)$  was used; ANOVA analyses were carried out to identify the significant factors affecting surface roughness, and the optimal cutting combination was determined by seeking the best surface roughness (response) and signal-to-noise ratio. Finally, confirmation tests verified that the Taguchi design was successful in optimizing milling parameters for surface roughness [15].

## 2 Research Methodology

The ASTM D638 type IV standard is selected as specimen for experiment. The reason for selecting ASTM D638 because it is suitable for the application of plastic material which is in line with this study that used ABS plastic as printed part. The SolidWorks software is used to draw the specimen for the experiments. The overall dimensions of the dog bone specimen are 19 mm width, 115 mm height and 3.5 mm thickness as shown in Fig. 2.



**Fig. 2.** CAD model of specimen (ASTM D638 type IV)

### 2.1 Selection of Parameter to Study

In general, the parameters of FDM machine are layer thickness, air gap, raster width, contour width, raster orientation and etc. These parameters are based on the type of 3D printed part of FDM machine used and in this project, CubePro machine are selected which means there are several process parameters in that machine. Focusing on optimizing process parameter for testing mechanical properties of surface roughness, there are four factor parameters selected to run the experiment. The types process parameters are print pattern, orientation (Y axis), support angle and sidewalk offset. There are two

fix parameters that are layer resolution is 200  $\mu\text{m}$  and print strength will be stronger. Layer resolution in 3D printing is a measurement of the layer height of each addition of material in the additive manufacturing or 3D printing process in which layers are compiled. It is one of the basic technical characteristics of each 3D printer, the layer height is basically the vertical resolution of the z-axis. Support angle point out to the angle of the raster pattern with respect to the X axis on the below part layer. The sidewalk offset is to set the offset distance between the part and the sidewalk. Then, the orientation and support angle is the position place the sample in  $0^\circ$ ,  $45^\circ$  and  $90^\circ$  position and the maximum angle to be supported.

The print pattern shows the inner structure of a design which have three pattern is cross, diamond and honeycomb. The pattern cross is faster in printing fill pattern meanwhile the diamond and honeycomb is strong print pattern but diamond with three directions cross bracing same with cross pattern and honeycomb with 3 directions cross bracing. Besides that, print strength is the strength of inner structure model that have four type that are hollow, strong, almost solid and solid. In this experiment, print strength are fix which selected is strong. As shown in Table 1 four parameters visualizing print pattern, orientation (Y axis), support angle and side walk layer considered as input parameters and based on literature survey. The studies of the ranges available in numbers of levels and their values are shown in Table 1.

**Table 1.** Parameters level and values

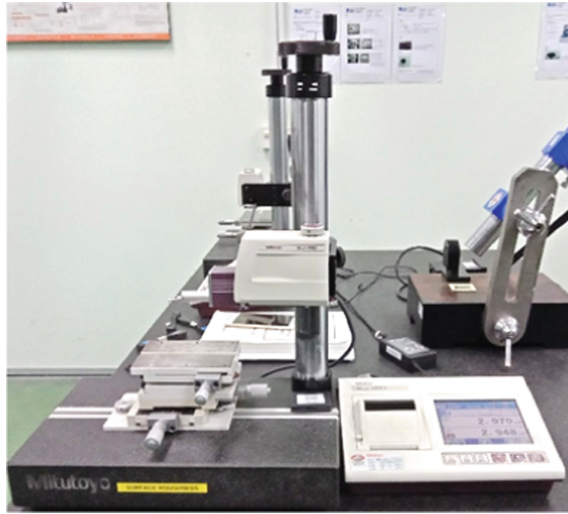
Factor	Level		
	I	II	III
Print pattern	Cross	Diamond	Honeycomb
Orientation (Y axis) ( $^\circ$ )	0	45	90
Support angle ( $^\circ$ )	0	45	90
Sidewalk offset (mm)	0.15	0.25	0.40

## 2.2 Surface Roughness Testing

Surface roughness test is a measurement of vertical deviation on the surface of a specimen in its ideal form. It also depends on the size of deviations on which the surface will either be rough or smooth. The surface roughness also known as surface profile ( $R_a$ ) which is expressed as a single numeric parameter and most commonly used from the other parameter. Other materials will interact differently on a rough surface due to the coefficient of friction. The surface roughness test will show the effect of combination process parameter based on Taguchi Method. Figure 3 shows the surface roughness tester Mitutoyo SJ-410 used in this study to measure roughness.

## 2.3 Experimental Setup

Taguchi Method is an effective tool introduced for the optimization of the product or process quality. In order to achieve the optimum performance of the produced part, the Taguchi method is a powerful method for experimental design using the orthogonal



**Fig. 3.** Surface roughness tester Mitutoyo SJ-410

array method. In this project, the number of experiment for orthogonal array L9 ( $3^4$ ) was chosen and nine pieces of samples specimen were determined for four parameters in each three levels. Number of runs are determined by referring number of level and parameter. Equation (4) is used to calculate the number of runs.

$$\text{Number of runs} = 1 + \text{NU}(\text{L}-1) \quad (4)$$

Where;

NU: Number of Parameter, L: Number of Level

Through all information about Taguchi method, the most suitable number of run is L9 ( $3^4$ ). The orthogonal array L9 is created based on the parameter and level in Table 1. Table 2 shows an orthogonal array L9 with values of parameters and levels.

**Table 2.** Orthogonal array L<sub>9</sub> ( $3^4$ )

Sample	Print pattern	Orientation (Y axis) (°)	Support angle (°)	Sidewalk offset (mm)
1	Cross	0	0	0.15
2	Cross	45	45	0.25
3	Cross	90	90	0.4
4	Diamond	0	45	0.4
5	Diamond	45	90	0.15
6	Diamond	90	0	0.25
7	Honeycomb	0	90	0.25
8	Honeycomb	45	0	0.4
9	Honeycomb	90	45	0.15

### 3 Result and Discussion

The samples of dog bone follow an ASTM D638 type IV with black ABS material that performed a trial run by using FDM CubePro. The sample of dog bone was fabricated with all parameter combinations studied from Taguchi's  $3^4$  design-of-experiment method. An orthogonal array of L9 was achieved in Minitab software, which gave a total of nine experiments. Figure 4 shows the sample of dog bone that are printed by using FDM CubePro 3D printer.



**Fig. 4.** Samples of dog bone ASTM D638 Type IV

Sample one is a combination of parameter print pattern (cross), orientation (Y axis) is  $0^\circ$ , support angle ( $0^\circ$ ) and sidewalk offset is 0.15 mm. For combination parameter sample number 2 is print pattern (cross), sidewalk offset (0.25 mm), orientation (Y axis) and support angle is  $45^\circ$ . Sample number 3 is print pattern (cross) sidewalk offset 0.4 mm and  $90^\circ$  for the orientation (Y axis) and support angle. The combination parameter for the sample number 4, 5 and 6 for the print pattern diamond and other orientations are (Y axis)  $0^\circ$ ,  $15^\circ$  and  $90^\circ$ . Meanwhile for the support angle  $45^\circ$ ,  $90^\circ$  and  $0^\circ$ . The parameter sidewalk offset is 0.4 mm, 0.15 mm and 0.25 mm for the sample number 4, 5 and 6. Next, print pattern (honeycomb), orientation (Y axis) is  $0^\circ$ , support angle ( $90^\circ$ ) and sidewalk offset (0.25 mm) for the sample number 7. For the combination parameter of sample number 8 is print pattern (honeycomb), orientation (Y axis) is  $45^\circ$ , support angle ( $0^\circ$ ) and sidewalk offset (0.4 mm). The last is sample number 9 used the combination parameter is print pattern (honeycomb), orientation (Y axis) is  $90^\circ$ , support angle ( $45^\circ$ ) and sidewalk offset is 0.15 mm. These explanations can also have referred to orthogonal array in Table 2.

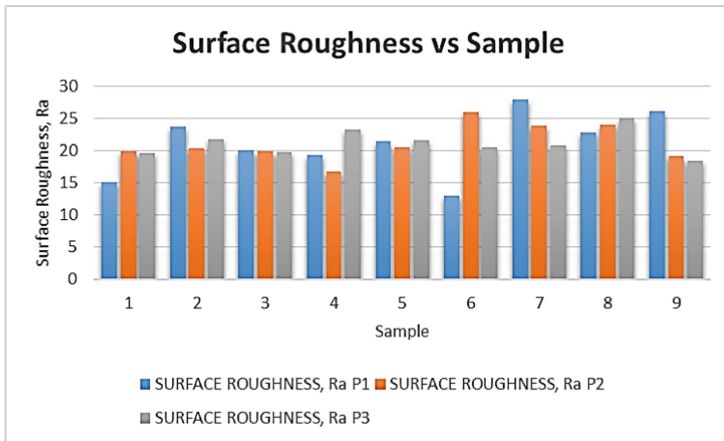
In this experiment, surface roughness (Ra) data are used for the Taguchi experiment. Table 3 shows the result of the Ra for P1, P2 and P3 measured by using surface

**Table 3.** The result of surface roughness (Ra)

Sample	Surface roughness, Ra (μm)			Sum (μm)	Average (μm)
	P1	P2	P3		
1	15.108	19.953	19.682	54.743	18.248
2	23.819	20.489	21.743	66.051	22.017
3	20.185	19.924	19.825	59.934	19.978
4	19.35	16.732	23.349	59.431	19.810
5	21.456	20.63	21.658	63.744	21.248
6	13.003	26.034	20.563	59.6	19.867
7	28.018	23.863	20.816	72.697	24.232
8	22.908	24.051	25.126	72.085	24.028
9	26.237	19.274	18.419	63.93	21.310

roughness machine. The result of Ra does not need to be measured by manual from the formula Arithmetic mean value, Ra because the result can be taken directly from the machine.

The average value for surface roughness Ra can be calculated from the three reading point which is P1, P2 and P3. The average Ra will be using in design-of-experiment (DOE) in Minitab software for the Taguchi Experiment. The graph for surface roughness (Ra) versus number of samples as shown in Fig. 5.



**Fig. 5.** Surface roughness, Ra versus sample

Next, the value of surface finish (Ra) will be compared between the P1, P2 and P3 from each sample. From surface roughness (Ra) of point P1 shows the highest is sample of 7 (28.018 μm) and the lowest is sample 6 (13.003 μm). Otherwise, the surface roughness (Ra) for the reading of point P2 the highest is sample 6 (26.034 μm)



and the lowest is sample 4 (16.732  $\mu\text{m}$ ). Meanwhile the surface roughness (Ra) of point P3 the highest is sample 8 (25.126  $\mu\text{m}$ ) and the lowest is sample 9 (18.419  $\mu\text{m}$ ). The measurement value can effect differences between surface roughness and stylus path. If the stylus path does not align with the lay of the roughness, then the reading of roughness will be lower or higher than expected.

For the Surface Roughness (Ra), Fig. 5 also demonstrates of the resulting data appears to be normal but recurrent in nature from minimum to maximum. Taguchi analysis will be utilized to clarify this phenomenon. The Ra value are identified at higher in others and lower in some runs, which implies that the combination of parameters in each run has the effect on the surface roughness characteristics. The average surface roughness of printed parts as shown in plotted graph as Fig. 6.

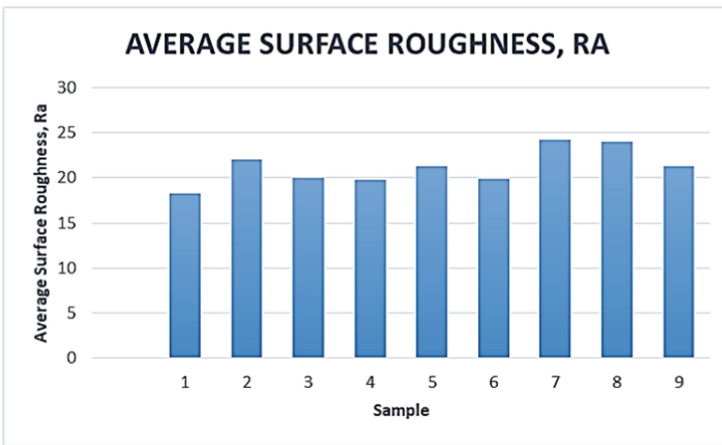


Fig. 6. The Average values of nine parts

### 3.1 Signal to Noise Ratio and Means

Signal-to-noise ratio is valuable for experiment to determine scaling factors, which are factors in which the mean and standard deviation are of different proportion. Scaling factors can be utilized to change the mean on target without influencing signal-to-noise ratios. According to Thamizhmanii et al. [16] the Taguchi design method uses a design parameter in which the factor can be control meanwhile a noise factor cannot be control which then might impact a product quality.

According to the DOE, nine experiment were conducted and all the surface roughness test data are presented in Table 4. The data points were determined using the ‘smaller-the-better approach’ because this study is focusing on minimising surface roughness in FDM CubePro 3D printer in optimal process parameter. For this reason, the ‘smaller-the-better’ equation was used for the calculation of S/N ratio. The Eq. (5)

is S/N ratio and Eq. (6) is MSD are calculated. MSD is the mean square deviation,  $y$  represents the value of surface roughness (Ra) and the number of test in one trial. Response Table for signal to noise ratio is shown in Table 4.

**Table 4.** Result of Taguchi design analysis

Sample	Print pattern	Orientation (Y axis)	Support angle	Sidewalk offset	Average Ra	Snra1	Mean1
1	Cross	0	0	0.15	18.248	-25.2241	18.2477
2	Cross	45	45	0.25	22.017	-26.8552	22.017
3	Cross	90	90	0.4	19.978	-26.011	19.978
4	Diamond	0	45	0.4	19.81	-25.9378	19.8103
5	Diamond	45	90	0.15	21.248	-26.5464	21.248
6	Diamond	90	0	0.25	19.867	-25.9625	19.8667
7	Honeycomb	0	90	0.25	24.232	-27.6879	24.2323
8	Honeycomb	45	0	0.4	24.028	-27.6145	24.0283
9	Honeycomb	90	45	0.15	21.31	-26.5717	21.31

$$S/N = -10 \log(\text{MSD}) \tag{5}$$

$$\text{MSD} = \frac{1}{2} \sum_{i=1}^n y_i^2 \tag{6}$$

The-smaller-the-better characteristic used to decide the smallest surface roughness (Ra) that would be perfect for this research. The S/N ratio analysed for optimum parameter of FDM CubePro 3D printer using Minitab software.

Moreover, the response table is a guided to select the best level for each factor. The Taguchi design was achieved a target with the mean and maximize the S/N ratio to minimum the surface roughness. The delta and rank value were used to identify the factors that have largest effect on each response characteristic. At that point, it helps in figuring out which levels of these factors has meet the objectives. The best level of a factor for one response characteristic is not quite the same as the best level for a different response characteristic. This problem determined is compulsory to predict the results for four combinations of factors levels to see which one produces the best result. The response table for Signal to Noise (S/N) and mean data presented in Table 5.

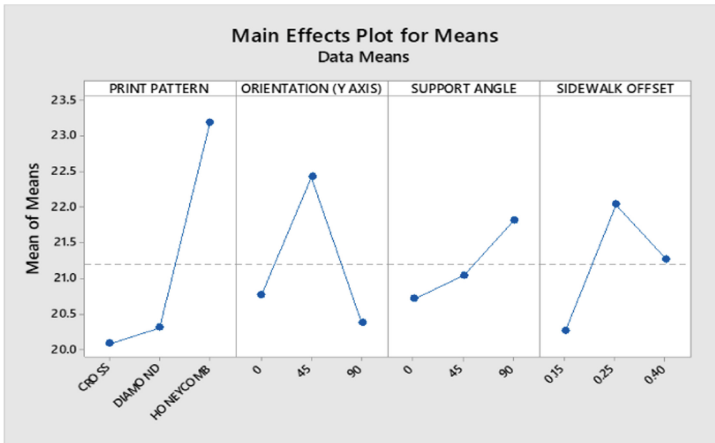
In these result, the response table shows the Signal to Noise. The print pattern is ranked 1 (Delta = 1.26). The second rank is orientation (Y axis) and followed by sidewalk offset and support angle. In addition, the ranks in a response table helps to identify which factors that have largest effect. In response table for means, print pattern is ranked 1 (Delta = 3.11) followed by orientation (Y axis), sidewalk offset and support angle. This rank chosen based on the highest to lowest delta value.

**Table 5.** Response table for signal to noise and mean

Level	Print pattern		Orientation (Y axis)		Support angle		Sidewalk offset	
	S/N	Mean	S/N	Mean	S/N	Mean	S/N	Mean
1	-26.03	20.08	-26.28	20.76	-26.27	20.71	-26.11	20.27
2	-26.15	20.31	-27.01	22.43	-26.45	21.05	-26.84	22.04
3	-27.29	23.19	-26.18	20.38	-26.75	21.82	-26.52	21.27
Delta	1.26	3.11	0.82	2.05	0.48	1.11	0.72	1.77
Rank	1	1	2	2	4	4	3	3

### 3.2 Prediction of Optimal Solution

The impact of control factor can be more certainly presented with response graphs in Figs. 7 and 8. The Fig. 7 shows the main effects plot for mean. This plot is to distinguish the parameters that influences the surface roughness response, which is proven by each parameter level. Hence, when the mean line is parallel to x-axis then it means that the parameter has no impact on response Ra and when the line is sloping then the parameter influences the response by its low and high level.



**Fig. 7.** Main effects plot for means

The print pattern, Orientation (Y axis), Support Angle and Sidewalk Offset potentially affect the Ra response since the mean line is inclined to x-axis. Consequently, print pattern at honeycomb level have higher average response than cross and diamond. Also, Orientation (Y axis) parameter 45° level is higher in average response than 0° and 90°, which means that the response is less when orientation (Y axis) is set to 90°, but differs when support angle parameter 90° level has high average response than 0° and 45°. Then, the sidewalk offset parameter 0.25 mm is higher in average than 0.15 mm and 0.40 mm.

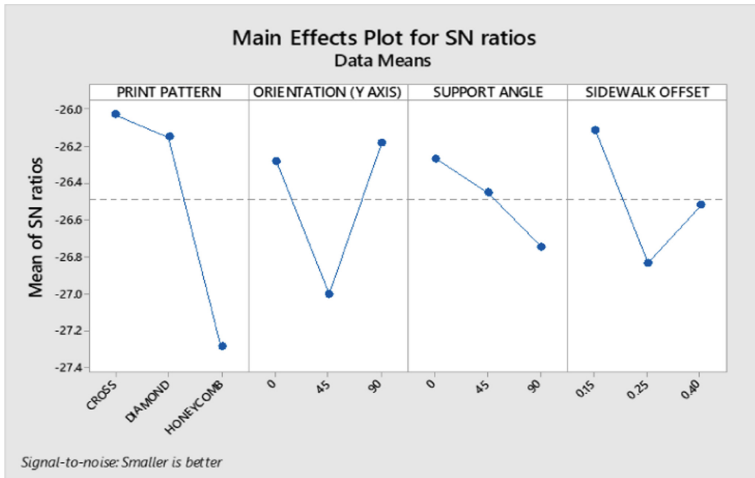


Fig. 8. Main effects plot for SN ratios

Based on Fig. 8 for main effects plot for S/N ratio, it can be identified as the optimal parameters to minimize surface roughness (Ra). The highest value is selected among all points. For the print pattern, the highest level is cross pattern compared to diamond and honeycomb. Meanwhile, orientation (Y axis) parameter 90° levels has highest average than 0° and 45°. Support angle parameter 0° has highest average than 45° and 90°. Next, sidewalk offset parameter 0.20 mm levels have higher value than 0.25 mm and 0.40 mm.

The prediction values for S/N ratio and mean are -25.224 and 18.248 respectively as shown in Table 6. Then, refer to Table 7, the confirmation of optimum result was produced by a combination of levels for all the four control factors parameter. From the analysis on the best surface finish, the results are print pattern (Cross), orientation (Y axis) is 0°, support angle (0°) and sidewalk offset is 0.15 mm. In any case, surface finish likewise relies on the nozzle. The different nozzle has dissimilar tip diameters and these factors influences the stability and precision of the extrusion procedure. Default values were used in order to gain optimize process parameter which are

Table 6. Prediction values

S/N ratio	Mean
-25.224	18.248

Table 7. Result of confirmation

Print pattern	Orientation (Y axis)	Support angle	Sidewalk offset
Cross	0	0	0.15

200  $\mu\text{m}$  for layer thickness and strong mode in print strength. Therefore, the optimum process parameter 3D printer type FDM, CubePro are cross print pattern,  $0^\circ$  Y axis orientation,  $0^\circ$  support angle and 0.15 mm sidewalk offset layer.

## 4 Conclusion

In conclusion, the optimum parameter condition for surface roughness of 3D printed part by FDM CubePro are cross print pattern,  $0^\circ$  Y axis orientation,  $0^\circ$  support angle and 0.15 mm sidewalk offset layer. A basic  $L_9$  ( $3^4$ ) orthogonal array was selected with nine experiments with four main factors each at three levels. Thus, it is proving that the Taguchi parameter design is a productive method to optimise the parameter setting in order to achieve the minimum value of surface roughness.

## References

1. Narang, R., Chhabra, D.: Analysis of process parameters of fused deposition modeling (FDM) technique. *Int. J. Future Revolut. Comput. Sci. Commun. Eng.* **3**(10), 41–48 (2017)
2. Mohamed, O.A., Masood, S.H., Bhowmik, J.L.: Optimization of fused deposition modeling process parameters: a review of current research and future prospects. *Adv. Manuf.* **3**(1), 42–53 (2015)
3. Kumar, S., Kannan, V.N., Sankaranarayanan, G.: Parameter optimization of ABS-M30i parts produced by fused deposition modeling for minimum surface roughness. *Int. J. Curr. Eng. Technol.* **3**, 93–97 (2014)
4. Levy, G.N., Schindel, R., Kruth, J.P.: Rapid manufacturing and rapid tooling with layer manufacturing (LM) technologies, state of the art and future perspectives. *CIRP Ann.* **52**(2), 589–609 (2003)
5. Mohamed, O.A., Masood, S.H., Bhowmik, J.L.: Optimization of fused deposition modeling process parameters: a review of current research and future prospects. *Adv. Manuf.* **3**(1), 42–53 (2015)
6. Bual, G.S., Kumar, P.: Methods to improve surface finish of parts produced by fused deposition modeling. *Manuf. Sci. Technol.* **2**, 51–55 (2014)
7. Athreya, S., Venkatesh, Y.D.: Application of Taguchi method for optimization of process parameters in improving the surface roughness of lathe facing operation. *Int. Refereed J. Eng. Sci.* **1**(3), 13–19 (2012)
8. Uttarwar, P.B., Raini, S.K., Malwad, D.S.: Optimization of process parameter on surface roughness (Ra) and wall thickness on SPIF using taguchi method. *Int. Res. J. Eng. Technol.* **2**(9), 781–784 (2015)
9. Ahmad, M.N., et al.: Optimization of vacuum casting process parameters using Taguchi method. In: 2018 Proceedings of Mechanical Engineering Research Day, pp 146–147 (2018)
10. Gaonkar, S., Karanjavkar, N., Kadam, S.N.: Taguchi method. *Int. J. Sci. Res. Sci. Eng. Technol.* **2**(2), 843–845 (2016)
11. Naiju, C.D., Anil, P.M.: Influence of operating parameters on the reciprocating sliding wear of direct metal deposition (DMD) components using Taguchi method. *Proc. Eng.* **174**, 1016–1027 (2017)

12. Pang, J.S., Ansari, M.N.M., Zaroog, O.S., Ali, M.H., Sapuan, S.M.: Taguchi design optimization of machining parameters on the CNC end milling process of halloysite nanotube with aluminium reinforced epoxy matrix (HNT/Al/Ep) hybrid composite. *HBRC J.* **10**(2), 138–144 (2014)
13. Ghani, J.A., Choudhury, I.A., Hassan, H.H.: Application of Taguchi method in the optimization of end milling parameters. *J. Mater. Process. Technol.* **145**, 84–92 (2004)
14. Tsai, Y.H., Chen, J.C., Lou, S.J.: An in-process surface recognition system based on neural networks in end milling cutting operations. *Int. J. Mach. Tools Manuf.* **39**(4), 583–605 (1999)
15. Zhang, J.Z., Chen, J.C., Kirby, E.D.: Surface roughness optimization in an end-milling operation using the Taguchi design method. *J. Mater. Process. Technol.* **184**(1–3), 233–239 (2007)
16. Thamizhmanii, S., Kamarudin, K., Rahim, E.A., Sapparudin, A., Hasan, S.: Optimizing surface roughness and flank wear on hard turning process using Taguchi parameter design. In: *World Congress on Engineering*, pp. 1068–1071 (2007)



# Factors that Entrapped the Malaysian Mobile Provider in the Red Ocean Traps

M. F. M. Sam<sup>2</sup>, H. Hafizuddin<sup>1</sup>(✉), B. C. Chew<sup>1</sup>, and Y. F. Yusof<sup>1</sup>

<sup>1</sup> Faculty of Technology Management and Technopreneurship,  
Universiti Teknikal Malaysia Melaka (UTeM), Malacca, Malaysia  
hafizuddin.hissamuddin@gmail.com

<sup>2</sup> Centre for Robotics and Industrial Automation (CeRIA),  
Fakulti Kejuruteraan Elektrik (FKE), Universiti Teknikal Malaysia  
Melaka (UTeM), Malacca, Malaysia

**Abstract.** The telecommunication industry in Malaysia is led by the 3 major companies that continuously compete over a small profit of pool to increase their market share in Malaysia. This has cause the telecommunication industry to be caught in the Red Ocean traps. Furthermore, in this research, the top three mobile providers which are Celcom, Digi and Maxis the factors that cases the Mobile Provide in Malaysia to be entrapped in the Red Ocean Traps. By resolving the Red Ocean traps of Mobile Provider in Malaysia, they can achieve a sustainable business and create new opportunity in the market. A qualitative interview is conducted to collect the respondent's answer for the analysis. The data is analyzed by using the qualitative method. The result of this research will be the causes and strategies to release Red Ocean traps of Mobile Provider in Malaysia. This research has been able to provide innovative suggestion that will help the Malaysian mobile providers to be sustainable within the business.

**Keywords:** Red Ocean traps · Telecommunication industry · Qualitative · Exploratory

## 1 Introduction

The telecommunication industry in Malaysia is led by the 3 major companies that continuously fighting with each other over a small profit of pool. Suruhanjaya Komunikasi Dan Multimedia Malaysia (2016) believes that there is an intensive competitive environment between the mobile providers in Malaysia for control over the market share which resulting to market saturation [3]. If we look back in 2015, SKMM have indicated that the growth of each providers has started to slow down as new player join in the fight and the characteristic of the Red Ocean Traps begin to show themselves within the telecommunication industry (such as competing in the existing market space, beat the competition and exploit the existing demand). According to Kim and Mauborgne Red Ocean is a trap that can hook the manager to the red ocean and prohibit them from exploring other option [2]. In addition, they also claim that as long as the companies gain a profitable growth, they will continue to have a head to head with their rival. Even if it means resulting in a bloody red ocean of rival over a small profit

of pool. Therefore, this research will be focusing on identifying the factors that cases the Mobile Provide in Malaysia to be entrapped in the Red Ocean Traps.

### 1.1 Research Question

The overarching research question is:

- i. What are the causes that have entrapped the Malaysian mobile providers in the Red Ocean trap?

### 1.2 Research Objective

Thus, the Research Objective is as follow:

- i. To examine the causes that have entrapped the Malaysian mobile providers in the Red Ocean trap.

## 2 Literature Review

### 2.1 Red Ocean Trap

Red Ocean can be defined as a market that had a clear boundary and rules which was set beforehand into the companies [3]. As a result, this company will compete to outperform their competitor in order to increase their market shares which eventually turn into an ocean of bloody red. Hence, it was called “Red” Ocean. Furthermore, for those who have been caught in the red ocean, there will be a decrease in profit and growth for their companies. This is due to the increase in the number of competitors in the market. Moreover, the Red Ocean was criticized by Kim and Mauborgne because its presence has made the market become much denser and intensive [3].

There are a lot of factors that could cause the red ocean to be emerge that could lead to market saturation and encourage competitor to be involve in an intense fight among them. However, this research has identified three factors that contribute to creation of the Red Ocean traps. Which is Intense Rivalry, Lack of Innovative Strategy and Obsession on Customer.

**A. Intense Rivalry.** According to Wilkinson [7], any fighting that occur between two competitors that involved in putting pressure on one another will be limiting both companies profit potential [7]. Since, it will affect the competitor environment and influence the ability of the existing firms to achieve profitability as stated by Porter [6]. In other word, the intensity fight between two rivals can make the market become more saturate and firmer will have started to eliminate those who occupied the market to expand their territories.

Resulting only the winner to stand at the top of the pyramid. Thus, decreasing the profit of each company.

**B. Lack of Innovative Strategy.** Porter have stated that there are two basic type of competitive advantage for a firm can possess which are either Low cost or High Value. They believe that a firm can only choose only one of them. Because of this, a lot of firm

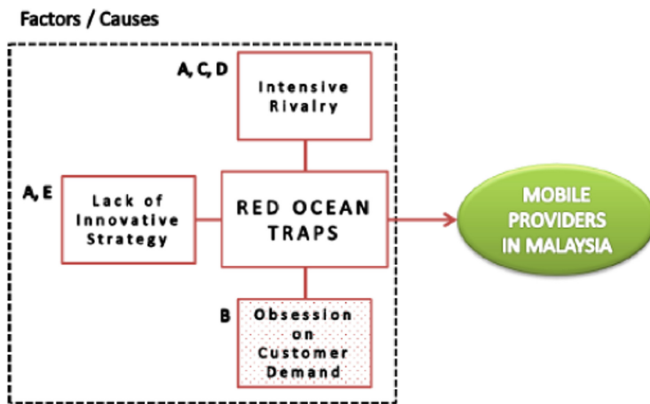


have entrapped in the current market which is believed to have turn into a Red Ocean. Kim and Mauborgne once mentioned that the current market situation is a good example of what the Red Ocean really is. They believe that, with only two option choice, the firms will have started to duplicate their rival strategy with hope to exploit the existing demand and get ahead start of their rival. Thus, creating a product without value in it.

**C. Obsession on Customer Demand.** From the perspective view of a marketer, generating new demand is the most important thing. However, this type of approach will only keep the companies to stay in the Red Ocean rather than getting out of it. The marketers assume that the customers are always right so much that they have averted their eyes from the vast opportunity that they could explore. They have been chain by the philosophy of “The Customer is the King” that cause them to create an improvise solution which could be used to gain a slight advantage over the rivals. Kim and Mauborgne [2] claims that a focus merely on an existing customer, tend to drive the company to create a better solution to counter the offer of their rivals [2]. If this approach continues to be implemented, these companies will never be able to escape the Red Ocean traps and explore new possibilities that cannot be gain in the Red Ocean Market.

**2.2 Theoretical Framework**

The theoretical framework below has been developed based on the research problem and literature review that relate one each other that have been identified and easier to understand by the researcher. The theoretical Framework is shown as below (Fig. 1):



Source:

- A. Kim and Mauborgne (2016) [3]
- B. Kim and Mauborgne (2015) [2]
- C. Wilkinson (2013) [7]
- D. Porter (2008) [6]
- E. Porter (1985) [5]

**Fig. 1.** Theoretical framework

### 3 Research Methods

The researcher has chosen the exploratory research since the researcher have a limited accessibility to the data especially on the current play of competition in Malaysian Telecommunication industry. One of top three mobile provider in Malaysia (which is Celcom Axiata Bhd) have been selected by the researcher to gain a deeper understanding of the current situation. The case study is conducted by using the qualitative method to conduct an in-depth interview on the Middle and Lower Management Level that are currently working in Celcom Sdn from four difference branch outlets which are Ipoh, Manjung, Taiping and Melaka. In this research, the case study is being used to investigate the reason why the mobile provider in Malaysia has been caught in the Red Ocean traps. Corresponding from that, judgmental sampling technique was chosen because of this technique work for the very small sample such as case study research and selected cases that have particularly informative. As a matter of fact, since most research projects undertaken for academic courses are usually time restricted, this research will be adopting the cross-sectional studies. It will allow the researcher to record all information at one point or even over a short period of time. Data collection along the period will allow the researchers to compare with the different dimension of each research objective at the same time. The focus of the case study is to investigate factor that causes the Red Ocean to emerge in the first place and how the Blue Ocean Strategy could save them from this trap. Therefore, it was decided that the result will be presented based in the objective of the research. Table 1 below shows the respondent from four different branches.

**Table 1.** Respondent's profile.

Organization	Branch outlet	Designation
Celcom Axiata Bhd	Ipoh	Outlet Manager
		Account Manager
	Manjung	Outlet Supervisor
		Outlet Executive
	Taiping	Outlet Manager
		Outlet Executive
	Melaka	Outlet Supervisor
		Outlet Executive

### 4 Discussion and Analysis

Based on the theoretical framework that have been constructed in the literature review, there are several factors that could cause the Red Ocean to emerge in the market which are Intense Rivalry, Lack of Innovative Strategy and Obsession on Customer. The researchers start to analyze each of the following factors:

**A. Intense Rival.** Primary and secondary data illustrated that the researcher admitted that Intense Rivalry is one of the factors that could contribute to the creation of the Red

Ocean Traps. The intense fighting among two competitors will limit both parties profit gain and growth since both of them will be applying pressure on one another. During one of the speeches of Dato Sri Mohd Nadzmi Bin Mohd Salleh in UTeM, the researcher has asked him whether the number of players in a market could affect the market saturation level and he said yes to it. Indicate that there are too many players in the telecommunication industry which further saturated the market.

According to Celcom's Account Manager in Ipoh, He stated that there are too many numbers of competitor in the telecommunication Industry. Especially the new comer such as U-Mobile, Onexox and Red One that started to make the market become more saturated. He noticed that this mobile provider companies will continue to fight with each other if its means that they can gain one step ahead of the others. They believe there will be only one winner that could control the market in Malaysia. This is very true since U-Mobile was able to gain 8.4% of the market share in 2015 which continue to increase when compare to its first entrance in 2008 [4].

One of their colleagues from Taiping states that the increase in number of players would also encourage the other player to be more aggressive in eliminating other if it means they can gain an upper hand. If we look back a few years back in 2016, the intense fighting among the player have cause caused Maxis to lose 384 000 subscribers while Digi was to gain 211 000 subscribers from those competition [1]. Resulting Celcom succeed in overtaking Maxis as the number 1 telecommunication industry in Malaysia. Thus, proven that if Celcom lose a customer, their rival will be able to gain an upper hand and will further increase the intense fighting.

The researcher believes that, the number of players has increased for the past few years have become a contributor to the intense fighting in the market. Each one of them is trying to secure a place in the market share and become a leader for the telecommunication industry. There a lot of factor that can contribute to the intense fight, but the main contributor is the introduction of the MNP System. After the introduction of the system, the fighting has become more intense to the point that stealing other's customer is a must in order to survive in this saturated market. Without knowing the consequence, they have entered the Red Ocean Traps.

**B. Lack of Innovative Strategy.** According to Celcom Outlet Executive from Taiping, there was a time when each mobile provider has their own signature number that could differentiate one user to another user (which are Celcom (013 and 019), Maxis (012 and 017) and Digi (016)). During this period, the mobile provider in Malaysia always compete in a friendly environment by coming up with new ideas and strategies that could make them the best provider in Malaysia. They will encourage each other to strive for a better future for both the users and company. However, after the introduction of the Mobile Number Portability (MNP) System, they have stop to generate new idea and focus more on eliminating other competitors. Thus, making them stuck in a stalemate competition.

Another reason why the lack of Innovative Suggestion could be considered one of the factors is because an outlet executive from Melaka notice that the player prefers to imitate their rival product rather than improving the current product. The higher up deem that, by investing more on Research and development, it would increase the cost and minimize the overall profit. Therefore, the product that being offer by the

telecommunication companies are almost identical with only a slight difference between them. A good example can be seen in one of the New Straits Time written by Zakariah [8] where the consumer is now facing difficulties to choose the best offer from this 3 Big Telecommunication companies [8]. The “Big Three” are currently been rolling out attractive package and the difference between them are only the price and the amount of data. For this reason, if this situation was not being resolve, the telecommunication industry in Malaysia will be forever stuck in a cycle.

**C. Obsession on Customer Demand.** Celcom Outlet Executive from Ipoh emphasize that the current telecommunication industry in Malaysia have been focusing more on the customer demand rather than the potential customer who could equally contribute to the company profit gains. He believed that the drawback of focusing on the customer demand would soon lead them to an endless cycle where no new market can be created. On the other hand, those who are from the Manjung Branch view it differently. They feel that this obsession on customer demand was triggered by both the company and the customers. Both party are equally at fault for creating the Red Ocean market. If one of them are not so obsessed in fulfilling and demanding on one another need and want, this kind of situation can be avoided and the MNP System would not be introduced in the first place.

However, both the manager and executive from Celcom Outlet Taiping disagree with this factor. They do not believe that being obsess with the customer is a bad thing since they are the one that bring profit and should treat them as a king. When in fact, thanks to the war between this Telco's, the one who gained benefit of it is only the customer but not for the companies itself. What worse, the RHB Investment Bank Bhd stated that the competition in the mobile space would remain too elevated due to more equitable spectrum re-allocation. This is because, the other telcoes would take this opportunity to grab more market share while Maxis and Celcom will likely to intensify the marketing campaigns to sustain their network investment for the subscriber. Thus, lower the chances of them getting out of the Red Ocean Traps.

The researcher concluded that, our telecommunication industry is too obsessed on the customer demand. They assume that the customers are always right and choose to take the easier ways. By diverting their focus from the potential customer, they tend to fulfill the demand of each one of their customers that could only provide a slight advantage over their competitor. They rather disregard the opportunity to growth and explore other's alternative just to follow the current trend. Even one of the respondents have mentioned that this kind of trend if it continues any longer, it will only bring disadvantage to our industry. Therefore, our telecommunication industry should realize that being obsesses with customer demand will not bring them any benefit; rather they should explore other opportunities that could provide a sustainable and long-term growth for the company.

## 5 Conclusion

After analyzed, the researcher found that the respondents understand all of factors that have been asked during the interview session. They are aware that the telecommunication industry in Malaysia have been caught in the Red Ocean traps and agreed that these traps will limit the profit gain and growth for their companies. Therefore, from all these factors, the most significance would be the Intense Rivalry and Lack of Innovative Suggestion while the remaining one would be the least significance which is the obsession on customer demand.

The first factor would be the Intense Rivalry that can be considered one of the most main catalyst that give birth to the Red Ocean Traps. Even though the respondents are aware of the intense fight among the provider, they do not have the power to stop it. They are afraid to give their rival an upper hand and would prefer to maintain the status. Furthermore, they also believe that the main causes of the Red Ocean traps are from the introduction of the MNP system in January 2007. From there onward, the saturation of the market has continued to increase and a lot of newcomer starting to enter the market. This statement can be supported by the report from SKMM (2015) where the newcomer company, U-Mobile was able to secure a place in the Market in 2008 [4]. It indicated that the MNP system has contributed to the intense fighting, lack of innovative suggestion and obsession on the customer demand.

Another significant factors that contributed to the creation of the Red Ocean Traps is the Lack of Innovative Strategy. The researcher noticed that the MNP System have also caused the telecommunication industry in Malaysia to be unable to produce new innovative strategy and maintain the friendly environment among the mobile provider's company. The inability to stop the intense fighting that happen in the market have cause the top management of each companies to take drastic decision without knowing the consequences of their choices. The researcher believe that their decision has cause them to be stuck in a stalemate and was unable to produce new idea that could difference them from one another. Even the New Straight time condemn them by implying that the main difference between their product to one another is only the price and the amount of data being offer. If this situation was not being resolved, the telecommunication industry in Malaysia will be forever stuck in a cycle and caused their growth potential to be halt and limited.

Lastly, there have one least important factor that cause the Red Ocean Traps to emerge which is the obsession on the customer. There has been a philosophy where "The Customer is the King" and they always right. If we look from the lens of the marketers, following this philosophy might be the right choice to make. However, for a company who wish to be the best in his area of expertise it might not be the best choices. Kim and Mauborgne once stated that merely focusing on the existing customer will not help them to generate new demand and improve its profit and revenue in long term planning [3]. So much that the researcher hopes that the telecommunication industry in Malaysia realize that being obsesses with customer demand will not bring them any benefit. Rather the higher ups should explore other opportunities that could provide a sustainable and long-term growth for the company.

## 6 Recommendation

The study can be continued in depth research for those who are interested in future. Hereby researcher would like to suggestion some steps for the continuous of this research. First, other researcher can generalize this research in other field of the industry that was facing the same problem such as the Smartphone Industry. The Smartphone Industry has started to show sign that they are entering the Red Ocean Traps. The researcher hopes that the result of this study can be used to provide an insight for their research and help them to identify different factors that could contributed the industry to be entrapped in the Red Ocean Traps. Second, this research can also be used to decrease the number of competitors in the market while increasing the profit and growth of the companies. The result of this research is open to every other research that would like to further research the Blue Ocean Strategy in order to come up with a better solution to escape the Red Ocean Traps.

**Acknowledgments.** The researchers feel thankful to Universiti Teknikal Malaysia High Impact Short Term Research Grant (PJP) which funds this publication.

## References

1. Howe, G.T.: Competition hots up for big 3 telcos. New Straits Times, 14 May 2016. <https://www.nst.com.my/news/2016/05/145535/competition-hots-big-3-telcos>
2. Kim, W.C., Mauborgne, R.: Red ocean traps. Harvard Business Review, March 2015. <https://hbr.org/2015/03/red-ocean-traps>
3. Kim, W.C., Mauborgne, R.: What is Blue Ocean Strategy. Blue Ocean Strategy (2016). <https://www.blueoceanstrategy.com/what-is-blue-ocean-strategy/>
4. Malaysia, S.K.: SKMM fact figures Q1 2016. Suruhanjaya Komunikasi dan Multimedia Malaysia (2016). <https://www.mcmc.gov.my/>
5. Porter, M.E.: Competitive Advantage: Creating and Sustaining Superior Performance. The Free Press, New York (1985)
6. Porter, M.E.: On Competition. Harvard Business School Publishing Corporation, Brighton (2008)
7. Wilkinson, J.: Intensity of rivalry. The Strategic CFO, 24 July 2013. <https://strategiccfo.com/intensity-of-rivalry-one-of-porters-five-forces/>
8. Zakariah, Z.: Telco price war: competition hots up, consumers spoilt for choice. New Straits Times, 30 January 2017. <https://www.nst.com.my/news/2017/01/208165/telco-price-war-competition-hots-consumers-spoilt-choice>



# Multi Response Optimisation of Injection Moulding Process Parameter Using Taguchi and Desirability Function

Vivekanandan Panneerselvam and Faiz Mohd Turan<sup>(✉)</sup>

Faculty of Manufacturing Engineering,  
Universiti Malaysia Pahang, Pekan, Malaysia  
faizmt@ump.edu.my

**Abstract.** In this study, the optimum injection molding process parameter of warehouse plastic pallets is identified. Compressive strength and part weight are the selected quality characteristic. Barrel temperature, injection speed and holding pressure are the selected process parameter. Taguchi optimization method and desirability function is used to identify the most effective process parameter on the compressive strength and part weight. Based on the conducted experiment, 241 °C of barrel temperature, 72 mm/s of injection speed and 11 MPa of holding pressure, optimise the compressive strength to 5242 kg and part weight to 11.6 kg. The optimised process parameters are studied with an actual experiment and the percentage error of optimised process parameter are identified which is 4.6% for compressive strength and 0.2% for part weight. Moreover, a quantitative relationship between the process parameter and the selected quality response is established using regression analysis. The percentage error of the prediction model for compressive strength is 10% and for part weight is 0.3%. Thus, the prediction model used in this study is effective and practical. This research is beneficial for all the plastic moulding industry which produce plastic pallets. The results can save cost on material consumption and also ensure high product quality.

**Keywords:** Injection moulding · Optimisation · Taguchi · Desirability function · Regression analysis

## 1 Introduction

Warehousing is an important part of any manufacturing industry as it is a link between producers and consumers. Plastic pallet is used by the manufacturing industry to keep its products in the warehouse for easy forklift handling. In the disposable of the warehouse, the use of plastic pallets material has grown rapidly for several years due to its performance, durability, and quality compared to wooden pallets. These plastic pallets are produced by a manufacturing company using injection moulding machines. Injection molding is known as an effective process for the mass production of plastic parts with complicated forms.

Determining optimal process parameter settings critically influences productivity, quality, and cost of production in the plastic injection molding (PIM) industry. Previously, production engineers used either trial-and-error method or Taguchi's

parameter design method to determine optimal process parameter settings for PIM. However, these methods are unsuitable in present PIM because of the increasing complexity of product design and the requirement of multi-response quality characteristics. Stability control of production is an important aspect of injection molding. However, challenges continue to exist with respect to improving product quality stability to achieve a faster forming speed and higher automation for injection molding because the injection process is usually disturbed by several inevitable variations. The difficulty in overcoming the fore-mentioned inevitable disturbances and achieving dynamic control of product quality is related to establishing a quantitative relationship between product quality and process variables.

In this research, the multi-response optimisation problem of injection molding of plastic pallets is studied systematically to produce a high-quality part with lower cost. Changes in processing conditions can lead to improvements or degradation of accuracy, shape, surface finish, and fracture resistance and many other part properties and characteristics. The primary use of process models is to predict these effects. So, a quality prediction model based on the process parameter is established to monitor product weight variation online.

## 2 Literature Review

First of all, most researchers did not conduct any confirmation test on the optimised process parameter. A confirmation test is to identify the gap between the optimised parameter and the actual experimental results. This is to confirm whether the optimisation method that has been used in any research is valid or not. Sajjan et al., Harshal et al., Osarenwindu et al., Sreedharan et al., Gurjeet, Pradhan et al., Rish et al. and Rathi [1–8], their optimised process parameters are not tested in the real experiment to validate their conducted studies. The gap or error between optimised parameter and the actual parameter is not studied in some of the previous researches. So, there is no evidence on the accuracy of the optimisation.

Furthermore, the research conducted by Altan [4] need a lot of computational work and it may cause an industry higher cost to own software like Matlab, Autocad and so on. Matlab was used to write a backpropagation type of algorithm which is used to train the prediction neural network. Other than that, 500,000 cycles need to be done in order to build this prediction neural network. This may cause severe cost on production, productivity and also higher lead time for the testing. Another study by Huizhuo et al. [9], used Mouldflow analysis to identify the influential process parameter before the experiment. The software is also used to analyse the quality index of the injection moulded parts. The Mouldflow Insight software (MPI) is very expensive and not a cost-effective method to optimise the process parameter for injection mouldings. Then, Researcher like Yizong et al. [10] used CADMOLD to do melt simulation for his studies. It is used to simulate the PS melt flow inside the mould cavity by lines propagate through the 3D model indicating the flow path of the PS melt. However, this method is quite costly and need to invest in the software to do such analysis. A small medium enterprise is not capable to buy or invest on the CADMOULD to conduct such studies and it is practically hard for the injection moulding industry to optimise the process parameter.



Finally, researchers also ignored the productivity of the injection moulding process in order to optimise the process parameter for better quality. Faruk et al. [11] studies involve time variable like cooling time and from the optimisation, it is identified that cooling time of the 40 s give the minimum flow shrinkage for the product. The optimal cooling time for minimum shrinkage is slightly higher which is the 40 s. This can directly influence the product cycle time and can lead to less production output. The study by Anand and Kumar [12] obtain optimal tensile strength with a process parameter of 220 °C for processing temperature, 130 Mpa for injection pressure, 20 s for the cooling time and 70 mm/sec of injection speed. Although the cooling time of 20 s can give higher tensile strength for PP material, it also can increase the cycle time of the whole process whereas can affect productivity. Rathi [8] believed that higher part weight is the better quality. Although it is technically correct, this will increase the cost due to the higher CPVC material consumption by the injection moulding machine in order to prevent shorts-shorts. Furthermore, this assumption of weight corresponds to short shorts possibilities cannot be applied for bigger products like a car bumper, containers or plastic pallets. Even a small tiny hole in the product cannot be seen in the part weight differences and this will lead to a wrong analysis on the short-shorts possibilities.

### 3 Methodology

Figure 1 below shows the research flowchart for the process parameter optimisation. This research consists of three main stages of process parameter optimisation. The stages are Phase 1: selecting key variable and quality response, Phase 2: optimising process parameter, and Phase 3: establishing a quantitative relationship. Before optimising the process parameter, the variables that need to be considered must be known

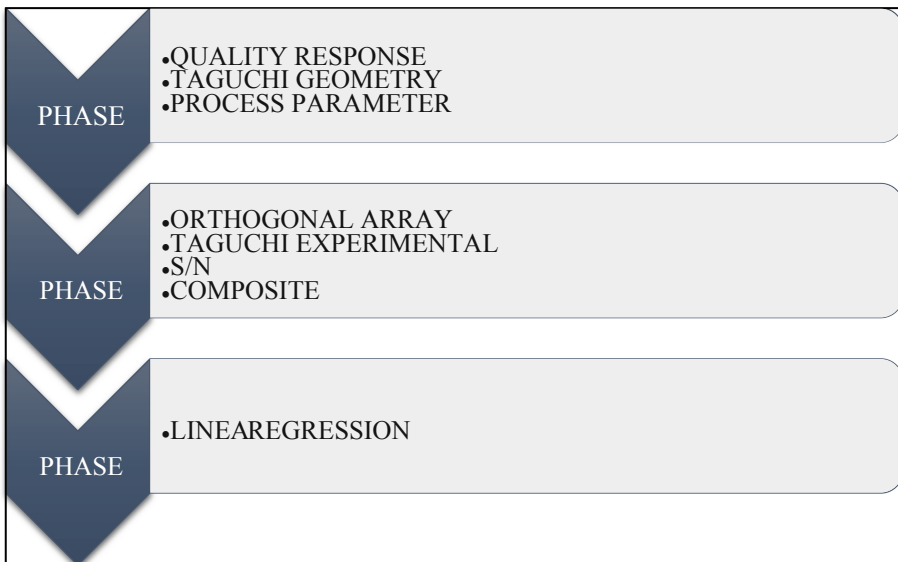


Fig. 1. Flow chart of optimisation

in order to have a successful parameter optimisation. The first phase is about determining all the component values required in design regarding the first objectives. The 2nd phase is to optimise the identified parameters and the 3rd is to establish a quantitative relationship between the process and quality.

### **3.1 Phase 1: Selecting Key Variable and Quality Response**

The first phase is about selecting a suitable process parameter which can directly influence the selected products quality. So, the first step in phase 1 is to select the quality of the product which we want to study and optimise. The quality of a product can be categorized into three properties: (a) dimensional properties (for e.g., weight, length, and thickness), (b) surface properties represented by the appearance of surface defects (for e.g., sink marks and jetting), and (c) mechanical or optical properties (for e.g., tensile and impact strength). Proper studies on previous researches have been done before selecting the important quality characteristics. Based on the studies conducted by Yang and Gao [13], the performance of a manufacturing process and its quality control are monitored through product weight because the quality is inversely proportional to variability and this is reflected in the product weight variation while product weight is closely related to other quality properties. Zhou et al. [14] also supported and considered part weight as an important quality characteristic in their studies. Optimisation of the weight of the plastic pallets is usually done by the operators in the plastic injection molding industry for material savings. Even though they can reduce the part weight as low as possible satisfying dimensional properties and surface properties but still they failed to satisfy the mechanical properties. This is due to the correlation between the part weight and the part compressive strength. A very low part weight can result in a low compressive strength which causes the plastic pallets to only cater a small amount of weight. Therefore, the compressive strength of the plastic pallets is also considered in this study for the part weight optimization. Once the quality characteristics are selected, their corresponding process parameters are found through several previous research works. A brief explanation is given in Sect. 4, Subsect. 4.1 for the selected process parameters. After the parameter is selected, the preliminary test had to be done to identify the maximum, minimum and average value of the parameter to construct the Taguchi experiment table.

### **3.2 Phase 2: Optimising Process Parameter**

In this phase, the design of the experiment is selected based on the orthogonal array table and the selected Taguchi design is used to run the experiment. After the experiment, each product weight is measured and tested for compression strength. Later, this data is used to perform S/N analysis for parameter optimisation. Finally, the composite desirability function is integrated with the Taguchi method for multi-response process parameter optimisation.

### 3.3 Phase 3: Establishing a Quantitative Relationship

In this phase, regression analysis is used to establish a quantitative relationship between the process parameter and the selected quality characteristics. Regression analysis mathematically describes the relationship between a set of independent variables and a dependent variable. There are numerous types of regression models that can be used. This choice often depends on the kind of data that we have for the dependent variable and the type of model that provides the best fit.

## 4 Results and Discussions

### 4.1 Selected Key Process Parameter

The initial melt temperature is affected by barrel heating and shear heat due to screw rotation. Barrel temperature is one of the frequently adjusted parameters in the plastic industry in order to get better quality results. Since this process parameter has a direct influence on the product quality, it has been selected for this research study. Adjustments in the melt specific volume can be achieved through the holding stage in which the main function involves compensating for the instability of the melt properties Zhou et al. [13]. Despite changes in the melt specific volume during the injection stage, it is still possible to control the holding stage to compensate for the melt specific volume. So, the holding pressure has been selected as another process parameter to study its influence on the compressive strength. Latest studies on compressive strength conducted by Gingtong et al. [14], they have selected three parameters like melt temperature, injection speed and holding pressure. Their studies show that the contribution of the injection speed to the quality characteristic is the highest compared to the other selected parameter. So, the injection speed has been selected in this study to be optimise for better quality output. Table 1 below shows the selected process parameter for this study.

**Table 1.** Selected process parameter

Process parameter	Reason	Source
Barrel temperature	Influence on melt specific volume	Zhou, Zhang, Mao, and Huamin [13]
Holding pressure	Influence on melt specific volume	Zhou, Zhang, Mao, and Huamin [13]
Injection speed	Higher significance effects on compressive strength	Gingtong, Nakpathomkun, and Pechyen [14]

## 4.2 Process Parameter Optimisation

A consistent experimental operation was applied to ensure similar conditions for the production of each test series. Prior to re-commencing production, a waiting time of 15 min was required to allow the barrel temperature to reach the setting number and become homogenous. Furthermore, a condition of thermodynamic equilibrium was indispensable for the reproducibility of the experiments. Thus, a total of 10 products were produced for each barrel temperature, and only the last 3 products were used for the measurement. Table 2 below shows the result of product weight and compressive strength after the testing.

**Table 2.** Experiment result

Test	Barrel temperature (°C)	Injection speed (mm/s)	Holding pressure (MPa)	Compressive strength (kg)	Part weight (kg)
1	240	72	11	5160.2	11.78
2	240	80	22	6376.7	11.78
3	240	88	33	6091.1	11.78
4	250	72	11	4407.8	11.70
5	250	80	22	4900	11.72
6	250	88	33	4454.9	11.62
7	260	72	11	5626.7	11.62
8	260	80	22	4716.1	11.63
9	260	88	33	4810.4	11.65

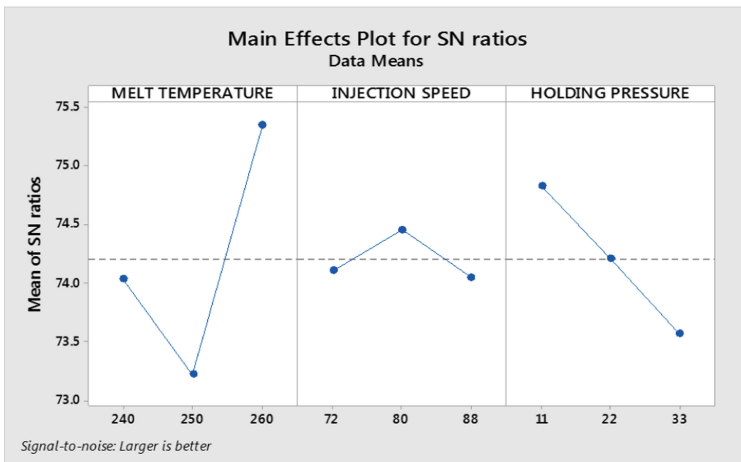
The test results were evaluated in terms of signal/noise (S/N) ratio. The S/N was calculated by larger is better for compressive strength and smaller is better for part weight. This is to determine the effect of injection parameters on selected quality characteristics. The calculated signal to noise ratio for both quality responses is listed as in Table 3 below.

From the signal to noise analysis the most significant parameter that affects the compressive strength and part weight is identified. It can be seen from Figs. 2 and 3 that the most important parameter for maximum compressive strength and minimum part weight is Barrel temperature followed by holding pressure. Injection speeds show the least effects on both selected quality characteristics. The figures also show that the most suitable value of each process parameter. The optimal injection moulding conditions for the maximum compressive strength were 260 °C barrel temperature, 11 MPa holding pressure, and 80 mm/s injection pressure. The optimal injection moulding conditions for the minimum part weight were 260 °C barrel temperature, 22 MPa holding pressure, and 80 mm/s injection pressure. However, Taguchi and signal to noise ratio alone cannot optimise multi responses. It has to be integrated with desirability functions in order to optimise both compressive and part weight quality.

The calculated signal to noise ratio of both compressive strength and part weight is converted into the dimensionless function using the desirability method. This is to

**Table 3.** S/N ratio for both responses

Test	Barrel temperature (°C)	Charging speed (mm/s)	Holding pressure (MPa)	Compressive strength (kg)	S/N ratio	Part weight (kg)	S/N ratio
1	240	72	11	5160.2	77.7169	11.78	-21.33
2	240	80	22	6376.7	76.0919	11.78	-21.36
3	240	88	33	6091.1	75.9343	11.78	-21.44
4	250	72	11	4407.8	75.793	11.70	-21.36
5	250	80	22	4900	75.9176	11.72	-21.39
6	250	88	33	4454.9	72.9768	11.62	-21.38
7	260	72	11	5626.7	75.0051	11.62	-21.39
8	260	80	22	4716.1	73.4728	11.63	-21.39
9	260	88	33	4810.4	73.6438	11.65	-21.36



**Fig. 2.** Signal to noise ratio plot for compression strength

integrate both responses into a dimensionless function called composite desirability. From this composite desirability, the most desirable value is considered as the optimal value. Table 4 below shows the individual desirability for each response and also the composite desirability.

The optimal values of the parameters are determined to maximise overall desirability (D), by applying a reduced gradient algorithm with multiple starting points. Figures 4 and 5 below shows the optimal parameter setting for individual responses. After investigating each response variable as an objective function individually, all response variables are optimised using the desirability function approach, while two response variables are considered as objective functions simultaneously.

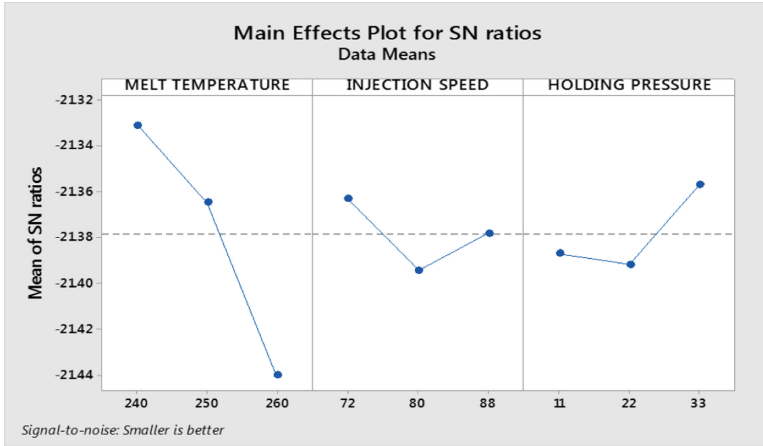


Fig. 3. Signal to noise ratio plot for part weight

Table 4. Desirability of both responses.

Compressive strength (kg)	Part weight (kg)	Compression individual desirability	Part weight individual desirability	Composite desirability
5160.2	11.79	0.190058	0.390147	0.272306
6376.7	11.82	0.137427	0.597395	0.286528
6091.1	11.8	0.084795	0.804643	0.261209
4407.8	11.725	0.47076	0.374216	0.419722
4900	11.75	0.418129	0.581464	0.493079
4454.9	11.63	0.681287	0.208032	0.37647
5626.7	11.645	0.751462	0.358285	0.518881
4716.1	11.655	1	0	0
4810.4	11.67	0.961988	0.192101	0.429883

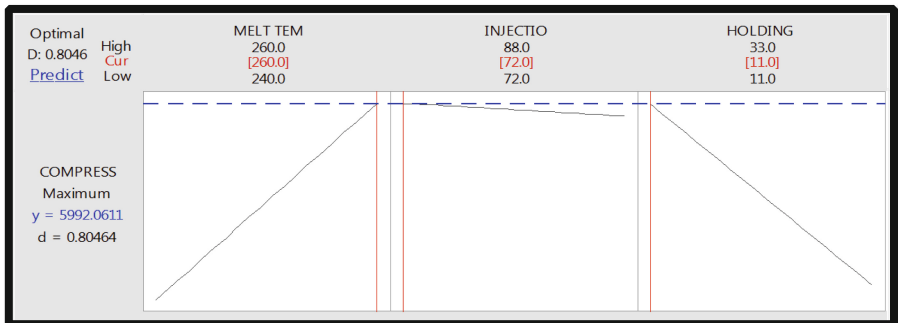


Fig. 4. Compressive strength as the response for individual optimization

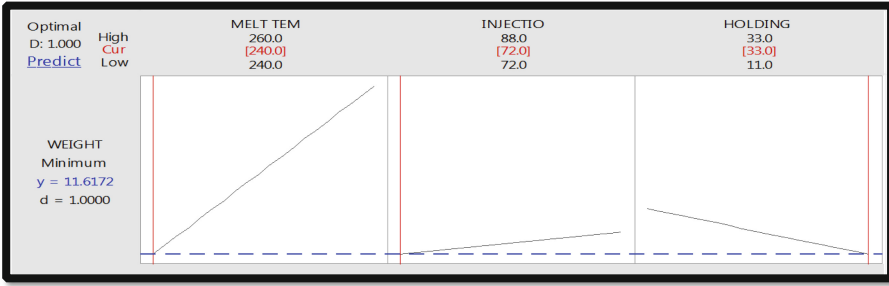


Fig. 5. Part weight as the response for individual optimisation

In Fig. 6, all the response variables are optimised simultaneously. Comparing the results obtained from the Taguchi design of experiment, the individual desirability function approach, and the composite desirability function approach, it can be seen that although optimising each response variable individually will provide a better result for each response variable but still the optimal parameter values will be different when each response variable is optimised individually. For example, considering the compressive strength variable as a response, the optimal values of factors barrel temperature, injection speed, and Holding pressure are obtained as 260, 72 and 11 respectively. However, when part weight is considered as a response variable, the optimal values are different. Considering the entire response variable as objective functions simultaneously in the composite desirability function method generates one general value for all the parameters of the algorithms, which leads to an optimal value of all the response variables. The summary of the results obtained from the composite desirability function approach is presented in Table 5.

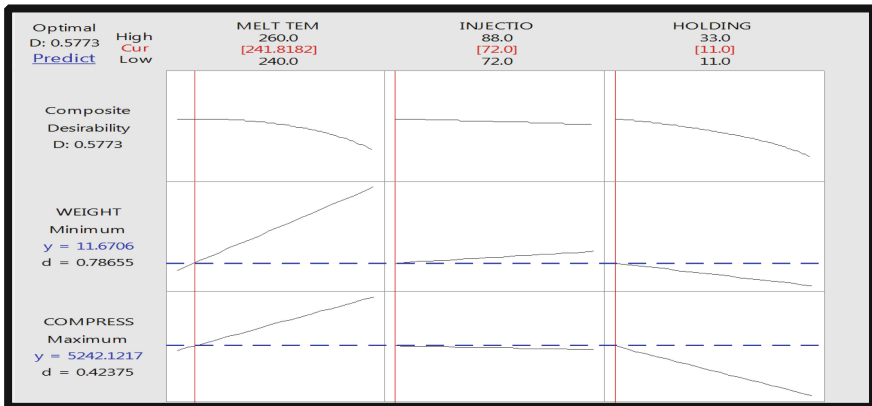


Fig. 6. Composite desirability function approach (multi responses optimisation)

**Table 5.** Results of multi-response optimisation

Responses	Factors			Predicted responses	Desirability value
	Barrel temperature	Injection speed	Holding pressure		
Compressive strength	241 °C	72 mm/s	11 MPa	5242 kg	0.57773
Part weight				11.67 kg	

The best set of process parameter is 241 °C of barrel temperature 72 mm/s injection speed and 11 MPa of holding pressure. This parameter will optimise the part quality to 5242 kg of compressive strength and can result in the part weight of 11.6 kg. Once the optimal combination of process parameters and their level was obtained, the final step is to verify the estimated result. A confirmation test is performed to validate the results of Taguchi optimisation and provide evidence that interaction effects between factors are low. In practice, it is very hard to state with confidence how close the experiment number must come to the predicted values for the agreement to be considered good. Hence, it can only be applied to the present set of parameters. The confirmation injection test was set up with the optimal combination using the same material and injection machine. A plastic pallet was moulded and compressive strength test is performed. The average compressive strength and part weight were calculated. The value of average compressive strength and part weight obtained from the confirmation experiment was then compared with the estimated value as shown in Table 6.

**Table 6.** Confirmation test of optimised parameter

Responses	Optimisation prediction	Actual result	Error
Compressive strength	5242 kg	5500 kg	4.6%
Part weight	11.67 kg	11.7 kg	0.2%

All experimental values are within a 20% difference from predicted results. As error values must be smaller than 20% for reliable statistical analyses, error values below 20% were accepted in the literature Kuram et al. [15]. The predicted results had very close values with the experimental results, thus the optimisation approach used in this study is effective and practical.

### 4.3 Quantitative Relationship Between Process Parameter and Quality

Regression analysis was a statistical tool for the investigation of relationships between variables. R-Square is correlation coefficient and should be between 0.8 and 1 in multiple linear regression analyses, Ozcelik [15]. The purpose of R-Square value is the prediction of future outcomes on the basis of other related data. It provides a measure of how well results are appropriate to be predicted by the model. A linear model between



injection moulding parameters and quality characteristics were created. The model is shown in Eqs. 1 and 2.

$$\begin{aligned} \text{Compressive strength} = & -23028 + 86.2 \text{ Barrel temperature} + 123.6 \text{ injection speed} \\ & - 42.6 \text{ holding pressure} \end{aligned} \quad (1)$$

$$\begin{aligned} \text{Weight} = & 9.827 + 0.00733 \text{ Barrel temperature} + 0.00125 \text{ injection speed} \\ & - 0.00182 \text{ holding pressure} \end{aligned} \quad (2)$$

The relationship between process parameters and the ensuing product quality is expressed in a mathematical equation using regression equation with an R(square) of 84% for compressive strength and R(square) of 82% for part weight. This means that, all the factors of the process explain 84% of the differences in the compressive strength and explain 82% of the differences on the part weight. The model result was best explained by values of the regression coefficient, R-square, close to 1.

## 5 Conclusion and Future Works

In this study, the optimal injection moulding process parameter of warehouse plastic pallets are identified. Compressive strength and part weight are selected as quality characteristics. Barrel temperature, injection speed, and holding pressure is selected as the process parameter based on previous researches. After that, the value of each process parameter is determined by running pre-testing. The selected process parameters are used to conduct an experiment based on Taguchi experimental design. The compressive strength and part weight for each experiment were identified. Those results are used to optimise the process parameter using Taguchi and desirability functions.

For Taguchi optimisation, S/N ratio is calculated for both responses and the optimal process parameter are identified. The optimal injection moulding conditions for the maximum compressive strength were 260 °C barrel temperature, 11 MPa holding pressure, and 80 mm/s injection pressure. The optimal injection moulding conditions for the minimum part weight were 260 °C barrel temperature, 22 MPa holding pressure, and 80 mm/s injection pressure. The calculated signal to noise ratio of both compressive strength and part weight is converted into the dimensionless function using the desirability method. The best set of process parameter that is optimised using desirability functions is 241 °C of barrel temperature 72 mm/s injection speed and 11 MPa of holding pressure which optimise the part quality to 5242 kg of compressive strength and 11.6 kg of part weight. The percentage error of optimised process parameter for compressive strength is 4.6% and for part weight is 0.2%. The response variable of the optimised process parameter had very close values with the experimental results, thus the optimisation approach used in this study is effective and practical.

Moreover, a quantitative relationship between the process parameter and the selected quality response is established using regression analysis. The constructed regression model can be validated using the R-square. The relationship between process parameters and the ensuing product quality is expressed in a mathematical equation using regression equation with an R-square of 84% for compressive strength and R-square of 82% for part weight. This means that all the factors of process explain 84% of the differences in the compressive strength and explain 82% of the differences on the part weight. The percentage error of the prediction model for compressive strength is 10% and for part weight is 0.3%. For reliable statistical analyses, error values must be smaller than 20%. Since comparisons were done according to average experimental values and the errors are within the acceptable range. Thus, the prediction model used in this study is effective and practical.

By optimisation, the product weight is reduced about 0.2 kg with optimum compressive strength. The pallet production for 1 day is about 1200 pieces, with 0.2 kg of material saving for each pallet, we can save around 240 kg of polypropylene per day and 7200 kg of material per month. The price range of 1 kg of recycled polypropylene in Malaysia is around Rm 2.70–Rm 2.90. Taking the minimum price, we can save around Rm 20,880 per month and RM 250,560 annually, ensuring better product quality.

Future developments of this work may be the extension of the DoE plan to other uninvestigated parameters, like packing time or injection pressure, and the mechanical characterization of the polymer through Charpy and Hopkinson bar tests. Moreover, in-cavity sensors information or barrel heater can be investigated. The relationship between the melt properties inside the barrel before the injection and the product quality can be studied. An online process parameter monitoring and adjustment can be achieved using the quantitative relationship between the Melt flow in the barrel and the product quality.

**Acknowledgments.** The author would like to give special thanks to Research & Innovation Department, Universiti Malaysia Pahang, Malaysia for funding this research project (RDU180322).

## References

1. Altan, M.: Reducing shrinkage in injection mouldings via the Taguchi, ANOVA and neural network methods. *Mater. Des.* **31**(1), 599–604 (2010)
2. Lal, S.K., Vasudevan, H.: Optimisation of injection moulding process parameters in the moulding of low density polyethylene (LDPE). *Int. J. Eng. Res. Dev.* **7**(5), 35–39 (2013)
3. Kale, H.P., Hambire, D.U.V.: Optimisation of injection molding process parameter for reducing shrinkage by using high density polyethylene (HDPE) material. *Int. J. Sci. Res.* **4**(5), 722–725 (2013)
4. Osarenmwinda, J.O., Olodu, D.D.: Optimisation of injection moulding process parameters in the moulding of high density polyethylene (HDPE). *J. Appl. Sci. Environ. Manag.* **22**(2), 203–206 (2018)
5. Sreedharan, J., Jeevanantham, A.K.: Analysis of shrinkages in ABS injection molding parts for automobile applications. *Mater. Today Proc.* **5**(5), 1274412749 (2018)

6. Singh, G., Pradhan, M.K., Verma, A.: Effect of injection moulding process parameter on tensile strength using Taguchi method. *World Acad. Sci. Eng. Technol., Int. J. Ind. Manuf. Eng.* **9**(10) (2015)
7. Pareek, R., Bhamniya, J.: Optimization of injection moulding process using Taguchi and ANOVA. *J. Sci. Eng. Res.* **4**(1) (2013)
8. Rath, M.M., Salunke, M.M.D.: Analysis of injection moulding process parameters. *Int. J. Eng. Res. Technol.* **1**(8), 1–5 (2012)
9. Shi, H., Xie, S., Wang, X.: A warpage optimization method for injection molding using artificial neural network with parametric sampling evaluation strategy. *Int. J. Adv. Manuf. Technol.* **65**(1–4), 343–353 (2013)
10. Yizong, T., Ariff, Z.M., Khalil, A.M.: Influence of processing parameters on injection molded polystyrene using Taguchi method as design of experiment. *Procedia Eng.* **184**, 350–359 (2017)
11. Kc, B., Faruk, O., Agnelli, J.A.M., Leao, A.L., Tjong, J., Sain, M.: Sisalglass fiber hybrid biocomposite: optimization of injection molding parameters using Taguchi method for reducing shrinkage. *Compos. Part A Appl. Sci. Manuf.* **83**, 152–159 (2016)
12. Fei, N.C., Mehat, N.M., Kamaruddin, S.: Practical applications of Taguchi method for optimization of processing parameters for plastic injection moulding: a retrospective review. *ISRN Ind. Eng.* (2013)
13. Zhou, X., Zhang, Y., Mao, T., Zhou, H.: Monitoring and dynamic control of quality stability for injection molding process. *J. Mater. Process. Technol.* **249**, 358–366 (2017)
14. Gingtong, T., Nakpathomkun, N., Pechyen, C.: Effect of injection parameters on mechanical and physical properties of super ultra-thin wall propylene packaging by Taguchi method. *Results Phys.* **9**, 987–995 (2018)
15. Kuram, E., Tasci, E., Altan, A.I., Medar, M.M., Yilmaz, F., Ozcelik, B.: Investigating the effects of recycling number and injection parameters on the mechanical properties of glass-fibre reinforced nylon 6 using Taguchi method. *Mater. Des.* **49**, 139–150 (2013)



# Utilization of Analytical Hierarchy Process (AHP) for Selecting the Best Design Concept of Conveyor System

K. N. Kamaludin<sup>1</sup>, L. Abdullah<sup>1</sup>(✉), M. N. Maslan<sup>1</sup>, R. Zamri<sup>1</sup>,  
M. Mat Ali<sup>1</sup>, M. S. Syed Mohamed<sup>1</sup>, and M. S. Noorazizi<sup>2</sup>

<sup>1</sup> Faculty of Manufacturing, Universiti Teknikal Malaysia Melaka,  
76100 Durian Tunggal, Melaka, Malaysia  
lokman@utem.edu.my

<sup>2</sup> Department of Engineering, Razak Faculty of Technology and Informatics,  
UTM Kuala Lumpur, Level 6 Razak Tower, Jalan Sultan Yahaya Petra,  
54100 Kuala Lumpur, Malaysia  
noorazizi@utm.my

**Abstract.** Accurate concept selection during product development is a crucial process. Inappropriate selection could reason the manufactured goods to have a high failure rate in the market. Analytical Hierarchy Process (AHP) offer as an alternative tool to cater decision-making process. AHP act as a tool in almost all applications related to decision-making problems. This paper presents the methodology and results of a case study which adopts AHP concept. The steps taken can be a guideline that will be able to assist designers or engineers, to effectively analyze various design criteria, alternatives at the conceptual design stage, and finally a precise decision-making.

**Keywords:** Analytical Hierarchy Process · Conceptual design selection · Product development process · Pairwise comparison · Conveyor development

## 1 Introduction

Material handling in manufacturing environment comprises the flow of a material or a product between one station to another via a carriage. It utilizes a broad range of manual, semi-automatic, and fully automatic machines and contains application of the inventory control of the materials during the industrial process. Material handling system is used in moving and controlling the goods throughout the process. By using the material handling system, the material that is transferred is in the right amount and can be reached the destination on time with minimum cost. The effective material handling can minimum the cost of operation, cycle time and decrease the damage. It helps to maximum the flexibility and higher automation and material flow in handling.

Material handling plays a significant role in a production exercise. It is a routine that need to undergo in each and every manufacturing plant. The process of material handling includes pick up, lie down and moving the material through manufacturing station.

In this paper, Analytic Hierarchy Process (AHP) is utilized for the purpose of choosing the best design concept of material handling system that integrates the qualitative and quantitative of each criterion in the decision structure. AHP is extensively applied as multi-variable-criteria decision investigation which decomposes the decision problem in a hierarchy structure and derives priorities from the value judgments of individual or in a group of decision making.

## 2 Review on Analytical Hierarchy Process AHP

According to [1, 2], the Analytic Hierarchy Process (AHP) has productively been used to the ranking process of decision-making problem which is extensively adopted in Multi-criteria decision making (MDCM) method. The Analytic Hierarchy Process (AHP) delivers a framework to endure with multiple criteria conditions which relating the logic, quantitative, qualitative and intuitive phases. [3] claim that the Analytic Hierarchy Process (AHP) is an efficient way created in late 1970 to set up the experience, instinct, and heuristic-based decision making into well-described approach by using the mathematical way of thinking. By using AHP method, the decision made can occur in two sequential which are hierarchy design and hierarchy evaluation.

Three rules of AHP are as follows [4–7]:

**I. Decomposition principle.** To trace the fundamental features in the problem, structuring of the hierarchy is required. The hierarchy works downward from the common objectives and aims to the options available. It is the typical process which works from general to more definite elements. The decision hierarchy will have more stages based on the difficulty of a problem.

**Table 1.** Measure of pair-wise relation [2]

Weightage intensity	Outline	Description
1	Identical score	Two factors are of equal score
3	Marginally extra score	Situation where marginally prefer one over another
5	Strong score	Situation where strong prefer one condition over another

(continued)

**Table 1.** (continued)

Weightage intensity	Outline	Description
7	Very strong score	Situation where very strong preferred and its superiority is showed in practice
9	Enormously strong score	The proof of preferring one over another is of the utmost possible order of confirmation
2, 4, 6, 8	In-between scores among two adjacent choice	Situation where settlement is required
Reciprocals	Reciprocals for inverse comparison	

**II. The principle of comparative judgments.** To carry out the pair-wise relations, the formation of the matrix is required. [4] had stated that the scale for the comparisons of the elements comprising equally into important, moderately important, strongly important, very strongly important and extremely important. These five verbal scales then converted into a judgment of numerical that corresponding to 1, 3, 5, 7, and 9. The scale of comparison is shown in Table 1.

**III. The principle of the synthesis of priorities.** From the second level down, the weight of priority is synthesized by multiplying the local priorities with the priority of the corresponding criterion in above level. Then, adding them for each of the factors in a level according to the factors that affected.

### 3 Framework of AHP via Conceptual Design

Six stages are defined during product development process [2]. Conceptual design is one of the stages and proven as a crucial stage. Expanded from product development process are the three process, (1) concept generation, (2) concept evaluation and (3) concept development. This paper focuses on (2) concept evaluation. AHP method is implemented for the development of the product, conveyor, to select the best design concept (Fig. 1).

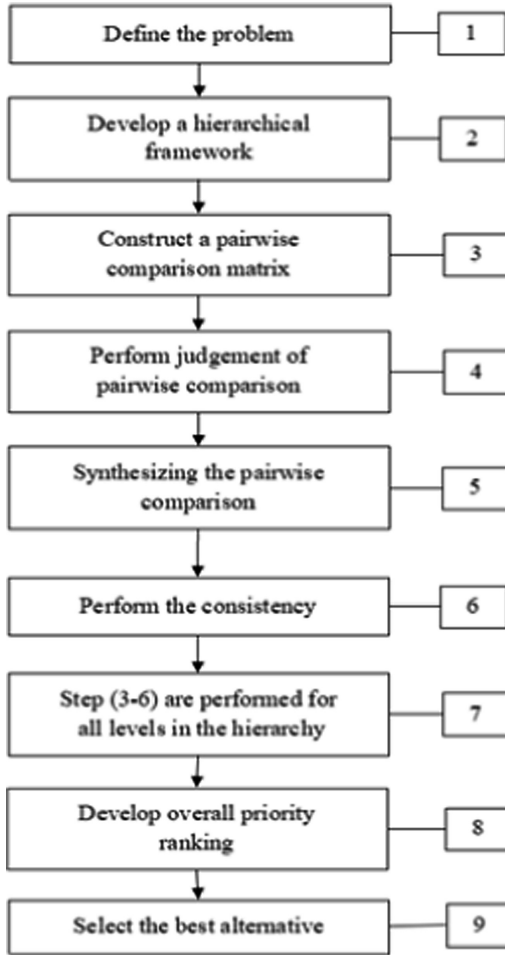


Fig. 1. The steps of the analytical hierarchy process (AHP) [2]

### 3.1 Step 1: Define the Problem

Selection of design concept for a conveyor system is presented in this research. A thorough study has been done for the types of conveyors to choose from. Four conveyor design is concluded as in Fig. 2. AHP will then be used to elect the most appropriate project.

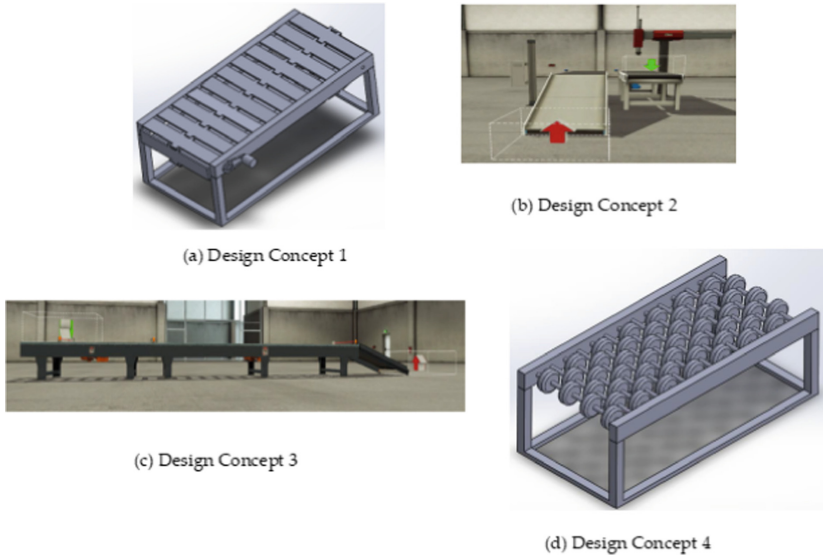


Fig. 2. Decision options - conveyor design concepts

### 3.2 Step 2: Develop a Hierarchy Model

Hierarchy model for forming design concept decisions using AHP is presented. A three stages ladder selection process is shown in Fig. 3:

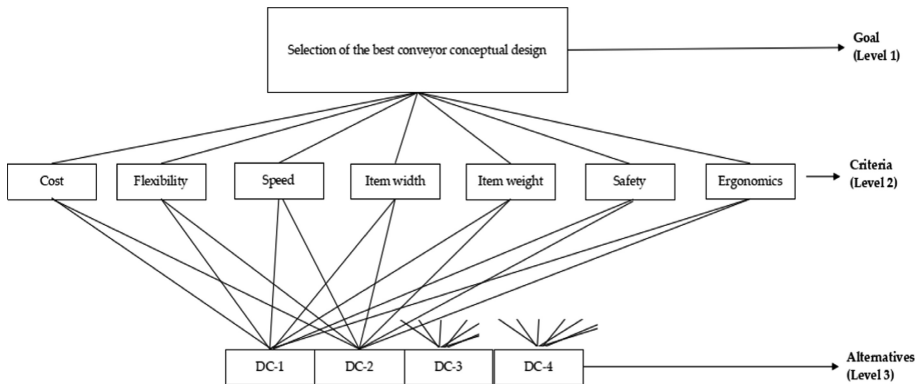


Fig. 3. A hierarchy model of design concept

**Level 1.** The main goals or the overall target is at the most top level of the ladder. To “choose the most appropriate conveyor conceptual design”, is the main overall goal.

**Level 2.** The next corresponding level is “criteria”, which will affect the selection and the development of the conveyor system design. As Fig. 3 shows, the criteria are: cost, flexibility, speed, item width, item weight, safety and ergonomics.



**Level 3.** The lowest level of the hierarchy, the “design concept (DC)” alternatives of the conveyor are known to be the least of the hierarchy level in decision options, presented in Fig. 2.

**3.3 Step 3: Creation of “Pair-Wise” Relation Matrix**

The major advantages in AHP is the utilization of “pair-wise” relation, to be able to extract precise “ratio-scale priorities” as shown in Table 2. Pair-wise is the basic to the AHP approach [2]. A pair-wise relation matrix of  $(n \times n)$ , is created for the least hierarchy, with an immediate higher level within the matrix. A matrix of “relative-rankings” for each hierarchy will be automatically created. Each element in the hierarchy will denote the number of matrices, whereas the number of elements at the hierarchy below associated, will denote the order of the matrix.

**Table 2.** Characteristics of design concepts

	Cost (€/h)	Speed (m/min)	Item width (cm)	Item weight (kg)	Flexibility (%)	Safety (%)	Ergonomics (%)
DC1	1.50–2.00	8–12	2–15	0–10	13–17	80–90	80–90
DC2	1.85–2.30	9–13	2–20	0–10	15–19	75–92	78–90
DC3	1.75–2.25	7–11	3–30	0–20	16–20	80–90	80–92
DC4	1.90–2.40	6–10	3–25	0–15	14–18	70–85	86–90

**3.4 Step 4: Judgement of Pair-Wise Relation Execution**

To execute pair-wise relation, the first step is to compare two nominated items, it’s “importance-relativity”. There would be  $n \times (n - 1)$  no of judgement needed during this process, in developing the set of matrices (as in step 3). Relation of each element by referring to the “measure of pair-wise relation” as in Table 1 is executed. Here is where developers experience, knowledge or surveys solidify the judgement. Engineering intuition is highly applicable in this step. As an example shown in Table 3, if “Cost” is a “very strong score factor” over “Speed”, then  $a = 7$ . This is performed to all of the “pair-wise” item [2].

**Table 3.** Pair-wise relation of criteria accordingly to overall target

Criteria	Cost	Flexibility	Speed	Item width	Item weight	Safety	Ergonomics
Cost	1	2	7	9	9	7	7
Flexibility	1/2	1	2	2	2	3	2
Speed	1/7	1/2	1	2	2	2	2
Item width	1/9	1/2	1/2	1	2	2	2
Item weight	1/9	1/2	1/2	1/2	1	2	2
Safety	1/7	1/3	1/2	1/2	1/2	1	2
Ergonomics	1/7	1/2	1/2	1/2	1/2	1/2	1
$\Sigma$	2.1508	5.333	13.5000	18.5000	18.5000	16.0000	13.5000

**3.5 Step 5: Analyzing/Synthesizing the Pair-Wise Relation**

In this step, to calculate the vectors of priorities, ANC (Average of normalized column) method is used. Elements of each column, is divided by the sum of the column. Then adding the element in each resulting row. This sum, will then be divided by the number of elements in the row (denote  $n$ ).

Mathematically, the above is written as:

$$W_i = \frac{1}{n} \sum_{j=1}^n \frac{a_{ij}}{\sum_i^n a_{ij}}, \quad i, j = 1, 2, \dots, n \tag{1}$$

The first priority vector calculations are summarized in the two tables below (Tables 4 and 5).

**Table 4.** Analyzed matrix: pair-wise relation of criteria

	Cost	Flexibility	Speed	Item width	Item weight	Safety	Ergonomics	Σ
Cost	1 ÷ 2.1508 = 0.4649	2 ÷ 5.333 = 0.3750	7 ÷ 12.0000 = 0.5833	9 ÷ 15.5000 = 0.5806	9 ÷ 17.0000 = 0.5294	7 ÷ 17.5000 = 0.4000	7 ÷ 18.000 = 0.3889	3.3222
Flexibility	1/2 ÷ 2.1508 = 0.2325	1 ÷ 5.3333 = 0.1875	2 ÷ 12.0000 = 0.1667	2 ÷ 15.5000 = 0.1290	2 ÷ 17.000 = 0.1176	3 ÷ 17.5000 = 0.1714	2 ÷ 18.0000 = 0.1111	1.1159
Speed	1/7 ÷ 2.1508 = 0.0664	1/2 ÷ 5.3333 = 0.0938	1 ÷ 12.0000 = 0.0833	2 ÷ 15.5000 = 0.1290	2 ÷ 17.0000 = 0.1176	2 ÷ 17.5000 = 0.1143	2 ÷ 18.0000 = 0.1111	0.7156
Item width	1/9 ÷ 2.1508 = 0.0517	1/2 ÷ 5.3333 = 0.0938	1 ÷ 12.0000 = 0.0833	1 ÷ 15.5000 = 0.0645	2 ÷ 17.000 = 0.1176	2 ÷ 17.5000 = 0.1143	2 ÷ 18.0000 = 0.1111	0.5946
Item weight	1/9 ÷ 2.1508 = 0.0517	1/2 ÷ 5.3333 = 0.0938	1/2 ÷ 12.0000 = 0.0417	1/2 ÷ 15.5000 = 0.0323	1 ÷ 17.0000 = 0.0588	2 ÷ 17.5000 = 0.1143	2 ÷ 18.0000 = 0.1111	0.5036
Safety	1/7 ÷ 2.1508 = 0.0664	1/3 ÷ 5.3333 = 0.0625	1/2 ÷ 12.0000 = 0.0417	1/2 ÷ 15.5000 = 0.0323	1/2 ÷ 17.000 = 0.0294	1/2 ÷ 17.5000 = 0.0286	2 ÷ 18.0000 = 0.1111	0.4005
Ergonomics	1/7 ÷ 2.1508 = 0.0664	1/2 ÷ 5.3333 = 0.0938	1/2 ÷ 12.0000 = 0.0417	1/2 ÷ 15.5000 = 0.0323	1/2 ÷ 17.000 = 0.0294	1/2 ÷ 17.5000 = 0.0286	1 ÷ 18.0000 = 0.0556	0.3476

**Table 5.** Priority vector (PV) calculation: weightage/n

Criteria	Weightage
Cost	3.3222/7 = 0.4746
Flexibility	1.1159/7 = 0.1594
Speed	0.7156/7 = 0.1022
Item width	0.5946/7 = 0.0849
Item weight	0.5036/7 = 0.0719
Safety	0.4005/7 = 0.0572
Ergonomics	0.3476/7 = 0.0497

### 3.6 Step 6: Executing Consistency Test

A degree of inconsistency can be expected, due to the relations judgment is carried out by the use of subjective substances. To assure that the judgement is consistent, consistency test is a necessary step. AHP incorporates consistency ratio [8–12]. The consistency test is concluded by the consistency ratio (CR). Consistency ratio (CR) is consistency index (CI) over random index (RI), as part 3.6.3 shows. Below, are the three steps to execute calculation of the consistency ratio (CR).

**Table 6.** New vector (NV) from eigenvalue

Criteria	Consistency value
Cost	$[(1 \times 0.4746) + (1 \times 0.1594) + (7 \times 0.1022) + (9 \times 0.0849) + (9 \times 0.0719) + (7 \times 0.0572) + (7 \times 0.0497)] \div 0.4746 = 7.7309$
Flexibility	$[(1/2 \times 0.4746) + (1 \times 0.1594) + (2 \times 0.1022) + (2 \times 0.0849) + (2 \times 0.0719) + (3 \times 0.0572) + (2 \times 0.0497)] \div 0.1594 = 7.4394$
Speed	$[(1/7 \times 0.4746) + (1/2 \times 0.1594) + (1 \times 0.1022) + (2 \times 0.0849) + (2 \times 0.0719) + (2 \times 0.0572) + (2 \times 0.0497)] \div 0.1022 = 7.6033$
Item Width	$[(1/9 \times 0.4746) + (1/2 \times 0.1594) + (1/2 \times 0.1022) + (1 \times 0.0849) + (2 \times 0.0719) + (2 \times 0.0572) + (2 \times 0.0497)] \div 0.0849 = 7.3707$
Item weight	$[(1/9 \times 0.4746) + (1/2 \times 0.1594) + (1/2 \times 0.1022) + (1/2 \times 0.0849) + (1 \times 0.0719) + (2 \times 0.0572) + (2 \times 0.0497)] \div 0.0719 = 7.1135$
Safety	$[(1/7 \times 0.4746) + (1/3 \times 0.1594) + (1/2 \times 0.1022) + (1/2 \times 0.0849) + (1/2 \times 0.0719) + (1 \times 0.0572) + (2 \times 0.0497)] \div 0.0572 = 7.1140$
Ergonomics	$[(1/7 \times 0.4746) + (1/2 \times 0.1594) + (1/2 \times 0.1022) + (1/2 \times 0.0849) + (1/2 \times 0.0719) + (1/2 \times 0.0572) + (1 \times 0.0497)] \div 0.0497 = 7.1550$

#### 3.6.1 Calculate the Eigenvalue ( $\lambda_{max}$ )

To calculate the weightage of criteria, the total of the adjusted pair-wise relation matrix has to be divided with the number of criteria. To calculate the consistency, the weightage of each criterion are then multiplied with the scale of the criteria. The maximum consistency of criteria in this case, is cost with a value of 7.7309 (Table 6).

#### 3.6.2 Calculate the Consistency Index (CI)

$$CI = (\lambda_{max} - n)/(n - 1)$$

$$\frac{7.7309 + 7.4394 + 7.6033 + 7.3707 + 7.1135 + 7.1140 + 7.1550}{7-1} - 7 = 0.0602. \tag{2}$$

**3.6.3 Calculate Consistency Ratio (CR)**

$$\begin{aligned}
 CR &= CI/RI \\
 &= 0.0602/1.32 = 0.0456
 \end{aligned}
 \tag{3}$$

To calculate the CR, CI is divided with the AHP Random Index. The Consistency Ratio is 0.0456. The value has to be less than 0.1 to considered as consistent. If the CR is higher than 0.1, the CR is defined as “inconsistent” [13–17] (Table 7).

**Table 7.** AHP random index table

Size of matrix ( <i>n</i> )	1	2	3	4	5	6	7	8	9	10	11	12
Random index (RI)	0	0	0.58	0.9	1.12	1.24	1.32	1.41	1.45	1.49	1.51	1.58

**3.7 Step 7: Repetition of Steps 3–6 to All Levels in the Hierarchy**

As calculated, all the value of CR for sub-criteria and alternatives is less than 0.1. Therefore, the result is deemed “acceptable” [18–21]. A detail example for criterion 1 “Cost”, and all the others sub-criteria, are as below (Tables 8, 9, 10, 11, 12, 13, 14).

**Table 8.** Consistency test for sub-criteria 1: cost

	DC-1	DC-2	DC-3	DC-4	Priority Vector (PV)	New Vector (NV)	NV/PV	Consistency Index (CI) = 0.0395
DC-1	1	3	5	7	0.5579	2.3556	4.2223	Consistency Ratio (CR) = 0.0439
DC-2	1/3	1	3	5	0.2633	1.0995	4.1757	
DC-3	1/5	1/3	1	3	0.1219	0.4919	4.0357	Note: As the value of CR is less than 0.1, the judgement is acceptable
DC-4	1/7	1/5	1/3	1	0.0569	0.2299	4.0403	
						Total	16.4739	
			Max eigenvalue ( $\lambda$ max)			4.1185		

**Table 9.** Consistency test for sub-criteria 2: flexibility

	DC-1	DC-2	DC-3	DC-4	Priority Vector (PV)	New Vector (NV)	NV/PV	Consistency Index (CI) = 0.00782	
DC-1	1	3	5	7	0.5393	2.3640	4.3835	Consistency Ratio (CR) = 0.0869	
DC-2	1/3	1	5	5	0.2950	1.3033	4.4179		
DC-3	1/5	1/5	1	3	0.1101	0.4438	4.0305	Note: As the value of CR is less than 0.1, the judgement is acceptable	
DC-4	1/7	1/5	1/3	1	0.0556	0.2283	4.1069		
						Total	16.9387		
			Max eigenvalue ( $\lambda$ max)					4.2347	

**Table 10.** Consistency test for sub-criteria 3: speed

	DC-1	DC-2	DC-3	DC-4	Priority Vector (PV)	New Vector (NV)	NV/PV	Consistency Index (CI) = 0.0663	
DC-1	1	3	3	5	0.4909	2.1519	4.3836	Consistency Ratio (CR) = 0.0737	
DC-2	1/3	1	3	5	0.2913	1.2420	4.2638		
DC-3	1/3	1/3	1	3	0.1507	0.6124	4.0639	Note: As the value of CR is less than 0.1, the judgement is acceptable	
DC-4	1/5	1/5	1/3	1	0.0670	0.2737	4.0847		
						Total	16.7959		
			Max eigenvalue ( $\lambda$ max)					4.1990	

**Table 11.** Consistency test for sub-criteria 4: width

	DC-1	DC-2	DC-3	DC-4	Priority Vector (PV)	New Vector (NV)	NV/PV	Consistency Index (CI) = 0.0663	
DC-1	1	3	3	5	0.4909	2.1519	4.3836	Consistency Ratio (CR) = 0.0737	
DC-2	1/3	1	3	5	0.2913	1.2420	4.2638		
DC-3	1/3	1/3	1	3	0.1507	0.6124	4.0639	Note: As the value of CR is less than 0.1, the judgement is acceptable	
DC-4	1/5	1/5	1/3	1	0.0670	0.2737	4.0847		
						Total	16.7959		
			Max eigenvalue ( $\lambda$ max)					4.1990	

**Table 12.** Consistency test for sub-criteria 5: weight

	DC-1	DC-2	DC-3	DC-4	Priority Vector (PV)	New Vector (NV)	NV/PV	Consistency Index (CI) = 0.0349	
DC-1	1	2	3	5	0.4560	1.9002	4.1671	Consistency Ratio (CR) = 0.0388	
DC-2	1/2	1	3	5	0.3238	1.3484	4.1643		
DC-3	1/3	1/3	1	3	0.1522	0.6161	4.0482	Note: As the value of CR is less than 0.1, the judgement is acceptable	
DC-4	1/5	1/5	1/3	1	0.0680	0.2747	4.0396		
						Total	16.4192		
			Max eigenvalue ( $\lambda$ max)					4.1048	

**Table 13.** Consistency test for sub-criteria 6: safety

	DC-1	DC-2	DC-3	DC-4	Priority Vector (PV)	New Vector (NV)	NV/PV	Consistency Index (CI) = 0.0754	
DC-1	1	3	5	3	0.5096	2.2338	4.3834	Consistency Ratio (CR) = 0.0837	
DC-2	1/3	1	3	3	0.2605	1.1201	4.2997		
DC-3	1/5	1/3	1	2	0.1265	0.5221	4.1269	Note: As the value of CR is less than 0.1, the judgement is acceptable	
DC-4	1/3	1/3	1/2	1	0.1034	0.4234	4.0943		
						Total	16.9043		
			Max eigenvalue ( $\lambda$ max)					4.2261	

**Table 14.** Consistency test for sub-criteria 7: ergonomics

	DC-1	DC-2	DC-3	DC-4	Priority Vector (PV)	New Vector (NV)	NV/PV	Consistency Index (CI) = 0.0475	
DC-1	1	3	5	7	0.5688	2.3817	4.1872	Consistency Ratio (CR) = 0.0528	
DC-2	1/3	1	3	3	0.2372	1.0085	4.2517		
DC-3	1/5	1/3	1	3	0.1280	0.5185	4.0510	Note: As the value of CR is less than 0.1, the judgement is acceptable	
DC-4	1/7	1/3	1/3	1	0.0659	0.2689	4.0803		
						Total	16.5702		
			Max eigenvalue ( $\lambda$ max)					4.1425	

### 3.8 Step 8: Finalizing Overall Priority Standing

After the consistency calculation is completed, the next process is to calculate the overall priority vector, and to multiply it with the weightage, to select the best design concept. The elements/points in Table 15 represent priority vectors for criteria, sub-criteria and alternatives.

**Table 15.** Priority vector × weightage for alternatives

Weightage / Priority Vector for alternatives					
Cost	DC1	0.5579	Width	DC1	0.4909
	DC2	0.2633		DC2	0.2913
	DC3	0.1219		DC3	0.1507
	DC4	0.0569		DC4	0.0670
Flexibility	DC1	0.5393	Weight	DC1	0.4560
	DC2	0.2950		DC2	0.3238
	DC3	0.1101		DC3	0.1522
	DC4	0.0556		DC4	0.0680
Speed	DC1	0.4909	Safety	DC1	0.5096
	DC2	0.2913		DC2	0.2605
	DC3	0.1507		DC3	0.1265
	DC4	0.0670		DC4	0.1034
			Ergonomic	DC1	0.5688
				DC2	0.2372
				DC3	0.1280
				DC4	0.0659

Priority Vector						
Cost	Flexibility	Speed	Width	Weight	Safety	Ergonomics
0.4746	0.1594	0.1022	0.0085	0.0719	0.0572	0.0497

Priority vector of the alternatives, according to the criteria is calculated and presented in Table 16. Overall priority vector is “priority vector for the design alternatives”, multiply by “priority vector of the criteria”. Example of the calculation are as below.

### 3.8.1 Design Concept 1

$$\begin{aligned}
 &= (\text{Priority Vector Cost}) \times (\text{DC1 Cost Weightage}) + (\text{Priority Vector Flexibility}) \\
 &\times (\text{DC1 Flexibility Weightage}) + (\text{Priority Vector Flexibility}) \times (\text{DC1 Flexibility Weightage}) \\
 &+ (\text{Priority Vector Flexibility}) \times (\text{DC1 Flexibility Weightage}) + (\text{Priority Vector Flexibility}) \\
 &\times (\text{DC1 Flexibility Weightage}) + (\text{Priority Vector Flexibility}) \\
 &\times (\text{DC1 Flexibility Weightage}) + (\text{Priority Vector Flexibility}) \times (\text{DC1 Flexibility Weightage}) \\
 &= (0.4746) (0.5579) + (0.1594) (0.5393) + (0.1022) (0.4909) + (0.0085) (0.4909) \\
 &+ (0.0719) (0.4560) + (0.0572) (0.5096) + (0.0497) (0.5688) = 0.4954
 \end{aligned}$$

**Table 16.** Final overall priority vector for the alternatives, with accordance to the criteria

	Cost	Flexibility	Speed	Width	Weight	Safety	Ergonomics	Overall priority
	<b>0.4746</b>	<b>0.1596</b>	<b>0.1022</b>	<b>0.0085</b>	<b>0.0719</b>	<b>0.0572</b>	<b>0.0497</b>	
DC-1	0.5579	0.5393	0.4909	0.4909	0.4560	0.5096	0.5688	0.4954
DC-2	0.2633	0.2950	0.2913	0.2913	0.3238	0.2605	0.2372	0.2543
DC-3	0.1219	0.1101	0.1507	0.1507	0.1522	0.1265	0.1280	0.1166
DC-4	0.0569	0.0556	0.0670	0.0670	0.0680	0.1034	0.0659	0.0574

### 3.9 Step 9: Best Design Concept Choice

Table 17 represents the ranking of AHP choice. Design concept-1 that has the largest value (0.4954 or 49.54%) comparing to the other design concepts. This emphasizes that it is the most appropriate design to be continued with, during the product development process. The second choice is then design concept-2 with a value of 0.2543 (25.43%), and the least design concept to be chosen is design concep-4.

**Table 17.** Design concept sorted from highest ranking to the lowest

No.	Best selection	
1	DC-1	0.4954
2	DC-2	0.2543
3	DC-3	0.1166
4	DC-4	0.0574



## 4 Conclusion

This research extracts the methodology of calculating and choosing the most appropriate design concepts at a conceptual design stage, by implementing analytical hierarchy process AHP. AHP can easily be adopted by designers and engineers, to determine a best design concept, based on a certain criterion (and with more sub-criteria) of a decision. Design concept 1 has been determined as the best design in this analysis, as it resulted the highest value of 0.4954, versus other concepts. Application of AHP can cater factors during product development process such as, strengthen the quality of a product, and decrease the duration time of product development process.

**Acknowledgement.** The authors would like to acknowledge the financial support by Universiti Teknikal Malaysia Melaka (UTeM) under short term grant scheme (PJP) Universiti Teknikal Malaysia Melaka with reference number PJP/2018/FKP(7C)/S01588.

## References

1. Saaty, T.L.: The Analytic Hierarchy Process. McGraw-Hill, New York (1980)
2. Ariff, H., Salit, M.S., Ismail, N., Nukman, Y.: Use of analytical hierarchy process (AHP) for selecting the best design concept. *J. Teknol.* **49**(1), 1–8 (2008). <https://doi.org/10.11113/jt.v49.188>
3. Vargas, L.G.: An overview of the analytic hierarchy process and its applications. *Eur. J. Oper. Res.* **48**(1), 2–8 (1990). <https://doi.org/10.1016/j.ejor.2004.04.028>
4. Fonseca, D.J., Uppal, G., Greene, T.J.: A knowledge-based system for conveyor equipment selection. *Expert Syst. Appl.* **26**(4), 615–623 (2004). <https://doi.org/10.1016/j.eswa.2003.12.011>
5. Chu, H.K., Egbelu, P.J., Wu, C.T.: ADVISOR: a computer-aided material handling equipment selection system. *Int. J. Prod. Res.* **33**(12), 3311–3329 (1995). <https://doi.org/10.1080/00207549508904876>
6. Hsiao, S.W.: Concurrent design method for developing a new product. *Int. J. Ind. Ergon.* **29**, 41–55 (2002). [https://doi.org/10.1016/S0169-8141\(01\)00048-8](https://doi.org/10.1016/S0169-8141(01)00048-8)
7. Ananda, J., Herath, G.: A critical review of multi-criteria decision making methods with special reference to forest management and planning. *Ecol. Econ.* **68**(10), 2535–2548 (2009). <https://doi.org/10.1016/j.ecolecon.2009.05.010>
8. Bhushan, N., Rai, K.: Strategic Decision Making Applying the Analytic Hierarchy Process. Springer, New York (2004)
9. Chan, F.T.S., Ip, R.W.L., Lau, H.: Integration of expert system with analytic hierarchy process for the design of material handling equipment selection system. *Mater. Process. Technol.* **116**(2), 137–145 (2001). [https://doi.org/10.1016/S0924-0136\(01\)01038-X](https://doi.org/10.1016/S0924-0136(01)01038-X)
10. Chatterjee, P., Athawale, V.M., Chakraborty, S.: Selection of industrial robots using compromise ranking and outranking methods. *Robot. Comput. Integrated Manuf.* **26**(5), 483–489 (2010). <https://doi.org/10.1016/j.rcim.2010.03.007>
11. Dongre, A., Mohite, N.Y.: Significance of selection of material handling system design in industry: a review. *Int. Eng. Res. Gen. Sci.* **3**(2): 76–79. (2015). <http://citeseerx.ist.psu.edu/viewdoc/download?10.1.1.735.2191&rep=rep1&type=pdf>
12. Forman and Gass: The analytic hierarchy process: an exposition. *Oper. Res.* **49**(4), 469–486 (2001). <https://doi.org/10.1287/opre.49.4.469.11231>

13. Ho, W.: Integrated analytic hierarchy process and its applications: a literature review. *Eur. J. Oper. Res.* **186**, 211–228 (2008). <https://doi.org/10.1016/j.ejor.2007.01.004>
14. Kim, K.S., Eom, J.K.: Expert system for selection of material handling and storage system. *Int. Ind. Eng. Theory Appl. Pract.* **4**(2), 81–89 (1997). <http://www.scopus.com/inward/record.url?scp=0031164007&partnerID=8YFLogxK>
15. Matson, J.O., Mellichamp, J.M., Swaminathan, S.R.: EXCITE: expert consultant for in-plant transportation equipment. *Int. J. Prod. Res.* **30**(8), 1969–1983 (1992). <https://doi.org/10.1080/00207549208948133>
16. Mergias, I., Moustakas, K., Papadopoulos, A., Loizidou, M.: Multi-criteria decision aid approach for the selection of the best compromise management scheme for ELVs: the case of Cyprus. *J. Hazard. Mater.* **147**(3), 706–717 (2007). <https://doi.org/10.1016/j.jhazmat.2007.01.071>
17. Malmborg, C.J., Agee, S.M.H., Choudhary, J.V.: A prototype expert system for industrial truck type selection. *Ind. Eng.* **19**(3), 58–65 (1987). <https://dl.acm.org/citation.cfm?id=29453>
18. Pugh, S.: *Total Design: Integrated Methods for Successful Product Engineering*. Addison Wesley Limited, Wokingham (1991)
19. Sari, K.: Selection of RFID solution provider. *Kybernetes* **42**(3), 448–465 (2013). <https://doi.org/10.1108/03684921311323680>
20. Sule, D.R.: *Manufacturing facilities: location, planning and design*, 2nd edn. PWS Publishing Company, Boston (1994). <https://doi.org/10.1080/03043799408928311>
21. Vargas, L.G.: An overview of the analytic hierarchy process and its applications. *Eur. J. Oper. Res.* **48**(1), 2–8 (1990). <https://doi.org/10.1016/j.ejor.2004.04.028>



# Fabrication of Polypropylene/Acrylonitrile Butadiene Rubber/Kenaf Core Composites: Effect of Polypropylene Maleic Anhydride as Compatibilizer

Nurul Syazwani Othman<sup>1</sup>(✉), Ragunathan Santiagoo<sup>1</sup>,  
Wan Azani Mustafa<sup>2</sup>, Nur Liyana Othman<sup>1</sup>,  
and Mohd Al Hafiz Mohd Naw<sup>2</sup>

<sup>1</sup> School of Environmental Engineering, Universiti Malaysia Perlis,  
Pusat Jejawi 3, 02600 Arau, Perlis, Malaysia

wanienurul91@yahoo.com, raguna@unimap.edu.my

<sup>2</sup> Faculty of Engineering Technology, Kampus Sg. Chuchuh,  
Universiti Malaysia Perlis, 02100 Padang Besar, Perlis, Malaysia

**Abstract.** The fabrication of polypropylene (PP)/acrylonitrile butadiene rubber (NBR)/kenaf core (KC) composites were investigated. Tensile and morphological properties of composites were evaluated with the addition of polypropylene maleic anhydride (PPMAH) as a compatibilizer. Five compositions of PP/NBR/KC with varied NBR loading (0–60 phr) were prepared with the addition of constant PPMAH ratio at 5phr. All the materials were melt mixed using a heated two-roll mill at temperature 180 °C and speed of 50 rpm. PP/NBR/KC compounds were compressed into 1 mm thin sheet by using a hot press machine and cut into a dumbbell shape specimen. The tensile test was conducted according to ASTM D 638 using a Universal Testing Machine. The results indicated that tensile strength slightly decreased with increasing NBR loading. However, it is interesting to observe that PP/NBR/KC composites with PPMAH compatibilizer have better tensile strength. Almost 43% improvement resulted for PP/NBR/KC/PPMAH composites with ratio 70/30/10. From scanning electron microscopy (SEM) analysis, composites with PPMAH compatibilizer show good attachment of KC filler with PP/NBR matrices.

**Keywords:** Kenaf core · Thermoplastic elastomer · Polypropylene · Acrylonitrile butadiene rubber · Tensile strength

## 1 Introduction

Thermoplastic elastomer (TPE) is a type of thermoplastic polymer as it can be melt-processed like plastic and recyclable [1, 2]. Due to the elastomeric component from rubber, TPE is a soft and flexible material. TPE was hardened when cooled and become soft when heated. The rubbery matrix in the composites contributed to the soft segments [3] while the reversible physical or chemical interaction of the macromolecules gave the hard segments crosslinks. The molecular networks were stacked together by

the physical crosslinks at the working temperature, whenever there is solid-to-liquid transitions occurred at elevated temperature as the crosslinks part will break.

Kenaf core is one of the natural fibres that have attention from many researchers to studied and added as a filler in PP/NBR matrices [4]. Cheap, renewable, recyclable and biodegradable make natural fibres become an alternative filler to replace the synthetic polymers [5]. Due to the hydrophilic characters of kenaf core and the hydrophobic characters of TPE polymers, this immiscibility is individually in charge of the decrease of mechanical properties. Thus, a compatibilizer was added into the formulation in order to improve the performance of PP/NBR/KC composites. In this research, PP/NBR/KC composites were fabricated with and without PPMAH compatibilizer to determined the tensile strength and observed the morphological part.

## 2 Materials and Method

### 2.1 Materials and Samples Preparation

PP grade 6331 was obtained from the Titan Pro Polymers (M) Sdn. Bhd, Johor Malaysia with melt flow index of 14 g/10 min at 230 °C. Kenafcorewas obtained from the National Kenaf and Tobacco Board (NKTB). The kenaf was first being dried in the oven for about 24 h at 80 °C in order to remove any moisture. Kenaf is then being shredded and turn into the powder form. The kenaf powder was sieved by using Endecott'ssiever with the size of less than 300 µm. For compatibilizer, maleic anhydride grafted polypropylene (PPMAH) were obtained from the Sigma Aldich Chemical. Table 1 shows the formulation of PP/NBR/KC composites with and without PPMAH compatibilizer.

**Table 1.** Formulation of PP/NBR/KC and PP/NBR/KC/PPMAH composites

Materials	PP/NBR/KC composites						PP/NBR/KC/PPMAH composites					
PP	100	80	70	60	50	40	100	80	70	60	50	40
NBR	0	20	30	40	50	60	0	20	30	40	50	60
KC	10	10	10	10	10	10	10	10	10	10	10	10
PPMAH	–	–	–	–	–	–	5	5	5	5	5	5

### 2.2 Preparation of Composites

Via the mixing process, all the materials were being mixed together according to the sequence, using a heated two-roll mill machine at temperature 180 °C with a rotating speed of 50 rpm. Firstly, PP was discharged, followed by NBR at minutes 4<sup>th</sup> and kenaf core at minutes 6<sup>th</sup>. The mixture was continuously mixed in order to make it homogeneous. Then, the compound was compressed using a hot press machine to get 1 mm thin sheets sample. Prior to the tensile test, all samples formulation were cut into dumbbell shape by using Wallace Die cutter model S6/1/6.A.

### 2.3 Tensile, Morphological and Chemical Testing

The tensile properties of PP/NBR/KC composites were analyzed to identify the tensile strength, Young's modulus, and elongation at break. The test was conducted followed the ASTM D 638 by using Instron Universal testing machine. The initial jaw separation distance was set to 50 mm and the crosshead speed of 5 mm/min. Five repetitions of samples from each composites formulation was evaluated.

The surface morphology of PP/NBR/KC composites was observed by using a scanning electron microscope (SEM). The cross-section of fracture composites surface morphology was sputter-coated with a thin platinum layer using JFC-1600 auto fine coater to avoid electrostatic charging and poor image resolution during the examination.

## 3 Result and Discussion

### 3.1 Tensile Properties

The tensile strength of PP/NBR/KC and PP/NBR/KC/PPMAH composites is presented in Fig. 1. The results showing that the tensile strength decreased with increasing NBR loading. Composites rigidity was reduced with the addition of the NBR. As the crystallinity portion of PP reduced, these will affect the rigidity and strength of the composites. NBR is a soft rubber material and purposely added into the formulation to give an elastic effect. By that being said, the crystallinity of the composites has reduced because of the addition of NBR in the composites [6].

However, the PP/NBR/KC/PPMAH composites showed better tensile strength compared to uncompatibilized composites. This might due to the better adhesion between PP/NBR matrices with KC filler. PP/NBR/KC/PPMAH composites composition 70/30/10/5 shows the highest percentage of improvement of tensile strength that is almost 43%. PPMAH have the ability to enhanced the interfacial adhesion between hydrophobic matrices and hydrophilic filler [7].

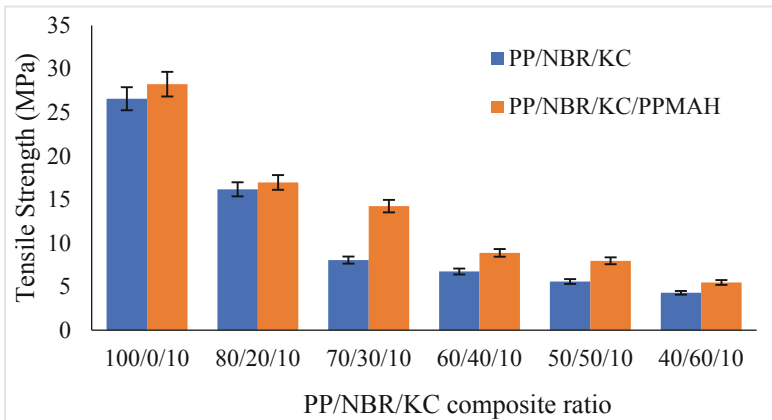
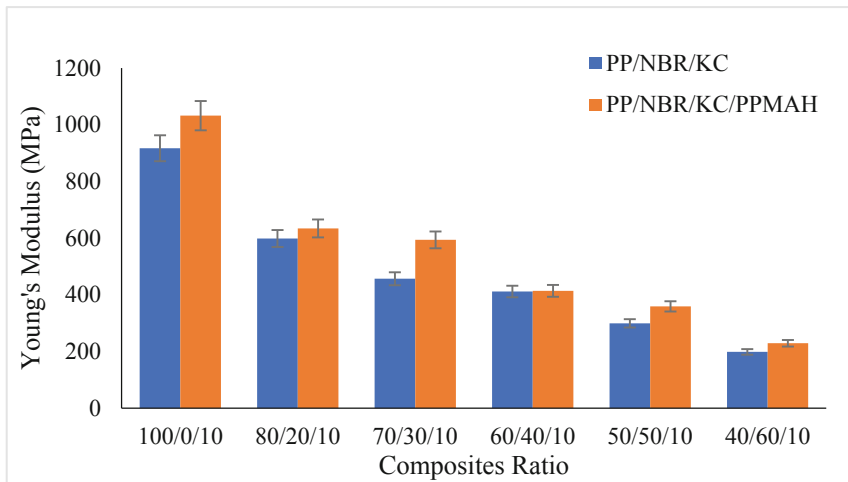


Fig. 1. Tensile strength of PP/NBR/KC and PP/NBR/KC/PPMAH composites

Figure 2 represents Young's modulus PP/NBR/KC and PP/NBR/KC/PPMAH composites. Young's Modulus is the mechanical property that measures the stiffness of a solid material [8]. This initiates the relationship between stress and strain in a material in the linear elasticity regime of a uniaxial deformation. From the graph, it can be seen that the increment of the NBR loading has reduced the stiffness of the composites. This shows that the increment rubber does not help much in improving the elasticity of the composites due to the presence of the hydrophilic KC fibre.

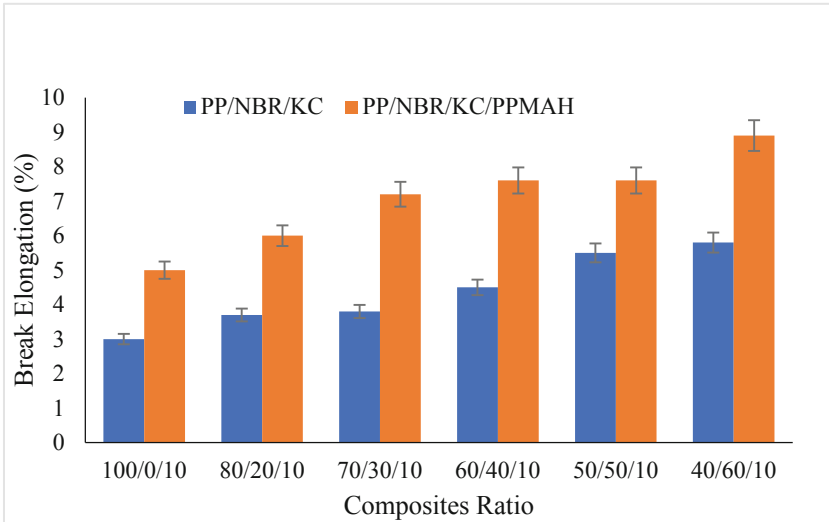
Meanwhile, for the PP/NBR/KC/PPMAH composites, has a higher Young's Modulus compared to the composites without PPMAH at a similar KC loading. This indicated that the addition of the PPMAH in the composites can reduce the interaction of hydrogen bond and force of intermolecular in PP. This finding was supported form several researchers [9, 10].



**Fig. 2.** Young's modulus of PP/NBR/KC and PP/NBR/KC/PPMAH composites

Figure 3 represents the elongation at break of PP/NBR/KC composites with and without PPMAH. From this observation, it can be seen that the elongation at break of the composites specimen increased when the NBR loading increased. The higher amount of NBR loading in the composites became the reasons for composites to reduce its resistance to elongation. This shows that the stiffness and brittleness of PP and NBR matrices are reduced.

However, PP/NBR/KC composites with addition of the PPMAH showed higher elongation at break compared to the composites without PPMAH compatibilizer a similar KC loading. In the previous study conducted by [11] stated that the compatibilizer reduces the interfacial energy between dipolar PP and NBR matrix phases, thus, it enhanced the interfacial adhesion. Similar findings were reported in the analysis of polypropylene maleic anhydride (PPMAH), polypropylene (PP) and acrylonitrile butadiene rubber (NBR) [12, 13].



**Fig. 3.** Break elongation of PP/NBR/KC and PP/NBR/KC/PPMAH composites

### 3.2 Morphological Properties

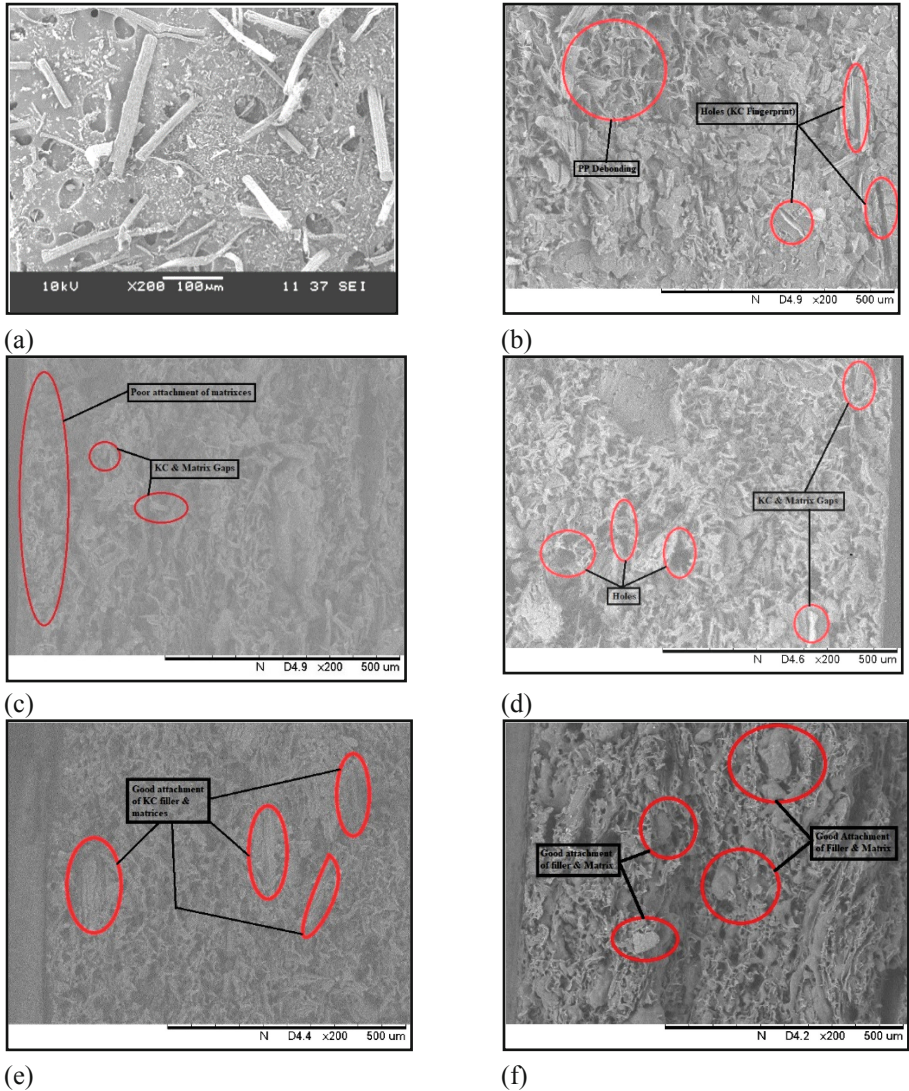
Scanning Electron Microscopy (SEM) was conducted to analyze the KC powder and surface fracture of the PP/NBR/KC composites with and without compatibilizer. The micrographs of each composite with difference NBR loading were studied. Figure 4(a) illustrated the SEM micrographs of KC filler. The KC filler used in the composites is in a powder form which size is less than 300  $\mu\text{m}$ . The raw and unprocessed KC has a rough surface. From the micrograph, it can be seen that the shape of KC filler is irregular and fibrous-like shape, it also seemingly likes cylindrical shape.

Figure 4(b) illustrates the tensile fracture surface of PP/KC (100/10) composites without the addition of the NBR and PPMAH at 200X magnification. From the observations of the SEM, Fig. 4.5 reveals that there are the holes KC fingerprints that can be seen it the figure. The PP de-bonding phenomena also occur. KC was appeared and was not wholly embedded into the PP matrix, KC fibres are also were extremely detached and pulled out from the matrix. The occurrences of some PP de-bonding phenomena indicated poor adhesion between the PP matrix and KC filler. These results were supported and proved as said by [14] in their journal that PP matrix and KC filler have an unsteady interfacial bonding.

Figure 4(c) and (d) shows the micrograph of the tensile fracture surfaces of PP/NBR/KC composites with NBR at 30 wt% and 60 wt% with a magnification of 200X respectively. Both micrographs show the quite poor attachment between KC filler and PP/NBR matrices. From the micrograph, it can be seen that the matrices were not in a good condition which PP and NBR matrices was not fully combined together thus, it cannot hold the KC filler properly. As more NBR was added, they probably formed many holes that are visible compared to the less NBR loading. This is not only due to the detachment of KC filler in matrices but also causes of NBR loading which



made the matrix became ductile. This lead to the decreased in tensile strength and increased the elongation at break of the composites. The similar finding reported in a previous study [7].



**Fig. 4.** (a) Kenaf core raw material; (b) Tensile fracture surface of PP/KC (100/10) composite at magnification X200; (c) Tensile fracture surface of PP/NBR/KC (70/30/10) at magnification X200; (d) Tensile fracture surface of PP/NBR/KC (40/60/10) at magnification X500; (e) Tensile fracture surface of PP/NBR/KC/PPMAH (70/30/10/5) at magnification X200; (f) Tensile fracture surface of PP/NBR/KC/PPMAH(40/60/10/5) at magnification X500



Figure 4(e) and (f) shows the micrograph of the tensile fracture surfaces of PP/NBR/KC/PPMAH composites with NBR loading at 30 wt% and 60 wt% with a magnification of 200X respectively. Both micrographs show an improvement in the attachment between KC filler and PP/NBR matrix with the presence of the PPMAH compatibilizer. Results show that with the addition of the PPMAH it has improved the dispersion and adhesion of KC filler in PP/NBR matrix. The similar findings show in the previous research conducted by [7] stated in the journal that improvement of filler and matrix adhesion is because of the presence of compatibilizer helps in reducing the dipolar energy between the PP and NBR phase which improved the nature of hydrophilic filler and hydrophobic matrices. Thus, the interfacial adhesion and dispersion of KC filler are improved.

## 4 Conclusion

Kenaf core is one of the natural fibre sources capable to replace the synthetic fibre in polymer composites applications. The tensile strength of thermoplastic elastomer of PP/NBR with the addition of kenaf decreased as NBR increased. However, composites with PPMAH compatibilizer produced better tensile strength and Young's modulus. From the morphological study, it can be proved the interfacial adhesion between KC filler and PP/NBR matrices resulted better distribute and fewer detachment sites were produced.

## References

1. Shanks, R., Kong, I.: Thermoplastic elastomers. *Thermoplast. Elastomers* (2012). <https://doi.org/10.5772/2038>
2. Mustafa, Z., Ragunathan, S., Othman, N.S., et al.: Thermoplastic elastomer composite using benzyl chloride treatment on kenaf core powder mixing with polypropylene and virgin acrylonitrile butadiene rubber. In: *IOP Conference Series: Materials Science and Engineering*, vol. 429, p. 012013 (2018). <https://doi.org/10.1088/1757-899X/429/1/012013>
3. Galpaya GDD. Processing characteristics, physical properties and morphological study of polypropylene (PP)/recycled acrylonitrile butadiene rubber (RNBr) blends 14 (2009)
4. Mustafa, Z., Ragunathan, S., Othman, N.S., et al.: Fabrication and properties of polypropylene and kenaf fiber composite. In: *IOP Conference Series: Materials Science and Engineering*, vol. 429, p. 012016 (2018). <https://doi.org/10.1088/1757-899X/429/1/012016>
5. Chandrasekar, M., Ishak, M.R., Sapuan, S.M., et al.: A review on the characterisation of natural fibres and their composites after alkali treatment and water absorption. *Plast. Rubber Compos.* **46**, 119–136 (2017). <https://doi.org/10.1080/14658011.2017.1298550>
6. Othman, N.S., Santiago, R., Zainal, M., et al.: Tensile and morphological studies of polypropylene/empty fruit bunch composite: effect of maleic anhydride-grafted polypropylene Tensile and morphological studies of polypropylene/empty fruit bunch composite: effect of maleic anhydride-grafted polypropylene. In: *Material Science and Engineering* (2018)

7. Mustafa, W.A., Zainal, M., Santiago, R., et al.: Structure analysis on polypropylene maleic anhydride (PPMAH)/polypropylene (PP)/recycled acrylonitrile butadiene rubber (NBRr)/banana skin powder (BSP) composites treatment. *J. Adv. Res. Fluid Mech. Therm. Sci.* **50**, 40–46 (2018)
8. Li, S., Lamminmäki, J., Hanhi, K.: Effect of ground rubber powder and devulcanizates on the properties of natural rubber compounds. *J. Appl. Polym. Sci.* **97**, 217–280 (2005)
9. Santiago, R., Zainal, M., Ting, S.S., Ramli, S.: Effect of polypropylene maleic anhydride (PPMAH) as a compatibilizer in polypropylene (PP)/ sugarcane bagasse (SCB) composites
10. Zainal, M., Aihsan, M.Z., Mustafa, W.A., Santiago, R.: Experimental study on thermal and tensile properties on polypropylene maleic academia baru experimental study on thermal and tensile properties on polypropylene maleic anhydride as a compatibilizer in polypropylene/sugarcane bagasse composite. *J. Adv. Res. Fluid Mech. Therm. Sci.* **43**, 141–148 (2018)
11. Khalf, A.I., Ward, A.A.: Use of rice husks as potential filler in styrene butadiene rubber/linear low density polyethylene blends in the presence of maleic anhydride. *Mater. Des.* **31**, 2414–2421 (2010). <https://doi.org/10.1016/j.matdes.2009.11.056>
12. Pang, A.L., Ismail, H.: Tensile properties, water uptake, and thermal properties of polypropylene/waste pulverized tire/kenaf (PP/WPT/KNF) composites. *BioResources* **8**, 806–817 (2013)
13. Joseph, A., George, S., Joseph, K., Thomas, S.: Melting and crystallization behaviors of isotactic polypropylene/ acrylonitrile-butadiene rubber blends in the presence and absence of compatibilizers and fillers. *J. Appl. Polym. Sci.* **102**, 2067–2080 (2006). <https://doi.org/10.1002/app.23986>
14. Sarifuddin, N., Ismail, H., Ahmad, Z.: The effect of Kenaf core fibre loading on properties of low density polyethylene/thermoplastic sago starch/Kenaf core fiber composites. *J. Phys. Sci.* **24**, 97–115 (2013)



# Pollutant Emission in Diesel Engine

Mohd Al Hafiz Mohd Naw<sup>1</sup>(✉), Mohd Hazwan Mohd Hanid<sup>1</sup>,  
Wan Azani Mustafa<sup>1</sup>, Mohd Shahir Kasim<sup>2</sup>,  
and Raja Izamshah Raja Abdullah<sup>2</sup>

<sup>1</sup> Faculty of Engineering Technology, Universiti Malaysia Perlis,  
Kampus UniCITI Alam, Sungai Chuchuh, 02100 Padang Besar, Perlis, Malaysia  
alhafiznawi@unimap.edu.my

<sup>2</sup> Faculty of Manufacturing Engineering, Universiti Teknikal Malaysia Melaka,  
Hang Tuah Jaya, 76100 Durian Tunggal, Melaka, Malaysia

**Abstract.** As for the diesel engine, it is well known as one of the largest contributors to environmental pollution, which cause by exhaust emission. Therefore, due to the energy constraint, the rising cost of raw petroleum and environmental change with the expanding request for vitality preservation and environmental protection further enhancement in fuel adaptability and emission reduction in a diesel engine are direly required. The outflows framed are indigent upon the engine configuration, power yield and working burden. The complete ignition of fuel prompts real diminishments in the development of fumes discharges. Complete on combustion will leads a significant mechanical power for the vehicle, which is perfect on the air-fuel mixture. With a specific end goal to diminish NO<sub>x</sub> and PM arrangement it is important to comprehend the components of its development.

**Keywords:** Emission · Diesel spray · Nitrogen Oxide · Particulate matter

## 1 Introduction

Nowadays, internal combustion engines (ICE) was the greatest invention in the world. This type of thermal engines is broadly utilized as a part of an industrial manufacturer which source of power for aircraft and road vehicles. Reaction from chemical energy that contains in the fuel will release energy by burning or oxidizing the fuel inside the engine and then it will produce mechanical power [1, 2]. Recalling the history of ICE in the early year 1800 such of many experimental studies are conducted on internal combustion engine operation. Due to this observation, in 1876 a German engine builder, Dr. N. A. Otto has to build up a first successful engine that calls “Otto gas engine”. This framework of the operating cycle is based on a French engineer named Beau de Rochas in 1862. Later on, the diesel engine was developed in 1893 by Rudolf Diesel [3, 4].

## 2 Pollutant Emission and Regulations in Diesel Engine

Figure 1 shows the raw emission data from real combustion and the composition in percent by weight of diesel engines. It shows that diesel engines have smaller fractions of pollutants. However, it's also resulted in the particulate matter, for example, solids that look like predominant soot and components as condensate [5]. Lately, the exhaust emission has been reduced dramatically like as shown in Figs. 2 and 3. This figure account for all vehicles has followed and met this stringent emission standard. Based

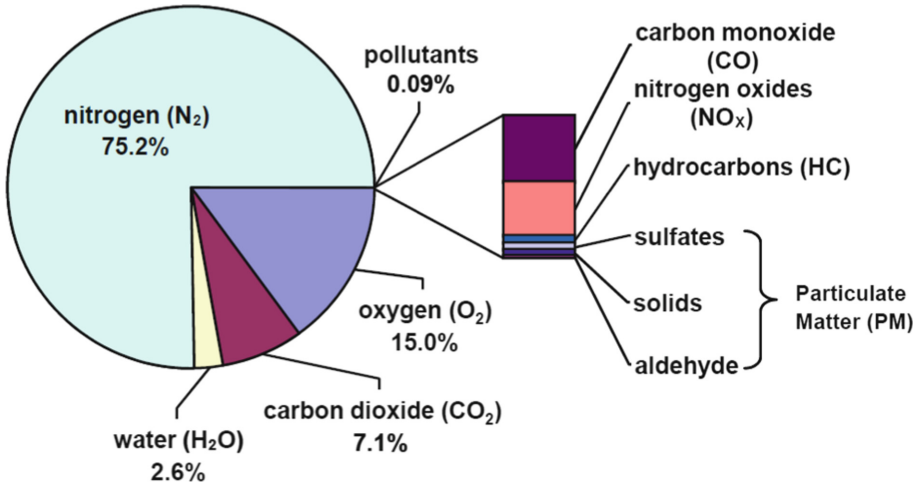


Fig. 1. Exhaust gas component during combustion in percent by volume of diesel engines [3, 4]

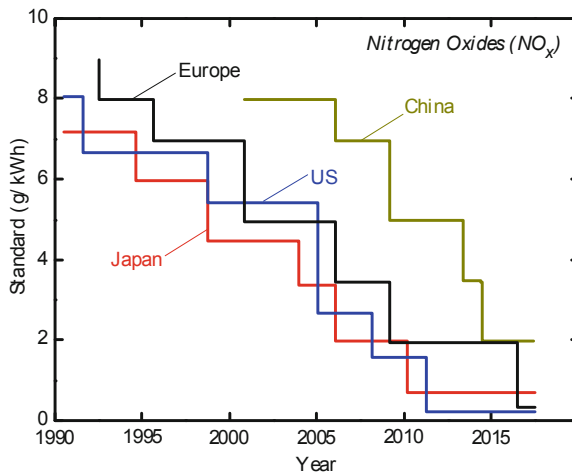


Fig. 2. NO<sub>x</sub> standards for heavy-duty vehicles in the United States, European Union, Japan and China [5]

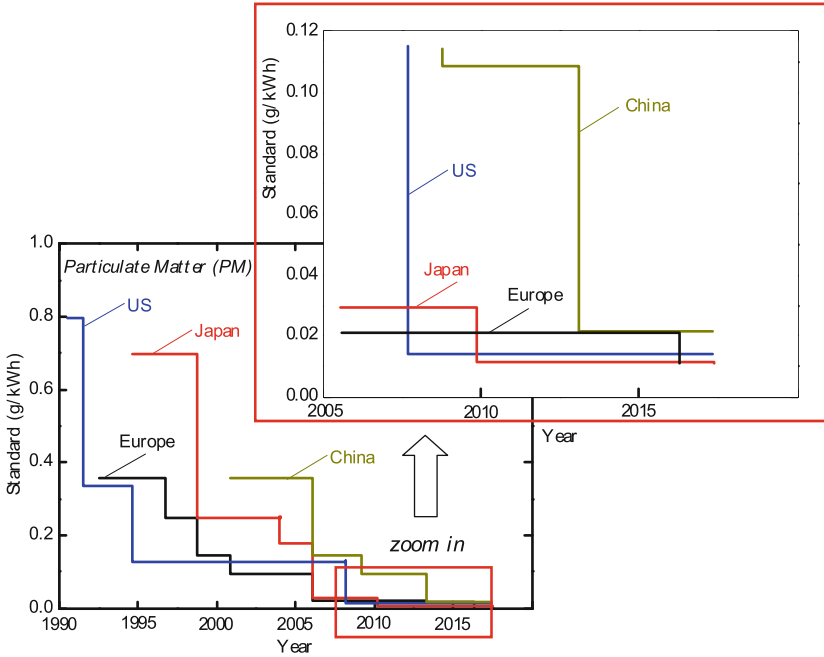


Fig. 3. PM standards for heavy-duty vehicles in the United States, European Union, Japan and China [5]

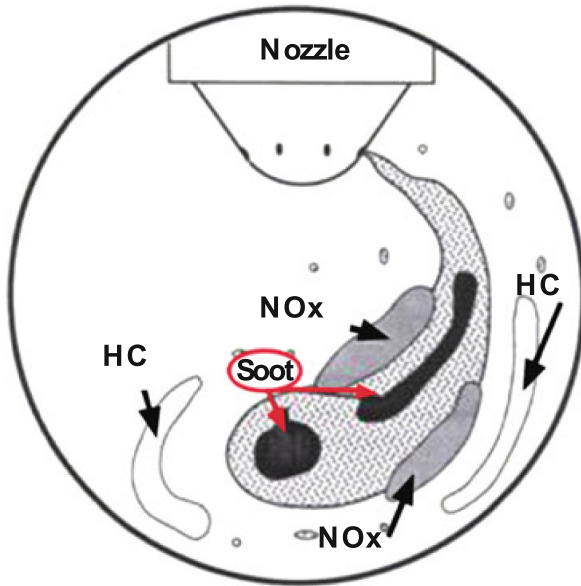


Fig. 4. Regions of pollutant production in a combustion chamber [7]

on information from Mollenhauer and Tschoke [6], Fig. 4 shows the formation of pollutant emission that occurred during combustion process [7]. As in the figure, the NO<sub>x</sub> is formed at high ambient temperature condition and excess air area. Further, unburned hydrocarbons occur due to the fuel was not fully oxidized and the low temperature outside the flame. In addition, the soot occurred at spray core region which air was in flawed phase. One of the point to improved and reduce the particulates is to generating greater turbulence. Therefore, the modern diesel engine has burned close to 95% of the particulates that formed in the engine.

## 2.1 Main Pollutant Emission

A brief explanation by a previous study [8] and others due to the main pollutant emissions such as Carbon Monoxide (CO), Hydrocarbons (HC), Particulate Matter (PM) and Nitrogen Oxides (NO<sub>x</sub>) are explained.

Carbon Monoxide (CO) - The emission occurred from the incomplete combustion where the oxidation process does not occur completely. Normally, this will cause at the time of starting and instantaneous acceleration of the engine where the rich mixtures are required. Further, based on the previous study that stated the CO is also emitted under lean condition due to chemical kinetic effects [9, 10]. It can be recognized as an odorless and colorless gas. It also harmful effect to human health when the emission was in the air is inhaled by the lungs and transmitted into the bloodstream [11]. Furthermore, this emission produced a large of droplets in a diesel engine and insufficient turbulence or swirl is created in the combustion chamber which is related to the present study.

Hydrocarbons (HC) - This emission results from the unburned fuels that lead to an insufficient temperature which occurs near the cylinder wall. At this period, the air-fuel mixture temperature is significantly less than the center of the cylinder [12, 13]. The emissions occur principally at light loads (lean air-fuel mixing) and it also exits in the engine crankcase, the fuel system. Results from atmospheric venting of vapors during fuel distribution and dispersing was one of the points on the present study. The hydrocarbons have played a significant role formation on ground-level ozone. Due to this condition, 50% of the emissions form was from vehicles. Further, emissions have the potential to cause respiratory tract irritation and cancer.

Particulate Matter (PM) - The particulate matter occurred from incomplete combustion of the hydrocarbons in the fuel and lube oil. Based on the previous study [14] the PM are typically spheres about 15-40 nm in diameter and more than 90% the size is smaller than 1  $\mu\text{m}$  in diameter. This emission is easy to recognize because of more than 50% of the emission are soot which seen as black smoke. The toxic has caused an important health problem such as premature death, asthma, lung cancer, and other cardiovascular issues [15, 16].

Nitrogen Oxides (NO<sub>x</sub>) - Last and not least emissions were nitrogen oxides. This emission results from major influences of the maximum temperature in the cylinder, the concentration of oxygen in the combustion and residence time. Furthermore, this emission was emitted early in the combustion process. Normally the NO is known as colorless and odorless gas, while NO<sub>2</sub> seen a reddish-brown gas with pungent odor [17, 18]. As we know the diesel vehicles have most contribute to NO<sub>x</sub>. This is being

one of the reasons to know the formation of the air-fuel mixture during the ignition delay period. This toxic can cause an effect on health hazards such as acidification, the formation of ozone, nutrient enrichment and smog formation [19]. The NO<sub>x</sub> can irritate the lungs and lower resistance to respiratory infection such as influenza [20, 21].

## 2.2 Alternative Combustion Methods

Neely et al. [22] have discussed on the distribution of soot and NO formation for the combustion diesel engine fuel via applying such a technique of Lower Temperature Combustion (LTC), Premixed Controlled Compression Ignition (PCCI), Homogenous Charge Compression Ignition (HCCI) and conventional diesel combustion. As we already know, the temperature and the local equivalence ratio of regular diesel combustion has enough soot peninsula. Today's diesel fuel with high-pressure injection system was enhanced and significantly reduce the soot emissions. In any case, if today's standard diesel combustion was utilized for rich burning, local identicalness proportion and temperature would be expanded further into the soot peninsula. Furthermore, the trend shape of  $\phi$  and T in case of LTC are most related to standard diesel combustion, however, the territory is moved to the lower temperature side of the soot peninsula. Additionally, the pattern of PCCI may not be so different from standard diesel combustion, but the local  $\phi$  is lower and permit low smoke rich ignition. The alternative combustion method can clearly be seen in Fig. 5 [22].

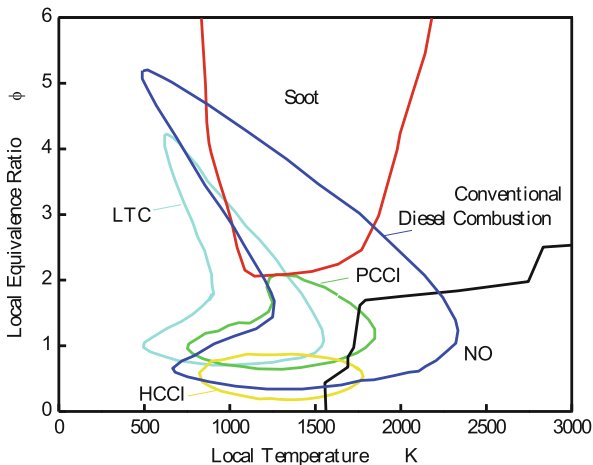
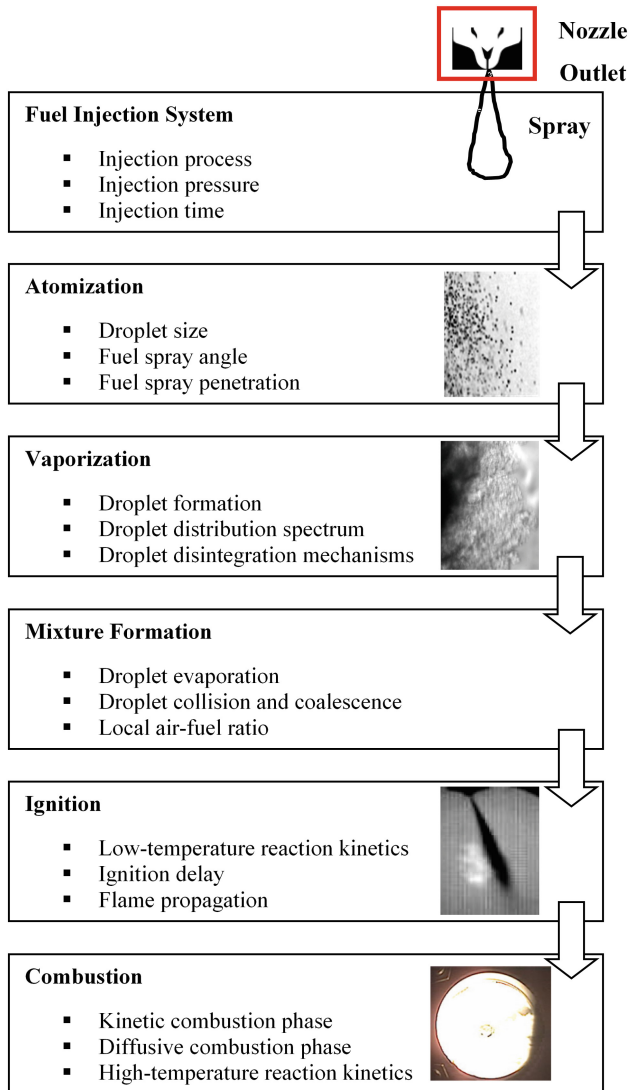


Fig. 5. Equivalence temperature diagram strategies [22]

## 2.3 Diesel Engine

Diesel engines or compression-ignition engines are often called that indicate by heterogeneous mixture formation and combustion. The cycle has involved with the intake of air, compression of air, fuel injection, mixture, ignition, combustion,

expansion, expansion, and exhaust. A compression ratio between 14 to 25 has been compressing the air into the top dead center (TDC) [23, 24]. Due to this condition, the fluid which has been injected into the combustion chamber will be atomized into small droplets. Then, the liquid fuel will be vaporized and mixed with air effect of change the pressure enhancement. At the end of compression, the combustion is initiated affected by high ambient temperature and pressures in the cylinder. Finally, the exhaust valve opens and remove the combustion completion. The cycle ends as the exhaust valve closed. Noted that, the formation of pollutant emissions such as particulate matter,



**Fig. 6.** Sub-processes after start of fuel injection leading to combustion diesel engines

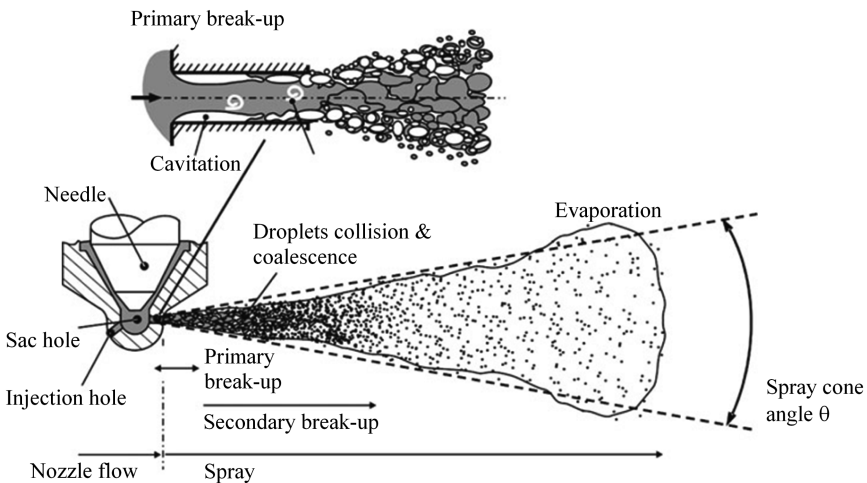


nitrogen oxides, and hydrocarbon will form caused by incomplete combustion. That is why a perfect setting on injection rate (fuel quantity and injection timing) and air supply will lead to high efficiency in the combustion process.

Hence, the ideal diesel engine acquires an extremely short ignition delay and hasty air motion in the combustion chamber. Due to this circumstance, the mixture formed during the ignition delay period is as primary on this present study. As reference from a previous study [25–27], Fig. 6 shows the sub-processes occur in diesel engines.

## 2.4 Diesel Spray Structure

Microscopic and macroscopic imaging experiments in diesel sprays are the most important part to identify the characteristics of the fuel spray structure. Spray penetration and cone angle are in macroscopic categories while droplets behavior, atomization, evaporation is in microscopic categories. As we can see in Fig. 7 [28] it shows the schematic of a typical full-cone spray structure which has been divided into several zones. As we already know, the spray is one of the area in a diesel engine that contributes significant energy during the combustion process. Due to spray research, it will lead an increasing engine performance, great energy of fuel consumption and control the pollutant emission of the exhaust.



**Fig. 7.** Schematics of full cone spray [28]

**Spray Penetration** - Spray penetration is defined as the maximum distance from nozzle exit to the top edge of the spray. It could be determined of reaction on stagnant air in the system. It forms with two factors; the fuel liquid momentum and the resistance of the surrounding gas. Here, it would be explained, due to the friction effect, the fuel kinetic energy is being transferred continuously to the liquid direction. The energy of the liquid will progressively deplete while the kinetic energy of the droplets have been decreasing and the movement of the droplets is mainly imposed by gravity,

surrounding gas and the liquid flow. As in this study [29, 30], the light droplet at the vicinity of injector outlet has moved as following the working liquid due to the less aerodynamic resistance of the droplets. The spray penetration also depends on nozzle geometry, injection pressure and liquid properties. The density, surface tension, and viscosity of the liquid properties will significantly effect on spray penetration. As a reference, the effect on ambient pressure into spray penetration clearly shows in Fig. 8 [31, 32]. Smaller surrounding ambient pressure shown peak tip penetration with a very short time elapsed. Contrary to large ambient pressure caused linear rise tip penetration within time elapse.

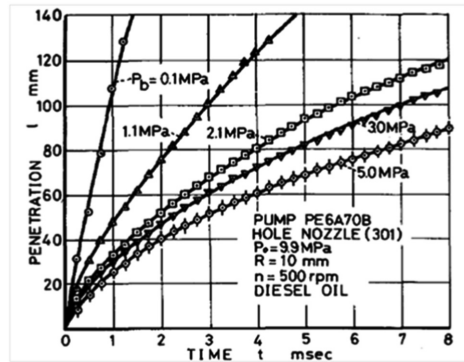


Fig. 8. Spray tip penetration [32]

Table 1. Parameters affecting liquid spray penetration distance [34]

System	Variable	Input	Effect on liquid sprays penetration distance (L)
Injector	Orifice diameter	↓	Strong decrease Linear decrease Strong decrease
	Injection pressure	↑	No significant effect, time to $L_{max}$ reduced No significant Weak increase
	Nozzle aspect ratio	↑	No significant effect
Engine	Ambient density	↑	Strong decrease Strong decrease initially, reduced sensitivity as Density increase Strong decrease
	Ambient temperature	↑	Strong decrease Strong decrease initially, reduced sensitivity as temperature Strong decrease
Fuel	Fuel type		Density increase as volatility decreases Can have significant effects
	Fuel temperature	↑	Linear decrease

It can be concluded that the spray tip penetration decreases with an increase in ambient gas pressure [25]. Summary of variable parameters that effecting spray penetration shall clearly be seen in Table 1. Based on the previous study [33] when the liquid has been influencing by high ambient temperature condition, it will reduce the density properties then it will shorter spray penetration. Furthermore, short spray penetration may lead to high emissions due to poor air utilization and inappropriate mixing rate. Table 1 [34] shown a summary such as a parameter that causes the penetration length.

**Spray Angle** - Spray angle measurement can be defined from two tangent lines which starting from nozzle exit onto the side edge of the spray boundary. The spray depth can be measured at several axial locations as follow with specifying the spray profile. The cone angle formed is relied on the effects of surrounding gas with the spray. Furthermore, the effect on large or small spray angle will depend on the nozzle, ambient density, and fuel properties. An example, when the fuel has been applying at high injection pressure which is under low ambient density environment, the size of the cone angle is increased [25].

**Droplets Size** - The droplet size formation have same criteria effect on the spray penetration and spray angle formation. Normally, injection pressure and ambient environment condition will greatly effect on size diameter formation of droplets [35]. It's found that when injection pressure rises the size of the droplets become smaller. As a reference, the effect on this injection pressure circumstances has been shown in Fig. 9 [25]. Furthermore, an influence on high ambient temperature will effect on droplets evaporation. As in the real combustion condition, the droplets can reach their critical state [36]. The smaller droplets size tend to evaporate completely within short time hiatus and for large droplets, it takes time to completely evaporate.

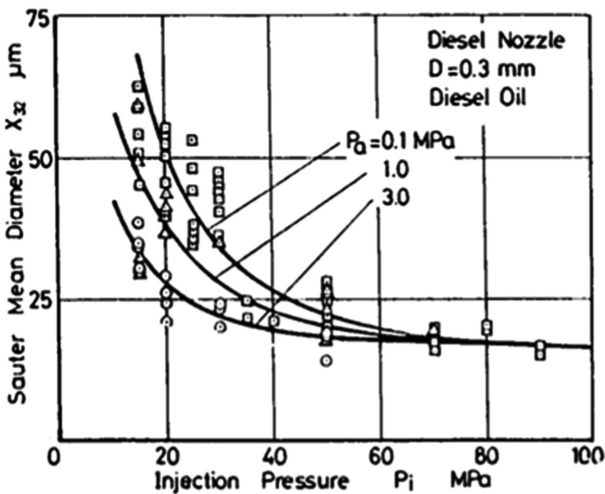


Fig. 9. The effect of ambient pressure and injection pressure on the Sauter mean diameter [25]

Evaporation - As in the evaporation regime, the phase has occurred due to the effect of heat at the liquid fuel. It makes the kinetic energy of the liquid molecules increased. This molecules become an attraction force and escape into the environment gas. Furthermore, affected by high ambient pressure and high ambient temperature will increased evaporation rate.

### 3 Conclusion

The purpose of this paper is to review the pollutant emission in a diesel engine. Structure and mechanism of the diesel engine were explained clearly. A few comparison and suggestion from previous research also was highlighted. The most obvious finding to emerge from this study is that the complete ignition of fuel prompts real diminishments in the development of fumes discharges. Complete on combustion will leads a significant mechanical power for the vehicle, which is perfect on the air-fuel mixture. With a specific end goal to diminish NO<sub>x</sub> and PM arrangement it is important to comprehend the components of its development. This research has thrown up many questions in need of further investigation. Further work needs to be done to establish whether pollutant emission in diesel engine effect on the living style on a long term period.

### References

1. Grimaldi, C.N., Millo, F.: Internal combustion engine (ICE) fundamentals. In: Handbook of Clean Energy Systems, pp. 1–32 (2015)
2. Oates, G.: Fundamentals of combustion. In: Aerothermodynamics of Aircraft Engine Components, pp. 1–43 (2012)
3. Heywood, J.B.: Internal Combustion Engines Fundamentals (1989)
4. Diesel, R.: The diesel oil-engine and its industrial importance. *Sci. Am.* **106**, 357–358 (2011). <https://doi.org/10.1038/scientificamerican04201912-357>
5. Handbook of diesel engines. *Choice Rev. Online* **48**, 48-3899–48-3899 (2013). <https://doi.org/10.5860/choice.48-3899>
6. Mollenhauer, K., Tschöke, H.: Handbook of Diesel Engines, 1st edn. Springer, Heidelberg (2010)
7. Van Basshuysen, R., Schaefer, F.: Internal Combustion Engine Handbook Basics, Components, Systems, and Perspectives (2011)
8. Reşitoğlu, I.A., Altinişik, K., Keskin, A.: The pollutant emissions from diesel-engine vehicles and exhaust aftertreatment systems. *Clean Technol. Environ. Policy* **17**, 15–27 (2015)
9. Nakajima, K., Yamakawa, Y.: Air pollution by motor vehicles. *J. Soc. Mech. Eng.* **73**, 990–999 (2017). [https://doi.org/10.1299/jsmemag.73.618\\_990](https://doi.org/10.1299/jsmemag.73.618_990)
10. Zhang, K., Yao, L., Li, G.: Analyzing the contribution of vehicles to air pollution, pp. 2842–2847 (2013)
11. Stork, C.M.: Carbon monoxide. In: Encyclopedia of Toxicology, 3rd edn, pp. 682–684 (2014)
12. Machado Corrêa, S., Arbilla, G.: Carbonyl emissions in diesel and biodiesel exhaust. *Atmos. Environ.* **42**, 769–775 (2008). <https://doi.org/10.1016/j.atmosenv.2007.09.073>

13. Li, R., Wang, Z., Xu, G.: Study on carbonyl emissions of diesel engine fueled with biodiesel. *Int. J. Chem. Eng.* **2017**, 1–12 (2017). <https://doi.org/10.1155/2017/1409495>
14. Burtscher, H.: Physical characterization of particulate emissions from diesel engines: a review. *J. Aerosol Sci.* **36**, 896–932 (2005). <https://doi.org/10.1016/j.jaerosci.2004.12.001>
15. Guevara, M.: Emissions of primary particulate matter. *Issues Environ. Sci. Technol.* **2016**, 1–34 (2016). <https://doi.org/10.1039/9781782626589-00001>
16. Grantz, D.A., Garner, J.H.B., Johnson, D.W.: Ecological effects of particulate matter. *Environ. Int.* **29**, 213–239 (2003)
17. Baukal, C.E., Bussman, W.: NO<sub>x</sub> emissions. In: *The John Zink Hamworthy Combustion Handbook—Fundamentals*, 2nd edn, vol. 1, pp. 417–477 (2012)
18. Hoekman, S.K., Robbins, C.: Review of the effects of biodiesel on NO<sub>x</sub> emissions. *Fuel Process. Technol.* **96**, 237–249 (2012)
19. Grewe, V., Dahlmann, K., Matthes, S., Steinbrecht, W.: Attributing ozone to NO<sub>x</sub> emissions: implications for climate mitigation measures. *Atmos. Environ.* **59**, 102–107 (2012). <https://doi.org/10.1016/j.atmosenv.2012.05.002>
20. Peel, J.L., Haeuber, R., Garcia, V., et al.: Impact of nitrogen and climate change interactions on ambient air pollution and human health. *Biogeochemistry* **114**, 121–134 (2013). <https://doi.org/10.1007/s10533-012-9782-4>
21. Kagawa, J.: Health effects of diesel exhaust emissions—a mixture of air pollutants of worldwide concern. *Toxicology* **181–182**, 349–353 (2002). [https://doi.org/10.1016/S0300-483X\(02\)00461-4](https://doi.org/10.1016/S0300-483X(02)00461-4)
22. Neely, G.D., Sasaki, S., Huang, Y., et al.: New diesel emission control strategy to meet US tier 2 emissions regulations. In: *SAE Technical Paper Series* (2010)
23. Reif, K.: *Diesel Engine Manag.* (2014). [https://doi.org/10.1007/978-3-658-03981-3\\_19](https://doi.org/10.1007/978-3-658-03981-3_19)
24. Konrad, R. (ed.): *Diesel Engine Management: Systems and Components* (2014)
25. Hiroyasu, H., Arai, M.: Structures of fuel sprays in diesel engines. In: *SAE Technical Paper Series* (2010)
26. McAllister, S., Chen, J.-Y., Fernandez-Pello, A.C.: *Fundamentals of Combustion Processes* (2011)
27. Fristrom, R.M.: Fundamentals of combustion. *Combust. Flame* **13**, 657 (2003). [https://doi.org/10.1016/0010-2180\(69\)90074-1](https://doi.org/10.1016/0010-2180(69)90074-1)
28. Baumgarten, C.: *Mixture Formation in Internal Combustion Engine*. Springer, Berlin (2006)
29. Nawi, M.A.M., Kidoguchi, Y., Nakagiri, M., et al.: Macro- and micro-scale observation on dynamic behavior of diesel spray affected by ambient density and temperature, pp. 1–9 (2014)
30. Abdullah, A.: Analysis of droplet evaporation process of diesel spray during ignition delay period. In: *COMODIA*, pp. 377–382 (2008)
31. Mimura, Y., Kidoguchi, Y., Miwa, K., Mohammadi, A.: A study on behavior of evaporating diesel spray and droplets. In: *Proceedings of the JSME Annual Meeting 2004.3*, pp. 165–166 (2017). [https://doi.org/10.1299/jsmemecjo.2004.3.0\\_165](https://doi.org/10.1299/jsmemecjo.2004.3.0_165)
32. Hiroyasu, H., Kadota, T.: Fuel drop-size distribution in diesel combustion chamber. *Trans. Jpn Soc. Mech. Eng.* **42**, 290–298 (2011). <https://doi.org/10.1299/kikai1938.42.290>
33. Fattah, I.M.R., Ren, W., Woo, C., et al.: Macroscopic spray characteristics of an evaporating diesel spray. In: *Proceedings of the Australian Combustion Symposium*, pp. 1–4 (2015)
34. Gulder, O.L.: Views on the structure of transient diesel sprays. *At. Sprays*. (2014). <https://doi.org/10.1615/atomizspr.v10.i3-5.70>
35. Desantes, J.M., Payri, R., Salvador, F.J., Gil, A.: Development and validation of a theoretical model for diesel spray penetration. *Fuel* **85**, 910–917 (2006). <https://doi.org/10.1016/j.fuel.2005.10.023>
36. Ashgriz, N.: *Handbook of Atomization and Sprays: Theory and Applications* (2011)



# A Bottle Neck Simulation System for a Generic Production Process

Azrul Haniedy Jamil<sup>1</sup>, Muhammad Nasiruddin Mahyuddin<sup>1</sup>(✉),  
Ahmad Rafeek Ibrahim<sup>2</sup>(✉), and Timothy Tong<sup>2</sup>

<sup>1</sup> School of Electrical and Electronics Engineering, Engineering Campus,  
Universiti Sains Malaysia, 14300 Nibong Tebal, Pulau Pinang, Malaysia  
nasiruddin@usm.my

<sup>2</sup> HP Malaysia Manufacturing Sdn Bhd,  
Batu Kawan Industrial Park, 14100 Simpang Ampat, Pulau Pinang, Malaysia  
ahmad.rafeek.ibrahim@hp.com

**Abstract.** The increase rate of consumer demands and stiff global competition among firms forced the industry to increase productivity by optimizing the production capacity to meet daily targeted yield. The presence of bottleneck problem, due to several triggering factors, is one of the root cause of low yield. Thus, to improve the yield whilst at the same time reducing the defects rate in the presence of bottle-neck, one need to seek the best model to accurately represent the production process. In this paper, bottle-neck detection algorithm is discussed and utilization rate for simulated setup of 2 different production topologies; series and parallel are discussed in the perspective of bottle-neck occurrence in the workstations being studied. The main aim of the simulation model is to monitor and analyze the system to pinpoint the bottleneck in the system. The scheduling algorithm is integrated in the proposed model in order to control the bottleneck occurrence, thereby, improving the productivity and meeting the targeted yield.

**Keywords:** Bottleneck detection · MATLAB simulink · Modelling · Scheduling

## 1 Introduction

The presence of bottleneck introduces a wide array of problem in machinery production. The impact of bottleneck toward the manufacturing line is the disruption of systematic process flow and the increase time and cost of the process limiting the yield [1]. The bottleneck may lead to one station has finished processing loads but because of the machine is still busy, the load cannot be delivered causing the next machine to be idle and waiting for item to be delivered [2]. Furthermore, Leporis [6] describe the term “bottleneck” is the point of congestion in a system that limit the production output and determines the capacity of the system. This is supported by [4] that stated the bottleneck machine will impede the system’s performance.

The dilemmas facing by today’s manufacturer are companies are more at risk for bottlenecks during production and need to identify and prevent the flaws in the process.

---

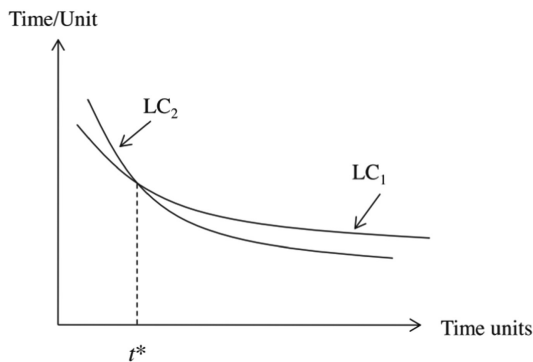
The original version of this chapter was revised: The second author name and the URL in Ref. [6] has been corrected. The correction to this chapter is available at [https://doi.org/10.1007/978-981-13-9539-0\\_56](https://doi.org/10.1007/978-981-13-9539-0_56)

© Springer Nature Singapore Pte Ltd. 2020, corrected publication 2021  
Z. Jamaludin and M. N. Ali Mokhtar (Eds.): SympoSIMM 2019, LNME, pp. 299–307, 2020.  
[https://doi.org/10.1007/978-981-13-9539-0\\_30](https://doi.org/10.1007/978-981-13-9539-0_30)

To further illustrate this impact, the definition of bottleneck as stated by [5] is the WIP (working in progress) level of different workstation may results in load imbalance thus creating delays and induce higher production costs. Furthermore, to identify the bottleneck parameter and it is important to define the bottleneck in order to minimize the impact on production.

The uncontrollable imbalance will induce bottleneck thus reducing the productivity of the workstation. Furthermore, the utilization rate of each workstation differs as the variable for the utilization rate depends on the output, heat capacity of each workstation and time [5]. Thus, the process is random and evolve with time. To further illustrate this effect, [6] deem that that the bottleneck is the machine that devoted most of the workload slowing or ceasing the work after a period of time. Researcher have developed various method for bottleneck detection and identifying bottleneck problems into analytical method and simulation method [7]. The simulation for bottleneck machine identification using simulated annealing proposed by Min [8] to minimize total tardiness by developing the scheduling optimization.

The work by Meerkov [9] states that the primary cause of bottleneck in a production system is the differences in machine learning curve between workstations and causes the bottleneck to keep shifting it position in a production system. Meerkov hypothesizes that learning curve is one of the factor to be considered as faster learning rate may cause the bottleneck to shift their position faster in the initial processing time compare to normal learning rate. Figure 1 illustrate the relationship between learning rate and bottleneck as the learning curve 2 (LC2) overtake the learning curve 1 (LC1) and the bottleneck for LC2 present before  $t^*$ .



**Fig. 1.** Example of two learning curves with different learning rate [9]

Based on the literature review, the bottleneck can be minimized by implementing queueing model to understand and define the bottleneck. Moreover, [10] state that queueing model needed to define the uncertainties and determine the performance of the multiple product. Furthermore, [11] conclude the queue model goal is to achieve an economic balance between the cost of service and the cost associated with average wait time to reduce the long wait time.

The work by [12] proposed that the hybridization of scheduling and queuing can be implemented. For example, [13] proposed that scheduling modelling progress from queuing model learns more characteristics of the manufacturing system and reflexed the manufacturing functions. However, the complex relationship between upstream and downstream machine in manufacturing line cause the increased of uncertainty issue, and require dynamic dispatching method [14]. To illustrate, the work proposed by Huang [4] done to observe the complexity of multiple lot scheduling by combining the heuristic search algorithm to schedule the manufacturing system using Petri net model. Moreover, [4] and [16] identified the bottleneck in serial configuration for production line by analyzing the relationship for manufacturing blockage and process of each machine. Based on the finding, scheduling is an integral part in the manufacturing line in which we can control or introduction correction for bottleneck.

Hence, this research aims to integrate the scheduling system for detecting the bottleneck using a simulation model. This paper summarizes the simulation approach for determining the bottleneck movement in the manufacturing.

## 2 Methodology

Figure 2 shows the generic model structure of a queuing model. This model is used as the principle structure model to represent a process in a factory plant whereby the occurrence of bottleneck is imminent amid the high capacity demand, the occurrence of unexpected machine downtime and some other influencing parameter affecting the committed yield at the end of the process.

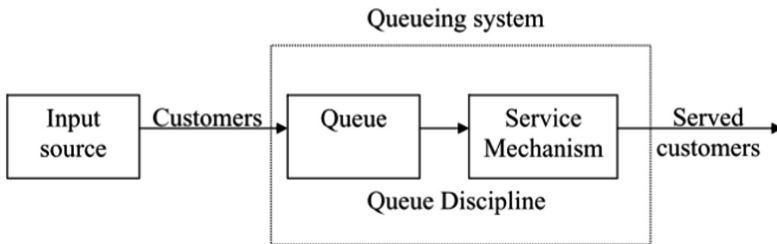


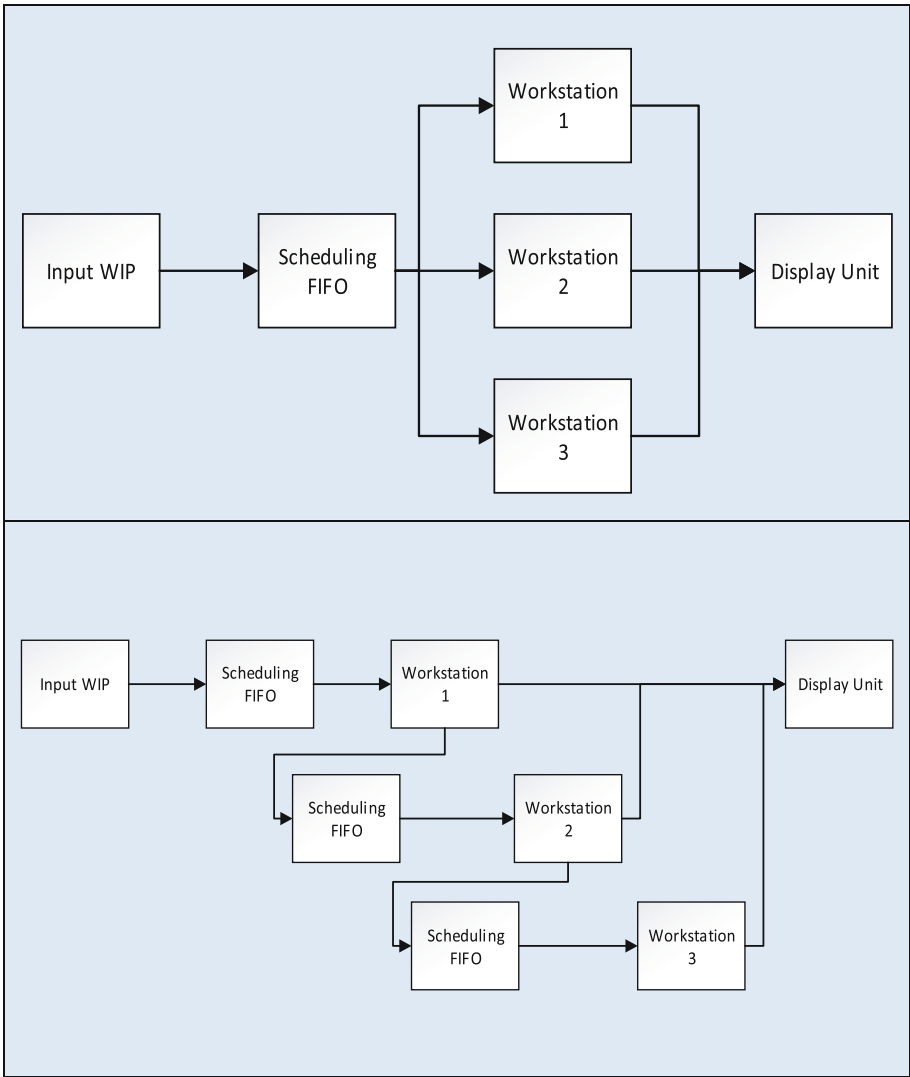
Fig. 2. The queuing model structure presented by [11]

The structure is considered as an ideal process of queuing in any process because the process flow is linear and without any error injection. Furthermore, to illustrate this problem, the shifting of workload in a workstation risks inducing bottleneck causing it to cease operation [6].

The proposed simulation model in Simulink will follow the framework architecture based on the queuing model provided by Wang in [13]. The Queuing Model comprises of test input, queue system, and output unit is taking into consideration. To identify the workstation that encountering bottleneck, the utilization rate of the workstation is observed for two possible process topological configuration; series



connection and parallel connection. Each sub-process has different number of dedicated machines depending on the tool requirement and together, they make up for a complete process for various distinctive product. Based on this basis, the basic block diagram for both of the framework topologies was developed. Figure 3 depicts the block diagram for both of the framework architecture.



**Fig. 3.** The basic block diagram for both series and parallel topology

In this paper, the theorem of Little’s law is incorporated to best represent the queuing model describing the process;

$$L = \lambda W \tag{1}$$

where the length of queue, L is equal to the arrival rate,  $\lambda$  multiplied by the waiting time W. The length of queue, L can be associate with the Work in Progress (WIP) because it is calculating the capacity of the system for each workstation. The dispatching rule used in the model primarily used first-in, first-out (FIFO) as the baseline for comparing the stimulated result in the proposed simulation framework. The parameter involve in the simulation is the initial buffer length is equal to zero; machine capacity is 50 lot can produce and the simulation duration is set by 4000 s time unit. The obtained simulated result will serve as the variability for the analysis to obtain the utilization rate of the machine in production line. The input source used the corresponding exponential distribution of inter-arrival time rate of the generate entity in the simulation. Furthermore, because of the stochastic results of utilization rate for each workstation, the distribution discipline used is Poisson distribution to simulate the output for the workstation.

**2.1 Bottleneck Detection Algorithm**

The work by Wang [14] introduces a method of detecting bottleneck using exponential mapping of the buffer length and smoothing of instantaneous bottleneck degree (IBD). This algorithm is obtained by improving the method based on the buffer length by multiple step function hence the response on the detected bottleneck is reserved [5]. This also to address the data fluctuation in bottleneck detection based on buffer length as it is difficult to reflect the degree of bottleneck in real production line. As the buffer length of bottleneck is spontaneous, a function transform known as, IBD is introduced:-

$$IBD = E(QL_s) = 1 - e^{-QL_s/T} \tag{2}$$

The characteristics of the transfer function is the function transform the buffer length into the range of (0, 1). The parameter, T is the bottleneck constant of the workstation. The transformed IBD induce time lag and exponential smoothing method is utilised to stabilise it. In the Eq. (2),  $\alpha$  is the smoothing factor denoting the variation of BD (bottleneck degree) known as BV (bottleneck variation) and can be set on sequence.

$$BV_s(t) = \alpha \cdot IBV_s(t) + (1 - \alpha) \cdot BV_s(t - 1) \tag{3}$$

The value  $\alpha$  also reflect on the sensitivity of variation of BD to IBD. It is worth noting that the bottleneck degree can be given a constant time, which can be identified after the aforementioned step as shown in the Eq. (3).

$$BD_{sb}(t) = \max BD_s(t) \tag{4}$$

The chosen algorithm for detecting bottleneck are able to satisfy the constraint for each of working station as it worth to point out that, the bottleneck constant,  $T$  is set individually hence this method can be applied to actual production line. In addition, this method of bottleneck detection can be develop to factor in machine maintenance and machine failure rate.

### 3 Result and Discussion

Figure 4 depicts the utilization rate of the workstation for parallel process for Workstation 1 (Fig. 4a), Workstation 2 (Fig. 4b) and Workstation 3 (Fig. 4c). By using Poisson distribution for each parallel workstation, the simulated result can be obtained in stochastic nature to observe the bottleneck characteristic in parallel process. It is to note that, the bottleneck occurs if the utilization rate reaches 1.

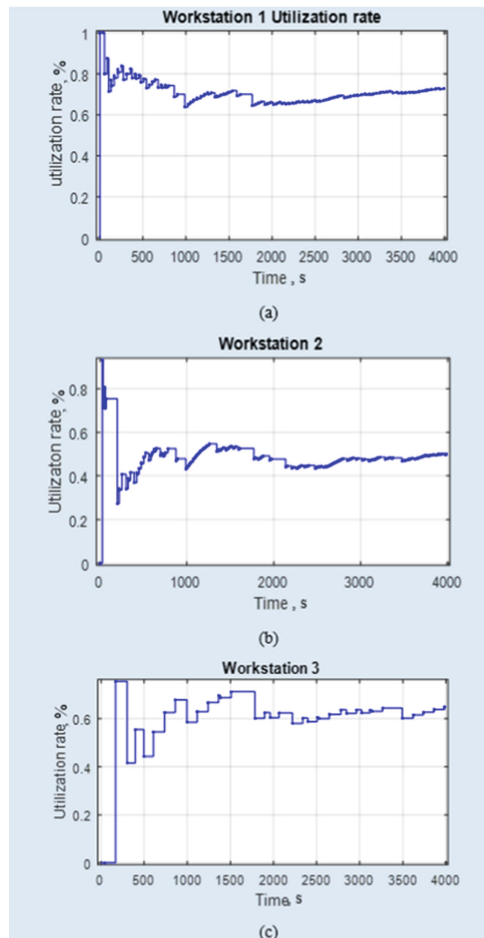
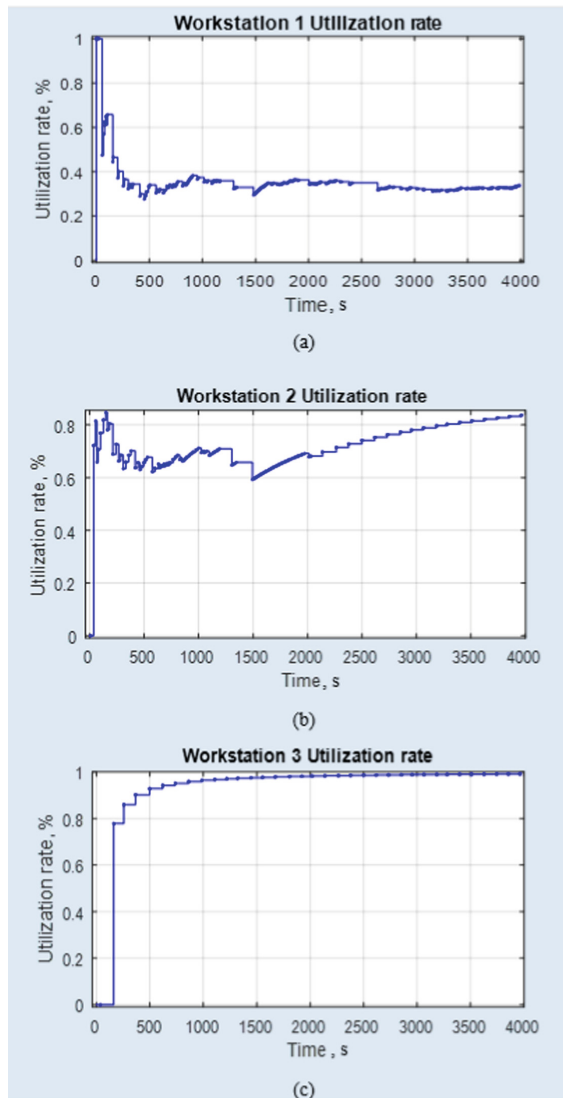


Fig. 4. The utilization rate of parallel process between workstation

By using Poisson distribution for each workstation, the stimulated result can be obtained in stochastic nature. The number of accumulating lots is high in workstation 1 and 3, thus bottleneck is detected in the simulation. Furthermore, the utilization rate for Workstation 2 averaging around 50% as it is waiting for the load to dispatch by the FIFO scheduling thus. Examining Fig. 3 in term of the FIFO dispatching rule, the rate of which load being distributed to the workstations is consistent.

Figure 5(a) (b) (c) depicts the utilization rate of the workstation for series process at Workstation 1, 2 and 3 respectively. By using Poisson distribution similar to the series process, the bottleneck observed on the load movement in series process.



**Fig. 5.** The utilization rate of series process between workstation

The number of accumulating load is high in workstation 1, thus bottleneck detected in the simulated result. The load distributed in the workstation 1 by FIFO dispatching rule is shifted to the next workstation that connected in series. The workstation 2 accumulated load while unstable during the first part of running stimulation shows the utilization rate increases after the fluctuation of bottleneck stabilised. The results show that the workstation 2 has a high uptime during the process. The results in Fig. 5 for workstation 3 reveals that the utilization rate encounters no bottleneck fluctuation thus the uptime for workstation 3 steadily increases to 90%. However, the high utilization rate may reach the machine capacity of the workstation and the probability for the machine downtime is possible based on the simulated result for the prototype.

The comparison between two processes can be approached by observing the FIFO dispatching rule on the distributed load to workstation. Whilst the observation on the load time of each bottleneck is similar in parallel process, however the magnitude of the utilization rate is different between workstation.

## 4 Conclusion

In this paper, the numerical model is designed to generate the simulation for the scheduling rule in the production line for manufacturing industry. In addition, the proposed model performance is based on the Simulink result to correspond with the actual MEMS manufacturing line to verify the validity of the model. In the model the scheduling optimization can be applied in the model to increase the accuracy of the model. Using software-based development, the possibility to adopt the production line process based on the Simulink proposed model in developing a software capable of coordinating the workloads and the tools in a system, and to monitor and analyze the system to pinpoint the bottleneck in the system and integrate scheduling in the proposed model.

Ultimately, the simulation model serves as an initial attempt to examine and analyse the method of detection of bottleneck based on the framework topology. There are other research question regarding bottleneck detection and how implementing scheduling can help improving the throughput that can be expand. For example, the model assumes that the constant value of the machine capacity rate in producing lot, while in actual practice, stochastic downtime and human travel time can affect the machine capacity. Thus, it would be interesting to extend the model to further analyse the variable.

## References

1. Ahmed, S.: Reduction of bottleneck operations in just-in-time manufacturing (1991). Retrospective Theses and Dissertations. Paper 16776
2. Bai, J., So, K.C., Tang, C.: A queueing model for managing small projects under uncertainties. *Eur. J. Oper. Res.* **253**(3), 777–790 (2016). <https://doi.org/10.1016/j.ejor.2016.02.052>
3. Glock, C.H., Jaber, M.Y.: Learning effects and the phenomenon of moving bottlenecks in a two-stage production system. *Appl. Math. Model.* **37**(18–19), 8617–8628 (2013). <https://doi.org/10.1016/j.apm.2013.03.043>

4. Huang, B., Sun, Y., Sun, Y.-M., Zhao, C.-X.: A hybrid heuristic search algorithm for scheduling FMS based on Petri net model. *Int. J. Adv. Manuf. Technol.* **48**(9), 925–933 (2010). <https://doi.org/10.1007/s00170-009-2329-8>
5. Lawrence, S.R., Buss, A.H.: Economic analysis of production bottlenecks. *Math. Probl. Eng.* **1**(4), 341–363 (1995). <https://doi.org/10.1155/S1024123X95000202>
6. Leporis, M., Králová, Z.: A simulation approach to production line bottleneck analysis. In: *International Conference on Cybernetics and Informatics*, pp. 1–10 (2010). [https://folk.ntnu.no/skoge/prost/proceedings/slovak\\_control\\_conference\\_2010/pdf/39\\_Leporis%20Kralova.pdf](https://folk.ntnu.no/skoge/prost/proceedings/slovak_control_conference_2010/pdf/39_Leporis%20Kralova.pdf)
7. Li, L., Chang, Q., Ni, J.: Bottleneck detection of manufacturing systems using data driven method, August 2007. <https://doi.org/10.1109/ISAM.2007.4288452>
8. Li, L., Min, Z.: An efficient adaptive dispatching method for semiconductor wafer fabrication facility. *Int. J. Adv. Manuf. Technol.* **84**(1–4), 315–325 (2016). <https://doi.org/10.1007/s00170-016-8410-1>
9. Meerkov, S.M.: Bottlenecks in Markovian production lines: a systems approach. *IEEE Trans. Rob.* **14**(2), 352–359 (1998). <https://doi.org/10.1109/70.681256>
10. Samson, O.O., Sunday, A.A., Anthony, I.C.: Bottleneck problem detection in production system using Fourier transform analytics. *Int. J. Mech. Eng. Technol. IJMET* **9**(12), 113–122 (2018)
11. Chiang, S.-Y., Kuo, C.-T., Meerkov, S.M.: DT-bottlenecks in serial production lines: theory and application. *IEEE Trans. Rob. Autom.* **16**(5), 567–580 (2002). <https://doi.org/10.1109/70.880806>
12. Tran, T.T., Terekhov, D., Down, D.G., Beck, J.C.: Hybrid queueing theory and scheduling models for dynamic environments with sequence-dependent setup times, pp. 215–223 (2013)
13. Wang, J.Y.: *Queueing Theory*, pp. 1–24 (2009). [https://doi.org/10.1016/S0723-2020\(11\)80062-7](https://doi.org/10.1016/S0723-2020(11)80062-7)
14. Wang, Z., Chen, J., Wu, Q.: A new method of dynamic bottleneck detection for semiconductor manufacturing line. In: *IFAC Proceedings Volumes (IFAC-PapersOnline)*, vol. 17. IFAC (2008). <https://doi.org/10.3182/20080706-5-KR-1001.3201>
15. Zhang, R., Wu, C.: Bottleneck machine identification based on optimization for the job shop scheduling problem. *ICIC Express Lett.* **2**(2), 175–180 (2008)
16. Zhu, X., Qiao, F., Cao, Q.: Industrial big data-based scheduling modeling framework for complex manufacturing system. *Adv. Mech. Eng.* **9**(8), 1–12 (2017). <https://doi.org/10.1177/1687814017726289>



# Study of Sawing Performance of Band Saw Machine on Honeycomb Structure Material

Chun-An Cheng<sup>(✉)</sup> and Chin-Chung Wei

National Formosa University,  
No. 64, Wenhua Rd., Huwei Township, Yunlin 632, Taiwan (R.O.C.)  
10674128@gm.nfu.edu.tw

**Abstract.** This article investigate the influence of different sawing angle and different band saw cutting speed by measuring the sawing vibration, motor current and shear stress caused by sawing. The band saw carrier stand are the closest fixing parts of the sawing point, the sawing vibration is measured by the axis vector of the two adjustable band saw carrier stand, so that we can understand the main vibration behavior occurring during the sawing process. Motor is the heart of the band saw machine, more current is needed to drive when the sawing resistance is large, in case to ensure the smooth cutting process, motor current monitoring system is established to monitor the motor current. The load cell is buried in the feeding plate to measure the sawing load, the shear stress is obtained after conversion. This study is to find correlation between cutting rate, band saw speed, and cutting angle of the honeycomb structure on vibration, motor current and shear stress.

**Keywords:** Band saw machine · Honeycomb structure material · Vibration · Shear stress · Motor current

## 1 Introduction

Honeycomb structure materials are widely used in aerospace industry, construction industry and vehicle manufacturing industry because of its high specific strength and stiffness, good corrosion resistance, low density, unique rebound resilience and shock absorption, etc. The honeycomb structure is typical hard-to-machining material, it has an axial uniform distribution of the hexagonal prism grid with orthotropic characteristics and the supportive matrix is full of short fibers, it's easy to occur buckling, degumming or breaking on the honeycomb structure. Using band saw machine to separate the honeycomb structure has not been used in the industry. Due to the structure properties and to obtained the sawing quality of the material, it is necessary to spin the band saw in high speed, but the life of the saw band is much reduced.

At present, honeycomb materials mainly include paper, aluminum, and Nomex honeycombs. As for properties of honeycomb, Zhang et al. [1] studied the collapse behavior under both shear and simple compression in the out-of-plane direction is analyzed, buckling debonding and fracture are identified as possible collapse mechanisms. Lee et al. [2] investigate the mechanical behavior and failure mechanism of honeycomb composite consisting of Nomex honeycomb core, compression and shear

strengths of honeycombs composites are discussed. Zhou et al. [3] study the mechanical performance and energy absorption property of two-layer Nomex honeycombs, compressive tests on different combinations were conducted and the experimental results compared with those from tests on single honeycomb specimens. For ultrasonic assisted cutting honeycomb, Hu et al. [4] studied the experiments of blade cutting of honeycomb composites with ultrasonic and non-ultrasonic assistance were executed by the control variable method.

The effects of the cutting depth, the blade inclined angle and the deflection angle on the cutting force were verified, which were reflected by the cutting force theoretical model. For Nomex honeycomb, Karakoç et al. [5] present an experimental method to obtain the effective in-plane compliance matrices of cellular structures using Nomex honeycomb cores without a priori assumptions such as orthotropic. For aluminum honeycomb, Qiu et al. [6] introduced typical machining defects and studied the machining characteristics of honeycomb core. All the cutting burrs and defects were found to locate on the line with entrance angle is equal to  $80^\circ$  and  $170^\circ$ .

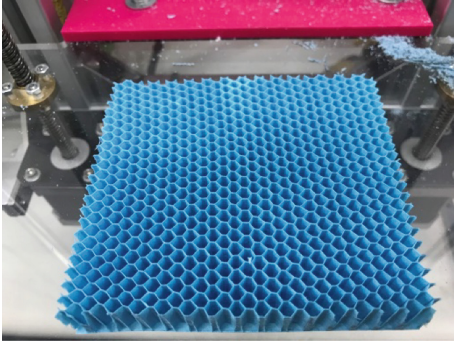
In summary, shear stress and compression in honeycomb structure has been analyzed, different way of machining honeycomb structure has been studied. Using a band saw to separate the material hasn't been studied, the best sawing parameters must be discussed including the associate of band saw speed, feeding rate and cutting angle. This article in order to investigate these parameters, captured the acceleration of the vibration, current of the motor to understand the relationship between signals.

## 2 Experiment Method

### 2.1 Experiment Setup

Experiment under different conditions were conducted to investigate the best cutting parameter. The work piece is paper hexagon honeycomb core shown in Fig. 1 with dimensions of  $80 \times 90 \times 15$  mm. The length of honeycomb cell wall is 3 mm and the thickness is 0.05 mm. The carpenter's glue method was used to hold the workpiece as to ensure the accuracy of cutting. The cutting experiment were carried out on self-made band saw machine with maximum band saw spindle speed of 1600 rpm. The cutting tool used in the tests was shown in Fig. 2 of which is made by Wikus and its specifications are M42 Ecoflex BiMetal  $1450 \times 13 \times 0.65 \times 10/14$  T. The sawing vibration were measured using a PCB Piezotronics accelerometer, coupled with a National Instruments 9174 compactDAQ. The motor current was captured by HIOKI AC/DC HiTESTER 3284, coupled with a memory HiCORDER MR8870. The detailed tool parameters are listed in Table 1. The band saw speed is calculated from the motor rotating speed.





**Fig. 1.** Honeycomb workpiece



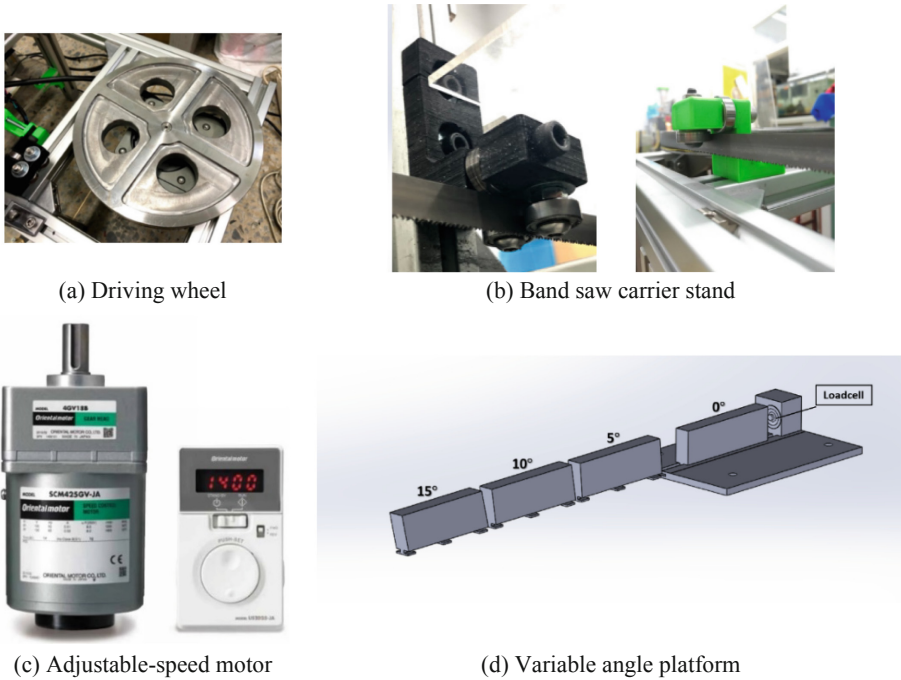
**Fig. 2.** Band saw blade

**Table 1.** The cutting tool parameters and cutting conditions

Band saw speed	502 m/min, 628 m/min, 753 m/min, 879 m/min, 1004 m/min
Cutting angle	0°, 5°, 10°, 15°
Cutting material	80 mm × 90 mm × 15 mm Paper Honeycomb
Band saw type	WIKUS ECOFLEX 1450 × 13 × 0.65 × 10/14T

## 2.2 Band Saw Machine

The band saw machine can be divided into four parts which is the saw bow system, the electronic motor control system, the feeding platform system, and the base of the machine. The saw bow system mainly contains the driving wheel shown in Fig. 3(a), the idle wheel and also the band saw blade. According to Du et al. [8], the saw band skew will obviously occur when the fixed tungsten steel in the guide arm further away from the cutting center. Therefore, placing the band saw carrier stand in the correct place is important as shown in Fig. 3(b). The electronic motor control system contains the stepper motor controlled by Arduino and the adjustable-speed motor by Oriental Taiwan as shown in Fig. 3(c). The stepper motor drive the feeding platform system, the maximum cutting area is 65 × 170 mm. In order to change the cutting angle, few angles platform is designed and printed by the 3D printer as shown in Fig. 3d. The base of the machine is made by aluminum extrusions, it can take care of both lightweight and structure rigidity. Normally, the band saw machine has the hydraulic cylinder oil tank and the cutting fluid tank, but in this experiment, the hydraulic cylinder has been replacing to stepper motor, and the coolant lubricant system is no need in cutting paper honeycomb material, because the general purpose of the band saw machine is to saw the steel material, so it is needed to use the hydraulic cylinder to clamp the material, but using the polyester resin to clamp the paper honeycomb on the fixture is enough.



**Fig. 3.** Different part of the band saw machine

### 3 Result and Discussion

#### 3.1 Sawing Vibration Analysis

In order to find the characteristic frequency of sawing on the honeycomb material, we capture original vibration data shown in Fig. 4, in this figure we can't find any significant frequency that can be description, so after making the Fourier transform, every frequency and their energy will obviously show in Visual Signal. Normally, the significant frequency will appear under 300 Hz. We discuss the four different angle on two different band saw speed. For the band saw operate on 800–1600 rpm without cutting, there is no significant frequency under 300 Hz as shown in Fig. 5. For 0° cutting angle to 15° cutting angle, we sort out the frequency of 45.5 Hz, 57.2 Hz, 80 Hz, 91.3 Hz, 102.8 Hz, 114.24 Hz are the most significant frequency to represent the honeycomb sawing. Other frequency only appear on specific cutting angle, such as 68.5 Hz only appear on 0°, 10° and 15°. 106.5 Hz only appear on 5° and 10°. 126 Hz only appear on 10° and 15° and 137 Hz appear on 5°, 10° and 15° as shown in Fig. 6, 7, 8 and 9.

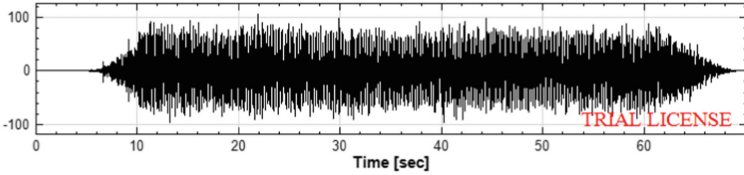


Fig. 4. Original vibration data

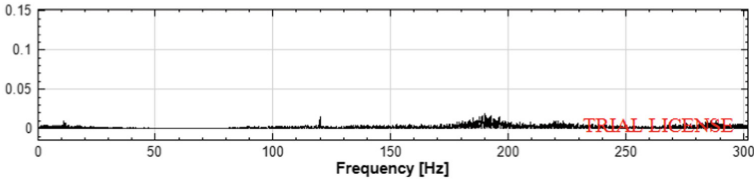
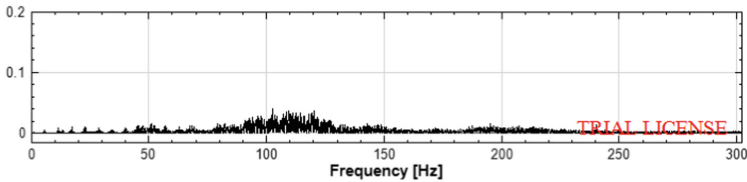
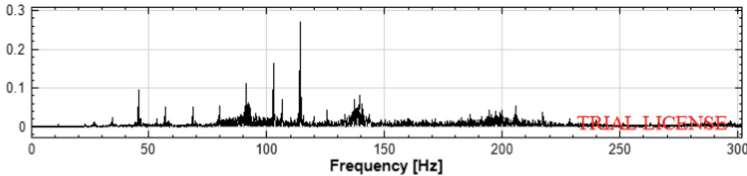


Fig. 5. Motor rotate without cutting



(a) 502 m/min

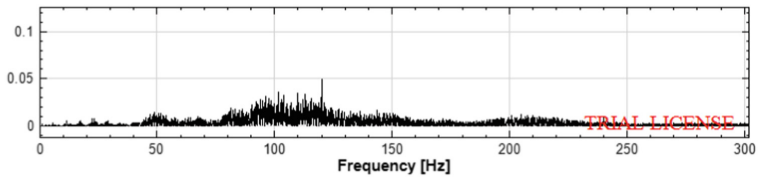


(b) 1004 m/min

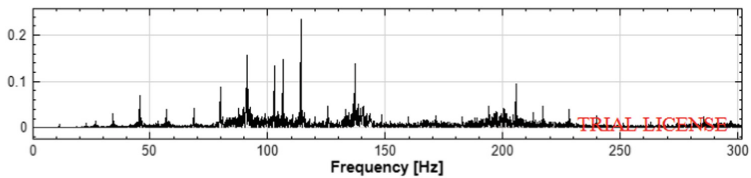
Fig. 6.  $0^\circ$  cutting angle compared with band saw speed

After analyzing the data through Fourier transform, discover that frequency changes over time, so using the Fast Short Term Fourier transform to show the Time-Frequency figure. In this figure we can understand the distribution of frequencies at different times. For the band saw rotate without cutting we figure out that the distribution of frequencies is similar when the band saw speed is low, by the band saw speed increase the distribution of frequencies will have a minor change. For  $0^\circ$  cutting angle, when compare the band saw speed at 502 m/min, the major frequency distributed on 803.35 Hz, the energy is 0.85 G, 1660.3 Hz, the energy is 1.465 G, 2784.9 Hz, the energy is 0.648 G, 5355.6 Hz, the energy is 2.65 G, around 6800 Hz and 12000 Hz of

the frequency is interpretation as friction as shown in Fig. 10. For the band saw speed at 1004 m/min, the major frequency distributed on 3374.1 Hz, the energy is 4.33 G, 4123.8 Hz, the energy is 1.4 G, 5837.7 Hz, the energy is 3.6295 G, the high frequency around 6800–10,300 Hz is also interpretation as friction as shown in Fig. 11. For 5°, 10° and 15° cutting angle time-frequency analysis they all have the same trend.

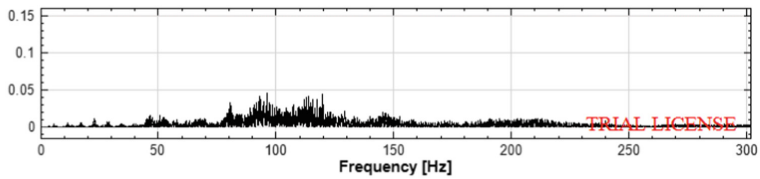


(a) 502 m/min

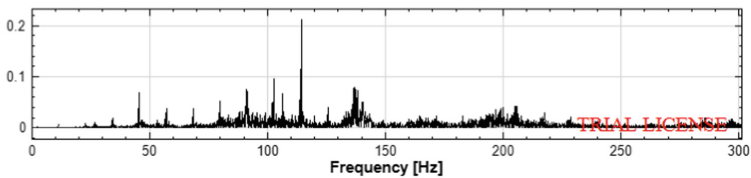


(b) 1004 m/min

**Fig. 7.** 5° cutting angle compared with band saw speed



(a) 502 m/min



(b) 1004 m/min

**Fig. 8.** 10° cutting angle compared with band saw speed

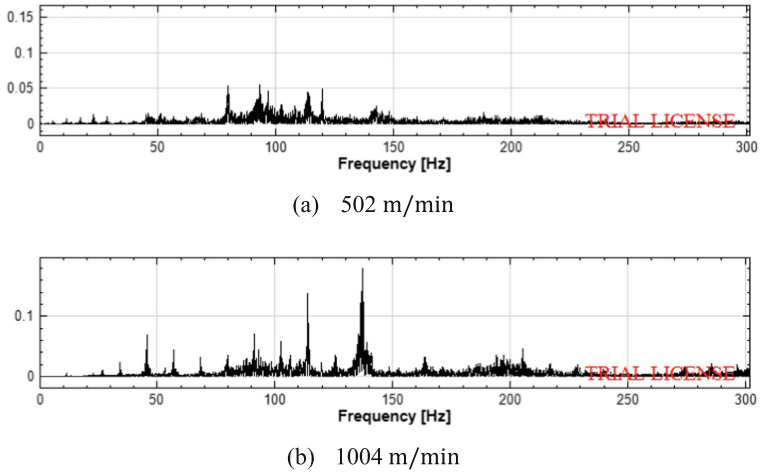


Fig. 9. 15° cutting angle compared with band saw speed

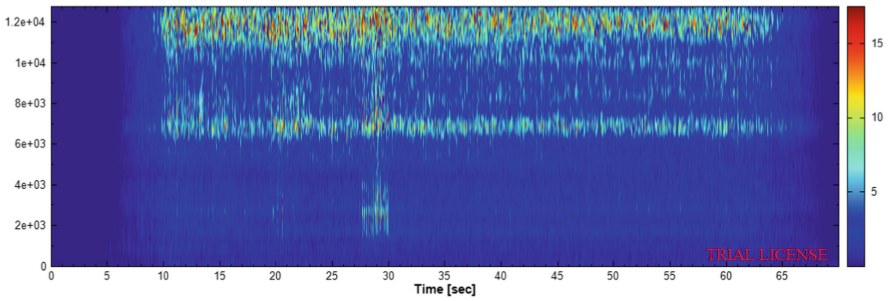


Fig. 10. Time-frequency of 0° cutting angle on band saw speed 502 m/min

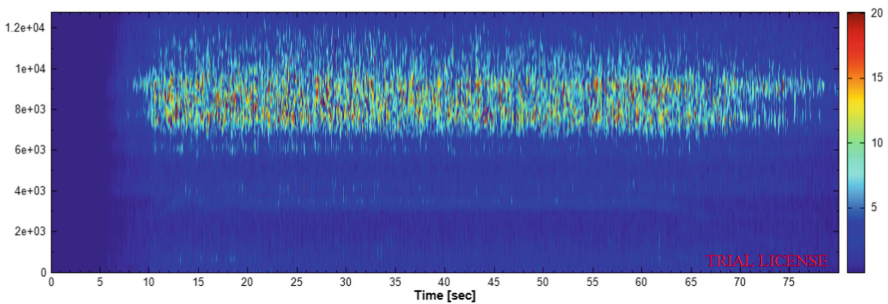
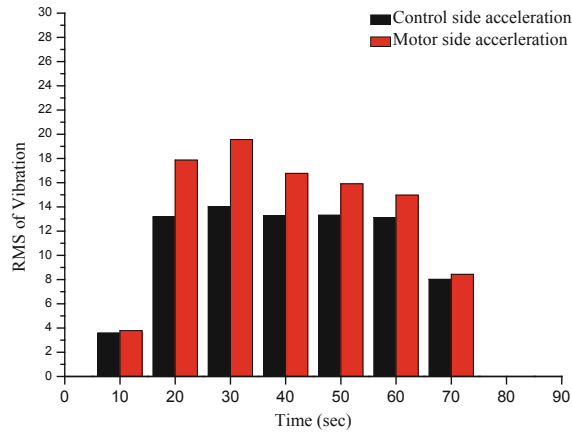
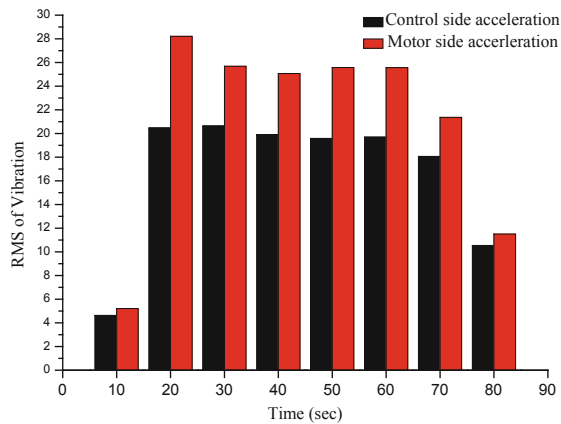


Fig. 11. Time-frequency of 0° cutting angle on band saw speed 1004 m/min

Although the band saw cutting at high speed has fewer low frequency, but after calculating the RMS (Root Mean Square) value of vibration, sawing with high speed has totally more vibration than sawing with low speed as shown in Fig. 12. It is because the more energy the motor gave to spin the driving wheel the more vibration it will cause vibration due to the machine stiffness isn't too strong to hold.



(a)



(b)

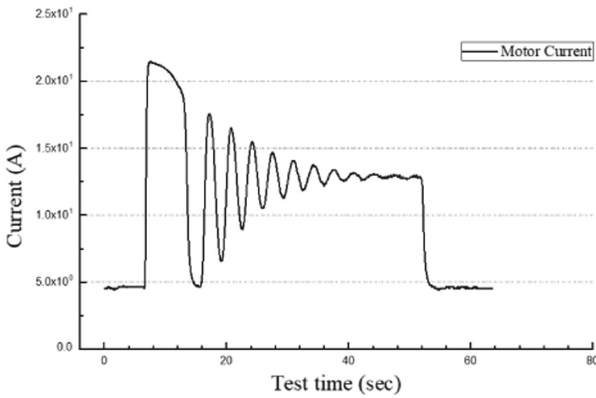
**Fig. 12.** RMS of vibration (a) Band saw speed 502 m/min cutting (b) Band saw speed 1004 m/min cutting

### 3.2 Motor Current Analysis

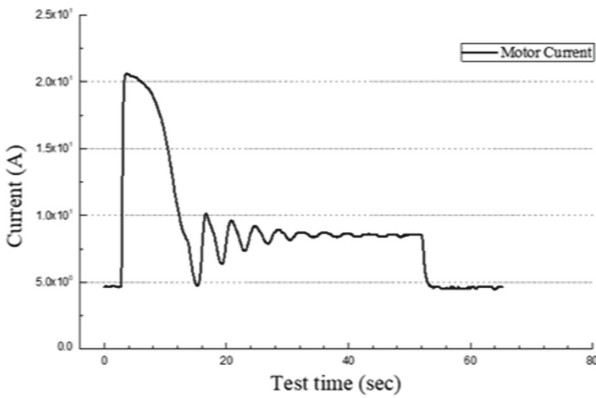
In addition to capture the motor current, we also calculated the motor torque by using the Equation [1].

$$\tau = \frac{I \times V \times E}{2 \times \pi \times f} \tag{1}$$

By measuring the motor current, the difference between the actual cutting and motor rotate without load can be obviously seen. First, the original signal of the motor rotate without load will decrease as the band saw speed increase as shown in Fig. 13. The initial current difference is almost none, but the sawing process will actually increase as shown in Fig. 14. From the analysis, when the band saw speed is 502 m/min, the difference between the original current and the sawing current will be



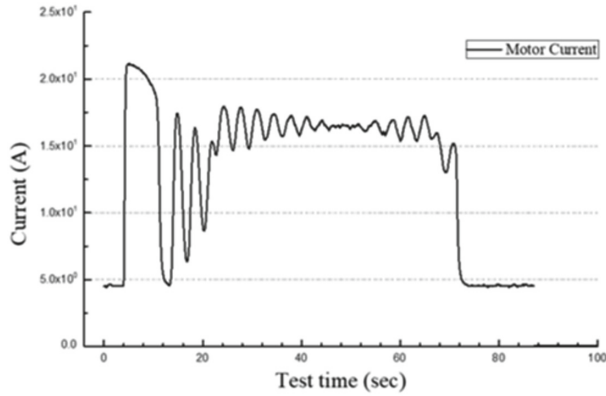
(a) 502 m/min



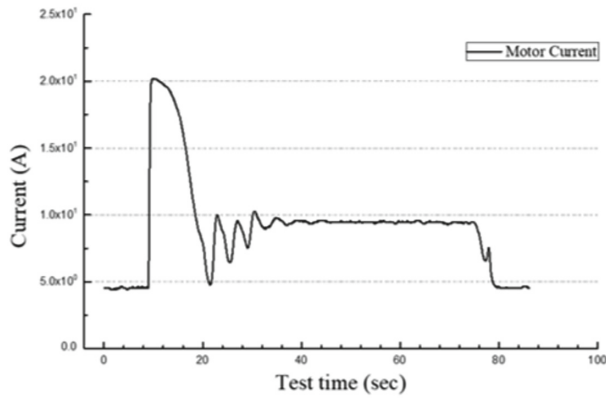
(b) 1004 m/min

**Fig. 13.** Motor current of different band saw speed rotate without load

larger than the band saw speed at 1004 m/min. By calculating the difference between the average of operate without load and the actual sawing current, when the band saw speed at 502 m/min, the difference is 3.74 A, band saw speed at 628 m/min, the difference is 2.52 A, band saw speed at 753 m/min, the difference is 1.68 A, band saw speed at 879 m/min, the difference is 1.58 A, band saw speed at 1004 m/min, the difference is 1.48 A as shown in Fig. 15.



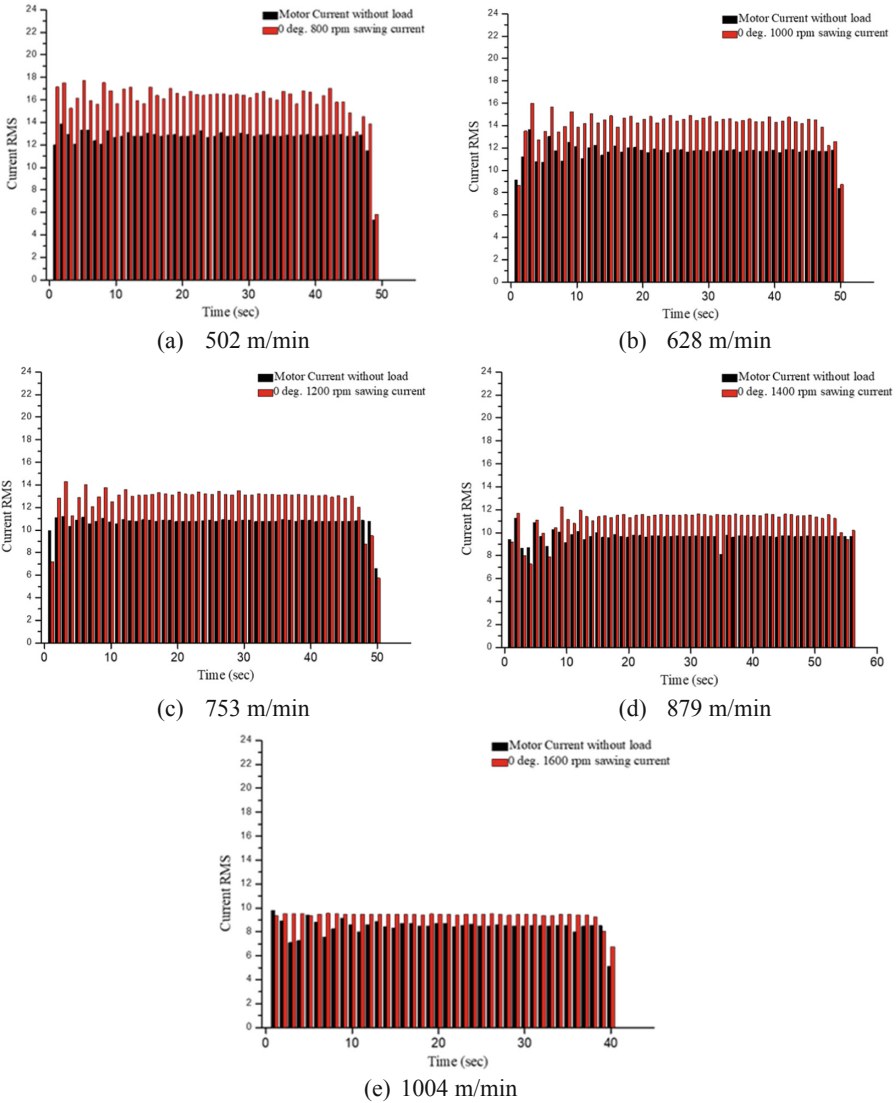
(a) 502 m/min sawing



(b) 1004 m/min sawing

**Fig. 14.** Motor current of different band saw speed sawing





**Fig. 15.** Motor current compare between operate without load and sawing

After converting the current into torque to understand the actually load difference on the sawing process by Equation [1], from low speed to high speed, respectively 1.79 N, 1.2 N, 0.8 N, 0.756 N, 0.709 N. The average of sawing torque is shown in Fig. 16. The torque of the motor decrease when the band saw speed increase, also the comparison between different cutting angle effects the torque, when the cutting angle at 0°, more torque is needed to drive the band saw, because it causes more resistance to it. When the cutting angle at 15°, torque needs to saw the material is about equal to the motor operate without load.

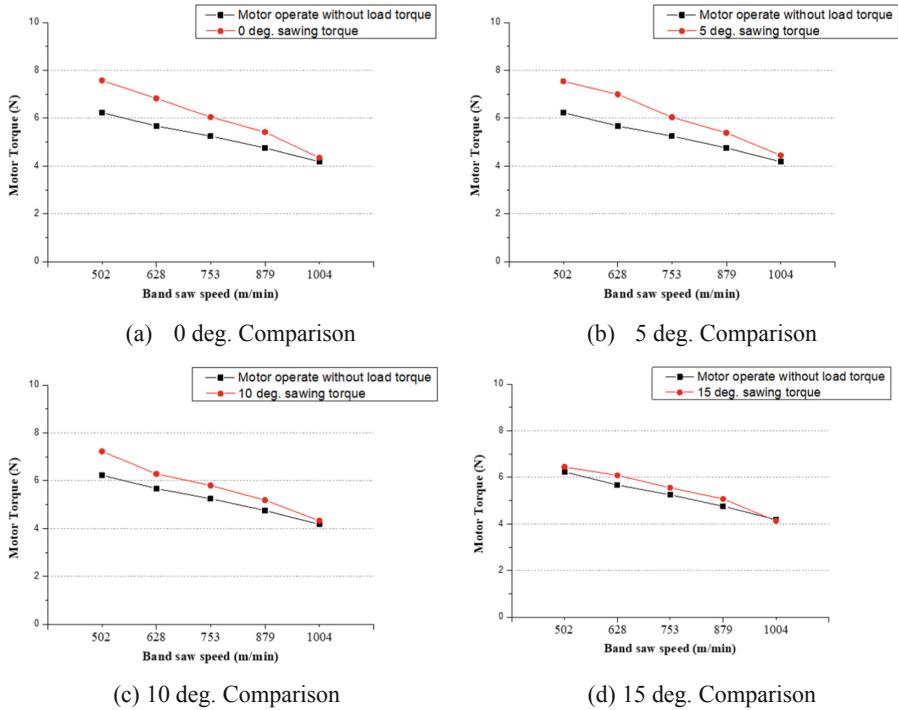


Fig. 16. Torque comparison between motor operate without load and sawing current

## 4 Conclusion

1. The significant frequency has been discussed based on different band saw speed sawing on different sawing angle. The most often appear frequency landing in 45.5 Hz, 57.1 Hz, 80 Hz, 91.3 Hz, 102.7 Hz, 114.3 Hz. High speed sawing vibration of low frequency is much less than low speed sawing, so increasing the band saw speed to saw the honeycomb material is effective. When the band saw speed increase, the less low frequency was discovered, so the mechanical vibration has inhibition. For the honeycomb material, the less vibration is produced, the cutting surface will be better.
2. The motor current difference between without load and sawing were discussed. Increasing the band saw speed is effective to reduce the current to drive the motor, it means that the sawing resistance is also reduced. By the experiment, band saw speed at 1004 m/min sawing only need 0.709 N more to cut the material. Conversely when the band saw speed at 502 m/min sawing, it need 1.79 N more to drive the motor to cut the material.

3. The cutting angle is also the main character of the sawing process. Experiment shows the torque comparison between different cutting angle and band saw speed, it is shown that the torque decrease when the band saw speed increase above the experiment, the torque also proves this discussion is right. As different cutting angle, it is shown that when the cutting angle increase, the difference between the torque of the low speed band saw sawing process decrease. It is necessary to study the blade entering material angle to find out the reason.
4. Above all, sawing vibration showed that increasing the band saw speed is effective to saw the material, because it's low frequency of vibration is much less than high speed sawing. The current analysis also showed that by increasing the band saw speed, it can reduce the current to drive the motor because the sawing resistance is much less than others. In these two issue, we found out that increasing the band saw speed to saw honeycomb is effective.

**Acknowledgements.** This research was undertaken at the Precision Machinery and Surface Science Laboratory of Department of Power Mechanical Engineering, National Formosa University. The authors gratefully acknowledge the support from the Ministry of Science and Technology (MOST 107-2221-E-150-015-).

## References

1. Zhang, J., Ashby, M.F.: *J. Mech. Sci.* **34**(6), 475–489 (1992)
2. Lee, H.S., Hong, S.H., Lee, J.R., Kim, Y.K.: *J. Mater. Sci.* **37**, 1265–1272 (2002)
3. Zhou, H., Ping, X., Xie, S., Feng, Z., Wang, D.: *J. Compos. Struct.* **185**, 524–536 (2018)
4. Hu, X.P., Yu, B.H., Li, X.Y., Chen, N.C.: 1st Crip Conference on Composite Materials Parts Manufacturing, CRIP-CCMPM 2017 (2017)
5. Karakoç, A., Freund, J.: *J. Compos. Struct.* **94**, 2017–2024 (2012)
6. Qiu, K., Ming, W., Shen, L., An, Q., Chen, M.: *J. Compos. Struct.* **164**, 58–67 (2017)
7. Roark, R.J., Young, W.C.: *Formulas for Stress and Strain*. McGraw-Hill Kogakusha, Tokyo (1975)
8. Du, W.M.: Master thesis, National Formosa University (2018)
9. Wu, S.-H., Huang, M.-S., Zhou, C.-E., Wei, C.-C.: *MATEC Web of Conferences*, vol. 201, p. 01001 (2018)
10. Jhang Jian, L.-H.: Master thesis, National Formosa University (2017)
11. Zhang, J.-B.: Master thesis, National Formosa University (2015)



# Improvement of Material Removal Rate (MRR) Through Ultrasonic Vibration Frequency in Machining Hardened Material

Azlan Ramli<sup>(✉)</sup>, R. Izamshah, and M. Akmal

Fakulti Kejuruteraan Pembuatan, Universiti Teknikal Malaysia Melaka (UTeM),  
Hang Tuah Jaya, 76100 Durian Tunggal, Melaka, Malaysia  
azlanramli@pms.edu.my, izamshah@utem.edu.my,  
akmalzak@student.edu.my

**Abstract.** Machining hardened D2 tool steel material for mold and die application facing many problems such as low material removal rate, poor machined surface, high cutting force, extreme machining temperature and rapid tool wear. A new machining strategies using rotary ultrasonic assisted end milling (RUAEM) is proposed aim to improve material removal rate (MRR) and machining time. To evaluate on the effectiveness, machining test were perform between conventional machining and RUAEM with different slurry concentration ranging from 0 to 20% alumina oxide contents. Taguchi statistical technique was used as the experiment design consists of independent variables i.e. cutting speed, feed rate, depth of cut, frequency vibration, amplitude vibration and abrasive slurry concentration with MRR as the machining response. The highest MRR with an average value of 161.58 mg/min was obtained from the combination of runs no. 12-e (Speed of 30 rpm, 45 mm/min feed rate, 30  $\mu$ m depth of cut, frequency of 27 kHz, 1  $\mu$ m amplitude and 20% concentration). From ANOVA analysis, it proved that the strongest machining parameter factor that affecting the material removal rate (MRR) are cutting speed (A), feed rate (B), depth of cut (C), % slurry concentration (E), cutting speed & depth of cut (AC), cutting speed & frequency (AD) and cutting speed & amplitude (AE). The result indicates that by adding ultrasonic frequency can improve the MRR values in machining hardened materials.

**Keywords:** Hardened D2 tool steel · RUAEM · Material removal rate

## 1 Introduction

Hardened D2 tool steel material is very popular material for mold and die industries especially in automotive, electronic and computer [1]. The problem existence in conventional machining of hardened D2 tool steel are low material removal rate, poor machined surface, high cutting force, extreme machining temperature and rapid tool wear [2–6]. In current process, slow machining are generally employed in order to control the machining performances i.e. surface roughness and tool wear which result in low MRR [7]. Therefore to solve with the discrepancies, new strategies with advanced machining technique are require to improve machining performance such as

rotary ultrasonic assisted machining. Rotary ultrasonic assisted machining is a non-conventional machining process which combined the ultrasonic vibration to the rotating end mill cutter [8]. The material removal mechanism during ultrasonic machining (USM) involved three main mechanics namely direct hammering of the abrasive particles on the workpiece, impact of the free-moving abrasive particles on the workpiece and erosion on the work surface due to cavitations effect of the abrasive slurry [9–11]. By incorporating the ultrasonic vibration frequency (20 kHz) to the rotating tool will help to increase the MRR apart from the normal shearing process performed by the milling cutter [12].

In order to perform the rotary ultrasonic assisted end milling (RUAEM) process, a custom ultrasonic pulse generator are developed consists of main pulse generation module, voltage driver, frequency controller and ultrasonic transducer. The high-frequency electrical signal is transmitted to the transducer which converts it into high frequency (15–20 kHz), low amplitude vibration (5 microns). The function of the transducer is to convert electrical energy into mechanical vibration using the principle of magnetostriction and transmitted to the rotating end mill tool as shown in Fig. 1.

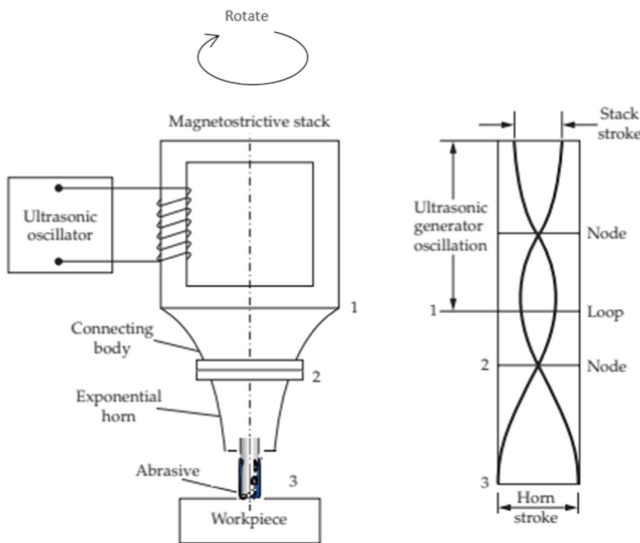


Fig. 1. Principle of RUAEM [13]

## 2 Methodology

### 2.1 Material

The work piece material used in an experiments was rectangular block of Hardened D2 Tool Steel with dimension 100 mm × 100 mm × 20 mm (W × L × H) and Rockwell hardness of 51 HRC. The chemical properties of hardened AISI D2 tool steel is shown in Table 1.

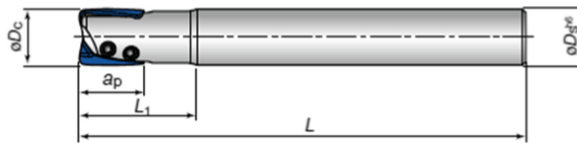
**Table 1.** Chemical properties of hardened AISI D2 tool steel

Composition	C	Si	Mn	Cr	Mo	V
% weight	1.55	0.3	0.4	11.8	0.8	0.8

Before the experiments test, the workpiece was skimmed down to 0.5 mm by vertical milling machine to remove any surface problem, cracks or any defect from previous manufacturing process [14].

## 2.2 Cutting Tool

A straight shank type EPH Hybrid TAC Mills with TiAlN/AlCrN coated carbide insert was used to perform the machining process. Figure 2 shows the cutting tool specification used in the experiment.

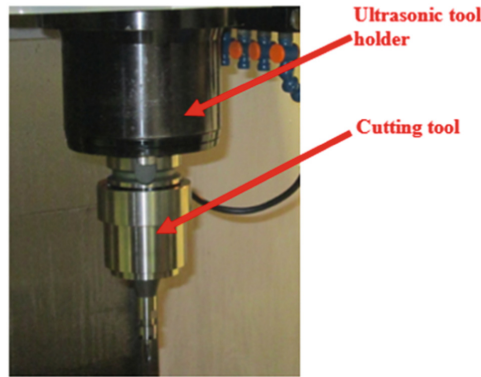


Type	XHGR110208ER
Shape	Rectangle
Grade	AH730
Coating	TiAlN
Applicable Material	Steel
Insert edge length	0.433"
Cutting length	0.394"
Corner radius	0.031"
Cutting edge material	C

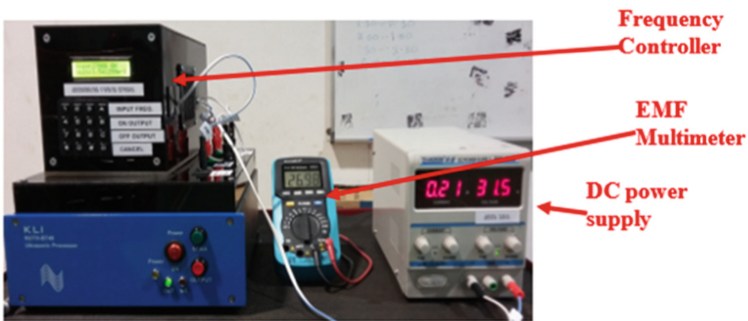
**Fig. 2.** Cutting tool specification

## 2.3 RUAEM Machine and Equipment

An ultrasonic tool holder type NUTH-BT40-ER-11 was used to perform the RUAEM process. The ultrasonic tool holder is controlled manually by ultrasonic processor using a frequency controller. The ultrasonic processor will transmit the high-frequency electrical signal to the transducer built inside the tool holder to produce a rotary vibration machining process. The operating frequency of the ultrasonic tool holder ranging between 20 to 27 kHz. The frequency output from frequency controller is measured using the EMF multimeter. Figures 3 and 4 show the ultrasonic tool holder and frequency controller respectively.



**Fig. 3.** Ultrasonic tool holder NUTH-BT40-ER-11 used in the experiments



**Fig. 4.** Experimental setup of DC power supply with ultrasonic processor and frequency controller

## 2.4 Machining Parameters and Design of Experiment (DoE)

The RUEAM independent variables studies consists of cutting speed, feed rate, depth of cut, vibration frequency, vibration amplitude and different percentage of Alumina Oxide concentration. While, the dependent variable is categorized as machining performance i.e. material removal rate (MRR). Table 2 shows the levels of independent variables values.

Taguchi statistical technique was used in this experiments to identify the control factors that affect the MRR. Table 3 shows the experimental runs for five (5) factors and three levels which that requires 27 experimental runs. All the machining conditions will be repeated 6 times for performing different machining techniques consists of conventional machining, ultrasonic machining and ultrasonic machining with difference slurry concentration i.e. 5%, 10%, 15% and 20%. The total experiment runs are 162 runs.

**Table 2.** Level of independent variables

Machining parameters variables	Level		
	- 1	0	+ 1
(A) Cutting speed, Vc (rpm)	30	90	150
(B) Feed rate, f (mm/min)	5	25	45
(C) Depth of cut, d ( $\mu\text{m}$ )	10	20	30
(D) Frequency vibration, f (kHz)	20	23	27
(E) Amplitude vibration, A ( $\mu\text{m}$ )	1	2	3
(F) Alumina oxide slurry (%)	0	10	20

**Table 3.**  $L^{27}$  orthogonal array for five factors and three levels ( $3^5$ )

Runs no.	Factor 1: (A) cutting speed	Factor 2: (B) feed rate	Factor 3: (C) depth of Cut	Factor 4: (D) frequency	Factor 5: (E) amplitude
1	0	1	-1	0	0
2	0	0	1	-1	-1
3	0	0	1	-1	0
4	1	1	0	-1	-1
5	1	1	0	-1	0
6	0	-1	0	1	-1
7	0	-1	0	1	0
8	1	0	-1	1	1
9	1	0	-1	1	0
10	0	1	-1	0	1
11	-1	-1	-1	-1	-1
12	-1	1	1	1	-1
13	1	-1	1	0	0
14	1	-1	1	0	-1
15	-1	-1	-1	-1	1
16	0	1	-1	0	-1
17	-1	-1	-1	-1	0
18	-1	0	0	0	-1
19	-1	1	1	1	1
20	-1	0	0	0	1
21	-1	1	1	1	0
22	1	-1	1	0	1
23	1	1	0	-1	1
24	0	0	1	-1	1
25	1	0	-1	1	-1
26	0	-1	0	1	1
27	-1	0	0	0	0



### 3 Results and Discussion

MRR is one of the important factor that used as the basic for measuring and rating the productivity of tools and machines. It was found that the mechanics of material removal process for RUAEM are complicated and the non-existence of the mechanistic model to quantify the rate of material removal precisely, it is therefore the most suitable and practical method to measure MRR are by measuring the weight of material losses per specific time depicted as:

$$MRR \left( \frac{mg}{min} \right) = \frac{\text{Weight before machining} - \text{Weight after machining}}{\text{Machining Time}} \tag{1}$$

The weight of the sample was measured using the precision weighing scale before performing the machining process. Once the machining process were completed, the sample will be cleaned using the ultrasonic cleaner machine before weighing for measuring the total of weight been removed. The machining slot are set to 100 mm in length and the time taken to complete the slot distance are recorded. The obtained MRR result are tabulated in Table 4 and Fig. 5.

**Table 4.** Experimental result for the material removal rate for RUAEM

Run	MRR (mg/min)			Run	MRR (mg/min)			Run	MRR (mg/min)			Run	MRR (mg/min)										
	1	2	Average		1	2	Average		1	2	Average		1	2	Average								
1	a	44.94	44.90	44.90	44.91	0	a	17.10	17.00	17.02	17.04	10	a	0.58	0.59	0.58	0.58	22	a	1.75	1.76	1.76	1.75
	b	45.14	45.09	45.09	45.10		b	17.19	17.09	17.10	17.13		b	0.61	0.60	0.61	0.61		b	1.70	1.79	1.80	1.79
	c	49.44	49.35	49.30	49.36		c	18.79	18.70	18.67	18.72		c	0.65	0.65	0.65	0.65		c	1.88	1.98	1.97	1.98
	d	51.69	51.60	51.52	51.61		d	19.60	19.60	19.50	19.57		d	0.69	0.67	0.66	0.68		d	2.06	2.03	2.05	2.06
	e	53.94	53.85	53.75	53.85		e	20.48	20.39	20.39	20.42		e	0.74	0.75	0.75	0.74		e	2.16	2.15	2.15	2.15
	f	44.95	44.90	44.90	44.91		f	17.02	17.00	16.94	16.98		f	0.59	0.59	0.59	0.59		f	1.76	1.76	1.76	1.75
2	a	51.01	50.99	50.96	50.98	9	a	17.10	17.00	16.99	17.03	10	a	44.95	44.90	44.85	44.90	23	a	89.78	89.80	89.80	89.80
	b	51.22	51.22	51.19	51.21		b	17.19	17.08	17.03	17.10		b	45.14	45.09	45.04	45.09		b	90.30	90.20	90.13	90.21
	c	56.14	56.08	56.02	56.08		c	18.78	18.70	18.67	18.71		c	49.44	49.35	49.25	49.35		c	98.81	98.80	98.72	98.78
	d	58.68	58.62	58.59	58.63		d	19.56	19.53	19.53	19.54		d	51.64	51.58	51.60	51.60		d	102.24	102.20	102.15	102.20
	e	61.21	61.17	61.11	61.16		e	20.41	20.38	20.35	20.38		e	53.93	53.85	53.75	53.84		e	122.15	122.06	121.96	122.06
	f	51.02	50.99	50.99	51.00		f	17.02	17.00	16.94	16.98		f	44.95	44.90	44.90	44.91		f	89.78	89.75	89.75	89.76
3	a	51.05	50.99	50.93	50.99	10	a	44.96	44.90	44.90	44.92	17	a	0.57	0.57	0.58	0.57	24	a	51.02	50.99	50.99	51.00
	b	51.26	51.22	51.16	51.22		b	45.15	45.09	45.09	45.11		b	0.61	0.59	0.59	0.60		b	51.28	51.22	51.19	51.23
	c	56.14	56.08	56.02	56.08		c	49.45	49.36	49.30	49.37		c	0.66	0.67	0.65	0.66		c	56.11	56.08	56.05	56.08
	d	58.70	58.65	58.59	58.64		d	51.66	51.60	51.59	51.62		d	0.68	0.67	0.66	0.67		d	58.67	58.66	58.67	58.66
	e	61.24	61.18	61.12	61.18		e	53.90	53.88	53.80	53.86		e	0.73	0.74	0.74	0.73		e	61.22	61.20	61.15	61.19
	f	51.02	50.99	50.99	51.00		f	44.95	44.90	44.90	44.91		f	0.59	0.59	0.58	0.59		f	51.02	50.99	50.99	51.00
4	a	89.59	89.78	89.65	89.77	11	a	0.58	0.57	0.58	0.58	18	a	24.02	23.99	23.99	24.00	25	a	17.00	17.00	17.00	17.01
	b	90.27	90.18	90.08	90.18		b	0.60	0.59	0.59	0.60		b	34.22	34.14	34.13	34.16		b	17.11	17.08	17.05	17.08
	c	96.84	96.75	96.65	96.75		c	0.65	0.65	0.65	0.65		c	37.41	37.32	37.38	37.37		c	18.73	18.70	18.67	18.70
	d	103.22	103.16	103.10	103.16		d	0.68	0.67	0.67	0.67		d	39.11	39.06	39.09	39.08		d	19.56	19.53	19.50	19.53
	e	117.74	117.70	117.65	117.70		e	0.72	0.72	0.73	0.72		e	40.83	40.76	40.74	40.78		e	20.38	20.36	20.35	20.37
	f	89.84	89.75	89.65	89.75		f	0.59	0.59	0.58	0.59		f	24.02	23.99	23.99	24.00		f	17.02	17.00	16.94	16.98
5	a	89.87	89.80	89.67	89.78	12	a	134.69	134.64	134.64	134.66	19	a	134.70	134.70	134.64	134.66	26	a	1.18	1.17	1.17	1.17
	b	90.28	90.20	90.09	90.19		b	135.41	135.31	135.22	135.31		b	135.39	135.38	135.27	135.35		b	1.19	1.19	1.18	1.19
	c	96.88	96.77	96.65	96.77		c	140.14	140.09	140.05	140.09		c	140.16	140.09	140.11	140.12		c	1.30	1.29	1.29	1.29
	d	103.24	103.20	103.10	103.18		d	154.81	154.80	154.74	154.78		d	154.84	154.80	154.80	154.81		d	1.35	1.35	1.34	1.35
	e	122.10	122.01	121.90	122.00		e	161.52	161.54	161.50	161.52		e	161.60	161.56	161.49	161.58		e	1.43	1.44	1.41	1.43
	f	89.84	89.75	89.65	89.75		f	134.69	134.64	134.60	134.64		f	134.69	134.64	134.60	134.64		f	1.18	1.17	1.17	1.17
6	a	1.16	1.15	1.15	1.15	13	a	1.74	1.75	1.75	1.74	20	a	34.09	33.99	33.99	34.02	27	a	34.03	33.99	33.99	34.01
	b	1.18	1.18	1.17	1.17		b	1.79	1.77	1.77	1.78		b	34.25	34.17	34.17	34.18		b	34.29	34.17	34.14	34.17
	c	1.30	1.29	1.27	1.29		c	1.96	1.97	1.97	1.96		c	37.49	37.38	37.32	37.40		c	37.41	37.38	37.38	37.39
	d	1.34	1.33	1.33	1.33		d	2.04	2.05	2.01	2.04		d	39.20	39.10	39.03	39.11		d	39.12	39.09	39.09	39.10
	e	1.40	1.41	1.40	1.40		e	2.13	2.13	2.13	2.13		e	40.89	40.80	40.79	40.82		e	40.82	40.80	40.80	40.80
	f	1.18	1.17	1.17	1.17		f	1.77	1.76	1.75	1.76		f	34.02	33.99	33.99	34.00		f	34.05	33.99	33.96	33.99
7	a	1.17	1.16	1.16	1.16	14	a	1.71	1.73	1.75	1.73	21	a	134.69	134.67	134.64	134.67						
	b	1.19	1.18	1.17	1.18		b	1.77	1.77	1.77	1.77		b	135.36	135.31	135.31	135.33						
	c	1.30	1.29	1.27	1.29		c	1.94	1.94	1.94	1.94		c	140.14	140.09	140.09	140.11						
	d	1.36	1.34	1.34	1.34		d	2.03	2.02	2.01	2.02		d	154.84	154.80	154.75	154.80						
	e	1.41	1.41	1.40	1.41		e	2.12	2.11	2.11	2.11		e	161.50	161.54	161.50	161.54						
	f	1.18	1.17	1.17	1.17		f	1.77	1.76	1.75	1.76		f	134.69	134.64	134.60	134.64						

Remarks: a-RUAEM with 0% slurry, b-RUAEM with 5% slurry, c-RUAEM with 10% slurry, d-RUAEM with 15% slurry, e-RUAEM with 20% slurry, f-conventional machining

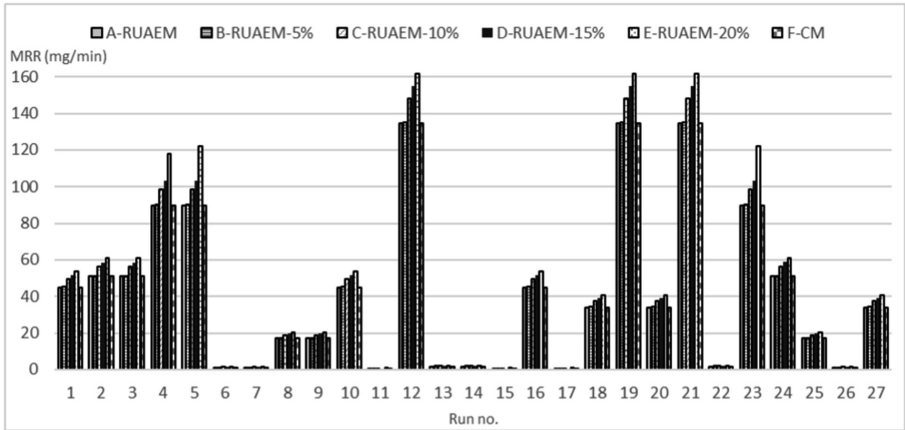


Fig. 5. Comparison of material removal rate between runs

According to Table 4, the average MRR value for all the runs varied between 0.562 and 161.58 mg/min with overall mean of 45.04 mg/min. The variations seen in the MRR values indicated that the studied factors i.e. cutting parameters has significant effect on the response values (MRR).

It can be observed that the combination of runs no. 12-e (Speed of 30 rpm, 45 mm/min feed rate, 30  $\mu$ m depth of cut, frequency of 27 kHz, 1  $\mu$ m amplitude and 20% concentration) produced the highest MRR with an average value of 161.58 mg/min. As with conventional milling process, the MRR value are dependent with the combination between feed rate and depth of cut values i.e. higher values will increase the MRR. However, for the case of RUAM, others than feed rate and depth of cut; frequency, amplitude and slurry concentration has direct effect on MRR values. In RUAM, additional material removal mechanism was created by the impact of abrasive particle to the workpiece surface which increase the MRR. Apart from that, the obtained result shows that the optimal combination of RUAM cutting parameter can increase the MRR values.

Meanwhile, the combination of run no. 11-f (Non-ultrasonic, speed of 30 rpm, 5 mm/min feed rate and 10  $\mu$ m depth of cut) produced the lowest MRR with an average value of 0.56 mg/min. Apart from the non-presence of ultrasonic vibration, one of the main reason for the lower MRR value obtained from the combination of this run was due to the combination of low feed rate as well with low depth of cut which removed the workpiece material lesser and slowly. Consequently, in both RUAM and conventional milling process, the selection of cutting parameters and vibrating parameters affects the MRR value. Therefore, in order to understand the effects and contribution of the parameter on the response clearly, statistical ANOVA are performed (Table 5).

**Table 5.** ANOVA result for the material removal rate (MMR)

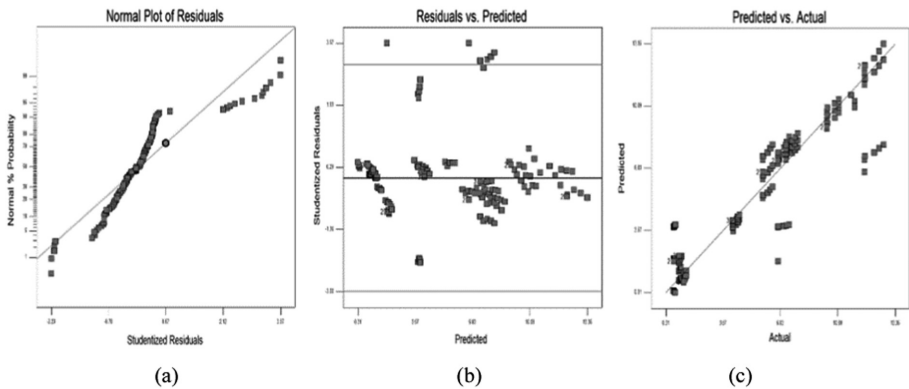
Source	Sum of squares	DF	Mean square	F value	<i>p</i> value	Prob > F	
Model	2012.96	21	95.86	44.39	<0.0001		Significant
A	35.03	1	35.03	16.23	<0.0001		
B	313.99	1	313.99	145.42	<0.0001		
C	78.29	1	78.29	36.26	<0.0001		
D	5.01	1	5.01	2.32	0.1298		
E	10.11	1	10.11	4.68	0.0322		
F	0.23	1	0.23	0.11	0.7443		
AB	7.36	1	7.36	3.41	0.0669		
AC	9.61	1	9.61	4.45	0.0367		
AD	16.58	1	16.58	7.68	0.0063		
AE	27.89	1	27.89	12.92	0.0005		
AF	0.04	1	0.04	0.02	0.8989		
BC	3.43	1	3.43	1.59	0.2098		
BD	2.63	1	2.63	1.22	0.2717		
BE	4.43	1	4.43	2.05	0.1543		
BF	2.44	1	2.44	1.13	0.2898		
CD	2.34	1	2.34	1.08	0.2996		
CE	3.15	1	3.15	1.46	0.2292		
CF	0.19	1	0.19	0.09	0.7682		
DE	2.94	1	2.94	1.36	0.2450		
DF	0.07	1	0.07	0.03	0.8565		
EF	0.14	1	0.14	0.06	0.8025		
Residual	302.28	140	2.16				
Lack of fit	64.21	112	0.57	0.07	1.0000		Not significant
Pure error	238.07	28	8.50				
Cor total	2315.24	161					

From the ANOVA, it shows that the generated model is significant, with *p* value of < 0.0001 and F value of 44.39 indicating that there is only a 0.01% chance that the model could occur due to noise. In addition, values of Prob > F less than 0.0500 indicate that the model terms are significant and in this case, the strongest machining parameter factor that affecting the MRR value in the design space are denoted in coded A, B, C, E, AC, AD and AE are significant model terms. The R-Squared of 0.870 is in reasonable agreement with the Adj R-Squared of 0.850 which shows the adequacy of the model in predicting the response in the design space. It shows that machining parameters i.e. speed, feed rate and amplitude strongly affect the MRR value.

Based on the limits of independent variable that have been studied, a two factor interaction mathematical equation for the MRR as a function of machining parameter are derived as:

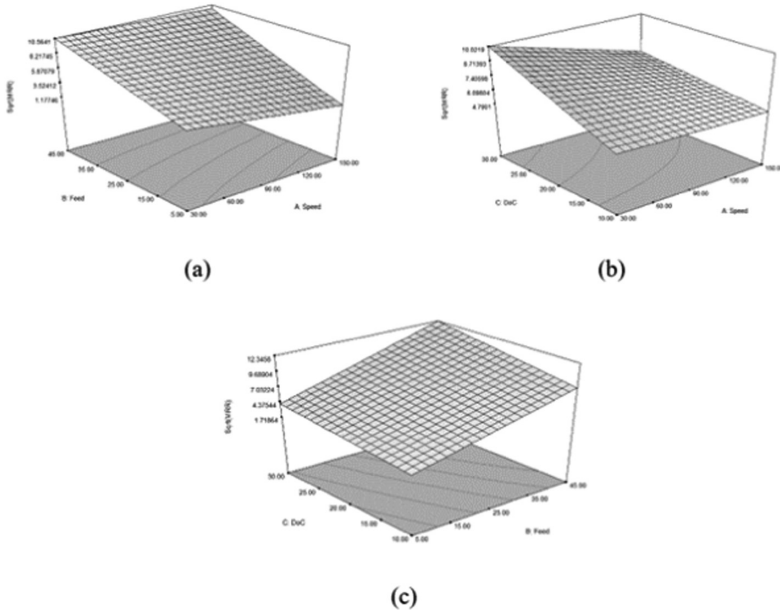
$$\begin{aligned}
 \text{Sqrt}(MRR) = & 6.59 - 1.00A + 3.69B + 1.62C \\
 & -1.25D + 1.26E + 0.19F + 0.72AB - 0.82AC + 0.91AD \\
 & - 0.96AE - 0.028AF + 0.44BC + 0.39BD \\
 & - 0.43BE + 0.24BF + 0.37CD - 0.35CE + 0.067CF \\
 & - 0.89DE + 0.14DF + 0.081EF
 \end{aligned}
 \tag{2}$$

It can be noted from the equation; the weak model terms were also included in order to maximize the fitness of the developed function. Furthermore, statistical diagnostic test to evaluate the fitness of the developed mathematical model are performed as shown in Fig. 6(a) to (c) which correspondingly show the Normal, Residuals vs Predicted, and Predicted vs Actual plots of residuals. It can be observed that, the Normal plot of residuals indicates that the residuals follow a normal distribution in a scatterplot straight line. In addition, the Residuals vs Predicted plot are also showing a randomly scattered (constant range of residuals across the graph) with just only one point outside the outlier limit. Lastly, from the Predicted vs Actual plots, it can be seen that the points were split evenly by 45° line which confirmed the model fitness.



**Fig. 6.** Statistical diagnostic test

To further analyzed the interaction between machining parameters and MRR in the design space graphically, 3d surface response plot were developed. As mention earlier, in regards of both technique i.e. conventional milling and RUAM the MRR value are greatly dependent with cutting speed, feed rate and depth of cut value. Figure 7 illustrated the two factors interaction of MRR between speed and feed rate; speed and depth of cut; feed rate and depth of cut respectively.



**Fig. 7.** The 3D surface response: (a) Interaction between cutting speed and depth of cut on MRR. (b) Interaction between cutting speed and depth of cut on MRR. (c) Interaction between feed rate and depth of cut on MRR

The 3d plots indicated that the highest MRR lies in the region in which feed rate and depth of cut were high whilst cutting speed are low. Obviously, the higher the feed rate and depth of cut values resulting in more material been removed in certain period of time thus increase the MRR value. In addition, the MRR value increases as the cutting speed decrease. One of the possible reason is when the cutting speed is low, the shearing process by the cutter teeth on the material can be done completely without any excessive material left thus increase the MRR value.

In the context of RUAM parameter, it was observed that vibration amplitude and abrasive slurry concentration has significant effect on the MRR value. Figure 8 shows the surface plot for the interaction between vibration amplitude and abrasive slurry concentration on MRR. It can be observed that the interaction between vibration amplitude and abrasive slurry concentration significantly affected the MRR value and can be model as two factor interaction function. The 3d plot indicated that the highest MRR lies in the region in which both factors were maximum.

The improvement on the MRR value can be relate with the additional material removal mechanism by the high energy hammering action i.e. high amplitude produced from the vibrated abrasive particles. Higher amplitude produced deeper chipping depth on the workpiece surface i.e. increase volume of material been removed. In addition, as the number of abrasive particles increases consequently increase the total microchipping area thus increase the MRR value.

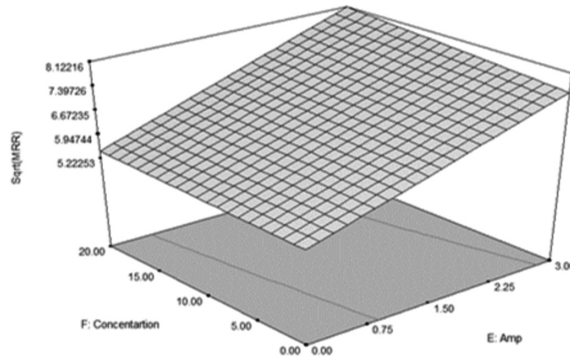


Fig. 8. Interaction between vibration amplitude and abrasive concentration on MRR

## 4 Conclusion

This paper presents the effectiveness of adding ultrasonic vibration to the conventional machining process in improving the MRR value for machining for hardened D2 material. The results from this study indicate that improvement on MRR value up to 17% can be achieved by using RUAM compared to conventional machining with the same cutting conditions. The RUAM improvement on the MRR value can be relate with the additional material removal mechanism by the high energy hammering action as well with the present of abrasive particles. Further research could be carried out to establish the effect of machining parameters on others machining performances such as surface roughness, cutting force and tool wear.

## References

1. Azlan, R., Izamshah, R., Kasim, M.S., Akmal, M., Nawi, M.: Improvement of machining performance using hybrid rotary ultrasonic milling (HRUAM) for Hardened D2 tool steel materials. *Int. J. Appl. Eng. Res.* **12**(23), 13506–13513 (2017)
2. Azlan, R., Izamshah, R., Hadzley, M., Kasim, M.S., Arfauz, M.: Experimental investigation of surface roughness using ultrasonic assisted machining of hardened steel. *Proc. Mech. Eng. Res. Day* **1**, 212–213 (2016)
3. Izamshah, R., Mo, J.P.T., Ding, S., Arfauz, M., Azam, M.A.: Effect of parameter condition on surface roughness for machining AISI D2 hardened steel. *J. Adv. Manuf. Technol.* **8**, 47–56 (2010)
4. Azlan, R., Izamshah, R., Hadzley, M., Kasim, M.S.: Surface evaluation of rotary ultrasonic assisted machining technique. In: *Advanced Processes and Systems in Manufacturing An International Conference 2016*, vol. 1, no. August, pp. 11–12 (2016)
5. Ramli, A., Abdullah, R., Izamshah, R., Bakar, A., Kasim, M.H., Shahir, M., Rahman, A.: Investigation on improvement of surface roughness using rotary ultrasonic assisted machining technique for hardened steel material. *J. Mech. Eng.* **3**(1), 119–134 (2017)
6. Izamshah, R., Mo, J.P.T., Ding, S., Arfauz, M., Azam, M.A.: Effect of parameter condition on surface roughness for machining AISI D2 hardened tool steel. *J. Adv. Manuf. Technol.* **8** (1), 47–56 (2014)

7. Tsai, M., Chang, C., Ho, J.: The machining of hard mold steel by ultrasonic assisted end milling. *Appl. Sci.* **6**(11), 373 (2016)
8. Kumar, J., Khamba, J.S., Mohapatra, S.K.: An investigation into the machining characteristics of titanium using ultrasonic machining. *Int. J. Mach. Mach. Mater.* **3**(1/2), 143–161 (2008)
9. Hocheng, H., Kuo, K.L.: Fundamental study of ultrasonic polishing of mold steel. *Int. J. Mach. Tools Manuf.* **42**(1), 7–13 (2002)
10. Chao, C.L., Chou, W.C., Chao, C.W., Chen, C.C.: Material removal mechanisms involved in rotary ultrasonic machining of brittle materials, vol. 329, pp. 391–396 (2007)
11. Agarwal, S.: International journal of machine tools and manufacture on the mechanism and mechanics of material removal in ultrasonic machining. *Int. J. Mach. Tools Manuf.* **96**, 1–14 (2015)
12. Ya, G., Qin, H.W., Yang, S.C., Xu, Y.W.: Analysis of the rotary ultrasonic machining mechanism. *J. Mater. Process. Technol.* **129**(1–3), 182–185 (2002)
13. Brehl, D.E., Dow, T.A.: Review of vibration-assisted machining. *Precis. Eng.* **32**(3), 153–172 (2008)
14. Kasim, M.S., Haron, C.H.C., Ghani, J.A., Sulaiman, M.A.: Prediction surface roughness in high-speed milling of Inconel 718 under Mql using Rsm method. *Middle East J. Sci. Res.* **13**(3), 264–272 (2013)



# The Effect of Carbon Fiber Reinforced Polymer (CFRP) Micro Drilling Parameter on Hole Accuracy

N. Syuhada Nasir<sup>(✉)</sup>, N. Ab Wahab, and H. Sasahara

Jabatan Teknologi Kejuruteraan Pembuatan, Fakulti Teknologi Kejuruteraan Mekanikal dan Pembuatan, Universiti Teknikal Malaysia Melaka, Durian Tunggal, Melaka, Malaysia  
nsyuhada\_mn@yahoo.com, norfariza@utem.edu.my

**Abstract.** The research was executed to study the effect of Carbon Fiber Reinforced Polymer (CFRP) micro drilling parameter on hole accuracy. The main contribution of this research is to improve manufacturing process of hole micro size by finding the optimum parameter for excellent hole accuracy. However, to obtain the optimum parameter, the behavior of hole quality must be investigated. The parameters considered in the experiment were machine spindle speed and cutting feed rate. The experiment was carried out by drilling CFRP panel using the router machine with micro drill bit (D0.9 mm) to make holes while a measuring microscope was used to observe and analyze the holes. The quality of hole created on each panel was compared, and at the same time, the hole diameter was measured to determine hole accuracy. In term of hole diameter, as the number of drilled holes increased, the diameter of holes reduced for both entry and exit hole. Minimum diameter of entry hole at spindle speed 8,000 rpm and 10,000 rpm were 0.8986 mm and 0.8973 respectively while maximum diameter of entry holes were 0.9297 mm and 0.9234 mm each. Similar pattern occurred at the exit holes as well. The result shows a linear relationship between hole accuracy, hole quality and number of drilled holes, it was also found that the spindle speed did not have a significant impact and there is a way to test the feed rate. In this regard, determining the excellent hole accuracy of CFRP is useful for mechanical assembly process of aircraft parts.

**Keywords:** CFRP composite · Delamination · Hole accuracy · Micro drill · Thrust force

## 1 Introduction

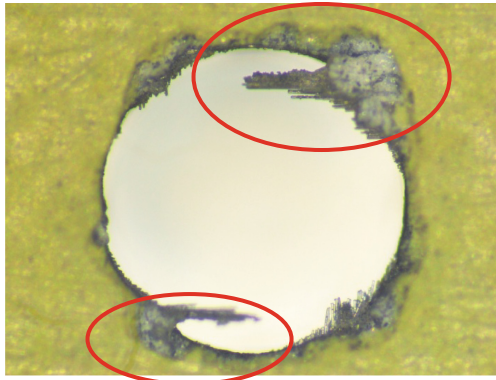
In the mid-1950s, fiber-reinforced polymer (FRP) composites were invented as replacements for metal-based materials. FRP were introduced to overcome the corrosion issues observed on metal parts. Consequently, hole-making operations are required to join the different FRP components [1]. The hole making process can be simply mentioned as a drilling process, however, drilling the carbon fiber reinforced polymers (CFRPs) is typically difficult due to its high structural stiffness and toughness [2]. Micro drilling has been widely used in the industry to drill micro sized holes as different



industries, such as the aerospace, electronics, medicine and automobile industries are keen to produce products and devices that are smaller, cheaper and faster to appeal to their customers [3].

Micro drilling is generally defined as the drilling process with drills with the diameter between 1  $\mu\text{m}$  and 1 mm to produce micro holes with diameters less than 0.5 mm and the aspect ratio greater than 10 [4]. Despite this description, there is still no specific standard which defines micro drilling. Micro drilling began to be used to be used widely as the components become smaller, smaller hole size is required to mount the components and consequently, the term Micro Drill was initiated. Micro drilling is also known as miniaturized drill, micro perforation, small diameter drilling technology, micro hole drilling, making tiny holes, and micro hole machining [3].

Precise drilling parameter is very essential to achieve high quality of holes. Moreover, in drilling CFRP panel, caution should be taken as particular defects, which do not occur when drilling metal-based materials, can occur. These defects include delamination, uncut fiber and hole surface damage [5] which will affect the accuracy of hole produced, as well as the diameter of the hole. Besides that, the desired hole diameter might not be achieved and this will lead to unfit bolt or rivet connection and consequently, creates a gap between the parts as opposed to producing a perfect connection of bolt or rivet to tightly join the parts. Figure 1 shows an example of an uncut CFRP composite panel fiber.



**Fig. 1.** Image of uncut fiber under microscope

In the aircraft industry, these kinds of defects are totally unacceptable as it will create problems when flying an aircraft. Environmental effects such as vibration and fraction could cause the connection between the bolts or the rivets to loosen when there is a gap between the parts. In addition, as the drilling process usually occurs during the finishing phase of assembly and the damage caused by the drilling process is hard to repair, about 60% of all CFRP part rejections are due to poor hole quality, which could be very expensive [6].

The discussion above justifies the significant of a study on the hole accuracy on CFRP panel. Studies on this topic will ensure the efficiency of the assembly of aircraft

part and to investigate the best parameter of micro drilling process. In turn, this will help ensure the reliability and consistency of the process. Therefore, this research will emphasize the impact of CFRP micro drilling process parameter on hole accuracy.

## 2 Methodology

This study involved the micro drilling process of CFRP composites and measured the process of hole diameter. The micro drilling process was carried out using Gantry Router, as shown in Fig. 2 while the hole was observed using Measuring Micrometer Nikon MM-800 (Fig. 3) while the hole diameter was measured using Data Processing Software E-MAX.

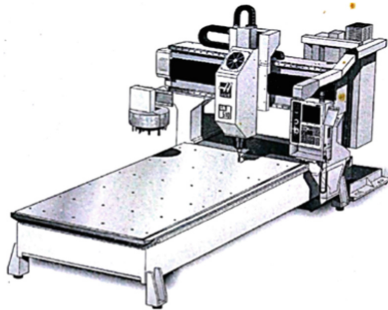


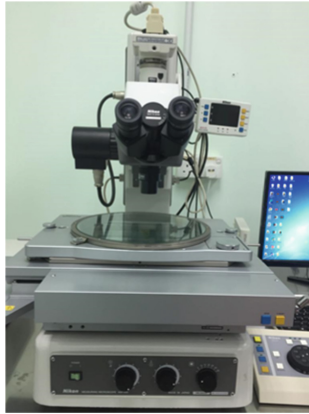
Fig. 2. Modelling of Gantry Router HAAS GR-510 [7]

Both processes took place in Jabatan Teknologi Kejuruteraan Pembuatan (JTKP) laboratory at Universiti Teknikal Malaysia Melaka (UTeM). A TiAlN coated solid carbide Micro drill bit, with a diameter of 0.9 mm and the tolerance of +0.004 mm, as shown in Fig. 4 was used. A CFRP composite laminates panel was used as the workpiece in this research.

### 2.1 Experimental Setup

Figure 5 illustrates the setup of the workpiece on a machine base with a holding fixture. A dyno meter was installed under the workpiece to measure the thrust force of the drilling process during the experiment. However, the dyno meter can be removed if the thrust force is insignificant in the research.

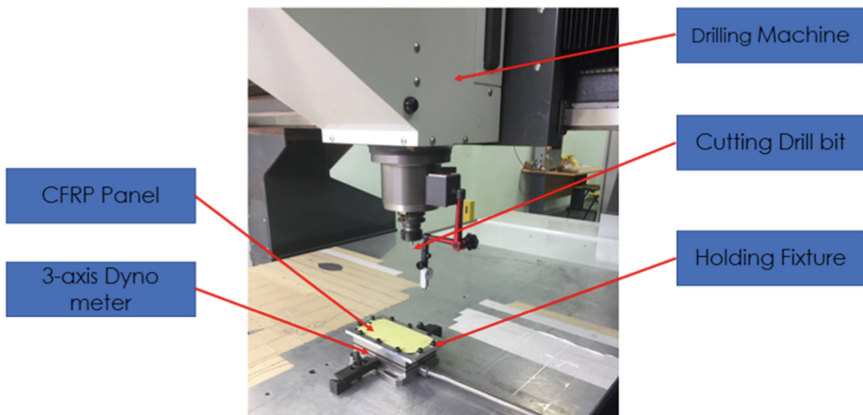
As the maximum thickness of the CFRP composite panel is 4 mm, the cutting depth of the machine was set to 5.5 mm to ensure the drill bit is able to drill through the hole. The same type of workpiece was used for all of the experiments. Similar workpiece setup was also applied for all the experiments.



**Fig. 3.** Measuring Micrometer Nikon MM-800



**Fig. 4.** Solid Carbide Drill Bit D0.9 +0.004 mm



**Fig. 5.** Setup of workpiece on the machine base

## 2.2 Process Parameter

The process parameters considered in this experiment were the spindle speed of the machine and the feed rate of the cutting tool. In order to produce a good hole quality, as well as to avoid delamination, the low feed rates (0.03–0.07 mm/rev) with higher cutting speed were used [8]. The process parameters used in this experiment are shown in Table 1.

**Table 1.** List of process parameter

Parameter	1	2
Spindle speed (rpm)	8000	10,000
Feed rate (mm/min)	200	200

## 2.3 Hole Quality Observation

During the initial phase, the machine drilled on up to 200 holes on the CFRP panel. Then, the quality of the holes was observed under a microscope. The experiment was repeated using a new drill bit and a different spindle speed. The hole diameter was then measured using a microscope and the difference between the diameters of the *n*th holes was observed. The purpose of changing the drill bit is to ensure that only the process parameter is varied when the fresh drill bits are used.

## 2.4 Measuring the Hole Diameter

The entry and exit diameter of hole were measured in this experiment using E-Max software. According to Girot [9] in the Aerospace Process Specification of Airbus, Bombardier and Embraer, the requirement for delamination of on the hole is 2.54 mm around the hole regardless of the hole diameter. The probe was chosen at the initial stage and a multi-point probe was used to detect the edge of the hole along the diameter of hole to form a perfect circle to measure the diameter of the hole. Approximately 100–150 points were captured along the hole diameter. In this regard, the higher the number of points captured reflects more accurate data measurement. Figure 6 presents the selection of probe used when the E-Max software was used.

After selecting the tool, the cursor was moved to the hole diameter and the probe simultaneously detected 10 points automatically. Once the point was selected, the input button was clicked to count the point into the measurement. The steps were repeated until up to 100 points were captured along the circle.

Finally, the hole diameter was calculated automatically after clicking the OK button. Then, the results were presented. The finding shown is up to 4 decimal places. Figure 7 shows that the hole diameter obtained is 0.9341 mm.

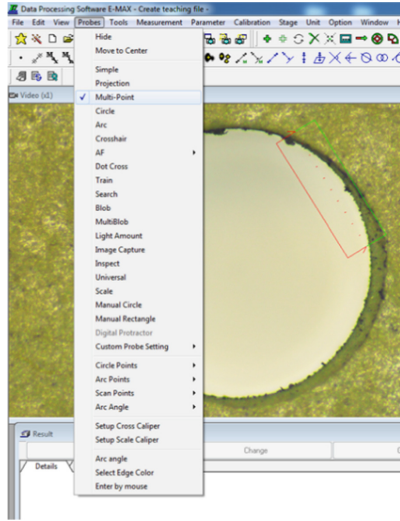


Fig. 6. Selection of the probe

 A screenshot of the 'Result' window in the software. It displays a table of measurement data for a circle. The table has columns for 'Actual', 'Nominal', 'Upper Tol.', 'Lower Tol.', 'Error', and 'Judge'. The 'Actual' values are: X: 0.6447, Y: -15.7554, Z: 0.0000, TRPOS: 0.0000, D: 0.9341, and Circularity: 0.0136.

Fig. 7. Result of the hole diameter

### 3 Result and Discussion

#### 3.1 Experimental Result of Hole Diameter

The spindle speed plays an important role in obtaining the perfect hole diameter with the maximum number of perfect holes to be drilled. By varying the spindle speed to between 8,000 rpm and 10,000 rpm, the entry and exit hole diameter from a similar range of nth hole was compared. The comparison results are shown in Tables 2 and 3, respectively.

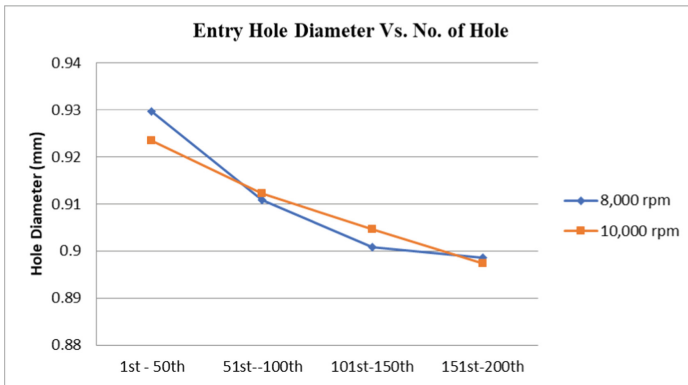
Table 2. Diameter of entry hole

Spindle speed (rpm)	Diameter of hole by range of n <sup>th</sup> hole (mm)			
	1 <sup>st</sup> -50 <sup>th</sup>	51 <sup>st</sup> -100 <sup>th</sup>	101 <sup>st</sup> -150 <sup>th</sup>	151 <sup>st</sup> -200 <sup>th</sup>
8,000	0.9297	0.9109	0.9008	0.8986
10,000	0.9234	0.9123	0.9046	0.8973

**Table 3.** Diameter of exit hole

Spindle speed (rpm)	Diameter of hole by range of n <sup>th</sup> hole (mm)			
	1 <sup>st</sup> -50 <sup>th</sup>	51 <sup>st</sup> -100 <sup>th</sup>	101 <sup>st</sup> -150 <sup>th</sup>	151 <sup>st</sup> -200 <sup>th</sup>
8,000	0.9267	0.8902	0.8879	0.8716
10,000	0.9262	0.9002	0.8974	0.8788

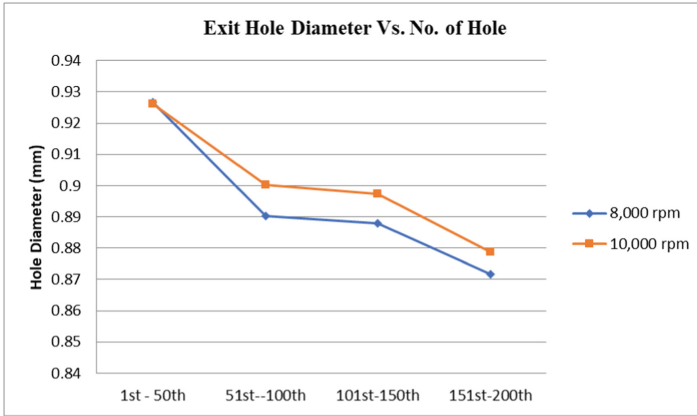
As observed from the table above, varying the spindle speed in the range between 8,000 rpm and 10,000 rpm did not have any significant impact on the hole accuracy. The similar trend was observed when the hole diameter was reduced as the number of drilled holes increased for both entry and exit holes, as shown in Figs. 8 and 9. In this light, the hole became smaller at the end of drilling process due to cutting tool wear. Meanwhile, when there are too many holes drilled, the cutting tool could deform the cutting edge which could affect the size of hole produced.

**Fig. 8.** Graph of comparison between entry hole diameter with number of drilled holes

### 3.2 Experimental Result of Hole Quality

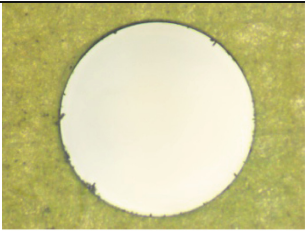
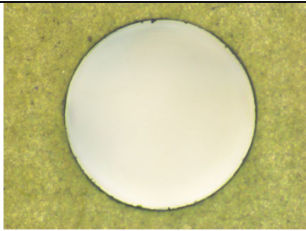
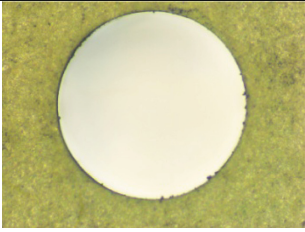
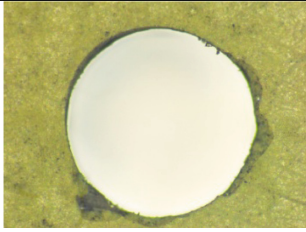
The quality of holes was also observed under a microscope. The hole conditions of different number of drilled holes were compared against each other. The range of hole compared are the 1<sup>st</sup>-50<sup>th</sup>, 51<sup>st</sup>-100<sup>th</sup>, 101<sup>st</sup>-150<sup>th</sup>, and 151<sup>st</sup>-200<sup>th</sup>. The image of entry and exit holes were captured and tabulated as shown in Tables 4 and 5, respectively.

Table 4 shows that the number of holes drilled did not have any significant impact on hole quality at the entry hole. However, the quality of exit hole become worse as more holes were drilled as shown in Table 5. Uncut fiber and delamination were observed when there are 51-100 holes and when there between 151 and 200 holes. Meanwhile, uncut fiber is commonly used as the first and last plies of the reinforcement



**Fig. 9.** Graph of comparison between exit hole diameter with number of drilled holes

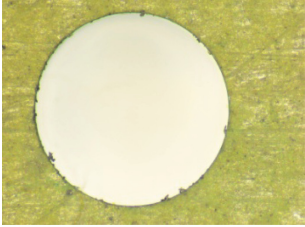
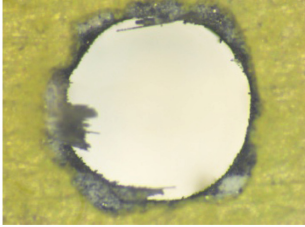
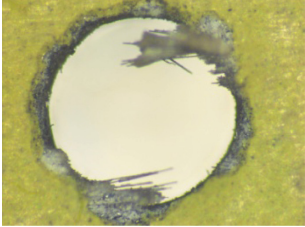
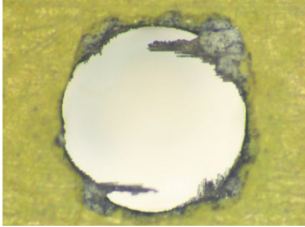
**Table 4.** Comparison of entry hole quality

Image of Entry Hole	
1 <sup>st</sup> -50 <sup>th</sup>	51 <sup>st</sup> -100 <sup>th</sup>
	
101 <sup>st</sup> -150 <sup>th</sup>	151 <sup>st</sup> -200 <sup>th</sup>
	

fibers, which were not cut during drilling process. Based on the previous study, the presence of uncut fiber is due to the lower spindle speed, which is not productive to drill CFRP composites panel.

Delamination was observed at the hole entry and exit points during the drilling process. However, the mechanism of the delamination has varied between the entry and

**Table 5.** Comparison of exit hole quality

Image of Exit Hole	
1 <sup>st</sup> -50 <sup>th</sup>	51 <sup>st</sup> -100 <sup>th</sup>
	
101 <sup>st</sup> -150 <sup>th</sup>	151 <sup>st</sup> -200 <sup>th</sup>
	

exit hole. It was observed that the peel-up delamination occurs at the entry of hole while push out delamination occurs at the exit of hole. As shown in Table 5, these are the push out delamination which occurs due to the thrust force during the cutting process. Besides that, the delamination at the exit of the hole is due to the decrease in the number of plies left to be drilled and the reduction in the hardness of the material. The deformation of material occurs easily as the material is easy to bend when the drill bit reaches the bottom layer of the composite's plies.

#### 4 Conclusion and Recommendation

In conclusion, it was found that the spindle speed of the drilling machine does not provide significant impact on hole accuracy with the feed rate of less than 0.10 mm/rev. As the spindle speed increased from 8,000 rpm to 10,000 rpm, the hole diameter is reduced in line with the number of holes drilled. In addition, as the number of hole increases, the hole quality becomes worse. It was also found that the uncut fiber and delamination occurred after the 50th hole at the exit hole while the hole quality on the entry hole only go worse after the 151st hole.

The knowledge from this research can be used in the industry to improve the manufacturing process, such as to reduce time and cost. In this light, the production of micro holes is essential to accommodate smaller bolts and nuts during the assembly



process. This is significant as the industry strives to produce smaller devices or joint to reduce weight and material consumption.

For future studies, variable feed rate could be used to study the impact of the process parameter on hole quality. Since the feed rate in this study was maintained by 0.0025 mm/rev, there was no outstanding different of hole accuracy observed. Furthermore, as the feed rate was reduced, the push out delamination factor was decreased to 37% for the CFRP composite panel [10]. Meanwhile, as mentioned in previous studies, delamination is influenced by spindle speed and feed rate.

**Acknowledgments.** This work is partially supported by Universiti Teknikal Malaysia Melaka (UTeM) and the Malaysia Ministry of Higher Education for the financial funding under Grant No. FRGS/2018/FTKMP-AMC/F00387.

## References

1. Hrechuk, A., Bushlya, V., Stáhl, J.E.: Hole-quality evaluation in drilling fiber-reinforced composites. *Compos. Struct.* **204**(July), 378–387 (2018)
2. Jaafar, M.F., et al.: Influence on thrust force and delamination for one shot drilling of carbon fibre reinforced plastic. *Int. J. Mech. Mechatron. Eng.* **19**(1), 43–56 (2019)
3. Hasan, M., Zhao, J., Jiang, Z.: A review of modern advancements in micro drilling techniques. *J. Manuf. Process.* **29**, 343–375 (2017)
4. Chang, D.Y., Lin, S.Y.: Tool wear, hole characteristics, and manufacturing tolerance in alumina ceramic microdrilling process. *Mater. Manuf. Process.* **27**(3), 306–313 (2012)
5. Fernández-Pérez, J., Cantero, J.L., Díaz-Álvarez, J., Miguélez, M.H.: Influence of cutting parameters on tool wear and hole quality in composite aerospace components drilling. *Compos. Struct.* **178**, 157–161 (2017)
6. Bai, Y., Wang, F., Jia, Z., Niu, B., Qian, B., Fu, R.: Novel drill structure for damage reduction in drilling CFRP composites. *Int. J. Mach. Tools Manuf.* **110**, 55–65 (2016)
7. Haas Automation Inc.: Gantry Router Operator's Addendum, California (2008)
8. Shyha, I.S., Aspinwall, D.K., Soo, S.L., Bradley, S.: Drill geometry and operating effects when cutting small diameter holes in CFRP. *Int. J. Mach. Tools Manuf.* **49**(12–13), 1008–1014 (2009)
9. Girot, F., Dau, F., Gutiérrez-Orrantia, M.E.: New analytical model for delamination of CFRP during drilling. *J. Mater. Process. Technol.* **240**, 332–343 (2017)
10. Sorrentino, L., Turchetta, S., Bellini, C.: A new method to reduce delaminations during drilling of FRP laminates by feed rate control. *Compos. Struct.* **186** (September 2017), 154–164 (2018)



# Hardness and Water Absorption Properties of Silicone Rubber Based Composites for High Voltage Insulator Applications

Najwa Kamarudin<sup>1</sup>(✉), Jeefferie Abd Razak<sup>1</sup>, Nurbahirah Norddin<sup>2</sup>,  
Noraiham Mohamad<sup>1</sup>, Lau Kok Tee<sup>2</sup>, Tony Chew<sup>3</sup>,  
and Nurzallia Mohd Saad<sup>3</sup>

<sup>1</sup> Fakulti Kejuruteraan Pembuatan, Universiti Teknikal Malaysia Melaka,  
Hang Tuah Jaya, 76100 Durian Tunggal, Melaka, Malaysia  
kanna.jwa@gmail.com, jeefferie@utem.edu.my

<sup>2</sup> Fakulti Teknologi Kejuruteraan, Universiti Teknikal Malaysia Melaka,  
Hang Tuah Jaya, 76100 Durian Tunggal, Melaka, Malaysia

<sup>3</sup> Saiko Rubber (Malaysia) Sdn. Bhd., Lot 53 & 54, Senawang Industrial Estate,  
70450 Seremban, Negeri Sembilan, Malaysia

**Abstract.** In almost all new-builds, replacement and upgrades, silicone rubber (SiR) material was an attractive alternative compared to traditional ceramic based insulators. This paper showcases the experimental findings to understand the physical properties of silicone rubber filled with various mineral fillers of calcium carbonate, silica and wollastonite minerals ( $\text{CaCO}_3$ ,  $\text{SiO}_2$  and  $\text{CaSiO}_3$ ) for high voltage insulator applications. The physical attributes have been analysed through the hardness and water absorption testing. An addition of mineral fillers into pure silicone rubber at different weight percentages of 5, 10, 20, 30 and 40 wt% had caused a significant improvement of hardness values which was clearly dominated by SiR/ $\text{CaSiO}_3$  composite samples of wollastonite mineral addition. In addition, in terms of water absorption, the stable water absorption behavior has again possessed by the SiR/ $\text{CaSiO}_3$  composite samples. Wollastonite mineral has responsible to improve SiR rubber physical properties due to their nature of hydrophobic and sharp edges morphologies, which advantages for hardness and water resistance. Hence, from these studies, it can be concluded that, the best performance of SiR based composites was clearly made known by SiR/ $\text{CaSiO}_3$  for both testings.

**Keywords:** Silicone rubber · Physical properties · Insulator · Wollastonite · Mineral fillers

## 1 Introduction

An electrical insulation has been recognized as an important aspect to be considered for high voltage outdoor application [1]. Previously, there are several types of high voltage insulators on transmission lines for outdoor applications, have been manufactured. The history of high voltage insulator has begun in 20th century, with porcelain as the only material being utilized for insulator applications. In 1940s, the development of

insulator was then continued with utilization of polymer insulator that replacing conventional materials like porcelain, glass and ceramic. This transformation had started with manufacturing of high voltage insulator by using epoxy resins as based raw materials [2].

The need for this major replacement was to eliminate the usage of expensive porcelain material, reduce the cost of manufacturing and most important to increase the tracking and erosion resistance of insulator, which has very important for high voltage insulator application [3]. Polymer material has chosen to replace previous types of insulator, due to their hydrophilic properties, which aids the process of dry band arcing that led into flashover phenomena [4]. Furthermore, polymeric insulators addressed most of the problems that faced by the porcelain insulators. Their advantages include light weight and flexible characteristics, which allows easier erection and commissioning of insulators, even at distant areas, including places with resistance to vandalisms [5]. These advantages over ceramic insulators have made them very attractive enough to be used for high voltage insulator applications.

Furthermore, polymeric insulators exhibit a hydrophobicity property which has suitable to be used in highly polluted areas. These kinds of properties make polymeric insulators are good for their usage. However, polymeric insulators also possessed certain drawbacks. While they are having commercial success, an obstacle occurred due to fluctuate hydrocarbon cost, limited manufacturing versatility and the utmost important part was an inadequate performance for outdoor high voltage application purposes [6]. Since the usage of polymeric insulators has not been developed until the late 1960s and 1970s, their expected life was still unknown [2].

In the real working environment, insulator for high voltage application exposed with unpredictable weather, moisture and etc., which led into environmental degradation. Hence, for this study, water absorption testing and hardness results are reported for resulted physical properties of produced SiR rubber composites filled with various types of mineral fillers of calcium carbonate, silica and wallastonite at different percentages of filler loadings for selected samples.

Water absorption testing was used to determine the amount of water absorbed under the specified conditions. Factors affecting water absorption are including the type of materials, additives used, temperature and immersion period. The data sheds light on the performance of tested materials in water or humid environments. Thus, water absorption is one of the most important failure factor in the development of composite insulator for high voltage application. It was because, some voids might be appeared at macroscopic interface between the sheath and the core of insulator rod for high voltage application, due to environmental factors [7]. Furthermore, insulator for high voltage (HV) are having drawback which was suffering from various environmental stresses, hence, water absorption testing has crucially important to determine their ability or resistance towards water diffusion [8].

Hardness is referred to as mean contact pressure or is also considered as resistance towards permanent indentation. Hardness is by far the most valuable and most widely used mechanical test for evaluating the physical properties for certain materials [9]. The purpose of hardness testing is to represent the effect of rubber crosslink establishment within the matrix of SiR rubber with the presence of different types of mineral fillers at difference percentages of filler loadings. Apart from that, by improving hardness, could

prove if the composite material is well design and fit with some of its properties [10]. It has been proved that hardness was continuously increased with increasing loading of filler addition, compared to unfilled material [11]. In a research paper also shows that the value of hardness for SiR/Al<sub>2</sub>O<sub>3</sub> composites has increased with increasing of filler volume fraction [12].

## 2 Methodology

The main material, silicone rubber (SiR) was obtained from Immortal Green Industrial Sdn Bhd and is used as matrix material. The type of SiR used was Elastosil R401/60S and it was supplied together with an Aux Heat Stabilizer H3. Mineral fillers were added into silicone rubber which consisted of silica and calcium carbonate derived from waste glass and cockle shell, respectively. Dicumyl Peroxide (DCP) acts as a curing agent to actively react with SiR with the presence of vinyl side group. Another filler type which is wollastonite (CaSiO<sub>3</sub>), was derived from the reaction between the silica from waste glass and calcium carbonate from the cockle shells, through simplified calcination heating process. In Table 1 shows different types of mineral fillers added into SiR.

**Table 1.** Types of mineral fillers added into SiR

Type of mineral fillers	Weight percentage (wt%)
Silica (SiO <sub>2</sub> )	5, 10, 20, 30 and 40
Calcium carbonate (CaCO <sub>3</sub> )	
Wollastonite (CaSiO <sub>3</sub> )	

### 2.1 Preparation of Materials

*Preparation of Wollastonite Powder.* In order to produce CaSiO<sub>3</sub>, there are two major important constituents are involved, which are CaCO<sub>3</sub> and SiO<sub>2</sub>. Both CaCO<sub>3</sub> and SiO<sub>2</sub> powders are prepared beforehand by utilizing the waste resources of cockle shells and waste glass bottles, respectively. The preparation was performed by weighing both calcium carbonate and silica based on 48.3%:51.7% ratio, which later undergoes the ball milling process at 20 rpm of milling speed for 45 min duration. The purpose of milling stage was to ensure the combination of CaCO<sub>3</sub> and SiO<sub>2</sub> powder could turn into homogenous powdery mixtures. Then, the powder mixture was calcined by heating it up into 1000 °C at heating rate of 10 °C/min for 3.5 h of heating duration. The cooling rate of 10 °C/min was used for the cooling purpose. Next, X-ray diffraction (X-RD) characterization tool was utilized to verify the crystal composition and phase presence of produced synthetic wollastonite (CaSiO<sub>3</sub>) made from waste glass bottles and waste cockle shells.

*Compounding of SiR/Mineral Filler Based Composites.* An internal mixer machine used was a Brabender Plasticorder mixer. The compounding process was performed at 7 min of mixing duration and 70 rpm of mixing speed. The capacity of an internal

mixer compounding chamber was 55.5 g per run, considering the volume of the machine and the density of SiR rubber. The mixing operation was started by adding pure silicone rubber at first minute then followed by the filler addition after then, at second minute. The mixing procedure of silicone rubber and filler was continued for a few minutes (about four minutes) before addition of DCP and Aux heat stabilizer at five minutes. The entire compounds are mixed together until the machine was automatically shut off at seventh minutes.

*Vulcanization of SiR/Mineral Filler Based Composites.* The compounded composite mixtures are weighed accordingly to ensure the amount of feed materials could be fitted into the size of mould. Then, the samples are rolled using a roller to make it flat with the purpose to fit into each space of the mould. While the SiR based composite blends were putted between two mylar sheets. All samples are compressed by using a hot press machine under the temperature of 175 °C and a pressure of 50 bar for 20 min of compression period. Then, the samples are taken out from the mould to be post-cured in a forced air heating oven for 24 h under 130 °C of post-cured temperature.

*Water Absorption Testing.* The selection of samples for water absorption test has been chosen from the samples which already undergoes the Inclined Plane Tracking (IPT) test, since those samples have been exposed to high voltage exposure. The samples dimension for this testing was based on ASTM D570 (1.00 cm × 1.00 cm × 0.60 cm). The samples were dried in an oven for a specified time and temperature and was subsequently placed in a desiccator, for conditioning purpose. Immediately, upon conditioning, the samples are weighed. The sample was then emerged in distilled water (300 ml), often at constant and controlled temperature of 23 °C for 24 h immersing period or until equilibrium has been reached. Samples are subsequently removed, patted dry with a tissue, and weighed again. The water swelling of each swollen sample was then recorded accordingly. The equipment used for data collection was a Mettler type precision balance. The samples measurement has been repeated by immersing it again until equilibrium was achieved. Percentage of weight change was calculated by using the following equation:

$$\text{Percentage Water Absorption} = \frac{(\text{Wet Weight} - \text{Dry Weight})}{\text{Dry Weight}} \times 100 \quad (1)$$

*Hardness Testing.* The hardness test of SHORE-A durometer was used in accordance to ASTM 2240. The samples are first conditioned at standard laboratory controlled temperature of 25 °C, for at least 3 h prior of the hardness testing. The reading was taken at a consistent interval between the indentation and measurement. The reading was taken immediately within one second, after the pressure foot has firmly contacted with the sample. Five measurements at different locations are usually taken for a sample and the mean value was determined as a final reading. The depth of the indentation was measured, which provides a measure of sample hardness. Values are based upon 100 point scale (accuracy ± 1.00 point).

### 3 Results and Discussions

#### 3.1 Characterization of Wollastonite ( $\text{CaSiO}_3$ )

Figure 1 displays an XRD pattern analysis result of synthetic wollastonite ( $\text{CaSiO}_3$ ) made from waste resources. It was proven that the tested powder sample was contained the characteristic of wollastonite crystal structure, having a chemical formula of calcium silicate ( $\text{CaSiO}_3$ ) that corresponded to the JCPDS reference code of 00-027-0088. It can be seen that from the intensity peaks of the wollastonite structure that has appeared to be the highest among others, and basically there were also the existence of small  $\text{SiO}_2$  and  $\text{CaO}$  peaks. The peak of  $\text{CaO}$  exist due to the reaction during calcination process as shown in Eq. 2. Thus, this XRD result was certainly convinced to prove the formation of wollastonite mineral due to the combination between cockles shells and waste glass bottles, from successful calcination heat treatment procedure.



This phase identification shows that the highest percentage of relative intensity was at position  $37.5^\circ$  of  $2^\circ$  theta, which dominantly referring into  $\text{CaSiO}_3$  phase. Hence, it has been proven that the  $\text{CaSiO}_3$  was successfully derived from the mixture of  $\text{CaCO}_3$  and  $\text{SiO}_2$  from waste sources.

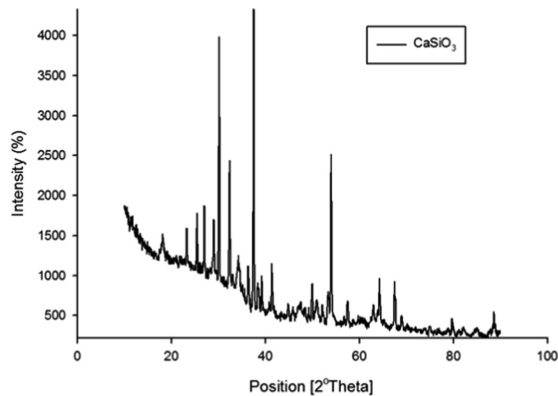
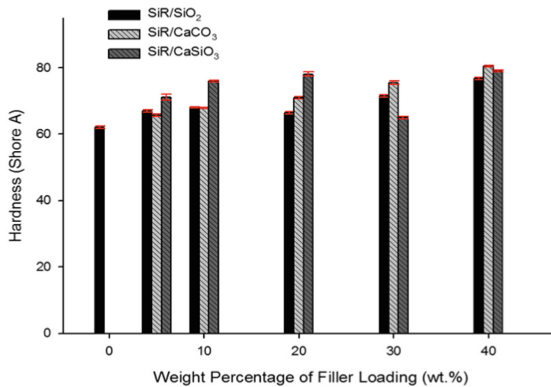


Fig. 1. X-Ray Diffraction (XRD) analysis on wollastonite

#### 3.2 Hardness Analysis

The purpose of hardness test is to represent the effect of rubber crosslink establishment within the matrix of SiR rubber with the presence of different types of mineral fillers at difference percentages of filler loadings. Figures 2 and 3 depict the hardness result before and after high voltage exposure. It can be seen that in Fig. 2 most of SiR based composites exhibit higher value of hardness, as compared than control sample. It was clearly shown that the filler-free control sample is the lowest in hardness performance,

compared than entire filled vulcanized SiR based composites. Basically, in this research, comparison of hardness behavior for produced composites before and after high voltage exposure was to evaluate the effects of HV application towards the macromolecules structure of SiR, and the role of added mineral filler in sustaining their physical properties. By comparing both hardness values between before and after HV exposure, it can be concluded that the hardness value after undergoing HV exposure were higher than prior of the testing, for each corresponding filler loadings.



**Fig. 2.** Hardness value for SiR based composites before undergoing an IPT test

Theoretically, it was common in rubber compounding ascribed to restriction of rubber chains to mobilise and slide pass one another, obstructed by filler aggregates [13]. This is attributed to the higher molecular interaction among filler and base matrix polymers. Hence, due to higher interaction, crosslinking in composites was found better after the HV exposure which has led into improved hardness values. This finding is correlated with research done by Khan et al. [3], where the value of hardness for SiR/nano-SiO<sub>2</sub> also improved due to good interaction between nano-SiO<sub>2</sub> and SiR matrix.

By focusing to the following Fig. 3, the hardness values show nonlinear increased at higher dosages above 30 wt% that may due to excessive filler agglomerations especially for calcium carbonate (CaCO<sub>3</sub>). It can be assumed that, the maximum filler loading up to 30 wt% is required to ensure the higher hardness results. An excessive filler is catastrophic and also able to lead into poor heat dispersion, hence poor performance of insulator [14]. However, samples of SiR/SiO<sub>2</sub> (20 wt%) and SiR/CaSiO<sub>3</sub> (30 wt%) show an abnormality of abruptly reduction in hardness values.

However, the highest hardness value was obtained by the sample of SiR/CaSiO<sub>3</sub> at the filler loading of 40 wt% at about 78.5 Shore-A values with 26% of increment than control unfilled sample. This positive improvement has occurred due to good interaction bonding between CaSiO<sub>3</sub> filler at higher level of filler loading, with SiR matrix. In addition, an interfacial strength depends significantly to the nature of bonding and the process applied [14].

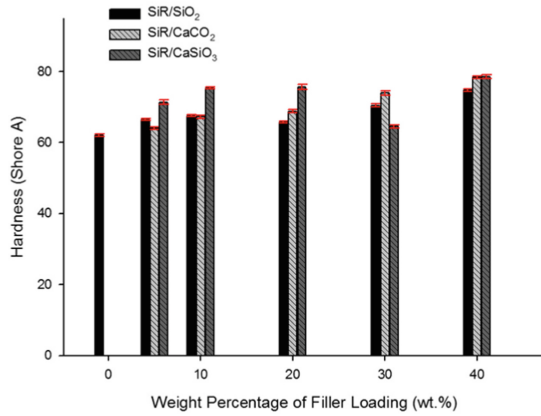


Fig. 3. Hardness value for SiR based composites after undergoing an IPT test

### 3.3 Water Absorption Analysis

The values of relative weight changes due to water absorption are depicted as in the following Fig. 4. Basically, for specific analysis of some attributes, the selection of samples are based on high-voltage inclined plane testing (IPT) test results that was applied beforehand. These includes the best, the worst and control sample from each respective different type of mineral fillers added into SiR based composites. For the purpose of investigating the performance of water absorption of produced SiR based composite with regard to different types of mineral fillers used, the SiR based composites filled with 30 wt% SiO<sub>2</sub>, 10 wt% CaCO<sub>3</sub>, and 40 wt% CaSiO<sub>3</sub> samples are selected for the testing purposes.

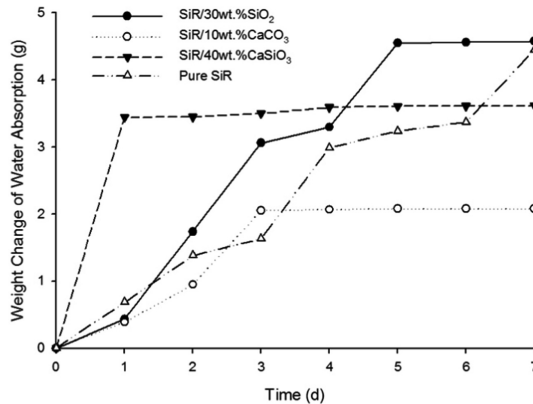


Fig. 4. Water absorption results



As clearly seen, the water absorption percentages were increased rapidly up to 24 h, while following to the next day it was increased gradually until reaching the saturation state. Since this observation was conducted at room temperature (RT), condition at lower humidity, an absorption of water has occurred slowly due to less interaction between water and hydrophobic polymeric composites surfaces [15]. It was clearly shown that, the stable water absorption behavior was possessed by the SiR/CaSiO<sub>3</sub> composite sample. The increased of water absorption content for SiR/CaSiO<sub>3</sub> composites, only occurred for the first day and later has remained constant on the following next six days of immersion period. At this state, the composites sample has reaching the saturation level at faster acceleration time, but the percentage absorption was among the lowest compared than others. This situation provides a good indication for produced SiR/CaSiO<sub>3</sub> based composites in water resistance characteristic. It was considered that the matrix-filler interaction are significantly provide the main path of water diffusing condition, and it was understood that the interfacial polarization was basically strengthened by the water absorption phenomena [16]. This path also was important in affecting the resulted dielectric properties.

Interestingly, the present findings have also discovered the unique observation based on percentages of filler loadings addition. As compared to pure SiR, the finding shows that SiR sample with an addition of mineral fillers are having stability in terms of water absorption even at first day of water immersion. This result proved that SiR based composites are having good binding interaction with all mineral fillers used in this study. The water molecules might be filled inside the volume holes and this condition provides the reason why the water-immersed sample are having the remain unchanged absorption values [7]. Slow absorption of water are not be able to trigger the degradation of material [17]. This characteristic has shown by SiR/CaSiO<sub>3</sub> based composites in their water resistance characteristic, which important for the real situation in HV application that directly exposed with environment.

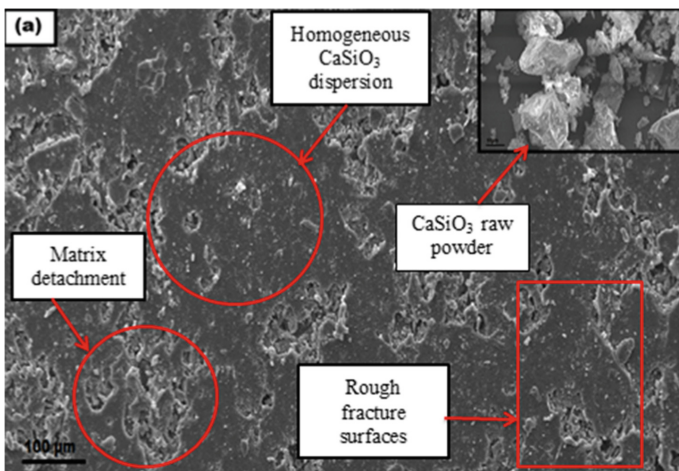


Fig. 5. Morphology of solid fracture surface of SiR/CaSiO<sub>3</sub>

López-Zaldívar et al. [18] has correlated the concept of filler addition into the rubber, that prone to cause greater porosity development and more air occlusion within the established sample. The content of water in the porosity can cause the diffusion into the core rod of insulator and has led into aging or worst degradation. Hence, lesser the porosity, lesser the water absorption uptake, thus, lesser the tendency of SiR based composites to experience early damages due to water absorption accelerated ageing condition. The morphology of solid fracture surface of SiR/CaSiO<sub>3</sub> based composites in the following Fig. 5 has supported this explanation, that the lesser the porosity, lower the percentages of water absorption.

## 4 Conclusion

In overall, the best performance of SiR based composites has shown by SiR/CaSiO<sub>3</sub> for both testings. SiR/CaSiO<sub>3</sub> based composites shows the best performance at highest filler loading in hardness testing. In water absorption testing, SiR/CaSiO<sub>3</sub> based composite shows the most stable water absorption behavior which can be seen clearly only for the first day and remained constant at the following 6 days of immersion period. In overall, the entire gathered experimental results are ample to justify the potential of this new advanced materials candidates for application of interest as insulator in HV purposes, which resistance towards wheather, moisture and local indentation or deformation.

**Acknowledgments.** The authors wish to extend their utmost appreciation to the Ministry of Higher Education (MOHE) Malaysia for funding this research work under RAGS/1/2015/TK0/FTK/03/B00120. Sincere appreciation to Faculty of Manufacturing Engineering and Faculty of Electrical Engineering Universiti Teknikal Malaysia Melaka (UTeM) for extensive support on laboratory and facilities. An expression of gratitude is also given to Immortal Green Industrial Sdn. Bhd and Saiko Rubber Sdn. Bhd for their support in research in terms of raw materials supply and processing machineries.

## References

1. Karthik, R., Raja, T.S.R., Madavan, R.: Enhancement of critical characteristics of transformer oil using nanomaterials. *Arab. J. Sci. Eng.* **38**(10), 2725–2733 (2013)
2. Hall, J.F.: History and bibliography of polymeric insulators for outdoor applications. *IEEE Trans. Power Deliv.* **8**(1), 376–385 (1993)
3. Khan, H., Amin, M., Ali, M., Iqbal, M., Yasin, M.: Effect of micro/nano-SiO<sub>2</sub> on mechanical, thermal, and electrical properties of silicone rubber, epoxy, and EPDM composites for outdoor electrical insulations. *Turk. J. Electr. Eng. Comput. Sci.* **25**(2), 1426–1435 (2017)
4. Prasenjit Biswas, V.M., Ganga, S., Moumita Naskar: Resistance to DC tracking and erosion of UV aged silicone rubber insulator. In: *International Conference on High Voltage Engineering and Technology (ICHVET-2015)* (2015)

5. Xuguang, L., Yougong, W., Fuyi, L.: Study on improving the tracking and erosion resistance of silicon rubber. In: Proceedings of 6th International Conference on Properties and Applications of Dielectric Materials 2000, vol. 1, pp. 342–345 (2000)
6. Sundhar, S., Bernstorff, A., Goch, W., Linson, D., Huntsman, L.: Polymer insulating materials and insulators for high voltage outdoor applications. In: Conference Record IEEE International Symposium Electrical Insulation, pp. 222–228 (1992)
7. Wang, Z., Jia, Z.D., Fang, M.H., Guan, Z.C.: Absorption and permeation of water and aqueous solutions of higherature vulcanized silicone rubber. *IEEE Trans. Dielectr. Electr. Insul.* **22**(6), 3357–3365 (2015)
8. Gao, Y., Wang, J., Liang, X., Yan, Z., Liu, Y., Cai, Y.: Investigation on permeation properties of liquids into HTV silicone rubber materials. *IEEE Trans. Dielectr. Electr. Insul.* **21**(6), 2428–2437 (2014)
9. Fernández, F.M.: Introduction to Hardness Testing. Library (Lond.) **11**, 81–82 (1977)
10. Yusup, R., Roslan, E.: Mechanical properties of CaCO<sub>3</sub> extracted from cockle shell with high density polyethylene (HDPE) for biomaterials in bone substitute application. *Sci. Int.* **30**(1), 91–95 (2018)
11. Ahmed, K.: Reinforcement of natural rubber hybrid composites based on marble sludge/silica and marble sludge/rice husk derived silica. *J. Adv. Res.* **5**(2), 165–173 (2014)
12. He, S., Hu, J., Zhang, C., Wang, J., Chen, L., Bian, X., Lin, J.: Performance improvement in nano-alumina filled silicone rubber composites by using vinyl tri-methoxysilane. *Polym. Test.* **67**(March), 295–301 (2018)
13. Wang, Y.M., Morris, M.D., Kutsovsky, Y.: Effect of fumed silica surface area on silicone rubber reinforcement. *Kautschuk Und Gummi Kunststoffee* **61**(3), 107–117 (2008)
14. Chen, Y.C., Lin, H.C., Lee, Y.D.: The effects of filler content and size on the properties of PTFE/SiO<sub>2</sub> composites. *J. Polym. Res.* **10**(4), 247–258 (2003)
15. Salama, S., Sirait, K.T., Kaerner, H.C.: Dielectric properties and surface hydrophobicity of silicone rubber under the influence of the artificial tropical climate. In: 1998 IEEE International Symposium on Electrical Insulating Materials. 1998 Asian International Conference on Dielectrical and Electrical Insulation. 30th Symposium on Electrical Insulating Materials (IEEE Cat. No.98TH8286), pp. 607–610 (1998)
16. Gao, N., Xie, H., Peng, Z.: Effect of water absorption on dielectric properties of EPDM/Al(OH)<sub>3</sub> composites. In: Proceedings of 6th International Conference on Properties and Applications of Dielectric Materials, vol. 2, no. I, pp. 905–907 (2000)
17. Lutz, B., Cheng, L., Guan, Z., Wang, L., Zhang, F.: Analysis of a fractured 500 kV composite insulator: identification of aging mechanisms and their causes. *IEEE Trans. Dielectr. Electr. Insul.* **19**(5), 1723–1731 (2012)
18. López-Zaldívar, O., Lozano-Díez, R., Herrero del Cura, S., Mayor-Lobo, P., Hernández-Olivares, F.: Effects of water absorption on the microstructure of plaster with end-of-life tire rubber mortars. *Constr. Build. Mater.* **150**, 558–567 (2017)



# Mechanical Properties and Fracture Morphological Observation of Recycled Polypropylene (*rPP*) Filled Dried Banana Leaves Fibre (DBLF) Composites: Effects of Sodium Hydroxide (NaOH) Surface Treatment

Thinakaran Narayanan<sup>1,2(✉)</sup>, Jeefferie Abd Razak<sup>1</sup>,  
Intan Sharida Othman<sup>1</sup>, Noraiham Mohamad<sup>1</sup>,  
Mohd Muzafar Ismail<sup>3</sup>, and Ramli Junid<sup>4</sup>

<sup>1</sup> Fakulti Kejuruteraan Pembuatan, Universiti Teknikal Malaysia Melaka,  
Hang Tuah Jaya, 76100 Durian Tunggal, Melaka, Malaysia  
thinakaran@kbs.gov.my, jeefferie@utem.edu.my

<sup>2</sup> Department of Mechanical Polymer, National Youth and High Skill Institute  
(IKTBN) Sepang, Bandar Baru Salak Tinggi, 43900 Sepang, Selangor, Malaysia

<sup>3</sup> Faculty of Electronic Engineering and Computer Engineering,  
Universiti Teknikal Malaysia Melaka,  
Hang Tuah Jaya, 76100 Durian Tunggal, Melaka, Malaysia

<sup>4</sup> Faculty of Mechanical Engineering, Universiti Malaysia Pahang,  
26600 Pekan, Pahang, Malaysia

**Abstract.** Disposal of after-used plastic based product has created worldwide problems on environmental pollution. This scenario has initiated the inventiveness to develop eco-friendly bio composites products. In this research, recycled waste polypropylene (*rPP*) was loaded with dried banana leaves fibre (DBLF), for *rPP*/DBLF composites fabrication. The effects of sodium hydroxide (NaOH) treatment on DBLF has studied based on the resulted mechanical and fracture morphological properties of produced *rPP*/DBLF composites. Dried banana leaves have been grounded into 30  $\mu\text{m}$  of fibre length, and *rPP* was taken from injection moulding scrap and crushed into finer *rPP* particles. The *rPP*/DBLF composites are prepared through double steps compounding method by using a melting device (230  $^{\circ}\text{C}$ , 95 rpm, 60 min) followed by an injection moulding process (210  $^{\circ}\text{C}$ , 30 s of residence time) for various amount of treated and untreated DBLF fibre loading at 0, 10, 20, 30 and 40 wt%. It was found that the tensile strength (TS) of treated NaOH-*rPP*/DBLF composite has significantly increased into about + 45.20% with 30 wt% of DBLF-NaOH loadings, in comparison to unfilled *rPP* sample. Loading of NaOH treated DBLF into *rPP* was enhanced the strength result which indicates successful reinforcement effects introduced by DBLF-NaOH filler. This could be explained by finer DBLF particle morphology as observed by SEM and presence of OH group from the successful NaOH treatment, which responsibly encouraged the mechanical interlocking and chemical bridging with *rPP*, for improved matrix-filler interaction, that significantly increased the TS. In overall, this study has successfully

highlighted the potential of DBLF filler to enhance the properties of *rPP*, as an additional choice of degradable plastic based composite for various promising applications.

**Keywords:** *rPP* · DBLF · Degradable plastics · Tensile · Fracture surfaces · NaOH · Surface treatment

## 1 Introduction

A wide-ranging application of thermoplastic materials has stricken most current industries, such as manufacturing industry, transportation industry, medical industry and many more other industries [1]. Due to plastic flexibility characteristic, the utilization of petroleum based non-biodegradable plastic are turn out to be endless. This scenario has cultivated the important of post-production on waste plastic, combined with natural fibres, which are currently available and feasibly being consumed as a secondary phase of the polymer matrix composites (PMC). The resulted composite also known as green composites. The bio composition between waste plastic and natural fibres have superior and outstanding mechanical properties as well as physical properties. Thermoplastic materials have been increasingly used for various applications [2]. In this research, the waste from injection moulding scrapped was consumed as matrix and the plant based natural fibres has been utilized to reinforce the matrix phase.

Natural fibres which were extracted from plant based are very attainable and abundant resources to substitute for high cost and non-renewable synthetic fibres. Natural fibres acquired low cost, low density, non-toxicity, possessed comparable strength and almost no waste disposal issues [3]. As we know, among the Southeast Asia nations, Malaysia having varieties of plant based fibres including coconut coir fibres, kenaf fibres, palm oil empty fruit bunch, banana fibres, pineapple fibres and etc. At this time, the consumption of plant based natural fibre are very popular and common in numerous engineering applications, such as in telecommunication, electrical and electronic industry [1–3]. The incorporation of natural fibres and waste recycled polypropylene (*rPP*) have extremely improving the mechanical strength of produced composites [4]. In this study, dried banana leaves fibre (DBLF) has been utilized as secondary phase for *rPP* matrix which was produced from an injection moulding process. So such a reason, the waste polypropylene was taken from an injection moulding operation, and was grinded into fine particles by using an industrial crusher. Then, several compounding step and hot compression technique were applied for *rPP*/DBLF composites production.

The cultivation of banana crops such as leaves, trunks, peels and etc. was becoming a primary factor causing more residue generated from an agricultural industry and these causes harmful threat to the environment [5]. Banana leaves rich in starch and contents cellulosic fibres and lignin [4, 5]. Cellulosic based fillers have been of superior interest that will offer great improvement to bio composites mechanical properties, as compared than those composites containing non-fibrous fillers [6]. The matured banana leaves contain of dry matter protein, lignocellulose fibres, starch as well as moisture. Banana tree yields big quantity of cellulosic residue which disposed into a landfill [7]. During

this degradation process, dried banana leaves emitted about 20% of methane gaseous which is 84 times more harmful than carbon monoxide, which is one of the main reason for global warming [8]. In addition, DBL can be used for industrial purpose without any extra cost [6–8]. In this study, DBL was derived from post-harvest of banana tree. Dried DBL was grinded by using a laboratory blender for converting it into DBLF powder. For this reason, to understand the role of DBLF as latest green functional filler for polymer matrix composites, their chemical treatment effects to the resulted mechanical and fracture morphological of *rPP*/DBLF composites were studied in this preliminary research.

## 2 Materials and Methods

### 2.1 Raw Materials

The materials used in this experiment for packaging application are recycled polypropylene (*rPP*) and dried banana leaves (DBL). *rPP* are collected from the waste generated by an injection moulding process in IKTBN Sepang. The purging or waste has been generated from teaching and learning activities held in the polymer processing laboratory at IKTBN Sepang. The *rPP* was originally virgin homopolymer polypropylene delivered by Titan PP Polymers (M) Sdn. Bhd. The collected *rPP* scrapped was first cleansed and isolated for any contamination or impurities elimination. Next, the *rPP* was filled into industrial crusher machine for grinding into fine particles. The process was repeated about two times to ensure *rPP* sizes homogeneity.

The dried banana leaves fibre were derived from dry banana petiole (one of the part from banana leaves) of *musa acuminata sp.* species. The petiole was separated from dried banana leaves then treated with sodium hydroxide (NaOH), that was heated at 80 °C for 30 min. The DBLF was further dried in a drying oven for 24 h at 80 °C for conditioning purpose. Next the DBLF was grinded by using an industrial blender and filtered into 30 µm of length size with *Analysette 3* vibratory sieve shaker. Lastly the merging process of *rPP*/DBLF composites was performed via double steps of melt-blending process.

### 2.2 *rPP*/DBLF Composites Preparation via Double Steps Melt-Blending Procedure

The *rPP*/DBLF composites with treated and untreated DBLF with numerous different loadings (0, 10, 20, 30 and 40 wt%) were formulated to evaluate the effects of sodium hydroxide (NaOH) surface treatment to the *rPP* filler for composites application. The double-steps melt-blending method was applied to combine the *rPP*/DBLF composites. At the beginning, the tuned melting device was set into 230 °C and mixing was performed within the period of 60 min at 95 rpm. Later on, the second melt-blending phase was followed by injection moulding and the samples was injected into specific dimension and shape of samples for tensile test. The moulding process was performed at 210 °C within 30 s of residence period, using DKM-188 Dakumar type injection

moulding machine. Produced samples were conditioned at 80 °C for 24 h in a drying oven, before carrying out the subsequent mechanical testing.

### 2.3 Fourier Transform Infrared Spectroscopy

The Fourier transform infrared (FTIR) spectroscopy technique was used to characterize the chemical structure for treated DBLF fibre with NaOH and untreated DBLF fibre. This analysis will determine the variations in measurement of fibre composition before and after the NaOH chemical treatment. Each spectrum was recorded in the range of 3600–400  $\text{cm}^{-1}$  at a resolution of 4  $\text{cm}^{-1}$  with 32 scans using an FTIR machine model JASCO FT/IR-6100 type A.

### 2.4 Tensile Testing of rPP/DBLF Composites

The tensile test for rPP/DBLF composites were performed in accordance to ASTM D638 – Type 1. Dimension of tensile test sample was monitored within  $\pm 1.00$  mm of thickness, overall width of 19.00 mm and gauge length at 50.00 mm. The test was carried out at controlled atmosphere of  $22 \pm 1$  °C, at relative humidity of 60%. Testing was performed at 10 mm/mins of cross-head speed by using a Universal Testing Machine (GoTech). For each loadings, about five samples were tested for data averaging purpose. For the case of this study, only tensile strength (TS) response was analysed and presented, to represent the reinforcement effects and properties improvement due to NaOH surface treatment performed towards DBLF green filler.

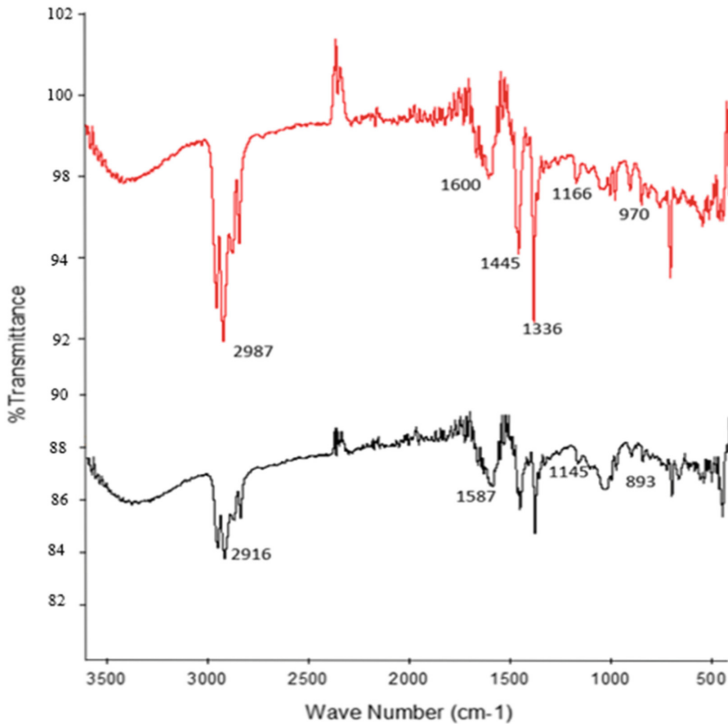
### 2.5 Fracture Surface Morphological Observation of rPP/DBLF Composites

The fracture surfaces of the selected samples of rPP/DBLF composite was observed under the Scanning Electron Microscope (SEM) observation. At first, the fractured surface was mounted onto the stub with carbon tape before being coated with gold-palladium (Au-Pd) thin conductive coating, using a sputter coater model Polaron E-1500, to eliminate the charging effects during observation. The fracture surface images were captured by using Zeiss Evo VPSEM at 7.00 kV accelerating voltage for  $100\times$  of magnification power at secondary electron detection.

## 3 Results and Discussion

The FTIR spectra of untreated and NaOH treated DBL fibre are as depicted in Fig. 1. NaOH treated DBLF fiber is referred to the red plots while the black plots is belongs to the untreated DBLF fiber. The spectrum of DBL fibre is subject where dominant peak at 2987  $\text{cm}^{-1}$ . The peak at about 2900  $\text{cm}^{-1}$  is referring to the C-H asymmetric and symmetric stretching from aliphatic saturated compounds which is parallel to the aliphatic moieties in cellulose and hemicellulose. Instead, the peaks in the region 1455  $\text{cm}^{-1}$  are due to C-H groups from various lignin. The intensity of the peak at 1366  $\text{cm}^{-1}$  is sharply reduced after presence of NaOH which is indicating C-H groups

in methyl and phenolic alcohol and results from bending vibration in the molecule. Apart from that, the peaks found at  $1145\text{ cm}^{-1}$  and  $893\text{ cm}^{-1}$  for untreated DBL fibre looks disappear at peak for NaOH treated. Different IR peaks at between untreated and treated DBLF as explained evidence of the success in performed alkaline treatment done into DBLF fiber.

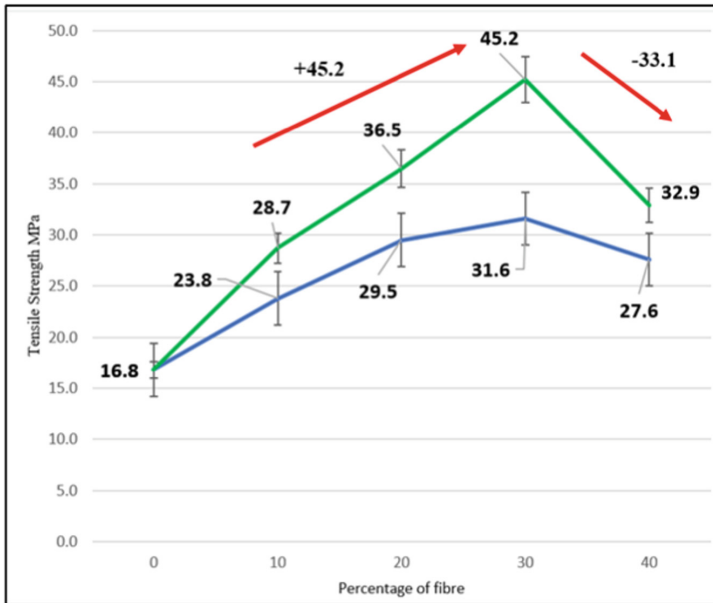


**Fig. 1.** FTIR spectrum for NaOH treated DBLF (red line) and untreated DBLF (black line)

The main aim of this investigation is to indicate the effectiveness of NaOH treatment towards the mechanical strength of produced rPP/DBLF composites (Fig. 2). Apart from mechanical properties, the effect of NaOH on fractured chemical structure of rPP/DBLF composite has been observe via scanning electron microscopy (SEM). The following Fig. 2 has presented the resulted tensile strength (TS) for rPP based composites filled with NaOH treated DBLF and untreated DBLF at various loadings (wt%). It was clearly found that, by treating DBLF with NaOH into rPP matrix, the TS was significantly increased up to +45.20% of positive improvement (refer to green plot), in comparison to the untreated DBLF sample. This absolute improvement was due to special ability of treated DBLF with NaOH that has improving the mechanical strength of produced rPP/DBLF composites. The alkaline treatment introduced to DBLF filler able to enhance the compatibility of DBLF which later provide the reinforcement effect into rPP matrix. However, this positive improvement is only applies

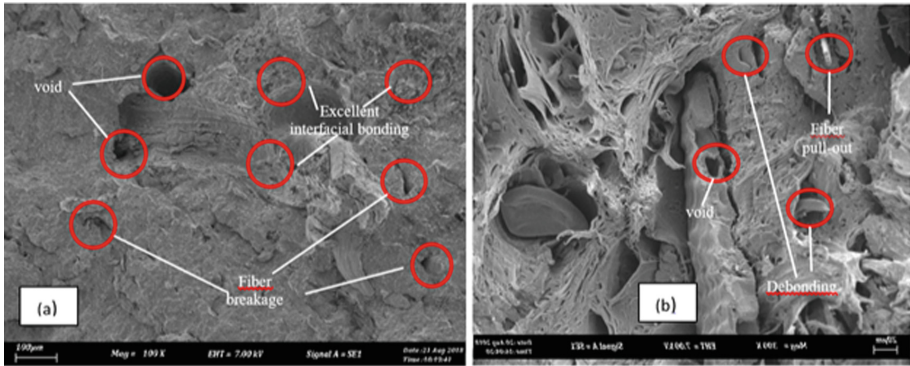


up to 30 wt% of DBLF addition, for both treated and untreated rPP/DBLF composites systems. Addition of DBLF filler more than this amount has reducing the composites performance, which responsible lowering the TS values. This properties reduction is due to agglomeration of DBLF where dispersion of filler was not effectively took place at maximum loading. Agglomeration of DBLF filler has responsible in avoiding the homogeneous load transfer during the tensile loading and prone to crack zone at the agglomeration site has caused the early premature failure of produced rPP/DBLF composites.



**Fig. 2.** TS plots for NaOH treated (green line) and untreated (blue line) DBLF at different wt% of loadings in rPP based composites

The fracture morphology of rPP/DBL composites was analysed to evaluate the effects of NaOH treatment into DBL fibre reinforced rPP at different loadings. This probe was investigated by referring based on the fracture surface of the tensile specimens. For untreated composition, it indicates very ineffective fibre matrix binding which is supported by the presence of cavities between fibre and the matrix and fibre pull-outs due to weak compatibility as displayed in Fig. 3(b). Meanwhile the compartment of the NaOH compatibilizer provides enhanced progress of the wettability of both fibre surface by the rPP matrix. The gaps between both composites were very less which is indicating superior adhesion and excellent wettability between the fibre and matrix as proven in Fig. 3(a). The effective diffusion for the period of blending avoids the unused area, thus it was indicated by providing the superior mechanical properties



**Fig. 3.** (a) Image of fractured surface of composite with NaOH treated DBLF, (b) Image of fractured surface of composites with untreated DBLF

compared to composites without the presence of treated DBLF-NaOH as filler inclusions.

## 4 Conclusions

In conclusion, from this study, the effects of DBLE fibre loadings as well as the effect of NaOH alkaline treatment towards the investigated tensile and fracture morphological properties of *rPP*/DBLF composites were fully explored and understood. Based on the experimental results, it was found that, about 30 wt% of treated DBLF addition has enough to enhance the TS for positive improvements compared to untreated DBLF. This study has successfully revealed that the improved interfacial adhesion and matrix-filler interaction, introduced by NaOH treated DBLF filler, are successfully enhanced the properties of *rPP* based composites. This positive finding provides another alternative of degradable plastic based composite to be selected and utilized for various promising applications.

**Acknowledgements.** Authors would like to extend their sincere appreciation to Ministry of Education, Malaysia (MOE) and Universiti Teknikal Malaysia Melaka (UTeM) for funding and supporting this research work under the FRGS research grant - FRGS/1/2018/TK05/UTeM/02/4. Sincere thanks to Faculty of Manufacturing (FKP), UTeM and Mechanical Polymer Department, IKTBN Sepang, for extensive support on laboratory and facilities until the completion of this research works.

## References

1. Ramesh, M., Sri Ananda Atraya, T., Aswin, U.S.: Processing and Mechanical property evaluation of banana fibre reinforced polymer composites. *Proc. Eng.* **97**, 563–572 (2014)
2. Yion, S., Tuladhar, R., Combe, M., et al.: Mechanical properties of recycled plastic fibres for reinforcing concrete. *Fibre Conc.* **2013**, 1–10 (2013)

3. Bolka, S., Slapnik, J., Rudolf, R.: Thermal and mechanical properties of biocomposites based on green PE-HD and hemp fibers. *Contem. Mater.* **VIII-1**, 80–90 (2017)
4. Batori, M., Jabbari, M., Akesson, D.: Production of pectin-cellulose biofilms: a new approach for citrus waste recycling. *Int. J. Polym. Sci.* **2017**, 1–7 (2017)
5. Mohapatra, D., Mishra, S., Sutar, N.: Banana and its by-product utilisation: an overview. *J. Sci. Ind. Res.* **69**, 323–329 (2010)
6. Marikkar, J.M.N., Tan, S.J., Salleh, A.: Evaluation of banana (*Musa* sp.) flowers of selected varieties for their antioxidative and anti-hyperglycemic potentials. *Int. Food Res. J.* **23**, 1988–1995 (2016)
7. Mukhopadhyay, S., Figueiro, R., Arpac, Y.: Banana fibres—variability and fracture behavior. *J. Eng. Fibre Fabr.* **3**, 39–45 (2008)
8. Abd Razak, J., Ahmad, S.H., Ratnam, C.T.: Effects of poly(ethyleneimine) adsorption on graphene nanoplatelets to the properties of NR/EPDM rubber blend nanocomposites. *J. Mater. Sci.* **50**, 6365–6381 (2015)



# Surface Roughness Analysis of Zirconia Dental Restoration Manufactured Through CNC Milling Machine

Rahimah Abdul Hamid<sup>(✉)</sup>, Wan Nur Amirah Wan Muhamad,  
Raja Izamshah, and Mohd. Shahir Kasim

Faculty of Manufacturing Engineering, Universiti Teknikal Malaysia Melaka,  
Hang Tuah Jaya, 76100 Durian Tunggal, Melaka, Malaysia  
rahimah.hamid@utem.edu.my

**Abstract.** The aim of the study was to characterize the chemical composition and surface roughness of zirconia dental restoration, fabricated by means of CNC milling machine. The chemical composition and surface roughness of the restoration were studied by SEM/EDS and surface roughness tester machine, respectively. The digitized metal restoration was used as a CAD reference model. Energy Dispersive Spectroscopy (EDS) showed the presence of carbon (C), copper (Cu) and silver (Ag) in the reference model, while the presence of zirconium (Zr) and oxygen (O) was confirmed in the zirconia disc which consists of more than 89% zirconium oxide. Meanwhile, all specimens yielded the *Ra* values lower than 0.5  $\mu\text{m}$ , except for point F which might be caused by the waviness profile due to the milling process. The improvement of the surface profile of the dental restoration could be achieved with some polishing techniques which are not considered in the present study.

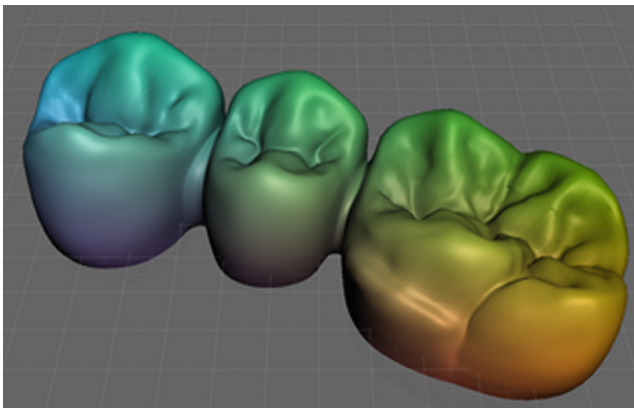
**Keywords:** Zirconia dental restoration · Surface analysis · SEM/EDS · CNC milling

## 1 Introduction

The introduction of CAD/CAM milling systems in the dental field enabled zirconia ceramics to be used as a standard material for dental prosthetic restorations. CAD/CAM milling systems provide a rapid and individual method for the manufacturing of zirconia dental restorations [1]. CAD/CAM dentures should have smoother and more hydrophilic surfaces than conventional dentures. However, the disadvantages of these systems include limited accuracy and possible introduction of microscopic cracks [2]. On the other hand, the surface roughness is one of the main properties which is responsible for the microbial attractiveness of denture surfaces [3]. Surface roughness is considered relevant for primary microbial adhesion. Microbial adhesion is enhanced with increasing surface roughness between 0.1 and 0.4  $\mu\text{m}$  [4]. Kim et al. [5] confirmed that different materials with extremely low surface roughness exhibit different amounts of bacterial adhesion. Bollen et al. [6] described the *Ra*-cut-off value of 0.2  $\mu\text{m}$  which means below this *Ra*-value, the surface roughness does not influence bacterial adhesion

or colonization. According to Rashid [7], the composition of a dental restorative material in addition to the surface structure influence the initial bacterial adhesion, and a rough material surface will accumulate more plaque. Therefore, the aim of the present study was to characterize the chemical composition and surface roughness of the zirconia dental restoration, fabricated by means of CNC milling machine. The testing hypothesis was that the surface roughness would be below  $0.5\ \mu\text{m}$  and the composition of the zirconia disc should consist of more than 89% zirconium oxide.

In order to get started, a metal restoration model was scanned using an oral scanner. Prostheses can be manufactured through oral data of patients that are acquired using intraoral scanners and allows the 3D modelling of a tooth of a patient, which is known as a digital oral impression [8]. In this study, however, the pre-fabricated restoration made of a metal was used to generate the digitized data, as shown in Fig. 1. The obtained scan data was then used as a CAD reference model (CRM), to produce a milled zirconia restoration model using Ardentia CNC milling machine. Since the composition of the metal restoration was unknown, the SEM/EDS machine was employed to initially identify the exact chemical composition of the master pattern. In addition, the zirconia disc was also examined for its chemical composition since the disc was obtained from the manufacturer and the production process of this block was unknown. According to Denry and Kelly [9], although many types of zirconia-containing ceramic systems are currently available, only three are used to date in dentistry. These are yttrium cation-doped tetragonal zirconia polycrystals (3Y-TZP), magnesium cation-doped partially stabilized zirconia (Mg-PSZ) and zirconia-toughened alumina (ZTA). Therefore, it is required to initially identify the elemental composition of the zirconia disc in order to examine the actual composition of the disc. Thus, the elemental analysis of the metal restoration and the zirconia disc was conducted as the first part of this study.



**Fig. 1.** Computer-aided design (CAD) reference model (CRM)

## 2 Materials and Method

### 2.1 Zirconia Disc

In this study, NexxZr T, which is dental zirconium oxide (Y-TZP ZrO<sub>2</sub>) from Sagemax Bioceramics, Inc. was used as the restoration material. The disc had undergone a sintering temperature between 1500–1530 °C. Table 1 shows the composition of the disc which was obtained from the manufacturer's website.

**Table 1.** Composition of the Zirconia disc as claimed in the manufacturer's website

Material	NexxZr T
Zirconium oxide ZrO <sub>2</sub>	≥ 89%
Yttrium oxide + Y <sub>2</sub> O <sub>3</sub>	4–6%
Hafnium oxide HfO <sub>2</sub>	≤ 5%
Aluminium Oxide Al <sub>2</sub> O <sub>3</sub>	<1%
Chemical solubility [μg/cm <sup>2</sup> ]	<100

### 2.2 Elemental Analysis

The internal structure of the metal crown was analyzed using energy dispersive spectroscopy (EDS). The purpose of this investigation was to use energy dispersive X-ray spectrometry (EDS) to characterize the chemical phases of a metal dental crown. Initially, the sample was sputter coated to avoid electrostatic discharge of the non-metallic sample. As a result of this coating process, the element of gold (Au) and palladium (Pd) were found in the analysis. Details of the data would be presented in Sect. 3.

### 2.3 Surface Roughness Measurements

For the surface roughness measurement, the fabricated dental restoration was evaluated using Mitutoyo surface roughness tester machine at some defined points. The specified points were selected at the buccal and lingual area of the restoration. The occlusal surface was not examined in this surface roughness measurement due to the uncertain structure of this region. *Ra* (roughness average) is the most commonly used surface roughness characteristic. It is determined as the arithmetic mean of absolute values of the roughness profile ordinates. The measurement areas were selected in consideration with the limitation of the surface roughness tester, which could only read the flat surface. In this context, the measurement has to be repeated several times and the specified measurement areas were as shown in Fig. 2.

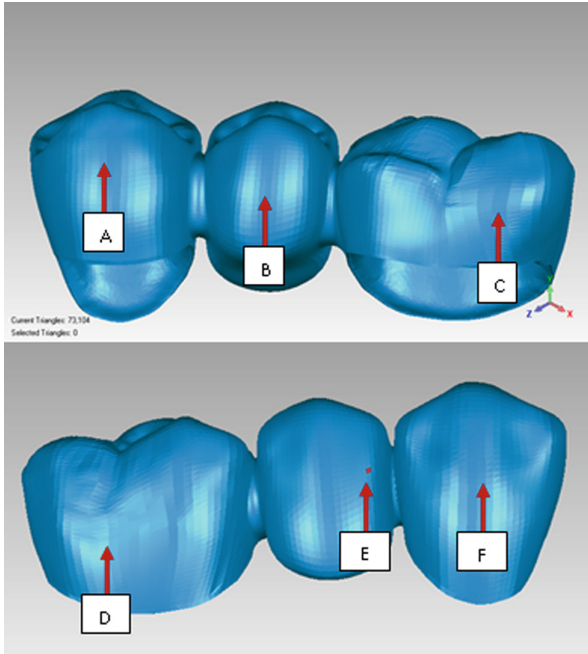


Fig. 2. The measurement points for the surface roughness analysis

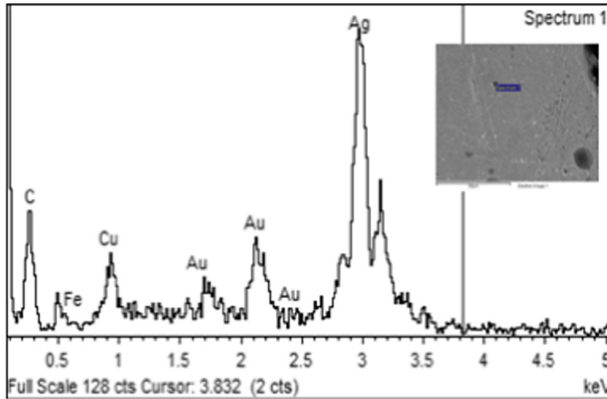
### 3 Results

#### 3.1 Elemental Composition

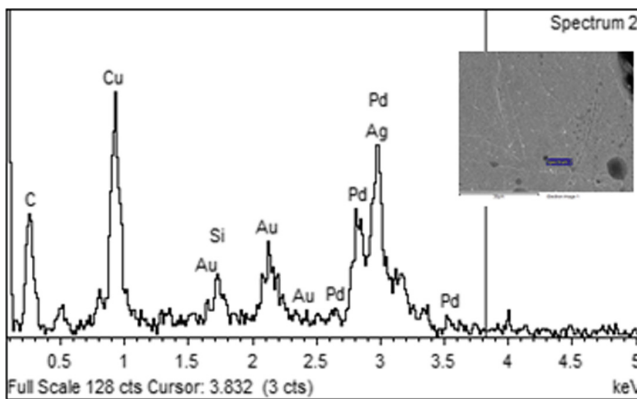
The predominant elements in the metal crown were carbon, copper, and silver in various compounds. These metal crown particles have slight variations in proportions of carbon (C), copper (Cu), and silver (Ag), as shown in Figs. 3, 4 and 5. In the first spectrum, the atomic percentage of carbon (C), copper (Cu), and silver (Ag) were 58.78%, 7.13%, and 30.34%, respectively. In the second spectrum, the atomic percentage of carbon (C), copper (Cu), and silver (Ag) were 79.32%, 8.97%, and 5.6%. The presence of silicone (Si) was identified around 1.23%. Meanwhile, in the third spectrum, the atomic percentage of carbon (C), copper (Cu), and silver (Ag) were 62.323%, 9.13%, and 25.42%. According to the result, the main elements of the reference model were carbon (C) and silver (Ag), with less than 10% composition of copper (Cu). As stated earlier, the presence of gold (Au) and palladium (Pd) in the sample was neglected due to the initial sputter coated of the non-metallic sample. Table 2 summarizes the obtained result.

**Table 2.** Elemental composition of the metal restoration in atomic percentage for all spectrums

Element	First spectrum	Second spectrum	Third spectrum
C (K)	58.78%	79.32%	62.33%
Si (K)		1.23%	
Cu (L)	7.13%	8.97%	9.13%
Pd (L)		3.65	
Ag (L)	30.34%	5.60%	25.42%
Au (M)	3.75	1.23	3.12
Totals	100.00	100.00	100.00

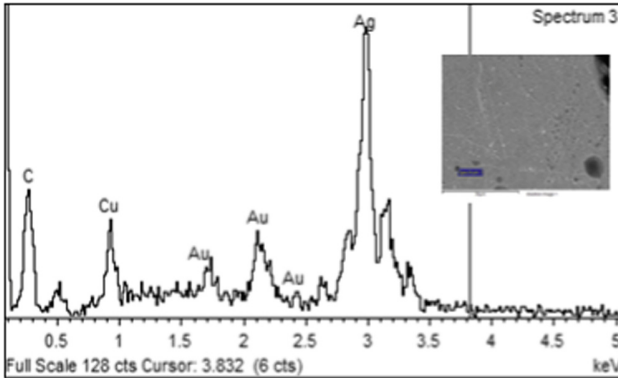


**Fig. 3.** Distribution of composition in the metal restoration for spectrum 1



**Fig. 4.** Distribution of composition in the metal restoration for spectrum 2



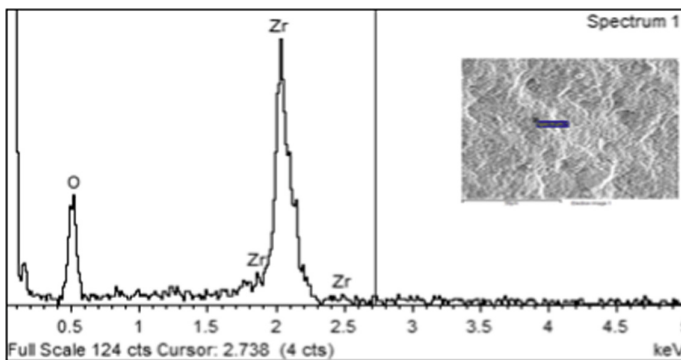


**Fig. 5.** Distribution of composition in the metal restoration for spectrum 3

Meanwhile, the predominant elements in the zirconia disc were zirconium (Zr) and oxygen (O) in various compounds. These zirconia disc particles have slight variations in proportions of zirconium (Zr) and oxygen (O), as shown in Figs. 6, 7, and 8. In the first spectrum, the atomic percentage of zirconium (Zr) and oxygen (O) were 36.88% and 63.12%, respectively. In the second spectrum, the atomic percentage of zirconium (Zr) was 100%. In the third spectrum, the atomic percentage of zirconium (Zr) and oxygen (O) were 46.49% and 53.51%. According to the result, the main elements of the reference model were zirconium (Zr) and oxygen (O). Table 3 summarizes the obtained result.

**Table 3.** Elemental composition of the zirconia block in atomic percentage for three spectrums

Element	First spectrum	Second spectrum	Third spectrum
O (K)	63.12%		53.51%
Z (L)	36.88%	100%	46.49%
Totals	100.00	100.00	100.00



**Fig. 6.** Distribution of composition in the zirconia disc for spectrum 1

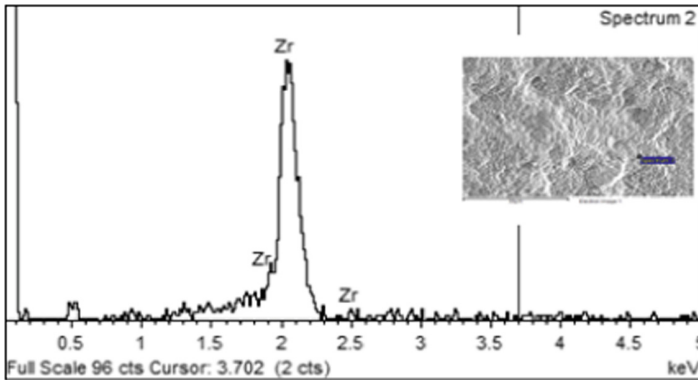


Fig. 7. Distribution of composition in the zirconia disc for spectrum 2

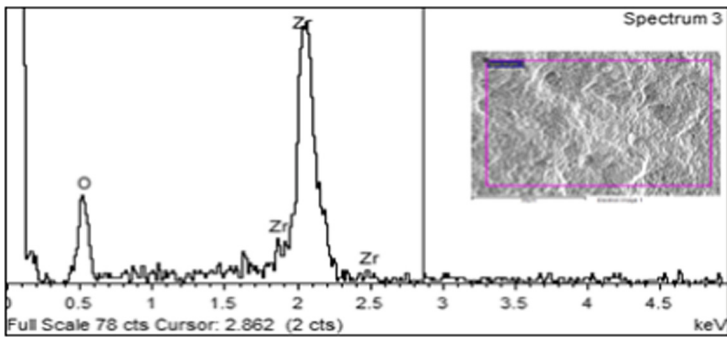
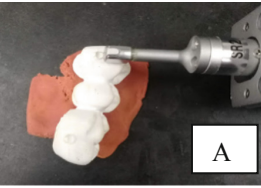
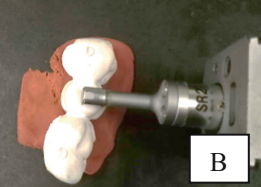
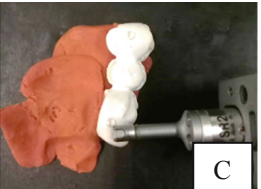
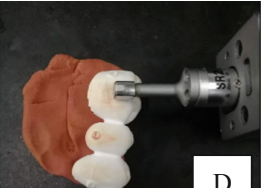

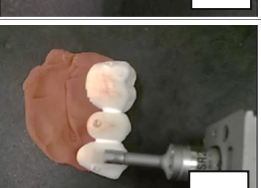


Fig. 8. Distribution of composition in the zirconia disc for spectrum 3

### 3.2 Surface Roughness Analysis Data

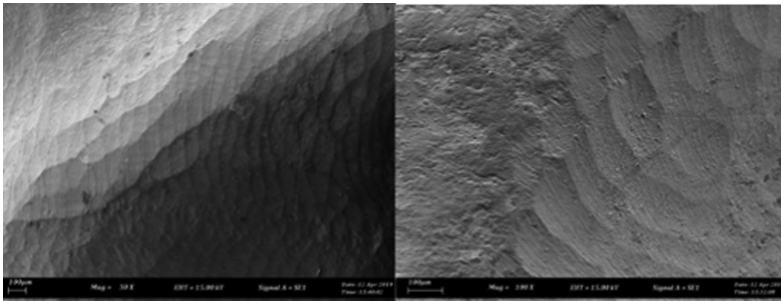
The average surface roughness of each measurement point is summarized in Table 4. All specimens yielded the  $R_a$  values lower than  $0.5 \mu\text{m}$ , except for point F. Three times of measurement were taken for each point and the average data was calculated in order to reduce the random error. The employed surface roughness tester exhibits a limitation in taking the measurement of the waviness surface which demanded multiple measurements to be conducted at some measurement points.

**Table 4.** Surface roughness data (*Ra*) for all measurement points

Measurement Point	Reading 1 <i>Ra</i> ( $\mu\text{m}$ )	Reading 2 <i>Ra</i> ( $\mu\text{m}$ )	Reading 3 <i>Ra</i> ( $\mu\text{m}$ )	Mean <i>Ra</i> ( $\mu\text{m}$ )
 A	0.04	0.03	0.04	0.037
 B	0.04	0.04	0.16	0.08
 C	0.29	0.38	0.32	0.33
 D	0.27	0.28	0.45	0.33
 E	0.42	0.55	0.36	0.44
 F	0.56	0.34	0.65	0.52

## 4 Discussion

The results of the present study confirmed the testing hypothesis that the composition of the zirconia disc consists of more than 89% zirconium oxide ( $ZrO_2$ ). According to literature, although many types of zirconia-containing ceramic systems are currently available, only three are used to date in dentistry. These are yttrium cation-doped tetragonal zirconia polycrystals (3Y-TZP), magnesium cation-doped partially stabilized zirconia (Mg-PSZ) and zirconia-toughened alumina (ZTA). In the present study, yttrium cation-doped tetragonal zirconia polycrystals (3Y-TZP) was employed. The composition of the zirconia disc according to the manufacturer's website should consist of Zirconium Oxide, Yttrium Oxide, Hafnium Oxide and Aluminium Oxide in the percentage of  $\geq 89\%$ , 4–6%,  $\leq 5\%$ , and  $<1\%$ , respectively. Biomedical grade zirconia usually contains 3 mol% yttria ( $Y_2O_3$ ) as a stabilizer (3Y-TZP). In this study, only the element of zirconium and oxygen were identified in all spectrums. Typically, the 3Y-TZP powder used in the fabrication of the disc contains a binder that makes it suitable for pressing. The binder is later eliminated during the pre-sintering step [9]. It also contains about 2 wt%  $HfO_2$ , classically difficult to separate from  $ZrO_2$ . These powders have only minor variations in chemical composition. The binder is eliminated during pre-sintering heat treatment. This step has to be controlled carefully by manufacturers, particularly the heating rate and the pre-sintering temperature.



**Fig. 9.** Enlarged images of zirconia restoration denture surfaces

As for the surface roughness study, all specimens yielded the  $R_a$  values lower than  $0.5 \mu m$ , except for point F. The periodic surface profile (waviness) might be originated from the milling process, as discussed by Steinmassl et al. [3]. The same effect could be observed in this study, as shown in Fig. 9. Nevertheless, the results almost confirmed the testing hypothesis that the surface roughness would be below  $0.5 \mu m$ . In the actual application, grinding or polishing the dental restoration would be performed to improve the surface roughness [7]. The polishing techniques have not been investigated in the present study. Therefore, the obtained result demonstrated the surface profile of the dental restoration without the polishing procedure. Since the results obtained were already below  $0.5 \mu m$ , the improvement of the surface roughness could be predicted if the polishing procedure is performed. As stated earlier, the surface roughness does not

influence bacterial adhesion or colonization if the *Ra* values are below 0.2  $\mu\text{m}$ . In this context, the study on bacterial adhesion might have to consider the available polishing techniques, in addition to the in-vitro study for the most accurate result. The fact that different polishing techniques may produce different results can also be explained by the fact that different systems for surface roughness evaluation have been used in different studies. Therefore, the surface roughness tester which has been used in this study might produce some measurement errors due to the limitation of the device which could only read the flat surface. As mentioned earlier, these can be estimated by comparing multiple measurements, and reduced by averaging multiple measurements.

## 5 Conclusion

The composition of the zirconia disc consists of more than 89% zirconium oxide ( $\text{ZrO}_2$ ) and the surface roughness of the unpolished zirconia restoration already demonstrated the values of *Ra* below 0.5  $\mu\text{m}$ . The improvement on the surface structure of the restoration could be done through several grinding or polishing techniques which require high skill of the dental technician. This is significant in reducing the tendency of bacterial adhesion and accumulation of plaque, affecting oral health. Different types of zirconia, in addition to a different type of CAD/CAM systems, produce slightly some variations in the surface roughness. The microstructure of each type of zirconia is also different due to the manufacturing process of the disc which might be explored in the future work.

**Acknowledgments.** The authors are grateful to the Universiti Teknikal Malaysia Melaka and the Ministry of Higher Education Malaysia for funding this research project through grant no: FRGS/2018/FKP-AMC/F00378.

## References

1. Ito, T., Hamid, R.A., Ichikawa, T.: Collaborative design and manufacturing of prosthodontics wire clasp. In: 23rd ISPE Inc. International Conference on Transdisciplinary Engineering, Curitiba, Parana, Brazil (2016)
2. Ebert, J., Özkol, E., Zeichner, A., Uibel, K., Weiss, Ö., Koops, U., Telle, R., Fischer, H.: Direct inkjet printing of dental prostheses made of zirconia. *J. Dent. Res.* **88**(7), 673–676 (2009). <https://doi.org/10.1177/0022034509339988>
3. Steinmassl, O., Dumfahrt, H., Grunert, I., Steinmassl, P.A.: Influence of CAD/CAM fabrication on denture surface properties. *J. Oral Rehabil.* **45**(5), 406–413 (2018). <https://doi.org/10.1111/joor.12621>
4. Tamada, M., Katakai, A., Yuasa, A., Terada, A., Kushimoto, T., Tsuneda, S.: Bacterial adhesion to and viability on positively charged polymer surfaces. *Microbiology* **152**(12), 3575–3583 (2006). <https://doi.org/10.1099/mic.0.28881-0>
5. Kim, H.Y., Yeo, I.S., Lee, J.B., Kim, S.H., Kim, D.J., Han, J.S.: Initial in vitro bacterial adhesion on dental restorative materials. *Int. J. Artif. Organs* **35**(10), 773–779 (2012). <https://doi.org/10.5301/ijao.5000153>

6. Bollen, C.M.L., Papaioanno, W., Van Eldere, J., Schepers, E., Quirynen, M., Van Steenberghe, D.: The influence of abutment surface roughness on plaque accumulation and peri-implant mucositis. *Clin. Oral Implants Res.* **7**(3), 201–211 (1996). <https://doi.org/10.1034/j.1600-0501.1996.070302.x>
7. Rashid, H.: The effect of surface roughness on ceramics used in dentistry: a review of literature. *Eur. J. Dent.* **8**(4), 571–579 (2014). <https://doi.org/10.4103/1305-7456.143646>
8. Jeong, Y.G., Lee, W.S., Lee, K.B.: Accuracy evaluation of dental models manufactured by CAD/CAM milling method and 3D printing method. *J. Adv. Prosthodont.* **10**(3), 245–251 (2018). <https://doi.org/10.4047/jap.2018.10.3.245>
9. Denry, I., Kelly, J.R.: State of the art of zirconia for dental applications. *Dent. Mater.* **24**(3), 299–307 (2008). <https://doi.org/10.1016/j.dental.2007.05.007>



# Design and Analyses of Semi-automated Portable Oil Spill Skimmer for Water Treatment Application

L. Abdullah<sup>(✉)</sup>, K. Santuso, Z. Jamaludin, R. Zamri,  
and M. N. Maslan

Faculty of Manufacturing, Universiti Teknikal Malaysia Melaka,  
76100 Durian Tunggal, Melaka, Malaysia  
lokman@utem.edu.my

**Abstract.** Oil spill response action plan is highly critical for preserving the ecosystem around the oil spillages area. During emergency situation, the action taken need to be responsive and effective to prevent the spillages from spreading widely and causes more harm to sea and water creature. Currently, several techniques were introduced with regards to response plan such as using booms, skimmers, barriers, storage barges, tanks and also vessel depending on the types of the spillages and the methods applied by the emergency response team. Owing to this reason, the project is conducted, to help providing an alternative for oil spillages response plan for water treatment application. Part of this project is designing prototype of portable oil spill skimmer to collect oil spillages in a different scales and area such as in the middle of the ocean, sea shore, water treatment facilities and reservoir. Radio frequency control is used as a controller for detection of location of the prototype while wireless camera for real-time monitoring. There are three analyses conducted for this project namely buoyancy force test, speed manoeuvring test, remote control coverage test and vision system coverage test. Results showed that the prototyped developed passed for the buoyancy force test. The maximum distance for coverage test using remote control is up to 50 m while it is improved to 60 m via vision system technique.

**Keywords:** Oil spill skimmer · Water treatment application · Oil spillage response plan

## 1 Introduction

Oils is defined as any neutral, nonpolar chemical substance, which is found in the form of viscous liquid at ambient temperatures and is both hydrophobic and lipophilic [1]. Oils have high carbon and hydrogen content and are usually flammable and slippery. Before oil is transported, reinjected or stored anywhere, the oil requires to pass through the field handling procedure, or oil processing on the production site [2].

Guidelines for oil or chemical handling procedures has been established [3]. In order to ensure that the wastes are safely handled, suitable containers are needed to be used by the waste generators. It is the responsibility of the waste generators to ensure that scheduled wastes are packed based on the composition in a manner suitable for

handling, storage and transportation [4]. According to [5], the supplier or owner of the chemicals should ensure that the warehouse keeper formally acknowledges receipt of information on hazards of the materials, recommendations for safe handling and instructions to be followed should spillage occur; seek confirmation that the implications of the information including those relating to first aid and emergency situations are understood. Seek confirmation that emergency arrangements are adequate and carry out the necessary inspections; be prepared to supply an emergency telephone number through which specialist advice may be obtained. All of the guidelines if were not followed and ignored will cause issues such as oil spillage that will bring negative impact to the environment and ecosystem.

There are several approaches to control oil spill pollution. Oil spill control measures aim to decrease and limit oil spills, as well as limit their spreading in the environment. This can be done in several ways, including the use of barriers and absorbent materials to mechanically recover the spilled oil is a commonly used method when the oil spill happens in a water environment, implying the use of physical barriers for the mechanical prevention of oil spreading. The main types of barriers used are booms, skimmers and natural and synthetic absorbing materials [6–8].

An oil skimmer is a device that is designed to remove oil floating on a liquid surface [9]. Depending on the specific design they are used for a variety of applications such as oil spill response, as a part of oily water treatment systems, removing oil from machine tool coolant and aqueous parts washers, and collecting fats oils and greases in wastewater treatment in food manufacturing industries [10–12]. The use of skimmers in industrial applications is often required to remove oils, grease and fats prior to further treatment for environmental discharge compliance. By removing the top layer of oils, water stagnation, smell and unsightly surface scum can be reduced. Placed before an oily water treatment system an oil skimmer may give greater overall oil separation efficiency for improved discharge wastewater quality [13–16]. It should be noted that all oil skimmers will pick up a percentage of water with the oil which will need to be decanted to obtain concentrated oil [17].

In this paper, methods on how to design and develop a semi-automated portable oil spill skimmer for water treatment application is presented. Four analyses are added and discussed to provide some solid judgement on the performance of the fabricated portable oil spill skimmer system.

## 2 Methodology

This project is divided into four parts of process. The four processes involved are as follows:

- i. Process 1: Design of body frame – this involved with designing the frame of oil spill skimmer system that able to float above the water with its weight (all equipment is mounted on the frame) including the weight of oil inside the storage tank.
- ii. Process 2: Design of the oil spills skimmer system – this include the selection of the materials to be used for the skimmer and the control circuit to make the skimmer function as required.



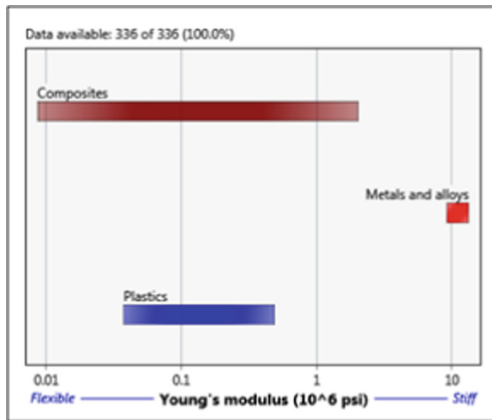
- iii. Process 3: Construction of the remote controlled system – construction of transmitter and receiver for communications between the remote control and the skimmer system. Radio frequency control will be used for good range of signal coverage.
- iv. Process 4: Selection of vision system – the wireless camera for the system to monitor real-time visual of the oil spills area.

**2.1 Process 1: Design of Body Frame Assembly**

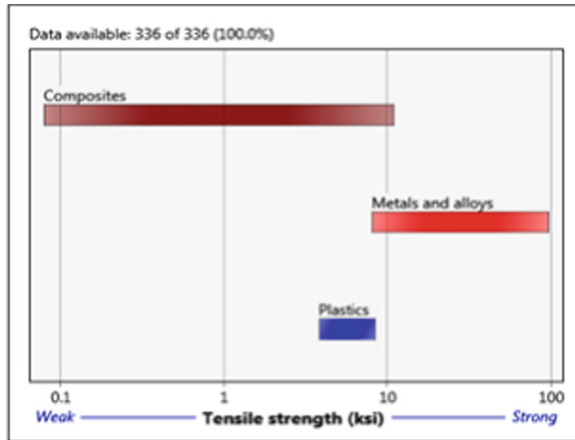
The selection of material of the body frame are selected based on the following requirements:

- i. Requirement 1: Water resistant
- ii. Requirement 2: Lightweight but durable
- iii. Requirement 3: Low chemical reaction with pure water and salt water

The above criteria are pre-requisite to ensure that the fully assembled system are able to perform its task accordingly without problem arise. Few suggestions to be decided in term of choices of material for the body frame like for this case is Polyvinylchloride (PVC), Wood and Aluminum. These three materials are considered to be selected for the body frame since it has been widely known to be used in boat construction. Analysis of material characteristics is performed using CES Edu Pack software. A group of materials are compared each other and one of the important parameter is the modulus of elasticity and tensile strength. The comparison results are shown in Figs. 1 and 2 respectively.

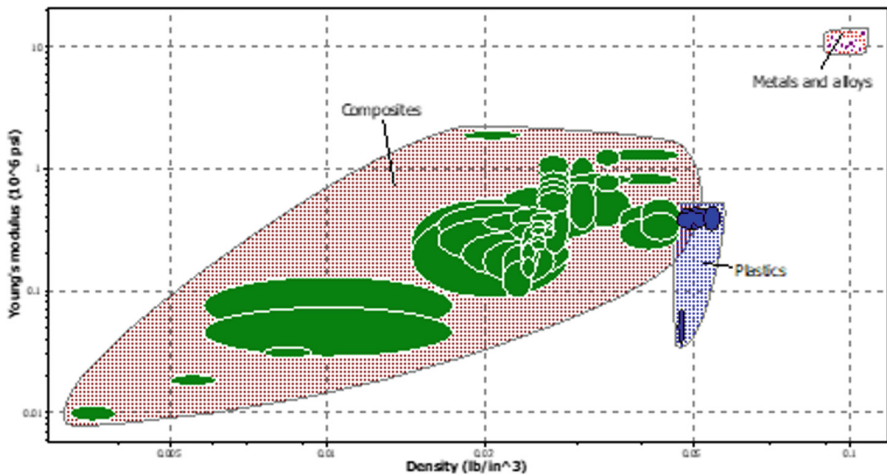


**Fig. 1.** Young’s modulus for composites (wood), metals and alloys (aluminium), and plastics (PVC)



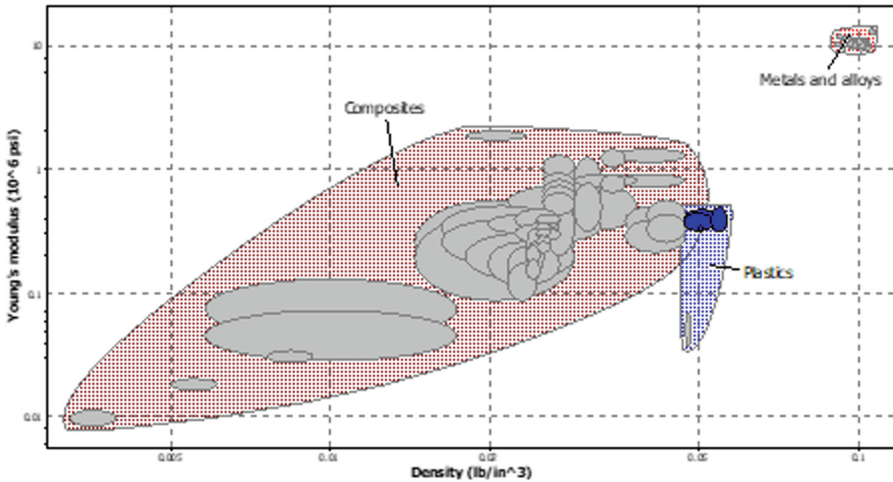
**Fig. 2.** Tensile strength for composites (wood), metals and alloys (aluminium), plastics (PVC)

Three different materials are inserted into a graph of Young's modulus versus density as shown in Fig. 3. The result from Fig. 3 indicates that aluminum has the highest Young's modulus and density while PVC is second while composites (wood) has a fairly large range value of Young's modulus and density.



**Fig. 3.** Young modulus versus density for composites (wood), metals & alloys (aluminium) and plastics (PVC)

On the other hand, the key selection parameter (boundary limit) for the body frame are with respect to durability; flammability, water (fresh and salt), organic solvents and UV radiation (sunlight). Using CES EduPack software, the result is shown in Fig. 4:



**Fig. 4.** The materials passes the limit (blue color)

The result from Fig. 4 portrays that plastics (indicates in blue color) passes the boundary set limit for the said purpose.

## 2.2 Process 2: Design of the Oil Spills Skimmer System

The selection of material for the oil spill skimmer system are selected based on the following requirement:

### i. Requirement: Material properties (Affinity with oil)

Study has been conducted to review the materials that are used as oil spills collector for skimmer type system. Few materials have been used as the collector with its intended purpose. As for this project, the important criteria are the property of the material. It is referring to material ability to attract oil. Scientifically, it is called property of material affinity (known as oleophilic material) that is essential during oil collecting process.

Furthermore, the consideration in term of capacity of water in the storage tank is crucial as it contributes to the effectiveness of the cleanup.

According to [3], the adhesion (oleophilic) skimmer is one of the most common types of mechanical recovery equipment. Oleophilic materials are substances that have affinity effectiveness attribute for oil absorption. The usage of oleophilic material in market is relatively new and its application for oil spill skimmer system is expected to increase steadily. Oleophilic materials are broadly divided into five types based on various material type:

- i. Polyethylene terephthalate (PET)
- ii. Polypropylene
- iii. Carbon-based sponges
- iv. Functional polymer sponges
- v. Kapok/milkweed seed hair.

In addition, in term of the type of structure for the skimmer to be applied in the system is roller type. The rotating roller will collect oil adhered to it before scrapped off to an oil storage tank. The amount of oil collected each time will be determined by the capacity of the tank.

### **2.3 Process 3 & 4: Construction of the Remote Controlled System and Selection of Suitable Vision System**

Selection of medium to control signal transmission for the remote controlled system is important in the development of portable oil skimmer system. In general, radio frequency remote control is a handheld, wireless device used to operate audio, video and other electronic equipment using radio frequency (RF) transmission. Unlike the common infrared (IR) remotes, RF remotes offer a flexibility in handling the device. For this project, remote control with medium frequency of (2.4 GHz) is preferred. It is because it is widely available for selection in the market as well as it is suitable to be used since its frequency bands is allowed legally in Malaysia without interrupting other specified service or systems.

On the other hand, selection of suitable vision system is crucial as well. According to [18], camera play a major role in vision system, thus, it is highly critical to select an appropriate specifications of camera to meet the objective. In general, the constraint for industrial usage as a whole is in term of space availability and environmental friendly. Designer for this equipment must take into account both two factors mentioned so that it meets the minimum standard. For this project, vision system is added for the purpose of visual aid to monitor the oil spillages around the portable oil skimmer system by capturing real-time videos where wireless camera will be utilized since it is easy to handle. Since it will be mounted on the skimmer system, waterproof camera with real-time video capture is the best option to perform the task.

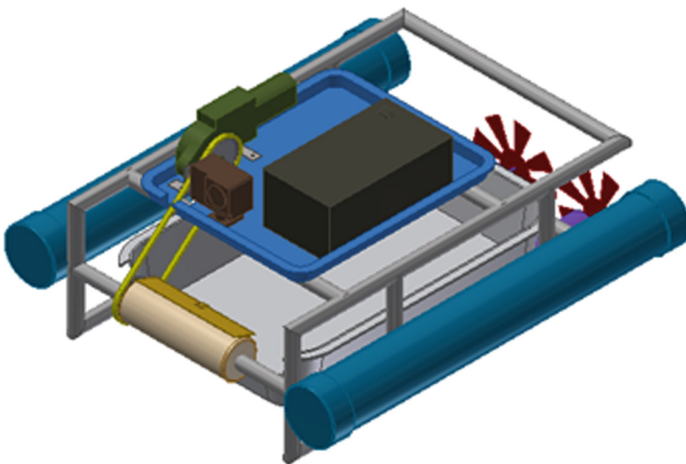
## **3 Development of Project**

The development process is divided into two parts. The first part is mechanical part of the project from chassis, hull and other mechanical parts. Second part is electronic part where process of wiring between main circuit, motor driver and wireless receiver circuit of remote control was done. During the process, there are criteria that need to be followed in order to fulfil the main objectives. Before the designing process of the Portable Oil Spill Skimmer can be proceed, the criteria of the project need to be studied and finalized. Design criteria regarding the objectives of the project, and other requirements such as the suitability of the design for the environment is tabulated in Table 1.

**Table 1.** Design criteria for portable oil spill skimmer [2]

Criteria	Requirements
Floatability	Low density
	Water resistant
	Lightweight (<10 kg)
Safety	No sharp edges
	Insulation from electrical shock
Oil absorption properties	Oleophilic
	Hydrophobic
Cost	Less or equal to RM2000
Ease of maintenance	Less obstruction
	Simple system architecture
Parts availability	Using common parts

The isometric and exploded view of the portable oil spill skimmer is shown in Figs. 5 and 6 respectively. The prototype design is inspired based on Catamaran boat concept where it is highly dependent on its hull at right and left side of the equipment to float. This design concept was chosen with the intention of preserving stability since the oil spillage tank is positioned at the center of the assembly. In addition, the chosen design is selected after undergo a stringent design selection using manufacturing design selection tool such as prioritization matrix and Analytical Hierarchy Process (AHP). Next, it uses DC motor as the driver to control the maneuvering of the system as well as controlling the oil collection system. The frame and hull of the system uses Polyvinyl chloride (PVC) while the roller for oil collection system uses Polypropylene (PP) material.



**Fig. 5.** Isometric view of design assembly

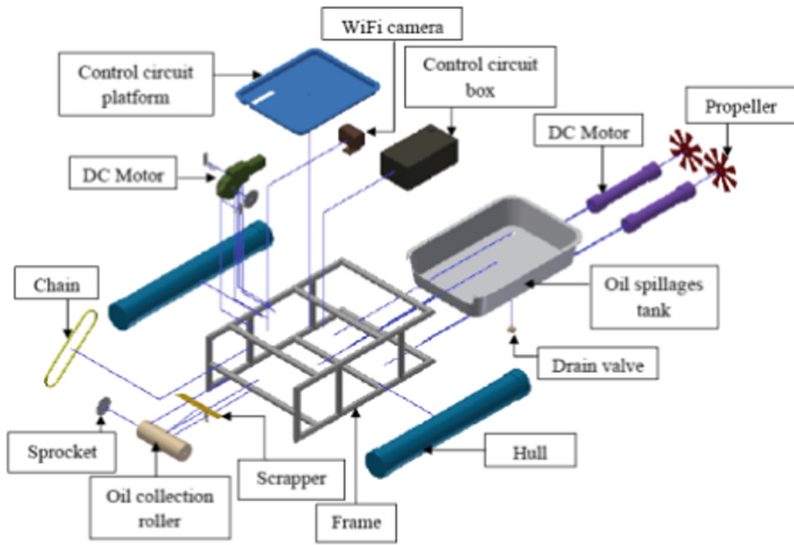


Fig. 6. Exploded view of design assembly

## 4 Results and Discussion

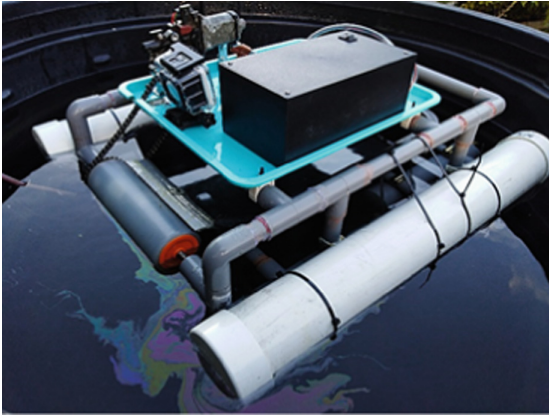
Basically, the obtained results are based on the output recorded from the actual field test conducted. There are four types of test conducted for the portable oil skimmer system namely:

- i. Buoyancy Force Test
- ii. Speed of Maneuvering Test
- iii. Remote control coverage Test
- iv. Wireless camera coverage Test

The result from the field test is then studied and analyzed accordingly to provide some solid indicator on the performance of the developed portable oil spill skimmer system.

### 4.1 Buoyancy Force Test

Buoyancy force or up thrust force, is the force exerted on an object that is wholly or partly immersed in a fluid (Fig. 7). Buoyancy is caused by differences in pressure acting on opposite sides of an object immersed in a static fluid thus results in a net upward force on the object. The magnitude of the force is proportional to the pressure difference. Archimedes' principle stated that buoyancy is equivalent to the weight of the fluid that would otherwise occupy the volume of the object [4].



**Fig. 7.** Buoyancy force test

The value of buoyancy force that is acted towards the system is calculated using Eq. (1) as follows:

$$\begin{aligned}
 \text{Buoyancy\_Force, } B &= \rho g V_{\text{displaced}} \\
 &= 1000 \text{ kg/m}^3 \times 9.81 \text{ m/s}^2 \times 0.0062 \text{ m}^3 \\
 &= 60.822 \text{ kg.m/s}^2
 \end{aligned} \tag{1}$$

where  $\rho$  = density of water with fix value of  $1000 \text{ kg/m}^3$ ,

$g$  = gravity ( $9.81 \text{ m/s}^2$ ) and

$V_{\text{displayed}}$  = volume of displaced fluid in unit  $\text{m}^3$ .

Archimedes discovered the hydrostatic principle which states that “a body completely or partially submerged in a fluid undergoes an upwards push equal to the weight of the displaced fluid.” The volume of the displaced water, when measured, will equal the volume of the object submerged in the water [11]. The result of this test shows that Portable Oil Spill Skimmer is partly immersed in the water, therefore it is suitable to perform the desired operations.

## 4.2 Speed of Maneuvering Test

Speed is the distance travelled per unit of time. It is how fast an object is moving. Speed is the scalar quantity that is the magnitude of the velocity vector. A higher speed means an object is moving faster. If it is not moving at all, it has zero speed. The optimization of speed for the Portable Oil Spill Skimmer is important in such way it will shorten the time to arrive at the location of the oil spillages. The higher the speed, the shorter the time taken for arrival. To determine the speed of the Portable Oil Spill Skimmer, test is done in a pool to check the speed of the Portable Oil Spill Skimmer.

The theoretical value of constant velocity of a moving object is calculated via Eq. (2) as follows:

$$\begin{aligned}
 \text{Speed, } V &= \text{distance, } d / \text{time, } t \\
 &= 3 \text{ m} / 6 \text{ s} \\
 &= 0.5 \text{ m s}^{-1}
 \end{aligned}
 \tag{2}$$

where;  $V$  = speed (m/s);  $d$  = distance traveled (m);  $t$  = time (s).

The speed of maneuvering test shows that the Portable Oil Spill Skimmer is capable for maneuvering to a desired location by remotely controlled. However, the maneuvering speed to one location is limited. Since the objective is to maneuvering the Portable Oil Spill Skimmer to variable location, it has achieved the objective. In other words, the capability of the system to reach the final location at the rate of 0.5 m in 1 s is sufficient and acceptable.

### 4.3 Remote Control Coverage Test

The purpose of testing the coverage of remote control is to check the signal acceptance by the wireless receiver, verified by response of the motor. Before the execution of this test, the distance of the remote control from the receiver were varied from one station to another. When signal is transmitted from the wireless remote control, test will be stopped when there is no signal accepted by the receiver.

**Table 2.** RF signal acceptance test

Station no.	Distance (m)	RF signal acceptance	Motor circuit response
1	5	Yes	Yes
2	10	Yes	Yes
3	15	Yes	Yes
4	20	Yes	Yes
5	25	Yes	Yes
6	30	Yes	Yes
7	35	Yes	Yes
8	40	Yes	Yes
9	45	Yes	Yes
10	50	No	No

Based on result from Table 2, it can be concluded that the range of RF signal acceptance is from 5 m up to 45 m before it lost its coverage at a distance of 50 m. So, the optimum range for controls the maneuvering of Portable Oil Spill Skimmer is not more than 50 m radius.



### 4.4 Wireless Camera Coverage Test

Wireless Camera coverage test was accomplished by measuring the signal intensity of Wireless Fidelity (WiFi) from zero distance until the farthest distance where the signal intensity are distorted. Two software used to perform the test; NetSpot software was used as the measurement tool for signal intensity measurement while SportLook software was used to capture the images to confirm the capture capability during test.

There are 5 station to test the signal and visual capabilities for the WiFi camera. At each location, signal intensity is measured in 5 min and the graph of signal is monitored and plotted using NetSpot software. The purpose of tabulating the graph is to determine the maximum visual capabilities for the Wifi Camera.

**Table 3.** WiFi camera signal coverage test

Station no.	Distance (m)	Measure duration (min)	WiFi signal intensity (average)	Visual capture capability
1	0	5	-25	Yes
2	20	5	-75	Yes
3	40	5	-80	Yes
4	60	5	-95	Yes
5	80	5	-100	No



**Fig. 8.** Wireless camera signal coverage test

Based on results from Table 3 and Fig. 8, it dictates that there is a degradation of signal intensity from one distance to another. The plotted graph is analyzed and described as follows:

Station 1: The signal intensity =  $-25$ , less deterioration during 5 min.

Station 2: The signal intensity experiencing degradation of 50 to average  $-75$ , deterioration occurs more than station 1.

Station 3: The signal intensity degrades to average 80, there was a signal disconnected recorded once.

Station 4: The signal intensity degrades to  $-95$ , there is 13 times signal disconnected recorded.

Station 5: Majority of the signal intensity is disconnected, only few times connected.

By referring to the observation made during the test, it is found that the image capture capability was lost at a distance of 80 m. To conclude on the analysis, the optimum distance for WiFi camera signal coverage is  $\leq 60$  m.

## 5 Conclusion

This paper presents the methodology on how to design and develop a semi-automated portable oil spill skimmer for water treatment application. Four analyses are added and discussed to provide some solid judgement on the performance of the fabricated portable oil spill skimmer system. The analyses are (i) Buoyancy force test (ii) Speed of maneuvering test (iii) Remote control coverage test and (iv) Wireless camera coverage test. Based on the recorded result, it can be concluded that the fabricated oil spill skimmer meet the minimum requirement to perform the task. The product could be extended or improved by adding some more unique features to further comprehend in term of its functionality.

**Acknowledgement.** The authors would like to acknowledge the financial support by Universiti Teknikal Malaysia Melaka (UTeM) under short term grant scheme (PJP) Universiti Teknikal Malaysia Melaka with reference number PJP/2018/FKP(7C)/S01588.

## References

1. Feng, L., Li, S., Li, Y., Li, H., Zhang, L., Zhai, J., Zhu, D.: Super-hydrophobic surfaces: from natural to artificial. *Adv. Mater.* **14**(24), 1857–1860 (2002). <https://doi.org/10.1002/adma.200290020>
2. Muizis, A.: Evaluation of the Methods for the Oil Spill Response in the Offshore Arctic Region. Bachelor's Thesis, Helsinki Metropolia University of Applied Sciences (2013)
3. Oasmaa, A., Källi, A., Lindfors, C., Elliott, D.C., Springer, D., Peacocke, C., Chiamonti, D.: Guidelines for transportation, handling, and use of fast pyrolysis bio-oil. 1. Flammability and toxicity. *Energy Fuels* **26**(6), 3864–3873 (2012). <https://doi.org/10.1021/ef300418d>
4. DOE: Guidelines for Packaging, Labelling, and Storage of Scheduled Waste in Malaysia (2014). <https://www.doe.gov.my/portalv1/en/info-untuk-industri/garis-panduan-buangan-terjadual/bahasa-english-guidelines-for-packaging-labelling-and-storage-of-scheduled-wastes-in-malaysia/314634>. Accessed 13 Apr 2019

5. DOSH: A Guide for Safe Warehousing of Packaged Hazardous Chemicals (2006). <http://www.dosh.gov.my/index.php/en/competent-person-form/occupational-health/guidelines/chemical/617-03-guidelines-on-storage-of-hazardous-chemicals-a-guide-for-safe-warehousing-of-packaged-hazardous-chemicals-2005?format=html&path=guidelines/chemical>. Accessed 13 Apr 2019
6. Fingas, M.: *The Basics of Oil Spill Cleanup*. CRC Press, Boca Raton (2012)
7. Fingas, M.F., Ka'aihue, L.: *Weather Windows for Oil Spill Countermeasures*. Prince William Sound Regional Citizens' Advisory Council, Valdez (2004)
8. Fingas, M.: *Oil Spill Science and Technology*. Gulf Professional Publishing, Houston (2011)
9. Broje, V., Keller, A.A.: Improved mechanical oil spill recovery using an optimized geometry for the skimmer surface. *Environ. Sci. Technol.* **40**(24), 7914–7918 (2006). <https://doi.org/10.1021/es061842m>
10. Broje, V., Keller, A.A.: Effect of operational parameters on the recovery rate of an oleophilic drum skimmer. *J. Hazard. Mater.* **148**(1–2), 136–143 (2007). <https://doi.org/10.1016/j.jhazmat.2007.02.017>
11. Prendergast, D.P., Gschwend, P.M.: Assessing the performance and cost of oil spill remediation technologies. *J. Clean. Prod.* **78**, 233–242 (2014). <https://doi.org/10.1016/j.jclepro.2014.04.054>
12. Ventikos, N.P., Vergetis, E., Psaraftis, H.N., Triantafyllou, G.: A high-level synthesis of oil spill response equipment and countermeasures. *J. Hazard. Mater.* **107**(1–2), 51–58 (2004). <https://doi.org/10.1016/j.jhazmat.2003.11.009>
13. Turan, O., Konovessis, D., Ventikos, N.P., Lemesle, P., Kakalis, N.M.P., Ventikos, Y.P.: Design and operation of small to medium scale oil-spill cleaning units. In: *Proceedings of the International Conference on Towing and Salvage of Disabled Tankers Safetow*, United Kingdom (2007)
14. Shi, N., Chen, R., Wang, K.: Study on domestic and foreign standards system for emergency response to oil spill on waters. In: *IOP Conference Series: Earth and Environmental Science*, vol. 237, no. 4, p. 042003. IOP Publishing (2019)
15. Wang, H., Xie, M., Goh, T.N.: A comparative study of the prioritization matrix method and the analytic hierarchy process technique in quality function deployment. *Total Qual. Manag.* **9**(6), 421–430 (1998). <https://doi.org/10.1080/0954412988361>
16. Reis, J.C.: *Environmental Control in Petroleum Engineering*. Elsevier, Amsterdam (1996)
17. Wang, G., Uyama, H.: Facile synthesis of flexible macroporous polypropylene sponges for separation of oil and water, 16 February 2016. <https://www.nature.com/articles/srep21265>
18. Prasad, P.B.: Machine vision systems and image processing with applications. *J. Innov. Comput. Sci. Eng.* **3**, 1–4 (2013)

# **Modelling and Simulation**



# Flow Analysis of Three Plate Family Injection Mould Using Moldflow Software Analysis

Noorfa Idayu, Mohd Amran Md Ali<sup>(✉)</sup>, Mohd Shahir Kasim,  
Mohd Sanusi Abdul Aziz, Raja Izamshah Raja Abdullah,  
and Mohd Amri Sulaiman

Fakulti Kejuruteraan Pembuatan, Universiti Teknikal Malaysia Melaka,  
Hang Tuah Jaya, 76450 Durian Tunggal, Melaka, Malaysia  
mohdamran@utem.edu.my

**Abstract.** Flow analysis of three plate family injection mould using pin point gate that consist of four cavities was studied. The responses investigated were volumetric shrinkage, in-cavity residual stress and deflection. The experiment was conducted using Taguchi method with L9 orthogonal array. The parameters involved in this study were mould temperature, melt temperature, injection time and cooling time. The plastic specimens were designed using CATIA V5 and the drawing was imported to Autodesk Moldflow Insight (AMI) simulation software environment. The feed system such as sprue, runner, pin-point gate and cooling system of three plate mould were designed inside the simulation software. Flow analysis was conducted under cool + fill + pack + warp analysis. From the flow analysis using Taguchi method, the lowest volumetric shrinkage obtained is 7.907%. For other responses, the lowest in-cavity residual stress and deflection found are 27.69 MPa and 0.9203 mm respectively. After optimization using optimized parameters, the value of volumetric shrinkage is reduced about 2.88% to 7.678%. In-cavity residual stress is reduced about 0.14% to 27.41 MPa, while deflection of plastic parts is reduced about 0.30% to 0.9176 mm. From ANOVA results, it is found that melt temperature is the most important factors affecting volumetric shrinkage, in-cavity residual stress and deflection of plastic parts.

**Keywords:** Flow analysis · Pin-point gate ·  
Three plate family injection mould · Optimization process

## 1 Introduction

Plastic injection moulding is a highly efficient means of producing variety of thermoplastic products and has many advantages. By using injection moulding process, complex and complicated shapes with excellent surfaces of plastic products can be produced in a short production cycles [1]. Injection moulding process is capable in producing products from plastic material where the molten polymer is injected at high pressure into a designed mould. Before any parts can be moulded a suitable injection mould must be well designed and manufactured [2]. During recent years, many programs for the computer simulation of injection moulding processes arose and the most used programs are Autodesk Moldflow and Cadmould. It was found that Autodesk

Moldflow Insight is widely used as numerical analysis tool for process optimization of the injection moulding process [3–6]. Hence, importance of CAE such as the development of computer simulation procedures that aims to mimicking the injection moulding process has the potential to replace the expensive experimental trial-and-error aspects that were associated with this process [7].

In order to determine the optimum process conditions, Öktem [8] has utilized design of experiment (DOE) called Taguchi method and managed to obtain optimum combination of process parameters. In general, Taguchi method employs a special design to learn the whole process parameters space with a small number of experiments only. Taguchi method uses specially constructed tables known as orthogonal array (OA) to design experiments. In Taguchi method, the results obtained from the experiment will be sent to the signal-to-noise (S/N) ratio. The S/N ratio is utilized to measure the quality characteristics as well as the significant process conditions through ANOVA analysis. This OA also makes the DOE very easy and it requires a lesser number of experiments that led to reduction of time, cost and effort [9].

In injection mould, the location of the injection gate is importance because it can influence the flow direction and melt solidification during and after filling. Kim selected pin-point gate in the numerical analysis and it was found that a proper gate location leads to a better flow in injection moulding process [10]. The design of feeding system especially gate system is crucial to eliminate the short shot, over filling and welding line defects in two-plate family mould [11]. So far to the authors' knowledge, mould that consists of more than one test sample such as tensile, impact, flexure and hardness test specimen was not exist. Usually, test sample was produced separately using a press machine that was more time consuming. So this research focuses on investigating the manufacturing of multi cavities of test samples inside one mould by using three plate mould through simulation method. Therefore, this study investigates the flow analysis of three plate mould that consist of tensile, impact, flexure and hardness test specimen using Moldflow software to optimize the injection moulding process parameters using Taguchi method.

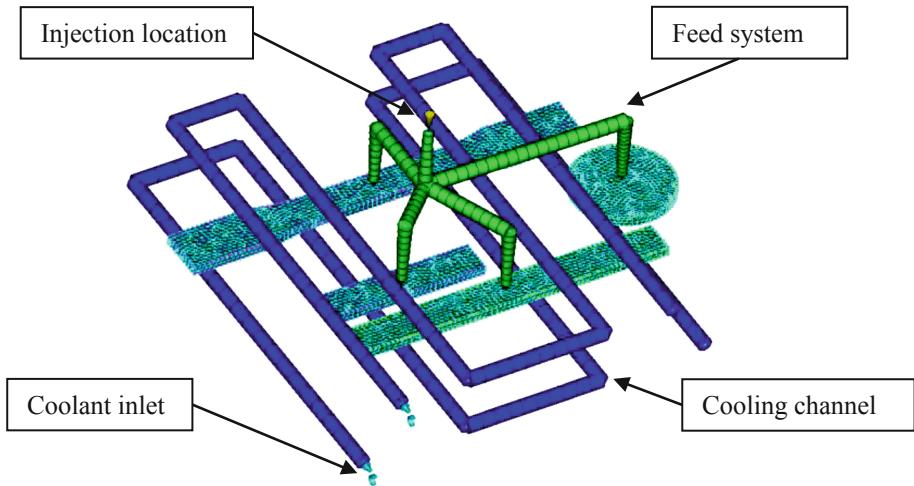
## 2 Experimental Method

### 2.1 Part Design

Autodesk Moldflow software is used to run a simulation towards plastic parts by using three plate mould design in injection moulding process. By using Moldflow software, recommended parameters value can be obtained. Before designing the sprue, runner and gate location for three plate mould design, the 3D drawing of four test specimens including tensile test specimen, impact test specimen, flexure test specimen and hardness test specimen was imported from CATIA 3D drawing to the Moldflow software environment.

Next, sprue, runner and gate location for three plate moulding attach with plastic parts was designed. The coolant system was also inserted into the drawing. Figure 1 shows a complete design of three plate moulding consist of feed system (pin-point gate,

runner and sprue), cooling system (cooling channels and inlets) and injection location inside the simulation environment. Material used in this simulation is polypropylene (3131 MU7) and its melt mass-flow rate (MFR) with 11 g/10 min.



**Fig. 1.** Design of three plate mould inside Autodesk Moldflow simulation software

## 2.2 Processing Parameters and Their Levels

By using Taguchi method, it can reduce the experimental trials and this method is used to determine the optimum level of process parameters [12]. The processing parameters value for injection moulding process of plastic parts by using three plate moulding design is obtained from simulation software. As a consequence, from simulation on the plastic part, the software has recommended few parameters such as mould temperature, melt temperature, injection time, and cooling time. Table 1 shows the processing parameters for injection process of plastic parts by using three plate moulding design where it has divided into three level of low, medium and high with four factors such as mould temperature, melt temperature, injection time, and cooling time.

**Table 1.** Process parameter of four factors with three levels setting

Process parameter	Level		
	Low	Medium	High
Mould temperature (°C)	15	25	35
Melt temperature (°C)	205	225	245
Injection time (s)	0.1	0.3	0.5
Cooling time (s)	10	18	26

Taguchi method with L9 orthogonal array was implemented and three level designs were used for experimental runs. Table 2 shows the Taguchi L9 orthogonal array experimental matrix that consists of total 9 runs that was generated through Minitab software.

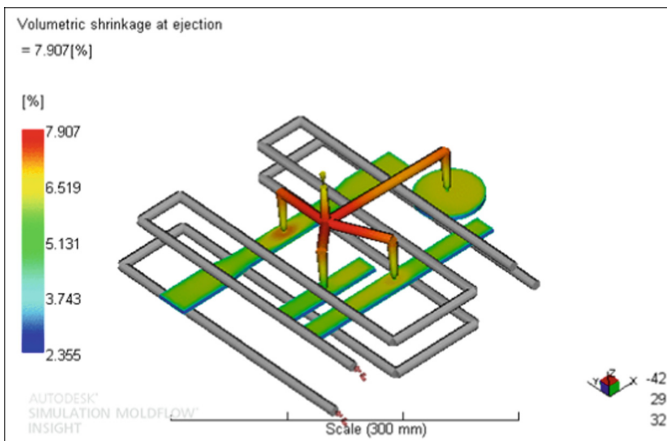
**Table 2.** Experimental matrix with Taguchi L9 orthogonal array

No.	Processing parameters			
	Mould temperature (°C)	Melt temperature (°C)	Injection time (s)	Cooling time (s)
1	15	205	0.1	10
2	15	225	0.3	18
3	15	245	0.5	26
4	25	205	0.3	26
5	25	225	0.5	10
6	25	245	0.1	18
7	35	205	0.5	18
8	35	225	0.1	26
9	35	245	0.3	10

### 3 Experimental Results

#### 3.1 Volumetric Shrinkage

Volumetric shrinkage is one of the common defects found in products from injection moulding process. In the Moldflow simulation, volumetric shrinkage found to be highest at injection point and lowest at local volume. Therefore, high shrinkage value can caused the reduction size of products. The results collected from Moldflow simulation were analysed and developed into signal-to-noise ratio in Minitab software. The lowest percentage values of volumetric shrinkage in simulation results symbolize the best injection part with less shrinkage phenomenon. Figure 2 shows the lowest volumetric shrinkage from run 1 from the analysis result of volumetric shrinkage.



**Fig. 2.** Simulation result of volumetric shrinkage from run 1 in Autodesk Moldflow software



In S/N ratio for volumetric shrinkage, the smaller the better characteristic arrangement is selected. Table 3 shows the corresponding S/N ratio for volumetric shrinkage generated from the Minitab software. The response table of S/N ratio for volumetric shrinkage for all parameters at different levels is shown in Table 4. From the table, volumetric shrinkage is significantly influenced by the melt temperature. Then it is followed by cooling time, injection time and mould temperature. The delta values for the parameters were 2.20, 0.55, 0.10 and 0.05 respectively.

**Table 3.** Signal to noise (S/N) ratio for volumetric shrinkage

No.	Volumetric shrinkage (%)	S/N ratio
1	7.907	-17.9602
2	9.690	-17.7265
3	10.570	-20.4815
4	8.203	-18.2795
5	9.009	-19.0935
6	10.800	-20.6685
7	8.280	-18.3606
8	9.551	-19.6010
9	10.05	-20.0433

**Table 4.** Response table of S/N ratio for volumetric shrinkage

Level	Mould temperature (°C)	Melt temperature (°C)	Injection time (s)	Cooling time (s)
1	-19.39	-18.20	-19.41	-19.03
2	-19.35	-19.47	-19.35	-19.59
3	-19.33	-20.40	-19.31	-19.45
Delta	0.05	2.20	0.10	0.55
Rank	4	1	3	2

Graph of S/N ratio for volumetric shrinkage is presented in Fig. 3. From the graph, the optimum parametric combination for volumetric shrinkage were at mould temperature 35 °C (Level 3), melt temperature 205 °C (Level 1), injection time 0.5 s (Level 3), and cooling time 10 s (Level 1).

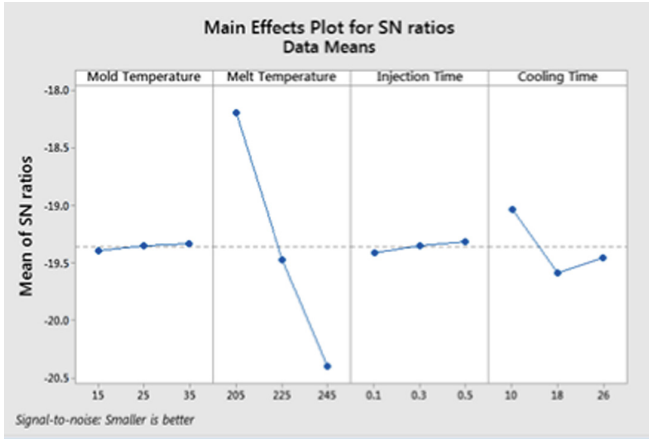


Fig. 3. Signal to noise (S/N) graph for volumetric shrinkage

By using ANOVA, the significance parameter level that affects the volumetric shrinkage can be determined. Table 5 represents the summary of ANOVA result. If the p-value is small than 0.05, then the parameter has a significant effect on the response. P-value for the melt temperature is 0.000 which is less than 0.05 and it indicates that melt temperature is a significant parameter for volumetric shrinkage of plastic parts.

Table 5. ANOVA result for volumetric shrinkage

Parameters	Mould temperature (°C)	Melt temperature (°C)	Injection time (s)	Cooling time (s)
R-Sq (%)	0.15	92.80	0.32	6.73
p-value	0.995	0.000	0.990	0.811
Rank	4	1	3	2

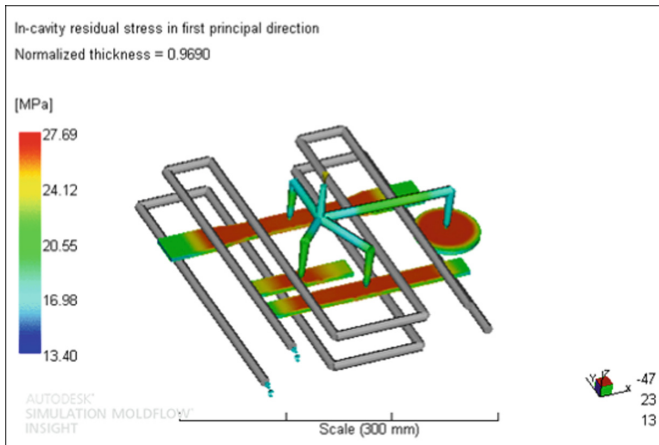
In Minitab software, Taguchi can predict the result of response for these optimal parameters setting. As recommended by S/N ratio analysis, the optimum parameters were set at mould temperature 35 °C (Level 3), melt temperature 205 °C (Level 1), injection time 0.5 s (Level 3), and cooling time 10 s (Level 1) and predicted optimum volumetric shrinkage percentage is 7.67867%. From all 9 runs, the best process parameters was run 1 where mould temperature 15 °C (Level 1), melt temperature 205 °C (Level 1), injection time at 0.1 s (Level 1) and cooling time at 10 s (Level 1) and the lowest percentage for volumetric shrinkage is 7.907%. Equation 1 shows the example of improvement calculation for volumetric shrinkage. From the calculation, the difference of percentage between values volumetric shrinkage before optimisation and after optimisation is 2.88%. Thus, it concluded that in order to accomplish the optimum percentage of volumetric shrinkage, the optimal process parameters can be achieved.

$$\text{Improvement (\%)} = \frac{|\text{before optimisation} - \text{after optimisation}|}{\text{before optimisation}} \times 100 \quad (1)$$

$$\text{Improvement (\%)} = \frac{|7.90700 - 7.67867|}{7.90700} \times 100 = 2.88\%$$

### 3.2 In-Cavity Residual Stress

In-cavity residual stress is an invisible unreleased stress in the material that occurred during filling the melt or packing process. Even though residual stress cannot be seen, but it may cause failure of parts during services and shorten their life time. In injection moulding process, it is better to produce a part that has a lower value of in-cavity residual stress. The lowest value for in-cavity residual stress has been recorded in Moldflow simulation is 27.69 MPa. Figure 4 shows the simulation result of in-cavity residual stress along with lowest response value which is from run 3.



**Fig. 4.** Simulation result of in-cavity residual stress from run 3 in Autodesk Moldflow software

In S/N ratio for in-cavity residual stress, the smaller the better characteristic arrangement is selected. Table 6 shows the corresponding S/N ratio for in-cavity residual stress generated from the Minitab software. The response table of S/N ratio for in-cavity residual stress for all parameters at different levels is shown in Table 7. From the table, in-cavity residual stress is significantly influenced by the melt temperature. Then it is followed by injection time, cooling time and mould temperature. The delta values for the parameters were 0.95, 0.24, 0.09 and 0.05 respectively.

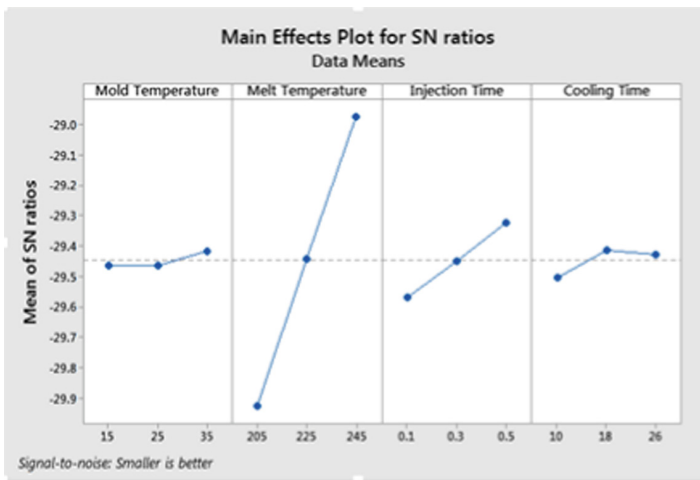
**Table 6.** Signal to noise (S/N) ratio for in-cavity residual stress

No.	In-cavity residual stress (MPa)	S/N ratio
1	32.06	-30.1193
2	29.60	-29.4258
3	27.69	-28.8465
4	31.34	-29.9220
5	29.48	-29.3905
6	28.42	-29.0725
7	30.67	-29.7343
8	29.88	-29.5076
9	28.19	-29.0019

**Table 7.** Response table of S/N ratio for in-cavity residual stress

Level	Mould temperature (°C)	Melt temperature (°C)	Injection time (s)	Cooling time (s)
1	-29.46	-29.93	-29.57	-29.50
2	-29.46	-29.44	-29.46	-29.41
3	-29.41	-28.97	-29.32	-29.43
Delta	0.05	0.95	0.24	0.09
Rank	4	1	2	3

Graph of S/N ratio for in-cavity residual stress is presented in Fig. 5. From the graph, the optimum parametric combination for in-cavity residual stress were at mould temperature 35 °C (Level 3), melt temperature 245 °C (Level 3), injection time 0.5 s (Level 3), and cooling time 18 s (Level 2).



**Fig. 5.** Signal to noise (S/N) graph for in-cavity residual stress

By using ANOVA, the significance parameter level that affects the in-cavity residual stress can be determined. Table 8 represents the summary of ANOVA result. If the p-value is small than 0.05, then the parameter has a significant effect on the response. P-value for the melt temperature is 0.000 which is less than 0.05 and it indicates that melt temperature is a significant parameter for in-cavity residual stress of plastic parts.

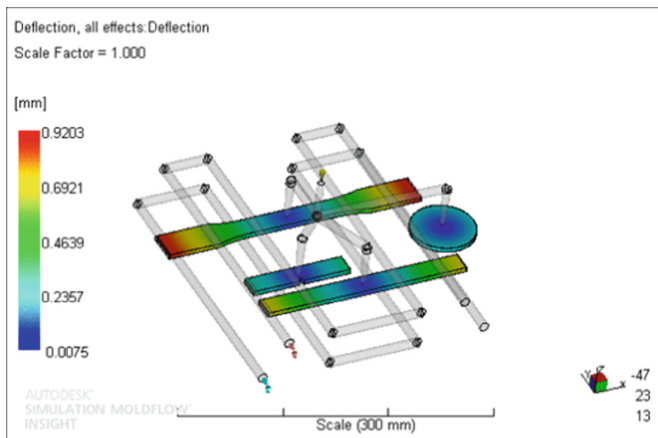
**Table 8.** ANOVA result for in-cavity residual stress

Parameters	Mould temperature (°C)	Melt temperature (°C)	Injection time (s)	Cooling time (s)
R-Sq (%)	0.41	92.29	6.14	1.16
p-value	0.988	0.000	0.827	0.966
Rank	4	1	2	3

As recommended by S/N ratio analysis, the optimum parameters for in-cavity residual stress mould temperature 35 °C (Level 3), melt temperature 245 °C (Level 3), injection time 0.5 s (Level 3), and cooling time 18 s (Level 2) and predicted in-cavity residual stress is 27.4133 MPa. From all 9 runs, the best process parameters was run 3 where mould temperature 15 °C (Level 1), melt temperature 245 °C (Level 3), injection time at 0.5 s (Level 3) and cooling time at 26 s (Level 3) and the lowest value for in-cavity residual stress is 27.69 MPa. It is found that by using the optimized parameters, in-cavity residual stress is improved by 0.14%.

### 3.3 Deflection

In injection moulding, higher values of deflection phenomenon can be as major cause of warpage on parts. Thus, it is essential to have the lower values of deflection to avoid other defects of part. From the analysis result, the lowest value for deflection is 0.9203 mm at run 6 as shown in Fig. 6.



**Fig. 6.** Simulation result of deflection from run 6 in Autodesk Moldflow software

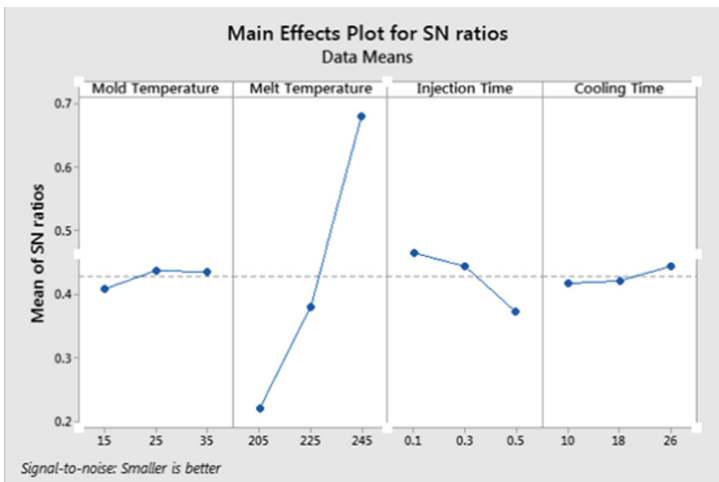
In S/N ratio for deflection, the smaller the better characteristic arrangement is selected. Table 9 shows the corresponding S/N ratio for deflection generated from the Minitab software. The response table of S/N ratio for deflection for all parameters at different levels is shown in Table 10. From the table, deflection is significantly influenced by the melt temperature. Then it is followed by injection time, mould temperature and cooling time. The delta values for the parameters were 0.4586, 0.0914, 0.0285, and 0.0251 respectively.

**Table 9.** Signal to noise (S/N) ratio for deflection

No.	Deflection (mm)	S/N ratio
1	0.9736	0.232389
2	0.9582	0.370877
3	0.9306	0.624739
4	0.9700	0.264565
5	0.9630	0.327474
6	0.9203	0.721412
7	0.9808	0.168391
8	0.9505	0.440958
9	0.9231	0.695025

**Table 10.** Response table of S/N ratio for deflection

Level	Mould temperature (°C)	Melt temperature (°C)	Injection time (s)	Cooling time (s)
1	0.4093	0.2218	0.4649	0.4183
2	0.4378	0.3798	0.4435	0.4202
3	0.4348	0.6804	0.6804	0.4434
Delta	0.0285	0.4586	0.4586	0.0251
Rank	3	1	2	4



**Fig. 7.** Signal to noise (S/N) graph for deflection

Graph of S/N ratio for deflection is presented in Fig. 7. From the graph, the optimum parametric combination for deflection were at mould temperature 25 °C (Level 2), melt temperature 245 °C (Level 3), injection time 0.1 s (Level 1), and cooling time 26 s (Level 3).

From ANOVA result, the significance parameter level that affects the deflection can be determined. Table 11 represents the summary of ANOVA result. If the p-value is small than 0.05, then the parameter has a significant effect on the response. P-value for the melt temperature is 0.000 which is less than 0.05 and it indicates that melt temperature is a significant parameter for deflection of plastic parts.

**Table 11.** ANOVA result for deflection

Parameters	Mould temperature (°C)	Melt temperature (°C)	Injection time (s)	Cooling time (s)
R-Sq (%)	0.40	95.18	4.03	0.39
p-value	0.988	0.000	0.884	0.988
Rank	4	1	2	3

As recommended by S/N ratio analysis, the optimum parameters for deflection mould temperature 25 °C (Level 2), melt temperature 245 °C (Level 3), injection time 0.1 s (Level 1) and cooling time 26 s (Level 3) and predicted deflection is 0.9176 mm. From all 9 runs, the best process parameters was run 6 where mould temperature 25 °C (Level 2), melt temperature 245 °C (Level 3), injection time at 0.1 s (Level 1) and cooling time at 18 s (Level 2) and the lowest value for deflection verified was 0.9203 mm. Therefore, it is found that before optimisation and after optimisation, deflection is improved about 0.3% by using the Taguchi method.

## 4 Conclusion

In this study, the flow analysis of three plate family injection mould design using pin-point gate was investigated. Taguchi method was employed to optimize the process parameters and ANOVA was used to determine the most significant parameter of each response. After optimization using the recommended optimum parameters, the value of volumetric shrinkage is reduced about 2.88% to 7.678%. In-cavity residual stress is reduced about 0.14% to 27.41 MPa, while deflection of plastic parts is reduced about 0.30% to 0.9176 mm. Furthermore, from the ANOVA result it is found that the most important parameters to minimize volumetric shrinkage, in-cavity residual stress and deflection of plastic part is melt temperature.

**Acknowledgments.** The authors would like to thank Faculty of Manufacturing Engineering, Universiti Teknikal Malaysia Melaka for providing facilities for this research to be conducted successfully. This research is funded by the Ministry of Higher Education through Fundamental Research Grant Scheme (FRGS) FRGS/2018/FKP-AMC/F00377.

## References

1. Jamsheed, M., Rahman, M.A., Moyeed, M.A., Ahmed, G.M.S.: Design and analysis of plastic injection mould for CAM BUSH with submarine gate. *Mater. Today Proc.* **2**(4–5), 2083–2093 (2015). <https://doi.org/10.1016/j.matpr.2015.07.203>
2. Malloy, R.A.: *Plastic Part Design for Injection Moulding: An Introduction*. Hanser Gardner Publications, Cincinnati (2011)
3. Amran, M.A.M., Idayu, N., Faizal, K.M., Sanusi, M., Izamshah, R., Shahir, M.: Part weight verification between simulation and experiment of plastic part in injection moulding process. *IOP Conf. Ser. Mater. Sci. Eng.* (2016). <https://doi.org/10.1088/1757-899X/160/1/012016>
4. Gheorghe, O.C., Florin, T.D., Vlad, G.T., Gabriel, D.T.: Optimization of micro injection molding of polymeric medical devices using software tools. *Procedia Eng.* **69**, 340–346 (2014). <https://doi.org/10.1016/j.proeng.2014.02.241>
5. Wen, T., Xia, C., Yang, C., Liu, L.: Optimization of processing parameters for minimizing warpage of large thin-walled parts in whole stages of injection molding. *Chin. J. Polym. Sci.* **32**(11), 1535–1543 (2014). <https://doi.org/10.1007/s10118-014-1541-7>
6. Amran, M., Salmah, S., Izamshah, R., Shahir, M., Amri, M., Mohamad, E., Sanusi, M., Sivarao, S., Marjom, Z., Umar, A., Musa, M.K., Abdullah, Z.: Warpage analysis of different number cooling channels for dumbbell plastic part in injection moulding. *Appl. Mech. Mater.* **761**, 8–11 (2015). <https://doi.org/10.4028/www.scientific.net/AMM.761.8>
7. Mukras, S.M.S., Al-Mufadi, F.A.: Simulation of HDPE mold filling in the injection molding process with comparison to experiments. *Arab. J. Sci. Eng.* (2015). <https://doi.org/10.1007/s13369-015-1970-9>
8. Öktem, H.: Optimum process conditions on shrinkage of an injected-molded part of DVD-ROM cover using Taguchi robust method. *Int. J. Adv. Manuf. Technol.* **61**(5–8), 519–528 (2012). <https://doi.org/10.1007/s00170-011-3750-3>
9. Kuram, E., Tasci, E., Ihsan, A., Metin, M., Yilmaz, F., Ozcelik, B.: Investigating the effects of recycling number and injection parameters on the mechanical properties of glass-fibre reinforced nylon 6 using Taguchi method. *Mater. Des.* **49**, 139–150 (2013). <https://doi.org/10.1016/j.matdes.2013.02.027>
10. Kim, H.S., Son, J.S., Im, Y.T.: Gate location design in injection molding of an automobile junction box with integral hinges. *J. Mater. Process. Technol.* **140**(1–3), 110–115 (2003). [https://doi.org/10.1016/s0924-0136\(03\)00700-3](https://doi.org/10.1016/s0924-0136(03)00700-3)
11. Amran, M.A., Hadzley, M., Amri, S., Izamshah, R., Hassan, A., Samsi, S., Shahir, K.: Optimization of gate, runner and sprue in two-plate family plastic injection mould. In: *AIP Conference Proceedings*, April 2015, pp. 309–313 (2010). <https://doi.org/10.1063/1.3377834>
12. Ali, M.A.M., Idayu, N., Izamshah, R., Kasim, M.S., Salleh, M.S., Sivarao, S.: Multiobjective optimization of injection moulding process parameters on mechanical properties using Taguchi method and grey relational analysis. *Int. J. Eng. Technol.* **7**, 14–16 (2018). <https://doi.org/10.14419/ijet.v7i3.7.16196>





# Optimization Process Parameters of Flat Plastic Part Having Side Gate System Using Flow Analysis Software

Mohd Amran Md Ali<sup>(✉)</sup>, Noorfa Idayu, Mohd Shukor Salleh, Mohd Najib Ali Mokhtar, Zulkeflee Abdullah, and Sivaraos

Fakulti Kejuruteraan Pembuatan, Universiti Teknikal Malaysia Melaka, Hang Tuah Jaya, 76450 Durian Tunggal, Melaka, Malaysia  
mohdamran@utem.edu.my

**Abstract.** Injection moulding process is one of the most important process in manufacturing plastic part. However, during injection process, many parameters are required to set-up at the injection machine monitor. Long time is needed to adjust the parameters in order to get high quality of product. Therefore, simulation software is essential to speed-up the setting process especially for producing new product. The objective of this research is to optimize the injection process parameters of melt temperature, mould temperature, injection time and cooling time. The responses of fill time and time to freeze are set the lowest the better meanwhile total part weight is set the higher the better. Taguchi method and analysis of variance (ANOVA) were performed to optimize all parameters. The plastic material used in this simulation analysis was polypropylene. The flat plastic part was designed using CATIA software and the design was transferred to the Moldflow simulation software. It found that, the lowest value for fill time and time to freeze is 0.2099 s and 12.21 s respectively. Meanwhile, the highest value of part weight is 4.5565 g. After optimization process, fill time shows no change. However, freeze time decreases for 0.4% to 12.16 s then total part weight increases for 0.12% to 4.620 g. ANOVA result shows that injection time was the most significant parameter for fill time meanwhile melt temperature was the most significant parameter for time to freeze and total part weight. Thus, these optimization parameters result can be used for future experimental work.

**Keywords:** Flow analysis · Side gate system · Optimization process · Injection mould · Taguchi method

## 1 Introduction

Injection moulding is the most important process in plastic industry. Product produced by injection moulding process are widely used in many applications. According to Tiusanen [1], injection moulding is cost effective process to produce a complex shape such as housing for electronic due to it can produce thousands of parts. To produce a good product, they are required several processes such as design the plastic part, mould fabrication and finally involve injection process in the injection moulding machine.

Diego [2] mentioned that injection moulding process are commonly used based on high volume productivity in producing the product.

In fabricated the injection mould, position of gate in injection moulding are very important in order to get a good product. This is important because between the runner and the cavity is a transition zone. According to Amran [3], the position of gate can affect the properties and appearance of finished part. In mould design stage, part design and process parameter are simulate using flow analysis software in order to reduce defects such as warpage [4], weld line [5] and short shots [6].

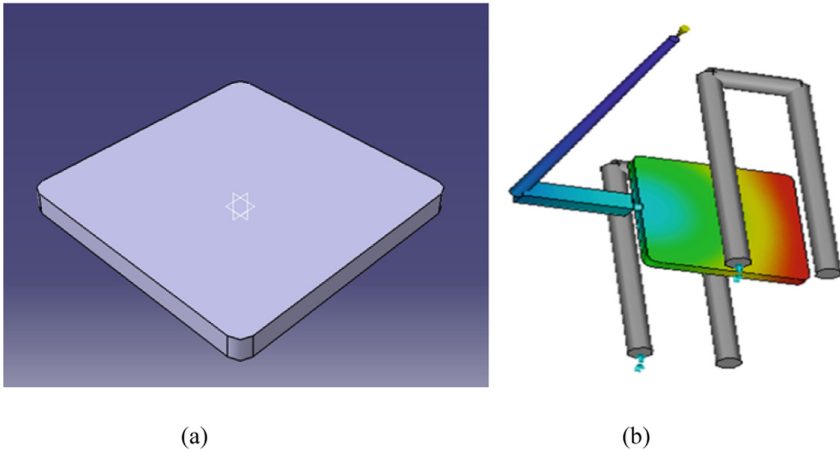
Moldflow software is the most effective analysis flow software that can used to reduce the defect in the injection moulding [7]. The injection moulding process can be optimized by using this software [8]. In order to get the good quality of plastic product, Taguchi method is a robust method to minimizing the defect of plastic. This method can be help by analysis of variance (ANOVA) which it can give the output to solve the problem [9].

This analysis used Moldflow simulation software in order to simulate the mould having side gate system. The injection process parameters that are investigated in this project are melt temperature, mold temperature, injection time and cooling time. These parameters can be optimized in order to reduce the output responses including to find the lowest fill time and time to freeze part meanwhile the highest output is set for total part weight. Taguchi method is used as the DOE to optimize the level input of parameter and ANOVA can give the most significant parameters that can affect the output responses.

## 2 Experimental Method

### 2.1 Plastic Part Design

The plastic part geometry in flat part shape was designed using CATIA software. The design of plastic part is very important in order to get the better result in the simulation. The part dimension of length, width and thickness are  $40 \times 40 \times 3$  (mm) respectively. Figure 1(a) shows the design flat plastic part. The design of the flat plastic part was transferred to the Autodesk Moldflow simulation to get the recommended process parameters for the part. This software can recommend the value of melt temperature, mould temperature, injection time and cooling time. This software also can determine the behavior of part design. Through this simulation, the problem of the product can be evaluated which is fill time, time to freeze part and total part weight. Figure 1(b) shows the simulation image of flat plastic part.



**Fig. 1.** (a) Design of flat plastic part and (b) simulation process of flat plastic part

Optimization process parameters are selected the highest value found from S/N ratio graph. Each higher parameters level is set in statistics software to find the improvement percentage. The improvement percentage is calculated from Eq. 1.

$$\% \text{ improvement} = \frac{\text{Lowest or highest analysis result} - \text{Optimize result}}{\text{Lowest or highest analysis result}} \times 100 \quad (1)$$

## 2.2 Analysis Parameters

There are four input parameters that are used during this analysis which are melt temperature, mould temperature, injection time and cooling time. The value of parameters as shown in Table 1 are recommended from the Moldflow simulation.

**Table 1.** Recommended process parameters

Parameters	Units	Value
Melt temperature	(°C)	215
Mould temperature	(°C)	25
Injection time	(s)	0.3
Cooling time	(s)	19

Table 2 shows the recommended level of parameters for using in this method. Taguchi method is used to design the analysis matrix. By using this method, the parameters are divided into three levels which are low, medium and high.

**Table 2.** Recommended process parameters

Parameters	Low level 1	Medium level	High level
Melt temperature (°C)	180	215	250
Mould temperature (°C)	15	25	35
Injection time (s)	0.2	0.3	0.4
Cooling time (s)	17	19	21

### 3 Analysis Result

Table 3 shows the result of flow simulation analysis of this study. Yellow colour in the table shows the lowest and highest of the analysis result. The target of analysis of fill time and time to freeze is the lowest the better meanwhile total part weight is the highest the better. Fill time is set the lowest the better because molten polymer can fill the cavity as soon as possible to reduce cycle time [10]. Further, time to freeze also is set the lowest the better to ensure that part can solidify as faster as well as the part can be ejected faster and reduce cycle time [11]. Meanwhile, total part weight is set the higher the better to ensure no void is generated in the injected part [12].

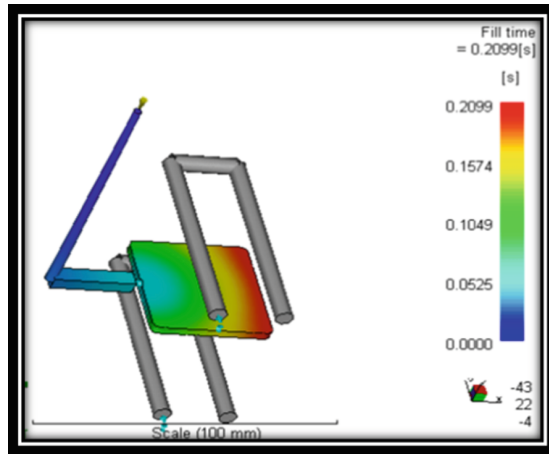
**Table 3.** Analysis result of the all responses

Run	Input parameters				Responses		
	Melt temp (°C)	Mold temp (°C)	Injection time (s)	Cooling time (s)	Fill time (s)	Time to freeze part (s)	Total part weight (g)
1	180	15	0.2	17	0.2130	12.31	4.5543
2	180	25	0.3	19	0.3191	12.26	4.5559
3	180	35	0.4	21	0.4235	12.21	4.5565
4	215	15	0.3	21	0.3150	14.64	4.5202
5	215	25	0.4	17	0.4207	14.79	4.5172
6	215	35	0.2	19	0.2115	14.71	4.5238
7	250	15	0.4	19	0.4209	16.83	4.4751
8	250	25	0.2	21	0.2099	16.73	4.4862
9	250	35	0.3	17	0.3149	16.93	4.4778

#### 3.1 Analysis Result of Fill Time

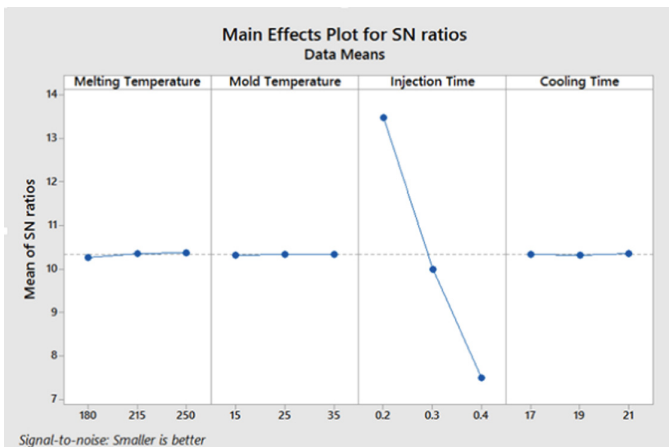
Fill time means that how fast or slow the plastic is injected into the mould. Fill time is very important because it can influence the amount of shear heating the plastic encounters. This situation can affect the material’s viscosity and temperature of the plastic. Hence, the fill time must have the lowest value to make the acceptable part. In this study, the smaller the batter characteristic were used during get the value of S/N ratio. Based on Table 3 above, the lowest value of fill time come from run 8 which is 0.2099 s. It is combination parameters which is melt temperature 250 °C, mould

temperature 25 °C, injection time 0.2 s and cooling time 21 s. Figure 2 shows the result of the flow simulation analysis for run number 8.



**Fig. 2.** Design Simulation result of fill time from run number 8

Figure 3 shows the graph of signal to noise ratio to represent the response of fill time. From the figure, it shows the optimum parameters combination which are melt temperature 250 °C (Level 3), mould temperature 25 °C (Level 2), injection time 0.2 s (Level 1) and cooling time 21 s (level 3). As shown in the figure, injection time dominated to the fill time compared to the others parameters.



**Fig. 3.** The graph of signal to noise ratio of fill time

The one-way (ANOVA) was used during this study to determine the significantly parameters that can affect the response of fill time. Table 4 shows the result of one-way ANOVA. This table shows the value of p-value which if the value is less than 0.05, it mean that the parameters are significant effect on the response. From the table, injection time is the most significant affected the response of fill time because the p-value of injection time is 0.00 which is lower than 0.05. Injection time has the highest value of R-square which is 99.97% compare to the others parameters. It means that the injection time can reduce the time of fill time during flow of molten polymer in mould cavity.

**Table 4.** ANOVA result of fill time

Input parameters	Melt temp. (°C)	Mold temp. (°C)	Injection time (s)	Cooling time (s)
R-Sq (%)	0.03	0.00	99.97	0.00
p-value	0.999	1.00	0.00	1.00
Rank	2	3	1	4

Improvement test is done after the optimize level parameters were identified. In this test, the lowest value of fill time required based on the optimum level of parameters. From the analysis result from Minitab software, it is found that the optimum parameters is 0.2099 s. This similar with the lowest value of fill time from the analysis result which is 0.2099 s. From the calculation from Eq. 1, the difference between the lowest value of analysis fill time with the optimize fill time is 0%. It means that the result is acceptable and the optimum parameters for the fill time of run number 8 is considered valid in order to achieve the lowest value of fill time.

**3.2 Analysis Result of Time to Freeze Part**

Time to freeze part mean that time taken to part frozen. Generally, the freeze time will vary depending on the molding parameters response to changing conditions on the real molding site. From the simulation, the result of freeze time can get directly. In order to get the best result for injection molding process, the value of responses which is freeze time must be lower. In Taguchi design, used the smaller is better to obtain the optimum process parameters. Table 3 above shows that the result of part freeze time for flow analysis is run 3 which has the lowest value which is 12.21 s with combination of melt temperature 180 °C, mould temperature 35 °C, injection time 0.4 s and cooling time 21 s. The simulation of part freeze time for run number 3 is shown in Fig. 4.

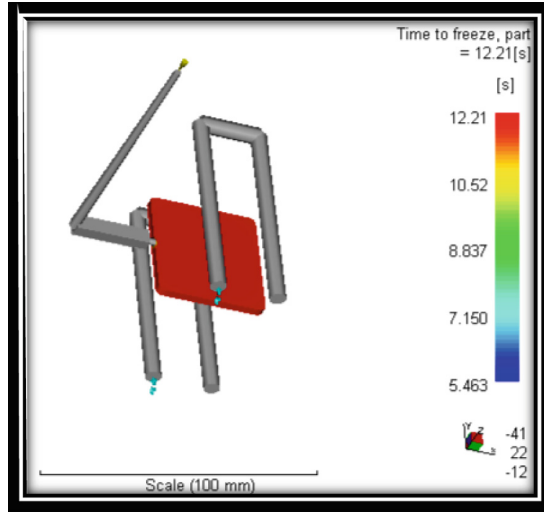


Fig. 4. Simulation result of time to freeze part for run number 3

Figure 5 shows the graph of signal to noise ratio to represent the response of time to freeze. From the figure, it shows the optimum parameters combination which is melt temperature 250 °C (Level 3), mould temperature 25 °C (Level 2), injection time 0.2 s (Level 1) and cooling time 21 s (level 3). As shown in the figure, melt temperature affected to the time to freeze compared to the others parameters.

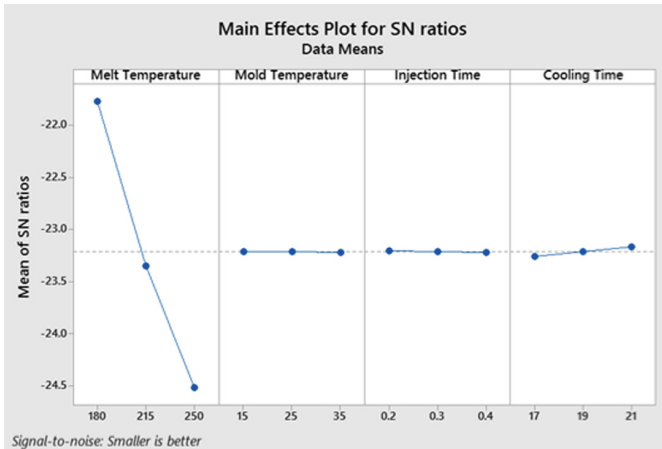


Fig. 5. The graph of signal to noise ratio for time to freeze

The result of ANOVA are shows in Table 5. In the table shows that the melt temperature has the lowest value of p-value which is 0.00 and this parameter is significant that affects the time to freeze part. Melt temperature also has the highest value

of R-square which is 99.88% compared the others parameters that mean melt temperature can reduce time to freeze part.

**Table 5.** ANOVA result of time to freeze part

Input parameters	Melt temp. (°C)	Mold temp. (°C)	Injection time (s)	Cooling time (s)
R-Sq (%)	99.88	0.00	0.00	0.11
p-value	0.00	1.00	1.00	0.997
Rank	1	4	3	2

When all influenced parameters were identified, improvement test were conducted. This test is to enhance the response time to freeze. This test is required the lowest value of time to freeze part based on the optimum parameter combination. The others requirement is optimized time to freeze part based on the optimal parameter that can get predicted value from S/N ratio. The value of time to freeze part based on the optimum combination is 12.21 s. It is included melt temperature 180 °C (Level 1), mould temperature 15 °C (Level 1), injection time 0.2 s (Level 1) and cooling time 21 s (Level 3). Result on the predicted value by using optimum parameter for time to freeze part is 12.16 s. Based on the calculation from Eq. 1, there is 0.4% improvement between the lowest value analysis result of time to freeze part and optimize time to freeze part. It means that the new set of parameters is found in order to achieve the lowest value of time to freeze part.

**3.3 Analysis Result of Total Part Weight**

The cavity weight result shows the weight of the plastic part, at the time the result was written. It can be animated, and changes with time. The result is written even when there is only one plastic part in the model analysis. The result from the simulation are converted into the signal to noise ratio by using the Minitab software. The value of total part weight must be higher to get the good result for injection molding process. The largest is better is selected during the Taguchi design. Figure 6 represents the graph of signal to noise ratio for the total part weight. This graph shows the combination of parameters which is melt temperature 250 °C (Level 3), mould temperature 25 °C (Level 2), injection time 0.2 s (Level 1) and cooling time 21 s (Level 3).

Table 6 shows the result ANOVA for each parameters. From the table, melt temperature has the lowest p-values compare to another parameter. The p-values for melt temperature is 0.000. That is mean melt temperature is significant parameter that effect the total part weight because the p-values is less than 0.005. Melt temperature also has the highest value of R-square which is 98.95% compared the others parameters that mean melt temperature can increase total part weight.



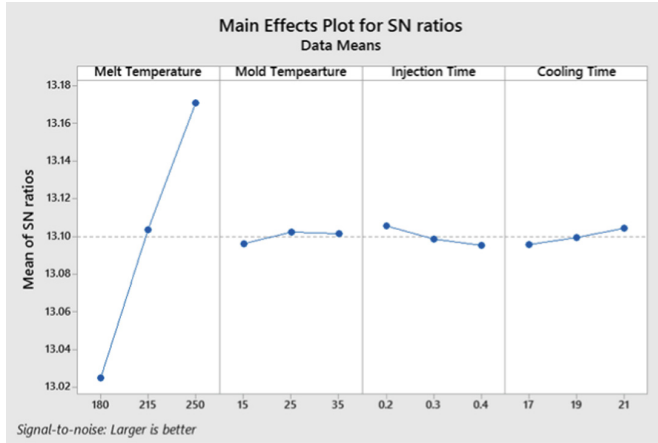


Fig. 6. The graph of signal to noise ratio for total part weight

Table 6. ANOVA result of total part weight

Input parameters	Melt temp. (°C)	Mold temp. (°C)	Injection time (s)	Cooling time (s)
R-Sq (%)	98.95	0.21	0.48	0.36
p-value	0.000	0.994	0.986	0.989
Rank	1	4	2	3

Improvement test is conducted when the optimization parameters are identified and can enhance the response of total part weight. The highest value of total part weight is required based on the optimum parameter combination. The next requirement was optimized the total part weight based on the optimal parameter setting that get from predicted value of response from S/N ratio. By using predict Taguchi result, this software can get the S/N ratio for selected new factor setting.

The highest value of total part weight from analysis work is 4.5565 g. This value come based on the optimum parameters combination collected from Fig. 6 above which are melt temperature 250 °C (Level 3), mould temperature 25 °C (Level 2), injection time 0.2 s (Level 1) and cooling time 21 s (Level 3). The value increases to 4.562 g after predicted using analytical software. From the calculation from Eq. 1, there was improvement 0.12% from the different between the highest values of total part weight in analysis result as compared to optimize value of total part weight found from statistical software. Its mean the new set of parameters was generated in order to achieve the highest value of total part weight.

## 4 Conclusion

Injection moulding parameters such as melt temperature, mould temperature, injection time and cooling time are optimized using flow analysis software. Three output responses are investigated that are fill time, time to freeze part and total part weight. The optimized parameters for fill time found are melt temperature 250 °C, mould temperature 25 °C, injection time 0.2 s and cooling time 21 s which the lowest fill time is 0.2099 s similar to analysis run. Meanwhile, time to freeze part shows optimization parameters are melt temperature 180 °C, mould temperature 15 °C, injection time 0.2 s and cooling time 21 s which the lowest time to freeze is 12.16 s reduces to 0.4%. Finally, total part weight shows optimization parameters are melt temperature 250 °C, mould temperature 25 °C, injection time 0.2 s and cooling time 21 s increases to 0.12%.

**Acknowledgments.** This research is under the grant FRGS/2018/FKP-AMC/F00377. The authors would like to thank Universiti Teknikal Malaysia Melaka (UTeM) for providing facilities for the research work done.

## References

1. Tiusanen, J., Vlasveld, D., Vuorinen, J.: Review on the effects of injection moulding parameters on the electrical resistivity of carbon nanotube filled polymer parts. *Compos. Sci. Technol.* **72**, 1741–1752 (2012). <https://doi.org/10.1016/j.compscitech.2012.07.009>
2. Diego, A.M., André, L.N.: Simulation of an injection process using a cae tool: assessment of operational conditions and mold design on the process efficiency. *Mater. Res.* **22**, 1–16 (2019). <https://doi.org/10.1590/1980-5373-mr-2018-0564>
3. Amran, M.A., Hadzley, M., Izamshah, R., Hassan, A., Samsi, S., Shahir, K.: Optimization of gate, runner and sprue in two-plate family plastic injection mould. *AIP Conf. Proc.* **1217**, 309–313 (2010). <https://doi.org/10.1063/1.3377834>
4. Amran, M., Salmah, S., Izamshah, R., Shahir, M., Amri, M., Mohamad, E., Sanusi, M., Sivaraos, Marjom Z., Al-Amani, U., Musa, M.K., Abdullah, Z.: Warpage analysis of different number cooling channels for dumbbell plastic part in injection moulding. *Appl. Mech. Mater.* **761**, 8–11 (2015). <https://doi.org/10.4028/www.scientific.net/AMM.761.8>
5. Baradi, M.B., Cruz, C., Régnier, G.: Mechanical characterization of frontal and flowing weld lines in injection-molded short fiber-reinforced thermoplastics. *AIP Conf. Proc.* **2055**, 1–5 (2019). <https://doi.org/10.1063/1.5084853>
6. Moayyedian, M., Abhary, K., Marian, R.: The analysis of short shot possibility in injection molding process. *Int. J. Adv. Manuf. Technol.* **91**, 3977–3989 (2017). <https://doi.org/10.1007/s00170-017-0055-1>
7. Moldflow Plastic Injection Moulding Design—Autodesk Moldflow Insight and Adviser. <https://www.autodesk.co.uk/products/moldflow/overview>. Accessed 18 Apr 2019
8. Amran, M.A.M., Idayu, N., Faizal, K.M., Sanusi, M., Izamshah, R., Shahir, M.: Part weight verification between simulation and experiment of plastic part in injection moulding process. *IOP Conf Ser: Mater. Sci. Eng.* (2016). <https://doi.org/10.1088/1757-899X/160/1/012016>

9. Ali, M.A.M., Idayu, N., Izamshah, R., Kasim, M.S., Salleh, M.S., Sivarao, : Multiobjective optimization of injection moulding process parameters on mechanical properties using Taguchi method and grey relational analysis. *Int. J. Eng. Technol.* **7**, 14–16 (2018). <https://doi.org/10.14419/ijet.v7i3.7.16196>
10. Nik, M.M., Shahrul, K., Abdul, R.O.: Modeling and analysis of injection moulding process parameters for plastic gear industry application. *ISRN Ind. Eng.* **2013**, 1–10 (2013). <https://doi.org/10.1155/2013/869736>
11. Pantani, R., De Santis, F., Brucato, V., Titomanlio, G.: Analysis of gate freeze-off time in injection molding. *Polym. Eng. Sci.* **44**, 1–17 (2004). <https://doi.org/10.1002/pen.20000>
12. López, A., Aisab, J., Martínez, A., Mercado, D.: Injection moulding parameters influence on weight quality of complex parts by means of DOE application: case study. *Measurement* **90**, 349–356 (2016). <https://doi.org/10.1016/j.measurement.2016.04.072>



# Conceptual Framework for Lean Manufacturing Implementation in SMEs with PDCA Approach

Jia Yuik Chong<sup>(✉)</sup> and Puvanasvaran A. Perumal

Faculty of Manufacturing Engineering,  
Universiti Teknikal Malaysia Melaka (UTEM), Hang Tuah Jaya,  
76100 Durian Tunggal, Melaka, Malaysia  
jackychongjy1988@live.com

**Abstract.** Implementation of lean manufacturing tools and practices in any type of organizations can bring many benefits, such as reducing waste and creating the value-added products to customers. There are a lot of frameworks have been developed in different industry worldwide, but still many companies find it is difficult to adopt the lean implementation especially for small and medium enterprises, SMEs. One of the critical challengers is due to lack of understanding of the real lean concept and inadequate of effective framework in SMEs. Thus, there is a strong need to develop a suitable framework specifically construct to suit SME's feature characteristic in order to SMEs can maximize the gain of lean benefits. Various main existing lean implementation frameworks and the common challenges faced during their lean journey are discussed. This present paper aims at developing an effective conceptual lean manufacturing framework that serves as a guideline to implement lean manufacturing in the industry and in attempt to overcome some of the limitations gap in main existing framework. It starts with the review of the main existing framework and highlighting the key elements adopt in SMEs. The proposed conceptual framework is constructed with detailed of four implementation phases in sequential process and included the 16 key components of step by step guidance flow. The PDCA cycles (Plan-Do-Check-Act) approach has been integrated into these difference four phases of lean manufacturing implementation with the adoption of feasibility lean practices to suit for SME's environment. This is to provide a simple and comprehensive framework for ease the SMEs lean practitioner to follow it accordingly in order to improve the organization's performance. However, the proposed framework is at conceptual stage, which it requires further study of practically implementation to be validated by future researches.

**Keywords:** Lean manufacturing · Conceptual framework · Small and medium enterprises · PDCA approach · Implementation

## 1 Introduction

Small and medium enterprise is the important sector and act as backbone in contributing national economy all over the world. There are a lot of global competitive challenges faced by every company especially for the small medium enterprises, SMEs. Many SMEs have been adopted many difference types of approaches in improving the production productivity efficiency performance goal and enhance the quality of the products. Lean manufacturing is one of the management systems which had been widely use and able to adopt into the SME's company practices in order to gain the lean benefits. Although there are a lot of existing lean manufacturing framework been established previously by the researches, but some company still find it's tough and face challenges to start implement the lean manufacturing till successfully [1]. This is due to small business have their own weakness which are always constraint by their structure, their lack of technical expertise, lack of financial support and other barriers [2, 3]. Therefore, the new lean manufacturing framework with the critical elements need to have integrated into the SME's feature characteristic in order to assist in guiding SME company for implementing the lean manufacturing successfully in long term.

In attempt to assist lean manufacturing implementation in SMEs, this paper proposes a conceptual framework which believe to be useful and suitable for lean practitioner. The research method for the study is divided into two phases. The first phase is focusing on structured literature review, which is to identify the common challenges faced by SMEs in lean manufacturing implementation, and critical review of the main existing framework. The second phase is focusing on development of propose conceptual framework in difference lean manufacturing implementation process stages.

## 2 Review of Existing Lean Manufacturing Frameworks

A framework is a set of simplified guidance for an organization to follow systematically, which is easy to understand and could assist the organization to follow efficiently in an implementable way [2, 3]. Most of the organization especially SMEs faced difficulties on lean manufacturing implementation and misapplication or misinterpretation of lean practices due to [3, 4];

- use the wrong tool to solve a problem
- use one tool to solve problem, use the same set of tools to solve problems
- lack of understanding about real concept and purpose of lean manufacturing by managers and employees

The misunderstanding is the main barrier of lean manufacturing implementation [5–7]. Therefore, development of the conceptual lean manufacturing framework is important to integrate the required suitable lean practices in different phases of implementation process steps to allow the practitioners understand clearly the requirements for implementing lean manufacturing effectively. The proposed a set of

characteristics criteria which must be fulfilled when developing the suitable framework for it to be considered applicable for SMEs [2]. These characteristics are:

- Systematic and easily understood;
- Simple in structure;
- Having clear links between the elements or steps outlined;
- General enough to suit different contexts;
- Represent a road map and a planning tool for implementation;
- Answers “how to?” and not “what is?” the initiative approach; and
- Implementable in SMEs.

Rose et al. [3] presented a conceptual framework with reviewed the SME characteristic of strength and weaknesses, but it does not highlight clearly the correlation linkage or steps of each other elements as a guideline. Mostafa et al. [7] discussed the 28 lean initiate implementation frameworks with listed down 9 critical success lean factors. This project-based framework structured to fit the lean implementation been proposed in 22 elements in four phases, which is not simple in the structure constructed and does not designed specially to suit SMEs characteristic needs. As SMEs top management are always want to see the fast result of lean benefits within the short period of lean implementation, so that the fast decision can be making for the next action taken [2, 3].

Amine et al. [8] proposed a framework which derived from the practical experiences of four SMEs in difference operating areas. This study of successful lean initiatives within SMEs presented plenty of elements (implementation process steps, tools and success factors) in 3 phases which are compliant with the characteristic criteria [2] and found suitable to apply in different types of SMEs. However, the identified elements need to be generalized and explore more others critical elements for enrichment or further improvement as per recommended by the authors. AlManei et al. [9] had presented the simple in structure framework with having clear links between the elements, but it did not provided details of the lean tools to be introduced and does not represent the lean methods roadmap. The model of Wong and Wong [10] is quite complicated to implement, which not general enough to suit others industry and not designed specifically for implement in SMEs. Okhovat et al. [9] presented the integrated framework by using PDCA driven cycle called, DMAIC which is very complicated in structure, and the framework is not specially designed focus on lean manufacturing implementation in SMEs. AlManie et al. [12] reviewed various lean implementation frameworks in various countries around the globe and the challenges for SMEs in lean implementation, but the key conclusion drawn is that is no unique roadmap to “leanness”; this needs to be tailored for every different organization.

Based on literature review carried out, noticed that there is still lack of suitable framework which considered universal or perfectly suit for applicability in SMEs according to their feature characteristic. Therefore, the propose of new effective conceptual framework is designed to serve as a guideline for lean manufacturing implementation in SMEs in attempted to fill-up this gap. The review of main existing framework is shown in the Table 1.

**Table 1.** Review of the main existing frameworks of lean implementation

Author	Key findings/description
Rose et al. [3]	The proposed conceptual framework comprised of SME's commitment, 15 feasible lean practices (based on basic, intermediate and advanced categories), external support and performance
Mostafa et al. [7]	28 lean implementation initiatives frameworks with respect to 9 critical success lean factors been reviewed. Proposed a 22 elements lean implementation framework constructed within four phases with integrated of monitoring and controlling
Amine et al. [8]	The proposed framework for lean implementation in SMEs presented the elements (implementation process steps, lean tools and success factors) in 3 phases, as integral framework derived from practical experiences of 4 SMEs and reviewed of the main existing framework in lean implementation
AlManei et al. [9]	A conceptual lean implementation framework based on change management theory with using eight steps of Kotter's model as basis and highlighting the lean tools roadmap use in sequence based on lean maturity
Wong and Wong [10]	This paper presents a framework consist of 3 parts that serves as a guideline to implement lean manufacturing which was developed through case studies conducted in four electrical and electronics companies in Malaysia
Okhovat et al. [9]	This paper presents a strategic framework which was developed through conceptual integration of three popular process improvement strategies, which are six-sigma, total productive maintenance and lean

### 3 Proposed Conceptual Lean Manufacturing Framework for SMEs

The proposed framework consists of 4 parts; the first part is the pre-implementation phase (Plan), where it serves as an overall project planning and problems identification stage for the lean manufacturing project to be carried out. The second part is the implementation phase (Do), which the lean practitioner will execute the lean tools and practices in a selected pilot project. The third part is the evaluation phase (Check), which acts as a checkpoint to analyze the result performance achieved in a specific allocated timeline with resources provided versus targeted goal, and the last fourth part is the post implementation phase (act) to standardize the successful lean result and lock it into the documentation for future continuous improvement reference in large scale run. There are 16 simple and easy to follow components been proposed, which including PDCA approaches are integrated built in into this difference of four phases in a structured manner. PDCA cycle is a systematic iterative four-stage approach for continually improving the process and help to solve the problems with implement the solutions in a methodical way.

Nawawi et al. [13] used the PDCA conceptual framework approach in linking the relationship between lean manufacturing and ergonomics in working assembly process. Therefore, PDCA approach is suitable to apply in lean manufacturing conceptual framework development as well. Apart from that, it is suggested that SMEs can choose the suitable lean practices which suit to their environment and within their control based on needs and lean maturity of the organization [3, 9]. Rose et al. [3] reviewed on past literature showed 15 practices which are feasible to be implemented in SME as shown in Fig. 1. These practices are divided into three categories; basic, intermediate and advanced, which can be apply into each of the difference phases in lean manufacturing framework to suit the needs. As example, it is recommended that the lean practitioner should start with the basic feasible lean practices first at the initial stage of lean manufacturing implementation, such as 5S, standardization and visual control before moving to the next intermediate level of feasible lean practices whichever applicable. Lastly, then only adopt high advance level of lean feasible practices when the project is achieving stable and maturity state. SMEs are not advised to start with advanced practices without considering implementing basic and intermediate practices. Figure 2 illustrates the proposed conceptual lean manufacturing implementation framework in SMEs with proper step by step guidance flow in sequence.

<b><u>Basic</u></b>	<b><u>Intermediate</u></b>	<b><u>Advanced</u></b>
Multifunction employees	Cell layout	Small lot sizes
5S	Preventive maintenance	Kanban
Visual control and display	Reduce set up time	Continuous flow
Standardization of operation	Continous improvement	Uniform workload
Quality control - SPC		
Quality circles		
Teamwork		

Fig. 1. Feasible lean practices for lean manufacturing implementation in SMEs [3]

### 3.1 Pre-implementation Phase (Plan)

This is the initial first phase of the lean manufacturing implementation, which the management leadership must provide the necessary support (which including financial, manpower and time resources) and commitment to the lean team in ensure the successful kick start of the lean implementation [2, 3, 8]. Grewal [14] presented the Value Steam Mapping as an initiative to implement lean manufacturing in small company by selection of the most important or critical product family, before the next step of current state map is drawn to identify the value-added and non-value added activities (waste).

Assessment of the current state and previously lesson learnt review [7] on lean implementation is important to prevent the occurrence of the similar mistake. Wong and Wong [10] stated that the current state need to be defined first, before moving to the future ideal state via three constructs, which are people, think lean and act lean.



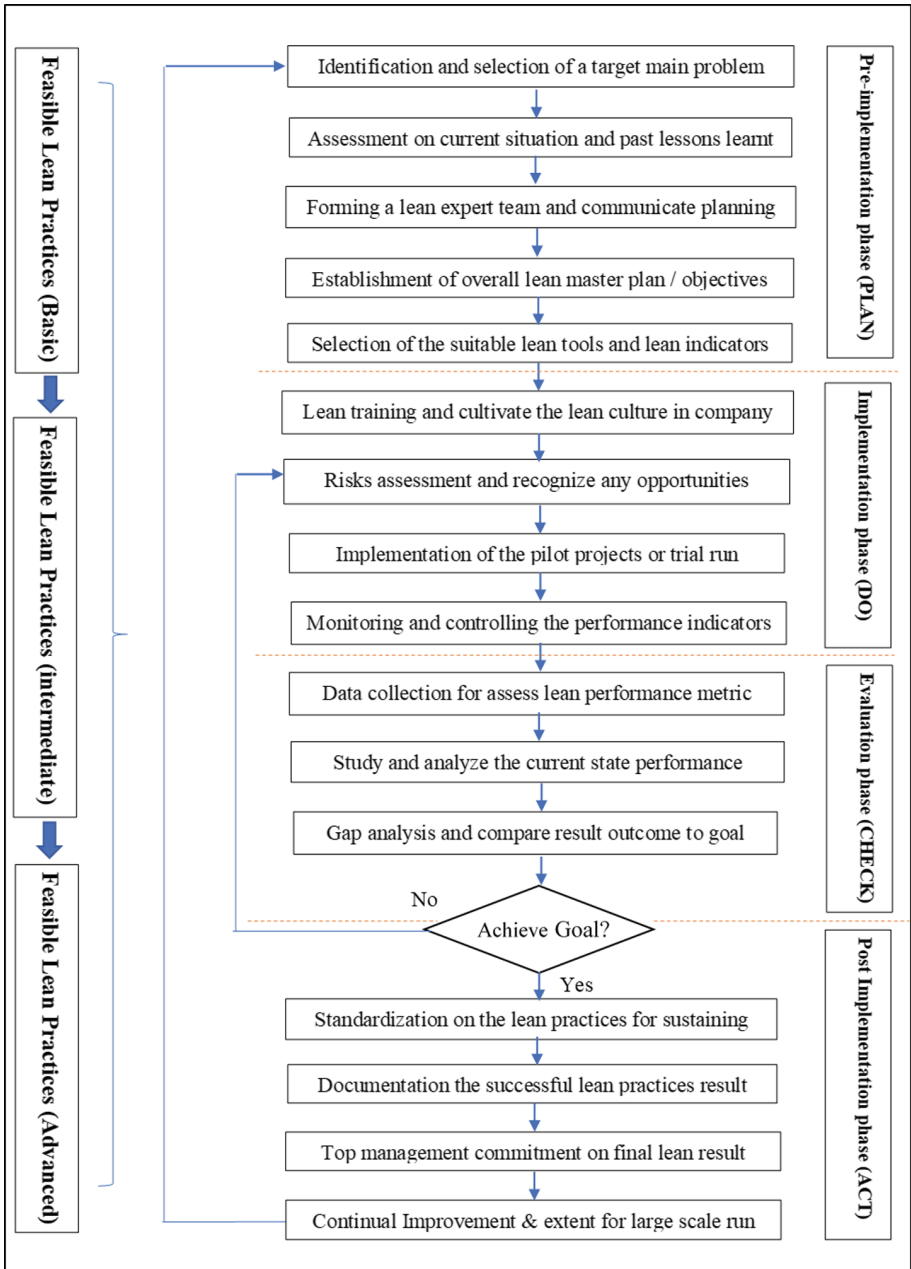


Fig. 2. The proposed framework for lean manufacturing implementation in SMEs

Mostafa et al. [7] highlighted that forming a lean expert team as one of the critical success factors on which the strong lean knowledge or experience will expedite the lean journey in the company via proper training and consultancy to the other employees. Worley and Doolen [15] stated that communication planning among the lean team and explaining to the employees is the key issue for successful implementation of a lean manufacturing.

Establishment of the overall lean master plan is enabling the team are in align with the common information sharing and understanding clearly each of their responsibility roles towards successful lean implementation goals within an identified the proper timeline due date. Selection of the suitable lean tools and performance indicators based on the lean objectives and target main problems to work on, so that lean team can be more focus in monitoring and controlling the progress in the project implementation stage.

### **3.2 Implementation Phase (Do)**

The implementation phase is the execution phase is by carry out the required lean tools concept and practices training programs to the employees in order to create the lean thinking culture awareness among them. This is human factor element is aimed to establish the more in-depth understanding of lean skills needed in lean manufacturing implementation to all the employees and their roles responsibilities towards the successful lean implementation [5, 7].

Hiring of the lean experts or consultant is the key success factor in lean implementation process [7, 11]. Risk assessment is performed to recognize any opportunity of improvement and to eliminate the possible lean barriers in lean manufacturing implementation. Implementation of the identified pilot work project or trial run is carried out with closely monitor and tracking the on-going performance in the mean-time interval.

### **3.3 Evaluation Phase (Check)**

In the evaluation phase, it serves as check point to assess the lean performance metric achieved. This is to analyze whether the lean manufacturing implemented is effective and bring the significant result for the company. Lean team will make the decision to continue proceed to the next phase or to discontinue this lean project, based on the results obtained comparing with lean goal established in the earlier planning stage. If the result did not meet the required goal expectation, the risks assessment shall be re-evaluating again to recognize those barriers or reasons of the lean failures and carry out the necessary action plan to recognize any others opportunity to improve it further.

### **3.4 Post Implementation Phase (Act)**

This post implementation phase will act as the standardization of the successful lean practices for sustaining the lean outcomes in the future long term. Documentation of the new lean practices established is important for team to lock down the successful lean experiences and result for future references as compared with previously result.

Top management and leadership commitment to review on the final lean result obtained is essential for them to decide whether is worth to continue or invest more with this project in the extent large scale based on the quick result of lean benefits gain with consideration of Return on Investment (ROI) for SME company in long term run [16]. Wong and Wong [10] stated before improvement process is commenced, the current state needs to be defined. Next, a vision of a future state needs to be proposed and developed. The PDCA cycle is still repeating and keep continuously for enhancement until SMEs can maximize the lean benefits gain in sustaining the lean implementation for long term.

## 4 Discussion and Conclusions

In the present study, the common challenges that SMEs face when during their lean journey have been discussed. Various lean implementation main existing frameworks were reviewed, as well several studies focused on the implementation of lean on SMEs in difference industry. This paper has proposed the conceptual framework for lean manufacturing implementation in SMEs based on structured literature review and compliant with the 9 critical success factors of Mostafa et al. [7], which are expert team building, situational analysis, lean communication planning, training process, lean tools, value stream mapping, lessons learned review, lean assessment, lean monitoring and controlling or lean sustaining. This could assist SMEs to implement the lean tools effectively by focusing on the sequential steps-by-steps flow in 4 differences phases as an easy to follow guideline. PDCA cycles approaches has been established to integrate built-in into this framework, as this is the fundamental and useful tools for implementing the lean manufacturing for continuous improvement, especially for the SME company. The feasible lean practices (basic, intermediate and advance) are suggested in this paper, which SMEs can choose the suitable practices based on their environment needs. The proposed adoption of lean practices can be based on three categories; least investment, feasible to apply in SME and recommended by researchers [17]. Another significant highlighted feature in the proposed framework is the management leadership commitment in reviewing the final lean result gain. This is very crucial because the support of the top management is the key element to decide a final call to go or no-go for the lean manufacturing implementation towards the next phase of large-scale run, especially in SMEs. In order to validate this framework, it is recommended that the future study will be carry out by developing a questionnaire survey for distributing to the SMEs for the data collection analysis as a case study.

**Acknowledgement.** I would like to thank the Universiti Teknikal Malaysia Melaka (UTEM) for granting me an opportunity to pursue this study. Not forgotten also, to appreciate Dr. Puvanasvaran for his guidance and support.

## References

1. Anvari, A., Norzima, Z., Rosnay, M., Hojjati, M., Ismail, Y.: A comparative study on journey of lean manufacturing implementation. *AIJSTPME* **3**, 77–85 (2010)
2. Yusof, S.M., Aspinwall, E.: A conceptual framework for TQM implementation for SMEs. *TQM Mag.* **12**(1), 31–36 (2000). <https://doi.org/10.1108/09544780010287131>
3. Rose, A., Deros, B., Rahman, M.: Development of framework for lean manufacturing implementation in SMEs. In: *The 11th Asia Pacific Industrial Engineering and Management Systems Conference* (2010)
4. Pavnaskar, S.J., Gershenson, J.K., Jambekar, A.B.: Classification scheme for lean manufacturing tools. *Int. J. Prod. Res.* **41**, 3075–3090 (2003). <https://doi.org/10.1080/0020754021000049817>
5. Norani, N., Deros, B., Abd Wahab, D., Nizam, M.N.A.: A framework for organisational change management in lean manufacturing implementation. *Int. J. Serv. Oper. Manage.* **12**, 101–117 (2012). <https://doi.org/10.1504/ijso.2012.046676>
6. Anand, G., Kodali, R.: Analysis of lean manufacturing frameworks. *J. Adv. Manuf. Syst.* **1** (9), 1–30 (2010). <https://doi.org/10.1142/S0219686710001776>
7. Mostafa, S., Dumrak, J., Soltan, H.: A framework for lean manufacturing implementation. *Prod. Manuf. Res. Open Access J.* **1**, 44–64 (2013). <https://doi.org/10.1080/21693277.2013.862159>
8. Belhadi, A., Touriki, F.E., El Fezazi, S.: A framework for effective implementation of lean production in small and medium-sized enterprises. *J. Ind. Eng. Manage.* **9**(3), 786–810 (2016). <https://doi.org/10.3926/jiem.1907>
9. Almani, M., Salonitis, K., Tsinopoulos, C.: A conceptual lean implementation framework based on change management theory. *Procedia CIRP* **72**, 1160–1165 (2018). <https://doi.org/10.1016/j.procir.2018.03.141>
10. Wong, Y.C., Wong, K. Y.: A lean manufacturing framework for the Malaysian electrical and electronics industry. In: *Proceedings of the 3rd International Conference on Information and Financial Engineering*, vol. 12, pp. 30–34 (2011)
11. Okhovat, M.A., Ariffin, M.K.A.M., Nehzati, T., Hosseini, S.A.: Development of world class manufacturing framework by using six-sigma, total productive maintenance and lean. *Sci. Res. Essays* **7**(50), 4230–4241 (2012). <https://doi.org/10.5897/SRE11.368>
12. AlManei, M., Salonitis, K., Xu, Y.: Lean implementation frameworks: the challenges for SMEs. *Procedia CIRP* **63**, 750–755 (2017)
13. Amin, A.N.M., Wan Mahmood, W.H., Kamat, S.R., Abdullah, I.: Conceptual framework of lean ergonomics for assembly process: PDCA approach. *J. Eng. Sci. Res.* **2**(1), 51–62 (2018). <https://doi.org/10.26666/rmp.jesr.2018.1.9>
14. Grewal, C.: An initiative to implement lean manufacturing using value stream mapping in a small company. *Int. J. Manuf. Technol. Manage.* **15**(3/4), 404 (2011). <https://doi.org/10.1504/ijmtm.2008.020176>
15. Worley, J.M., Doolen, T.L.: The role of communication and management support in a lean manufacturing implementation. *Manage. Decis.* **44**(2), 228–245 (2006)
16. Motwani, J.: A business process change framework for examining lean manufacturing: a case study. *Ind. Manage. Data Syst.* **103**(5), 339–346 (2003). <https://doi.org/10.1108/02635570310477398>
17. Rose, A.M.N., Deros, B.Md., Rahman, M.N.Ab. & Nordin, N.: Lean manufacturing best practices in SMEs. In: *The 2011 International Conference on Industrial Engineering and Operations Management* (2011)



# Comparisons in L<sub>32</sub> 2k-Factorial and L<sub>25</sub> Taguchi for the 16 nm FinFET Statistical Optimization Applications

Ameer Farhan Roslan<sup>(✉)</sup>, Fauziyah Salehuddin,  
Anis Suhaila Mohd Zain, Khairil Ezwan Kaharudin,  
Abdul Razak Hanim, Haroon Hazura, and Siti Khadijah Idris

Faculty of Electronics and Computer Engineering,  
Universiti Teknikal Malaysia Melaka, Jalan Hang Tuah Jaya,  
76100 Durian Tunggal, Melaka, Malaysia  
ameerfarhan@aol.com

**Abstract.** This project examines and analyzes the process parameter variance towards on-state drive current ( $I_{ON}$ ) and leakage current ( $I_{OFF}$ ) towards the 16 nm double-gate FinFET (DG-FinFET) device by the implementation of 2k-factorial design, with comparisons made against an L<sub>25</sub> Taguchi statistical method. Alterations with two levels for six process parameters consisting of the threshold voltage ( $V_{TH}$ ) doping dose,  $V_{TH}$  doping tilt, polysilicon doping dose, polysilicon doping tilt, Source and Drain (S/D) doping dose and S/D doping tilt will be done to analyze and improve the results of both  $I_{ON}$  and  $I_{OFF}$ . The physical characteristics of the device will be defined on the ATHENA module, with the ATLAS module then used to characterize its electrical properties. Consideration is made with the responses from both modules by the assistance of the L<sub>32</sub> 2k-factorial design to reduce the device's variability as well as maximizing the value of  $I_{ON}$  while minimizing the  $I_{OFF}$  value. By achieving both values, the  $I_{ON}/I_{OFF}$  ratio are able to be maximized in order to reduce the power consumption of the device subsequently. The most dominant factor towards both  $I_{ON}$  and  $I_{OFF}$  values is identified with polysilicon doping tilt, showcasing the largest standardized effects at the end of this experiment. The optimum values achieved with 2k-factorial design with  $I_{ON}$  and  $I_{OFF}$  at 1648.48  $\mu\text{A}/\mu\text{m}$  and 42.096 pA/ $\mu\text{m}$  respectively while achieving better  $I_{ON}/I_{OFF}$  ratio with  $39.160 \times 10^6$  as its  $I_{ON}$  have surpassed the value of  $I_{ON}$  achieved in Taguchi method that was valued at 1559.96  $\mu\text{A}/\mu\text{m}$ . Importantly, the results acquired have met the predictions of the International Technology Roadmap Semiconductor (ITRS) 2013 for the year 2020.

**Keywords:** DG-FinFET ·  $I_{ON}$  implantation · 2k-factorial design · Taguchi method · NMOS device

## 1 Introduction

In today's standard, various of electronic devices that not only limited to laptops or phones, like audio system, home system and even smart electrical appliances have CMOS technology embedded in them, just like how Apple HomePod speakers fabricated with an A8 processor that holds a 20 nm CMOS die technology. Metal Oxide Semiconductor Field Effect Transistor (MOSFET) is one primary component in CMOS technology that also comprises of many other different types of MOSFETs in multi-gate FET (MuGFET) that comprises of Silicon-on-insulator MOSFET, Flexgate, Pi-gate, Trigate and FinFET to name a few [1].

The reduction in scaling is purposed for smaller, rapid and cost-reduced technology. However, disadvantage in scaling down is primarily due to higher process parameter variation towards wafer fabrication [2, 3]. Mitigating these disadvantages and other issues such as short-channel effect (SCE), threshold voltage ( $V_{TH}$ ) roll-off and drain induced barrier leakage (DIBL) can be challenging but the implementation of FinFET have proven to have overcome the SCEs by reducing the large leakage current and subthreshold swing (SS) while the performance of the transistor can be enhanced while the scaling process is furthered [4–6].

Understanding the process variations alongside its own manufacturing modeling are rather fundamental to allow prediction of devices characteristics as well as its performance that are prior to the fabrication process as these allows adequate information towards parameters' impact minimizations while exploiting the performance yielding [7, 8]. The electron drift characteristics inside the channel has been heavily affected by the influence of SCEs. In this Double-gate FinFET (DG-FinFET) design, the silicon depletion depth has been reduced whilst the gate length has been referred to in considering the gate oxide thickness. Since the process parameter variations have impacted in influencing the outcomes of the  $V_{TH}$ , drive current, the off-state leakage current ( $I_{OFF}$ ) and also towards SS, these values can also be optimized by manipulating the process variation parameters it selves. Defining the electrical characterization from the aforementioned process parameters however can also be challenging [9].

Nevertheless, the robustness of devices, especially for Polysilicon/Silicon Dioxide (PolySi/SiO<sub>2</sub>)-based DG-FinFET can still be advanced with the implementation of numerous statistical methods [10–17]. Other than Taguchi optimization methods thrived by Salehuddin et al. and Kaharudin et al., 2k-factorial design can also be used in many experimental cases specifically in DG-FinFET design optimization [16–18]. In this work, the application of 2k-factorial is compared against Taguchi method, analyzed and discussed.

## 2 Methodology

### 2.1 Device Fabrication Using ATHENA and ATLAS Modules

By employing both ATHENA and ATLAS modules from Silvaco International for the 16 nm DG-FinFET fabrication enables both physical and electrical properties for the device to be constructed and analysed prior to the actual fabrication. This does not only

enable cheaper construction for every changes made for each parameters unlike the actual construction, but this method also allows immeasurable properties based from the simulated construction to be analysed from when the actual fabrication does not able to. Following to that the identification has been towards the selection of five geometrical parameters that have been chosen due to its aptitude in activating the effects on output responses whilst minor manipulation is made towards its variations as in Table 1. Conclusively, variation took its place towards the output when fluctuations occurs to the process parameters against local parameter variations that are 30% from the overall [19].

**Table 1.** Value of the geometrical parameters set

Parameters	Value (nm)
Gate Length, $L_G$	16
SiO <sub>2</sub> Thickness, $T_{OX}$	3.25
Main substrate (silicon) length, $L_C$	35
Polysilicon Length, $L_{DM}$	17.3
Silicon Thickness, $T_{FIN}$	18.7

A <100> orientation took its place towards the P-type main substrate as the oxide layer is being constructed on the silicon bulk top for which is operated as mask throughout the implantation of P-well.  $1 \times 10^{17}$  atom/cm<sup>3</sup> of Boron is then infused into the silicon substrate before the gate oxide with dry oxygen condition is applied for 875 °C to a 3% of Hydrochloric acid (HCl). Dielectric layer meanwhile secludes both of source and drain (S/D) away from gate terminal that against the conductive channel. By implementing Boron in the channel region with  $1.95 \times 10^{13}$  atom/cm<sup>3</sup> with 5 keV of energy, responses towards  $V_{TH}$  is achieved. This proves that small modifications on gate concentration can significantly influences changes and therefore through the most significant variations obtained, the parameter variations are able to be elected. So when the formation of multi-layered structure is accomplished the polycrystalline silicon deposited on the wafer before polysilicon is conformed.

Before the construction of sidewall spacer took its place on the silicon and polysilicon surfaces with Silicon Nitride (Si<sub>3</sub>N<sub>4</sub>) layer, an implantation of indium dope is implanted by  $1.17 \times 10^{13}$  atom/cm<sup>3</sup> along with 1 keV of energy. This allows the SCEs to be minimized for when the n-type S/D areas to have doped to p-type substrate's sides. As Arsenic is implanted with 3 keV energy to  $22 \times 10^{18}$  atom/cm<sup>3</sup> of dose for S/D implantation, the compensate implantation meanwhile enables reductions to side capacitance. By depositing aluminium and patterning from the contact window's initial formation within the S/D region, the process of metallization took its place and only then, the structure is mirrored before it is concluded with electrode definition as in Fig. 1.

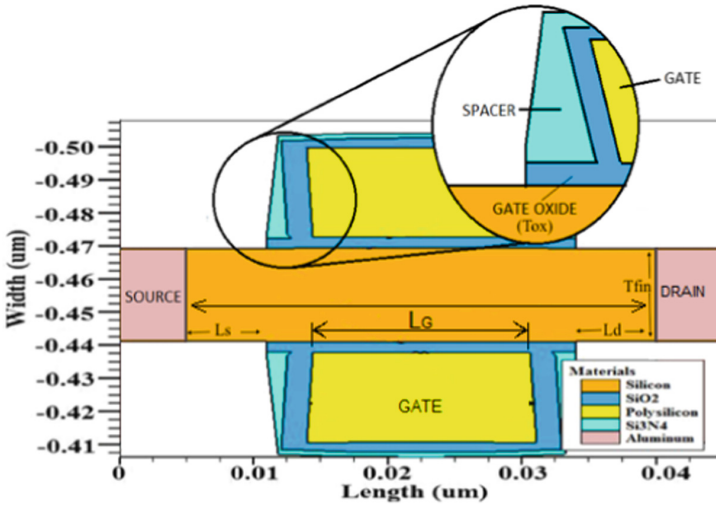


Fig. 1. Simulated structure of the PolySi/SiO<sub>2</sub>-based DG-FinFET

2.2 2k-Factorial as Method of Optimization

The 2k-factorial design or the 2<sup>k</sup> designs are defined as a major set of building blocks for numerous experimental designs for which denotes the designs comprises of k factors with two levels for each factor [19, 20]. Compared to other statistical methods like Taguchi method or Grey relational analysis, these method requires minimal number of levels with just two used for larger number of factors. Based on Yates notation, the optimizations of six different parameters that represents the factors are levelled to two where each of the combinations allows coded factors data for the aforementioned combinations where the notion is visually explained as in Fig. 2. The representation of “ab” denotes high level for both A and B which is +1, while (1) represents low level or -1 for both A and B. Meanwhile, “a” and “b” denote from when A is high level or +1 with low level at B, and for when A is low levelled as B is high levelled or +1 respectively. These representations signify which level in every k factors are at.

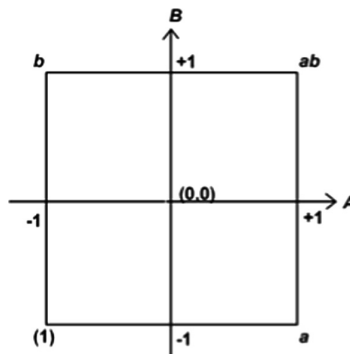


Fig. 2. Plot of the region of experimentation in two dimensions for Yates notion



The 2k effect signifies the change in means of factor for both high and low level. Therefore, the minus of averages of observations at high level against the low level of A would yield the following notation A [20]:

$$A = \bar{y}_{A+} - \bar{y}_{A-} \tag{1}$$

With B using similar approach albeit in different direction:

$$B = \bar{y}_{B+} - \bar{y}_{B-} \tag{2}$$

Meanwhile the notation AB is:

$$AB = \frac{ab + (1)}{2n} - \frac{a + b}{2n} \tag{3}$$

However, since in this experiment six factors are used for two levels, these aforementioned principle allows other different applications with different characterizations to be used in these 2k-designs. In Yates notation, the contrasts of observations are showcased by columns that has equivalent amount of pluses and minuses for each column. That said the general form of an effect for k factors is:

$$\text{Effect} = \left(1/2^{(k-1)}n\right) [\text{contrast of the totals}] \tag{4}$$

Succeeding to that the effect variance can be achieved by applying the following general form used in (4):

$$\begin{aligned} \text{Variance (Effect)} &= \left[1/(2^{(k-1)}n)\right]^2 2^k n \sigma^2 \\ &= \sigma^2 / 2^{(k-2)}n \end{aligned} \tag{5}$$

The sum of squares for the effect meanwhile is:

$$SS(\text{effect}) = (\text{contrast})^2 / 2^k n \tag{6}$$

### 2.3 Design of Experiment for 2k-Factorial

Four available options are given in 2k-factorial design of experiment (DOE) for six process parameters which are full factorial, half fraction, quarter fraction and 1/8 fraction with each requires 64, 32, 16 and eight experiment runs respectively. Even though, 1/8 fraction and quarter fraction offers less experiment runs, an L<sub>32</sub> half fraction is chosen as it allows more combinations of process parameter to take place while does not requires as much of experiment runs as the full factorial. Table 2 shows the experimental layout for six process parameters with random orthogonal array combinations generated. The process parameters and values for each level in low level and high level is represented in Table 3.

**Table 2.** L<sub>32</sub> 2k-factorial design array

Experiment no.	Process parameter level					
	Polysilicon Doping Dose (A)	Polysilicon Doping Tilt (B)	S/D Doping Dose ©	S/D Doping Tilt (D)	V <sub>TH</sub> Doping Dose €	V <sub>TH</sub> Doping Tilt (F)
1	-1	1	-1	1	1	1
2	1	1	1	-1	1	-1
3	1	-1	-1	-1	1	-1
4	-1	1	-1	1	-1	-1
5	1	1	-1	-1	1	1
6	1	1	1	1	1	1
7	1	1	-1	1	1	-1
8	1	-1	1	-1	-1	-1
9	1	1	1	1	-1	-1
10	-1	-1	1	-1	-1	1
11	1	-1	1	-1	1	1
12	-1	1	-1	-1	1	-1
13	-1	1	1	-1	-1	-1
14	1	1	-1	1	-1	1
15	1	-1	-1	1	-1	-1
16	-1	-1	-1	-1	-1	-1
17	1	-1	1	1	1	-1
18	-1	1	-1	-1	-1	1
19	-1	-1	1	1	-1	-1
20	1	-1	1	1	-1	1
21	-1	-1	1	1	1	1
22	1	1	-1	-1	-1	-1
23	-1	1	1	-1	1	1
24	1	-1	-1	-1	-1	1
25	-1	1	1	1	1	-1
26	1	1	1	-1	-1	1
27	-1	-1	-1	1	1	-1
28	1	-1	-1	1	1	1
29	-1	-1	-1	1	-1	1
30	-1	-1	1	-1	1	-1
31	-1	-1	-1	-1	1	1
32	-1	1	1	1	-1	1

**Table 3.** Control factors of 16 nm DG-FinFET and its levels

Symbols	Control Factors	Units	(-1)	(+)
A	V <sub>TH</sub> Doping Dose	atom/cm <sup>3</sup>	4.465 × 10 <sup>13</sup>	4.485 × 10 <sup>13</sup>
B	V <sub>TH</sub> Doping Tilt	deg. (°)	5	7
C	Polysilicon Doping Dose	atom/cm <sup>3</sup>	3.58 × 10 <sup>14</sup>	3.60 × 10 <sup>14</sup>
D	Polysilicon Doping Tilt	deg. (°)	-22	-20
E	S/D Doping Dose	atom/cm <sup>3</sup>	1.20 × 10 <sup>18</sup>	1.22 × 10 <sup>18</sup>
F	S/D Doping Tilt	deg. (°)	72	74

### 3 Results

#### 3.1 Multiple Properties of 16 nm DG-FinFET

The drive current (I<sub>ON</sub>) and leakage current or OFF-current (I<sub>OFF</sub>) responses is incorporated in the findings for the design electrical properties whereby these selected properties are optimized maximally for I<sub>ON</sub>, and minimally for I<sub>OFF</sub> by the execution of 2k-factorial design. The conducted experiments follow the combinations in Table 2 of L32 random array to examine the changes of multiple electrical properties based on modification in control factors. Table 4 depicts the values of I<sub>ON</sub> and I<sub>OFF</sub> obtained from 32 experiments based on the L32 2k-factorial design implementation.

**Table 4.** I<sub>ON</sub>, I<sub>OFF</sub> and I<sub>ON</sub>/I<sub>OFF</sub> of 16 nm DG FinFET Device

Experiment no.	I <sub>ON</sub> (μA/μm)	I <sub>OFF</sub> (pA/μm)	I <sub>ON</sub> /I <sub>OFF</sub> ratio (×10 <sup>6</sup> )
1	1804.86	87.270	20.681
2	1677.92	46.839	35.823
3	1675.89	45.928	36.489
4	1804.86	87.270	20.681
5	1677.1	46.710	35.904
6	1797.36	78.951	22.765
7	1796.96	78.780	22.810
8	1676.71	46.055	36.407
9	1797.36	78.951	22.765
10	1684.33	50.976	33.041
11	1676.71	46.055	36.407
12	1684.71	51.716	32.577
13	1685.53	51.858	32.503
14	1796.96	78.780	22.810
15	1795.68	77.472	23.179
16	1683.51	50.836	33.116
17	1796.07	77.641	23.133
18	1684.71	51.716	32.576
19	1803.98	85.994	20.978

(continued)

**Table 4.** (continued)

Experiment no.	$I_{ON}$ ( $\mu A/\mu m$ )	$I_{OFF}$ (pA/ $\mu m$ )	$I_{ON}/I_{OFF}$ ratio ( $\times 10^6$ )
20	1796.07	77.641	23.133
21	1803.98	85.994	20.978
22	1677.10	46.711	35.904
23	1685.53	51.858	32.503
24	1675.89	45.928	36.489
25	1805.25	87.460	20.641
26	1677.92	46.839	35.823
27	1803.58	85.807	21.019
28	1795.68	77.472	23.179
29	1803.58	85.807	21.019
30	1684.33	50.976	33.041
31	1683.51	50.836	33.116
32	1805.25	87.460	20.641

**3.2 Factor Effects Estimation with Regard to  $I_{ON}$  and  $I_{OFF}$**

Six control factors have been analyzed in Taguchi Method to have affected the output responses in the 16 nm DG-FinFET device. Thence the analysis is done by using the same control factor A, B, C, D, E and F in order to observe the trends of the factors against the output responses variations in  $I_{ON}$  and  $I_{OFF}$  with tabulation of results as in the respective Tables 5 and 6.

**Table 5.** Estimation of factor Effect, Coefficient, T-value and P-value for  $I_{ON}$

Term	Effect	Coef	SE Coef	T-value	P-value
A	-7.7575	-3.8787	0.0259	-149.95	0.000
B	1.2425	0.6212	0.0259	24.02	0.000
C	0.6075	0.3037	0.0259	11.74	0.000
D	119.7550	59.8775	0.0259	2314.89	0.000
E	-0.0000	-0.0000	0.0259	-0.0000	1.000
F	0.0000	0.0000	0.0259	0.0000	1.000

**Table 6.** Estimation of factor Effect, Coefficient, T-value and P-value for  $I_{OFF}$

Term	Effect	Coef	SE Coef	T-value	P-value
A	-6.693	-3.346	0.175	-19.09	0.000
B	1.109	0.555	0.175	3.16	0.000
C	0.157	0.078	0.175	0.45	0.004
D	33.557	16.779	0.175	95.74	0.659
E	-0.0000	-0.0000	0.175	-0.0000	1.000
F	0.0000	0.0000	0.175	0.0000	1.000

The p-values obtained were equivalent to zero for four control factors which indicates that the tested factors A ( $V_{TH}$  Doping Dose), B ( $V_{TH}$  Doping Tilt), C (Polysilicon Doping Dose), and D (Polysilicon Doping Tilt) are significant to the  $I_{ON}$  values whereby factor E (S/D Doping Dose) and F (S/D Doping Tilt) are inconsequential based on Table 5 as opposed to optimization done with Taguchi method where these process parameters contribute to the output responses. In Table 6 however, factor A and B were observed to be the most significant with zero p-values, trailed by actor C and D with 0.004 and 0.659 respectively as factor E and F were once again insignificant even towards  $I_{OFF}$  values. Through the analysis of the estimation effect managed through Tables 5 and 6, normal plots were formed based on standardized effects of  $I_{ON}$  and  $I_{OFF}$  as in Figs. 3 and 4 respectively.

In Fig. 3, the standardized effects normal plot indicates that the  $I_{ON}$  values react strongly to the control factor A and D, as suggested by points that represent both factors to be distributed away from the straight line. However, factor B and C were also significant to the values of  $I_{ON}$  whereby factor E and F are both located near and on the straight line which indicates the factors to have not significantly effecting the values of  $I_{ON}$ . Meanwhile, for  $I_{OFF}$  the normal plot for its standardized effects as in Fig. 4 shows that only factor A, B and D that are significant towards  $I_{OFF}$  characteristics as each point is spread away from the straight line as factor C, E and F were all insignificant towards the characteristics of  $I_{OFF}$ . That said, the points that are within the line region are ignored with the points only to be considered more significant as it diverges away from the line.

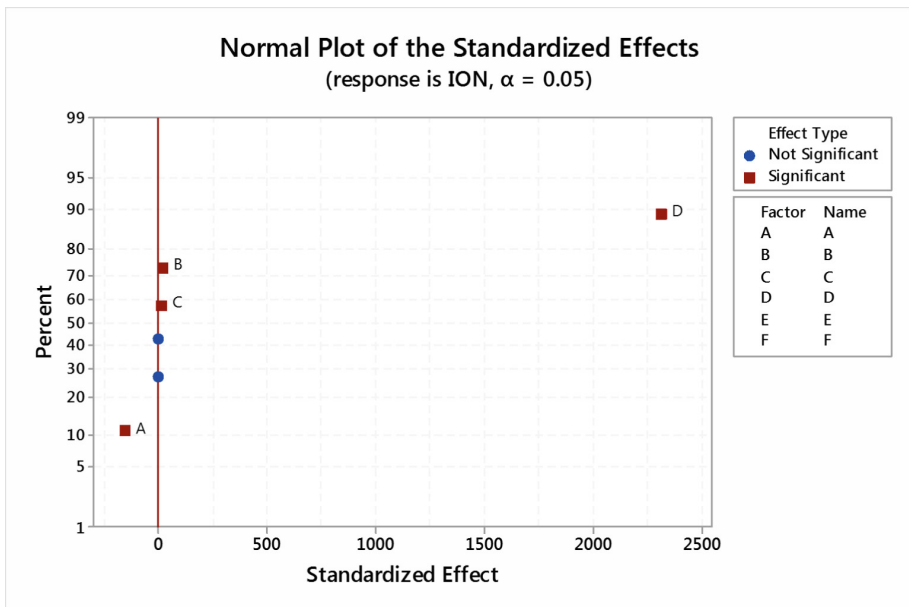


Fig. 3. Normal plot of standardized effects for  $I_{ON}$  for 16 nm DG-FinFET

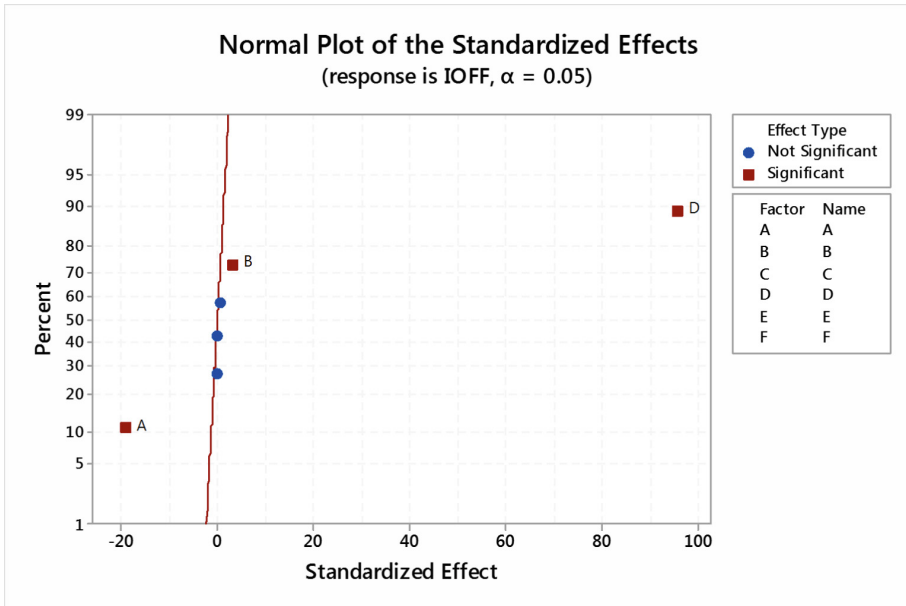


Fig. 4. Normal plot of standardized effects for  $I_{OFF}$  for 16 nm DG-FinFET

95% confident level is implemented that serves as a guide for each of the respective control factor and its effects for the  $2k$ -factorial analysis. Therefore, standardized effects for both  $I_{ON}$  and  $I_{OFF}$  were presented in the Pareto charts form whereby, a confident line in each chart suggests factors that are significant and ones that are not as shown in Figs. 5 and 6, with factor effects surpasses the confident line considered as significant factors.

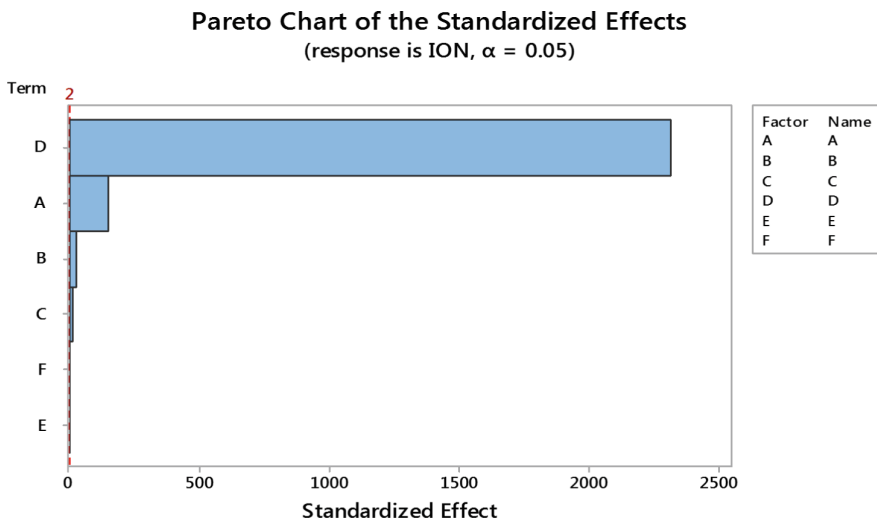
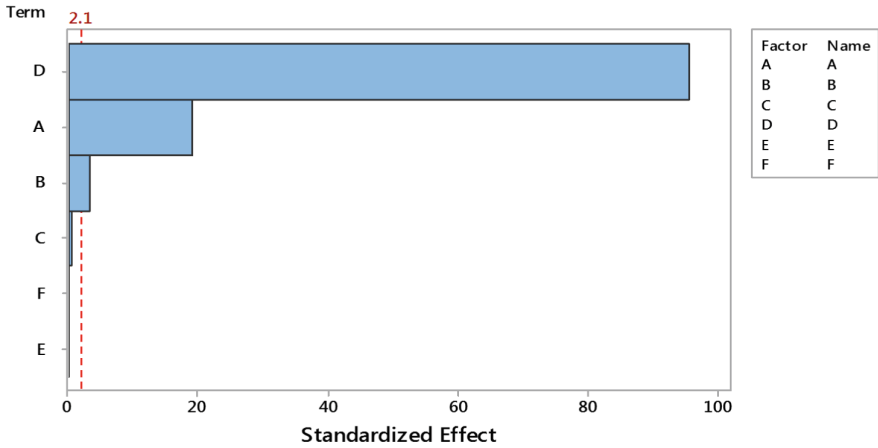


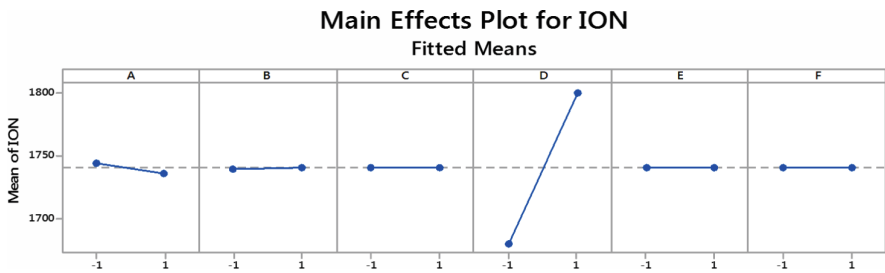
Fig. 5. Pareto chart for the  $I_{ON}$  standardized effects for 16 nm DG-FinFET

**Pareto Chart of the Standardized Effects**  
(response is IOFF,  $\alpha = 0.05$ )

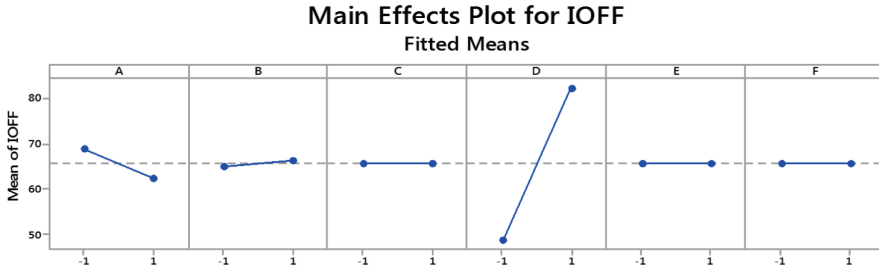


**Fig. 6.** Pareto chart for the  $I_{OFF}$  standardized effects for 16 nm DG-FinFET

Factor A and D in Fig. 5 are proven to be significant against the  $I_{ON}$  variation whereby these main effect excelled in surpassing the confident line with factor B and C to have surpassed the confident line as well to indicate both as significant factors behind A and D. The Pareto chart for the  $I_{OFF}$  response in Fig. 6 meanwhile depicts factor A, B and D to have exceeded the confident line. These patterns prove that factor E and F were not significant for neither  $I_{ON}$  nor  $I_{OFF}$  variation responses, with C to be below the confident line only for  $I_{OFF}$  contrary to its significance in  $I_{ON}$  variations. Subsequent to that, main effects plot for both  $I_{ON}$  and  $I_{OFF}$  were also performed as portrayed in Figs. 7 and 8 respectively. The impact of factor D towards both  $I_{ON}$  and  $I_{OFF}$  variations can be seen in both main effect plots whereby the slopes for factor D suggested larger gradient in between low level and high level of the control factor D. Overall, the increment towards  $I_{ON}$  of the device can be achieved if factor B and D is set at high level, with factor A set at low level.



**Fig. 7.** Main effect plot for  $I_{ON}$  for 16 nm DG-FinFET



**Fig. 8.** Main effect plot for  $I_{OFF}$  for 16 nm DG-FinFET

In addition to that, the trends are similar in  $I_{OFF}$  as to the main effects plot for  $I_{ON}$ , with exception that the  $I_{OFF}$  value should be minimized when factor B and D are set to high level with value of factor A reduced. Evidently, factor E and F does not show indication of being the contribution factor to the rise and fall in terms of values for both  $I_{ON}$  and  $I_{OFF}$ . Similar to previous normal plot, factor does contribute to the variations in  $I_{ON}$  but from Fig. 8, it is implying that factor C does not contribute to the changes in  $I_{OFF}$ .

### 3.3 Analysis of Variance

In analysis of variance (ANOVA), all control factors including the non-significant factors were comprised as well in the full model as this is due to the fact that ANOVA process is convoluting multiple of properties. That said, investigation towards residual error in this model can be accomplish through the ANOVA formed specifically for  $I_{ON}$  and  $I_{OFF}$ . Since the residual error probability is vital in measuring the significance of certain factor, the p-value is applied. By using 95% confident level, it is required for a factor to have less than 0.05 of factor effects to achieve factor of significant [21]. The ANOVA for each  $I_{ON}$  and  $I_{OFF}$  for the device is tabulated in Tables 7 and 8 respectively.

**Table 7.** ANOVA for  $I_{ON}$  for 16 nm DG-FinFET

Source	DF	Adj SS	Adj MS	F-value	P-value
A	1	481	481	22486.24	0.000
B	1	12	12	576.85	0.000
C	1	3	3	137.90	0.000
D	1	114730	114730	5358714.63	0.000
E	1	0.00	0.00	0.00	1.000
F	1	0.00	0.00	0.00	1.000
Error	25	1			
Total	31	115227			



**Table 8.** ANOVA for  $I_{OFF}$  for 16 nm DG-FinFET

Source	DF	Adj SS	Adj MS	F-value	P-value
A	1	358.32	358.32	364.55	0.000
B	1	9.85	9.85	10.02	0.004
C	1	0.20	0.20	0.20	0.659
D	1	9008.65	9008.65	9165.27	0.000
E	1	0.00	0.00	0.00	1.000
F	1	0.00	0.00	0.00	1.000
Error	25	24.57			
Total	31	9401.59			

### 3.4 Optimization Analysis via Desirability Function

The implementation of desirability function is done in order to optimize both  $I_{ON}$  and  $I_{OFF}$  concurrently whereby through the multiple level settings that is determined beforehand, the optimal solution can be achieved. With both weight and importance set at one, the preset condition for multi-response optimization of the  $I_{ON}$  and  $I_{OFF}$  were analyzed as in Table 9.

**Table 9.** Preset Condition of  $I_{ON}$  and  $I_{OFF}$  for multiple response optimization 16 nm DG-FinFET

Response	Goal	Lower	Target	Upper	Weight	Importance
$I_{ON}$	Maximum	1675.89	1805.25		1	1
$I_{OFF}$	Minimum		45.93	87.46	1	1

The optimization plot for the  $I_{ON}$  and  $I_{OFF}$  in Fig. 9 showcases the best combination that depicts the optimal result that can be achieved based on the horizontal line on each of control factor. That said, the vertical lines set on which level should each of the control factor valued at in obtaining optimum results simultaneously. Factor A, C and F were predicted to have high level that represents  $4.485 \times 10^{13}$  atom/cm<sup>3</sup>,  $3.6 \times 10^{14}$  atom/cm<sup>3</sup>, and 74° respectively. Low level is anticipated for factor B with actual value of 5°. However, factor D was optimally coded at 0.2596 with factor E is expected to be 0.0 that carries the actual values of -22.256° and  $1.21 \times 10^{18}$  atom/cm<sup>3</sup> respectively. Succeeding to the combination of the optimization plot, the best settings for the control factors with respect to the optimal level after the optimization plot is documented for  $I_{ON}$  and  $I_{OFF}$  as in Table 10.

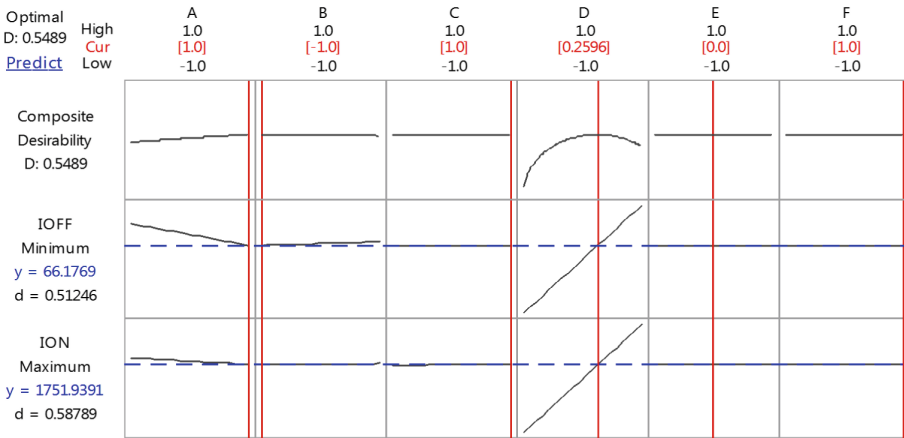


Fig. 9. Optimization plot for  $I_{ON}$  and  $I_{OFF}$  for 16 nm DG-FinFET

### 3.5 Confirmation Test

The performance of the predicted optimum level for the control factor were confirmed by implementing the confirmation test against the performance of the actual pre-optimized simulated values. Table 10 depicts each control factor alongside its coded values, actual and best value based on the combination settings from the optimization plot preceded for the 16 nm DG-FinFET.

Table 10. Best setting of control factors based on the Optimum Level post-optimization plot for multiple response

Symbol	Control factors	Units	Actual value	Best value
A	$V_{TH}$ Doping Dose	atom/cm <sup>3</sup>	$4.485 \times 10^{13}$	$4.485 \times 10^{13}$
B	$V_{TH}$ Doping Tilt	deg. (°)	5	5
C	Polysilicon Doping Dose	atom/cm <sup>3</sup>	$3.60 \times 10^{14}$	$3.60 \times 10^{14}$
D	Polysilicon Doping Tilt	deg. (°)	-22.2596	-22.2596
E	S/D Doping Dose	atom/cm <sup>3</sup>	$1.21 \times 10^{18}$	$1.21 \times 10^{18}$
F	S/D Doping Tilt	deg. (°)	74	74

The combinations from the best setting of an  $L_{25}$  Taguchi method,  $L_{32}$  2k-factorial design, and the actual experiment result are compared with respect to the prediction made by the ITRS 2013 for the year 2020. Based on Table 11, the  $I_{ON}$  obtained from 2k-factorial best setting combination is 1648.48  $\mu A/\mu m$  for which successfully exceeds the prediction of ITRS 2013 with 11.38% higher than the prediction, as it is also higher than  $I_{ON}$  from Taguchi optimization albeit lower than the pre-optimized value. This trend is also follows the  $I_{OFF}$  valuation in the 2k-factorial design, with it being lower than the pre-optimized but higher than the value produced by Taguchi method as it meets the prediction from the ITRS 2013 by 57.90% lower. Subsequently, this has

brought the  $I_{ON}/I_{OFF}$  ratio achieved to be substandard in comparison to Taguchi method's  $I_{ON}/I_{OFF}$  ratio with  $39.160 \times 10^6$  for the 2k-factorial as it attained the desired value which is higher to that of the pre-optimized experiment and the ITRS 2013 prediction.

**Table 11.** Comparisons of best optimization combination between Optimized values of Taguchi method, 2k-factorial design, pre-optimized and prediction from the ITRS 2013

Device characteristics	Pre-optimized values	Optimized values		ITRS 2013 prediction
		Taguchi	2k-factorial	
$I_{ON}$ ( $\mu A/\mu m$ )	1689.53	1559.96	<b>1648.48</b>	$\geq 1480$
% Difference from targeted output value	12.40	5.13	11.38	–
$I_{OFF}$ ( $pA/\mu m$ )	52.285	33.027	<b>42.096</b>	$\leq 100$
% Difference from targeted output value	47.77	66.97	57.90	–
$I_{ON}/I_{OFF}$ ratio	$32.486 \times 10^6$	$47.233 \times 10^6$	<b><math>39.160 \times 10^6</math></b>	14.80
% Difference from targeted output value	54.44	68.67	62.21	–
SS (mV/dec)	97.526	96.933	<b>96.291</b>	N/A
% Difference from targeted output value	–	–	–	N/A

## 4 Conclusion

Ultimately, the  $L_{32}$  2k-factorial is proven to be reliable and workable in optimizing the values for two responses in  $I_{ON}$  and  $I_{OFF}$  respectively. As the polysilicon doping tilt is identified as the most dominant control factor amongst the six process parameters, the  $V_{TH}$  doping tilt,  $V_{TH}$  doping dose are both significant in contributing to the changes of the responses. The polysilicon doping dose however is proven to have only capable in signifying the changes for the  $I_{ON}$  while it is less significant for the variations in  $I_{OFF}$ . Through the optimization process, the  $L_{32}$  2k-factorial have not been able to bettered the  $I_{ON}/I_{OFF}$  ratio produced by Taguchi method. However, 2k-factorial design holds bigger advantage in that it saves a lot of time for the completion of tests, with less experiment runs required with 32 tests needed as opposed to more experiments for Taguchi method, which requires 100 tests due to the consideration in noise factor with two levels for the latter. Despite that, the implementation of 2k-factorial is proven to have improved the  $I_{ON}/I_{OFF}$  ratio against the pre-optimized value for which makes the device to require less power for its operation. Therefore, it is concluded that the polysilicon doping tilt have played a significant role in contributing the largest effect towards the performance of  $I_{ON}$  and  $I_{OFF}$ , and subsequently the  $I_{ON}/I_{OFF}$  ratio against six other control factors. It is observed that the optimized values from the 2k-factorial have met the requirement of the ITRS 2013 for the year 2020.

**Acknowledgements.** The authors would like to thank the Ministry of Higher Education (MOHE) for sponsoring this work under project (FRGS/1/2017/TK04/FKEKK-CeTRI/F00335) and MiNE, CeTRI, Faculty of Electronics and Computer Engineering (FKEKK), Universiti Teknikal Malaysia Melaka (UTeM) for the moral support throughout the project.

## References

1. Bhattacharya, D., Jha, N.K.: FinFETs: from devices to architectures. *Adv. Electron.* **2014**, 1–21 (2014). <https://doi.org/10.1155/2014/365689>
2. Mallik, A., Ryckaert, J., Mercha, A., Verkest, D., Ronse, K., Thean, A.: Maintaining Moore's law: enabling cost-friendly dimensional scaling. In: *Proceedings of the SPIE 9422, Extreme Ultraviolet (EUV) Lithography VI*, 94221N (2015)
3. Vidya, S., Khan, A., Kamat, S.V., Venkatesh, V.: 3D FinFET for next generation nano devices. In: *2018 International Conference on Current Trends Towards Converging Technologies (ICCTCT)* (2018). <https://doi.org/10.1109/icctct.2018.8550967>
4. Kwon, D., Chatterjee, K., Tan, A.J., Yadav, A.K., Zhou, H., Sachid, A.B., Salahuddin, S.: Improved subthreshold swing and short channel effect in FDSOI n-channel negative capacitance field effect transistors. *IEEE Electron Device Lett.* **39**(2), 300–303 (2018)
5. Gill, A., Madhu, C., Kaur, P.: Investigation of short channel effects in bulk MOSFET and SOI FinFET at 20 nm node technology. In: *2015 Annual IEEE India Conference (INDICON)* (2015). <https://doi.org/10.1109/indicon.2015.7443263>
6. Wang, M.C., Rao, Z.Y., Liu, H.Y., Tuan, F.Y., Liao, W.S., Lan, W.H.: DIBL effect gauging the integrity of nano-node n-channel FinFETs. In: *2017 6th International Symposium on Next Generation Electronics (ISNE)* (2017). <https://doi.org/10.1109/isne.2017.7968704>
7. Saxena, S., Member, S., Hess, C., Karbasi, H., Rossoni, A., Tonello, S., Mcnamara, P., Lucherini, S., Minehane, S., Dolainski, C., Quarantelli, M.: Variation in transistor performance and leakage in nano-scale technologies. *IEEE Trans. Electron Devices* **55**, 131–144 (2008)
8. Chang, R.D., Lin, P.H.: Simulation study of implantation angle variation and its impact on device performance. In: *2016 21st International Conference on Ion Implantation Technology (IIT)* (2016). <https://doi.org/10.1109/iit.2016.7882906>
9. Elgomati, H.A., Majlis, Burhanuddin Yeop, Ahmad, I., Salehuddin, F., Hamid, F.A., Zaharim, Azami, Mohamad, T.Z., Apte, P.R.: Statistical Optimization for process parameters to reduce variability of 32 nm PMOS transistor threshold voltage. *Int. J. Phys. Sci.* **6**, 2372–2379 (2011)
10. Mah, S.K., Ahmad, I., Ker, P.J., Tan, K.P., Faizah, Z.A.N.: Modeling, simulation and optimization of 14 nm high-K/metal gate NMOS with Taguchi method. In: *2018 IEEE International Conference on Semiconductor Electronics (ICSE)* (2018). <https://doi.org/10.1109/smelec.2018.8481293>
11. Noor Faizah, Z.A., Ahmad, I., Ker, P.J., Menon, P.S., Afifah Maheran, A.H.: VTH and ILEAK optimization using Taguchi method at 32 nm bilayer graphene PMOS. *J. Telecom. Electron. Comput. Eng.* **9**, 105–109 (2017)
12. Othman, N.A.F., Azhari, F.N.N., Wan Muhamad Hatta, S.F., Soin, N.: Optimization of 7 nm strained germanium FinFET design parameters using Taguchi method and Pareto analysis of variance. *ECS J. Solid State Sci. Technol.* **7**(4), 161–169 (2018)
13. Goncalves, F., Duarte, C., Alves, P.: Development of an evaluation platform for statistical characterization of MOSFET model parameters. *UPorto J. Eng.* **3**(1), 39–49 (2017). [https://doi.org/10.24840/2183-6493\\_003.001\\_0004](https://doi.org/10.24840/2183-6493_003.001_0004)

14. Saha, R., Bhowmick, B., Baishya, S.: Statistical dependence of gate metal work function on various electrical parameters for an n-channel Si step-FinFET. *IEEE Trans. Electron Devices* **64**(3), 969–976 (2017). <https://doi.org/10.1109/ted.2017.2657233>
15. Mei, S., Raghavan, N., Bosman, M., Pey, K.L.: Stochastic modeling of FinFET degradation based on a resistor network embedded metropolis Monte Carlo method. *IEEE Trans. Electron Devices* **65**, 440–447 (2018). <https://doi.org/10.1109/ted.2017.2785041>
16. Salehuddin, F., Zain, A.S.M., Idris, N.M., Yamin, A.K.M., Hamid, A.M.A., Ahmad, I., Menon, P.S.: Analysis of threshold voltage variance in 45 nm N-channel device using L27 orthogonal array method. *Adv. Mater. Res.* **903**, 297–302 (2014)
17. Kaharudin, K.E., Salehuddin, F., Zain, A.S.M., Aziz, M.N.I.A.: Taguchi modelling with the interaction test for higher drive current in WSix/TiO<sub>2</sub> channel vertical double gate NMOS device. *J. Theor. Appl. Inf. Technol.* **90**, 185–193 (2016)
18. Kaharudin, K.E., Hamidon, A.H., Salehuddin, F.: Design and optimization approaches in double gate device architecture. *Int. J. Eng. Technol.* **6**, 6 (2014)
19. Kaharudin, K.E., Salehuddin, F., Zain, A.S.M., Aziz, M.N.I.A.: Impact of different dose, energy and tilt angle in source/drain implantation for vertical double gate PMOS device. *J. Telecommun. Electron. Comput. Eng.* **8**, 23 (2016)
20. Montgomery, D.: Design and analysis of experiments. In: *Blocking and Confounding in the 2k Factorial Design*, 9th edn., pp. 306–344. Wiley, New York (2017)
21. Salehuddin, F., Kaharudin, K.E., Elgomati, H.A., Ahmad, I., Apte, P.R., Nopiah, Z.M., Zaharim, A.: Comparison of 2k-factorial and Taguchi method for optimization approach in 32 nm NMOS device. In: *Mathematical Methods and Optimization Techniques in Engineering*, pp. 125–134 (2013)



# Energy Consumption Clustering Analysis in Residential Building

Muhammad Aiman Razak<sup>1</sup>, Fitri Yakub<sup>1(✉)</sup>,  
Nur Najwa Izzati Sulaiman<sup>1</sup>, Mohd Zamzuri Ab. Rashid<sup>1,2(✉)</sup>,  
Sheikh Ahmad Zaki Shaikh Salim<sup>1</sup>, Zainudin A. Rasid<sup>3</sup>,  
and Aminudin Abu<sup>3</sup>

- <sup>1</sup> Wind Engineering for (Urban, Artificial, Man-Made) Environment Laboratory,  
Malaysia-Japan International Institute of Technology (MJIT),  
University Teknologi Malaysia,  
Jalan Sultan Yahya Petra, 54100 Kuala Lumpur, Malaysia  
mfitri.kl@utm.my, zamzuri@utem.edu.my
- <sup>2</sup> Centre for Robotics and Industrial Automation,  
Fakulti Kejuruteraan Elektrik Universiti Teknikal Malaysia Melaka,  
76100 Durian Tunggal, Melaka, Malaysia
- <sup>3</sup> Intelligent Dynamic System Laboratory,  
Malaysia-Japan International Institute of Technology (MJIT),  
University Teknologi Malaysia,  
Jalan Sultan Yahya Petra, 54100 Kuala Lumpur, Malaysia

**Abstract.** Demand for electricity has been rapidly increasing in the residential sector as it is one of the necessities proportional to the increase in human population. However, most of the occupants less aware on how to use energy efficiently. The major factors that contribute to the energy consumption in residential buildings consumption are due to occupant's activities and their lifestyle. Some of the occupants also not realize that they have used the electrical energy inefficiently because they utilize inefficient household appliances. As a result, inefficient energy has caused waste of energy. Waste of electrical energy will not only impact the costs of processing energy resources; it also impacts our environment. In order to save the electricity, we have to improve the energy efficiency by conserving or improving the efficiency. By improving the efficiency, the consumer should be able to know the household appliances that use high power consumption via their electrical appliances. The main aim of this project is to implement the clustering techniques to the measured data and to determine the most energy usage in home appliances using MATLAB simulation. In order to determine the number of cluster data for household appliances, the measured data will go through certain techniques that usually being used in clustering.

**Keywords:** Energy consumption · MATLAB · Residential building · Household appliance · Clustering

## 1 Introduction

An increased number of development project in residential area has makes a great impact on national developments and increase the energy demand. Negative impacts can be reduced by making energy household more energy efficient. Various resources have been used to generate electricity such as hydroelectric, natural gases, wind generators, nuclear, coal, oil, tidal power, solar energy and geothermal sources. With the varieties of resources, the electricity can be generated and distributed to the entire nation. Despite that, it has risen the environmental concern as it is affecting the environment. The cleanliness of electricity depends on its source. For example, fossil fuel-based electricity generation released emissions of pollutants and greenhouse gases which contribute the significant portion to the world greenhouse gas emissions and CO<sub>2</sub>. By improving the efficiency, the consumer should be able to know the household appliances that use high power consumption via their electrical appliances.

An energy usage profile is a time-series data that can reveal a lot about energy efficiency. Clustering can be used to build the energy usage profile. It has the ability to measure the similarity between the data sets and group them based on energy usage by using clustering technique. The data can be organized into homogenous groups, maximizing the similarity and dissimilarity within and between a group. Clustering also allows us to compare and contrast the similar energy usage tendencies and find a way to improve the energy efficiency [1]. So, the consumer is aware of their energy usage and reduce it efficiently.

The major factors that contribute to the energy consumption in residential buildings consumption are due to occupant's activities and their lifestyle. The longer the occupants stay indoors, a lot of energy goes to waste. According to Chakraborty [2] between 2 to 20% of the 40% of energy consumed by buildings is misused through ineffective appliances. This refers to electricity leakage consuming energy without achieving the principal. The increase of energy consumption in the residential building is due to the economic status of the occupants.

In order to determine the number of cluster data for household appliances, the sampled data will go through certain techniques before we applied the techniques on real data to determine the most energy usage in home appliances using MATLAB simulation. The aim of this project is:

1. To develop clustering group using clustering techniques from the measured data
2. To develop energy usage profile

Data measurement of electrical energy for each household appliances such as air conditioner, heater, iron and etc. are collected from 20 houses in PPR Desa Rejang. The data from each house has been measured within 1 year from March 2016 until August 2017. All the associated coding and simulation will be used on MATLAB for clustering purpose. This project is to help the occupants to reduce their monthly energy consumption and save the energy by reducing the electricity on specific home appliances for energy efficient purpose. The measured data used for the clustering technique is hourly power and energy consumption data.

## 2 Motivation

This section will start with a concept of the machine learning. For better understanding, the types of machine learning and categories of algorithms in machine learning will be discussed before we focused on the clustering approach and techniques used. The method that is used to analyze the data will be explained in this chapter.

### 2.1 Machine Learning

Machine learning is a way to make computer create a program that can deal with problems without programming. It makes the computer learn something from the data. There are different types of task in machine learning such as is supervised learning, unsupervised learning, semi-supervised learning. Conventionally, there are two different types in machine learning which is supervised learning and unsupervised learning [3] (Fig. 1).

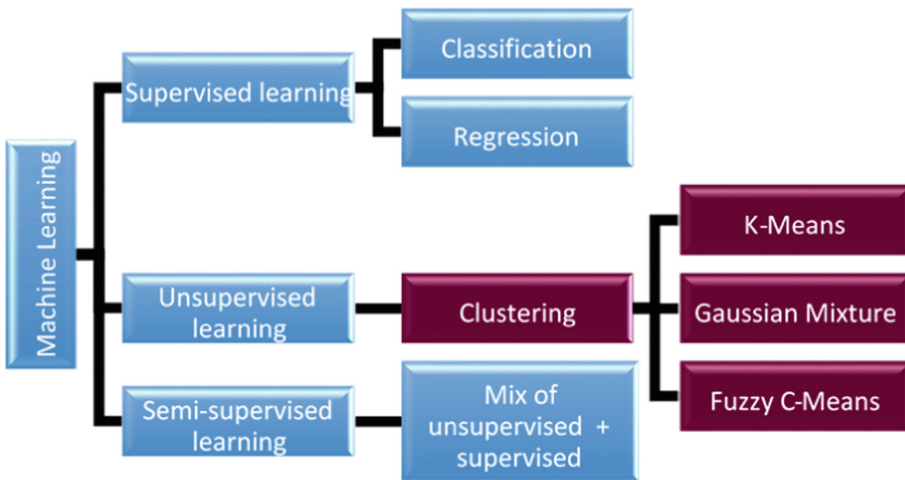


Fig. 1. Types of machine learning

Supervised learning is where the algorithms learn to predict the output from the input data. Supervised learning has two categories of algorithms, classification, and regression. For unsupervised learning, it has only one category of algorithms which is clustering (Fig. 2).



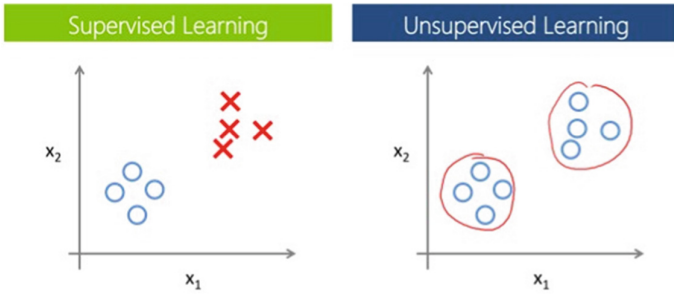


Fig. 2. Supervised and unsupervised learning

Recently, semi-supervised learning is introduced to the world. Semi-supervised learning is a mixing of supervised learning and unsupervised learning. Some of the data is labelled but most of it is unlabelled. The learning is based on assumption. The boundary of each cluster from unlabelled data can be find more accurately. For example, one unlabelled data can run the clustering algorithm and used labelled points to assign a class to each cluster. Based on the assumption, if the points are in the same cluster, they are likely in the same class. Then, unsupervised learning technique can be used to discover and learn the structure of input variable.

### 2.2 Classification

Classification is a process of classifying something according to shared qualities of characterization by trying to predict a discrete number of values. The common algorithms that are usually used in classification are Support Vector Machines (SVM), Naive-Bayes, and discriminant analysis (Fig. 3).

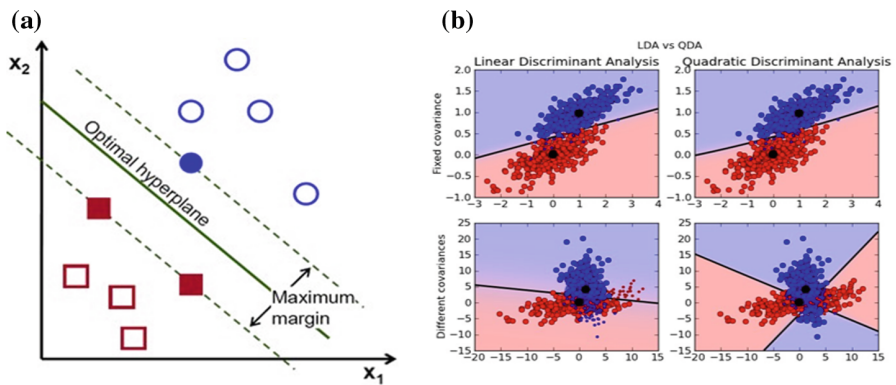


Fig. 3. (a) Support vector machines [4] (b) discriminant analysis [5]

A classification is a form of data analysis that extracts models describing important data classes [6]. Classification is known as supervised learning because of the training data a class label information is given. In data, classification has 2 step process, consisting of training step and classification step [7]. During learning the step, classification algorithm needs a training dataset from the main data to learn and determine class label. Then, the training dataset is later used to predict the classifier label. The test set is used for later to the real dataset for prediction purposes.

Classification and prediction techniques usually used for data mining research as it has the capability to process a large amount of data. There are numerous applications that used classification approach, including performance prediction, manufacturing and medical diagnosis.

### 2.3 Regression

Another category of supervised learning is a regression. In regression, we focus on predicting the continuous-valued output. The common algorithms used in the regression are linear regression and neural network (Fig. 4).

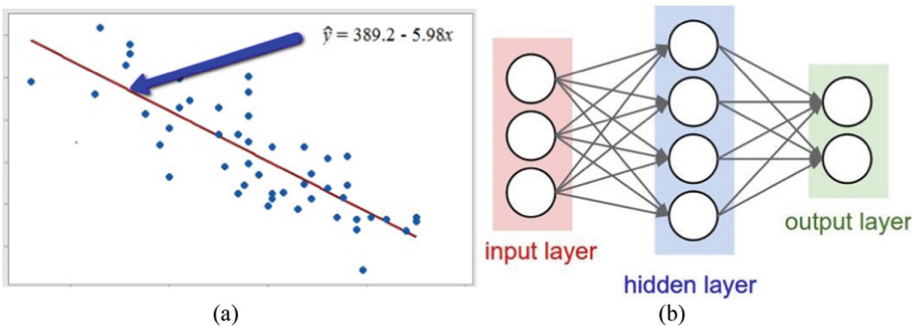


Fig. 4. (a) Linear regression [8] and (b) neural network [9]

### 2.4 Clustering

Data mining technology is used to identify patterns and trends of a large volume of data. A different approach has been used to extract these unknown raw data set which is widely used for business and real-time application. All of these data set will be classified and clustered using clustering analysis. Unlike classification, the class label for each dataset is unknown. Clustering is also known as supervised learning as its class label information are not provided. Other than that, clustering is a form of learning by observation, rather than learning by examples.

Classification is a process of grouping a set of data into multiple groups or clusters so that the objects within the cluster have high similarity, but very dissimilar to objects in other clusters. Dissimilarities and similarities are assessed based on the attribute values describing the objects and distance measure. Clustering is widely applied as data mining tool in biology, security, business intelligence and Web search. There are

various clustering techniques that can be applied to data analysis such as partitioning method, hierarchical method, density-based methods and grid-based methods. Each subset is a cluster where objects in a cluster are similar to one another, and yet dissimilar to the objects in another cluster [10]. In addition, the set of clusters is called clustering. Different clustering method will produce different clustering even in the same dataset. The clustering algorithms will produce partitioning between clusters. Cluster analysis can be used to observe the characteristics of each cluster and focus on particular set of clusters for further analysis.

Sometimes, clustering is called automatic classification because it can automatically find the groupings. It is also called data segmentation as it partitions large data set into groups according to their similarity. One of the reasons that clustering approach is chosen is due to its ability to analyse the large unlabelled dataset. However, for clustering, it is hard to provide a crisp categorization because the categories may overlap, and it may have the features from several categories.

## 2.5 Partitioning Method

In partitioning method, each object must belong to exactly one group. Most partitioning methods are distance-based. The examples of approaches that are usually used in partitioning method are the k-means and the k-medoids. This method works well for finding spherical-shaped cluster for small to medium-size databases. However, this method needs to be extended if we want to cluster a very large data [11] (Fig. 5).

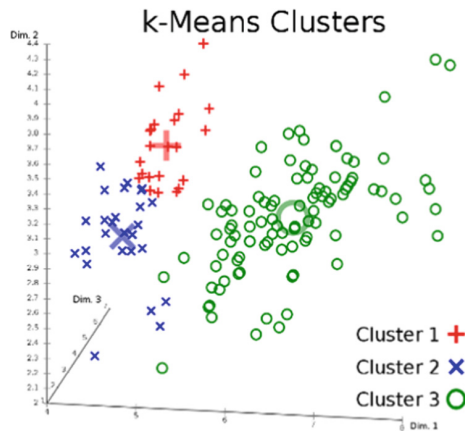


Fig. 5. K-means [12]

## 3 Research Methodology

In this chapter, the data that has been measured is tested to figure out which techniques is suitable for the objective of this project. In order to identify the cluster, box plot is plotted to show the visual representation of the data. Then, the measured data will be

used as the data points to produce the clustering results. Based on boxplot, we can determine the number of clusters from the data point using MATLAB implementation. In this chapter, the focus will be on Fuzzy C-Means clustering algorithm, K-Means clustering algorithm and Gaussian Mixture Model clustering algorithm to test the sampled data and later, the techniques are applied as mentioned above to the measured data. The results obtained from the techniques are described in the next chapter (Fig. 6).

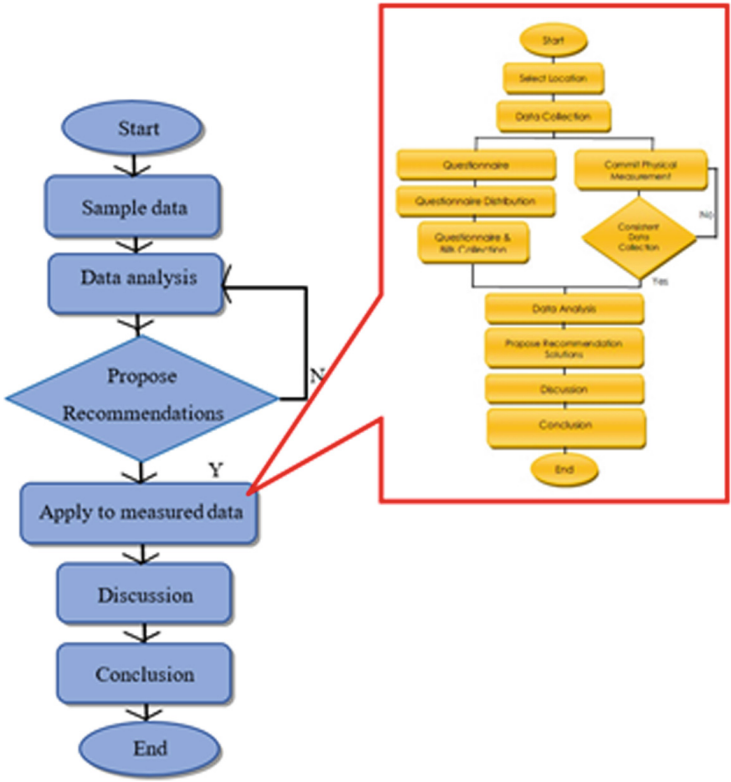


Fig. 6. Flowchart of study

### 3.1 Fuzzy C-Means Clustering Algorithm

As a start, this project plots the measured data into boxplot to represent the data, to determine the number of clustering, implemented the clustering technique and simulated using MATLAB. The data involved in this project is hourly power and electricity energy consumption for each house. To produce clustering results, FCM clustering algorithm is used as clustering algorithm because the number of clustering is not known. The algorithm relies on the user to specify the number of clusters present in the set of data to be clustered. The popularity and usefulness of fuzzy C-means result from

three facts. The algorithms are simple; they are very effective at efficiently finding minimisers of objective function: give dataset [13].

$$X = \{x_1, x_2, \dots, x_n\} \quad (1)$$

The algorithms work by assigning membership to each data points corresponding to each cluster center due to the distance between cluster center and data point. The nearer the distance of data to the cluster center, the more the membership to the particular cluster center. After each iteration membership and cluster center will be updated according to the formula.

$$\mu_{ij} = \frac{1}{\sum_{k=1}^c \left(\frac{d_{ij}}{d_{ik}}\right)^{\left(\frac{2}{m}-1\right)}} \quad (2)$$

$$v_j = \left(\frac{\sum_{i=1}^n (\mu_{ij})^m x_i}{\sum_{i=1}^n (\mu_{ij})^m}\right), V_j = 1, 2, \dots, c \quad (3)$$

where,  $n$  is the number of data,  $v$  represents the  $j^{th}$  cluster center,  $m$  is the fuzziness index  $m \in [1, \infty]$ ,  $c$  represents the number of clusters center,  $\mu_{ij}$  represents the membership of  $i^{th}$  data to  $j^{th}$  cluster center,  $d_{ij}$  represents the Euclidean distance between  $i^{th}$  data and  $j^{th}$  cluster center.

The main objective of fuzzy c-means algorithm to minimize the objective function:

$$J(U, V) = \sum_{i=1}^N \sum_{j=1}^c (\mu_{ij})^m \|x_i - v_j\|^2 \quad (4)$$

where,  $\|x_i - v_j\|$  is the Euclidean distance between  $i^{th}$  data and  $j^{th}$  cluster center.

### 3.2 Gaussian Mixture Model Clustering Algorithm

One of the clustering that is often used for clustering is Gaussian Mixture Models (GMM). It clustered by assign the data points and represents it in the probability density function. The mixture models use an Expectation Maximization (EM) algorithm to assigns the posterior probabilities to each density with respect to each observation. The clusters can be determined by maximized the probabilities. The probabilities indicate the probability of belonging for each cluster. To converge a local optimum, an iterative algorithm is used.

Algorithmic Step for Expectation Minimization (EM) Clustering.

Let  $X = \{x_1, x_2, x_3, \dots, x_n\}$  be the set of data points,  $V = \{\mu_1, \mu_2, \mu_3, \dots, \mu_c\}$  be the set of means of Gaussian and  $P = \{p_1, p_2, p_3, \dots, p_c\}$  be the set of probability of occurrence of each Gaussian.

1. Initialization  $i^{th}$  iteration.

$$\lambda_t = \left\{ \begin{array}{l} \mu_1(t), \mu_2(t), \dots, \mu_c(t), \sum_1(t), \\ \sum_2(t), \sum_c(t), p_1(t), p_2(t), \dots, p_c(t) \end{array} \right. \quad (5)$$

E-step

2. The ‘expected’ classes of all data points for each class is computed using:

$$\begin{aligned} P(w_i|x_k, \lambda_t) &= \frac{P(x_k|w_i, \lambda_t)P(w_i|\lambda_t)}{P(x_i, \lambda_t)} \\ &= \frac{p(x_k|w_i, \mu_i(t), \sum_i(t))p_i(t)}{\sum_{j=1}^c p(x_k|w_j, \mu_j(t), \sum_j(t))p_j(t)} \end{aligned} \quad (6)$$

M-step

3. The ‘maximum likelihood  $\mu$ ’ of given data class membership distribution is computed using:

$$\begin{aligned} \mu_i(t+1) &= \frac{\sum_k (w_i|x_k, \lambda_t)x_k}{\sum_k (w_i|x_k, \lambda_t)}, p_i(t+1) \\ &= \frac{\sum_k p(w_i|x_k, \lambda_t)}{R} \end{aligned} \quad (7)$$

where, ‘R’ is the number of data points.

## 4 Result and Discussion

In this chapter, the result for each clustering technique is shown and further discussed. In this chapter also the results of all clustering techniques are further discussed and explained. A summary of comparison between each clustering techniques with the manual clustering will be discussed later in this chapter.

### 4.1 Research Scenario

The hourly power and energy data consumption has been measured and collected from 19 houses in PPR Desa Rejang starting from March 2016 until August 2017. Each energy and power consumption data for each house has been monitored, measured and labelled as D1 until D19 (19 houses). The details of the houses and duration of measured data for energy and power consumption data has been summarized on the Table 1 below (Fig. 7).

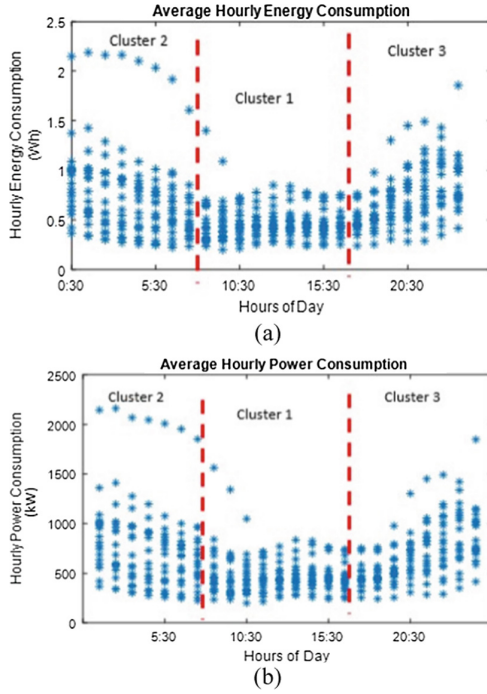
**Table 1.** Details of the duration of measured energy and power consumption

Houses	Duration
D1, D2, D3, D4, D7	March 2016 – June 2016
D5	March 2016 – May 2016
D6	March 2016 – April 2016
D8, D9	March 2016 – November 2016
D10	May 2016 – November 2016
D11	August 2016 – January 2017
D12, D15	August 2016 – November 2016
D13, D14, D16, D17, D18	August 2016 – August 2017
D19	September 2016 – August 2017

**Fig. 7.** PPR Desa Rejang

## 4.2 Clustering Analysis

Before proceeds with the clustering techniques, the measured data has been averaged and plot into a scattered graph. It is used to review the overall data and predicts the clusters boundary and also the number of clusters. The results for each of clustering technique for FCM, K-Means and GMM are shown in different graph below to show the similarities and differences for each of the techniques used. The results are shown below (Fig. 8):

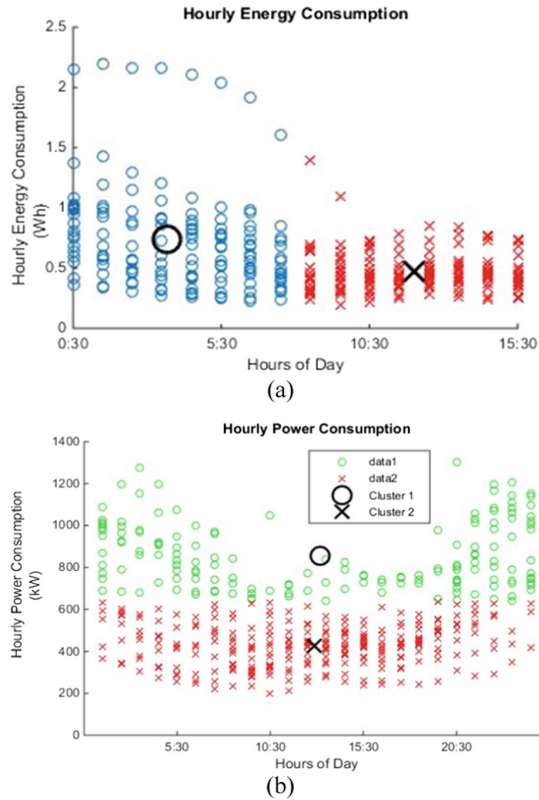


**Fig. 8.** Average of hour (a) energy and (b) power consumption in scattered graph

### 4.3 Fuzzy C-Mean Analysis

Based on the clustering plot using Fuzzy C-Means in Fig. 9, cluster group are divided in two group where cluster 1 represents the highest energy consumption started from 0.30 am until 7.30 am, while cluster 2 represents the lowest energy consumption within 24 h. The orientation of clustering group is different in hourly power consumption, but the representation for each cluster is nearly the same as in hourly energy consumption.





**Fig. 9.** Average of hourly (a) energy and (b) power consumption using fuzzy c-means

#### 4.4 K-Means Clustering Analysis

The plot using K-Means clustering technique in Fig. 10(a) shows that cluster 2 in the left plot is completely separated from the other two clusters. Cluster 1 contains the lowest energy consumptions 9.30 am until 16.30 pm. Cluster 3 is in the right is the medium energy consumption within 24 h while cluster 2 is the highest energy usage starts from 0.30 am until 8.30 am. Meanwhile in Fig. 10(b), the clustering analysis of power usage is different due to the iterations. Cluster 1 is in lower plot, cluster 2 is at the center of the plot and cluster 3 is at the upper plot. It clearly shown that each cluster represent the highest and lowest power usage for every hour within 24 h each house.

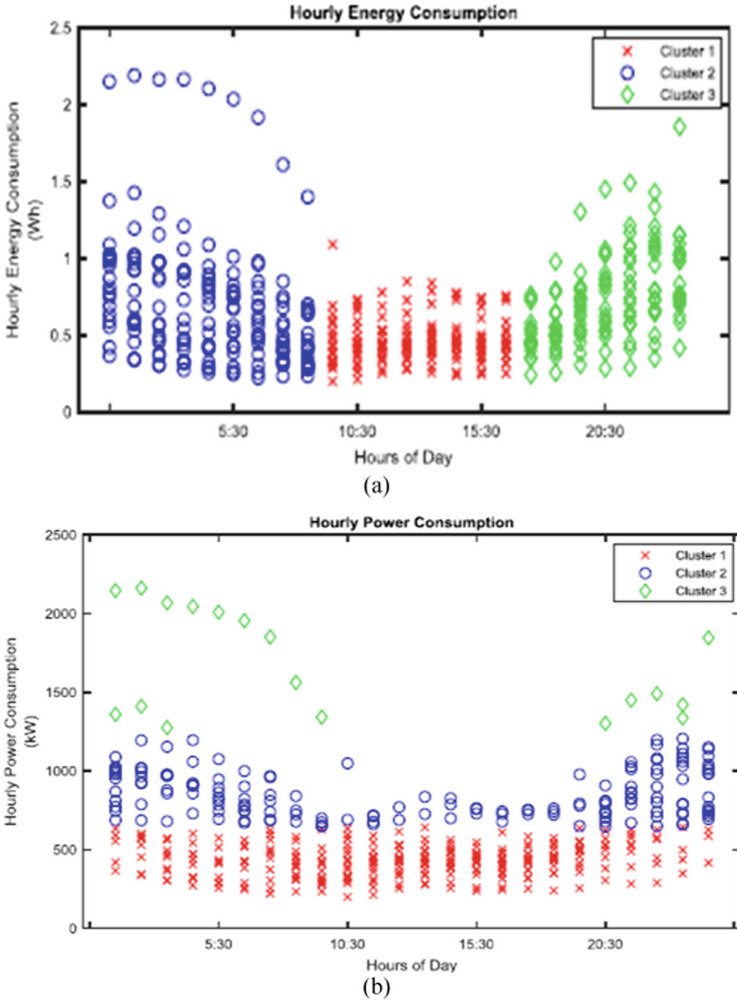
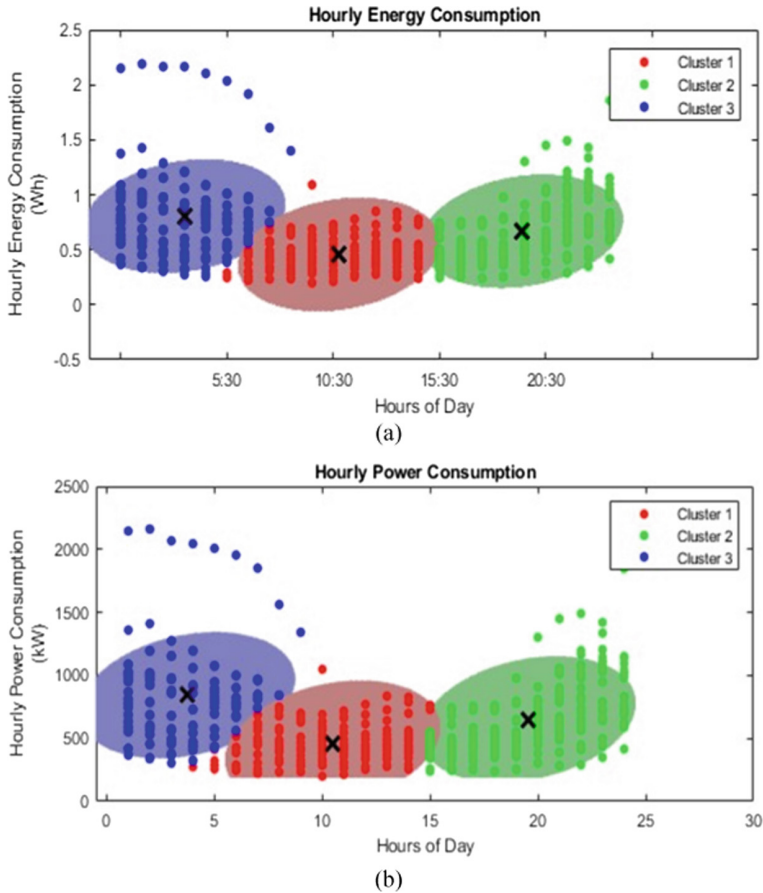


Fig. 10. Average of hourly (a) energy and (b) power consumption using k-means

### 4.5 Gaussian Mixture Model Analysis

Gaussian Mixture Model clustering technique for energy and power consumption has shown the same results for both plots. The clustering group has been divided into three groups that shows lowest, medium and highest energy and power usage which is as the same as other two clustering technique as shown in Fig. 11.

Based on results in Fig. 11, we can conclude that the least energy consumption that being used by occupants is between 10:30 am until 17:30 pm while the highest energy consumption is between 0:30 am until 9:30 am. When comparing all of the three clusters, it shows that GMM is more accurate and flexible as it can be assigning the data point to exactly one cluster called hard clustering or assign it to be more than one



**Fig. 11.** Average of hourly (a) energy and (b) power consumption using gaussian mixture model

cluster called soft clustering. Other than that, compared to other clustering technique, GMMs appear to be the most appropriate clustering technique to use as it can accommodate the clusters from different sizes and correlation structures within them.

## 5 Conclusion

In a nutshell, the objective for this project is to develop the clustering group using clustering analysis techniques from the hourly measured power and energy data consumption is successfully achieved through FCM, K-Means and GMM. After various clustering method has been applied to the measured data, can be concluded that the most accurate clustering method for this research is Gaussian Mixture Model. It has been proved that GMMs has abilities to accommodate the clusters from different sizes

and correlation structures within them and also its flexibility to assign more clustering groups. In energy and power usage, finally prove that one of the factors that contribute to the high energy and power consumption is the inefficient energy usage and also the activities that occupants do in the house.

## References

1. Rahman, A., Rahman, K.A., Leman, A.M., Mubin, M.F., Yusof, M.Z.M., Hariri, A., Salleh, M.N.M.: Energy consumption analysis based on energy efficiency approach: a case of suburban area. In: International UNIMAS STEM 9th Engineering Conference 2016, 2003 (2016). <https://doi.org/10.1051/mateconf/20178702003>
2. Chakraborty, A., Pfaelzer, A.: An overview of standby power management in electrical and electronic power devices and appliances to improve the overall energy efficiency in creating a green world. *J. Renew. Sustain. Energy* **3**(2), 023112 (2011). <https://doi.org/10.1063/1.3558870>
3. Ghiassi, N., Mahdavi, A.: Reductive bottom-up urban energy computing supported by multivariate cluster analysis. *Energy Build.* **144**, 372–386 (2017). <https://doi.org/10.1016/j.enbuild.2017.03.004>
4. Zhang, G., Wang, G.G., Farhangi, H., Palizban, A.: Data mining of smart meters for load category based disaggregation of residential power consumption. *Sustain. Energy Grids Netw.* **10**, 92–103 (2017). <https://doi.org/10.1016/j.segan.2017.03.006>
5. Chévez, P., Barbero, B., Martini, I., Discoli, C.: Application of the K-Means clustering method for the detection and analysis of areas of homogeneous residential electricity consumption at the Great La Plata Region, Buenos Aires, Argentina. *Sustain. Cities Soc.* **32**, 115–129 (2017). <https://doi.org/10.1016/j.scs.2017.03.019>
6. Diao, L., Sun, Y., Chen, Z., Chena, J.: Modeling energy consumption in residential buildings: a bottom-up analysis based on occupant behavior pattern clustering and stochastic simulation. *Energy Build.* **147**, 47–66 (2017). <https://doi.org/10.1016/j.enbuild.2017.04.072>
7. Nilashi, M., Dalvi-Esfahanic, M., Ibrahima, C., Bagherifard, K., Mardanie, A., Zakuan, N.: A soft computing method for the prediction of energy performance of residential buildings. *Measurement* **109**, 268–280 (2017). <https://doi.org/10.1016/j.measurement.2017.05.048>
8. Wang, E.: Decomposing core energy factor structure of U.S. residential buildings through principal component analysis with variable clustering on high-dimensional mixed data. *Appl. Energy* **203**, 858–873 (2017). <https://doi.org/10.1016/j.apenergy.2017.06.105>
9. Zadeh, L.A.: Fuzzy sets. *Inf. Control* **8**(3), 338–353 (1965)
10. Nilashi, M., Ibrahim, O.B.: A model for detecting customer level intentions to purchase in B2C websites using TOPSIS and fuzzy logic rule-based system. *Arab. J. Sci. Eng.* **39**(3), 1907–1922 (2014)
11. Nilashi, M., Ibrahim, O., Ithnin, N.: Hybrid recommendation approaches for multi-criteria collaborative filtering. *Expert Syst. Appl.* **41**(8), 3879–3900 (2014)
12. Farokhi, N., Vahid, M., Nilashi, M., Ibrahim, O.: A multi-criteria recommender system for tourism using fuzzy approach. *J. Soft Comput. Decis. Support Syst.* **3**(4), 19–29 (2016)
13. Nilashi, M.: An overview of data mining techniques in recommender systems. *J. Soft Comput. Decis. Support Syst.* **3**(6), 16–44 (2016)
14. Lavin, A., Klabjan, D.: Clustering time-series energy data from smart meters. *Energy Effic.* **8**(4), 681–689 (2014). <https://doi.org/10.1007/s12053-0149316-0>



# The Power Level Control of a Pressurised Water Reactor Nuclear Power Plant

Jothi Letchumy Mahendra Kumar, Anwar P. P. Abdul Majeed<sup>(✉)</sup>,  
Muhammad Aizzat Zakaria, Mohd Azraai Mohd Razman,  
and Mohd Ismail Khairuddin

Innovative Manufacturing, Mechatronics and Sports Laboratory,  
Universiti Malaysia Pahang, 26600 Pekan, Pahang Darul Makmur, Malaysia  
ama.jeed@ump.edu.my

**Abstract.** The control system of a reactor core in a Nuclear Power Plant (NPP) is non-trivial to ensure safe operation of a nuclear power plant. Owing to the complex and non-linear characteristics of a nuclear power plant, it is, therefore, essential to control the power in load following condition through the regulation of the reactor core. The aim of this paper is to evaluate the efficacy of different variation of classical control schemes, namely, P, PI, PD and PID to control the power level output. The reactor core model is based on the H.B. Robinson Pressurised Water Reactor NPP. The control schemes evaluated were tuned based on the Ziegler-Nichols tuning method. It was demonstrated through the following simulation investigation that the PID control scheme is appropriate in regulating the power level.

**Keywords:** Pressurized water reactor · Reactor core · PID controller

## 1 Introduction

In order to address the 2 Degree Scenario (2DS) and to actively ratify the United Nations Sustainable Development Goals (UNSDG), particularly goal 13 on climate action, the role of Nuclear Power Plants (NPPs) is non-trivial [1]. Nuclear power along with other relevant technologies can generate energy which provides high living standards, a clean atmosphere as well as a viable economy. Moreover, nuclear power has been demonstrated over the years that it yields significantly lower greenhouse gas (GHG) discharges as compared energy generated from fossil technologies [2, 3], suggesting its sustainability and its ability in mitigating the 2DS.

The general working principle of an NPP is that continuous fission process of the atoms in the nuclear fuel produces heat that in turn generates steam that drives the turbine of a generator [4]. This process eventually produces electricity. To date, there are more than 440 NPPs globally, in which approximately 60% of it are pressurised water reactors (PWRs) [5]. PWRs use light water for neutron moderation and reactor heat removal. The water inside the primary cooling circuit of a PWR is under high pressure does not convert into steam even under elevated temperature. The primary circuit and the secondary circuit are completely separated, and heat generated will be

transferred from the primary circuit to the secondary circuit. These reactors often utilise Uranium 235 (U235) as its fuel [6].

Nonetheless, it is worth noting that an NPP is a complex and nonlinear system. Owing to its intricate characteristics, it is difficult and challenging to control the power and temperature of the nuclear reactor. In addition, it gets more arduous in the event there is a wide range of power fluctuation that transpires in load-following conditions. Hitherto, researchers have attempted in modelling the reactor core by means of different approaches [1]. It is worth noting that one of the approaches that has been extensively used is the the point kinetic modelling owing to its ability in capturing the dynamics of the model as well as to its simplicity. Through this approach, the nuclear reactor is modelled through point kinetics model with six groups of delayed neutrons and two thermal feedbacks due to the effect of both the fuel and coolant temperature [7].

Different types of control schemes have been investigated over the past few decades. Nevertheless, amongst the control schemes, the Proportional–Integral–Derivative controller is one of the most widely used in the NPP industry primarily owing to its simplicity and robust performance [8]. This paper shall investigate the efficacy of the various configuration of the classical PID control scheme, i.e., P, PI, PI and PID in controlling the power lever of a PWR NPP modelled based on the R.H. Robinson NPP. A point kinetic modelling technique is used in which a linearised plant model is attained.

## 2 System Modelling

The reactor core model is modelled based on the point kinetic equations with six groups of delayed neutrons. This model is often used to construct PWR core models at the full power level. It is worth noting that it is the simplest model to be used without losing any generality. This linearised equation is formed based on H.B. Robinson NPP that produces 2200 MWth at full power [9]. The reactor model may be expressed in the transfer function form with respect to its core reactivity ( $\Delta\rho$ ) and power ( $\Delta P$ ) as shown in Eq. (1) below [10].

$$G(s) = \frac{\Delta P}{\Delta\rho} = \frac{12500s^3 + 18540s^2 + 5640s + 413}{s^4 + 401.4s^3 + 589s^2 + 198s + 18} \quad (1)$$

## 3 Control Schemes

The control schemes that will be used to control the PWR NPP power level as previously mentioned are the Proportional (P), Proportional-Integral (PI), Proportional-Derivative (PD), Proportional-Integral-Derivative (PID) classical control schemes, respectively. The generalised PID control scheme is given by the Eq. (2), where the  $K_p$ ,  $K_i$  and  $K_d$ , are the control gains which are tuned based on the Ziegler-Nichols (Z-N) formulation in frequency response as per Eq. (3). The proportional, integral time and derivative time gains are given by  $K_p$ ,  $T_i$  and  $T_d$ , respectively. The overall system is

evaluated on the MATLAB Simulink platform (Fig. 1). Table 1 lists the gains computed via the aforesaid formulation.

$$u(t) = K_p e(t) + K_i \int_0^t e(t) dt + K_d \frac{d}{dt} e(t) \tag{2}$$

$$D_c(s) = K_p \left( 1 + \frac{1}{T_i s} + T_d s \right) \tag{3}$$

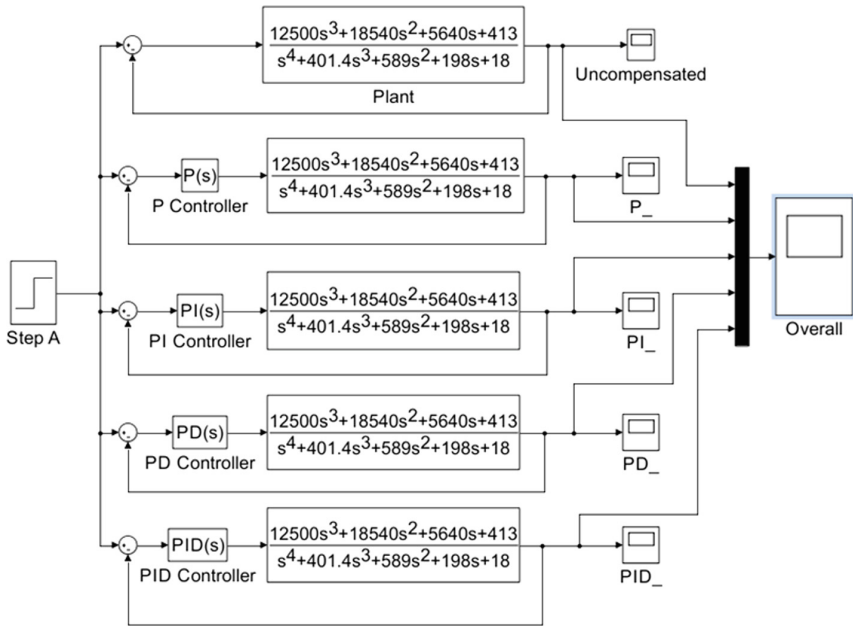


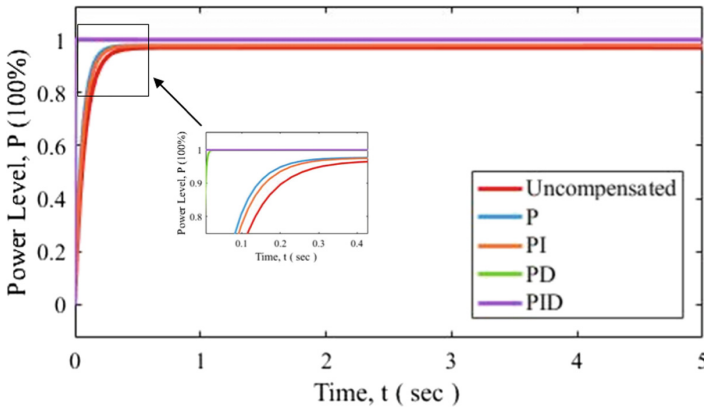
Fig. 1. The Simulink block of the evaluated schemes on the NPP reactor model

### 4 Results and Discussion

Figure 2 depicts the comparison of the control schemes tuned via the Z-N method. The systems were excited through step response that mimics the reactivity of the control rod motion at 100%. The transient performance of the control schemes evaluated are tabulated in Table 2. It could be seen from the table that the PID control scheme is able to achieve a desirable zero steady state error that is much desired in an NPP [10]. It is also apparent that the PID scheme has a much faster rise time against other controllers. In addition, it is also evident that the PID scheme settles much faster in comparison to the other control schemes evaluated, that in turn, suggesting that the initial larger overshoot yielded by the PID scheme does not affect much the performance of the

**Table 1.** Controller gains obtained via the Z-N method

Controller	$K_p$	$T_i$	$T_d$
P	1.37908	N/A	N/A
PI	1.24117	18.6	N/A
PD	1.65489	N/A	1.65
PID	1.65489	1.0039	1.0009



**Fig. 2.** The performance to the classical control schemes against the uncompensated system

**Table 2.** The transient response performance of the control schemes evaluated

Controller	Maximum overshoot (%)	Rise time (s)	Settling time (s)	Steady state error
Uncompensated	0.0000	0.1712	0.3049	0.0308
Compensated with P	0.0000	0.1250	0.2236	0.0224
Compensated with PI	0.0000	0.1394	0.2507	0.0230
Compensated with PD	0.0264	0.0064	0.0115	0.0012
Compensated with PID	0.0292	0.0011	0.0019	0.0000

system. It is noteworthy to mention that the PD scheme does also provide a reasonably good transient response, suggesting its efficacy in load trajectory tracking.



## 5 Conclusion

The study evaluated different configuration of the classical PID control scheme on a linearised point reactor model that were tuned based on the Z-N approach. The plant reactor model is based on the H.B. Robinson PWR NPP. It was demonstrated from the present investigation that the PID control scheme provides the best transient response in achieving 100% power level in comparison against other classical control schemes evaluated. Future investigation will be carried out through the utilisation of optimisation techniques (for instance, Particle Swarm Optimisation, Simulated Kalman Filter, Genetic Algorithm amongst others) in further improving the performance of the present PID gains attained from the present study as it is well-known that the Z-N method provides generalised gains that are required to be further fine-tuned.

## References

1. Li, G., Wang, X., Liang, B., Li, X., Zhang, B., Zou, Y.: Modeling and control of nuclear reactor cores for electricity generation: a review of advanced technologies. *Renew. Sustain. Energy Rev.* **60**, 116–128 (2016). <https://doi.org/10.1016/j.rser.2016.01.116>
2. IAEA: Nuclear Power for Sustainable Development Booklet. International Atomic Energy Agency 1–10 (2017)
3. Lenzen, M.: Life cycle energy and greenhouse gas emissions of nuclear energy: a review. *Energy Convers. Manag.* **49**, 2178–2199 (2008). <https://doi.org/10.1016/j.enconman.2008.01.033>
4. Lamarsh, J.R., Baratta, A.J.: Introduction to Nuclear Engineering. Prentice Hall, Upper Saddle River (2001)
5. Rowinski, M.K., White, T.J., Zhao, J.: Small and medium sized reactors (SMR): a review of technology. *Renew. Sustain. Energy Rev.* **44**, 643–656 (2015)
6. Manual, R.C., Water, P., Systems, R.: Pressurized Water Reactor (PWR) Systems
7. Vadivel, M., Karthigaivel, R., Selvakumaran, S.: Control of PWR nuclear reactor power using soft computing techniques based proportional-integral-derivative design. *Int. J. Appl. Eng. Res.* **9**, 30605–30619 (2014)
8. Cammi, A., Fiorina, C., Guerrieri, C., Luzzi, L.: Dimensional effects in the modelling of MSR dynamics: moving on from simplified schemes of analysis to a multi-physics modelling approach. *Nucl. Eng. Des.* **246**, 12–26 (2012). <https://doi.org/10.1016/j.nucengdes.2011.08.002>
9. Kerlin, T.W., Katz, E.M., Thakkar, J.G., Strange, J.E.: Theoretical and Experimental Dynamic Analysis of the H. B. Robinson Nuclear Plant. *Nucl. Technol.* **30**, 299–316 (1976). <https://doi.org/10.13182/NT76-A31645>
10. Liu, C., Peng, J.F., Zhao, F.Y., Li, C.: Design and optimization of fuzzy-PID controller for the nuclear reactor power control. *Nucl. Eng. Des.* **239**, 2311–2316 (2009). <https://doi.org/10.1016/j.nucengdes.2009.07.001>



# Mesh WSN in Midstream and Downstream of Oil and Gas Industry

A. S. Azman<sup>1</sup>(✉), M. Y. Lee<sup>1</sup>, S. K. Subramaniam<sup>2</sup>, and F. S. Feroz<sup>2</sup>

<sup>1</sup> Department of Electronic and Computer Engineering,  
Fakulti Kejuruteraan Elektronik dan Kejuruteraan Komputer,  
Universiti Teknikal Malaysia Melaka, Durian Tunggal, Malaysia  
{M021820013, M021820002}@student.utem.edu.my

<sup>2</sup> Center for Telecommunication Research and Innovation (CeTRI),  
Fakulti Kejuruteraan Elektronik dan Kejuruteraan Komputer,  
Universiti Teknikal Malaysia Melaka, Durian Tunggal, Malaysia  
{siva, shahnaz}@utem.edu.my

**Abstract.** Wireless Sensor Networks (WSN) has been used in the oil and gas industry since its implementation cost is less as compared to the wired solution. WSN can be found in a wide range of applications starting from the exploration stage up to the storage and refining stages. Thenceforth, there are a lot of problems faced by past researchers. The security, robustness, energy constraint and scalability are some of the challenges and they are interrelated with each other. These problems could affect the power consumption, network lifetime or economical aspect. This paper will discuss the solution, method, and algorithm that have been proposed by the researchers in midstream and downstream of the oil and gas industry. Later, it was found that the energy conserving solution is the most focused topic and IEEE 802.15.4 standard has been used by most of the researcher.

**Keywords:** Wireless sensor network · WSN · Oil and gas · Pipeline

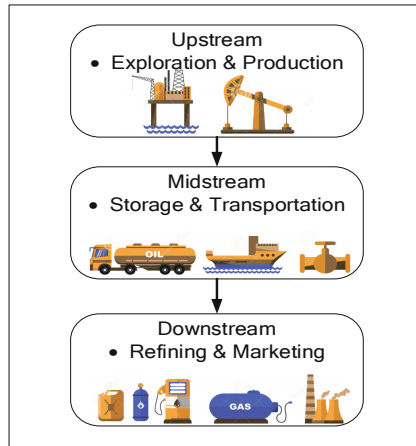
## 1 Introduction

WSN has recently become a top research focus and created new challenges for researchers. This is because it has created a wide interest from both research and industrial perspective. WSN is the cooperative network that consists of a collection of sensor nodes that collect and control the environment allowing communication between the surrounding environments with peoples or computers. WSN has been used in many applications such as intrusion detecting, medical monitoring, fish farm, air quality monitoring, agriculture, and so on [1–3]. However, the key area of this paper is in the oil and gas industry.

There are three sectors in the oil and gas industry which is upstream, midstream and downstream. Upstream is an area where the process of extracting the raw material commences. The materials commonly exist in the extreme environment location such as deserts, deep-water and underground.

Midstream is the process of storing and transporting the materials drawn from upstream to the downstream sector. The transportation medium could be via pipelines, truck, ship or rail.

Downstream sectors include the refining and marketing the final product such as petrol, diesel, cooking gas or lubricants. However, the midstream sector is also known as the downstream sector. Figure 1 shows an overview of all these three sectors.



**Fig. 1.** Sectors in the oil and gas industry

The process of exploration, transporting, refining, and so on requires critical monitoring since it involves the safety of the area and environmental issue. Hence, the need for WSN in the oil and gas industry is high.

### 1.1 Necessity of WSN in the Oil and Gas Industry in Midstream and Downstream Sectors

As known, wired communication requires a lot of processes even before the installation. It requires pre-planning and higher cost as compared to the wireless solution. It is still difficult to maintain and locate the fault in the wired system. In addition, a wired system can be easily reached and intruded by unauthorized personnel.

Therefore, there is a need for a wireless solution which is a wireless sensor network (WSN). WSN resolves the requirement of the oil and gas industry such as the need for multiple sensor deployments at the same place [1]. This is because some area needs critical monitoring such as pipeline which could corrode or leak because of the humidity or vibration that exceed the threshold [2]. The possible sensors that could be installed in the oil and gas industry are temperature, visual, acoustic, radar, magnetic, infrared and so on [1]. In pipeline transportation, the risk is bigger and has more incident history as compared to railway transportation [3].

The usage of temporary sensor contributes to the need for the WSN in the oil and gas industry. Hence, WSN can be the best option since it has better flexibility, cheaper

and shorter installation time of the sensor since the intervention of wired medium is less [4]. Most of the network device can be powered up using a battery since the network device is not power hungry [5].

The maintenance cost and time is another point to this topic. The worst case, if one node is not functioning, the other node can run as usual without interrupting the other node and in a meanwhile, the ruined node can be fixed. Hence this eliminates the need for temporary shutdown.

Apart from that, WSN is needed since there is the presence of a high number of dangerous and remote locations [1]. With WSN, the human intervention can be reduced to monitor the condition of the machinery, pipelines, wellhead and other properties or tools. However, the deployment of WSN has drawn some problems and challenges to the researchers.

## **2 Technical Challenges of WSN**

The need for WSN is very high since it helps the oil and gas industry in a variety of aspects. However, there are some challenges in WSN deployment that were discovered by the past researchers that have high potential to affect the industry.

### **2.1 Security**

The security is one of the major challenges in deploying WSN since attackers can easily intercept the radio frequency of WSN. In addition, they may able to modify or eavesdrop the WSN. There are attacks called energy exhaustion and Denial of Service (DoS) which is correlated with the vulnerability of the link layer. With the usage of WSN, it is hard to avoid the implementation of multi-hop technique but this can cause packet injection, suppression or modification attack which in turn causes the data alteration. In addition, with multi-hop technique, there is a chance of maintenance and route construction attack [6].

### **2.2 Energy Constraint**

The energy source is the main important part of WSN since it determines the network lifetime. This issue has been more prominent for the underwater WSN since it requires more power as compared to the common onshore WSN. In addition, the installation of new batteries or any power sources could risk one's life since the depth could be hundreds of meters below the sea level. Security issue can affect energy consumption as well as mentioned previously [6].

### **2.3 Robustness**

Interference such as varying large number of nodes, dynamical topological update, and energy dependence can affect the robustness in WSN based system. Robustness is important in the oil and gas industry to prevent malicious attacks and node failures.

Hence, the improved strategies of algorithm and robustness enhancing are required so that WSN based system able to withstand such risks [6].

## 2.4 Scalability

Scalability is important in WSN to increase production since the downtime will be reduced through self-healing or self-organizing technique. Scalability is the ability to maintain the network performance even the number of nodes is increasing which is also related to routing overhead, a higher density of the network, or failure detection and recovery. In addition, scalability can be affected by the vendors or different protocol issue. The underwater WSN has more scalability issue such as high packet loss due to low bandwidth, high attenuation, and low speed. Apart from that, limited memory and high power usage during packet transmission can cause the scalability issue as well [6].

## 3 Proposed Solution by Past Researchers

This section will discuss the method or solution that have been proposed by the past researchers to improve the problems that could affect the performance of the WSN. The downstream of oil and gas is the main focus of this paper. As mentioned earlier, the main challenges in WSN deployment are security, energy constraint, robustness and scalability of the WSN.

In terms of security, the network layer could be attacked through packet replication, false routing, blackhole, wormhole or sinkhole attack. Such attack could cause degradation of the wireless network and reduce the performance of the WSN. The misbehaving node indicates the presence of the attack and such node is detected with the implementation of watchdog. The authors in [7] have analyzed method which works efficiently during wormhole attack through simulation using the parameters as shown in Table 1. The promiscuous mode Ad Hoc on Demand Routing protocol (AODV) with extensions (promiscuous mode) has shown better end-to-end delay and throughput as compared to simple AODV protocol. In addition, it can prevent an attack during a robust network and can be implemented in the design of new attack barrier.

**Table 1.** Parameters used in the simulation by the authors in [7]

Parameters	Values
Standard	802.11
Number of nodes	20
Routing protocol	AODV
Packet size	1,000 bytes
Traffic generator	CBR
Grid dimension	800 m × 800 m
Propagation ground	Two-ways ground
Antenna	Omnidirectional
Queue length	50

In terms of energy consumption, the authors in [8] have proposed a gas leakage detection and smart alerting system using the Internet of Things (IoT). There are two WSN systems that were proposed by the authors which are Gas Leak Detection and Localization System through Wireless Sensor Network and Context-Adaptive Multimodal Wireless Sensor Network for Energy-Efficient Gas Monitoring. In the first system, Gas Leak Detection and Localization System through Wireless Sensor Network, the authors have implemented WSN on the moving node to detect and locate the carbon dioxide (CO<sub>2</sub>) gas leaking. The collected data will be displayed at the monitoring center as the concentration of CO<sub>2</sub> gas.

The second system as in [8] which is Context-Adaptive Multimodal Wireless Sensor Network for Energy-Efficient Gas Monitoring was developed by the authors purposely to reduce the power consumption of the nodes because the gas sensor uses a high amount of power. The node uses a pyroelectric infrared sensor and metal oxide semiconductor gas sensor which finally draw 8 $\mu$ A of sleep current. This is done by adjusting the behavior of the node and the measuring frequency of the gas concentration according to the presence of people and from the neighbor nodes. The authors highlighted that the performance of the system has followed the expectations and models after the WSN with 36 nodes has been installed in a four-story building.

The researchers in [9] have proposed a new multi-layered routing protocol namely Shortest Path Routing (SPR). The algorithm created by the researchers purposely to furnish energy effectiveness and faster handling. The researchers have simulated SPR using NS2 Underwater Sensor Network Simulation Tool (USNeT) simulator using the parameter as listed in Table 2. It was then compared with other protocols which are Vector-Based Forwarding (VBF) and Depth Based Routing (DBR). As a result, SPR has shown more energy efficient, better end-to-end delay, longer network lifetime, and better delivery ratio as compared to VBF and DBR.

**Table 2.** Parameters used in the simulation for SPR routing protocol

Parameters	Values
Grid dimension	1,000 m $\times$ 1,000 m $\times$ 300 m
Number of nodes	50
Distance between sensor node and sink node	1,500 m
Frequency	20 kHz
Bandwidth	50 Kbps
Length of the packet header	532 bytes

The authors in [10] have proposed the distributed algorithm to sense dynamic environmental phenomena with an assumption centralized server is not utilized to gather the sensors data. The sensors will self-organize and become disperse groups by choosing a few sensors as group heads (GH). The remaining sensors will accumulate themselves according to the nearest GH. There are two GH nomination algorithms introduced by the authors which are Last Group Head (LGH) and Distributed Group Head (DGH) nomination algorithm. The authors have used NS2 network simulator

using IEEE 802.15.4 to validate the experiments and analysis using parameters listed in Table 3. The results have shown that with the proposed algorithm, the power consumption of the WSN has been reduced by 54 to 66% as compared to a direct nomination algorithm. The authors have highlighted that by reducing the size of the received information, the power of reporting data can be further reduced by 33% by decreasing the size of the information of the reported phenomena.

**Table 3.** Parameters used in simulation by the authors in [10]

Parameters	Values
$E_{trans}$	1.8 $\mu$ J/byte
$E_{receive}$	2.1 $\mu$ J/byte
k	10 bytes
Number of sensor node	1,000
Number of GH node	5, 10, 50, 100, 200, 300, 500
Sensor speed	0–5 ms
$\alpha$	2

The authors in [11] have proposed an architectural model of WSN purposely to maximize the lifetime of the operating nodes and to detect the leakage or other types of damage monitoring in oil and gas pipelines. The authors have evaluated the effectiveness of the scheme of same distance placement for lifetime maximization of WSN using Tmote (802.15.4) energy model and ideal energy model. The authors concluded that the node lifetime will decrease as the number of sensor node increase based on same distance placement scheme.

The authors in [12] have used SimpliMote which is a sensor board with the algorithm to solve leak interrupt detection, network creation and specific routing of top priority data with reliability using linear topology. The novelty of the proposed solution is the data routing while labeling them into different priorities, the removal of noise for custom nodes, and enables the network to stay alive. The system was compared with Arduino-based Libelium Waspote and the results have shown that SimpliMote is two times more energy preserving, timely and reliable. This is due to the powerful microcontroller of the SimpliMote which has software interrupts and time synchronization which allows better data flow handling and responding to serious situations.

The proposed system in [13] uses JenNet network with IEEE 802.15.4 standard which operated using 2.4 GHz ISM band and supports star, linear and tree network topologies. It also has a self-healing features for robust communication. The proposed system uses three types of nodes which has been listed in Table 4. As mentioned by the authors, the wind sensor is used in the system to ease the emergency-repair workers by sending wind information such as wind direction and wind speed. The End Device has the sleep mode capability since energy consumption is the main constraint when deploying the WSN. Apart from that, the Coordinator and the Router is not programmed with the sleep mode since they must keep alive so that the data will not be missed during the data transmission.

**Table 4.** Purpose and components of each node using JN5148

Node	Purpose	Standard
Coordinator	Setting up the networks and collect wind direction and speed data	802.15.4
Router	Grant transmission of data between end devices and coordinator	
Child Node	Collect gas concentration, humidity, and temperature data	

The authors in [14] mentioned that the major issue in the underwater deployment of WSN is the robustness of the network and become worse if the deployment reaches hundred of kilometers. The capacity and heterogeneity of the sensor nodes lead to the ineffectiveness data transmission from the underwater sensor node to the surface sink node. The authors have proposed Enhanced Underwater Linear Wireless Sensor Network Deployment (EULWSND) and experimented EULWSND using parameters as in Table 5 and compared the existing data collection algorithm with the proposed algorithm using AquaSim. The proposed WSN overtakes the Dynamic Address Routing Protocol for Pipeline Monitoring (DARP-PM) which is more packet transmission with 20.5% and fewer overhead with 17.4%.

**Table 5.** Simulation parameters for the proposed routing protocol

Parameters	Values
Transport agent	UDP
Channel bandwidth	25 kHz
Number of sinks	5
Number of nodes	20–200
Dimension of the network	12,600 m × 500 m
Distance between nodes	100, 250, 400, 500 m
Maximum length of the pipeline	90,000 m
Packet size	12 bytes
Time of simulation	1,000 s

In terms of scalability, as known by many, the likelihood for the leakage or burst of the pipelines is high that it requires critical monitoring and inspection which then requires robust, low energy, and scalable mechanism. The researchers in [15] have proposed a scalable simulation and design using parameters in Table 6 by focusing the non-real-time long-distance aboveground pipelines as the main targets for the WSN to be deployed by implementing the Radio Frequency Identification (RFID) technology. The WSN operates according to the nodes where only one node is working at a time while the rest are sleeping and can be awakened up by interrupt-driven, location-based, and time-based technique. The authors have presented an improved power consumption as a result and highlighted that it can be further improved by extending the distance range between the RFID tags but unfortunately it can cause degradation.



**Table 6.** Parameters for simulation by the researchers in [15]

Parameters	Value
Total node period, T	10–70 h
Number of nodes, N	1–60
Distance between nodes	10–500 m

Apart from the solution for the challenges stated earlier, the authors in [2] have proposed an IoT based architecture which can be used in all three sectors of oil and gas which is upstream, midstream and downstream. The authors highlighted that the proposed solution is presented purposely to achieve the smallest human intervention possible in the industry. The Smart Object (SO) is used to detect any anomalous events and to detect if there is a person entering the restricted area as well as the movement of a person. The SO is equipped with the active RFID and motion sensor. Therefore, if someone illegally tries to break in, tap the power, or steal, the authorities will be notified beforehand.

The authors in [16] used Zigbee for hydrogen sulfide (H<sub>2</sub>S) gas safety monitoring system and Ultra 1000 as a gas sensor. There are four types of node that were used in the system which is Special End Node (SEN), Worker End Node (WEN), relay node and coordinator node as listed in Table 7. The proposed system must be cheap and open source as highlighted by the authors. The results obtained from the conducted experiment is 4 s of average response time which is faster than the benchmarked time response (120 s). A rechargeable battery with 250 mAh capacity of the WEN can be used up to 45 h which is about two working days.

**Table 7.** Components and purpose of respective nodes

Node	Purpose	Standard
SEN	Sensing toxic or flammable gas	802.15.4
WEN	Track and alert the worker	
Relay node	Forward packets	
Coordinator node	Act as a gateway	

Table 8 shows a summary of the findings from the past researches discussed earlier. This helps in giving a clear picture of what has been done and what not.

**Table 8.** Summary of findings from past research

Re-searchers	Proposed method	Types of re-search	IEEE Stand-ard	Improvement on				
				De-lay	Through-put	Packet Deliv-ery Ratio (PDR)	Energy consu-mption	Overh-ead
[7]	Promiscuous mode AODV	S	802.11	Yes	Yes	Yes	Yes	-
[8]	Usage of low power device and sensors	H	-	-	-	-	Yes	-
[9]	Shortest Path Routing Protocol	S	-	Yes	-	Yes	Yes	-
[10]	GH election algorithm	S	802.15.4	-	-	-	Yes	-
[11]	Equal distance placement scheme	S	802.15.4	-	-	-	Yes	-
[12]	SimpliMote accompanied with algo-rithms	S, H	802.15.4	-	-	-	Yes	-
[13]	Usage of low power device	H	802.15.4	-	-	-	Yes	Yes
[14]	EULWSND Routing Protocol	S	-	-	-	Yes	-	Yes
[15]	Mathematical modelling	S	-	-	-	-	Yes	-

S – Simulation
H - Hardware

Security
 Energy constraint

Robustness
 Scalability

## 4 Conclusion and Suggestion

WSN is widely used in a various application in the oil and gas industry mainly in mid-stream and downstream section since a long time ago and there is a variety of challenges faced by the researchers and the industry. There are a lot of improvements have been done since then in every aspect. The energy conserving technique, method or algorithm were the most popular topic for the researchers to improve on as can be seen in Table 8.

Besides, the IEEE 802.15.4 standard has been used the most by the researchers in both simulation and hardware implementation. There is no specific parameter that could be drawn as the ideal parameters for each respective solutions.

Some of the researchers have not mentioned the parameters used in their research. It is highly recommended for the researchers to show these parameters as it could be very helpful for future research. Apart from that, the future research should focus on the scalability issue since the geographical area of the oil and gas industry is wide and it needs a large number of nodes.

**Acknowledgments.** The authors would like to thank the Ministry of Higher Education - Malaysia, Universiti Teknikal Malaysia - Melaka for their support, lab facilities, sincere encouragement, and assistance.

## References

1. Akhondi, M., Carlsen, S., Asa, S.: Applications of wireless sensor networks in the oil, gas and resources industries. In: 2010 24th IEEE International Conference on Advanced Information Networking and Applications, pp. 941–948. IEEE (2010)
2. Khan, W.Z., Aalsalem, M.Y., Khan, M.K., Hossain, S.: A reliable internet of things based architecture for oil and gas industry. In: 2017 19th International Conference on Advanced Communication Technology (ICACT), pp. 705–710. IEEE (2017)
3. Green, K.P., Jackson, T.: Safety in the transportation of oil and gas: pipelines or rail? *Fraser Res. Bull.*, pp. 1–14 (2015)
4. Yu, H., Guo, M.: An efficient oil and gas pipeline monitoring systems based on wireless sensor networks. In: 2012 International Conference on Information Security and Intelligent Control, pp. 178–181. IEEE (2012)
5. Chraim, F., Erol, Y.B., Pister, K.: Wireless gas leak detection and localization. *IEEE Trans. Ind. Inform.* **12**(2), 768–779 (2016)
6. Aalsalem, M.Y., Khan, W.Z., Gharibi, W., Khan, M.K., Arshad, Q.: Wireless sensor networks in oil and gas industry: recent advances, taxonomy, requirements, and open challenges. *J. Netw. Comput. Appl.* **113**, 87–97 (2018)
7. Kaur, D., Singh, P.: Various OSI layer attacks and countermeasure to enhance the performance of WSNs during wormhole attack. *Int. J. Netw. Secur.* **5**(1), 62 (2014)
8. Imade, S., Rajmanes, P., Gavali, A., Nayakwadi, P.V.N.: Gas leakage detection and smart alerting system using IOT. *Int. J. Innov. Res. Stud.* **8**(5), 291–298 (2018)
9. Gomathi, R.M., Manickam, J.M.L.: Energy efficient shortest path routing protocol for underwater acoustic wireless sensor network. *Wirel. Pers. Commun.* **98**(1), 843–856 (2018)
10. Safia, A.A., Al Aghbari, Z., Kamel, I.: Phenomena detection in mobile wireless sensor networks. *J. Netw. Syst. Manage.* **24**(1), 92–115 (2016)
11. Monir, F., Das, S., Roychowdhury, P.: A study on wireless sensor network deployment and lifetime maximization of wireless sensor nodes in natural gas pipeline monitoring system. *J. Commun. Eng. Syst.* **6**(3), 1–10 (2016)
12. Ali, S., et al.: SimpliMote : a wireless sensor network monitoring platform for oil a gas pipelines. *IEEE Syst. J.* **12**(1), 778–789 (2016)
13. Guo, X., Wang, Y., Wei, X.: Design of WSN-based environment monitoring system on repair of gas leakage. In: The 27th Chinese Control and Decision Conference (2015 CCDC), pp. 3340–3344. IEEE (2015)
14. Ahmed, Z., Bakar, K.A.: An enhanced underwater linear wireless sensor network deployment strategy for data collection. *Int. Innov. Comput.* **8**(4), 39–45 (2018)
15. Almazyad, A.S., et al.: A proposed scalable design and simulation of wireless sensor network-based long-distance water pipeline leakage monitoring system. *Sensors* **14**(2), 3557–3577 (2014)
16. Aliyu, F., Al-shaboti, M., Garba, Y., Sheltami, T., Barnawi, A., Morsy, M.A.: Hydrogen sulfide (H<sub>2</sub>S) gas safety system for oil drilling sites using wireless sensor network. *Procedia - Procedia Comput. Sci.* **63**, 499–504 (2015)



# Wireless Sensor Networks in Midstream and Downstream in Oil and Gas Industry

M. Y. Lee<sup>1(✉)</sup>, A. S. Azman<sup>1</sup>, S. K. Subramaniam<sup>2</sup>, and F. S. Feroz<sup>2</sup>

<sup>1</sup> Fakulti Kejuruteraan Elektronik dan Kejuruteraan Komputer,  
Universiti Teknikal Malaysia Melaka, Durian Tunggal, Malaysia  
{M021820002, M021820013}@student.utem.edu.my

<sup>2</sup> Centre for Telecommunication Research and Innovation (CeTRI),  
Fakulti Kejuruteraan Elektronik dan Kejuruteraan Komputer,  
Universiti Teknikal Malaysia Melaka, Durian Tunggal, Malaysia  
{Siva, Shahnaz}@utem.edu.my

**Abstract.** Oil and gas industry can be considered to be one of the biggest corporations worldwide. It involves complex and critical process and machinery for the exploration, extraction, refining, transporting and marketing petroleum product. Hence, it is important to have a system to control, monitor, maintain and secure the industrial assets. Wireless Sensor Network (WSN) have the capability to sense, process and communicate hence, making it one of the best solutions to the existing problem in the oil and gas industry. This paper discussed the challenges faced during deploying the WSN and give an overview of the solution proposed by past researches.

**Keywords:** Wireless sensor network · Oil and gas · WSN

## 1 Introduction of WSN Deployment in Oil and Gas Industry

WSN is a group of miniature sensors, each proficient to sense, process and communicate, but when deployed in a group, form a network which collectively monitors the state of the physical world. These sensors each have the ability to process gathered data and to communicate with each another without wires [1]. This technology will give a big impact on the industry world especially the oil and gas industry as the industrial operations involved in this industry are complex, critical and dangerous. Since the WSN offers various benefits, this technology has been used not only in oil and gas sector but also in other sectors such as agricultural sector, acoustics sector, environmental management and other [2–5].

According to the U.S. Energy Information Administration Office [6], the world energy demand will have 7% growth which is higher than the 4% average growth rate from 2005 to 2015. By 2030, it is forecasted that the natural gas plant liquid (NGPL) production will increase by 38% compared to 2018 level.

Oil and gas industry is certainly popular for their dangerous and critical process involved. To ensure the assets are in defectless condition, some obstacles must be overcome by the company. The issues faced by this industry include terrestrial issues, environmental, and safety. One of the major issues encountered by the company is to detect the condition of the pipeline that carries oil and gas [7]. The oil and gas

operations are separated into three main levels which are upstream, midstream and downstream. Upstream is a level where the crude oil or the raw material are being extracted. This level usually exists in a dangerous and extreme environment location such as deep-water and underground. Midstream is where the storage and transporting process took place. The raw material from the upstream is transported here by underground pipe, ship or truck. Downstream, on the other hand, is where the refining and marketing process took place. The crude oil is refined into products such as petrol, diesel, or lubricants. The overall view of these sectors is shown in Fig. 1.

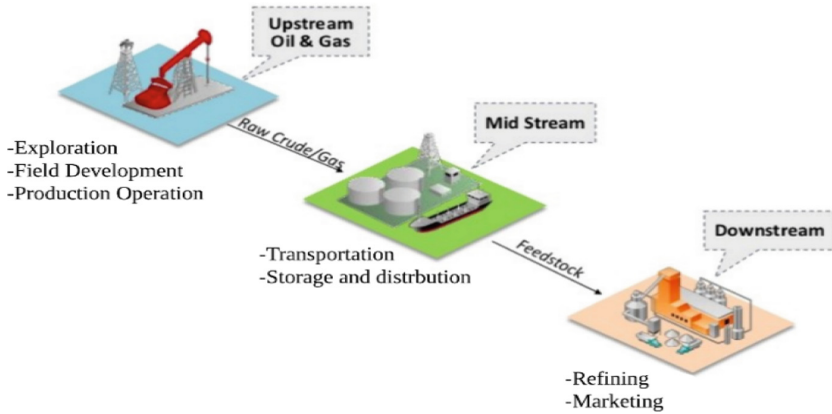


Fig. 1. Subdivisions of oil and gas industrial operation

## 2 Challenges in Deployment of WSN

Although the WSN is highly benefited to the oil and gas industry, there are some challenges in deploying the WSN. These obstacles must be considered in order to have an outstanding network system. Figure 2 showed the overall view of challenges in the deployment of WSN.

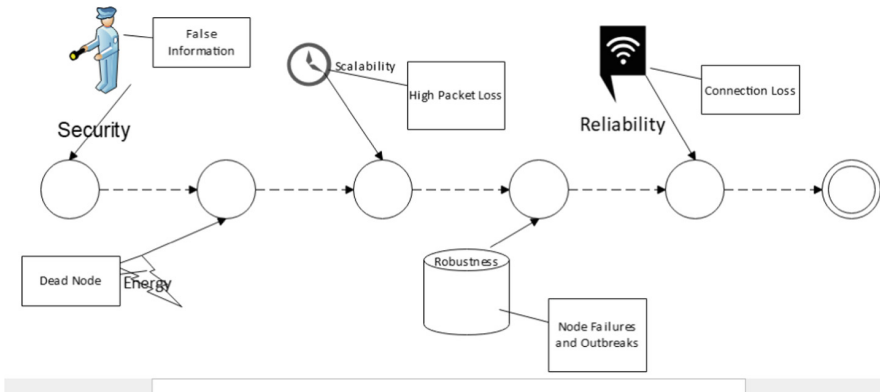


Fig. 2. Overall views of challenges in deployment of WSN

## 2.1 Energy Consumption

Energy consumption is one of the most critical challenges that will affect the efficiency of WSN. The network lifetime is a major aspect especially to the linear topology deployment of WSN. If the network is on a large scale, a huge amount of energy is required to transmit the packets. The idea of preparing an alternative energy harvesting device is applicable in terrestrial but not appropriate in underground nodes. Besides, batteries replacement for WSN can be challenging and costly as the deployment of WSN is usually in extreme and dangerous environment.

## 2.2 Security

There are two types of security in the oil and gas industry, equipment and communication protocols. Since the nodes are deployed to function without human intervention, an unauthorized person can attack the network and this will disrupt the whole network system [8]. Without a good security measurement, the attackers can trigger false alarm and inspection during the false alarm is a serious problem which will hinder the production. Since the deployment of WSN is usually multi-hop, the adversary can inject, suppress or modify packet to interfere with the data collection.

## 2.3 Reliability

In the oil and gas industry, a reliable communication system is indispensable. When an abnormal event is detected, the nodes are required to collect and send the data within a specific time as the failure to do so will lead to catastrophic accidents. The performance of WSN is depended on the wireless signal and since the signal in the underground and underwater is unstable, the reliability of the network will be affected. Moreover, the strength of the wireless signals can be affected by the changing temperature and humidity.

## 2.4 Robustness

Robustness allows a system to handle a large amount of data. In the oil and gas industry, it is a vital issue as there are many undefined interferences during the process. The WSN system is expected to have the ability to handle such errors during the execution. Enhanced algorithms and plans are needed so that the WSN can survive node failures and malicious outbreaks.

## 2.5 Scalability

Scalability is achieved when the performance of WSN is not affected by the number of nodes in the network. Scalability is accomplished by reducing the downtime through self-healing technique. Scalability can be affected by routing overhead, high network density, failure detection and recovery. Also, different wireless sensor product, protocol and standards make the work harder. The terrestrial condition makes the challenge to achieve scalability higher. Limitation such as high attenuation, low bandwidth and

speed will lead to high error rate and packet loss. In addition, the scalability will also be affected by restricted memory and high energy consumption.

### 3 Existing Solution

In this section of the study, the solution that has been proposed or explored by other researchers is summarized.

The authors in [9] highlighted that network lifetime as a critical factor that is influenced by limited power supply specifically in a WSN deployment. The authors then presented strategies such as grid, linear sequential and parallel with several deployment approaches which include decreasing distance, uniform, random and triangular. Experiments and simulations are done to verify that the WSN routing protocols will have a positive impact on the WSN lifetime.

In another study, the author [10] proposed an algorithm which cartel the benefits of both Clustering and Compressive Sensing-based strategy. Characteristic such as optimal size and distribution of cluster are discussed in this paper. The authors also mentioned that the network lifetime of the WSN is due to “Hot Spot Problem” and the rotation of the role for Cluster Head. To overcome this, the authors suggested that a Backup Cluster Head along with a new mechanism to replace the role of Cluster Head and Backup Cluster Head which is called Energy-Efficient Compressive Sensing-based clustering Routing (EECSR). This study showed that the EECSR has better energy efficiency and lifespan compared to the existing clustering algorithm.

The author in the study of an overview of routing techniques highlighted the strength of a linear topology in the deployment of WSN which is the simplicity to deploy and robustness in a diverse environment. This study also mentioned the design, classification and trials that exist in linear WSN. Several routing parameters such as reliability, energy proficiency, coverage, delay, sensor’s mobility, route discovery and maintenance are considered and analyzed during the summarization of types if linear WSN. The author also mentioned that the major problem faced by this topology is that if a single node dies, the network lifetime will be affected [11].

On the other hand, the researchers in [12] have considered making research on the deployment of 100 WSN nodes for monitoring Oil and gas pipelines. This paper includes the description and analyzation of steps included for designing a Cross-Layered Protocol Stack to increase the performance and energy efficiency. The researchers also mentioned the advantages of WSN. The protocol proposed by the researches contains Routing, Time Synchronization, Media Access Controls protocols and Topology Control. The proposed protocol shows characteristic such as low energy consumption and memory usage.

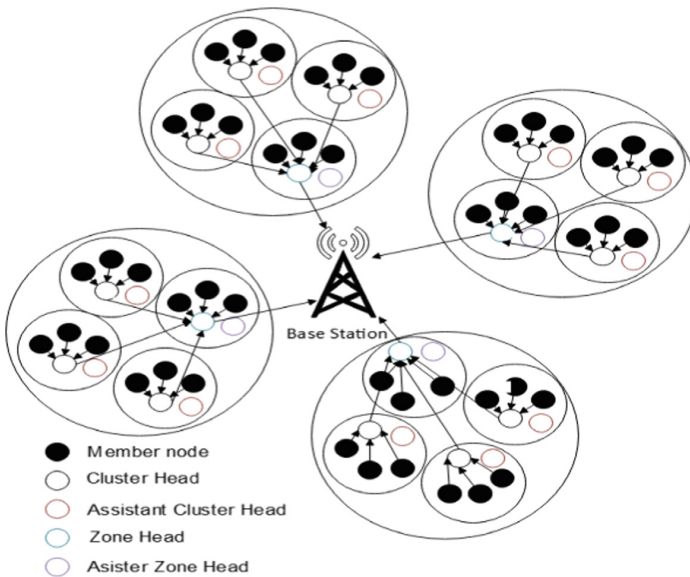
The next author [13] stated that the critical challenge faced by WSN is the non-uniform power consumption and network lifetime is the most crucial barriers in deploying it. The studies focused on strategic node placement in order to increase network performance. The author suggested a non-uniform scheme named as linearly decreasing distance (LDD) to ensure the energy consumption is steady. This is done by slowly moving the nodes closer towards the gateway. This study proposed that this

scheme (LDD) and strategic placement of the gateway will increase the network performance. The Simulation configuration for this study is shown in Table 1.

**Table 1.** Simulation configuration

Parameter	Value
Number of sensors	20
Pipeline length	300 m
Initial energy	2 J
Communication range	100 m
Channel model	Free space propagation
MAC	TDMA
Model	Zigbee

The author in this study [14] mentioned that during the deployment of WSN in a severe environment, the sensor’s power which can affect the power efficiency and lifetime of the sensor is a critical issue. Furthermore, the author also brought up issues such as the security of the data since WSN are deployed in an unattended location. To overcome such obstacles, the researches proposed a novel routing protocol called Secure and Low-energy Zone-based Routing Protocol (SeLeZoR). This protocol works by dividing the nodes of the WSN into small group and clusters. Figure 3 showed the overall network structure of the protocol and the simulation parameters are listed in Table 2.



**Fig. 3.** SeLeZoR network structure



**Table 2.** Simulation parameter

Parameter	Value
Network size	500 m * 500 m
MAC	802.11
Routing protocols	SELEZOR SECLEACH
Number of zones	6
Number of clusters	42
Number of nodes per cluster	3–4
Transmission rate	250 m
Node distribution	Random
Initial energy	17 J
Data packet size	512 bytes
Payload size	30 to 70 bytes
Number of packets	200
Path loss model	Two-ray model

In this research, the author [15] have presented a WSN monitoring solution named REMONG for collecting data from oil and gas pipelines. This solution focused on reliability, security and power efficiency factors. It can detect leakage and reports pipeline health. This system consists of three parts which are Dashboard, GYU and Middleware. For communication, this system uses ZigBee modules. This proposed solution is able to monitor the oil and gas pipelines without human intervention and this can save time and resources. Table 3 shows the experimental parameter used in this research.

**Table 3.** Experimental parameter

Parameter	Value
Model	ZigBee
Maximum data rates	250 kbps
Maximum data transmission range	3200 m
Routing	AODV
Maximum payload size	255 bytes

In [16] the author proposed a system that combines JenNet network with IEEE 802.15.4 standard. This proposed system supported several network topologies such as star, linear and tree. It also has a self-healing features for robust communication. The proposed system uses three different types of nodes. To tackle the main issues faced by the industry in deploying WSN which is power constraint, this system contains sleep mode capability. To further ease the workers for emergency maintenance, a wind sensor is placed in the system to indicate the wind speed and other information.

In the next paper [17], the author presented a technique which is called SimpliMote. This system uses ZigBee technique to detect leakage in oil and gas pipelines. The

author integrated a custom sensor board with algorithms that use low power to detect leakages, localization, actuation and parameter sensing. To validate the proposed system, the author prepared a testbed of 3-meter-long pipeline and filled it with pressurized fluid to simulate the oil and gas pipeline. Valves are used to create leaks for the system to detect.

The author in [18] has presented a cathode protection monitoring system by collecting the cathode data in time and integrate the WSN technology with GPRS and internet for the transmission. This system is used for terrestrial oil and gas pipes and has the ability to regulating the protection mode of cathode protection on request. The author also used the cluster technique to reduce the power consumption of the proposed system. Table 4 shows the hardware components involved in the proposed system.

**Table 4.** Hardware components

Subnet	Node	Description
WSN	Sensor node	Monitoring potential data
	Cluster head	Collecting the data and transfer to sink
	Sink node	Assembling all sampling data and transfer them to the monitoring centre
	PDA sink node	On-site maintenance
Internet	Database server	Storing data
	Web service server	Communicating with sink and provide web service

**Table 5.** Summary of existing solution

Author	Proposed method	Standard	Parameter					
			Energy	End to end delay	Security	Packet delivery ratio	Throughput	Packet delivered time
[9]	Linear sequential deployment scheme	N/A	YES	N/A	N/A	N/A	N/A	N/A
[10]	EECR algorithm	N/A	YES	N/A	N/A	N/A	N/A	N/A
[11]	Linear sensor network		YES	YES	N/A	N/A	N/A	N/A
[12]	Cross-layered protocol stack	N/A	YES	N/A	N/A	YES	N/A	YES
[13]	LDD	Zigbee	YES	N/A	N/A	N/A	N/A	N/A
[14]	SeLeZoR	IEEE 802.11	YES	N/A	YES	YES	N/A	N/A
[15]	REMONG	Zigbee	YES	N/A	YES	N/A	N/A	N/A
[16]	Environment monitoring system	Zigbee	YES	N/A	N/A	N/A	N/A	N/A
[17]	SimpliMote	Zigbee	YES	N/A	N/A	N/A	YES	YES
[18]	Cathod protection monitoring system	N/A	YES	N/A	N/A	YES	N/A	YES

## 4 Conclusion

WSN technology has the potential to provide a proper and efficient monitoring system, especially in the oil and gas industry. Although various challenges or obstacles such as energy consumption, robustness and other, plenty of improvement have been done. In this paper, a review of the technique that has been used or proposed by the past researches is presented. According to Table 5 which summarize all the existing technique, most researches are interested in tackling the power consumption challenges.

The most popular standard among researches are Zigbee or IEEE 802.15.4 due to the distance of the coverage is much wider compared to Wi-Fi. On the other hand, researches tend to prefer cluster topology in order to tackle the energy constraint in WSN. However, some of the researches have not presented the parameters used in their research. These parameters are important to enable improvement in the future. Other than that, it is highly recommended that future researches put more effort into solving the challenges regarding security and scalability.

**Acknowledgements.** The authors also acknowledge the since encouragement, assistance and support from the Ministry of Higher Education Malaysia, Universiti Teknikal Malaysia Melaka.

## References

1. Khan, W.Z., Aalsalem, M.Y., Gharibi, W., Arshad, Q.: Oil and gas monitoring using wireless sensor networks: requirements, issues and challenges. In: Proceedings - 2016 International Conference on Radar, Antenna, Microwave, Electronics, and Telecommunications, ICRAMET 2016, pp. 31–35 (2017)
2. Sheng, Z., Yang, S., Yu, Y., Vasilakos, A., McCann, J., Leung, K.: A survey on the ietf protocol suite for the internet of things: Standards, challenges, and opportunities. *IEEE Wirel. Commun.* **20**(6), 91–98 (2013)
3. Parra, L., Sendra, S., Lloret, J., Rodrigues, J.J.P.C.: Low cost wireless sensor network for salinity monitoring in mangrove forests. *Proc. IEEE Sens.* **2014**, 126–129 (2014)
4. Srbínovska, M., Gavrovski, C., Dimcev, V., Krkoleva, A., Borozan, V.: Environmental parameters monitoring in precision agriculture using wireless sensor networks. *J. Clean. Prod.* **88**, 297–307 (2015)
5. Felemban, E., Shaikh, F.K., Qureshi, U.M., Sheikh, A.A., Bin Qaisar, S.: Underwater sensor network applications: a comprehensive survey. *Int. J. Distrib. Sens. Netw.* (2015)
6. U.S. EIA: Annual energy outlook 2019 with projections to 2050. In: Annual Energy Outlook 2019 with Project to 2050, vol. 44, no. 8, pp. 1–64 (2019)
7. Aalsalem, M.Y., Khan, W.Z., Gharibi, W., Khan, M.K., Arshad, Q.: Wireless sensor networks in oil and gas industry: recent advances, taxonomy, requirements, and open challenges. *J. Netw. Comput. Appl.* **113**, 87–97 (2018)
8. Khan, W.Z., Hossain, M.S., Aalsalem, M.Y., Saad, N.M., Atiquzzaman, M.: A cost analysis framework for claimer reporter witness based clone detection schemes in WSNs. *J. Netw. Comput. Appl.* **63**, 68–85 (2016)
9. Khan, A., Imran, M., Noreen, M., Tariq, M., Shoaib, M., Subhan, F.: Impact of node deployment and routing for protection of critical infrastructures. *IEEE Access* **7**, 1 (2019)
10. Wang, Q., Lin, D., Yang, P., Zhang, Z.: An energy-efficient compressive sensing-based clustering routing protocol for WSNs. *IEEE Sens. J.* **PP**(c), 1 (2019)

11. Abbas, M.Z., Abu Bakar, K., Ayaz, M., Mohamed, M.H.: An overview of routing techniques for road and pipeline monitoring in linear sensor networks. *Wirel. Netw.* **24**(6), 2133–2143 (2018)
12. Shah, S., Anupama, K.R., Sahu, S., Kamalampet, S.K., Kamdar, N., Vyas, D.: A wireless sensor network based pipeline monitoring system, pp. 412–419 (2014)
13. Alnuem, M.: Performance analysis of node placement in linear wireless sensor networks. *J. Emerg. Trends Comput. Inf. Sci.* **5**(1), 1–8 (2014)
14. Lloret, J., Amjad Mehmood, S.S.: A secure and low-energy zone-based wireless sensor networks routing protocol for pollution monitoring. *Wirel. Commun. Mob. Comput.* **16**, 654–666 (2016)
15. Saeed, H., Ali, S., Rashid, S., Qaisar, S., Felemban, E.: Reliable monitoring of oil and gas pipelines using wireless sensor network (WSN) - REMONG. In: *Proceedings of the 9th International Conference on System of Systems Engineering: The Socio-Technical Perspective*, pp. 230–235 (2014)
16. Guo, X., Wang, Y., Wei, X.: Design of WSN-based environment monitoring system on repair of gas leakage. In: *Proceedings of the 2015 27th Chinese Control and Decision Conference, CCDC 2015*, pp. 3340–3344 (2015)
17. Ashraf, A., et al.: SimpliMote: a wireless sensor network monitoring platform for oil and gas pipelines. *IEEE Syst. J.* **12**(1), 778–789 (2016)
18. Liu, P., Huang, Z., Duan, S., Wang, Z., He, J.: Optimization for remote monitoring terrestrial petroleum pipeline cathode protection system using graded network. *Int. J. Smart Home* **9**(6), 51–64 (2015)



# Performance Analysis of n-Channel VDG-MOSFET with High Dielectric Permittivity

Ameer F. Roslan, K. E. Kaharudin<sup>(✉)</sup>, F. Salehuddin, A. S. M. Zain, A. R. Hanim, H. Hazura, S. K. Idris, and Z. A. M. Napiah

Micro and Nano Electronics (MiNE), CeTRI,  
Faculty of Electronics and Computer Engineering,  
Universiti Teknikal Malaysia Melaka, Jalan Hang Tuah Jaya,  
76100 Durian Tunggal, Melaka, Malaysia  
khairilezwan@yahoo.com.my

**Abstract.** The use of high dielectric permittivity in vertical double gate MOSFET (VDG-MOSFET) can overcome the problem of power dissipation and leakage current. In this paper, we investigated the performance potential of Titanium dioxide ( $\text{TiO}_2$ ) which has been deposited on silicon for use as a high-permittivity gate insulator and tungsten silicide ( $\text{WSi}_2$ ) for use as metal gate based on 2-D numerical simulations. The analysis and optimization of n-channel VDG-MOSFET is conducted, using a combination of  $L_9$  orthogonal array (OA) of Taguchi method and grey relational analysis (GRA). Four process parameters which are  $V_{\text{TH}}$  implant energy, halo implant dose, source/drain (S/D) implant dose and S/D implant tilt angle are optimized to obtain the desired value of on-current ( $I_{\text{ON}}$ ), off-current ( $I_{\text{OFF}}$ ) and subthreshold slope (SS). The design of experiment (DoE) is based on the  $L_9$  OA of Taguchi method and then the experimental data for multiple responses are converted into a single unit called grey relational grade (GRG). The most optimal level of four process parameters towards multiple responses are selected based on the highest GRG. Based on the analysis of variance (ANOVA), the most significant factor is observed to be S/D implant dose with 35.6% factor effect on GRG. The optimized value for  $I_{\text{ON}}$ ,  $I_{\text{OFF}}$  and SS after the optimization approach are 1599.3  $\mu\text{A}/\mu\text{m}$ , 865.5  $\text{pA}/\mu\text{m}$  and 68.02 mV/dec respectively with 0.8362 of GRG.

**Keywords:** High-permittivity · ANOVA · On-current · Off-current · VDG-MOSFET

## 1 Introduction

For the past few decades, Moore's law have been the guiding force for MOSFET's miniaturization [1]. As the MOSFET dimension is reduced, the process parameter variations become the main factor affecting the electrical properties [2]. These increased variations play a significant role in determining the value of  $I_{\text{ON}}$ ,  $I_{\text{OFF}}$  and SS of the device. Hence, it is required to take statistical variations into account during the design cycle of the MOSFET. Determining the correlation between process parameter variations with the MOSFET's properties, like doping concentration, doping energy and doping tilt angle have always been a complicated task [3]. The Technology

Computer Aided Design (TCAD) do not always provide a sufficiently physical correlation between various MOSFET's properties and MOSFET's process parameters. Therefore, various of statistical approaches have been implemented to increase the efficiency of the TCAD simulation for robust designs [4–7].

The most recent approach for improving the statistical variations of process parameters in MOSFET have been done using Taguchi method. For instance, Salehuddin *et al.* utilized Taguchi method to optimize process parameters in 45 nm technology node MOSFET for a desired threshold voltage ( $V_{TH}$ ) and  $I_{OFF}$  characteristic [8–10]. Furthermore, Afifah *et al.* also employed Taguchi method to optimize several process parameters in 22 nm gate length high- $k$ /metal-gate MOSFET for a nominal  $V_{TH}$  and lower  $I_{OFF}$  characteristic [11–13]. However, Taguchi method is only restricted to a single response and not applicable for multi-response optimization problems. Hence, Taguchi-based grey relational analysis (GRA) has been proposed to solve those problems in many of engineering applications [14–17].

The grey system theory was introduced by Deng *et al.* in 1982 to solve problems with poor, incomplete and uncertain information [18]. Basically, the GRA is based on the grey system theory that can be utilized to solve complicated interrelationships among multiple responses [19]. Optimization of the multiple responses can be converted into optimization of a single grey relational grade (GRG). In the present study, the process parameters of  $TiO_2/WSi_2$ -based vertical double-gate MOSFET, i.e.  $V_{TH}$  implant energy, halo implant dose, S/D implant dose and S/D implant tilt angle are optimized for obtaining desirable responses. Confirmation test is carried out to verify the optimal process parameters predicted by GRA. The ANOVA is also conducted to determine the level of significance for each process parameter towards GRG

## 2 Experiment Procedure

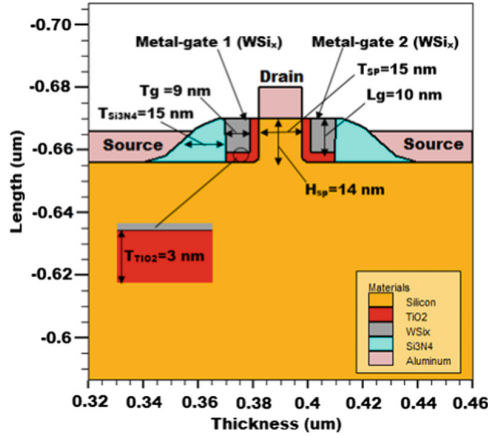
### 2.1 Process and Device Simulation

ATHENA module of Silvaco TCAD tools is the software used to perform process simulation for the  $TiO_2/WSi_2$ -based vertical double-gate MOSFET. The design is based on the previous report in [20]. The process simulation is initiated by defining the <100> orientation of p-type (boron doped) silicon substrate. The ultrathin silicon pillar is developed through etching process in order to separate the two vertical metal gates ( $WSi_2$ ). The metal-gate work function of 4.5 eV is applied to the  $WSi_2$  gate in order to stabilize the  $V_{TH}$  [21]. The silicon substrate is then doped with  $1.81 \times 10^{12}$  atom/cm<sup>3</sup> of boron at 20 keV and tilted at 7°. Next, the oxide layer is etched and replaced with  $TiO_2$ . The 10 nm gate length of  $WSi_2$  is deposited on the top of thin  $TiO_2$  layer. The halo implant process is then performed by doping the substrate with  $2.87 \times 10^{13}$  atoms/cm<sup>3</sup> of indium at 170 keV and tilted at 24°. The process is then followed by nitride spacer deposition. The S/D implant is performed with an arsenic dosage of  $2.21 \times 10^{18}$  atoms/cm<sup>3</sup> at 3 keV and tilted at 76°. Finally, compensation implant is employed with a phosphor dosage of  $2.51 \times 10^{12}$  atom/cm<sup>3</sup> at 60 keV and tilted at 7°. The aluminum layer is deposited on the top structure's surface and any unwanted aluminum is etched to develop the contacts. Table 1 shows the detail of

parameters used in the simulation. The completed cross section of 10 nm  $L_g$   $TiO_2/WSi_2$ -based n-channel VDG-MOSFET is depicted in Fig. 1.

**Table 1.** Parameters used in the simulated  $TiO_2/WSi_2$ -based n-channel VDG-MOSFET device

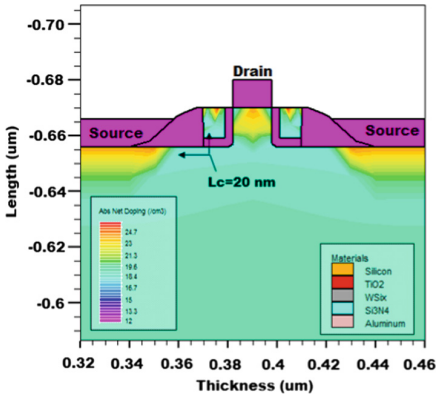
Parameters	Value
Gate Length, $L_G$	10 nm
Gate Thickness ( $T_g$ )	9 nm
Silicon Pillar Height ( $H_{sp}$ )	14 nm
Silicon Pillar Thickness ( $T_{sp}$ )	15 nm
$TiO_2$ Thickness	3 nm
Spacer Nitride Thickness ( $T_{Si_3Ni_4}$ )	15 nm
Channel Length ( $L_c$ )	20 nm
Metal-gate Workfunction (WF)	4.5 eV



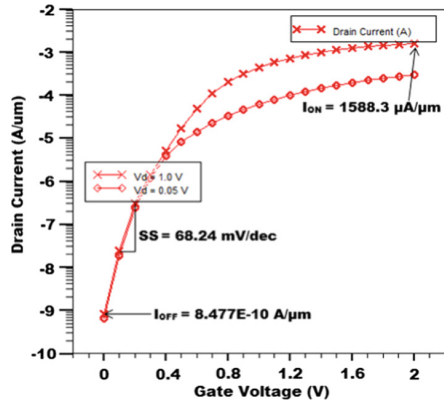
**Fig. 1.** Cross section of 10 nm  $L_g$  of  $WSi_x/TiO_2$ -based vertical double-gate NMOS

The device simulation of the  $TiO_2/WSi_x$ -based vertical double-gate NMOS device is carried out using an ATLAS module of Silvaco TCAD tools. Figure 2 illustrates the contour mode of the device, showing the tabulation of silicon,  $WSi_2$ ,  $TiO_2$ , silicon nitride ( $Si_3Ni_4$ ) and aluminum. Figure 3 depicts the subthreshold  $I_D$  vs.  $V_G$  curve at  $V_D = 0.05$  V and  $V_D = 1.0$  V for the device. The value of  $I_{ON}$ ,  $I_{OFF}$  and  $SS$  is extracted from the curve. The initial value of  $I_{ON}$ ,  $I_{OFF}$  and  $SS$  are observed to be 1588.3  $\mu A/\mu m$ , 847.7 pA/ $\mu m$  and 68.24 mV/dec respectively. The subthreshold swing ( $SS$ ) is extracted from the inverse slope of  $\log_{10} I_D$  vs  $V_{GS}$  characteristic shown in (1) [22]:

$$SS = \left[ \frac{d(\log_{10} I_{DS})}{dV_{GS}} \right]^{-1} \quad (1)$$



**Fig. 2.** Contour Mode of 10 nm Lg of WSi<sub>2</sub>/TiO<sub>2</sub>-based n-channel VDG-MOSFET



**Fig. 3.** Graph of subthreshold drain current ( $I_D$ )-gate voltage ( $V_G$ )

**2.2 L9 Orthogonal Array (OA) of Taguchi Method**

Taguchi method is an efficient and systematic approach to find the most optimal combination of process parameters. This method relies on the special OA of experiments that only requires less experimental runs. Since four process parameters are involved, the L<sub>9</sub> OA of Taguchi method had been utilized in this current study. Table 2 shows the list of process parameters and their levels. Table 3 shows the combination of levels of process parameters with their corresponding responses. The information listed in Table 3 is used to study the effects of process parameters on  $I_{ON}$ ,  $I_{OFF}$  and SS characteristics.

**Table 2.** Process parameters of TiO<sub>2</sub>/WSi<sub>2</sub>-based n-channel VDG-MOSFET

Symbol	Control factors	Units	Level 1	Level 2	Level 3
A	V <sub>TH</sub> Implant Energy	keV	20	22	24
B	Halo Implant Dose Tilt	atom/cm <sup>3</sup>	2.87E13	2.89E13	2.91E13
C	S/D Implant Dose	atom/cm <sup>3</sup>	2.21E18	2.23E18	2.25E18
D	S/D Implant Tilt Angle	deg. (°)	76	77	78

**2.3 Grey Relational Analysis (GRA)**

In the current study, the multiple responses for the device have been investigated using GRA. Using GRA approach, the multiple responses of the device like  $I_{ON}$ ,  $I_{OFF}$  and SS are converted into single grey relational grade (GRG). The following steps are performed for this method:

*Step 1*

All the response values obtained from L<sub>9</sub> OA of Taguchi method are normalized in the range of 0 to 1. These responses are categorized into different performance characteristics where  $I_{ON}$  is higher-the-better performance characteristics and  $I_{OFF}$  and SS are



**Table 3.** L<sub>9</sub> orthogonal array table for responses

Experiment no.	Parameter Level				I <sub>ON</sub> (μA/μm)	I <sub>OFF</sub> (pA/μm)	SS (mV/dec)
	A	B	C	D			
1	1	1	1	1	1588.3	8.477	68.24
2	1	2	2	2	1577.4	8.354	68.45
3	1	3	3	3	1567.5	8.203	68.67
4	2	1	2	3	1581.6	8.446	68.37
5	2	2	3	1	1589.3	8.483	68.21
6	2	3	1	2	1576.9	8.351	68.46
7	3	1	3	2	1592.8	8.610	68.14
8	3	2	1	3	1581.3	8.447	68.37
9	3	3	2	1	1589	8.484	68.23

lower-the-better performance characteristics. The following equations are used to normalize the responses respectively [23]:

$$x_i^*(k) = \frac{x_i(k) - \min x_i(k)}{\max x_i(k) - \min x_i(k)}, \text{ higher - the - better} \tag{2}$$

$$x_i^*(k) = \frac{\max x_i(k) - x_i(k)}{\max x_i(k) - \min x_i(k)}, \text{ lower - the - better} \tag{3}$$

where  $x_i^*(k)$  and  $x_i(k)$  are the sequence after data pre-processing and comparability sequence.  $\Delta_{oi}(k)$  is the deviation sequence of the reference sequence  $x_o^*(k)$  and the comparability sequence  $x_i^*(k)$  as shown in (4) [23]:

$$\Delta_{oi}(k) = |x_o^*(k) - x_i^*(k)| \tag{4}$$

*Step 2*

After data normalization is done, a grey relational coefficient (GRC) is measured with the pre-processed sequence. The GRC is defined as follows [23]:

$$\zeta_i(k) = \frac{\Delta_{\min} + \zeta \Delta_{\max}}{\Delta_{oi}(k) + \zeta \Delta_{\max}} \tag{5}$$

where  $\zeta$  is a  $n$  identification coefficient. Since all the process parameters are given with equal preference,  $\zeta$  is taken as 0.5, while  $\Delta_{\max}$  and  $\Delta_{\min}$  are the maximum and minimum absolute difference.

*Step 3*

After computing all the GRCs, the grey relational grade (GRG) is computed by averaging the GRCs corresponding to each response. The GRG represents multiple responses with different types of characteristic. The overall evaluation of multiple responses based on GRG is defined as follows [23]:

$$\gamma_i = \frac{1}{n} \sum_{k=1}^n \xi_i(k) \tag{6}$$

*Step 4*

The predicted GRG, using the optimal level of process parameters can be computed using (7) [23]:

$$\hat{\gamma} = \gamma_m + \sum_{i=1}^q (\gamma_i - \gamma_m) \tag{7}$$

where  $\gamma_m$  is the total means of GRG,  $\hat{\gamma}$  is the mean of GRG at optimal level and q is the number of process parameters.

### 3 Results and Discussion

Table 4 shows the normalized sequence of all the responses based on their corresponding performance characteristics. The deviation sequence is then computed using (4) and summarized in Table 5.

**Table 4.** Normalized response values for conducted experiments

Experiment No.	I <sub>ON</sub>	I <sub>OFF</sub>	SS
Reference Sequence	1	1	1
1	1588.3	8.477	68.24
2	1577.4	8.354	68.45
3	1567.5	8.203	68.67
4	1581.6	8.446	68.37
5	1589.3	8.483	68.21
6	1576.9	8.351	68.46
7	1592.8	8.610	68.14
8	1581.3	8.447	68.37
9	1589	8.484	68.23

These values are converted into GRC using (5). The GRG for each experiment is computed by averaging the GRC for for I<sub>ON</sub>, I<sub>OFF</sub> and SS. The rank of each experiment is tabulated based on the highest GRG as shown in Table 6. The higher level of GRG implies the quality of multi-response characteristics.

**Table 5.** Deviation sequences

Experiment no.	$I_{ON}$	$I_{OFF}$	SS
Reference sequence	1	1	1
1	1588.3	8.477	68.24
2	1577.4	8.354	68.45
3	1567.5	8.203	68.67
4	1581.6	8.446	68.37
5	1589.3	8.483	68.21
6	1576.9	8.351	68.46
7	1592.8	8.610	68.14
8	1581.3	8.447	68.37
9	1589	8.484	68.23

**Table 6.** GRC with GRG and their rank

Experiment No.	Parameter Level			GRG	Rank
	$I_{ON} \xi_i (1)$	$I_{OFF} \xi_i (2)$	SS $\xi_i (3)$		
1	0.7376	0.4262	0.7260	0.6299	4
2	0.4510	0.5741	0.4609	0.4953	8
3	0.3333	1	0.3333	0.5555	5
4	0.5304	0.4557	0.5353	0.5071	6
5	0.7833	0.4209	0.7910	0.6651	2
6	0.4431	0.5790	0.4530	0.4917	9
7	1	0.3333	1	0.7778	1
8	0.5238	0.4548	0.5353	0.5046	7
9	0.7690	0.4200	0.7465	0.6452	3

Based on Table 6, experiment row no. 7 had the best multi-response characteristics among the others due to its highest GRG. Since the design of experiments is orthogonal, the GRG at different levels can be separate out. For example, the mean of the GRG for factor A ( $V_{TH}$  implant energy) at level 1 can be computed by averaging the GRG at the experiment row 1 to 3 as level 1 had been allocated for column factor A as shown in Table 3. All the computed GRG for all the process parameters are listed in Table 7.

**Table 7.** Average GRG by process parameter levels

Symbol	Process parameters	Grey relational grade		
		Level 1	Level 2	Level 3
A	$V_{TH}$ Implant Energy	0.5602	0.5546	0.6425
B	Halo Implant Dose Tilt	0.6383	0.5550	0.5641
C	S/D Implant Dose	0.5421	0.5492	0.6661
D	S/D Implant Tilt Angle	0.6467	0.5883	0.5224

The GRGs for each process parameters are then converted into factor effect graph for better interpretation of optimal value for each of the process parameters as depicted in Fig. 4. Generally, the higher GRG indicates the better the overall quality of the responses. Figure 4 shows the most optimal value of process parameters based on the highest GRG which are  $A_3B_1C_3D_1$ .

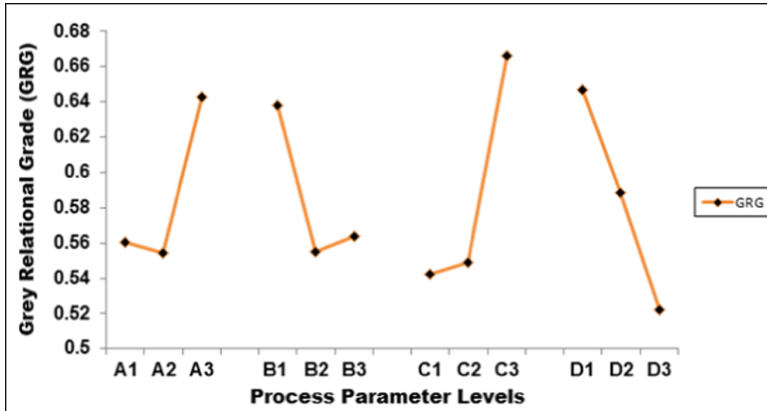


Fig. 4. Factor effect plot of GRGs for multiple responses

In order to investigate the importance of certain process parameter towards GRG, the analysis of variance is carried out. The ANOVA table consists of parameters such as the sum of squares (SSQ), degree of freedom (DF), variance or mean square (MS), F-value and percentage of the effect of each process parameter. The results of ANOVA revealed that factor C (S/D implant dose) is the most significant process parameter with 35.6% factor effect on GRG, followed by factor D (S/D implant tilt angle) with 28.3% factor effect on GRG, factor A ( $V_{TH}$  implant energy) with 17.8% factor effect on GRG and factor B (halo implant dose) with 15.3% factor effect on GRG. The completed ANOVA table and the percentage contributions of process parameters on the GRG are shown in Table 8 and Fig. 5. Finally, confirmation test is carried out to verify the optimal combination level of process parameters, predicted by  $L_9$  OA of Taguchi-based GRA. The optimal combination of process parameter levels that resulted in the highest GRG is  $A_3B_1C_3D_1$ .

Table 8. Results of ANOVA for GRG

Process parameter	DF	SSQ	MS	F-ratio	Percentage contribution ( $\rho$ )
$V_{TH}$ Implant Energy	2	0.015	0.0073	8.8	17.8
Halo Implant Dose Tilt	2	0.013	0.0063	7.6	15.3
S/D Implant Dose	2	0.029	0.0146	17.6	35.6
S/D Implant Tilt Angle	2	0.023	0.0116	14	28.3
Error	3	0.0025	0.00083	–	3
Total	11	0.0825	0.0405	–	100

Table 9 shows the best process parameters setting of the device. The device is re-simulated using the optimized level of process parameters (A<sub>3</sub>B<sub>1</sub>C<sub>3</sub>D<sub>1</sub>). The predicted GRG of the optimal level of process parameters as shown in (8) for the device can be computed using (7) as follows [23]:

$$\hat{\gamma} = \gamma_m + \sum_{i=1}^4 (\gamma_i - \gamma_m) \tag{8}$$

$$\hat{\gamma} = 0.5858 + (0.6425 - 0.5858) + (0.6383 - 0.5858) + (0.6661 - 0.5858) + (0.6467 - 0.5858)$$

$$\hat{\gamma} = 0.8362$$

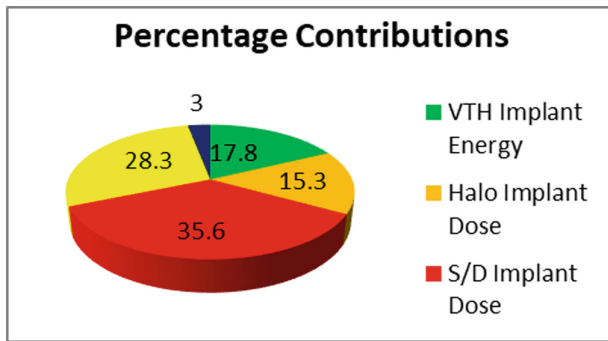


Fig. 5. Percentage contributions of factors on the GRG

Table 9. Optimal level of process parameter

Symbol	Process parameter	Units	Optimal value
A	V <sub>TH</sub> Implant Energy	atom/cm <sup>3</sup>	24
B	Halo Implant Dose Tilt	deg. (°)	2.87E13
C	S/D Implant Dose	atom/cm <sup>3</sup>	2.25E18
D	S/D Implant Tilt Angle	deg. (°)	76

The improvements in GRG with optimized process parameters for multiple responses are summarized in Table 9. The GRG of process parameters after optimization is improved by 24.7%. The highest GRG implies how close multiple responses to their desired value are. Based on Table 10, I<sub>ON</sub> is improved by 0.69% after the optimization. On top of that, the I<sub>ON</sub> characteristic is increased by 7.46% compared to ITRS 2013 prediction. The I<sub>OFF</sub> characteristic is slightly increased by 2.06% from the value before optimization. However, the I<sub>OFF</sub> characteristic is still under 100 A/μm as predicted by ITRS 2013 [24]. The SS characteristic after the optimization has slightly decreased by 0.32% from the value before the optimization. It is obviously proved that the I<sub>ON</sub>, I<sub>OFF</sub> and SS characteristics of the device could be simultaneously optimized using a L<sub>9</sub> OA of Taguchi-based GRA method.

**Table 10.** Improvements in GRG and responses with optimized process parameters

Condition description	Before optimization (first set of experiment row)	After optimization using L9 OA of Taguchi-based GRA	ITRS 2013 prediction [24]
Level	A1B1C1D1	A3B1C3D1	N/A
$I_{ON}$ ( $\mu A/\mu m$ )	1588.3	1599.3	$\geq 1480$
$I_{OFF}$ ( $A/\mu m$ )	$8.477E-10$	$8.655E-10$	$\leq 100$ n
SS (mV/dec)	68.24	68.02	N/A
GRG	0.6299	0.8362	N/A

Improvement in GRG = 24.7%

## 4 Conclusion

In this study, L<sub>9</sub> OA of Taguchi-based GRA method has been applied to simultaneously optimize multiple responses of TiO<sub>2</sub>/WSi<sub>2</sub>-based n-channel VDG-MOSFET. The most significant process parameter identified from the ANOVA is S/D implant dose with 35.6% factor effect on GRG. The highest I<sub>ON</sub> characteristic obtained from the analysis is observed to be 1599.3  $\mu A/\mu m$ . There is a slight improvement of 0.69% compared to the I<sub>ON</sub> characteristic before the optimization. The other responses of the device like I<sub>OFF</sub>, and SS characteristic are observed to be within the acceptable range. The final results have justified that the L<sub>9</sub> OA of Taguchi method is able to optimize multiple responses simultaneously in the TiO<sub>2</sub>/WSi<sub>2</sub>-based n-channel VDG-MOSFET.

**Acknowledgments.** The author would like to thank to the Ministry of Higher Education (MOHE) for sponsoring this work under project (FRGS/1/2017/TK04/FKEKK-CeTRI/F00335) and MiNE, CeTRI, Faculty of Electronics and Computer Engineering (FKEKK), Universiti Teknikal Malaysia Melaka (UTeM) for the moral support throughout the project.

## References

1. Rezali, F.A., Mazhar, M., Aida, N., Othman, F., Muhamad, S.W.: Performance and device design based on geometry and process considerations for 14/16-nm FinFETs stress engineering. *IEEE Trans. Electron Devices* **63**(3), 974–981 (2016)
2. Chen, C.Y., Lin, J.T., Chiang, M.H.: Comparative study of process variations in junctionless and conventional double-gate MOSFETs. *IEEE Nanotechnol. Mater. Devices Conf. IEEE NMDC* **2013**, 1–2 (2013)
3. Saxena, S., Member, S., Hess, C., Karbasi, H., Rossoni, A., Tonello, S., Mcnamara, P., Lucherini, S., Minehane, S., Dolainy, C., Quarantelli, M.: Variation in transistor performance and leakage in nanometer-scale technologies. *IEEE Trans. Electron Devices* **55**(1), 131–144 (2008)
4. Mutlu, A.A., Rahman, M., Member, S.: Statistical methods for the estimation of process variation effects on circuit operation. *IEEE Trans. Electron. Packag. Manuf.* **28**(4), 364–375 (2005)

5. Shedabale, S., Ramakrishnan, H., Yakovlev, A., Russell, G., Chattopadhyay, S.: Statistical modelling of the variation in advanced process technologies using a multi-level partitioned response surface approach. *IET Circuits Devices Syst.* **2**(5), 451–464 (2008)
6. Elgomati, H.A., Majlis, B.Y., Salehuddin, F., Ahmad, I., Zaharim, A., Hamid, F.A.: Optimizing 35 nm NMOS devices  $V_{TH}$  and  $I_{LEAK}$  by controlling active area and halo implantation dosage. In: *IEEE Regional Symposium on Micro and Nanoelectronics (RSM)*, Malaysia, pp. 286–290 (2011)
7. Kaharudin, K.E., Salehuddin, F., Zain, A.S.M., Aziz, M.N.I.A.: Taguchi modeling with the interaction test for higher drive current in WSix/TiO<sub>2</sub> channel vertical double gate NMOS device. *J. Theor. Appl. Inf. Technol.* **90**(1), 185–193 (2016)
8. Salehuddin, F., Zain, A.S.M., Idris, N.M., Yamin, A.K.M., Hamid, A.M.A., Ahmad, I., Menon, P.S.: Analysis of threshold voltage variance in 45 nm n-channel device using L27 orthogonal array method. *Adv. Mater. Res.* **903**, 297–302 (2014)
9. Salehuddin, F., Ahmad, I., Hamid, F.A., Zaharim, A., Hashim, U., Apte, P.R.: Optimization of input process parameters variation on threshold voltage in 45 nm NMOS device. *Int. J. Phys. Sci.* **6**(30), 7026–7034 (2011)
10. Salehuddin, F., Ahmad, I., Hamid, F.A., Zaharim, A., Elgomati, H.A., Majlis, B.Y.: Impact of SALICIDE and source/drain implants on leakage current and sheet resistance in 45 nm NMOS device. *J. Telecommun. Electron. Comput. Eng.* **2**(1), 35–41 (2010)
11. Afifah Mahteran, A.H., Menon, P.S., Ahmad, I., Salehuddin, F., Zain, A.S.M.: Process parameter optimization for minimum leakage current in a 22 nm p-type MOSFET using Taguchi method. *J. Telecommun. Electron. Comput. Eng.* **8**(9), 19–23 (2016)
12. Afifah Mahteran, A.H., Menon, P.S., Ahmad, I., Salehuddin, F., Mohd Zain, A.S., Noor Faizah, Z.A., Elgomati, H.A.: Control factors optimisation on threshold voltage and leakage current in 22 nm NMOS transistor using Taguchi method. *J. Telecommun. Electron. Comput. Eng.* **9**(2–7), 137–141 (2017)
13. Afifah Mahteran, A.H., Menon, P.S., Ahmad, I., Shaari, S., Elgomati, H.A., Salehuddin, F.: Design and optimization of 22 nm gate length high-k/metal gate NMOS transistor. *J. Phys. Conf. Ser.* **431**, 1–9 (2013)
14. Aggarwal, N., Sharmar, S.K.: Optimization of process parameters by Taguchi based grey relational analysis. *Int. J. Curr. Eng. Technol.* **4**(4), 2792–2796 (2014)
15. Muthuramalingam, T., Mohan, B.: Taguchi-grey relational based multi response optimization of electrical process parameters in electrical discharge machining. *Indian J. Eng. Mater. Sci.* **20**, 471–475 (2013)
16. Prayogo, G.S., Lusi, N.: Application of Taguchi technique coupled with grey relational analysis for multiple performance characteristics optimization of EDM parameters on ST 42 steel. *AIP Conf. Proc.* **1725**, 020061–1–020061–7 (2016)
17. Singh, B., Kasdekar, D.K., Parashar, V.: Application of GRA for optimal machining parameter selection in EDM. *Int. J. Hybrid Inf. Technol.* **8**(1), 371–382 (2015)
18. Deng, J.: Introduction to grey system. *J. Grey Syst.* **1**(1), 1–24 (1989)
19. Ramu, I., Srinivas, P., Vekatesh, K.: Taguchi based grey relational analysis for optimization of machining parameters of CNC turning steel 316. *IOP Conf. Ser. Mater. Sci. Eng.* **377**, 012078 (2018). <https://doi.org/10.1088/1757-899x/377/1/012078>

20. Kaharudin, K.E., Salehuddin, F., Zain, A.S.M., Aziz, M.N.I.A., Manap, Z., Salam, N.A.A., Saad, W.H.M.: Multi-response optimization in vertical double gate PMOS device using Taguchi method and grey relational analysis. In: IEEE International Conference on Semiconductor Electronics (ICSE), Kuala Lumpur, pp. 64–68 (2016). <https://ieeexplore.ieee.org/document/7573592>
21. Ana, F., Najeeb-ud-din, : Gate workfunction engineering for deep sub-micron MOSFET's: motivation, features and challenges. *Int. J. Electron. Commun. Technol.* **2**(4), 29–35 (2011)
22. Yadav, V.K., Rana, A.K.: Impact of channel doping on DG-MOSFET parameters in nano regime-TCAD simulation. *Int. J. Comput. Appl.* **37**(11), 36–41 (2012)
23. Deepak, Doreswamy, Beedu, Rajendra: Multi response optimization of process parameters using grey relational analysis for turning of Al-6061. *IOP Conf. Ser. Mater. Sci. Eng.* **225**, 012092 (2017). <https://doi.org/10.1088/1757-899x/225/1/012092>
24. ITRS: International technology roadmap semiconductor (2013). <http://www.itrs2.net/2013-itrs.html>





# Study of Gauss–Newton and Total Variation Image Reconstruction Approach in Imaging the Phantom in Concrete Using Electrical Resistance Tomography

Vernoon Ang<sup>1</sup>, M. H. F. Rahiman<sup>1(✉)</sup>, and R. A. Rahim<sup>2</sup>

<sup>1</sup> Centre of Excellence for Advanced Sensor Technology (CEASTech),  
Universiti Malaysia Perlis, Pauh Putra Campus, 02600 Arau, Perlis, Malaysia  
hafiz@unimap.edu.my

<sup>2</sup> Faculty of Electrical and Electronic Engineering,  
Universiti Tun Hussein Onn Malaysia, 86400 Batu Pahat, Johor, Malaysia

**Abstract.** This paper is to evaluate different imaging method to reconstruct the image of phantom located in a concrete medium. This research uses three types of image reconstruction technique such as NOSER prior, Laplace prior and Total Variation (TV) to image the different numbers and sizes of steel in concrete. The reconstructed images undergo image quality assessment using Mean Structural Similarity Index (MSSIM) to evaluate the similarity compared to the reference image. The TV algorithm is found most superior after comparing with all the cases stated to reconstruct the better image for Electrical Resistance Tomography system in concrete structure application.

**Keywords:** Electrical Resistance Tomography ·  
Image reconstruction algorithm · MSSIM · Prior

## 1 Introduction

Electrical Resistance Tomography (ERT) is well known as noninvasive imaging technique and potential system among industrial process, geophysical and as well as in the medical field. For example, successful utilization of ERT system can be seen in industrial process monitoring [1, 2], geophysical [3, 4] and medicine application [5–7]. Imaging method such as ERT system mainly depends on the boundary voltage measurements to reconstruct the resistivity or conductivity distribution of a medium. ERT is classified as a soft field tomography type. Soft field tomography such as ERT, when a current is excited into a medium through a pair of electrode, the electric field will propagate throughout the entire medium. The ERT system is operated where the attachment of an array of electrodes on the surface of a medium and current is injected into the medium via the electrodes. Boundary voltages are measured and collected from the electrodes. Imaging reconstruction of the internal conductivity of the medium is carried out by using the measured boundary voltages. The purpose of this study is conducted to investigate the behaviour of image reconstruction algorithm given cases such as embedded varies a number of steel and different sizes of steel in concrete. The

outcome of this study will help the ERT system in determining the superior algorithm to localise phantom in a concrete medium.

## 2 Simulation Parameters

This study applies a current injection method like adjacent or neighbouring method. The concrete medium is mounted with 16 electrodes at equidistant. The current of 10 mA is excited into a pair of electrode and boundary voltages are measured from the remaining pair of electrodes except for the current injection electrode as shown in Fig. 1. The concrete and circular electrodes are used with a diameter of 155 mm and 10 mm respectively. Next, the current injection is then switched to another pair and the remaining electrode pairs are utilized for voltage measurement. The same procedure is repeated until 16 sets of voltage measurement are recorded. This method yields 208 measurements using this formula  $M = N(N-3)$  where  $M$  is the total number of measurements and  $N$  is the number of electrodes.

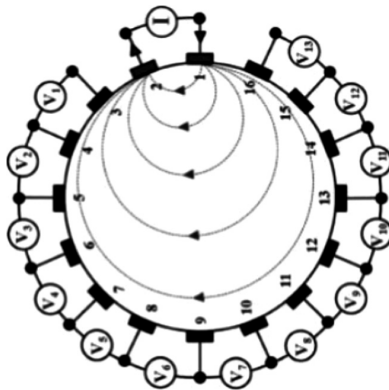


Fig. 1. Adjacent current injection method

## 3 Image Reconstruction Algorithms

Electrical Impedance and Diffuse Optical Reconstruction Software (EIDORS) is utilized for image reconstruction in this simulation study. The image is reconstructed by using measurement collected from simulation studies. EIDORS is an open source software [8] and it uses Matlab as its platform to perform high-speed image reconstruction process [9]. Hence, this study will use the Gauss–Newton (GN) approach and Total Variation from EIDORS to conduct image reconstruction for different numbers and sizes of steel in concrete.

## 4 Image Analysis

In this paper, the Mean Structural Similarity Index (MSSIM) is applied to compare the similarity between two images. MSSIM is an improved technique for image quality assessment compared to conventional techniques such as Peak Signal to Noise Ratio (PSNR) and Mean Squared Error (MSE). A number of experiments have been carried out in image quality assessment performance, it is apparently MSSIM yielded a better outcome in analyzing the image quality compared to PSNR and MSE [10, 11]. The MSSIM technique compares between a reference image and reconstructed image and the assessment will be indexed in the range from 0 to 1. As the index number is closer to 1, it can be indicated that the reconstructed image is likely alike with the reference image. MSSIM can be defined as shown in Eqs. 1 and 2.

$$MSSIM(X, Y) = \frac{1}{M} \sum_{j=1}^M SSIM(x_j, y_j) \quad (1)$$

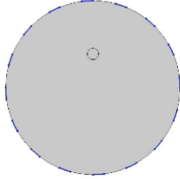
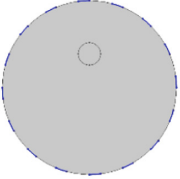
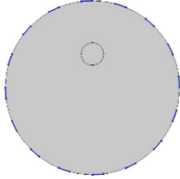
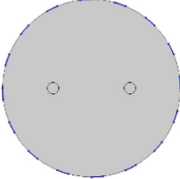
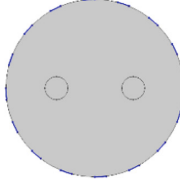
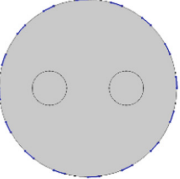
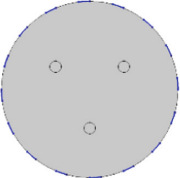
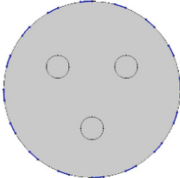
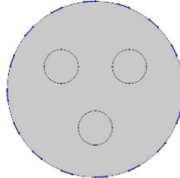
$$SSIM(x, y) = [l(x, y)]^\alpha \cdot [c(x, y)]^\beta \cdot [s(x, y)]^\gamma \quad (2)$$

Where  $X$  = the reference image,  $Y$  = the reconstructed image,  $x$  and  $y$  = image content at the  $j$ th local window,  $M$  = number of local windows of the image,  $l(x, y)$  = luminance comparison function,  $c(x, y)$  = contrast comparison function,  $s(x, y)$  = structure comparison function and  $\alpha$ ,  $\beta$  and  $\gamma$  = parameters applied to adjust the relative importance of the three components.

## 5 Result and Discussion

In this section, the investigation of different numbers and sizes of steel are carried out on a concrete medium. For each concrete, it is embedded with 1 to 3 piece(s) of steel and the size of the steel increased from 5 mm, 10 mm until 15 mm as shown in Fig. 2. Each case is simulated and the boundary voltages measurement is feed into three types of image reconstruction algorithms such as NOSER prior, Laplace prior and Total Variation. Reconstructed images are analyzed through MSSIM in order to evaluate the similarity compared to the reference image.

Figures 3, 4 and 5 presents the image reconstruction from NOSER, Laplace and TV algorithms based on simulation results in 2D view for concrete embedded with 1–3 piece(s) of steel in it. The reconstructed image from NOSER is not preserving the image edge in shaping the phantom as image reconstructed using Laplace or TV algorithm. While on the other hand, the Laplace algorithm yields better in shaping the circular phantom because it has the properties of edge preserving. The TV algorithm demonstrated clearer in presenting the image of the circular phantom. NOSER and TV algorithm shows better in localizing the position of the phantom compared to Laplace. The images reconstructed from Laplace algorithm shows smearing effect which unable the location of the phantom to be pinned precisely (Figs. 3, 4 and 5).

	5mm	10mm	15mm
1 steel			
2 steel			
3 steel			

**Fig. 2.** Concrete medium embedded with 1 to 3 piece(s) of steel and different size of the radius of the steel

The MSSIM indexes produced are tabulated as shown in Tables 1, 2 and 3 for three types of algorithms with different numbers of steel and sizes of steel in the concrete medium. From Figs. 9, 10 and 11, the graph clearly demonstrated that the TV algorithm achieved the highest MSSIM index reading following by NOSER algorithm and Laplace algorithm.

Overall, MSSIM shows that the increased size of the steel does not yield any significant changes in all the algorithms for each number of steel cases. In 5 mm of steel size case, MSSIM significantly presented major increment in the index obtained for 2 pieces of steel compared to 1 and 3 piece(s) of steel when using NOSER and TV algorithm. However, Laplace algorithm produces a higher index of MSSIM for 2 and 3 pieces of steel compared to 1 piece of steel. In addition, the same phenomenon happened in the 10 mm case. Next, for 15 mm steel size, overall for all the steel number, there are no major changes except for TV algorithm in reconstructing the 2 pieces of steel phantom.

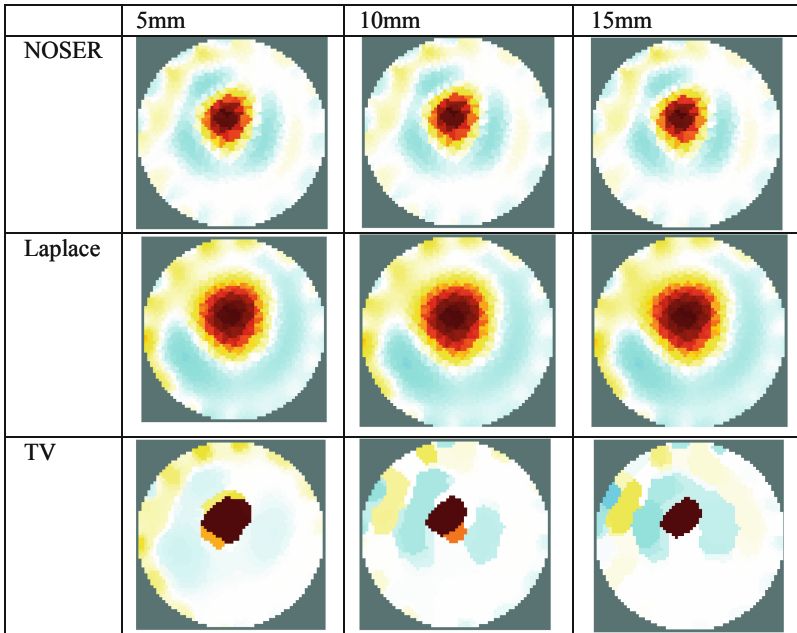


Fig. 3. Image reconstruction simulation results in the 2D view for concrete with 1 piece of steel

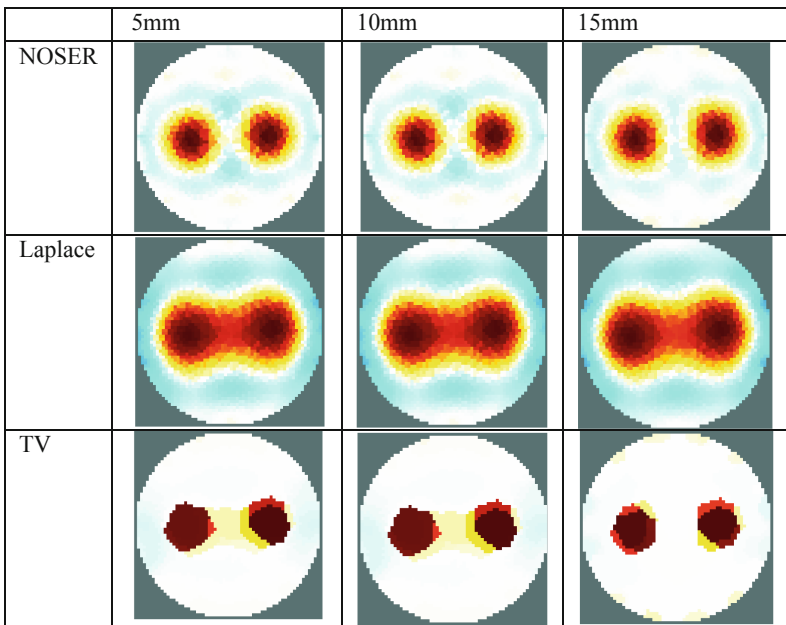


Fig. 4. Image reconstruction simulation results in the 2D view for concrete with 2 pieces of steel

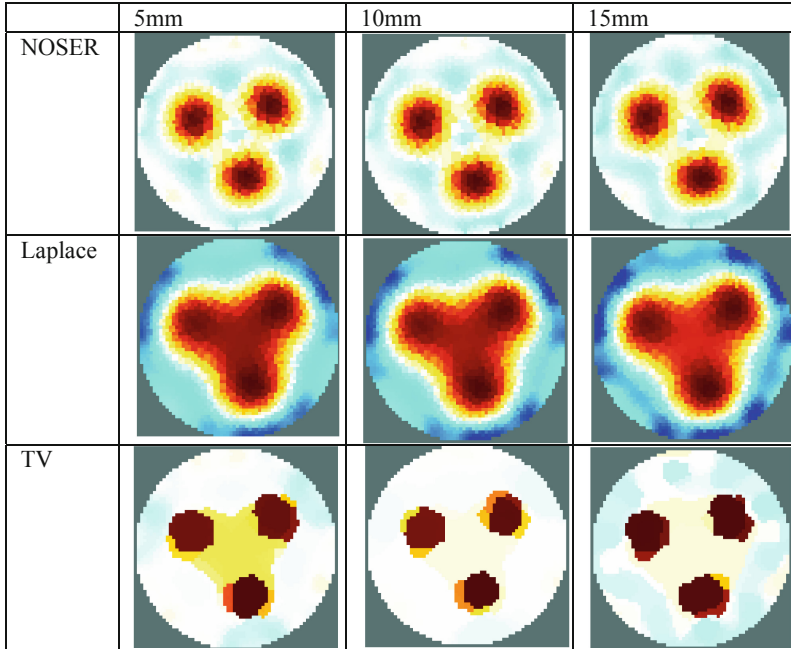


Fig. 5. Image reconstruction simulation results in the 2D view for concrete with 3 pieces of steel

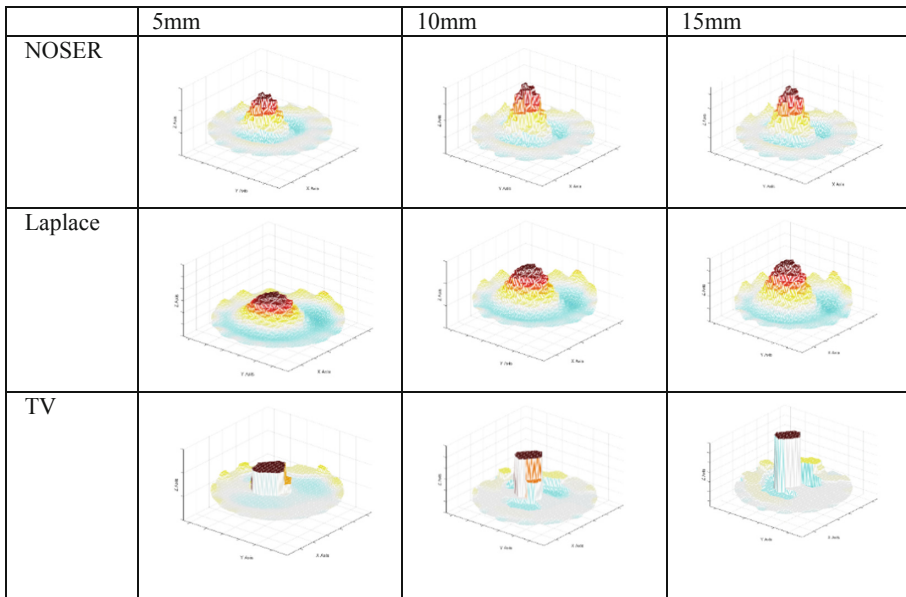
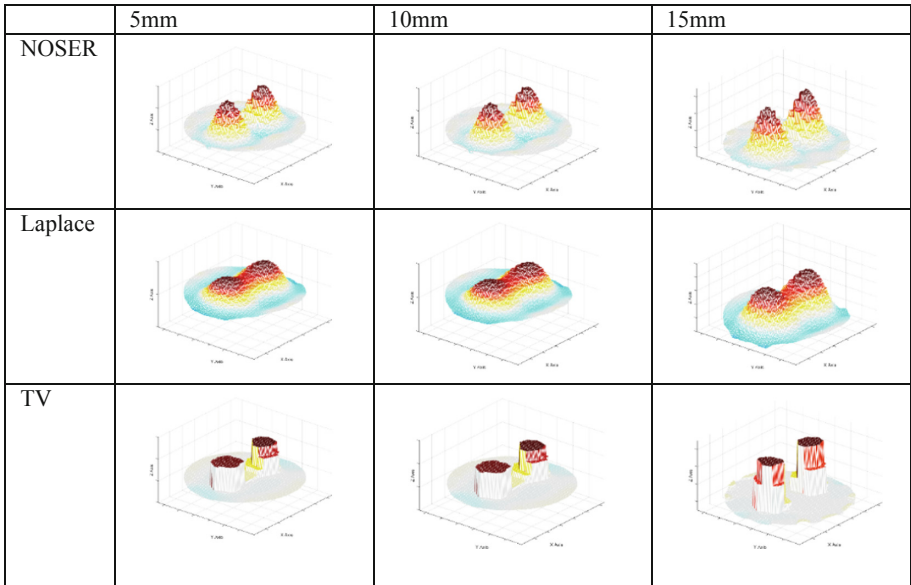
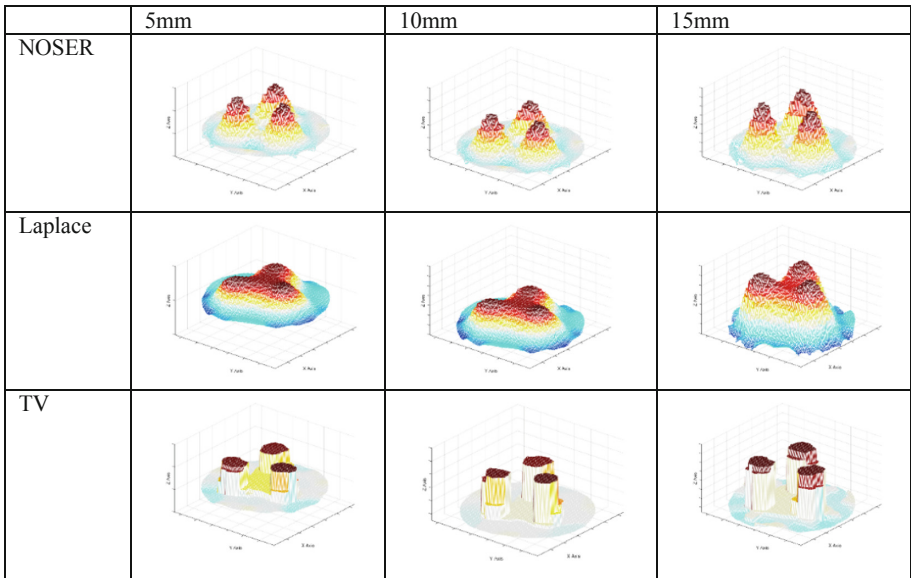


Fig. 6. Image reconstruction simulation results in the 3D view for concrete with 1 piece of steel



**Fig. 7.** Image reconstruction simulation results in the 3D view for concrete with 2 pieces of steel



**Fig. 8.** Image reconstruction simulation results in the 3D view for concrete with 3 pieces of steel

**Table 1.** MSSIM analysis result of three image reconstruction algorithms for concrete medium embedded with 1 piece of steel

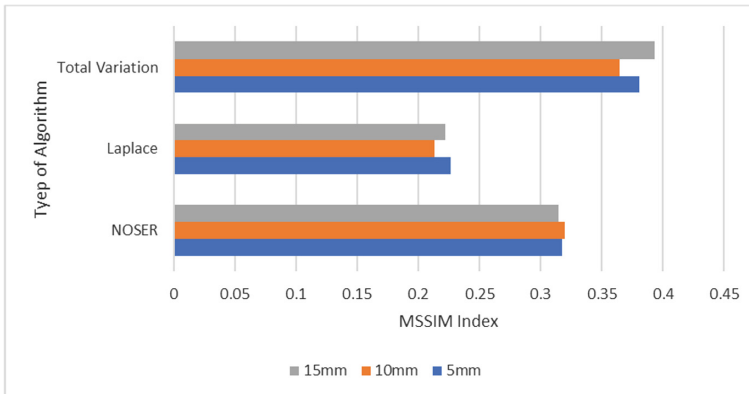
Phantom size for 1 steel	5 mm	10 mm	15 mm
NOSER	0.3177	0.3199	0.3146
Laplace	0.2266	0.2135	0.2220
TV	0.3804	0.3642	0.3931

**Table 2.** MSSIM analysis result of three image reconstruction algorithms for concrete medium embedded with 2 pieces of steel

Phantom size for 2 steels	5 mm	10 mm	15 mm
NOSER	0.3714	0.3705	0.3334
Laplace	0.2659	0.2653	0.2691
TV	0.5399	0.4274	0.5221

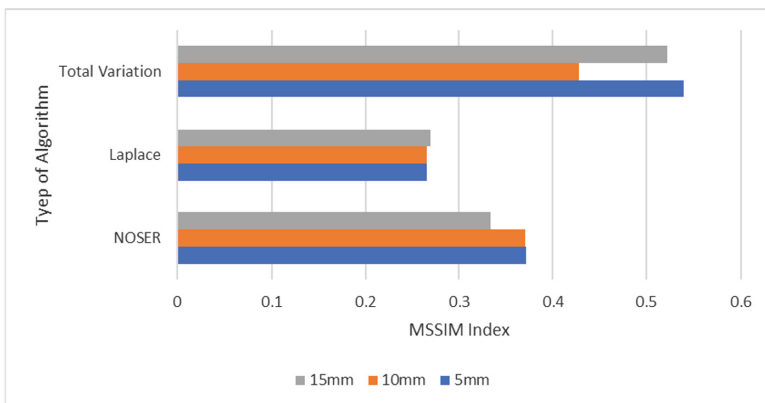
**Table 3.** MSSIM analysis result of three image reconstruction algorithms for concrete medium embedded with 3 pieces of steel

Phantom size for 3 steels	5 mm	10 mm	15 mm
NOSER	0.2811	0.2986	0.2695
Laplace	0.2757	0.2640	0.2403
TV	0.4252	0.4877	0.4387

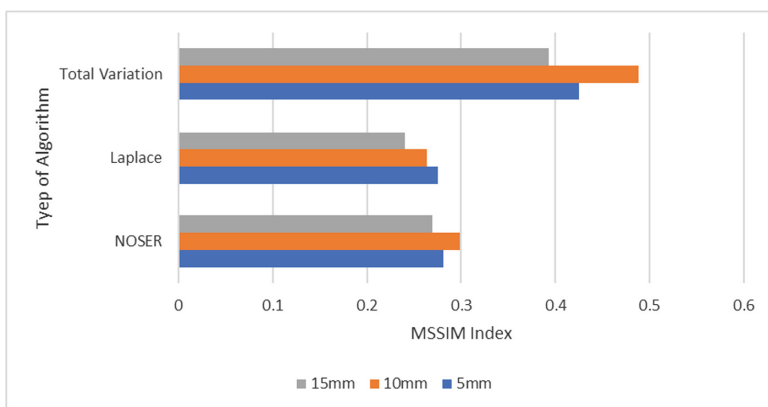


**Fig. 9.** Comparison of the three types of algorithm for concrete with 1 piece of steel





**Fig. 10.** Comparison of the three types of algorithm for concrete with 2 pieces of steel



**Fig. 11.** Comparison of the three types of algorithm for concrete with 3 pieces of steel

## 6 Conclusion

As a nutshell, this research has successfully implemented GN approach to study different numbers of steel and sizes of steel in a concrete medium. MSSIM index has been utilized for image assessment of the reconstructed images. Parameters such as shape, size, and position are the key element in this study. The implementation of the GN algorithm has produced outstanding reconstructed images in demonstrating the shape, size, and position. By comparing among the applied GN algorithm prior, Total Variation has the advantage to demonstrate how close the reconstructed image to the reference image by having the highest MSSIM index in all the cases. In future work, several GN algorithm priors can be added to the present work to compare and analyze in order to find a superior and suitable algorithm to help the ERT system in the localizing the phantom in concrete structure application which requires precision and accuracy.

**Acknowledgments.** The author is grateful for the funding from the Ministry of Science, Technology and Innovation (MOSTI), Malaysia under Science Fund Grant (Project NO. 03-01-15-SF0249).

## References

1. Bolton, G.T., Hooper, C.W., Mann, R., Stitt, E.H.: Flow distribution and velocity measurement in a radial flow fixed bed reactor using electrical resistance tomography. *Chem. Eng. Sci.* **59**, 1989–1997 (2004)
2. Vlaev, D., Wang, W., Dyakowski, T., Mann, R., Grieve, B.D.: Detecting filter-cake pathologies in solid–liquid filtration: semi-tech scale demonstrations using electrical resistance tomography (ERT). *Chem. Eng. J.* **77**, 87–91 (2000)
3. Bentley, L.R., Gharibi, M.: Two- and three-dimensional electrical resistivity imaging at a heterogeneous remediation site. *Geophysics* **69**, 674–680 (2004)
4. Kouli, M.: Investigation of waste disposal areas using electrical methods: a case study from Chania. *Environ. Geol.* **51**, 1249–1261 (2007)
5. Mueller, J.L., Isaacson, D., Newell, J.C.: A reconstruction algorithm for electrical impedance tomography data collected on rectangular electrode arrays. *IEEE Trans. Biomed. Eng.* **46**, 1379–1386 (2000)
6. Osterman, K.S., Kerner, T.E., Williams, D.B., Hartov, A., Poplack, S.P., Paulsen, K.D.: Multifrequency electrical impedance imaging: preliminary in vivo experience in breast. *Physiol. Meas.* **21**, 99–109 (2000)
7. Brown, B.H., Barber, D.C., Seagar, A.D.: Applied potential tomography: possible clinical applications. *Clin. Phys. Physiol. Meas.* **6**, 109–121 (1985)
8. William, R.B., Adler, A., Lionheart, W.R.B.: Uses and Abuses of EIDORS: An Extensible Software Base for EIT Uses and Abuses of EIDORS An Extensible Software Base for EIT, pp. 1–21. University of Manchester, Manchester (2006)
9. Lionheart, W.R.B.: EIT reconstruction algorithms: pitfalls, challenges. *Physiol. Meas.* **25**, 125–142 (2004)
10. Wang, Z., Bovik, A.C., Sheikh, H.R., Simoncelli, E.P.: Image quality assessment: from error measurement to structural similarity. *IEEE Trans. Image Process.* **13**, 600–612 (2004)
11. Horé, A., Ziou, D.: Image quality metrics: PSNR vs SSIM. In: 20th International Conference on Pattern Recognition, vol. 23, pp. 2366–2369 (2010)



# Temperatures Distribution and Contact Area of the Peaks of Three-Dimensional Rough Surfaces

Shin-Yuh Chern, Wei-Lun Liu, Jeng-Haur Horng<sup>(✉)</sup>,  
Qiong-Mao Jiang, and Jin-Long Lin

Department of Power Mechanical Engineering, National Formosa University,  
Yunlin, Taiwan  
jhorng@gmail.com

**Abstract.** All surfaces are rough. When two surfaces slide over each other, the contact temperature and contact area of peak have the different distribution under different operating parameters, and affects the tribology properties, precision, reliability and of contact pairs. In this work, a 3D Finite Element Method is used to analyze the temperature distribution and contact area of the peaks and valleys of designed asperity of sliding contact surfaces. The affecting parameters include pressure, roughness, sliding speed and Peclet number of rough surfaces. Analysis results showed that the increase of contact pressure makes up to the contact area and surface temperature increase simultaneously. The temperature rise parameter of peaks was larger than those of valleys as speed increases. However, the effect of pressure on the temperature rise of the non-contact zone is greater than the effect of velocity. The temperature rise parameter and contact area of asperity peaks of decreased as surface roughness increased. At the same surface roughness, the more the surface asperity number, the lower is the contact area and maximum temperature rise parameter. The relationship between contact pressure, sliding speed and asperity density can be used as a reference for surface engineering design of parts.

**Keywords:** Peak temperature · Contact area · Surface roughness · Contact pressure · Finite Element Method · Surface peak

## 1 Introduction

At present, the surface roughness of various micro-mechanical components and precision machinery has reached the micron or nano level after precision machining. From a microscopic point of view, an extremely smooth surface also can be seen that the surface is filled with many different asperities with peaks and valleys. When the two surfaces are under the relative contact movement, the contact of the surface asperities that causes friction, wear and high temperature. The temperature rises on the e peaks of the surface asperity will results in material deterioration, precision degradation, and component failure. Therefore, the relationship between contact temperature and performance of components is worthy to study.

Blok and Jaeger [1, 2] pioneered the studies of temperature rise at the contact peak of surfaces due to sliding and heating sources. They proposed simplified regression equations to calculate temperature rise as a function of sliding speed, applied load, friction coefficient, and material properties. In the latest years, substantial progress in the modeling of contact temperature problems has been made, resulting in more realistic simulations to account for surface roughness. The Finite Element Method has been proven to be an effective method to investigate the contact temperature of deformation peaks [3, 4]. The grinding temperature and the character of temperature distribution, predicted by FEM analysis by Zhang [4] are in good agreement with experimental data. All topographies of engineering surfaces have multiple peaks; however, most contact temperature analyses focused on temperature distribution and asperity distortion of a single peak. Another problem in analyzing surface temperature is the determination of the friction coefficient; the friction coefficient is difficult to predict in advance. Friction coefficients are different for various contact conditions, including contact load, sliding speed, surface roughness, and material properties. Lin [5] described the thermal behavior of single asperity in an apparent area of contact by means of a fractal method. A new expression of the temperature rise parameter ( $T/f$ ) was introduced to describe fluctuations in thermal parameters. The work by Hornig [6] proposed a somewhat simplified analysis of the friction coefficients of two rough surfaces. FEM is a potentially useful method to study peak and valley temperatures within multiple asperity surfaces. In 2011, Chern et al. [7] used 2-D FEM method to study the temperature rise parameters for multiple asperity surfaces under limited operation conditions in 2016, Kennedy [8], analyze the relationship of surface temperature and heat convection under sliding condition for the different surface roughnesses by FEM. In his continuation paper [9], it was found that temperature rise promotes oxidation and increases wear. However, 2-D simulation is not enough to examine the temperature characteristic of discrete 3-D asperities of real surface. In this work, 3-D asperity pattern surface is studied to investigate the peak temperature and contact area properties of two sliding surfaces.

## 2 Theory and Simulation

As shown in Fig. 1, a 3-D contact model was constructed using a deformable rough surface, which width  $w$  and height  $w$ , and a rigid flat block which length  $l$  and height  $w$ . The upper block had 1, 4, 9, 16, 25 sinusoidal peaks on the bottom contact area. In this work, giving a normal pressure ( $P$ ) in the y-axis direction, as shown in Fig. 1. With velocity  $V$ , the upper block slides along the lower block, friction heat was generated due to the friction work on the contact patches, and is denoted by  $Q$ , and  $Q = fWV$ , where  $f$  is the coefficient of friction and  $W$  is the applied load. The real friction heat flux,  $Q_f$ , can be expressed as follows:

$$Q_f = Q/A_r \quad (1)$$

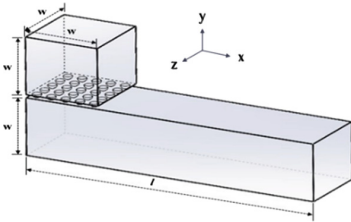
where  $A_r$  is the real contact area of contact bodies. The real contact area can be calculated from contact mechanics analyses of FEM, and is different for the various

applied pressures, sliding speeds, and surface roughness values. Convection and radiation are neglected in this study. The heat is conducted into the two contact bodies within the real contact area at the contact interface. The heat flux entering body 1 is  $Q_f \alpha$ , where  $\alpha$  is the overall heat partitioning factor, and the heat flux entering body 2 is  $Q_f (1 - \alpha)$  [10].

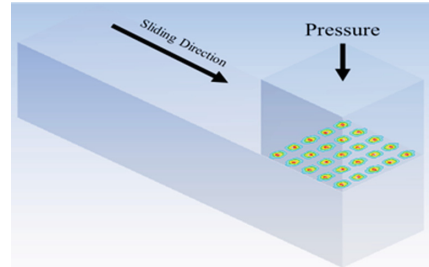
$$\left(1 + \frac{k_1}{k_2} \sqrt{\frac{1 + P_{e2}}{1 + P_{e1}}}\right)^{-1} \quad (2)$$

where  $k$  is the thermal conductivity and  $P_e$  is the Peclet number.  $P_{e1}$  denote the Peclet number of body 1. The general transient thermal equilibrium equation for this contact model can be described as follows:

$$\rho c (\partial T / \partial t) = \nabla k \nabla T + \dot{q} \quad (3)$$



**Fig. 1.** Geometry of 3-D contact model



**Fig. 2.** Schematic diagram of peak temperature and contact area of asperity

where  $T$  is the micro-temperature,  $\rho$  is the density, and  $c$  is the specific heat.  $\dot{q}$  is the heat rate by volume. Figure 2 shows the peak temperature distribution on the rough surface with 25 asperities under a fixed pressure and sliding speed of FEM analysis, where red color presents the higher temperature contact zone and green color presents the lower temperature contact zone. It also indicated that contact area is discrete distribution from this temperature rise diagram.

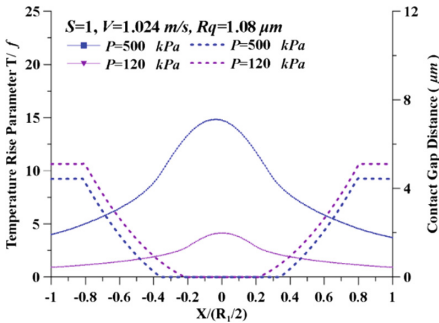
### 3 Results and Discussion

In this study, a physical system with  $w = 1280 \mu\text{m}$ ,  $l = 5120 \mu\text{m}$ ,  $S = 1, 4, 9, 16, 25$ ; density,  $\rho = 2.7 \times 10^3 \text{ kg/m}^3$ ; specific heat capacity,  $c = 9.0 \times 10^8 \text{ W}^\circ\text{C/kg}$ ; and coefficient of thermal expansion  $2.4 \times 10^{-5} \text{ mm/K}$  were considered. The mechanical properties of the upper and lower blocks, including Young's modules of  $7 \times 10^{10} \text{ Pa}$ , Poisson's ratio of 0.3, were used in this work. A sinusoidal wave was used to simulate the asperity surface. The studied cases for calculating peak temperature are shown in Table 1. Consequently, the Peclet number range is from 0.044 to 31.85.

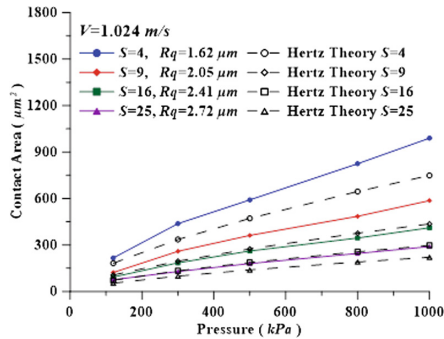
**Table 1.** Parameters for calculating peak temperatures of surface asperity

Asperity number	1, 4, 9, 16, 25
Roughness ( $\mu\text{m}$ )	1.08, 1.62, 2.05, 2.41, 2.72
Pressure (kPa)	120, 300, 500, 800, 1000
Velocity (m/s)	1.024, 2.048, 5.120, 10.24

A new expression of the temperature rise parameter ( $T/f$ ) was used in this work to describe the variation in thermal property because friction coefficient is different for the different operation conditions. Figure 3 shows that temperature rise parameter and contact spot radius increased as contact pressure increased at the same sliding speed and 1 asperity on surface. The variation of contact area at the different asperity numbers can be shown in Fig. 4. The dash line is the calculated results from the Hertz theory. It shows that contact area increased when the contact pressure or peak number increase. Under the same contact pressure and asperity size, more asperity numbers on surface have smaller contact area than that on surface. This reason is that contact area is proportional to the square of the pressure according to the Hertz theory. Comparing the present analysis with Hertz theory, we find that two kinds of analysis method have the same trend. However, the deviation of two kinds of data is smaller under the lower contact pressures because the assumption of the Hertz theory is elastic contact condition. Taking 25 peaks on the surface as an example, the error at 120 kPa is 28.96% and the error at 1000 kPa is 23.78%.

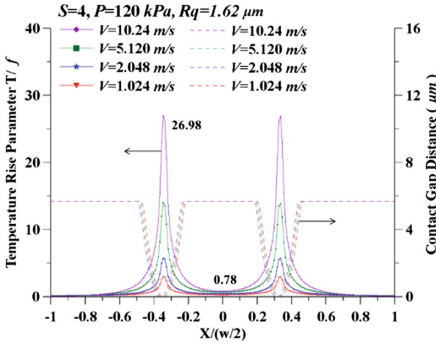


**Fig. 3.** Temperature rise parameter and contact gap versus contact position at the different contact pressure for the  $V = 1.024$  m/s

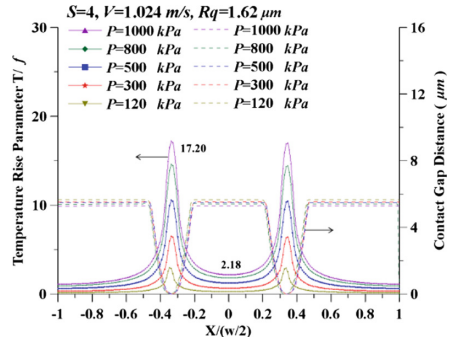


**Fig. 4.** Contact areas from numerical results and Hertz theory versus pressure at the different asperity numbers for the  $V = 1.024$  m/s

Figures 5 and 6 shows that temperature rise parameter and contact gap versus contact position at the different sliding speeds and contact pressures for the  $S = 4$ ,  $P = 120$  kPa and  $Rq = 1.62 \mu\text{m}$ . From Fig. 5, we can found that temperature rise parameter of peaks increase significantly as the sliding speed increases. The temperature rise parameter at the center of valleys almost constant as the sliding speed increases. The increasing rate of the temperature rise parameter of peaks was larger

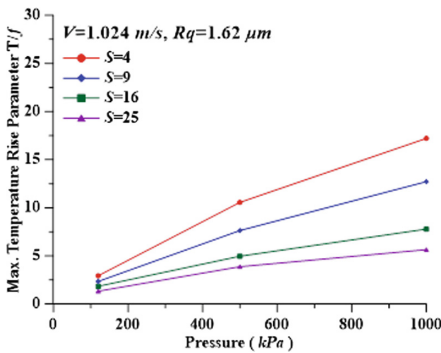


**Fig. 5.** Temperature rise parameter and contact gap versus contact position at the different velocities for the  $S = 4$ ,  $P = 120$  kPa, and  $R_q = 1.62$   $\mu\text{m}$

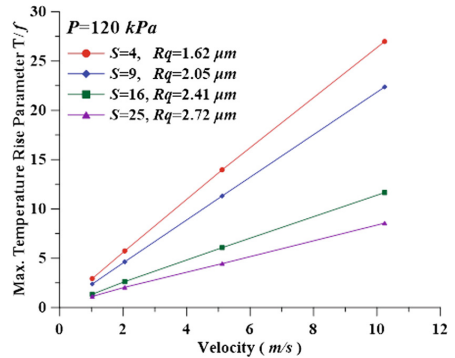


**Fig. 6.** Temperature rise parameter and contact gap versus contact position at the different pressures for the  $S = 4$ ,  $P = 120$  kPa, and  $R_q = 1.62$   $\mu\text{m}$

than those of valleys at the load of 120 kPa and the sliding speed of 10.24 m/s, the temperature rise parameter at the peak is reach up to 26.98. The increases of contact pressure also give up to the temperature rise parameter of peaks and valley increases, as shown in Fig. 6. However, the increasing rate of the temperature rise parameter of peaks and valleys almost the same. Comparing Figs. 5 and 6, we can found that the effect of contact pressure on the temperature rise parameter of valley is larger than that effect of sliding speed. The main factor affecting the peak temperature of surface asperity is sliding speed.



**Fig. 7.** Max. temperature rise parameter versus pressure at the different peak numbers for the  $V = 1.024$  m/s and  $R_q = 1.62$   $\mu\text{m}$



**Fig. 8.** Max. temperature rise parameter versus Velocity at the peak numbers for the  $P = 120$  kPa

If the number of asperities on the surface increases, the asperity shrinks so that the surface roughness values are the same. Figure 7 shows that the effect of contact

pressure and asperity number on temperature rise parameter for the constant sliding speed and surface roughness. Regardless of the contact pressure, it indicates that not only more surface asperity number but also ratio of asperity number to roughness value will induce the temperature rise parameter decreases. The results of Fig. 8 also have the same trend. More asperity number or asperity density has lower temperature rise parameter for different sliding speeds.

## 4 Conclusions

3-D Finite Element Method transient model was used to analyse the contact spot temperature and real contact area of rough surfaces. The main factor affecting the peak temperature is sliding speed. However, the main factor affecting the valley temperature is contact pressure. More asperity number and ratio of asperity number to roughness value on the surface will decrease the peak temperature rise parameter and contact area. The relationship between contact pressure, sliding speed and asperity density can be used as a reference for surface engineering design of parts.

**Acknowledgement.** The authors are grateful for the financial supports provided by Ministry of Science and Technology, Taiwan through the contracts MOST 105-2221-E-150-005-MY3 and 107-2221-E-150-009-MY3.

## References

1. Blok, H.: Theoretical study of temperature rise at surfaces of actual contact under oiliness lubricating conditions. *Proc. Inst. Mech. Eng.* **2**, 222–235 (1937)
2. Jaeger, J.C.: Moving sources of heat and the temperature at sliding surfaces. *J. Proc. R. Soc. NSW* **76**, 203–224 (1942)
3. Zwierczy, P.T., Varad, K.: Thermal stress analysis of a railway wheel in sliding-rolling motion. *ASME J. Tribol.* **136**, 1–8 (2014)
4. Zhang, X.F., Lin, B., Xi, H.: Validation of an analytical model for grinding temperature in surface grinding by cup wheel with numerical and experimental results. *Int. J. Heat Mass Transf.* **58**, 29–42 (2013)
5. Lin, J.F., Chung, J.C., Chen, J.W., Liu, T.C.: Thermal analysis of the transient temperatures arising at the contact spots of two sliding surfaces. *ASME J. Tribol.* **127**, 694–704 (2005)
6. Horng, J.H., Wei, C.C., Tsai, H.J., Shiu, B.C.: A study of surface friction and particle friction between rough surfaces. *Wear* **267**, 1257–1263 (2009)
7. Chern, S.Y., Horng, J.H., Chen, S.H.: Study of temperature distributions of sliding block with asperity surface. *SIA* **43**, 1509–1513 (2011)
8. Kennedy, F.E., Tian, X.: Modeling sliding contact temperatures including effects of surface roughness and convection. *J. Tribol.* **138**, 042101-1–042101-9 (2016)
9. Kennedy, F.E., Lu, Y., Baker, I., Munroe, P.R.: The influence of sliding velocity and third bodies on the dry sliding wear of Fe<sub>30</sub>Ni<sub>20</sub>Mn<sub>25</sub>A<sub>125</sub> against AISI 347 stainless steel. *Wear* **374–375**, 63–76 (2017)
10. Tian, X., Kennedy, F.E.: Maximum and average flash temperatures in sliding contacts. *ASME J. Tribol.* **116**, 167–174 (1994)





# The Study of Light Effect on Surface Roughness of Metallic Surface by Using Vision System Technique

R. Zamri<sup>1</sup>(✉), M. N. Maslan<sup>1</sup>, M. S. Syed Mohamed<sup>1</sup>, L. Abdullah<sup>1</sup>,  
M. Mat Ali<sup>1</sup>, and M. S. Noorazizi<sup>2</sup>

<sup>1</sup> Fakulti Kejuruteraan Pembuatan,  
Universiti Teknikal Malaysia Melaka (UTeM), Hang Tuah Jaya,  
76100 Durian Tunggal, Melaka, Malaysia  
ruzaidi@utem.edu.my

<sup>2</sup> Department of Engineering and Technology,  
Razak Faculty Technology and Informatics, Universiti Teknologi Malaysia,  
54100 Kuala Lumpur, Malaysia

**Abstract.** This paper describes the image processing method which is one of the non-contact method is applied to measure the mean gray value ( $G_a$ ) used to predict and calculate the value of surface roughness ( $R_a$ ) on the specimen. All the specimens image are captured in different light source environment exposure which is Red LED light, white fluorescent and yellow bulb by using Omron CCD camera. The captured image of each specimen are processed by using MATLAB software as to calculate  $G_a$  value on the defect area of the captured image. By using formulation, the  $G_a$  value is then transform into surface roughness value and compared with manually measured surface roughness ( $R_a$ ) data. It is found that there is significant effect on surface roughness measurement from different light source, which effect the accuracy of the surface roughness reading. The outcome of the study clearly indicates the effectiveness of white fluorescent light to be used as light source for surface roughness measurement for metallic surface.

**Keywords:** Light effect · Surface roughness · Metallic surface · Vision system

## 1 Introduction

Nowadays, machine vision is one of the equipment and method that applied the vision-based automatic measurement and experimental investigation for instance applications as production check-up, production process control, and robots-guided in advanced industries. The potential of machine vision technology is very wide and it depends on the applications [1]. Not only that, image processing have been successfully used in predicting tool life with the combination of artificial intelligent [2].

However, some of conventional machine vision are still developing such as markets-metrology, defect recognition, image tracing, and bar-code reader. Unfortunately, only at a pace reflecting the maturity of the technology give a lot of advantage to its consumers. Besides that, the latest machine vision algorithms depend on

controlled parts presentation, lighting and optics for robust and faster processing [3]. Users have been considering *Graphical User Interface* (GUI) on new machine vision applications that work flexible in generally independent situations.

For example, the camera captures and freeze the image of the object placed on a moving conveyor. The crucial information of parameter is acquired from the image of the object and a script file or algorithms is generated by the software and the image is saved as a template for further measurements. When the measurement starts, the images of the objects which come under the camera are captured and the script is run which compares the images with the template and reflects status either accept or unaccepted on the GUI depending on how many the crucial dimensions of the image matches with the template.

The apparent and material color of the experiment matters have a vital associated and usually are the main factors on the subsequent of camera image [4]. Colors engross a huge amount of the most visible occurrence light in addition to the revealed surface effects so that the reflection proportion is additionally condensed. In this respect it is also significant whether there is only a simply penetrable thin coat of paint on the object or the experiment item is completely coloured.

## 2 Surface Roughness Measurement

Surface roughness testers are basic instruments utilized for surface roughness measurement applications. To acquire surface roughness information, Mitutoyo Surftest SJ-301 is utilized. Fundamentally, a precious stone stylus is navigated over the specimen and a piezoelectric pickup records all vertical development. Crests and valleys are recorded and changed over into a known estimation of given parameter. Parameters contrast by the way they approach taking a gander at peaks and valleys. The parameter that is ordinarily utilized is  $R_a$  which is simple and proficient. Different parameters can be more particular and valuable relying upon the application prerequisites. The parameters enable to characterize surface roughness precisely and efficiently. This surface roughness tester is necessary for any application that works with surface requirements.

## 3 Surface Defect Detection System Model

There are several steps in developing the surface defect detection. Every step has its function and proper steps as to create a sustainable system. The flow to develop surface defect detection is depicted in Fig. 1. The illumination in this research is using fluorescent lights, red LED light and yellow bulb. The surface defect detection algorithm consists of the main file and the function file. The purpose of having separate function files is to isolate the binary image operation with the main file which performs the gray image operation. The binary image operation is performed to find the coordinate ( $x_1$ ,  $y_1$  and  $x_2$ ,  $y_2$ ) or the location of the straight line defect on the specimen. The coordinate or location of straight line defect obtained will be used to crop the straight line defect on gray image and to preserve the characteristic of the original gray

pixel. When the location of the straight line defect is identified, the main file will read the point from the function file. This enables the main file to use the point's location to crop straight line defect directly on the gray image.

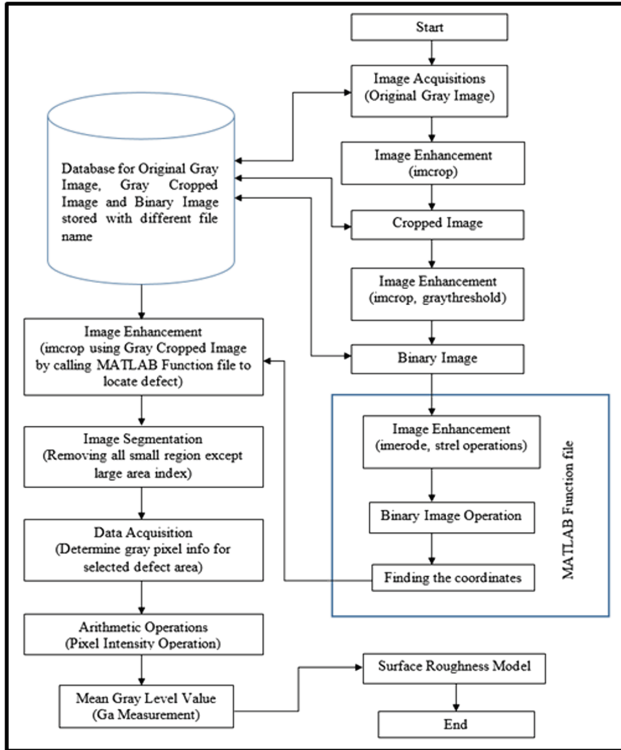


Fig. 1. Flow chart for the development of surface defect detection system

Other steps involved in defect detection algorithm are image acquisition, image enhancement, image segmentation, data acquisition, and arithmetic operation. Defect detection model is established to predict the precise and accurate surface roughness measurement for the developed defect detection system. The model predicts the value of surface roughness respective of the Ga obtained from the particular defect. It involves image processing algorithm development by using MATLAB software. Table 1 shows the complete apparatus used for the Surface Defect Detection System.

**Table 1.** Apparatus used for the surface defect detection system

Apparatus	Specifications
Light Source	Red LED, white fluorescent, yellow bulb
CCD Camera	Omron F500 vision system
Personal computer	DELL Precision T3400 Workstation
Specimen	JIS 3141 SPCC Cold Rolled Steel
MATLAB	Image processing toolbox
Microsoft Excel	Linear ModelDevelopment
Frame Grabber	EasyCAB USB 2.0 Video Capture
Surface roughness tester	Mitutoyo Surftest SJ-301

In data acquisition, there are four important data to extract from the image and the important final data is mean gray pixel value ( $Ga$ ) or in Eq. 1 represent by  $T$ .

- $P$  = pixels\_in\_region\_k;
- $R$  = mean(I(idx));
- $Q$  = length (idx);

$$T = \text{sum}(\text{abs}(\text{int16}(P) - R))/Q \tag{1}$$

The equation for  $T$  is the combination of several parameters of such as  $P$ ,  $R$  and  $Q$ .  $P$  is a measurement of pixel value for every single pixel in region  $k$  which is the scratch line and  $k$  in this case should only represent one continuous straight line defect.  $R$  is the mean pixel measurement of every pixel in region  $k$ .  $Q$  is the length or quantity of pixel in region  $k$ . According to [5], the arithmetic of gray level ( $Ga$ ) can be expressed as:

$$Ga = \left( \sum (|g_1 - g_m| + |g_2 - g_m| + \dots + |g_n - g_m|) \right) / n \tag{2}$$

where  $g_1, g_2, g_3 \dots g_n$  are the gray level pixel values of surface image along one line and  $g_m$  is the average of gray level values and  $g_m$  can be determined as:

$$g_m = \left( \sum (g_1 + g_2 + \dots + g_n) \right) / n \tag{3}$$

when the equation is applied in MATLAB on real image application, the same equation is written as Eq. 1.

During the training phase to develop the model, the following steps are conducted and the model equation including the steps is as below [6] (Table 2).

$$y = mx + c \tag{4}$$

**Table 2.** Sequence to estimate the coefficient of M and C

No.	Sequence
1.	Measure the surface value Ra by using stylus profilometer equipment
2.	Capture the image of the work piece with the straight line defect
3.	Determine the $Ga(x)$ value of the straight line defect ROI from the image
4.	Employ linear regression, ordinary least square and robust regression model to estimate the coefficients of m and c by applying equation in (1)

The sequence has been employed to the model are linear regression, ordinary least square and robust regression. For simple linear regression, the model takes the form of [7],

$$y_i = \beta_1 x_{i1} + \cdots + \beta_p x_{ip} + \varepsilon_i = X_i^T \beta + \varepsilon_i \quad i = 1, \dots, n \quad (5)$$

and these n equation is stack together to form,

$$y = X\beta + \varepsilon \quad (6)$$

## 4 Experimental Setup

The experimental setup for data capturing is illustrated in Fig. 2. This section discusses the development of defect detection model by using vision system which is able to detect straight line defect and obtained the Ga only at the particular defect or ROI. Figure 2 shows the schematic diagram for surface detection system. Firstly, the images are taken by CCD (Charged-couple Device) camera in the form of gray scale and saved in the computer database. There are three types of image that are created and named according to their function in the defect detection algorithm. The 'OGIS001.jpg' file stands for 'Original Gray Image Sample 001' referring to 'raw gray image sample number one' taken from CCD camera. Whereas 'grayS001.jpg' file stands for 'gray cropped image sample number one' and 'binerS001.jpg' file is referring to 'binary image sample number one'. Every straight line defect samples are created to have these three types of image file and the defect detection algorithm will be using all these files for image processing purposes. Defect detection algorithm is developed by using MATLAB R2014b software. The important parameter involved in defect detection model is Ra in micron and Ga in pixel unit. The purpose of the defect detection model is to predict the Ra measurement of straight line defects by using Ga data obtained from the gray image.

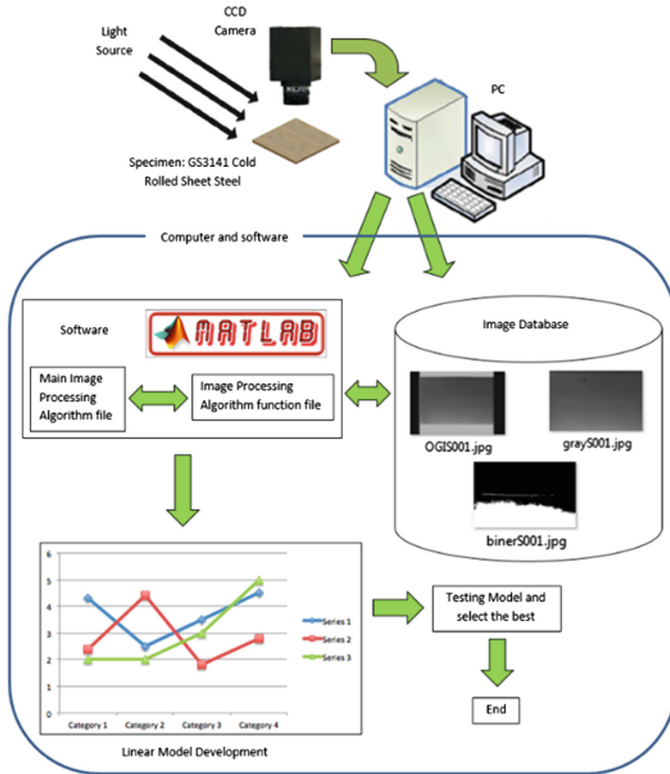


Fig. 2. Schematic diagram of experimental setup

## 5 Surface Roughness ( $R_a$ ) Model Calculation

Table 3 shows the results measured by MITUTOYO surface measurement tool in surface roughness ( $R_a$ ) unit. There are total 20 specimen measured 10 times for each specimen and the average  $R_a$  are calculated as the actual result for  $R_a$ . This step is used to show the relationship between mean gray value ( $G_a$ ) calculated in MATLAB software with the actual surface roughness ( $R_a$ ) measured by MITUTOYO surface measurement tool. Table 4 show the  $G_a$  data for Red LED, White fluorescent and yellow bulb respectively.

The model is  $Y = mX + C$  is generated which  $Y$  is representing surface roughness ( $R_a$ ) while  $X$  represent mean gray value ( $G_a$ ). Each of the data from different light source developed as model in order to calculate new surface roughness ( $R_a$ ). In order to calculate the new surface roughness ( $R_a$ ) for every light source and the mean gray value ( $G_a$ ) for each specimen should be substitute into the model equation. The new  $R_a$  for every light source shows in Table 4.

$R$  is the relationship between the anticipated qualities and the watched estimations of  $Y$ .  $R$  square is the square of this coefficient and shows the level of variety clarified by the relapse line out of the complete variety. This esteem will in general increment with

Table 3. Surface roughness measurement

Surface Roughness (Ra)	Specimen																			
	1	2	3	4	5	6	7	8	9	10	11	12	13	14	15	16	17	18	19	20
1	1.19	1.32	1.34	1.13	1.55	1.33	1.22	1.20	1.21	1.57	1.24	1.30	1.24	1.21	1.14	1.14	1.31	1.56	1.09	1.12
2	1.20	1.19	1.25	1.15	1.32	1.45	1.20	1.31	1.27	1.44	1.33	1.17	1.43	1.42	1.19	1.22	1.21	1.54	1.22	1.09
3	1.26	1.22	1.35	1.14	1.36	1.60	1.17	1.27	1.21	1.45	1.33	2.01	1.48	1.18	1.06	1.26	1.36	1.56	1.22	1.14
4	1.22	1.28	1.29	1.14	1.34	1.60	1.23	1.25	1.25	1.7	1.28	1.33	1.26	1.27	1.16	1.19	1.17	1.53	1.24	1.17
3	1.19	1.32	1.45	1.25	1.60	1.61	1.12	1.24	1.39	1.58	1.15	1.28	1.14	1.38	1.17	1.19	1.37	1.57	1.21	1.19
6	1.13	1.32	1.35	1.24	1.46	1.66	1.23	1.14	1.36	1.67	1.28	1.51	1.22	1.09	1.25	1.33	1.26	1.55	1.07	1.16
7	1.21	1.29	1.42	1.15	1.29	1.54	1.12	1.19	1.35	1.69	1.19	1.47	1.24	1.15	1.13	1.24	1.25	1.61	1.21	1.05
8	1.23	1.19	1.29	1.21	1.29	1.44	1.18	1.23	1.35	1.51	1.21	1.26	1.22	1.35	1.31	1.26	1.26	1.53	1.21	1.13
9	1.16	1.23	1.51	1.21	1.27	1.71	1.16	1.29	1.23	1.77	1.19	1.44	1.14	1.36	1.11	1.23	1.38	1.62	1.12	1.10
10	1.15	1.20	1.34	1.23	1.33	1.40	1.16	1.17	1.39	1.67	1.22	1.45	1.22	1.29	1.23	1.27	1.23	1.60	1.26	1.15
Average	1.19	1.26	1.36	1.19	1.38	1.53	1.18	1.23	1.30	1.61	1.24	1.42	1.26	1.27	1.18	1.23	1.28	1.57	1.19	1.13

**Table 4.** Ga and new Ra under 3 types of light source with respect to manually measured Ra

Specimen	Mean Gray Value (Ca) Red LED	Mean Gray Value (Ga) White Fluorescent	Mean Gray Value (Ga) Yellow Bulb	MITUTOYO Surface Roughness (Ra)	New Ra for Red LED (Ra)	New Ra for White Fluorescent (Ra)	New Ra for Yellow Bulb (Ra)
1	2.9966	4.3592	3.8083	1.19	1.31	1.27	1.31
2	3.0385	4.6233	4.1970	1.26	1.31	1.27	1.31
3	3.5941	12.2534	6.7929	1.36	1.33	1.33	1.30
4	3.2758	5.5398	10.9835	1.19	1.32	1.29	1.28
5	4.0769	6.4626	12.0417	1.38	1.35	1.30	1.27
6	3.7783	14.0930	9.9077	1.53	1.34	1.41	1.28
7	2.4850	4.3370	3.6615	1.18	1.29	1.27	1.32
8	3.1942	8.6824	7.2695	1.23	1.32	1.33	1.30
9	3.4592	9.2000	4.4539	1.30	1.33	1.34	1.31
10	2.7548	8.1209	4.4636	1.61	1.30	1.32	1.31
11	0.9825	5.7389	3.9281	1.24	1.23	1.29	1.31
12	1.2805	3.6225	2.7197	1.42	1.25	1.26	1.32
13	2.4785	3.9750	9.2553	1.26	1.29	1.26	1.29
14	0.9912	3.5232	4.1763	1.27	1.20	1.21	1.33
15	1.3651	4.1543	5.8872	1.18	1.25	1.27	1.30
16	1.7948	4.0267	3.0000	1.23	1.26	1.27	1.32
17	3.9745	9.1526	15.8288	1.28	1.34	1.34	1.26
18	3.8755	3.6569	3.0153	1.57	1.20	1.21	1.33
19	4.3592	6.7101	9.6013	1.19	1.36	1.30	1.29
20	1.5360	7.6500	9.8793	1.13	1.26	1.32	1.28



extra indicators in the model. Along these lines, one can falsely get higher *R square* by expanding the quantity of *Xs* in the model. To evade this impact, balanced *R square* is utilized. When you contrast models and their intricacy, you should then depend on *Adj R square*. Anticipated *R square* is another measure that tends to the issue of overfitting the information and clarify the forecast power for future perceptions [7]. From data observed, the value of *R* is 0.7459 for red LED. This is a moderate positive correlation, which means there is a tendency for high *X* variable scores go with high *Y* variable scores (and vice versa). The value of  $R^2$ , the coefficient of determination, is 0.5564. However, for white fluorescent light the value of *R* is 0.9565 shows strong positive correlation, which means that high *X* variable scores go with high *Y* variable scores (and vice versa). The value of  $R^2$ , the coefficient of determination, is 0.9149. For yellow bulb, the value of *R* is  $-0.9584$ . This is a strong negative correlation, which means that high *X* variable scores go with low *Y* variable scores (and vice versa). The value of  $R^2$ , the coefficient of determination, is 0.9185.

## 6 Conclusion

In conclusion, the study discussed the ability of machine vision that is one of non-contact method to measure the surface roughness (*Ra*) based on the mean gray value (*Ga*) data on the captured images from different light source environment exposure which are Red LED light, White Fluorescent light and Yellow Bulb. After all the analysis have been done, the study found that the White Fluorescent light source have the strongest correlation which can be determine as the best model which suitable to be used as light source for defect detection on metallic surface.

**Acknowledgements.** The authors acknowledge the support from Faculty of Manufacturing Engineering, Universiti Teknikal Malaysia Melaka (UTeM) and collaboration partners from Department of Engineering and Technology, Razak Faculty Technology and Informatics, Universiti Teknologi Malaysia, 54100 Kuala Lumpur, Malaysia for the combine effort.

## References

1. Golnabi, H., Asadpour, A.: Design and application of industrial machine vision systems. *Robot. Comput. Integr. Manuf.* **23**(6), 630–637 (2007)
2. Mikołajczyk, T., Nowicki, K., Bustillo, A., Pimenov, D.Y.: Predicting tool life in turning operations using neural networks and image processing. *Mech. Syst. Signal Process.* **104**, 503–513 (2018)
3. Khalik, A.A.A., Eissa, A.H.A.: Understanding color image processing by machine vision for biological materials. INTECH, 2012
4. Datta, R., Joshi, D., Li, J.I.A., Wang, J.Z.: Image retrieval: ideas, influences, and trends of the new age. *ACM Comput. Surv.* **40**(2), 1–60 (2008)
5. Kumar, R., Kulashekar, P., Dhanasekar, B., Ramamoorthy, B.: Application of digital image magnification for surface roughness evaluation using machine vision. *Int. J. Mach. Tools Manuf.* **45**(2), 228–234 (2005)

6. Chauhan, J.D., Modi, C.K., Pithadiya, K.J.: Comparison of redescending and monotone M estimator for surface roughness estimation using machine vision. *Second Int Conf. Emerg. Trends Eng. Technol.* **2**, 464–469 (2009)
7. Mudrak, E.: *Interpreting Linear Models: Regression and ANOVA*, 1st edn. Wiley, Hoboken (2017)

# **Robotics**



# The Design and Development of an Interactive Teaching Tool for Robotics and Control System Course Using Rapid Control Prototyping Solution

Richard Lee Jiang Hong, Muhammad Nasiruddin Mahyuddin<sup>(✉)</sup>,  
Mohd Rizal Arshad, and Yeong Chin Koo

School of Electrical and Electronic Engineering,  
Universiti Sains Malaysia (USM), Gelugor, Pinang, Malaysia  
nasiruddin@usm.my

**Abstract.** Control systems of robot manipulators offer many challenges in education where the students must learn robot dynamics and control structures, and understand relations between the control parameters, and the systems performance. Interactive simulation is aimed at improving the understanding and intuition for the abstract parts of the control of robot courses. Implementation of the control design on a robot manipulator significantly impress and improve the understanding towards the control system learning. This paper presents an application of interactive simulation designed by using the National Instrument's (NI) LabVIEW to teach control systems of robots by using the Rapid Control Prototyping method. The application considers a nonlinear robot arm and two control modules: computed torque control and PID control. For the computed torque control module, user can directly manipulate graphical representation of the systems such as choice in controller gains, desired trajectories and obtain instant feedback on the effects. PID control module will be the implementation on PID control to a well-developed 2 degree of freedom (DOF) planar robot arm through NI MyRIO-1900. User can visualize the performance of the real robotic system and manipulate the control parameters through user interface. These features make the interactive learning tool stimulating and of high pedagogical value.

**Keywords:** Robotic arm control · Teaching apparatus · NI myRIO · PID control · Control course

## 1 Introduction

Robotic arm systems, in particular, a serial-linked type, can be found in the production assembly line of any modern industry. Their functions and features can be varied from material handling, assembly, welding, loading and unloading of a machine or tool. To achieve such functions, some robots are configured for operation by teaching technique and repetition [1]. Most of the robot arms are programmable numerically to execute

certain specific task which require precision and repetition thereby, eliminating the disadvantage traits owned by human workers which are prone to error and exhaustion.

The robot arm system aforementioned requires a control system which allows precise motion to be commanded in particular for machining and assembling parts. The robotic arm control system ought to be reliable to be used in the assembly line of a factory. Without a reliable control system to control the robot in the assembly line, defects in the finished product are possible and incur cost to the associated company of the product.

This requirement demands for an engineer, preferably from a mechatronics engineering background, who possesses the fundamental knowledge in both robotics and controls system.

His or her strong theoretical knowledge in robotics and control system should be complemented with an adequate hands-on skills and exposure in programming the robot. Such requirement can be guaranteed if we have graduates from the local university which provides the facility (in addition to a comprehensive control engineering course syllabus) with laboratory equipment that effectively teaches the undergraduate engineering students about robot arm control system.

Nowadays, control system course, in particular, robotic control system lacks in the aspect of bridging the understanding gap between the theory and the practical aspect of the robotic control system. Formal control system education normally involves a set of theoretical lectures where students follow the induction of mathematics manipulation to build control concept. This is, seldom, complemented by practical activities in a form of laboratory exercises which could pedagogically induce students' interest and passion towards the subject. Lack of interesting practical activities and lecture-driven course are more likely to lure the students to boredom state, adversely affecting their understanding in mastering the principle [2]. A survey carried out in Jordanian Universities shows that out of 83.74% students vote for implementation of aids in teaching as the factor that increase student's enjoyment in learning process [3]. An intuitive and yet interesting pedagogical tool is a need in the course of the graduates learning experience to induce the interest of the students in control theory learnt in the lecture [4].

In this paper, a new pedagogical tool which helps the students in learning the principle and concept of robotic arm control system is to be discussed. The newly invented tool will be implemented in the School of Electrical and Electronics Engineering, Universiti Sains Malaysia, to assist the undergraduates in their learning of the control system subjects. The tool comprises of three aspects: software (National Instrument (NI) LabVIEW), hardware (self-built mechanical robotic manipulator arm with Brushless-DC (BLDC) motor (with its drivers) and quadrature encoders) and the software-hardware interfacing modules (NI myRIO).

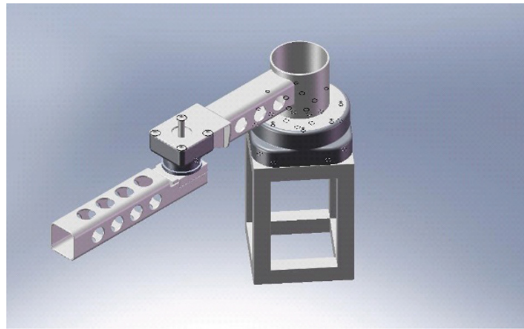
## 2 Software-Robotic Manipulator Robot Arm

The software part of the tool consists of a National Instrument LabVIEW which is a type of Rapid Prototyping Software for instrumentation, signal processing and control, suited for our Control Design and Prototyping needs. The LabVIEW allows the control designer to work in two environments hand-in-hand which are termed as Virtual Instruments or Vis. The VIs are further classified into two:- the codings pane and the

Graphical User Interface(GUI). Simultaneous access and ease of configuration to both panes accelerates the design and development of control system for our robotic system.

### 3 Hardware-Robotics Manipulator Robot Arm

Figure 1 shows a two-degrees-of freedom (2DOF) planar robot manipulator system which was self-built, equipped with a BLDC motor at each of its joints for actuation. Two quadrature incremental encoders are connected to its drive shaft to feedback the current angular position of the robot arm links. The BLDC motors are driven by its associated Voltage-based driver.



**Fig. 1.** The CAD design of the two degrees of freedom (2 DOF) planar mechanical robotic arm system used in the newly setup of Control System Laboratory experiment

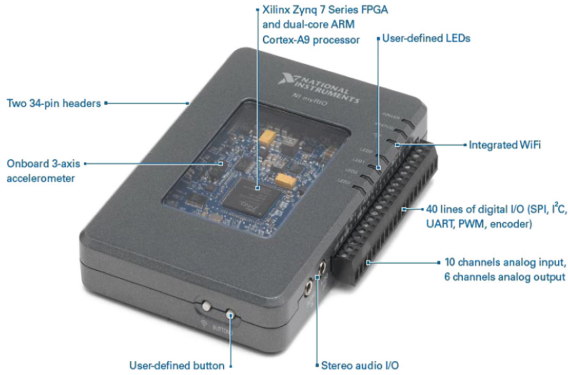
### 4 Software-Hardware Interfacing Modules (NI's MyRIO)

Figure 2 shows NI's myRIO forms the 'heart' of our pedagogical tool or the Robotic Arm Control Laboratory experiment equipment. It is not an ordinary Data-Acquisition board(DAQ) because on board, it is packed with dual-core ARM processor for number crunching application and Xilinx Zynq FPGA for huge parallel data processing application. The software codes and the control algorithm designed in LabVIEW can be downloaded into myRIO once, and act as a standalone computer which controls the robotic arm.

## 5 Two DOF Planar Robot Manipulator Model and Controller Design

### 5.1 Kinematics Model

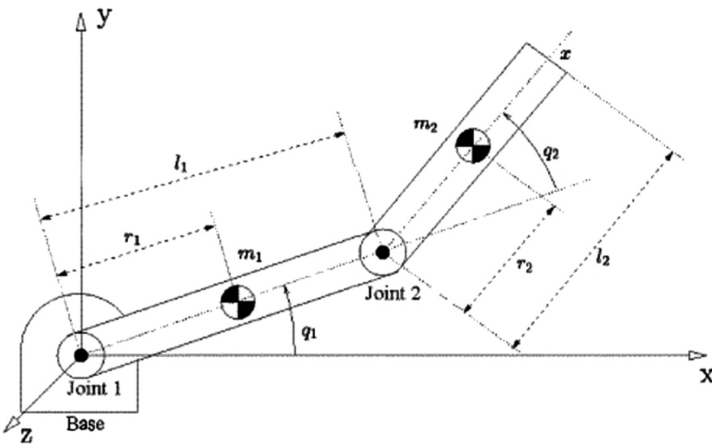
Kinematics model relates the position and orientation of end-effector and spatial position of joint-link. The kinematics analysis is divided into forward kinematics and inverse kinematics. Forward kinematic describes the transformation from joint space to Cartesian space whereas inverse kinematic describes the transformation from Cartesian space to joint space.



**Fig. 2.** National Instrument’s myRIO is fully packed with useful peripheral and state-of-the-art features such as dual-core processor ARM as well as Xilinx.Zynq FPGA, 3-axis accelerometer, sufficient Digital/Analog IOs and PWM signal generator

The two degrees of freedom (DOF) planar robot manipulators with two revolute joints can be represented in a diagram as illustrated in Fig. 3. The joint variables are  $q_1$  and  $q_2$ . The link length for the first link and second link are denoted by  $l_1$  and  $l_2$  respectively whereas the mass of first and second links are represented by  $m_1$  and  $m_2$ . Through simple trigonometric manipulation, the forward kinematic model is obtained by:

$$\begin{aligned} x &= l_1 \cos(q_1) + l_2 \cos(q_1 + q_2) \\ y &= l_1 \sin(q_1) + l_2 \sin(q_1 + q_2) \end{aligned} \tag{1}$$



**Fig. 3.** A Schematic diagram of the 2-DOF planar robot manipulator

### 5.2 Dynamic Model

The complex dynamic system of the serial link manipulators are commonly modelled by using Euler-Lagrange or Euler-Newton formulation. Under reasonable assumption, the resulting dynamic model of any n degree of freedom robot manipulators can be expressed in a general form:

$$M(q)\ddot{q} + C(q, \dot{q})\dot{q} + g(q) = \tau \tag{2}$$

where  $\ddot{q}$ ,  $\dot{q}$  and  $q$  are the  $n \times 1$  vector of joint angular acceleration, joint velocity and joint angle respectively,  $M(q)$  is the  $n \times n$  symmetric positive definite manipulators inertia matrix,  $C(q, \dot{q})$  is the  $n \times n$  vector of centrifugal and Coriolis torques,  $g(q)$  is  $n \times 1$  vector of gravitational torques and  $\tau$  is the  $n \times 1$  vector of applied torques input.

The resulting form of the robot model elements can be given by:

$$\begin{aligned} M(q) &= \begin{pmatrix} (\frac{1}{3}m_1 + m_2)l_1^2 + \frac{1}{3}m_2l_2^2 + m_2l_1l_2C_2 & m_2[\frac{1}{3}l_2^2 + \frac{1}{2}l_1l_2C_2] \\ \frac{1}{3}m_2l_2^2 + \frac{1}{2}m_2l_1l_2C_2 & \frac{1}{3}m_2l_2^2 \end{pmatrix} \\ C(q, \dot{q}) &= \begin{pmatrix} -\frac{1}{2}m_2l_1l_2S_2\dot{\theta}_2 & -\frac{1}{2}m_2l_1l_2S_2(\dot{\theta}_1 + \dot{\theta}_2) \\ \frac{1}{2}m_2l_1l_2S_2\dot{\theta}_1 & 0 \end{pmatrix} \\ g(q) &= 0 \end{aligned} \tag{3}$$

### 5.3 PID Control

The PID controller algorithm as three unique parameters; proportional, integral, and derivative values. The Proportional part determines the reaction to the error, the Integral part determines the reaction based on the sum of recent errors and the Derivative part determines the reaction to the rate at which the error has been changing. The averaged sum of these actions is used to control the angular joints position of the robot manipulators so to follow the desired joint position. Each joint of the manipulators is treated as an individual system to be controlled.

The PID controller signal can be defined by:

$$\begin{aligned} u(t) &= Kp + Ki/s + Kd \cdot s \\ u(t) &= Kp(1 + 1/Ti/s + Td \cdot s) \end{aligned} \tag{4}$$

where  $K_p, K_I, K_D$  are tuning parameters which related to proportional gain, integral gain and derivative gain respectively.  $T_I$  is the integral action time, and  $T_d$  is the derivative action time. The best results are tuned using the knowledge of Ziegler Nichols method.



## 5.4 Computed Torque Control

Computed torque control or nonlinear control is a model-based control method which utilizes dynamics model of a system to compute the control torque signals that input to the system, given the present state of the system in order for the system to achieve desired motion. The control scheme makes direct use of the dynamic model of the manipulators to cancel the effect of inertia tensor, Coriolis and centrifugal force gravity, and friction. This method is a well-known modern system theory which is an application of feedback linearization of nonlinear system [5–15].

Regardless of frictional force, actuator dynamic and disturbance of the in the manipulators system, the computed torque control law can be governed by the following equation:

$$\tau = M(q)[\ddot{q}_d + K_d\dot{\tilde{q}} + K_p\tilde{q}] + C(q, \dot{q})\dot{q} + g(q) \quad (5)$$

where  $K_p$  and  $K_d$  are positive definite design matrices which refer to position control gain and derivative control gain respectively whereas  $q_d, \dot{q}_d, \ddot{q}_d$  correspond to the desired joint position, velocity and acceleration respectively.  $\tilde{q} = q_d - q, \dot{\tilde{q}} = \dot{q}_d - \dot{q}$  are called position error vector and velocity error vector respectively. Notice that the  $K_p\tilde{q} + K_d\dot{\tilde{q}}$  terms in (5) denote the PD type controller. Computed torque control implements the feedback linearization to compensate for the nonlinearities present in the manipulator dynamics whilst inserting the servo term which takes the form of PD controller.

## 5.5 Trajectory Planning

The task for the planar robot manipulators is described as a smooth point to point (PTP) motion by using joint space technique which consist series of time-dependent functions of all joint variables and their first two derivatives. These are generated to describe the desired motion of the manipulators. In this case, a 5th degree polynomial function is adopted to obtain trajectories with continuous joints position, velocity, and acceleration as:

$$\begin{aligned} q(t) &= a_0 + a_1t + a_2t^2 + a_3t^3 + a_4t^4 + a_5t^5 \\ \dot{q}(t) &= a_1 + 2a_2t + 3a_3t^2 + 4a_4t^3 + 5a_5t^4 \\ \ddot{q}(t) &= 2a_2 + 6a_3t + 12a_4t^2 + 20a_5t^3 \end{aligned} \quad (6)$$

By defining the coefficients of the polynomial result:

$$\begin{aligned}
 a_0 &= q_i \\
 a_1 &= \dot{q}_i \\
 a_2 &= \frac{1}{2} \ddot{q}_i \\
 a_3 &= \frac{1}{2T^3} [20(q_f - q_i) - (8\dot{q}_f + 12\dot{q}_i)T - (3\ddot{q}_f - \ddot{q}_i)T^2] \\
 a_4 &= \frac{1}{2T^4} [-30(q_f - q_i) + (14\dot{q}_f + 16\dot{q}_i)T + (3\ddot{q}_f - 2\ddot{q}_i)T^2] \\
 a_5 &= \frac{1}{2T^5} [12(q_f - q_i) - 6(\dot{q}_f + \dot{q}_i)T - (\ddot{q}_f - \ddot{q}_i)T^2]
 \end{aligned} \tag{7}$$

where  $t_f$  and  $t_i$  are the initial and final time instant respectively.  $q_i, \dot{q}_i$  and  $\ddot{q}_i$  are joint position, velocity and acceleration at respectively whereas  $q_f, \dot{q}_f$  and  $\ddot{q}_f$  are the joint position, velocity, and acceleration at respectively.

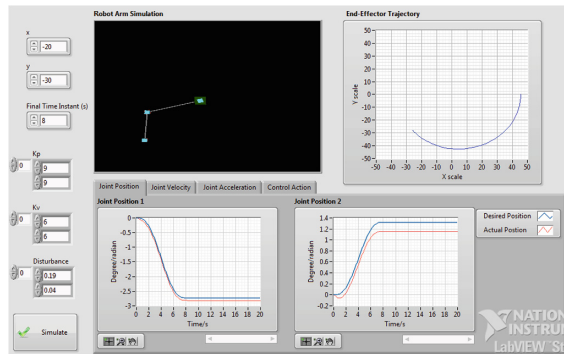


Fig. 4. Graphical User Interface (GUI) for computed-torque Control Module

### 5.6 Computed Torque Control Module

The main graphical user interface is depicted in Fig. 4. It is designed as a dynamic picture in the sense that the interface is built up in an interactive manner where the user can change a parameter and immediately see its influence without typing a single command. The left part of the GUI consists a number of choices and parameters which includes setting of desired x-y Cartesian coordinate of end-effector and the parameters  $K_{p1}, K_{p2}, K_{d1}$  and  $K_{d2}$  which are the elements in the control gain matrices.

Disturbance was introduced by using bounded Band-Limited White noise to simulate the effects of noise which maybe emitting from mechanical components. A simulation button is created to simulate the robot arm motion after user confirms the control parameters. The right part of the GUI shows the animated robot arm motion, end-effector trajectory, the system responses, particularly the joint positions, velocity, acceleration, and the control actions.

### 5.7 PID Control Module

The PID control module is the implementation of PID control to the 2-DOF planar robot manipulators with interactive graphical user interface (GUI). The main unit is a robot frame with two links jointed together by revolute joints. Two brushless DC motors controlled by motor drivers are attached to each joint of the robot to provide rotary motion for the joints.



**Fig. 5.** The hardware of two-DOF Planar Robot Manipulator

The two-DOF planar robot manipulator is shown in Fig. 5. Encoders are used to read and feedback the actual position at each joint to microprocessor for error calculation. MyRIO-1900 is used as the microprocessor to send the computed PID control signals to the motor drivers and keep track the angular position of each links via the encoders. In contrast with computed torque module, the desired joint positions of the set point are constant (step set-point). Similarly, inverse kinematics solution is used to obtain the desired joints position from the Cartesian space specified by user. PID control system is used to control the joint positions to follow the desired set position with the aid of the feedback of the actual joint positions from the encoders. User can set new desired end-effector position, change the PID gains at the bottom right part of the GUI and visualize how the real robot arm motion and its end-effector trajectory is simulated at the upper right part.

## 6 Results and Discussion

Several experiments are carried out to ensure that the computed torque control system work on the motion control of the dynamic model of the robot manipulators. It is to note that for computed-torque control module, the students are only allowed to use the simulated dynamics scenario. Hardware implementation for the computed-torque will be implemented in the future once the safety issue mechanism is resolved. The students, however, have the opportunity to implement a rather safe PID control mechanism on the real two-DOF planar robot system. They are able to learn intuitively the effects of derivative and integral terms of the PID controller on the transient and steady-state performance of the dynamical system.

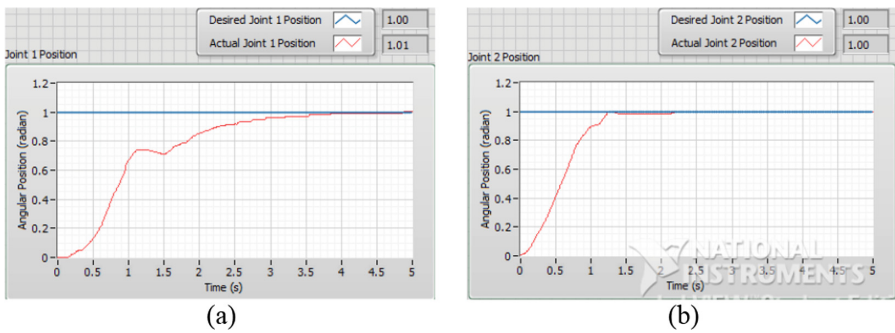


Fig. 6. The practically-implemented result of a PI controlled robot arm

Figure 6 shows the performance for the practically-implemented position control by using PI controller. The integral term added to the system eliminates the residual steady-state error that occurs with the case of a pure proportional controller shown in Fig. 7. However, since the integral term responds to accumulated errors from the past, it can cause the present value to overshoot the set point value.

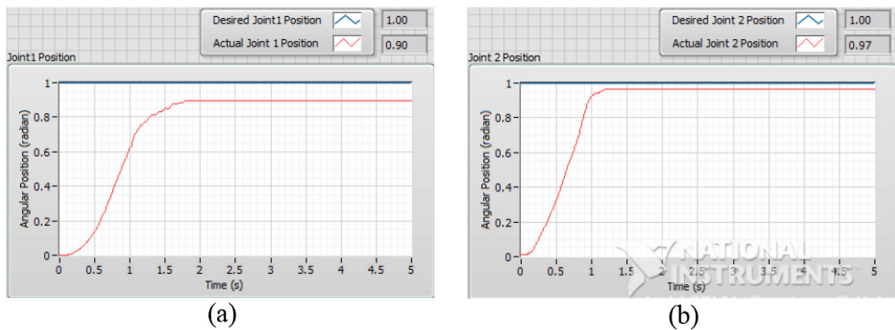
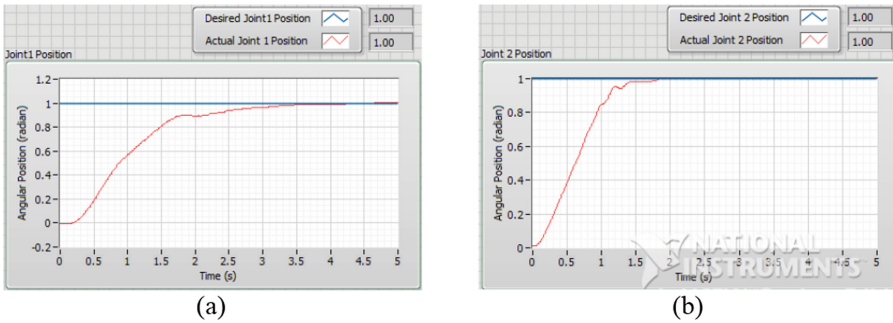


Fig. 7. The practically-implemented result of a PD controlled robot arm



**Fig. 8.** The practically-implemented result of PID controlled robot arm

Figure 7 shows the performance for the position control by using PD controller. The controller eliminates the undesired overshooting of the system yet it unable to compensate for the steady state errors. The derivative action predicts system behaviour and thus improves settling time and stability of the system.

Figure 8 shows the performance for the position control by using PID controller. The system shows less oscillation compared to PI control and the joint positions reach the desired positions set with no steady state error. PID controller combine the advantages of both PI and PD controller which reduces the undesired overshoot and able to eliminate completely the steady state error of the system.

## 7 Conclusion

A two-DOF planar robot manipulators system trainer with interactive simulation of control systems has been developed and described in this paper. The highly interactive of LabVIEW has been found to be a key issue in the GUI design. The tool is divided in two modules according to the control objective: computed torque control module and PID control module. The former includes attractive robot arm simulation with tunable parameters; the latter involves implementation of PID control in the developed planar robot arm to visualize the system performance. The system has a strong pedagogical potential to be used as a natural complement to traditional training and education on the control of robots to quickly gain an insight and motivation.

**Acknowledgements.** The authors are also particularly thankful to School of Electrical and Electronics Engineering, USM for the provision of funds to support the project. In addition, the authors are thankful to National Instrument for their provision of myRIO to be able for the authors to carry out their work in the DreamCatcher Innovate Competition. The authors are also thankful to Timur Automation Sdn. Bhd. for their provision of brushless DC (BLDC) motor and quadrature encoders in this project for without their in-kind assistance this project will not be completed.

## References

1. Rivas, D., Alvarez, M., Velasco, P., Mamarandi, J., Carillo-Medina, J.L., Bautista, V., Galarza, O., Reyes, P., Erazo, M., Perez, M., Huerta, M.: BRACON: control system for a robotic arm with 6 degrees of freedom for education systems. In: Proceedings of 6th International Conference on Automation, Robotics and Applications (ICARA), Queenstown, pp. 358–363, (2015)
2. Mora, R.: School is so boring: high-stakes testing and boredom at an urban middle school. Univ. Pennsylvania Grad. Sch. Educ. Online Urb. Educ. J. **9**(1), 1–9 (2011)
3. Suryadi, I., Widodo, R.J.: Control systems in our daily life. In: Li, D. (Ed.) Volume I: First IFIP TC 12 International Conference on Computer and Computing Technologies in Agriculture (CCTA 2007), Wuyishan, China, pp. 239–251. Springer, Boston (2007)
4. Shui-Chun, L., Ching-Chih, T.: Development of a self-balancing human transportation vehicle for the teaching of feedback control. IEEE Trans. Educ. **52**(1), 157–168 (2009)
5. Satyanarayan, M.: Fundamental challenges in mobile cloud computing. In: Proceedings ACM Symposium Principles of distributed Computing. ACM Press, New York (1996)
6. Craig, J.J.: Introduction to Robotics: Mechanics and Control. Prentice Hall, Pearson (2005)
7. Mark, S.H., Spong, W., Vidyasagar, M.: Robot Modeling and Control (2006)
8. Bejczy, A.K.: Dynamic analysis for robot arm control. In: Proceedings of American Control Conference, pp. 503–504 (1983)
9. Dixon, W.E.: Control of robot manipulators in joint space. Int. J. Robust Nonlinear Control **16**, 945–946 (2006)
10. Frank, D.M.D., Lewis, L., Abdallah, C.T.: Robot Manipulator Control: Theory and Practice, 2nd edn. Marcel Dekker Inc, New York (2004)
11. Doering, E.: NI myRIO Project Essentials Guide: Electrical and Computer Engineering Department Rose-Hulman Institute of Technology (2014)
12. Ganesan, N., Gopalakrishnan, K.: Design and control of 3-DOF articulated robotic arm using LabVIEW and NI-myRIO. Int. J. Innov. Res. Electr. Electron. Instrum. Control Eng. **3**, 2015
13. Mahyuddin, M.N., Khan, S.G., Herrmann, G.: A novel robust adaptive control algorithm with finite-time online parameter estimation of a humanoid robot arm. Robot. Auton. Syst. **62**(3), 294–305 (2014)
14. Mahyuddin, M.N., Herrmann, G., Khan, S.G.: A novel adaptive control algorithm in application to a humanoid robot arm. In: Lecture Notes (Book Chapter) in Advances in Autonomous Robotics, vol. 7429, pp. 25–36. Springer, Berlin (2012)
15. Na, J., Mahyuddin, M.N., Herrmann, G., Ren, X., Barber, P.: Robust adaptive finite-time parameter estimation and control for robotic systems. Int. J. Robust Nonlinear Control **25**, 3045–3071 (2014)



# Emotional States Analyze from Scaling Properties of EEG Signals Using Hurst Exponent for Stroke and Normal Groups

Choong Wen Yean<sup>1</sup>✉, Wan Khairunizam<sup>1</sup>,  
Mohammad Iqbal Omar<sup>1</sup>, Murugappan Murugappan<sup>2</sup>,  
Zunaidi Ibrahim<sup>3</sup>, Bong Siao Zheng<sup>1</sup>, Shahrman Abu Bakar<sup>1</sup>,  
Zuradzman Mohamad Razlan<sup>1</sup>, and Wan Azani Mustafa<sup>4</sup>

<sup>1</sup> School of Mechatronic Engineering, Universiti Malaysia Perlis (UniMAP),  
Arau, Perlis, Malaysia

wenyea0412@gmail.com, wendy880806@gmail.com,  
{khairunizam, iqbalomar, shahrman,  
zuradzman}@unimap.edu.my

<sup>2</sup> Department of Electronics and Communication Engineering,  
Kuwait College of Science and Technology, Kuwait City, Kuwait  
m.murugappan@gmail.com

<sup>3</sup> Sustainable Advanced Manufacturing,  
University of Sunderland, Sunderland, UK  
zunaidi@yahoo.com

<sup>4</sup> Faculty of Engineering Technology,  
Universiti Malaysia Perlis, Kangar, Malaysia  
wanazani@unimap.edu.my

**Abstract.** Emotion is regulated by the interconnection of the brain network. Each emotion is a different mental state, where the neuronal oscillations differ for different emotions. The EEG signal has been a useful method to analyze emotions. Furthermore, the neuronal oscillation can be observed by analyzing the scaling properties of EEG signal. In this study, the EEG signal was used as the source of emotions of stroke patients and normal subject. The Hurst Exponent (HURST) was estimated from the EEG signal to analyze the auto-correlation of the signal. The estimated HURST indicated that all emotions in this work were exhibit positive correlation in the time scale, also the neuronal oscillation for every emotions experimented were statistically different.

**Keywords:** Emotion · Electroencephalogram (EEG) · Stroke · Hurst exponent (HURST) · Scaling properties

## 1 Introduction

Emotion is the psychophysiological experience in human that influenced by stimuli. It is an instant response of human to the stimuli they perceive. The emotion is controlled and processed by the brain, it involves many neural structures of the brain, where the emotional experiences of human are controlled and regulated by brain networks that formed by the interconnection between different brain regions [1, 2]. There are two

types of emotion, the positive emotion and the negative emotion. Positive emotions are the pleasant feeling such as happy, excited, delighted and satisfied, whereas the negative emotions are unpleasant emotions such as anger, sadness, annoyed and afraid [3, 4]. The emotions and health are interrelated, where the feedback or responses towards one's feeling will be expressed by their appearances.

The emotional states of human can hardly be classified into discrete or distributed emotions and are known to be continuum in nature. However, there is the "discrete emotion theory", which claimed that there are basic emotions that can be classified discretely. According to "discrete emotion theory", some emotions are distinguishable on the basis of biological and physiological. Silvan Tomkins proposed the discrete emotions as affect programs in 1962 and 1963, and concluded there are eight affect programs, they were surprise, interest, joy, rage, fear, disgust, shame, and anguish [5–7]. As influenced by Tomkin's studies, Paul Ekman introduced the "discrete emotion theory" in 1972, the six basic emotions introduced were anger, disgust, fear, happiness, sadness and surprise [8, 9]. According to Ekman, the emotions are universal and are distinguishable among all states of human. To date, the Ekman's six basic emotions have been widely used for the emotion-related studies.

In normal communication between human beings, the emotions are recognized through facial expressions and sometimes through body gestures or other physical appearances. However, emotions recognized through the physical appearances in some people are not possible, such as patients with stroke and Parkinson's disease, who possibly have problem to control their facial expression. Hence, researchers started working on analyzing the changes of internal feelings through biosignals, such as the brain signal or Electroencephalogram (EEG). The biosignals provide more reliable information about subjects' emotional state changes, since it cannot be controlled by the subjects and it reflects internal feelings of the subject by monitoring their physiological responses.

As a matter of fact, the EEG signals reveal different mental states as well as the degree of the mental states experienced. In this study the different emotional states represented the mental states with varies degree of experiences in the subject, hence the degree of emotional experiences can be assessed through the application of the non-linear feature extraction from the EEG signal. Also, this study aims to analyze the severity level of emotional impairment in the stroke patients with left and right brain damage by the comparison among the normal group and the stroke groups.

This paper was organized as follows: Sect. 1 introduces the background of emotions and emotion recognition. Section 2 presents the literature reviews of EEG signal processing by using non-linear features. Section 3 explains the methodology of this study. Section 4 reports the results and discussion of emotion analysis in EEG signal. Lastly, Sect. 5 concludes the findings of this study.

## 2 Literature Reviews

The feature extracted from the EEG signal plays a significant role in accurately identify the subject's responses. There were a number of features implemented in the emotion analysis using EEG signal, either using linear or non-linear features. EEG signal



exhibits non-linear characteristics, therefore non-linear analysis performs better than linear analysis in EEG signal processing [10].

From past studies, different non-linear features have been used and reported as effective methods for analyzing EEG signals. For instance, different HOS-based features were used to analyze the EEG signals in two emotional states, calm and negative emotion Hosseini [11]. Bispectrum features, approximate entropy (ApEN), Hurst Exponents (HURST) and Detrended Fluctuation Analysis (DFA) were used to analyze the emotional EEG signals of Parkinson's disease patient [12]. In the study of mental states using different types of music, the different non-linear features, the Correlation Dimension, Lyapunov exponent, HURST, and Approximate Entropy, have been implemented [13].

HURST was first designed to model the Nile river, it is used to determine the optimum dam size for the reservoir system [14]. Later, HURST has been applied in financial markets, it has been used to predict the long-term effect of the time series in observing the fractal nature of financial markets [15]. Accordingly, the HURST is valid for other natural system as well. In EEG signal processing, HURST has been used to identify the persistence of the trends in time series, and to characterize the EEG signals in different states [13, 16, 17].

In addition, researchers reported the existence of the long-range temporal correlation (LRTC) in EEG signals [18–20]. The LRTC indicates that the event in the past has an effect on the event in future. In other words, the LRTC in EEG signals indicates that the interaction of the underlying neuronal population is able to operate over a broad temporal scale. The correlation of the oscillatory brain activity has been investigated to occur after at least 5 s [18]. Furthermore, the LRTC showed an association to the severity of depression [20]. The LRTC in EEG signals can be characterized by using scaling exponent, such as Hurst exponent [21, 22] and detrended fluctuation analysis (DFA) [20, 21, 23].

HURST relates to the autocorrelations of the time series, it can be expressed in the H value, for instances the H value between 0.5 and 1 shows positive correlation in the time series, the H between 0 and 0.5 shows anti-correlation in time series, and the H at 0.5 indicates there is no correlation behavior in the time series [24].

## 3 Methodology

### 3.1 EEG Database

EEG database used in this study was taken from [25], this EEG database involved three groups of subjects, they were the stroke patients with left brain damage (LBD) and right brain damage (RBD), and also the normal control (NC), each of the group contained 15 subjects. Therefore, there were a total of 15 subjects  $\times$  3 groups = 45 subjects.

The emotions from the database were stimulated by using audio-visual stimuli in the form of video clips, the six stimulated emotions in the EEG database were anger, disgust, fear, happiness, sadness, and surprise. The data were collected using a 14 channel wireless EEG Epoc Emotiv headset at sampling frequency of 128 Hz. The

electrodes were placed over the entire scalp based on the international standard 10–20 system. There were 6 trials for each emotion, therefore the total number of trials of the six emotional states were 36. Each trial varies between 46 and 60 s.

### 3.2 Signal Pre-processing

The raw EEG signals of stroke patients (LBD and RBD) and NC were used for pre-processing to remove the effects of noises and artefacts that caused interference to the raw EEG signals. The artefacts due to eyes blink were removed by using thresholding method, where the potential higher than  $80 \mu\text{V}$  and lower than  $-80 \mu\text{V}$  were offset from each EEG raw signals.

Next, a 6<sup>th</sup> order Butterworth bandpass filter was used to filter the EEG signals. The filtering was performed with cut-off frequencies from 0.5 Hz to 49.0 Hz to extract the theta to gamma frequency band.

### 3.3 Feature Extraction

The characteristics that representing the emotional states in EEG signals were extracted from three frequency bands, the alpha (8–13) Hz, beta (13–30) Hz and gamma (30–49) Hz bands. After the pre-processing, the total number of sample in each channel was 5000. Signal segmentation divided the EEG signal into smaller epoch for feature extraction, with the 6 s segmentation, there were 768 samples in each epoch. Consequently, there were 6 epochs for each channel, and the HURST was estimated from each epoch.

This study used the Rescaled Range Statistics (RRS) method to estimate HURST, the RRS method is used to evaluate the variability of data in time series, RRS can be used to analyze the persistence, stochastic, or mean reversion in the data [26]. The RRS-based HURST were estimated from the amplitude envelope of the oscillatory EEG to investigate the amplitude fluctuations of the neuronal EEG. The detailed discussion of HURST estimation and interpretation can be found in [26].

### 3.4 Statistical Validation

The extracted features were tested for their statistically significant among the six emotions, one-way analysis of variance (ANOVA) was used to test the significant changes among the six emotions for the three groups, LBD, RBD and NC, respectively. The features were validated as statistically significant if the p-value is less than or equal to 0.05.

## 4 Results and Discussion

The six discrete emotional experiences of the stroke patients and normal subjects were analyzed by applying HURST to the EEG signals. The HURST is a fractal analysis that analyze the signal by scaling method, thus the relation of the events in EEG signal can be studied from the HURST value. In this work, the events to study were the different

emotional experiences. Therefore, the HURST was used to investigate the presence and the persistency of the emotional experiences.

The estimated RRS-based HURST were validated for the significant different among the six emotions, the results of the ANOVA were presented in Table 1. As shown in Table 1, all the HURST are statistically significant among the six emotions with p-value less than 0.05, for all subject groups in alpha, beta and gamma frequency bands.

**Table 1.** ANOVA among the six emotions

Group	Alpha	Beta	Gamma
LBD	0.0002	<0.001	<0.001
RBD	0.0039	<0.001	<0.001
NC	<0.001	<0.001	<0.001

The HURST estimated from the EEG signal represented the neural oscillation of the underlying signal. From the results, the HURST of the six emotions were statistically different, which indicated the neuronal oscillation of the emotional states are statistically different.

As shown in Figs. 1, 2 and 3, the estimated HURST from the emotional EEG of LBD, RBD and NC have shown the presence of LRTC with the average HURST value between 0.5 and 1, in alpha, beta and gamma bands. Therefore, the six emotional states of LBD, RBD and NC have positive correlation in the EEG signal. Thus, indicated the interaction of the underlying neuronal population is able to operate over a broad temporal scale.

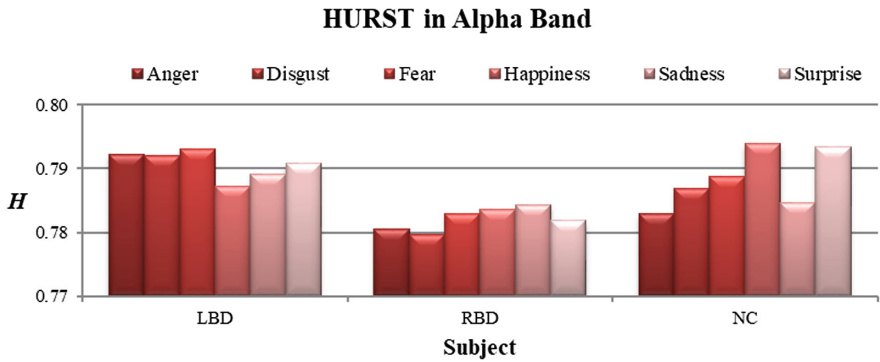
In Fig. 1, the RBD group has lower HURST than LBD and NC groups, the RBD group has the lowest value in disgust emotion, and the highest value in sadness emotion. Meanwhile, the LBD has the lowest value in happiness emotion and the highest value in fear emotion. For NC group, the anger emotion has the lowest value while the happiness emotion has the highest value.

Likewise, the Fig. 2 shows the RBD group has the lowest HURST value compared to LBD and NC group in the beta band. However, the HURST values are overall smaller than in the alpha frequency band in Fig. 1. In beta band, all the three groups have the lowest value in sadness emotion, whereas the highest values are in the disgust, fear and happiness emotions, respectively for LBD, RBD and NC groups.

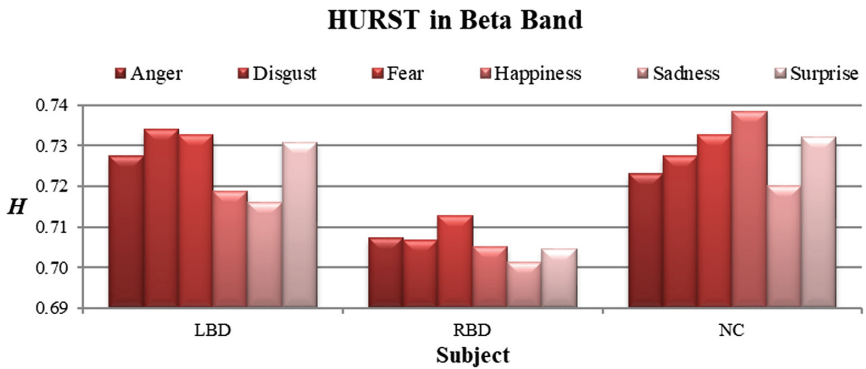
Moreover, the RBD has the lowest HURST compared to LBD and NC in gamma band as shown in Fig. 3. The LBD group has the lowest value in happiness emotion whereas the RBD and NC groups both have the lowest value in sadness emotion. Similarly to Fig. 2, which is beta band, the gamma band shown in Fig. 3 also has the highest values in the disgust, fear and happiness emotions, respectively for LBD, RBD and NC groups.

Overall, the results from Figs. 1, 2 and 3 show that the alpha frequency band has the highest HURST than beta and gamma bands. Also, the RBD has the lowest HURST compared to LBD and NC in all frequency bands. The highest average HURST for NC is the happiness in all frequency bands. Unlike the NC, the stroke groups have highest average HURST for negative emotions. The LBD has highest for fear (alpha) and

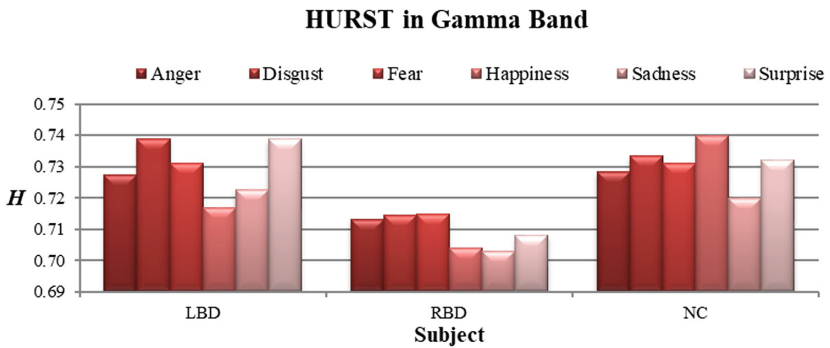
disgust (beta and gamma), whereas the RBD has highest average HURST for sadness (alpha) and fear (beta and gamma).



**Fig. 1.** Estimated HURST of all emotional states from alpha frequency band



**Fig. 2.** Estimated HURST of all emotional states from beta frequency band



**Fig. 3.** Estimated HURST of all emotional states from gamma frequency band

As has been noted, HURST can be used to represent different mental states. Consequently, the HURST values differ significantly in this current work and can be used to interpret as the degree of emotional experiences, it can be used to explain which emotion has not been experienced in stroke patient but normal subject do. Indeed, in this study the happiness emotion has lower degree of experience in both the stroke groups, but it is the highest emotional experience in the normal group, which complement to the fact that stroke patients are prone to negative emotions than positive emotions [27, 28]. Additionally, the RBD group has the lowest HURST value which suggests that the RBD group has higher degree of severity in emotion impairment compared to the LBD group, which has been reported in previous studies [29].

## 5 Conclusion

This study presented the scaling properties of emotional EEG signals of stroke patients and normal subjects. The LRTC in the emotional EEG has been observed in all subject groups in alpha, beta and gamma frequency bands, and the neuronal oscillation of each emotional state were validated as statistically different. The HURST was highest for happiness emotion, which is the positive emotion and lowest for the sadness emotion, which is the negative emotion, in the NC group. Furthermore, the RBD group has the lowest HURST compared to the LBD and NC.

**Acknowledgements.** TUSB Research UniMAP supports this research under the research Grant 2017/08/0006.

## References

1. Stam, C.J., van Straaten, E.C.W.: The organization of physiological brain networks. *Clin. Neurophysiol.* **123**(6), 1067–1087 (2012). <https://doi.org/10.1016/j.clinph.2012.01.011>
2. LeDoux, J.E., Brown, R.: A higher-order theory of emotional consciousness. *Proc. Natl. Acad. Sci.* **114**(10), E2016–E2025 (2017). <https://doi.org/10.1073/pnas.1619316114>
3. Nezlek, J.B., Kuppens, P.: Regulating positive and negative emotions in daily life. *J. Personal.* **76**(3), 561–580 (2008). <https://doi.org/10.1111/j.1467-6494.2008.00496.x>
4. Snyder, S.A., Heller, S.M., Lumian, D.S., McRae, K.: Regulation of positive and negative emotion: effects of sociocultural context. *Front. Psychol.* **4**(JUL), 1–12 (2013). <https://doi.org/10.3389/fpsyg.2013.00259>
5. Tomkins, S.S.: *Affect, Imagery, Consciousness*, vol. 1. America (1962)
6. Tomkins, S.S.: *Affect, imagery, consciousness: II*. In: *The Negative Affects* (1963). <https://doi.org/10.1037/14351-000>
7. Colombetti, G.: From affect programs to dynamical discrete emotions. *Philos. Psychol.* **22**(4), 407–425 (2009). <https://doi.org/10.1080/09515080903153600>
8. Ekman, P.: An argument for basic emotions. *Cogn. Emot.* **6**, 169–200 (1992). <https://doi.org/10.1080/02699939208411068>
9. Ekman, P.: Are there basic emotions? *Psychol. Rev.* **99**(3), 550–553 (1992). <https://doi.org/10.1037/0033-295X.99.3.550>

10. Yuvaraj, R., Murugappan, M., Ibrahim, N.M., Omar, M.I., Sundaraj, K., Mohamad, K., Palaniappan, R., Satiyan, M.: Emotion classification in Parkinson's disease by higher-order spectra and power spectrum features using EEG signals: a comparative study. *J. Integr. Neurosci.* **13**(01), 89–120 (2014). <https://doi.org/10.1142/S021963521450006X>
11. Hosseini, S.A.: Classification of brain activity in emotional states using HOS analysis. *Int. J. Image Graph. Signal Process.* **4**(1), 21–27 (2012). <https://doi.org/10.5815/ijigsp.2012.01.03>
12. Yuvaraj, R., Murugappan, M., Ibrahim, N.M., Sundaraj, K., Omar, M.I., Mohamad, K., Palaniappan, R.: Optimal set of EEG features for emotional state classification and trajectory visualization in Parkinson's disease. *Int. J. Psychophysiol.* **94**(3), 482–495 (2014). <https://doi.org/10.1016/j.ijpsycho.2014.07.014>
13. Natarajan, K., Acharya, R.U., Alias, F., Tiboleng, T., Puthusserypady, S.K.: Nonlinear analysis of EEG signals at different mental states. *Biomed. Eng. Online* **3**(1), 7 (2004). <https://doi.org/10.1186/1475-925X-3-7>
14. Hurst, H.E.: Long-term storage capacity of reservoirs. *Trans. Am. Soc. Civ. Eng.* **116**, 770–799 (1951)
15. Mandelbrot, B.B., Wallis, J.R.: Noah, Joseph, and operational hydrology. *Water Resour. Res.* **4**(5), 909–918 (1968). <https://doi.org/10.1029/WR004i005p00909>
16. Hosseini, S.A., Akbarzadeh-T, M.R., Naghibi-Sistani, M.B.: Qualitative and quantitative evaluation of EEG signals in epileptic seizure recognition. *Int. J. Intell. Syst. Appl.* **5**(6), 41–46 (2013). <https://doi.org/10.5815/ijisa.2013.06.05>
17. Lahmiri, S.: Generalized Hurst exponent estimates differentiate EEG signals of healthy and epileptic patients. *Phys. A* **490**, 378–385 (2018). <https://doi.org/10.1016/j.physa.2017.08.084>
18. Watters, P.A., Martin, F.: A method for estimating long-range power law correlations from the electroencephalogram. *Biol. Psychol.* **66**(1), 79–89 (2004). <https://doi.org/10.1016/j.biopsycho.2003.09.001>
19. Lee, J.M., Kim, D.J., Kim, I.Y., Park, K.S., Kim, S.I.: Nonlinear-analysis of human sleep EEG using detrended fluctuation analysis. *Med. Eng. Phys.* **26**(9), 773–776 (2004). <https://doi.org/10.1016/j.medengphy.2004.07.002>
20. Bornas, X., Fiol-Veny, A., Balle, M., Morillas-Romero, A., Tortella-Feliu, M.: Long range temporal correlations in EEG oscillations of subclinically depressed individuals: their association with brooding and suppression. *Cogn. Neurodyn.* **9**(1), 53–62 (2014). <https://doi.org/10.1007/s11571-014-9313-1>
21. Hartley, C., Berthouze, L., Mathieson, S.R., Boylan, G.B., Rennie, J.M., Marlow, N., Farmer, S.F.: Long-range temporal correlations in the EEG bursts of human preterm babies. *PLoS ONE* **7**(2), e31543 (2012). <https://doi.org/10.1371/journal.pone.0031543>
22. Sheng, H., Chen, Y., Qiu, T.: Multifractional property analysis of human sleep EEG signals. *Int. J. Bifurc. Chaos* **22**(04), 1250080 (2012). <https://doi.org/10.1142/S0218127412500800>
23. Nikulin, V.V., Brismar, T.: Long-range temporal correlations in electroencephalographic oscillations: relation to topography, frequency band, age and gender. *Neuroscience* **130**(2), 549–558 (2005). <https://doi.org/10.1016/j.neuroscience.2004.10.007>
24. Mansukhani, S.: The Hurst Exponent: Predictability of Time Series. *INFORMS* (2012). Retrieved from <http://analytics-magazine.org/the-hurst-exponent-predictability-of-time-series/>
25. Bong, S.Z., Wan, K., Murugappan, M., Ibrahim, N.M., Rajamanickam, Y., Mohamad, K.: Implementation of wavelet packet transform and non linear analysis for emotion classification in stroke patient using brain signals. *Biomed. Signal Process. Control* **36**, 102–112 (2017). <https://doi.org/10.1016/j.bspc.2017.03.016>

26. Voss, J.: Rescaled Range Analysis: A Method for Detecting Persistence, Randomness, or Mean Reversion in Financial Markets (2013). Retrieved from <https://blogs.cfainstitute.org/investor/2013/01/30/rescaled-range-analysis-a-method-for-detecting-persistence-randomness-or-mean-reversion-in-financial-markets/>
27. Bogousslavsky, J.: William Feinberg lecture 2002: emotions, mood, and behavior after stroke. *Stroke* **34**(4), 1046–1050 (2003). <https://doi.org/10.1161/01.STR.0000061887.33505.B9>
28. Robinson, R.G., Jorge, R.E.: Post-stroke depression: a review. *Am. J. Psychiatry* **173**(3), 221–231 (2016). <https://doi.org/10.1176/appi.ajp.2015.15030363>
29. Yuvaraj, R., Murugappan, M., Norlinah, M.I., Sundaraj, K., Khairiyah, M.: Review of emotion recognition in stroke patients. *Dement. Geriatr. Cogn. Disord.* **36**(3–4), 179–196 (2013). <https://doi.org/10.1159/000353440>



# Rover Car Outdoor Localization for Navigation Tracking Using Differential Global Positioning System Estimation

Wi Kang Chew<sup>1</sup> and Muhammad Aizzat Zakaria<sup>1,2</sup>(✉)

<sup>1</sup> Innovative Manufacturing, Mechatronics and Sport (iMAMS) Laboratory,  
Faculty of Mechanical and Manufacturing Engineering,  
Universiti Malaysia Pahang, Pahang, Malaysia  
maizzat@ump.edu.my

<sup>2</sup> Automotive Engineering Center (AEC),  
Universiti Malaysia Pahang, Pahang, Malaysia

**Abstract.** GPS is a technique that has become very popular for outdoor positioning. Due to the error in satellite signal, the GPS receivers determine the accuracy of a current location with about 100 m in latitude and 156 m in longitude. Autonomous vehicles depend on positioning accuracy in navigation tracking. Inaccuracy of positioning will cause the autonomous vehicles moving in dangerous way. So in this paper, Differential Global Positioning System (DGPS) experiment will be introduced to improve the accuracy of the positioning data. In the experiment, reference station and rover station will receive the positioning data from GPS satellites and the positioning data collected from reference station will be used to calculate the errors and the errors correction will then be transferred to rover station to improve the accuracy of positioning data. The results obtained will be discussed based on the range and average of positioning errors and the Differential Global Positioning System (DGPS) improvement at different time.

**Keywords:** GPS · DGPS · Autonomous · Localisation · Navigation · Tracking

## 1 Introduction

Global Positioning System (GPS) is a satellite-based radio navigation system that has been operated by United Air Force and it is owned by the U.S government. GPS is also a global navigation satellite system that offers geolocation and time information to a GPS receiver anywhere on Earth when there is unobstructed line of sight to four or more GPS satellites. A weak GPS signals can be affected by obstacles such as mountains and building blocks [1].

GPS is widely used in public sector for navigation purposes such as traffic or geological as a primary use of data. GPS is well suited for most navigational applications with an overall accuracy of approximately 25 m, based upon governmental selective availability [2]. Furthermore, GPS is also used for applications that related to



newly developed autonomous devices such as lawnmowers or drones. These devices also mainly use GPS as a primary source for navigation. However, GPS only provides limited level of precision and accuracy. Besides, the autonomous ground moving vehicles require a high level of accuracy to be able to follow a defined path and do not overpass a defined area. In addition, the flying objects require the same accuracy in vertical domain [3, 4] (Fig. 1).

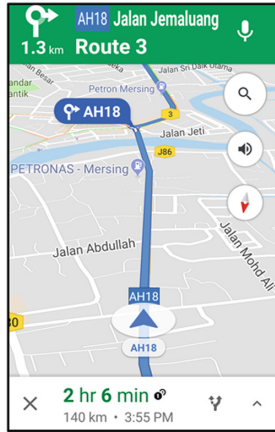


Fig. 1. GPS navigation

Position augmentation of GPS is a technique for increasing the accuracy of object's position to remove and decrease errors that caused by the signal propagation errors and clock biases. The position augmentation methods of GPS such as DGPS and RTK (Real Time Kinematics) are widely used for providing better improvements on the accuracy of position [5–7]. However, the systems are expensive to implement compared to the existing GPS [8].

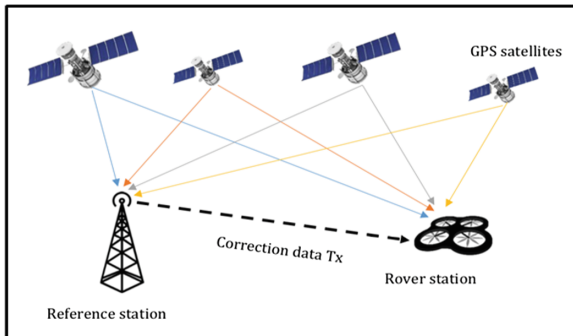


Fig. 2. Principal scheme of DGPS [9]

DGPS was designed to alleviate the error of systematic of Selective Availability (SA). The error of positioning from 100 m can be improved to about 10 cm. DGPS can be composed by the Reference Station and Rover Station. In Fig. 2, Reference Station is stationary situated at a fixed and location and then calculates the errors correction between known and computed positioning data. Next, rover station would use the error corrections for alleviating the error of positioning and improving the accuracy of positioning. The estimated correction can be done by position domain of DGPS [10].

## 2 Methodology

### 2.1 Mathematical Modelling

Position domain of DGPS is very simple to understand where the difference the known and measured position is calculated and then to augments the position, the calculated position difference is added to the measurement of rover [11]. In position domain of DGPS, the computed coordinates  $\vec{X}_{RS}$  is subtracted from the known coordinates of reference station. The position difference is denoted as vector  $\delta_x$ .

$$\vec{\delta}_x = \vec{X}_{RS,known} - \vec{X}_{RS} \quad (1)$$

The error corrections are then applied to the measured position from rover station which is used for mitigating the position error, and improving the accuracy of positioning.

$$\vec{X}_{rover,DGPS} = \vec{X}_{rover,measured} + \delta_x \quad (2)$$

### 2.2 Flowchart of the DGPS Experiment

For DGPS experiment, DGPS algorithm is first to be understood by the researcher to prevent any mistakes on experimental design of DGPS. Next, reference station and rover station are required to setup for collecting positioning data. The positioning data that is collected from the Reference Station are used for average error monitoring and errors calculation and the corrected data will be transferred to rover station to correct the positioning data and calculate the offset between GPS and DGPS. The details of the experimental setup on reference station and rover station will be explained on the next section (Fig. 3).

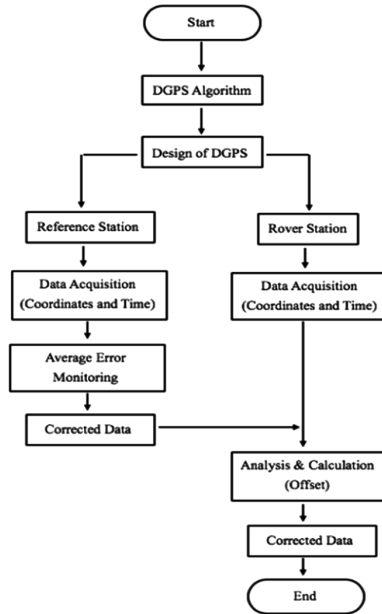
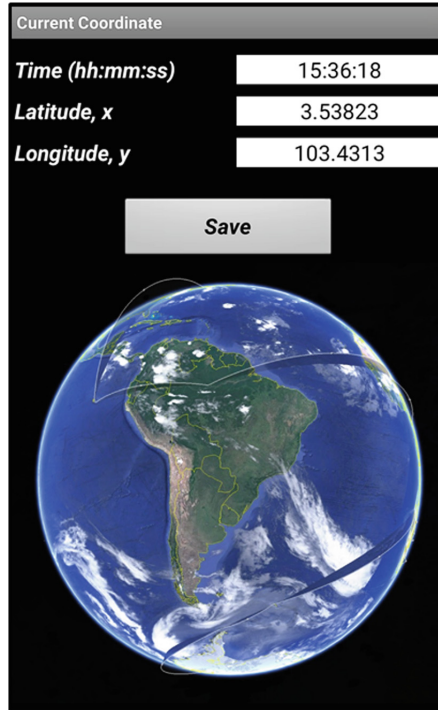


Fig. 3. Flow chart of DGPS experiment

### 2.3 Reference Station

DGPS operation uses a reference station at a fixed and known position to receive positioning data, calculate and eliminate errors to improve the accuracy of positioning data [12, 13]. So before the experimental setup on reference station, an Android apps which is named “Current Coordinate” is built via MIT App Inventor for collecting positioning data and time. The apps will be used together with “Auto Clicker” apps to auto-collect the positioning data constantly. Note that “Auto Clicker” apps can be downloaded from Google Play Store.

“Current Coordinate” apps is built and the layout of the apps is as shown in Fig. 4. The “Current Coordinate” apps showed the time (in hours: minutes: seconds), latitude, x and longitude, y. To use the apps, the location services on phone is required to be turned on for receiving the location information. After the location service is turned on, latitude, x and longitude, y will be shown accordingly based on the location. Due to the accuracy of GPS, the latitude, x and longitude, y would change from time to time.



**Fig. 4.** Own-built android app “Current Coordinate”

The experimental flow chart of reference station is shown in Fig. 5. First, an Android phone is required to install “Current Coordinates” and “Auto Clicker” apps. Next, the Android phone is connected with power supply to prevent battery drainage during positioning data collection and prevent any movement of the phone to make sure the phone is in static so the data collected is more accurate and the analysis of data will be correct. Then, the location service on phone is required to turn on for receiving the positioning data. Next, the location where the phone is fixed is checked on google maps. After that, the “Current Coordinates” apps is opened for checking the functionality. When the positioning data is receiving, “Auto Clicker” apps is then used for automatically clicking the **Save** button on “Current Coordinates” apps every second in 24 h to collect the current positioning data. The data collected will be used for calculating and analysing the errors. The results will be explained in the next section.

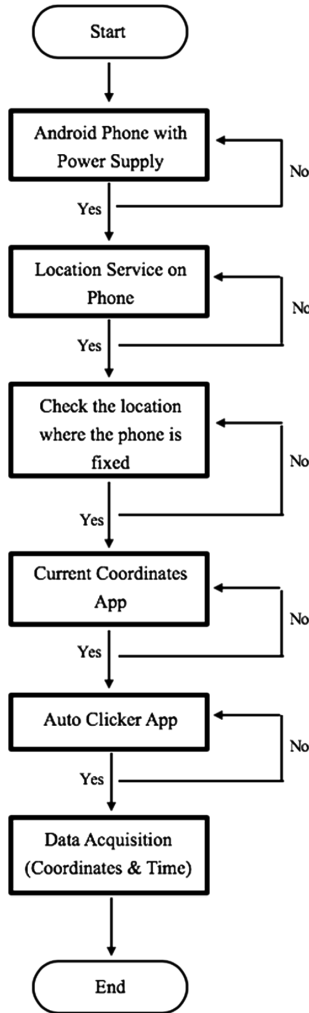


Fig. 5. Experimental flow chart of reference station

### 2.4 Rover Station

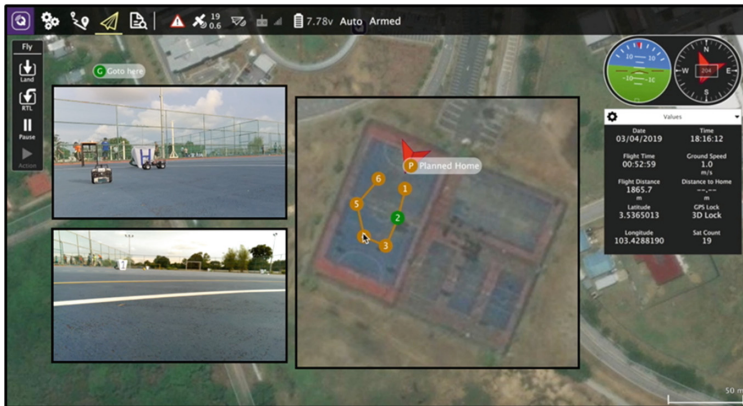
DGPS correction information is transmitted by the reference station to rover station to adjust the accuracy of positioning data.

Figure 6 showed the experimental setup of Rover Station. Rover used is 1972 Ford Bronco Ascender™ 1/10 RTR. Components such as GPS Neo-8m Module with compass, receiver, radio telemetry, power module, lithium polymer battery, servo and ESC motors are connected to Pixhawk 2.4.8 Controller. Software such as Mission Planner is used for setting up the program and creating the mission on it [14]. Figure 7 showed that the autonomous mission via QGroundControl Software. There are

6 waypoints on the map showed in Fig. 7 and the rover will move according to the points with the aid of GPS module on rover.



**Fig. 6.** Experimental setup of Rover Station



**Fig. 7.** Autonomous mission via QGroundControl Software

### 3 Results and Discussions

In this section, results on Reference Station and Rover Station will be discussed accordingly.

#### 3.1 Reference Station

In Reference Station, the results are discussed based on different time range (in 24 h, from 12 am to 8 am, from 8 am to 4 pm and from 4 pm to 12 am). The location where the phone is fixed is (3.54106, 103.41937) via Google maps. Next, the positioning data

at the same location are collected every second via “Current Coordinates” apps. The fixed coordinate from Google maps is then used to subtract the collected positioning data from phone for calculating the errors. The results such as coordinates distribution, errors distribution, error of latitude, x (m) and error of longitude, y (m) are discussed.

### 24 Hours

Figures 8 and 9 showed the coordinates distribution at the same location in 24 h and the errors distribution in 24 h respectively. From the graph, some coordinates are far away from the fixed and known coordinates. The minimum and maximum of the error in latitude, x are  $-153.18$  m and  $231.99$  m respectively whereas the minimum and maximum of the error in longitude, y are  $-87.69$  m and  $114.33$  m respectively. The large range on errors occurred might due to different effect such as climatic change and unstable of GPS system on GPS sensor.

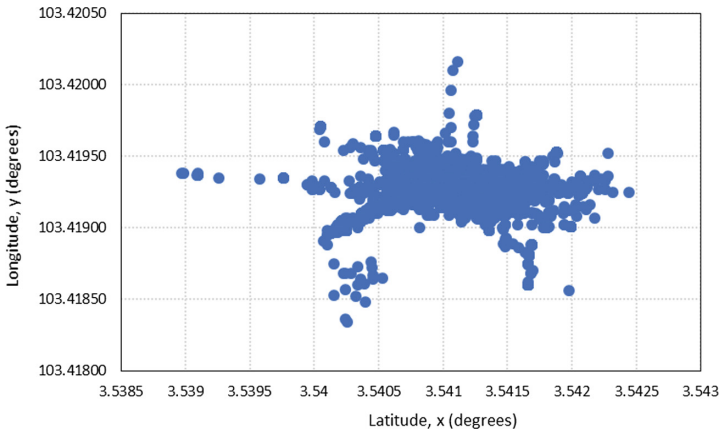


Fig. 8. Coordinates distribution in 24 h

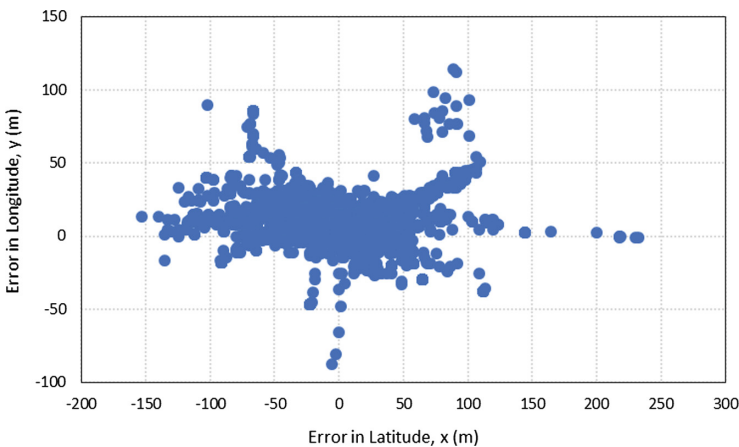
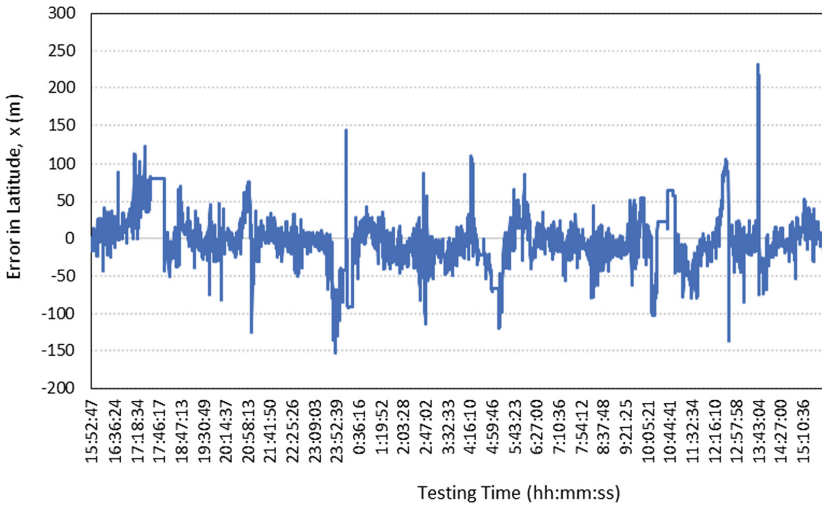
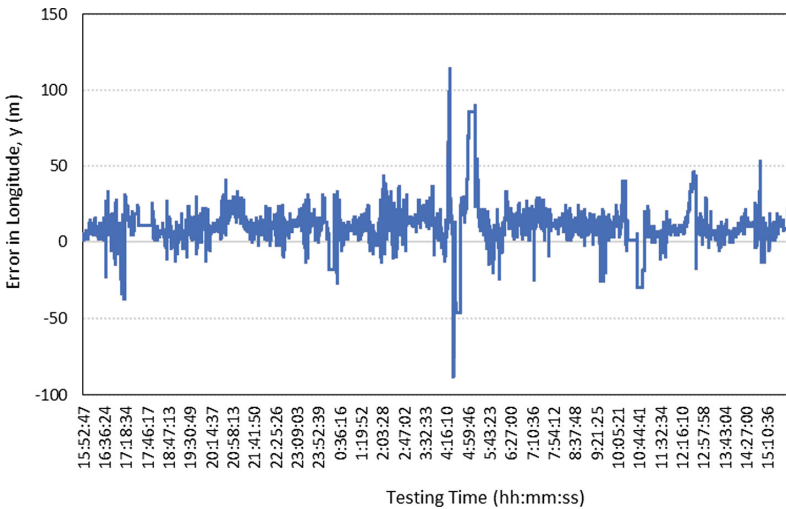


Fig. 9. Errors distribution in 24 h



**Fig. 10.** Graph of error in latitude,  $x$  (m) vs testing time (in 24 h)



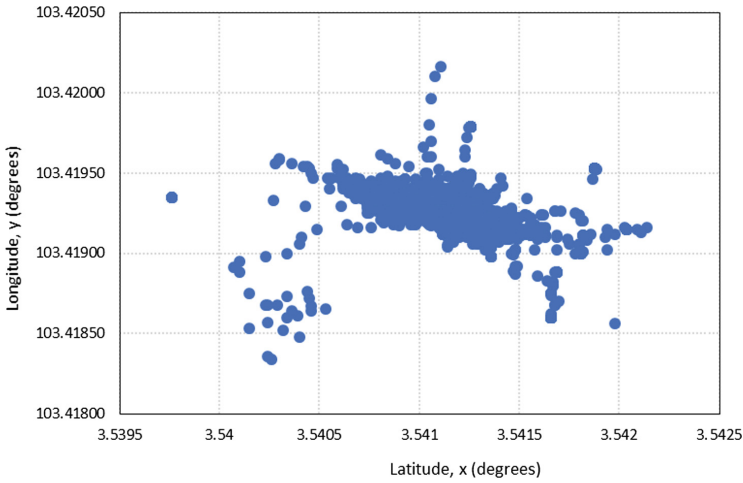
**Fig. 11.** Graph of error in longitude,  $y$  (m) vs testing time (in 24 h)

Figures 10 and 11 showed that the graph of error in latitude,  $x$  (in meters) versus testing time (in 24 h) and the graph of error in longitude,  $y$  (in meters) versus testing time (in 24 h) respectively. The high changes in the amplitude of both graphs occurred due to the cloudy and heavy raining. Besides, the GPS positioning data is quite unstable over 24 h even the GPS receiver is in static form and without climatic change. The average of error in latitude,  $x$  is  $-2.91$  m and average of error in longitude,  $y$  is  $10.78$  m.

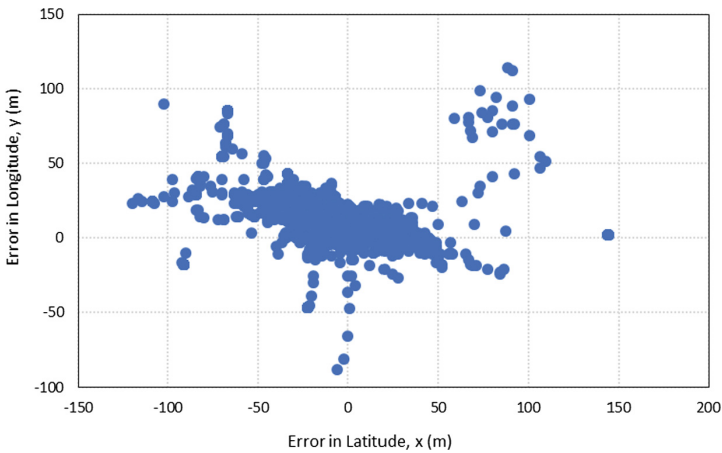


**From 12 am to 8 am**

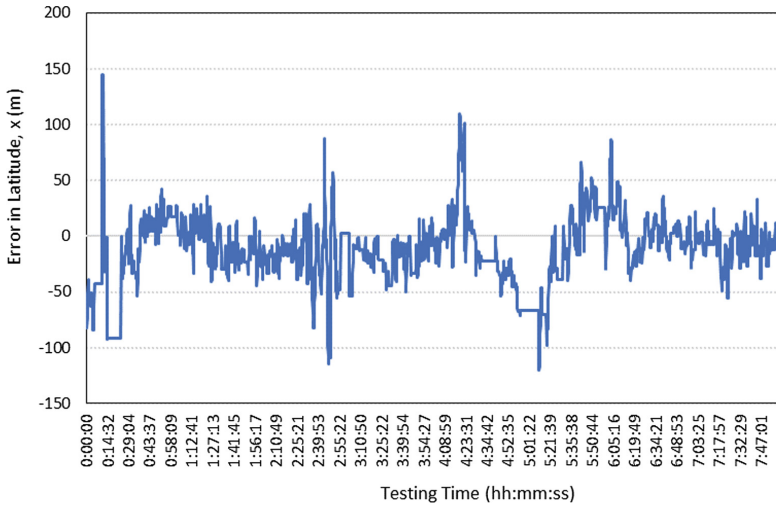
Figures 12 and 13 showed the coordinates distribution from 12 am to 8 am and the errors distribution from 12 am to 8 am respectively. From the graph, some coordinates are far away from the fixed and known coordinates. The minimum and maximum of the error in latitude, x are  $-119.88$  m and  $144.30$  m respectively whereas the minimum and maximum of the error in longitude, y are  $-87.69$  m and  $114.33$  m respectively. The large range on errors occurred might due to different effect such as climatic change and unstable of GPS system on GPS sensor. From the time range of 12 am to 8 am, data distribution is less accurate and less precise compared to other time range.



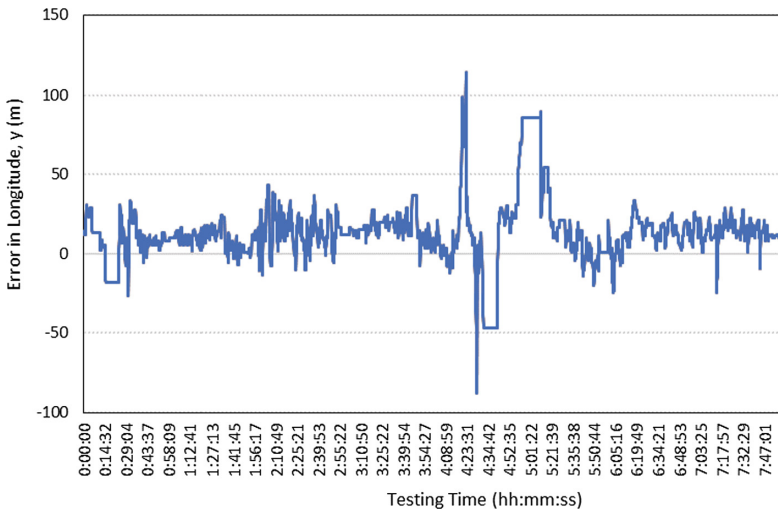
**Fig. 12.** Coordinates distribution from 12 am to 8 am



**Fig. 13.** Errors distribution from 12 am to 8 am



**Fig. 14.** Graph of error in latitude,  $x$  (m) vs testing time (from 12 am to 8 am)

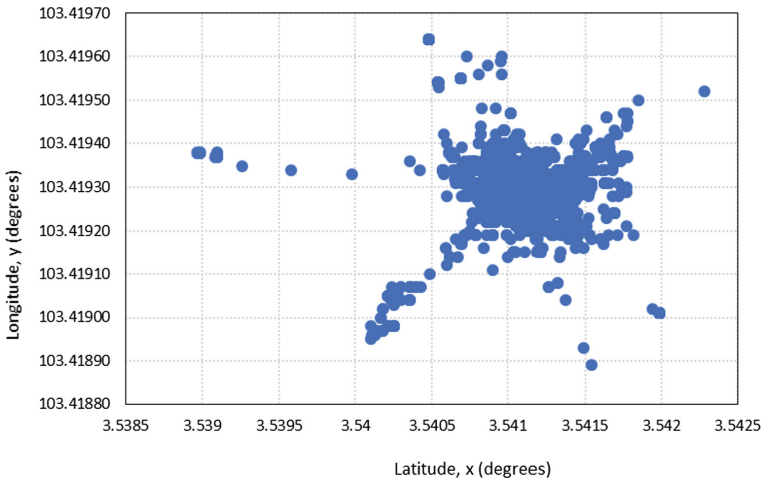


**Fig. 15.** Graph of error in longitude,  $y$  (m) vs testing time (from 12 am to 8 am)

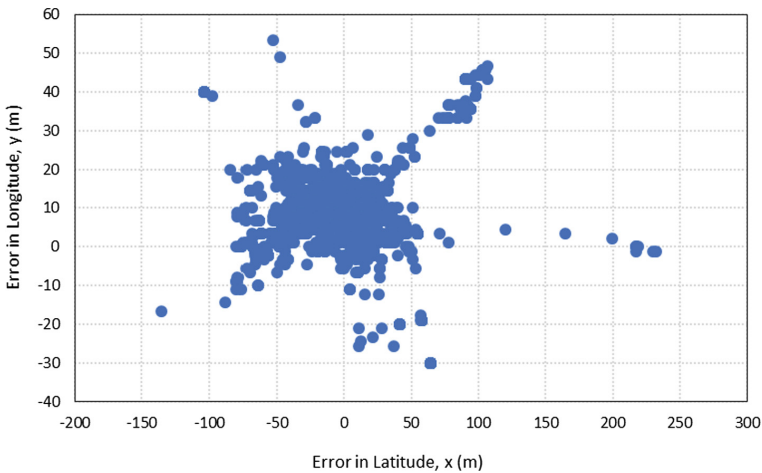
Figures 14 and 15 showed that the graph of error in latitude,  $x$  (in meters) versus testing time from 12 am to 8 am and the graph of error in longitude,  $y$  (in meters) versus testing time from 12 am to 8 am respectively. The high changes in the amplitude of both graphs occurred due to the cloudy and heavy raining. Besides, the GPS positioning data is quite unstable from 12 am to 8 am even the GPS receiver is in static form and without climatic change. The average of error in latitude,  $x$  is  $-12.21$  m and the average of error in longitude,  $y$  is  $13.32$  m.

**From 8 am to 4 pm**

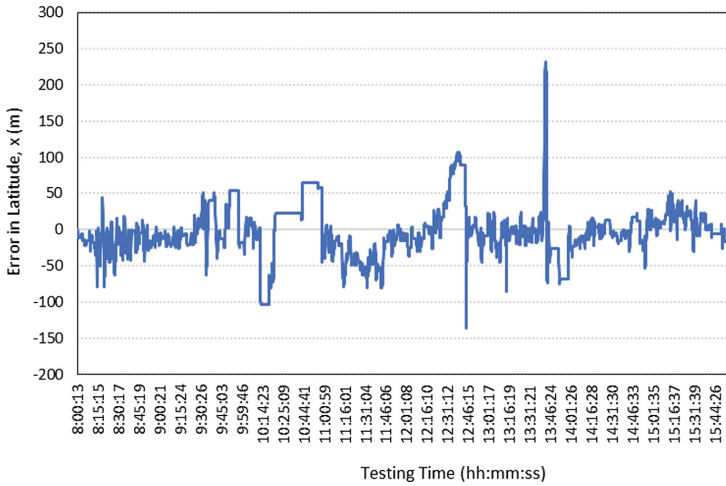
Figures 16 and 17 showed the coordinates distribution from 8 am to 4 pm and the errors distribution from 8 am to 4 pm respectively. From the graph, some coordinates are far away from the fixed and known coordinates. The minimum and maximum of the error in latitude,  $x$  are  $-135.42$  m and  $231.99$  m respectively whereas the minimum and maximum of the error in longitude,  $y$  are  $-29.97$  m and  $53.28$  m respectively. The large range on errors occurred might due to different effect such as climatic change and unstable of GPS system on GPS sensor. From the time range of 8 am to 4 pm, the data distribution is more accurate and more precise compared to other time range.



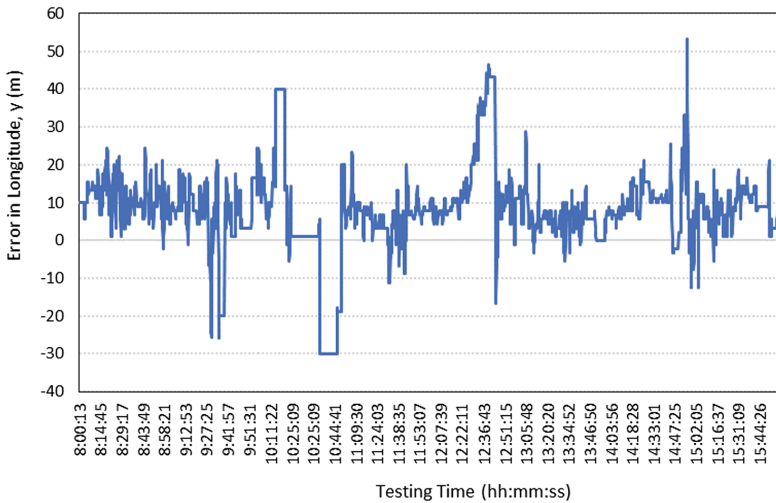
**Fig. 16.** Coordinates distribution from 8 am to 4 pm



**Fig. 17.** Errors distribution from 8 am to 4 pm



**Fig. 18.** Graph of error in latitude,  $x$  (m) vs testing time (from 8 am to 4 pm)

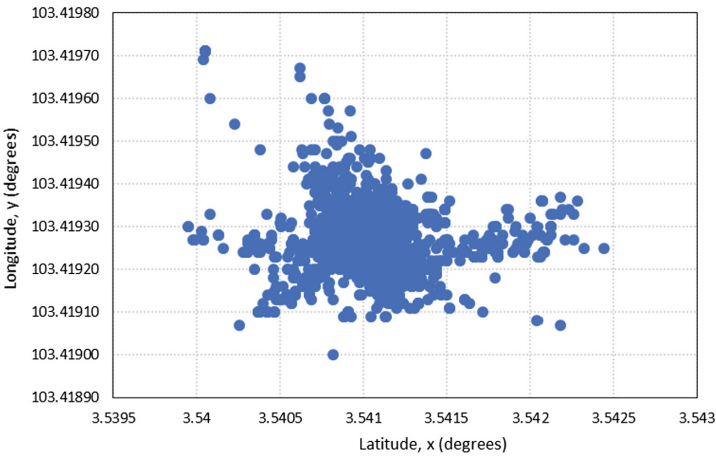


**Fig. 19.** Graph of error in longitude,  $y$  (m) vs testing time (from 8 am to 4 pm)

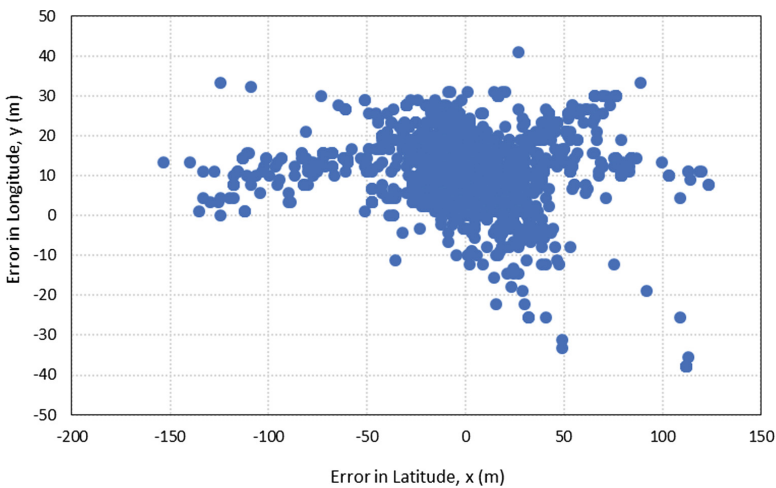
Figures 18 and 19 showed that the graph of error in latitude,  $x$  (in meters) versus testing time from 8 am to 4 pm and the graph of error in longitude,  $y$  (in meters) versus testing time from 8 am to 4 pm respectively. The high changes in the amplitude of both graphs occurred due to the cloudy and heavy raining. Besides, the GPS positioning data is quite unstable from 8 am to 4 pm even the GPS receiver is in static form and without climatic change. Average of error in latitude,  $x$  is  $-3.33$  m and average of error in longitude,  $y$  is  $7.77$  m.

**From 4 pm to 12 am**

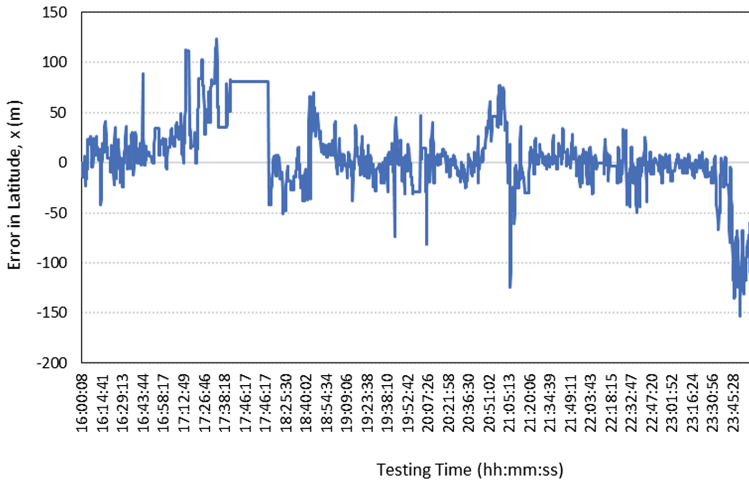
Figures 20 and 21 showed the coordinates distribution from 4 pm to 12 am and the errors distribution from 4 pm to 12 am respectively. From the graph, some coordinates are far away from the fixed and known coordinates. The minimum and maximum of the error in latitude,  $x$  are  $-124.32$  m and  $123.21$  m respectively whereas the minimum and maximum of the error in longitude,  $y$  are  $-37.74$  m and  $41.07$  m respectively. The large range on errors occurred might due to different effect such as climatic change and unstable of GPS system on GPS sensor. From the time range of 4 pm to 12 am, the data distribution is less accurate but more precise compared to other time range.



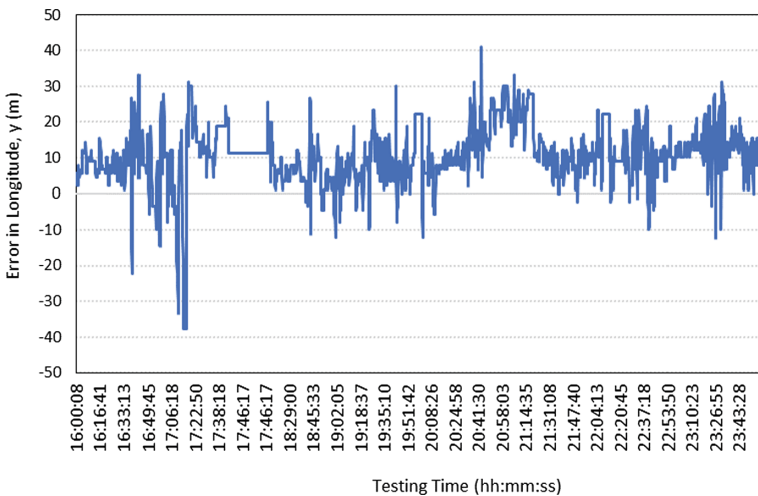
**Fig. 20.** Coordinates distribution from 4 pm to 12 am



**Fig. 21.** Errors distribution from 4 pm to 12 am



**Fig. 22.** Graph of error in latitude, x (m) vs testing time (from 4 pm to 12 am)



**Fig. 23.** Graph of error in longitude, y (m) vs testing time (from 4 pm to 12 am)

Figures 22 and 23 showed that the graph of error in latitude, x (in meters) versus testing time from 4 pm to 12 am and the graph of error in longitude, y (in meters) versus testing time from 4 pm to 12 am respectively. The high changes in the amplitude of both graphs occurred due to the cloudy and heavy raining. Besides, the GPS positioning data is quite unstable from 4 pm to 12 am even the GPS receiver is in static form and without climatic change. Average of error in latitude, x is 6.66 m and average of error in longitude, y is 11.11 m.

**Table 1.** Comparison of the range of errors in latitude, x (m) and longitude, y (m) in different time range

Time	Error in latitude, x (m)		Error in longitude, y (m)	
	Min	Max	Min	Max
24 h	-153.18	231.99	-87.69	114.33
From 12 am to 8 am	-119.88	144.30	-87.69	114.33
From 8 am to 4 pm	-135.42	231.99	-29.97	53.28
From 4 pm to 12 am	-124.32	123.21	-37.74	41.07

**Comparison of the Range and Average of Errors in Different Time Range**

Table 1 showed that the range of errors in latitude, x (m) and longitude, y (m) in different time range. In 24 h, the minimum and maximum of error in latitude, x are -153.18 m and 231.99 m respectively whereas the minimum and maximum of error in longitude, y are -87.69 m and 114.33 m respectively. By comparing the time range (from 12 am to 8 am, from 8 am to 4 pm and from 4 pm to 12 am), it showed that the time range from 4 pm to 12 am has the smallest range of error occurred in latitude, x (min = -124.32 m and max = 123.21 m) and longitude, y (min = -37.74 m and max = 41.07 m) and followed by the time range from 8 am to 4 pm and from 12 am to 8 am.

**Table 2.** Comparison of the average of errors in latitude, x (m) and longitude, y (m) in different time range

Time	Average of error in latitude, x (m)	Average of error in longitude, y (m)
24 h	-2.91	10.78
From 12 am to 8 am	-12.21	13.32
From 8 am to 4 pm	-3.33	7.77
From 4 pm to 12 am	6.66	11.11

Table 2 showed that the comparison of the average of error in latitude, x (m) and longitude, y (m) in different time range. In 24 h, the error in latitude, x is -2.91 m and the error of longitude, y is 10.78 m. By comparing the time range (from 12 am to 8 am, from 8 am to 4 pm and from 4 pm to 12 am), it showed that the time range from 8 am

to 4 pm has smallest average of error which has the offset of  $-3.33$  m in latitude, x and  $7.77$  m in longitude, y and the positioning accuracy is followed by the time range from 4 pm to 12 am ( $6.66$  m in latitude, x and  $11.1$  m in longitude, y) and the time range from 12 am to 8 am ( $-12.21$  meters in latitude, x and  $13.32$  m in longitude, y).

### 3.2 Rover Station

In Rover Station, the results are discussed based on comparison of GPS and DGPS at different time to analyse the improvement on DGPS method. The errors correction calculated from Reference Station is transferred to Rover Station for alleviating the error of positioning and improve the positioning accuracy. It is the improvement on rover's localization.

#### Improvement of DGPS at 8 am

In Fig. 24, it showed that the comparison between latitude, x in GPS and DGPS versus time (s). It occurred an average of  $-0.51$  m error in GPS which means the DGPS has improved  $-0.51$  m in latitude, x at 8 am. In Fig. 25, it showed that the comparison between longitude, y in GPS and DGPS versus time (s). It occurred an average of  $1.69$  m error in GPS which means the DGPS has improved  $1.69$  m in longitude, y at 8 am.

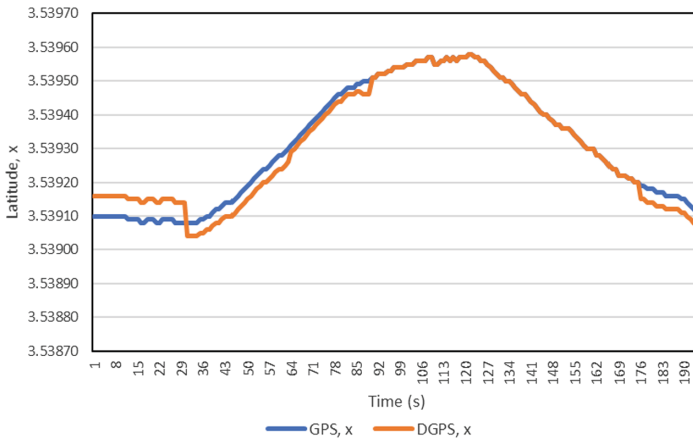


Fig. 24. Comparison between latitude, x in GPS and DGPS vs time (s)



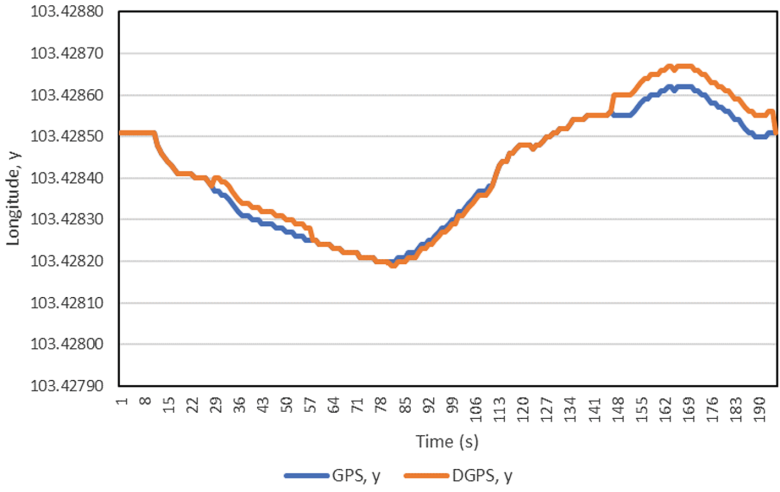


Fig. 25. Comparison between longitude, y in GPS and DGPS vs time (s)

**Improvement of DGPS at 4 pm**

In Fig. 26, it showed that the comparison between latitude, x in GPS and DGPS versus time (s). It occurred an average of  $-0.83$  m error in GPS which means the DGPS has improved  $-0.83$  m in latitude, x at 4 pm. In Fig. 27, it showed that the comparison between longitude, y in GPS and DGPS versus time (s). It occurred an average of  $-4.37$  m error in GPS which means the DGPS has improved  $-4.37$  m in longitude, y at 4 pm.

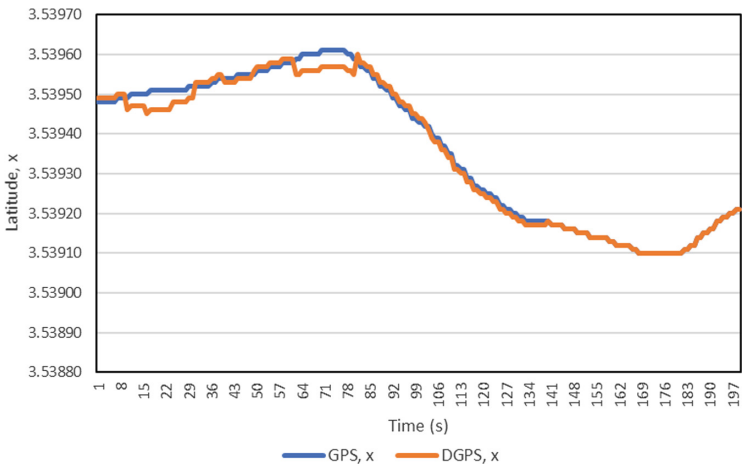
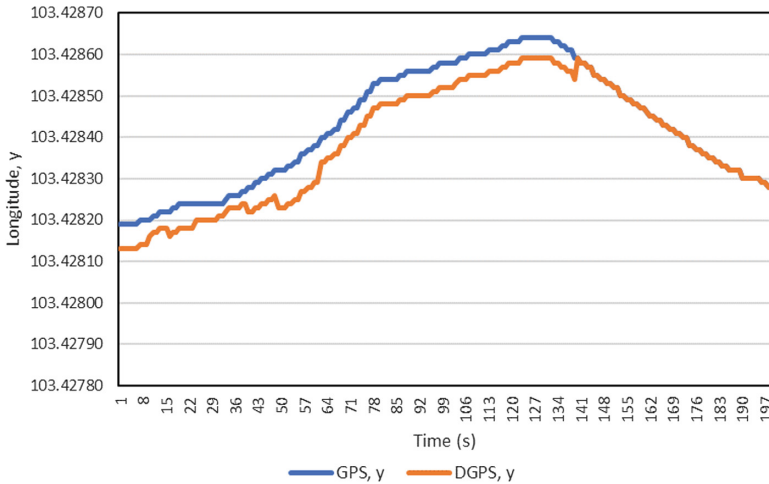


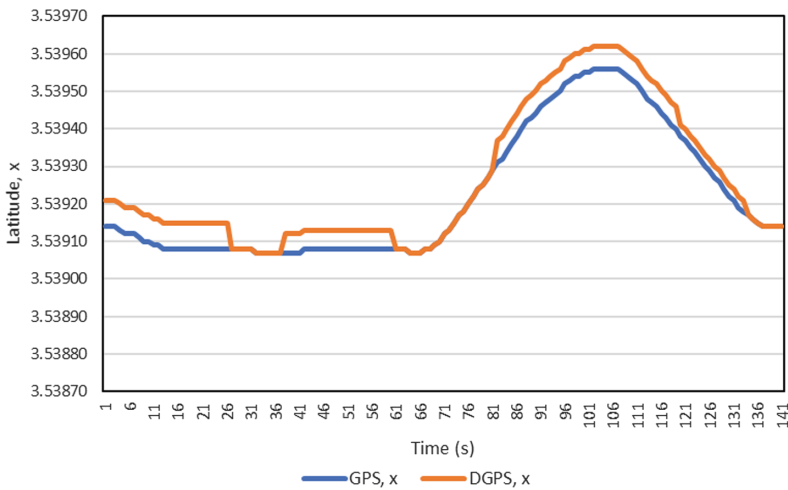
Fig. 26. Comparison between latitude, x in GPS and DGPS vs time (s)



**Fig. 27.** Comparison between longitude, y in GPS and DGPS vs time (s)

**Improvement of DGPS at 12 am**

In Fig. 28, it showed that the comparison between latitude, x in GPS and DGPS versus time (s). It occurred an average of 4.46 m error in GPS which means the DGPS has improved 4.46 m in latitude, x at 12 am. In Fig. 29, it showed that the comparison between longitude, y in GPS and DGPS versus time (s). It occurred an average of 2.05 m error in GPS which means the DGPS has improved 2.05 m in longitude, y at 12 am.



**Fig. 28.** Comparison between latitude, x in GPS and DGPS vs time (s)

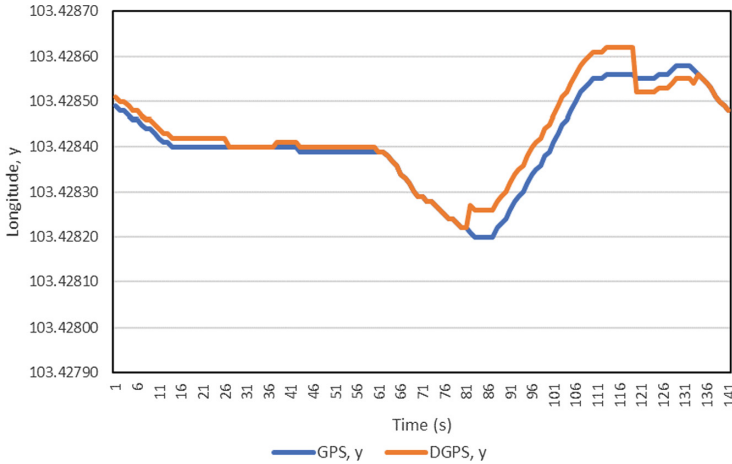


Fig. 29. Comparison between longitude, y in GPS and DGPS vs time (s)

**Improvement of DGPS at Different Time**

Table 3 showed that the improvement of DGPS in latitude, x and longitude, y at different time. By comparing them, it shown that time at 12 am has the largest error which are 4.46 m in latitude, x and 2.05 m in longitude, y. By transferring the error correction to rover station, the localization on rover can be improved by 4.46 m in latitude, x and 2.05 m in longitude, y. The second largest error is time at 4 pm which has the error of -0.83 m in latitude, x and -4.37 m at longitude, y. The smallest error is time at 8 am which has the error of -0.51 m in latitude, x and 1.69 m in longitude, y. By transferring both error corrections to rover station, the localization on rover can be improved by -0.83 m in latitude, x and -4.37 m in longitude, y at 4 pm and -0.51 m in latitude, x and 1.69 m in longitude, y at 8 am.

Table 3. Improvement of DGPS in latitude, x and longitude, y at different time

Time	Improvement in latitude, x (m)	Improvement in longitude, y (m)
8 am	-0.51	1.69
4 pm	-0.83	-4.37
12 am	4.46	2.05

**4 Conclusion**

From the positioning data collected, the results showed that the accuracy of GPS is unstable over 24 h. When there is climatic change, the accuracy of GPS would becoming lower due to weaker GPS signals are transmitted to the GPS receiver. Due to lower positioning on GPS, DGPS method would be applied to improve the accuracy of GPS because autonomous vehicles need more accurate positioning data for navigation

tracking in outdoor environment. The accurate positioning could prevent the accident on the road.

In Reference Station, it can be seen that time range from 4 pm to 12 am has the smallest range of error by comparing the time range (from 12 am to 8 am, from 8 am to 4 pm and from 4 pm to 12 am) which followed by time range from 8 am to 4 pm and time range from 12 am to 8 am. By comparing the average of error at different time ranges, we can see that time range from 8 am to 4 pm has the smallest average of error on positioning data which followed by time range from 4 pm to 12 am and time range from 12 am to 8 am. Largest range of error at certain time range does not means the average of error occurred is the highest but it somehow affect the positioning data due to climatic change, unstable GPS system, weak GPS signals and low quality of GPS receiver.

In Rover Station, it can be seen that time at 12 am, DGPS has the best improvement on rover's localization since the error corrections are the most which followed by time at 4 pm and 8 am. The errors calculated on GPS is the improvement on DGPS. The best improvement on rover's localization can be said that it has the large range of error and average of error on positioning data.

**Acknowledgements.** This research is supported by Ministry of Education Malaysia (Higher Institution Sector under FRGS Grant RDU1803130) and Universiti Malaysia Pahang.

## References

1. Michalski, A., Czajewski, J.: The accuracy of the global positioning systems. *IEEE Instrum. Meas. Mag.* **7**, 56–60 (2004). <https://doi.org/10.1109/MIM.2004.1288779>
2. Hunter, T., Kosmalski, W., Truong, P.: Vehicle navigation using differential GPS, pp. 392–398 (1990). <https://doi.org/10.1109/PLANS.1990.66205>
3. Sun, Q., Odolinski, R., Xia, J., Foster, J., Falkmer, T., Lee, H.: Validating the efficacy of GPS tracking vehicle movement for driving behaviour assessment. *Travel Behav. Soc.* **6**, 32–43 (2017). <https://doi.org/10.1016/j.tbs.2016.05.001>. ISSN 2214-367X
4. Han, S., Zhang, Q., Reid, J.: A navigation planner for automatic tractor guidance using machine vision and DGPS. *IFAC Proc. Vol.* **34**, 209–214 (2001). [https://doi.org/10.1016/S1474-6670\(17\)41707-1](https://doi.org/10.1016/S1474-6670(17)41707-1)
5. Dariusz Lapucha, K.L.M.: Investigation of Real-Time Accuracy of the DGPS Method. U.S. Army Corps of Engineers Topographic Engineering Center, Surveying and Mapping Research and Development Program Technical report, TEC-0024, John E. Chance and Associates, Inc. (1992)
6. Mertikas, S.P.: Differential Global Positioning System Navigation: A Geometrical Analysis. Technical report, Geodesy and Geomatics Engineering UNB (1983)
7. Morgan-Owen, G.J., Johnston, G.T.: Differential GPS positioning. *Electron. Commun. Eng. J.* **7**, 11–21 (1995). <https://doi.org/10.1049/ecej:19950104>
8. Matosevic, M., Salcic, Z., Berber, S.: A comparison of accuracy using a GPS and a low-cost DGPS. *IEEE Trans. Instrum. Meas.* **55**(5), 1677–1683 (2006). <https://doi.org/10.1109/TIM.2006.880918>
9. Chen, S., Wang, Y., Chen, F.: A study of differential GPS positioning accuracy, pp. 361–364 (2002). <https://doi.org/10.1109/ICMMT.2002.1187711>

10. Tang, C.: Accuracy and Reliability of Various DGPS Approaches. Master Thesis, University of Calgary (1996)
11. Svaton, M.: Low-Cost Implementation of Differential GPS Using Arduino. Master Thesis, Linkoping University (2016)
12. Shao, M., Sui, X.: Study on differential GPS positioning methods. In: 2015 International Conference on Computer Science and Mechanical Automation (CSMA), Hangzhou, pp. 223–225 (2015). <https://doi.org/10.1109/csma.2015.51>
13. Farrell, J., Givargis, T.: Differential GPS reference station algorithm-design and analysis. *IEEE Trans. Control Syst. Technol.* **8**(3), 519–531 (2000). <https://doi.org/10.1109/87.845882>
14. Maurer, J.: Outdoor Localization and Navigation for Mobile Robots. Master Thesis, IST (2012)



# Dynamic Compensation Controller with Feedback Linearization Technique of 3 Degree of Freedom Exoskeleton Robotic Arm for Upper Limb Rehabilitation Purpose

Muhammad Taha Ansari, Nur Fasiah Mohd Sobri,  
and Muhammad Nasiruddin Mahyuddin<sup>(✉)</sup>

School of Electrical and Electronics Engineering, Universiti Sains Malaysia,  
Pulau Pinang, Malaysia  
nasiruddin@usm.my

**Abstract.** A dynamic compensation controller for an exoskeleton robotic arm is designed for the application of upper limb rehabilitation. In this paper, the proposed dynamic compensation controller with robust feature is studied and compared against the conventional PID and sliding-mode controller. The exoskeleton robotic arm need to be controlled to assist post-stroke patient in rehabilitation. The motion executed by the exoskeleton is very crucial as it determines the effectiveness of the physiotherapy assisted by the robotic technology. The assisted therapy is expected to resolve the problem of difficulty of the stroke patient to visit physiotherapist at clinics or hospital by providing an equivalent therapy service back at home. The robotic solution is not to be considered to replace the job of the physiotherapist but rather serves to complement the existing clinical practice. In this paper, we are focusing on rehabilitation of upper limb impairment [1].

**Keywords:** Exoskeleton · Robotic arm · Dynamic compensation controller · Rehabilitation · Assistive therapy

## 1 Introduction

Stroke is one of the diseases cases which is increasing at an alarming rate worldwide. The main factors for stroke are high cholesterol level and hypertension. The mean age for occurrence of stroke in person is around the age of 54.5 to 62.6 years old [2].

Physiotherapy is the treatment used for the stroke's survivor to recover their muscle motor coordination. The person undergoes series of therapy sessions to improve their severe muscle impairments caused by stroke. Physiotherapy sessions are monitored by a physiotherapist who co-ordinates with the stroke survivors and plans complete recovery schedule for the them. The physiotherapist has an opportunity to build rapport with the person and affect both attitude and behavior, for example encouraging individuals to realize their problems, take initiative and do efforts to recover and return to previous activities [3]. However, number of physiotherapists are much less to monitor a vast number of stroke survivors, keeping in mind the number of stroke cases are

increasing rapidly every year. Besides that, the hurdle is the space and equipment required to accommodate the stroke survivors for rehabilitation.

Moreover, the cost incurred for every physiotherapist session and a specialized knowledge and skills of physiotherapy are needed in a way that each person's recovery progress is monitored to ensure each session provides effective treatment. Therefore, an exoskeleton robot provides solution to assist the therapy session whereby the person can undergo the therapy session without the presence of human therapist [4]. However, the assistive force exerted by the exoskeleton robot needs to be controlled when interacting with the stroke survivor. There lies the control problem for the assistive function in which the exoskeleton robot is to be controlled by a nonlinear controller for a wide range of stroke survivor's arm weight. It is to reemphasize that the proposed method is complementary and not a complete replacement solution for the human physiotherapists or the therapy sessions.

In this paper, a simulation of a single robotic arm is presented, and a suitable controller is designed to be able to control the simulated exoskeleton robotic arm for various type of users with different mass distribution (weight). The controller should be able to compensate the effects of nonlinearities of the robotic arm itself as well as the distinctive mass characteristics of the stroke survivors.

## 2 Methodology and System Definition

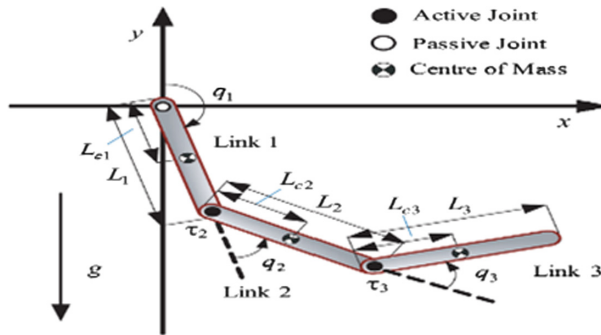
There are three types of controller that are designed to simulate the exoskeleton of 3 degree-of-freedom (DOF) planar robot arm. The controllers are PID controller, Robust PID controller and the dynamic compensation controller. Before designing the controllers, the derivation of robotic arm is done by considering the kinematics and dynamics of the 3 DOF planar robot arm model [9]. Next, the MATLAB Function is used to program the code for 3 DOF planar robot arm model. SIMULINK block diagram is designed after programming the code for simulating the position of the arm. MATLAB Function and SIMULINK block diagram are important tools for designing each of the controller. The length for each of the body segment of the exoskeleton and the user's arm are unchangeable as they can be seen in Table 1 and so same values are applied to all three controllers. However, the mass for each of the body segment of the exoskeleton and user's arm will be slightly different as the mass of the exoskeleton will be 0.2 kg lighter than the user's arm as mentioned in Table 2 (as illustrated in Fig. 1).

**Table 1.** Mean length for each of the body segment [5]

Body segment	Male	Female	Average
Shoulder	34.08 cm	31.19 cm	32.64 cm
Elbow	26.99 cm	24.34 cm	25.67 cm
Wrist	19.38 cm	18.05 cm	18.72 cm

**Table 2.** Mass for the exoskeleton and human arm [5]

Body segment	Exoskeleton		Human arm	
	Male	Female	Male	Female
Shoulder	2.13 kg	1.51 kg	2.23 kg	1.71 kg
Elbow	1.19 kg	0.82 kg	1.39 kg	1.02 kg
Wrist	0.32 kg	0.22 kg	0.52 kg	0.42 kg



**Fig. 1.** The 3 DOF planar robot arm model [7]

### 2.1 Kinematics Derivation for 3 DOF Planar Robot

Kinematics of the robot will enable us to calculate the desired location and orientation of each joint [6]. Denavit-Hartenberg (D-H) representation is used to obtain the kinematic configurations of the exo-skeleton 3 DOF planar robot (shown in Fig. 2) and the respective D-H parameters used in this project are shown in Table 3 below.

**Table 3.** D-H parameters for 3 DOF planar robot u

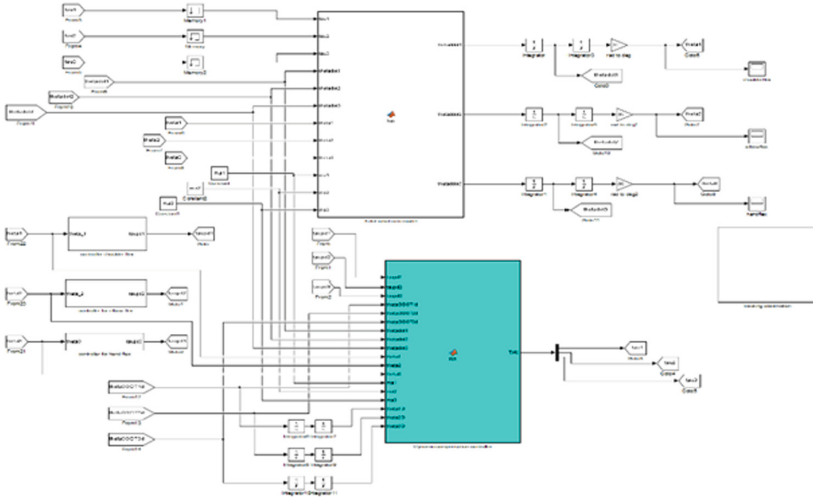
#	$\alpha$	$a$	$D$	$\theta$
1	0	0	0	$\theta_1$
2	0	$l_1$	0	$\theta_2$
3	0	$l_2$	0	$\theta_3$

## 3 Dynamic Modelling

### 3.1 DOF Planar Robot Dynamic Modelling

The mass matrix  $M(\theta)$  (1), centrifugal and Coriolis matrix  $V(\theta, \dot{\theta})$  (2) and the gravity vector  $G(\theta)$  (3) of the exoskeleton robot arm were considered to be unified with the patient upper hand. Table 2 presents further information in terms of exoskeleton masses and the human arm according to the corresponding limb.





**Fig. 2.** System diagram for dynamic compensation controller

The mass matrix of the system is

$$M(\theta)\ddot{\theta} = \begin{bmatrix} m_{11} & m_{12} & m_{13} \\ m_{21} & m_{22} & m_{23} \\ m_{31} & m_{32} & m_{33} \end{bmatrix} \begin{bmatrix} \ddot{\theta}_1 \\ \ddot{\theta}_2 \\ \ddot{\theta}_3 \end{bmatrix} \tag{1}$$

The Centrifugal and Coriolis matrix of the system is

$$V(\theta, \dot{\theta}) = \begin{bmatrix} v_{11} & 0 & 0 \\ v_{21} & 0 & 0 \\ v_{31} & 0 & 0 \end{bmatrix} \begin{bmatrix} \dot{\theta}_1 \\ \dot{\theta}_2 \\ \dot{\theta}_3 \end{bmatrix} \tag{2}$$

Gravity vector of the system is written as

$$G(\theta) = \begin{bmatrix} r_{11} \\ r_{12} \\ r_{13} \end{bmatrix} \tag{3}$$

The rigid body of dynamic is given in the following equation

$$M(\theta)\ddot{\theta} + V(\theta, \dot{\theta}) + G(\theta) = \tau \tag{4}$$

### 3.2 Simulink Block Diagram

The motion of the unified exoskeleton robot arm (assumed to be strapped with the respective stroke patient limb) were simulated in terms of motion by the shoulder flexion, elbow flexion and wrist flexion. All of the joints' range of motion have their own set points. The set point for the shoulder start at 0° and finish at 60°. Next, for the elbow and wrist, both start at 0° and finish at 45°. The paper consists of the comparison between three types of controllers implemented in the exoskeleton which are PID controller, Robust PID controller and dynamic compensation controller with feedback linearization technique. Figure 3 shows the block diagram of the presented system.

## 4 Controller Design

Three different types of controller for 3 DOF planar robotic arm exoskeleton have been developed. The first controller comprised of the basic PID controller will be evaluated its performance against the robust PID controller. This is latter contrasted with proposed controller which includes dynamic compensation controller in which nonlinear terms are eliminated at the output by adding feedback linearization technique.

### 4.1 PID Controller

A controller is needed to command the exoskeleton to follow the input given by the stroke survivor. Therefore, PID controller is chosen to control the exoskeleton since it includes the proportional, integral and derivative actions.  $K_P, K_i, K_d$ , gains are set to not equal to zero i.e.  $K_P, K_i, K_d \neq 0$  to get PID control. The standard form of a PID controller is presented in the following equation.

$$C_{PID}(s) = K_P \left( 1 + \frac{1}{T_i S} + T_d S \right) \tag{5}$$

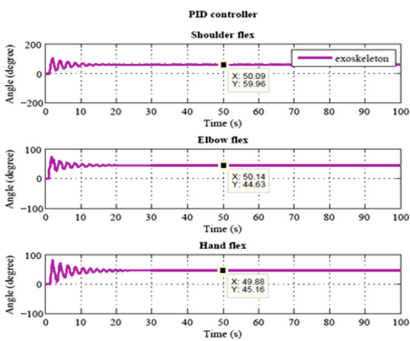


Fig. 3. PID controller for male exoskeleton

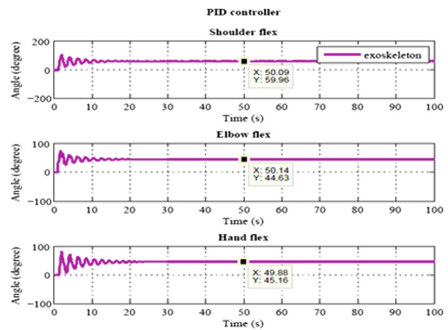


Fig. 4. PID controller for female exoskeleton

Figures 3 and 4 shows the results for the exoskeleton using the mass of male and female that had been mentioned in Table 2 respectively with the specific set point for each joint labelled on the y-axis. The set point for the shoulder starts at 0° and finish at 60° while the set points for the elbow and wrist starts at 0° and finishes at 45°. The results show that the controller was struggling at the earlier of sampling time to have a stable system over time.

### 4.2 Robust PID Controller

PID controller was forced to smoothen the closed loop system throughout the sampling time. Thus, three low pass filters were used to smoothen the system. However, the controller still faced the difficulty to have a stable system at the early of sampling time even though the system was smoother compare to the PID controller alone. Figures 5 and 6 shows the simulation results for both male and female with the specific set point for each joint that had been mentioned earlier in the PID controller. From the results, it can be seen clearly that the controller did not reached the set points for each joint. This is because the controller took long time to make the system stable and smooth.

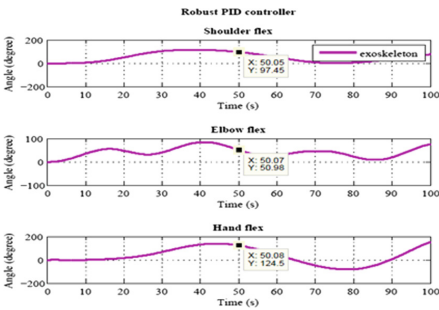


Fig. 5. Robust PID controller for male exoskeleton

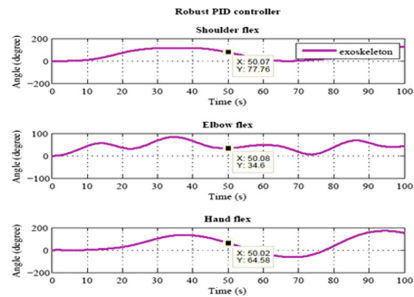


Fig. 6. Robust PID controller for female exoskeleton

### 4.3 Dynamic Compensation Controller with Feedback Linearization Technique

The nonlinearity error that occurred in PID and Robust PID controller had made the closed loop system to have a tough time in simulation. Therefore, the error equation for the closed loop system was characterized by the following equation.

$$\tau = M(\theta)\ddot{\theta} + V(\theta, \dot{\theta}) + G(\theta) + K_p\tilde{\theta} + K_d\dot{\tilde{\theta}} \tag{6}$$

where,  $\tilde{\theta} \in R^{n \times 1}$  is the generalized vector of the state which contains the angular position responsible for the shoulder, elbow and wrist flexion.

$$\theta = [\theta_1 \theta_2 \theta_3]^T \tag{7}$$

Thus, feedback linearization technique was used to overcome the inherent nonlinearity dynamic of robotic arm. The combination of the nonlinear effect of a system would be exactly cancelled by a nonlinear term in the control law so that the overall stiffness of the closed loop system will always stay constant. This is under the assumption that the information about the exoskeleton and the user’s arm parameters are known by the controller.

The linearizing model-based portion and servo law portion were the two parts that were used to perform the linearizing function in a closed loop system. The model-based portion and servo law portion of the exoskeleton of 3 DOF planar robot arm were shown in the following equations.

The model-based portion of the control is

$$\tau = \alpha \tau' + \beta \tag{8}$$

Where

$$\alpha = M(\theta)\ddot{\theta} \tag{9}$$

$$\beta = V(\theta, \dot{\theta}) + G(\theta) \tag{10}$$

and the servo law portion represent as below

$$\tau' = \ddot{\theta}_d + K_p \tilde{\theta} + K_d \tilde{\dot{\theta}} \tag{11}$$

The set point for the shoulder start at 0° and finish at 60° while the set point for the elbow and wrist starts at 0° and finishes at 45° respectively. Figures 7 and 8 show the simulation results after the implementation of the feedback linearization technique in the closed loop system with the specific set point for each joint labelled on the y-axis.

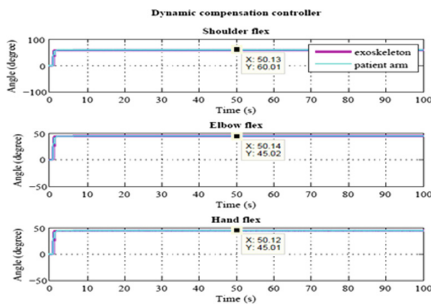


Fig. 7. Dynamic compensation controller for male

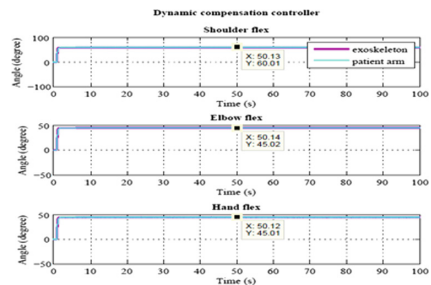
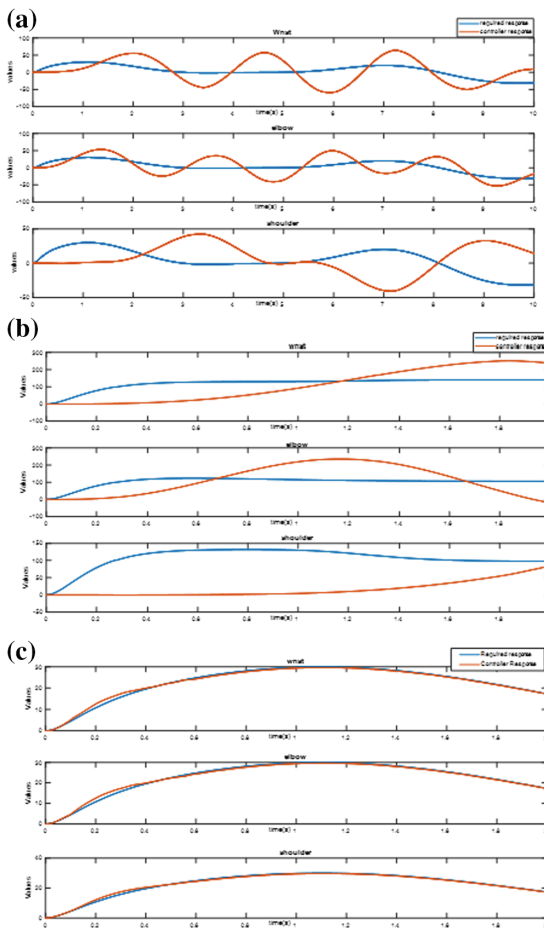


Fig. 8. Dynamic compensation controller for female

### 5 Comparative Results

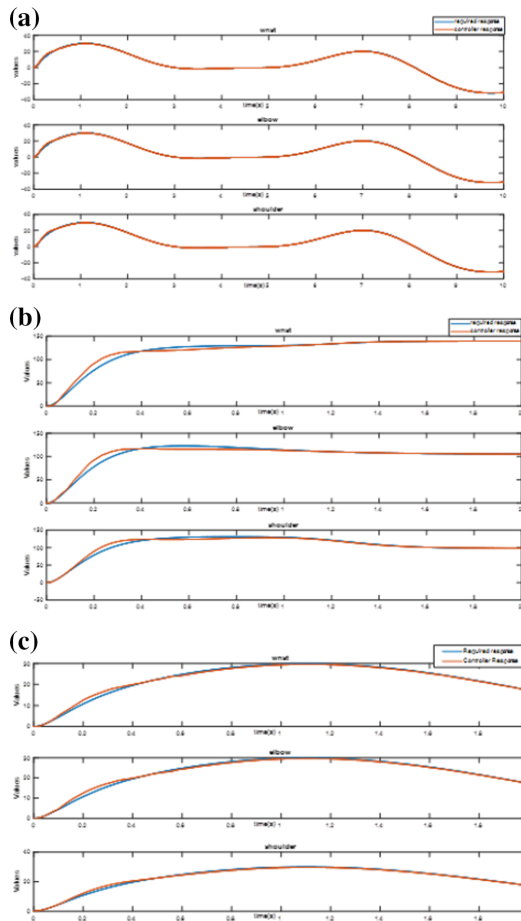
This paper has developed controller for 3 DOF planar robotic arm exoskeleton. The controllers for the exoskeleton were built in sequence starting from the basic knowledge on PID controller continued with some improvised robust PID controller and lastly by using the feedback linearization technique.

The presented controllers are tested on 3 different controllers, two with two seconds input based on the actual response of shoulder, elbow and wrist flexion and the third one is 10 s continuous movements [8]. It can be clearly seen from the results Fig. 9 that for either input the robust PID acting alone without the non-linear function struggles to track the desired motion.



**Fig. 9.** (a) PID response on 10 s input. (b) PID response on 2 s actual input. (c) PID response on 2 s harmonic input

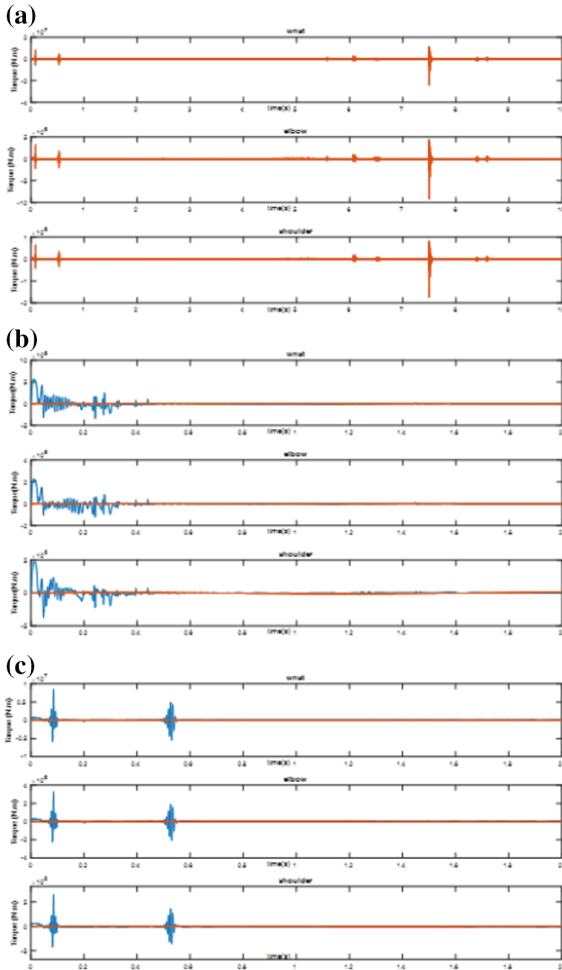
The Dynamic compensation controller with feedback linearization technique have shown better tracking performance on all the inputs as shown in Fig. 10.



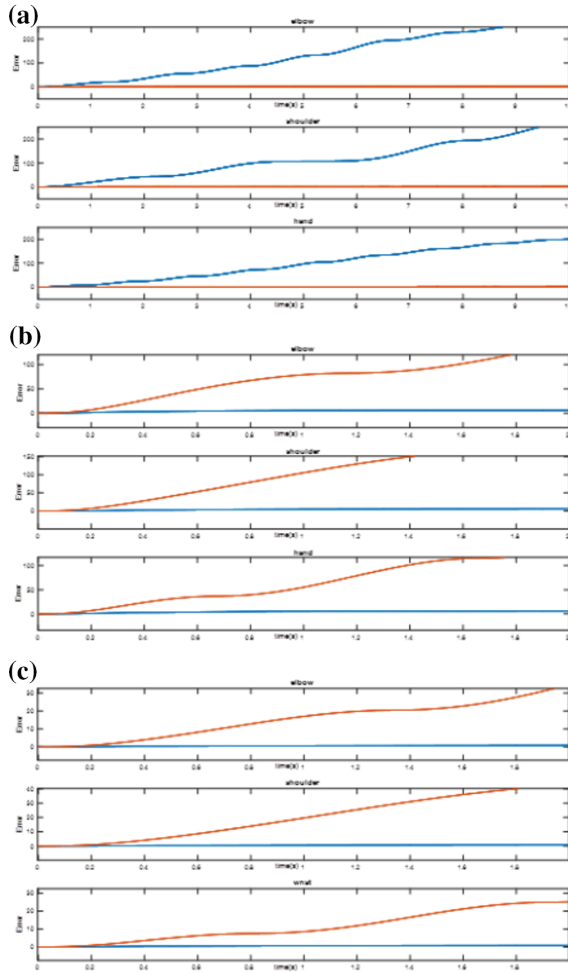
**Fig. 10.** (a) DCC response on 10 s input. (b) DCC response on 2 s actual input. (c) DCC response on 2 s harmonic input

From Fig. 11, it can clearly be seen from the torque comparison of both the controllers for all three inputs that the robust PID controller’s torque is too high and faced the difficulty to obtain the stability at the start of sampling time in contrast to the dynamic compensation controller the torque results are astonishing and reached the stability much faster than the robust PD controller.

The difference can also be seen from the integral absolute error (IAE) comparison Fig. 12 that the error kept increasing for robust PID controller which is undesirable whereas on the other hand for the dynamic compensation controller the integral absolute error was not propagative. The proposed dynamic compensation controller with feedback linearization technique have proved to eliminate all the undesired extremities and tracking problems.



**Fig. 11.** (a) Torque comparison for 10 s input. (b) Torque comparison for 2 s actual input. (c) Torque comparison for 2 s harmonic input



**Fig. 12.** (a) IAE comparison for 10 s input. (b) IAE comparison for 2 s actual input. (c) IAE comparison for 2 s harmonic input

## 6 Conclusion

The purpose of the presented paper is to design a controller through which the 3 DOF planar robot arm and the user’s arm can co-operate. In order to get a smooth, linear and stable system, feedback linearization technique is implemented in the system to compensate for the nonlinearity exists in the robotic arm dynamics and user’s arm.

From the results, by comparing the performance of presented controllers, it can clearly be seen that without the feedback linearization technique in the dynamic compensation controller, it is difficult to get the desired results using a linear controller which in turn, adversely affect the therapy effectiveness.



## References

1. Veerbeek, J., et al.: Clinical Practice Guideline for Physical Therapy after Stroke (Dutch: KNGF-richtlijn Beroerte) (2014)
2. Kw, L., Sh, G.: Burden of stroke in Malaysia. *Int. J. Stroke* **7**(2), 165–167 (2012)
3. Klabber Moffett, J.A., Richardson, P.H.: The influence of the physiotherapist-patient relationship on pain and disability. *Physiother. Theory Pract.* **13**(1), 89–97 (1997)
4. Sánchez-Sánchez, P., Reyes-Cortés, F.: Cartesian Control for Robot Manipulators. InTechOpen (2010)
5. Gordon, C.C., Churchill, T., Clauser, C.E., Bradtmiller, B., McConville, J.T., Tebbetts, I., Walker, R.A.: Anthropometric Survey of U.S. personnel: summary statistics interim report for 1988 (1989)
6. Niku, S.B.: *Introduction to Robotics: Analysis, Systems, Applications*. Prentice Hall, Upper Saddle River (2001)
7. Lai, X., Pan, C., Wu, M., Yang, S.X.: Control of an underactuated three-link passive–active–active manipulator based on three stages and stability analysis. *Dyn. Syst. Meas. Control* **137**, 021007 (2014)
8. Kasehagen, B., et al.: Assessing the reliability of ultrasound imaging to examine peripheral nerve excursion: a systematic literature review. *Ultrasound Med. Biol.* **44**(1), 1–13 (2017)
9. Bitzer, S., Havoutis, I., Vijayakumar, S.: Synthesising novel movements through latent space modulation of scalable control policies. In: *International Conference on Simulation of Adaptive Behavior*. Springer, Berlin (2008)



# PLC Based Automated Coolant Supply System for Machining AISI 304L in CNC Milling

Farizan Md Nor<sup>1,2(✉)</sup>, Fairul Azni Jafar<sup>2,3</sup>, Aisyah Jamri<sup>2</sup>,  
Wan Nur Izzati Wan Md Hatta<sup>2</sup>, and Mohd Hadzley Abu Bakar<sup>2,3</sup>

<sup>1</sup> Department of Technology and Process,  
Kolej Kemahiran Tinggi MARA Kuantan, Km 8, Jalan Kuantan Gambang,  
25150 Kuantan, Pahang, Malaysia

farizan@kuantan.kktm.edu.my

<sup>2</sup> Faculty of Manufacturing Engineering,  
Universiti Teknikal Malaysia Melaka, Hang Tuah Jaya,  
76100 Durian Tunggal, Melaka, Malaysia

<sup>3</sup> Advanced Manufacturing Centre (AMC),  
Faculty of Manufacturing Engineering, Universiti Teknikal Malaysia Melaka,  
Hang Tuah Jaya, 76100 Durian Tunggal, Melaka, Malaysia

**Abstract.** In machining operation, cutting fluids plays an important role to the surface quality of a product. However, the toxicity of cutting fluids can give negative impact to the human health and environmental problems. There are many techniques that have been explored by researchers for green manufacturing such as dry cutting, high pressure cooling technique, wet cooling technique, mist cooling technique and minimal quality lubricant technique. This research work proposed to explore the MQL concepts in the CNC milling using the application of Programmable Logic Control (PLC) which is able to control the duration time for coolant supply during the machining process. The performance of the new system was evaluated by measuring the surface roughness and the quantity of the cutting fluids used during the machining process. The results show that the best surface roughness can be obtained with less amount of coolant quantity during the machining operation. Automated coolant system can minimize the use of coolant and able to reduce the coolant recycle period. Therefore, the automatic coolant supply for CNC machine has the potential to be implemented as a new method to the machining process for green cutting.

**Keywords:** PLC · Automated coolant supply · CNC milling · Surface roughness · Coolant quantity

## 1 Introduction

In metal cutting operation, the proper selection of cutting parameter and cutting fluids are very important to obtain the optimum quality of a product. During machining operation, the friction between the chip-tool interface and the workpiece will generate heat due to shearing action and can affect the surface roughness as well as the tool life. The selection of efficient methods of cooling is very important and needs to be considered because it can reduce the amount of coolant used and can obtain the optimum

surface roughness. According to Kiyak and Cakir [1] and Boswell and Chandrantilleke [2], the surface roughness is increase while dimensional sensitiveness of workpiece is decrease due to generated friction.

Kiyak and Cakir [1] also stated that some approaches have been used to protect cutting tool from heat such as the uses of coolant to cool the cutting tool and the workpiece as well as to lubricate them. Cutting fluid acts as lubricant at the friction zone and washes away the chips at the cutting area. Furthermore, it can prevent the corrosion of chips and machine tool by carrying away the heat generated during machining and permits maximum cutting speed hence the time for machining reduce and productivity of manufacturing increase.

There are four problems occurs at the CNC machining when using the conventional coolant method which is high coolant recycle frequency, increase the production cost and waste, the machine coolant easily contaminated and harmful for the health and environment. The analysis is focusing on the effect of the coolant to the tool wear, depth of cut and the feed rate while using the conventional flooded lubricant compare to the minimal quantity lubricant (MQL). Due to the particular disadvantages, the research had been done before using the idea of MQL method with the help of PLC.

This paper has been written with the following sequence. First, we explain briefly the background and motivation of the research work. Section 2 describing those related works while Sect. 3 is explaining the methodology conducted in this research work. In Sect. 4, the whole results of the research work are discussed with intention to analyse the performance of the proposed automated coolant supply system in achieving good surface roughness when cutting workpiece in CNC milling machine.

## 2 Related Works

This research work is an inspiration to improve the wet cooling technique. The wet cooling technique has been widely used in the past with an application of a stable flow of the coolant to the tool and workpiece. It is clearly seen that this system produced a lot of waste when large amount of fluid being projected to the workpiece. In addition, it only needs a small amount of coolant to cool down the temperature of the tool and workpiece. That is when the minimum quantity lubricant (MQL) method has been introduced. Moreover, continuous flow of the coolant causes the increase in production cost because the coolant has to undergo recycle frequency in 2 to 3 weeks' time.

### 2.1 Dry Machining

Dry machining is a process of metal removal without using coolant. There are many advantages of using the dry machining such as able to complete eliminate the harmful cutting fluid, reduce production cost on the cutting fluid, able to achieve high surface finish with high speed, and the operation time will be reducing. The Engineer [3] state that dry machining is becoming more prevalent, in milling especially. In drilling, coolant is required because the tool has prolonged exposure to the material and fluid is essential to evacuate the chips. And dry machining in turning is rare as the cutting edge

is constantly in contact with the workpiece, so without some cooling, the cutting edge will eventually fail. Milling is the main beneficiary.

## 2.2 Wet Cooling

Conventional wet lubricant used the flooded coolant system during the machining process. Petrilin [4] stated that cooling mixture, cutting lubricant, cutting fluid and coolant are common terms that refer to a liquid applied for both cooling and lubricating the tool/workpiece interface while machining. All cutting generates unwelcome friction at that interface. The presence of coolant ensures that the friction between the two surfaces is reduced and lubrication significantly enhances the metal-removal process. Everybody in the business has used flooded coolant practically forever and knows that it works. They are probably also aware that it has its drawbacks, including The cost of buying, maintaining and disposing of cutting fluid, which is estimated to account for 7 to 17% of the cost of machining parts, the need to clean parts after machining and to remove as much fluid as possible from chips before recycling, and Health problems from handling or working around conventional coolants include skin irritation or allergic reactions, asthma, bronchitis and other respiratory difficulties. It's possible that long-term exposure to some coolant additives could lead to cancer.

## 2.3 Minimum Quantity Lubrication (MQL)

MQL will decrease the amount of machining fluid to solve the problems from the conventional method [5]. Minimum quantity lubrication (MQL) machining has achieved noticeable attention in both academic and industry research areas due to its minimum costs and maximum environmental protection. This paper focuses on the analysis of the effects of MQL parameters such as the flow rate of lubricant and the air-oil mixture ratio on cutting performances in terms of cutting force, cutting temperature, and residual stress. Additionally, the cutting performances in MQL machining are also compared with the dry and flood cooling machining. The reduction of the cutting force and cutting temperature is the results from the uses of the cutting fluid. For MQL machining, there is a maximum effective flow rate of lubricant and it is influenced by the cutting speed. When the flow rate of lubricant is beyond the maximum effective value, the air-oil mixture ratio will no longer affect the cutting performances in machining. This research can support the process planning in achieving the desired residual stress profile by strategically adjusting the MQL parameters. Benefits and challenges of minimum quantity lubricant propose that when properly applied, whether externally or through the tool, MQL can lead to improved surface finish and increased tool life [6]. It also has a positive impact on emissions and waste, boosting a facility's overall health, safety and environmental profile.

From the three application method for coolant supply, MQL method is the best method compare to the dry machining and the conventional wet machining. Therefore, MQL concept has been chosen to be the basis for this research work and it is believed that this method can gives many advantages to improve the machining operation. Moreover, the application of programmable logic controller (PLC) to control the time of coolant supply will be able to minimize the quantity of the coolant. The aim of this

research work is to improve the quality of AISI 304L under CNC automated coolant supply method by replacing the conventional flooded coolant system.

### 3 Methodology

#### 3.1 Automated Coolant Supply System

In this research work, a PLC system by using CX programmer as a connector between PLC system and the CNC machine was developed. CX programmer able to creates the advance programs using data blocks of identical data types or different data. The uses of the CX programmer able to create the advance programs using data blocks of identical data types or different data types. Other than that, this programmer also makes a development of PLC programs with a simple drag and drop configurations. Figure 1 shows the Ladder diagram schematic in CX programmer software. This program can create ladder diagram which consist of start and stop button, light, timer 1, timer 2 and valve to control the overall system of automatic coolant supply. A Nozzle is attached to the CNC machine to control the coolant flow according to the duration of period time that have been set by CX programmer. Therefore, the timer 1 will start to run simultaneously with the light. After certain period time, timer 2 start to run and the cycle will repeat continuously until the stop button is pressed.

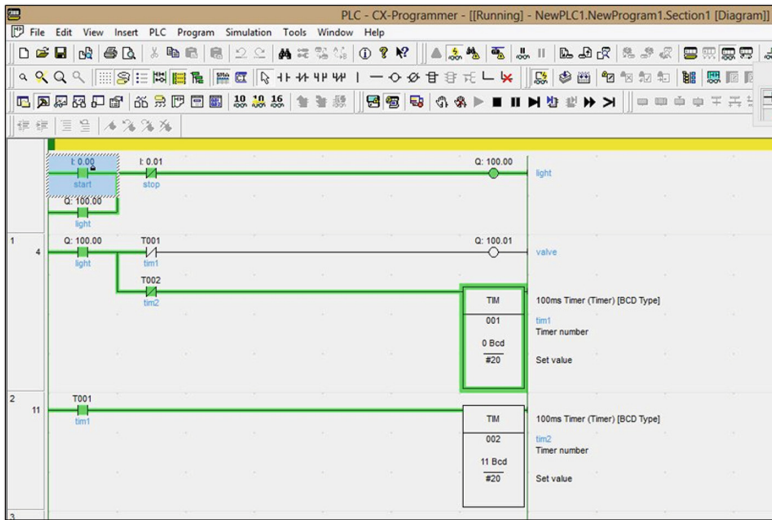
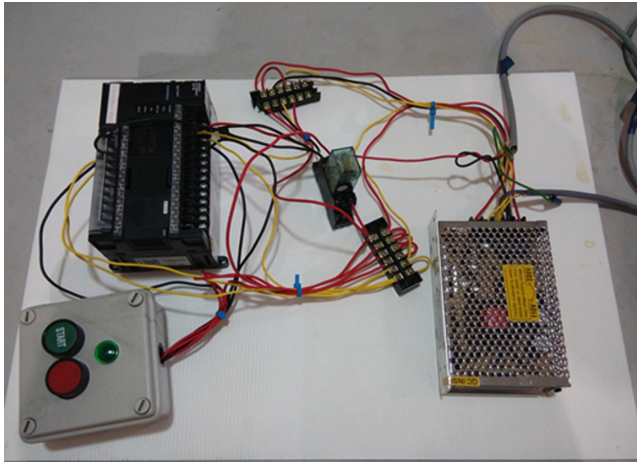


Fig. 1. Ladder diagram schematic in CX programmer software

Hardware development consist of two main components which is electrical part and mechanical part. The electrical part is located at the side of the CNC machine while the mechanical part is attached at the nozzle that supply the coolant of the CNC machine

(Fig. 2). For the mechanical part, a nozzle has been design by using SOLIDWORK software to control the coolant supply with high pressure (Fig. 3). Furthermore, this design is very convenient for the fast responds of the coolant supply during the experimental operation. The importance of the nozzle is to build the connection between the coolant supplies with the PLC system that consist the ladder diagram program.



**Fig. 2.** Electrical and wiring part of the system



**Fig. 3.** Mechanical part – fabricated nozzle

### 3.2 Experimental Setup

Experiments were carried out on CNC milling machine to analyse the performance of the new coolant supply system for each of the duration time and to observe the surface roughness.

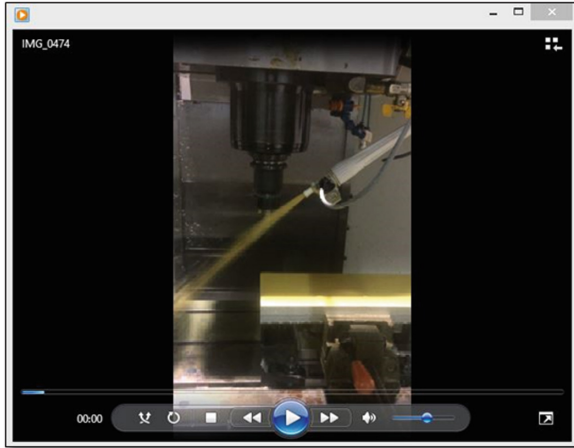


Fig. 4. Coolant start to eject



Fig. 5. Coolant stop ejecting after the designated time

A series of experiments were conducted as to ensure the performance of the automated coolant supply system. The experiments consist of 2 s, 3 s, 4 s, 5 s, 10 s, 15 s, 20 s and 25 s time period and undergo the milling process for 150 mm cutting length of the aluminium block. This system is designed to control the amount of coolant automatically according to time setting by the application of CX programmer so that the amount of the coolant supply for the machining process can be reduced. For example, for the interval time of 2 s, the valve will be opened 2 s for coolant flow and will be closed for 2 s to stop the flow of coolant. Figure 4 and Fig. 5 shows the coolant start to ejecting and stop according to time setting respectively. For this experiment, there are 3 sets of cutting (Run 1, Run 2 and Run 3) that were carried out for each interval time and the cutting tool is changed for every single interval time. The purpose of changing the cutting tool is to obtain a fair comparable result of surface roughness for each interval time since it is believed that new cutting tool should be used to cut the workpiece for each interval time for a fair comparison to identify the best interval time.

#### 4 Results and Discussion

The surface roughness results for the initial test for Run 1, Run 2 and Run 3 are shown in Figs. 6, 7 and 8 respectively. Table 1 shows the average result of the surface roughness for the three runs of the initial test where the milling tool is changed for each of the interval time. From the plotted graph, Run 1, Run 2 and average result show that the interval time of 3 s has the best surface roughness while in the graph plotted for Run 3, the best surface roughness goes for the 25 s interval time. These results resulting for inconsistent data obtained, which causing the decision to find the best interval time based on the surface roughness condition become not relevant.

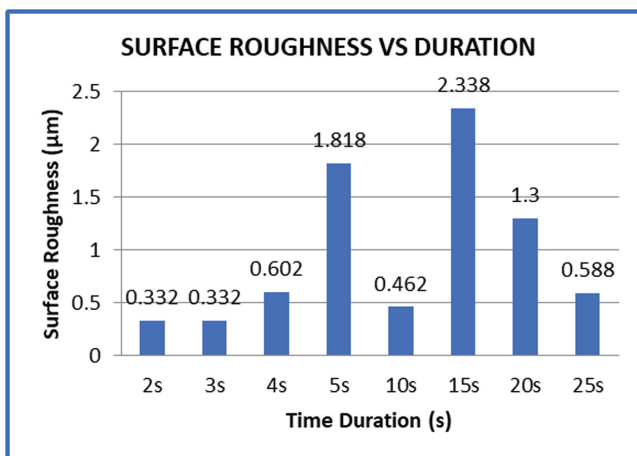


Fig. 6. Graph plotted based of the data in Run 1



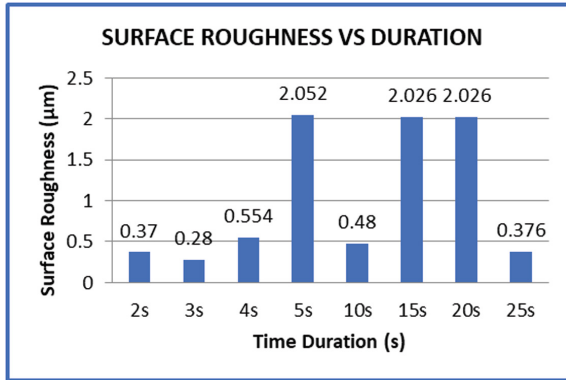


Fig. 7. Graph plotted based of the data in Run 2

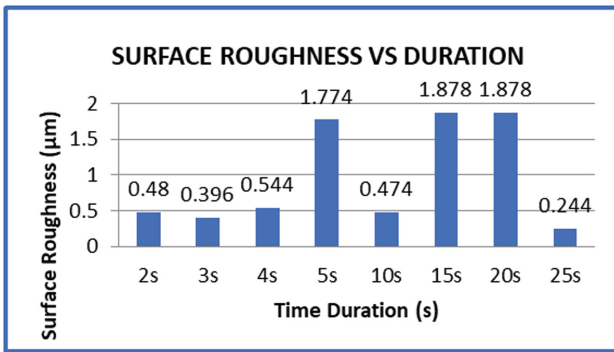
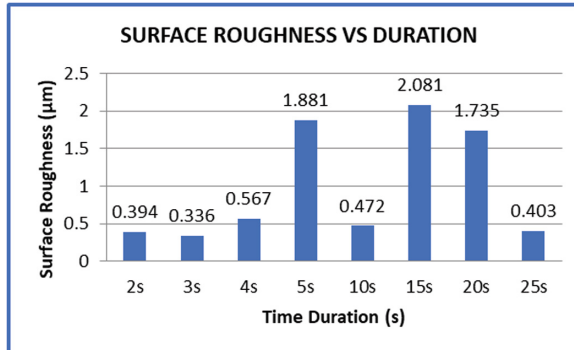


Fig. 8. Graph plotted based of the data in Run 3

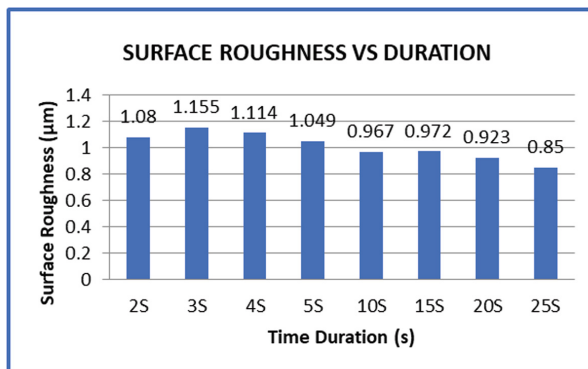
Table 1. Average surface roughness for Experiment 1

Coolant supply interval time (s)	Surface Roughness ( $\mu\text{m}$ )			
	Run 1	Run 2	Run 3	Average
2 s	0.332	0.37	0.48	0.394
3 s	0.332	0.28	0.396	0.336
4 s	0.602	0.554	0.544	0.567
5 s	1.818	2.052	1.774	1.881
10 s	0.462	0.48	0.474	0.472
15 s	2.338	2.026	1.878	2.081
20 s	1.3	2.026	1.878	1.735
25 s	0.588	0.376	0.244	0.403

Moreover, the average result in Fig. 9 shows that interval time of 5 s, 15 s and 20 s have a drastically bad surface roughness while the others have merely similar surface roughness which is less than 1  $\mu\text{m}$ . This inconsistent data is probably coming from the human error during changing the milling tool in the experiment. There are many factors that will affect the surface roughness of the workpiece which one of the cause is human error. Through these results, it comes to our decision that the cutting tool should not be changed during performing experiment in this research work as it will give negative effects and cause for inconsistent data obtained.



**Fig. 9.** Average surface roughness for 3 run experiment



**Fig. 10.** Average surface roughness for the extra experiment

Therefore, another extra experiment was conducted to overcome the issue of the first experiment, where in this extra experiment the cutting tool is not changed during the experiment and the same cutting tool is used for all the interval times.

Table 2 shows the result of the surface roughness for the extra experiment which undergoes only one set of the experimental machining process without changing the milling tool for each of the time period. According to Fig. 10, it is observed that the

result of the surface roughness of the workpiece is more consistent compare to the first experiment. This finding shows that the machining operation with changing the milling tool produced a promising result. Therefore, machining operation without changing the cutting tools will result for the better and consistent surface roughness of the workpiece.

**Table 2.** Average surface roughness for the extra experiment

Interval time (s)	Surface roughness ( $\mu\text{m}$ )
2 s	1.08
3 s	1.155
4 s	1.114
5 s	1.049
10 s	0.967
15 s	0.972
20 s	0.923
25 s	0.85

Generally, the best surface roughness is at 25 s interval time as shown in Fig. 10. It is clearly seen that the results of the surface roughness value are decreasing from time interval 3 s until 25 s, although there is a slight increase between the surface roughness obtained in 3 s form the result of 2 s. According to Table 2, the best surface roughness is obtained during time interval of 25 s with the value 0.85  $\mu\text{m}$ . The result proves that a better surface result can be obtained even with less amount of coolant supply which indirectly proving the potential application of the proposed automated coolant supply system. Drilling with external coolant which is widely practiced may not be a good significance in machining. This is parallel with the findings of Jessy et al. [7], where they stated that the chips formation during machining are tended to emerge from the cutting zone to machining zone through coolant. When the coolant is supplied to the cutting zone, the chips cannot emerge from the cutting zone if the amount of coolant is too big.

According to a separately conducted test by using a flooded condition of coolant supply without any time-based control, the roughness of the workpiece after the cutting has been conducted was recorded at 0.331  $\mu\text{m}$ . From the observation of automated coolant supply system, the best surface roughness is obtained at 25 s interval time and the value is 0.85  $\mu\text{m}$ . Perhaps that the best value of surface roughness for automated coolant supply for 25 s is more trending towards flooded coolant system. Although the roughness of the workpiece in flooded condition is quiet good compared to the roughness value in 25 s interval time, further investigation needs to be carried out to verify this issue as the current research work had not consider for the optimum cutting parameter condition such as spindle speed, feed rate, depth of cut and so on.

Moreover, further study needs to be executed for future work to observe the effect on surface roughness by increasing the interval time more than 25 s. It is believing that with the increasing of interval time, the minimum surface roughness will be obtained. This is because as the time interval increased, this allows the chips move away from the cutting zone more easily and cause an improvement in the surface roughness.

## 5 Conclusion

This paper presents the experimental results in terms of surface roughness when milling AISI 304L by application of the new development of coolant supply system. Experimental observations reported in this study point out that this new lubricating system may generate economic advantages for production system and manufacturers due to the reduction of the amount of coolant use with a view to sustainability for green manufacturing. The analyses of the results indicated that the human error detected while changing the milling tool during machining operation is giving big impact to the result of machining performance. Therefore, machining operation without changing cutting tools is better than changing cutting tools because by reduction of human error it can improve the surface quality of a product and also the cost of cutting tool.

Another experiment will be conducted by applying Dyno Ware software to evaluate the effect of force especially during opening and closing the valve and to ensure that the flow of coolant is consistent throughout the different experiments. It is recommended to explore the relationship between the nozzle size and the surface roughness of work-piece and also use the other interval time to test the performance of this system.

**Acknowledgments.** The authors would like to acknowledge the financial support provided by Majlis Amanah Rakyat (MARA), Universiti Teknikal Malaysia Melaka (UTeM) and technical support provided by Faculty of Manufacturing Engineering, UTeM.

## References

1. Kiyak, M., Cakir, O.: Examination of machining parameters on surface roughness in EDM of tool steel. *J. Mater. Process. Technol.* **191**(1), 141–144 (2007)
2. Boswell, B., Chandrantilleke, T.T.: Air-Cooling used for metal cutting. *Am. J. Appl. Sci.* **6**(2), 251–262 (2009)
3. The Engineer: The benefits of dry machining (2016). <https://www.theengineer.co.uk/the-benefits-of-dry-machining/>. Accessed 20 May 2018
4. Petrillin, A.: Which is better: dry or wet machining? Technical report, Cutting Tool Engineering (2016)
5. Ji, X., Zhang, X., Liang, Y.S.: Modeling the effects of Minimum Quantity Lubrication on machining force, temperature, and residual stress. *Int. J. Mach. Sci. Technol.* **18**(4), 547–564 (2014)
6. Probst, E.: Benefits and challenges of minimum quantity lubrication. Technical report, Modern Machine Shop (2016)
7. Jessy, K., Dinakaran, D., Rao, V.S.: Influence of different cooling methods on drill temperature in drilling GFRP. *Int. J. Adv. Manuf. Technol.* **76**(1–4), 609–621 (2015)



# Non-static Vision Guided Pneumatic Pick and Place Robotic System with Shared Supervisory Control

Ahmad Anas Yusof<sup>(✉)</sup>, Shakti Kumaran Asohkumaran,  
and Muhammad Arif Aiman Ramli

Faculty of Mechanical Engineering, Universiti Teknikal Malaysia Melaka,  
Hang Tuah Jaya, 76100 Durian Tunggal, Melaka, Malaysia  
anas@utem.edu.my

**Abstract.** The purpose of this research is to develop a vision guided pneumatic pick and place robotic system with shared supervisory control where it is highly desirable in the current industry and is in line with the industrial revolution 4.0 that is currently being developed around the globe. In this research, a non-static Pixy camera CMUcam5 is being used as the vision sensor that provides cues to the movement of the pick and place system in an automatic mode. The sensor will receive the data from the image captured and process it to do the desired task. The system uses Arduino microcontroller and the PS2 controller starter kit wireless transmitter or SKPSW, which is tested in the manual and automatic mode. The supervisory control project is developed by using the PS2 controller as a base system that will send the data from the remote control and send output data to the system. Operational test results show that the shared supervisory control is well executed in both manual and automatic mode. The vision sensor also guides the pick and place robot to handle two objects in the automatic modes with successful attempts.

**Keywords:** Shared supervisory control · Vision sensor · Pixy camera · Pick and place robotic system

## 1 Introduction

The basic concept in shared supervisory control is to provide a remote-control capability for a human supervisor to generate commands to a site with the help of multiple sensors for improve situational awareness [1]. Vision-guided robots are a quickly emerging area of industrial and autonomous robotics. The robots that are equipped with advanced vision systems are typically far more adept and flexible than robots that operate without a vision. The robots are basically a machine fitted with one or more cameras used as sensors to provide a secondary feedback signal to the robot controller to more accurately move to a variable target position, thus making them highly anticipated in a wide range of applications. Such technology is rapidly transforming production processes by enabling robots to be highly adaptable to shared supervisory control and more easily implemented [2]. Prior work in the use of visual information specifically for grasping has resulted in various insight. Many of these proposed

systems use a static camera and a calibrated coordinate transformation from the camera frame to the manipulator frame. Static camera configuration eliminates problems with moving cameras, but introduces the need for stereo-baseline calibration and camera-to-manipulator coordinate transform calibration. Others uses alternative to gripper, such as a basket and grapple as the end effector. This eliminates mechanical alignment issues, allows calibration error, and tolerates noise in both sensing and manipulator positioning. There are also methods where the objects' location is known and the objects maintained constant movements with no velocity and direction changes.

This simplifies the issues of calibrating camera transformations on the robot, but limited the flexibility of the system. By limiting these factors, the control of the robot is simplified, and the control system could accurately predict object position for a given point in time. There are also studies on using movable camera vision, where robot motion causes camera motion, without requiring the vision system to track the end-effector, which is usually required for closed-loop control with a static camera [3–9]. Thus this paper presents the development of a movable camera used in an automatic movement of a pick and place robotic system that tracks work pieces from above and moves with the motion of the robots. Shared supervisory control is also developed, where human and robot can mutually solve the given task.

## 2 Methodology

This section describes the test rig and programming setup for the test. The functionality of the pneumatic pick and place robotic system with shared supervisory control is one of the crucial aspects need to be taken in the industry especially in manufacturing industries to enhance the productivity of the output and it is a good platform to keep developing the robotic technology that is useful for the human being. An operational test has been conducted based on four functionalities, which are the manual mode, shared supervisory control, vision sensor and automatic mode operations.

### 2.1 Test Rig Setup

In this case of study, a pick and place robotic system with five pneumatic cylinders are used, which creates five degree of freedom movement for gripper, gripper rotation, downward movement, rotation of the body and forward movement [10]. Based on the semi-cylindrical coordinate movement system, the pneumatic pick and place robotic system is pre-programmed for a shared supervisory control, by the use of a microcontroller and related computer programming. A wireless PS2 controller with its transmitter and receiver is used to control the pick and place robotic system, as shown in Fig. 1. The control system has been developed by using Arduino Uno microcontroller and the SKPSW wireless transmitter. The related button on the PS2 controller is used to switch a pre-programmed manual and automatic movement based on C programming language.

Arduino Uno serves as the main brain to control the movements, while Pixy camera CMUcam5 serves as the vision sensor that processes images captured into the pre-programmed algorithm [11, 12]. Figure 2 illustrates the Pixy camera used in the test while Fig. 3 shows the assigned movement of pneumatic pick and place system in

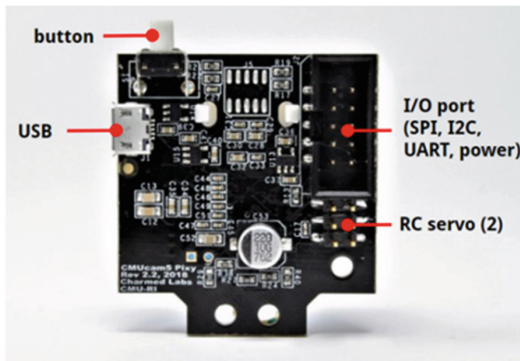


**Fig. 1.** The assigned movement of the mini robot in the PS2 controller

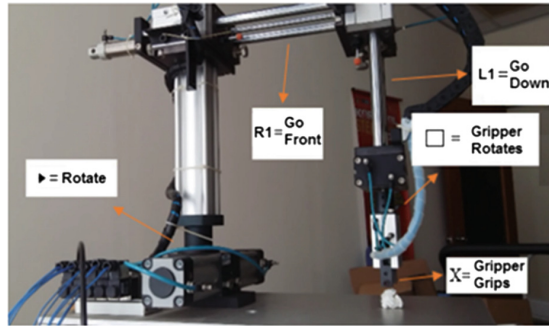
manual mode. Relays are used to control the solenoid valves, which eventually control the pneumatic system, as shown by the assigned connection for relays in Table 1.

**Table 1.** Assigned connection for relays

Relay module number	Arduino pin	Function	Button
2	6	Gripper operation	X
4	10	Downward movement	L1
5	9	Forward movement	R1
1	8	Gripper rotation	□
7	7	Robot rotation	▶

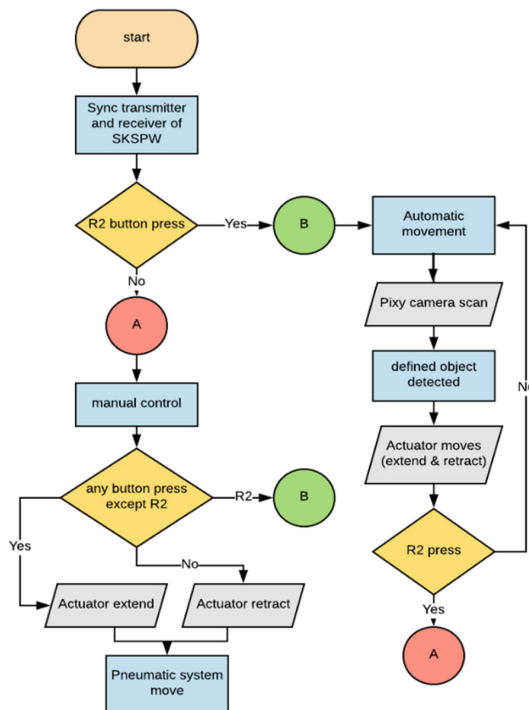


**Fig. 2.** The pixy camera CMUCam5



**Fig. 3.** The assigned movement of pneumatic pick and place system in manual mode

Prior to the pneumatic pick and place operation, the Pixy camera is positioned and calibrated on top of the pneumatic gripper, facing down directly on a pre-designated position located under the gripper. This is important due to the end-to-end movement of the system, since the pneumatic system depends on the 5/2-way directional control valves. The angle of Pixy facing downward is also crucial in order for the Pixy to detect objects with suitable distance under the gripper for automatic mode operation. Figure 4 illustrates the flowchart for manual and automatic mode operation based on the selection of using the R2 button.



**Fig. 4.** Simplified flowchart for manual and automatic mode operation



## 2.2 Programming Setup

In this research, the shared supervisory control is based on Arduino Uno microcontroller, with Arduino IDE software, which allows researcher to write sketches, a form of Arduino programming language. The Arduino programming language is based on a very simple hardware programming language called processing, which is similar to the C language. The algorithm, pseudocodes and programming codes are presented in this section.

**Algorithm.** The algorithm presents in this project defines the initialization and operation set of steps for the test. The initialization algorithm involves the setting parameters, the outputs and the inputs in the program. The written algorithm for the operation test is as follows:

### Program to run Pick and Place System using Microcontroller

```

Initialize
  Set  Predetermine location
      Manual Mode
      Automatic Mode
      Pixy Signature 1 colour
      Pixy Signature 2 colour
      Pixy Camera
      PS2 Shield
Output
Gripper
  Horizontal Cylinder
  Vertical Cylinder
  Gripper Rotary Actuator
  Main Rotary Actuator
Input
  Pixy Signature 1
  Pixy Signature 2
  PS2 Button X
  PS2 Button L1
  PS2 Button R1
  PS2 Button R2
  PS2 Button 
  PS2 Button 
Operation
  If PS2 Button R2 pushed in Automatic Mode
    Change to Manual Mode
  If PS2 Button R2 pushed in Manual Mode
    Change to Automatic Mode
  If PS2 Button X pushed in Manual Mode

```

```

    Gripper Grasps the Object
  If PS2 Button X released in Manual Mode
    Gripper Ungrasps the Object
  If PS2 Button R1 pushed in Manual Mode
    Horizontal Cylinder Extends
  If PS2 Button R1 released in Manual Mode
    Horizontal Cylinder Retracts
  If PS2 Button L1 pushed in Manual Mode
    Vertical Cylinder Extends
  If PS2 Button L1 released in Manual Mode
    Vertical Cylinder Retracts
  If PS2 Button  pushed in Manual Mode
    Gripper Rotary Actuator Rotates Counter Clockwise
  If PS2 Button  released in Manual Mode
    Gripper Rotary Actuator Rotates Clockwise
  If PS2 Button  pushed in Manual Mode
    Main Rotary Actuator Rotates Counter Clockwise
  If PS2 Button  released in Manual Mode
    Main Rotary Actuator Rotates Clockwise
  If Pixy Signature 1 in Automatic Mode at predeter-
  mined location      Vertical Cylinder Extends
    Gripper Grasps the Object
    Vertical Cylinder Retracts
    Horizontal Cylinder Extends
    Vertical Cylinder Extend
    Gripper Ungrasps the Object
    Vertical Cylinder Retracts
    Horizontal Cylinder Retracts
  If Pixy Signature 2 in Automatic Mode at predeter-
  mined location      Vertical Cylinder Extends
    Gripper Grasps the Object
    Vertical Cylinder Retracts
    Main Rotary Actuator Rotates Counter Clockwise
    Gripper Ungrasps the Object
    Main Rotary Actuator Rotates Clockwise

```

**Pseudocodes.** The pseudocodes for the experiment use high level style syntax such as IF, Else-IF and Call, which describes the selections in the program. The written pseudocodes for the test are as follows:

```

function Automatic Mode Signature 1
{
    Start;
    Vertical Cylinder Extends;
    Gripper Grasps the Object;
    Vertical Cylinder Retracts;
    Horizontal Cylinder Extends;
    Vertical Cylinder Extends;
    Gripper Ungrasps the Object;
    Vertical Cylinder Retracts;
    Horizontal Cylinder Retracts;
    Stop;
}
function Automatic Mode Signature 2
{
    Start;
    Vertical Cylinder Extends;
    Gripper Grasps the Object;
    Vertical Cylinder Retracts;
    Main Rotary Actuator Rotates Counter Clockwise;
    Gripper Ungrasps the Object;
    Main Rotary Actuator Rotates Clockwise;
    Stop;
}
function Manual Mode
{
    Start;
    if (X button press)
    {
        Gripper Grasps the Object;
    }
    Gripper Ungrasps the Object;
    if (R1 button press)
    {
        Horizontal Cylinder Extends;
    }
}

```

```

    Horizontal Cylinder Retracts;
if (L1 button press)
{
    Vertical Cylinder Extends;
}
    Vertical Cylinder Retracts;
        if ([ ] button press)
    {
Gripper Rotary Actuator Rotates Counter Clockwise;
    }
    Gripper Rotary Actuator Rotates Clockwise;
if (> button press)
{
    Main Rotary Actuator Rotates Counter Clockwise;
}
    Main Rotary Actuator Rotates Clockwise;
    Stop;
}
Start;
Sync transmitter and receiver of SKSPW;
if(R2 button press)
{
Automatic Mode;
    Pixy Camera Scan;
    if (Pixy Camera Detects Signature 1)
        {
            call Automatic Mode Signature 1;
        }
    Pixy Camera Scan;
    if (Pixy Camera Detects Signature 2) {
        call Automatic Mode Signature 2;
    }
}
    Pixy Camera Scan;
if (R2 button press)
{
call Manual Mode;
}
Automatic Mode;
Stop;

```

**Programming Codes.** The programming codes used in the experiment are shown below. Note that the programming is suited for manual and automatic mode, using five

5/2-way pneumatic directional control valves, which controls five degree of movement of the pick and place robotic system. The codes in the form of Arduino sketches for the operation test are as follows:

```
// Writing Arduino sketches for controlling five 5/2-way
valves on a
// pneumatic pick and place system with shared superviso-
ry control in the
// form of manual mode and automatic mode operation. The
automatic mode
// detects 2 objects with different colours in pre-
determined end-to end
// position.
// Codes written by Muhammad Arif Aiman bin Ramli
B041410233
// 11 April 2018
// Faculty of mechanical Engineering
// Universiti Teknikal Malaysia Melaka

#include <SoftwareSerial.h> //declare class object
#include <Cytron_PS2Shield.h> //PS2 ps2 = PS2(); //PS2
class object: ps2
#include <SPI.h>
#include <Pixy.h>
Cytron_PS2Shield ps2(2,3);
Pixy pixy;
int signature = 0;
int x = 0; //positon x axis
int y = 0; //position y axis
int Xmin = 70; //min x position
int Xmax = 200; //max x position
int Ymin = 60; //min y position
int Ymax = 140; //max y position
static int i = 0;
int c=2;
#define gripper 6
#define front 9
#define head 8
#define down 10
#define turn 7
```

```
void setup()
{
  pinMode(front,OUTPUT);
  pinMode(gripper,OUTPUT);
  pinMode(head,OUTPUT);
  pinMode(down,OUTPUT);
  pinMode(turn,OUTPUT);
  Serial.begin(9600);
  ps2.begin(9600); //initialize the main board to use de-
  sired (baudrate, rx, tx)//This baudrate must same with
  the jumper setting at PS2 shield
  Stop();
  pixy.init();
}
void loop()
{
  while(millis()<5000)
  {
    scan();
  }
  uint16_t blocks;
  blocks = pixy.getBlocks();
  scan();
  if(c==1)
  {
    if(ps2.readButton(PS2_RIGHT_2) == 0)
    // if button R2 is pressed (0 = pressed, 1 = released)
    {
      c=2;
    }
    else if(signature==1 && blocks && x>=Xmin && x<=Xmax &&
    y>=Ymin && y<=Ymax)
    {
      sig1();
    }
  }
}
```

```

else if(signature==2 && blocks && x>=Xmin && x<=Xmax &&
y>=Ymin && y<=Ymax)
{
sig2();
}
else
{
Stop();
}
}
else if(c==2)
{
if(ps2.readButton(PS2_RIGHT_2) == 0) // if button R2 is
pressed (0 = pressed, 1 = released)
{
c=1;
}
if ( ps2.readButton(PS2_SQUARE) == 0) //0 = pressed, 1 =
released
{
digitalWrite(head, HIGH);
}
else
{
digitalWrite(head, LOW);
}
if ( ps2.readButton(PS2_CROSS) == 0)
{
digitalWrite(gripper, HIGH);
}
else
{
digitalWrite(gripper, LOW);
}
if ( ps2.readButton(PS2_RIGHT) == 0)
{
digitalWrite(turn, HIGH);
}
else
{
digitalWrite(turn, LOW);
}
}

```

```
if ( ps2.readButton(PS2_LEFT_1) == 0)
{
digitalWrite(down, HIGH);
}
else
{
digitalWrite(down, LOW);
}
if ( ps2.readButton(PS2_RIGHT_1) == 0)
{
digitalWrite(front, HIGH);
}
else
{
digitalWrite(front, LOW);
}
}
}

void sig1() // when signature 1 detected, run this func-
tion { digitalWrite(head,LOW);
digitalWrite(turn,LOW);
digitalWrite(down,LOW);
digitalWrite(front,LOW);
delay(100);
digitalWrite(gripper,HIGH);
delay(700);
digitalWrite(gripper,LOW);
delay(700);
digitalWrite(down,HIGH);
delay(2000);
digitalWrite(gripper,HIGH);
delay(1000);
digitalWrite(down,LOW);
delay(2000);
digitalWrite(front,HIGH);
delay(3000);
digitalWrite(down,HIGH);
delay(2000);
digitalWrite(gripper,LOW);
delay(1000);
```



```

digitalWrite(down,LOW);
delay(2000);
digitalWrite(front,LOW);
delay(3000);
}
void sig2() // when signature 2 detected, run this function {
digitalWrite(head,LOW);
digitalWrite(turn,LOW);
digitalWrite(down,LOW);
digitalWrite(front,LOW);
delay(100);
digitalWrite(gripper,HIGH);
delay(700);
digitalWrite(gripper,LOW);
delay(300);
digitalWrite(down,HIGH);
delay(2000);
digitalWrite(gripper,HIGH);
delay(1000);
digitalWrite(down,LOW);
delay(2000);
digitalWrite(turn,HIGH);
delay(3000);
digitalWrite(gripper,LOW);
delay(1000);
digitalWrite(turn,LOW);
delay(3000);
}
void Stop() // stop the running program then set the system to the default position
{
digitalWrite(front,LOW);
digitalWrite(gripper,LOW);
digitalWrite(head,LOW);
digitalWrite(down,LOW);
digitalWrite(turn,LOW);
}
void scan() // scan the object via Pixy
{
uint16_t blocks;
blocks = pixy.getBlocks(); //receive data from pixy
signature = pixy.blocks[i].signature; //get object's signature
x = pixy.blocks[i].x; //get x position y =
pixy.blocks[i].y; //get y position }

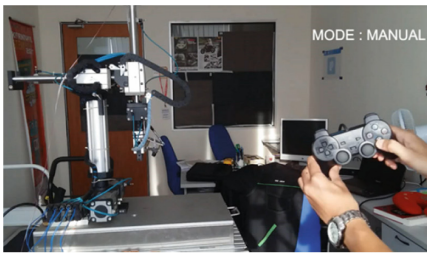
```

### 3 Results and Discussions

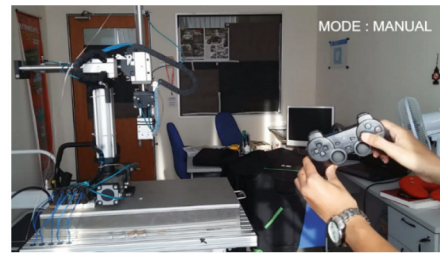
The test results on the communication between the Pixy camera, the PS2 controller and the pneumatic pick and place robotic system have been illustrated in Figs. 5, 6, 7, 8 and 9. The operation test has been conducted in order to perform the required task in manual and automatic mode and to check for the functionality of the vision sensor and the shared supervisory control.

#### 3.1 Manual Mode Operational Test

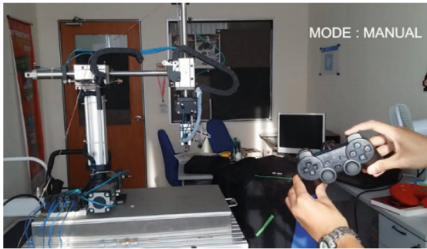
In manual mode control, five buttons are used to control five movements of the pneumatic pick and place robotic system. The operator may use the shared supervisory control by pushing button R2, to interchangeably opt for manual or automatic mode. Figure 5(a) shows that the gripper grasps the object when button X is pushed.



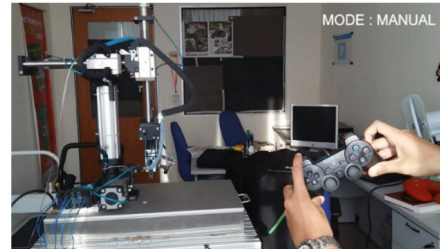
(a) The gripper grasps the object by pushing button X



(b) The gripper rotates by pushing button □



(c) The pick and place robot extend forward by pushing button R1



(d) The pick and place robot extend downward by pushing button L1



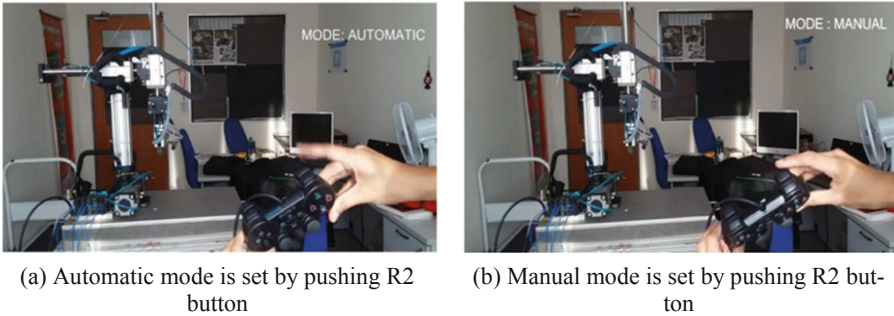
(e) The pick and place robot rotates 180° anti-clockwise by pushing button ►

**Fig. 5.** Robot's movement in manual mode.

The gripper releases the grasp when the push button X is released. Downward movement is controlled by button L1, while R1 controls the forward movement. Gripper and the whole robot rotation movement are controlled by button  $\square$  and  $\blacktriangleright$ , respectively. All movements are illustrated in Fig. 5(a) to (e).

### 3.2 Shared Supervisory Control Functionality

The basic architecture of the system provides a shared control capability with simultaneous multiple sensors for input, which in time can help the operator to generate commands and parameterization to send to the remote site. In the experiment, the operator may use the shared supervisory control by pushing button R2, to interchangeably opt for manual or automatic mode. In the test, as illustrated in Fig. 6(a) and (b), it was shown that the pick and place system is set in an automatic mode when button R2 is pushed. The automatic mode has been programmed to interact with two objects with different colours.

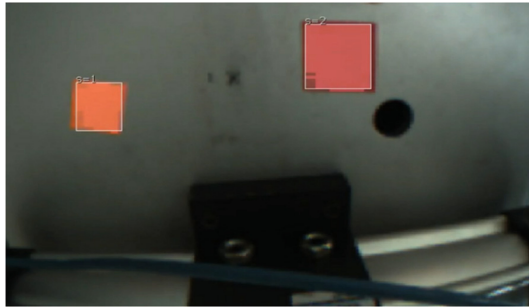


**Fig. 6.** Changing manual mode to automatic mode and vice versa

### 3.3 Vision Sensor Functionality

Vision sensor coding is based on an open source Pixy view software that is small, affordable price and easy to use. The camera can distinguish around seven different unique colours and processes 50 frames per second equal to 20 ms per image. Figure 7 shows the detection of the orange and red objects, designated as signature 1 ( $S = 1$ , for orange object) and signature 2 ( $S = 2$  for red object) in the Pixy view software. The codes for the sensor are as follows:

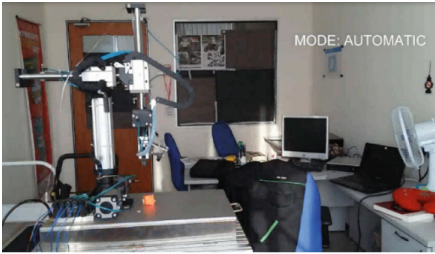
```
void scan() // scan the object via Pixy
{
  uint16_t blocks;
  blocks = pixy.getBlocks(); //receive data from pixy
  signature = pixy.blocks[i].signature; //get object's signature
  x = pixy.blocks[i].x; //get x position y =
  pixy.blocks[i].y; //get y position }
```



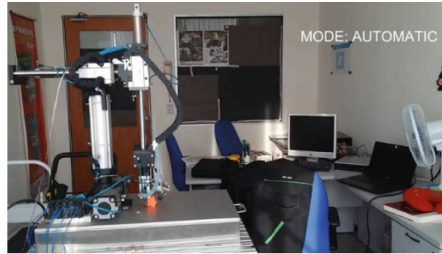
**Fig. 7.** Detection of orange and red objects

### 3.4 Automatic Mode Operational Test

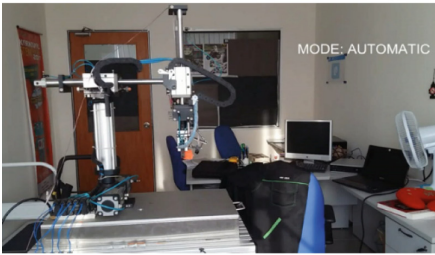
In the automatic mode control test, two objects with different colours are used. The pick and place robot is subjected to a simple material handling routine. The robot is pre-programmed to detect red and orange objects. The proposed robot-vision system then detects the object in a predetermined location of the object. If the orange object is detected, the pick and place moves vertically downward at a fixed speed of 4 cm/s along the y-axis of the image, as illustrated in Fig. 8(a) and (b). The gripper then grasps the object, and moves vertically upward with the same velocity. Upon reaching the maximum height, the arm then moves forward to convey the object to a new location. The location of the target is designated at the end of the fully extended condition. At the designated target, the robot will then move downward, and release the object as illustrated in Fig. 8(c)–(e).



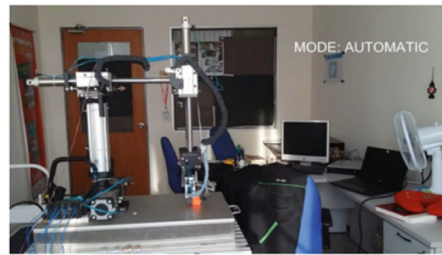
(a) The gripper moves downward to grasp the orange object at the designated starting point



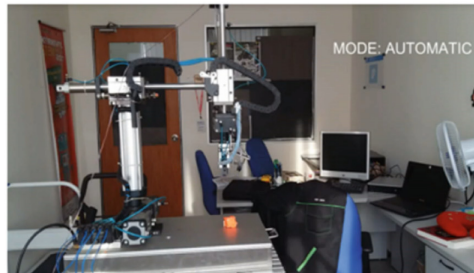
(b) The gripper grasps the orange object



(c) The object is raised, transferred horizontally to a designated receiving point



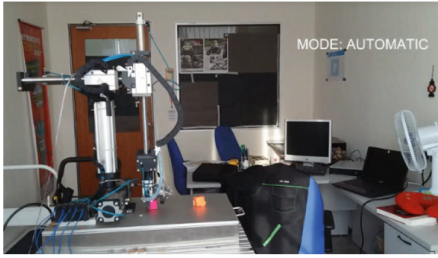
(d) The gripper transfers the object to the designated position



(e) The gripper releases the object

**Fig. 8.** Grasping process of an orange object

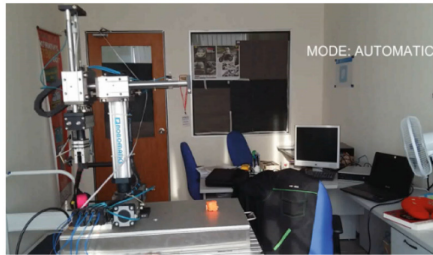
The image of the object is continuously being captured and analyzed by the microcontroller and the pixy camera. If a red object is detected, the pick and place robot will follow the same step, where it moves vertically downward at a fixed speed of 4 cm/s along the y-axis of the image, as illustrated in Fig. 9(a) and (b). The gripper then grasps the object, and moves vertically upward with the same velocity. Upon reaching the maximum height, the arm then rotates to the left in an 180° counter-clockwise swing to convey the object to a new location. The location of the target is designated at the end of the fully rotation condition. At the designated target, the robot will then release the object as illustrated in Fig. 9(c).



(a) The gripper grasps the red object at the designated starting point



(b) The gripper grasps and lifts the red object



(c) The gripper transfer the object to another designated position and release it

**Fig. 9.** Grasping process of a red object

## 4 Conclusion

The study on the development of the pneumatic pick and place robotic system with shared supervisory control has been presented in this paper. There are many ways of control method in the development of a pick and place robotic system. The Arduino microcontroller has been used in the study, with program codes that is introduced to operate the pneumatic pick and place robotic system in manual and automatic mode, for shared supervisory control. Pixy camera CMUcam5 is used as the main input sensor to work as the vision sensor during the automatic mode operation test. The test has been conducted in order to understand the ability of the Pixy camera to detect and differentiate red and orange in different circumstances. It is noted that the pick and place robotic system manages to differentiate between both coloured objects, and transferred the objects to the designated locations. However, due to the usage of 5/2-way directional control valves on the system, it can only operate in the end-to-end movement, which limits the object to be placed only at a specific designated target and not at any random positions. Future development will involve the improvement of the system in handling objects at random positions.



## References

1. Gavriel, S.: Handbook of Human Factors and Ergonomics, 4th edn. Wiley, Hoboken (2012)
2. Lian-Wang, L., Hsin-Han, C., Hsum, L.I.: Development and control of a pneumatic-actuator 3-DOF translational parallel manipulator with robot vision. *Sensors* **19**(1459), 1–26 (2019)
3. Allen, P., Timcenko, A., Yoshimi, B., Michelman, P.: Automated tracking and grasping of a moving object with a robotic hand-eye system. *IEEE Trans. Robot. Autom.* **9**(2), 152–165 (1993)
4. Brandt, S., Smith, C., Papanikolopoulos N.: The Minnesota robotic visual tracker: a flexible testbed for vision guided robotic research. In: Proceedings of the IEEE International Conference on Systems, Man, and Cybernetics, pp. 1363–1368 (1994)
5. Buttazzo, G., Allotta, B., Fanizza, F.: Mousebuster: a robot system for catching fast moving objects by vision. In: Proceedings of the IEEE International Conference on Robotics and Automation, pp. 932–937 (1993)
6. Houshangi, N.: Control of a robotic manipulator to grasp a moving target using vision. In: Proceedings of the IEEE International Conference on Robotics and Automation, pp. 604–609 (1992)
7. Koivo, A.: On adaptive vision feedback control of robotic manipulators. In: Proceedings of the IEEE Conference on Decision and Control, pp. 1883–1888 (1991)
8. Schrott, A.: Feature-based camera-guided grasping by an eye-in-hand robot. In: Proceedings of the IEEE International Conference on Robotics and Automation, pp. 1832–1837 (1992)
9. Charmedlabs (2019). Pixy CMUcam5. <http://charmedlabs.com/default/pixy-cmucam5/>. Accessed 1 Apr 2019
10. Yusof, A.A., Ismail, I., Bakri, S., Nor, M.K.M., Ahmad, R.: Preparation, field observation and survey on STEM engagement of 5-axis pick-and-place pneumatic robotic arm remote-manipulation. In: Proceedings of Intelligent Manufacturing & Mechatronics Symposium, pp. 219–230 (2018)
11. Candelas, F.A.: Experiences on using Arduino for laboratory experiments of automatic control and robotics. *IFAC PapersOnLine* **48**(29), 105–110 (2015)
12. Arduino (2019). Arduino Board Uno. <https://store.arduino.cc/usa/arduino-uno-rev3>. Accessed 1 Apr 2019



# Correction to: A Bottle Neck Simulation System for a Generic Production Process

Azrul Haniedy Jamil, Muhammad Nasiruddin Mahyuddin,  
Ahmad Rafeek Ibrahim, and Timothy Tong

**Correction to:**  
**Chapter “A Bottle Neck Simulation System for a Generic Production Process” in: Z. Jamaludin and M. N. Ali Mokhtar (Eds.): *Intelligent Manufacturing and Mechatronics*, LNME,**  
[https://doi.org/10.1007/978-981-13-9539-0\\_30](https://doi.org/10.1007/978-981-13-9539-0_30)

The original version of the chapter was inadvertently published with an incorrect second author name “Zedenka, K.” in Ref. [6] which has now been corrected to “Králová, Z.” and an incorrect URL also corrected. The chapter has been updated with the changes.

---

The updated version of this chapter can be found at  
[https://doi.org/10.1007/978-981-13-9539-0\\_30](https://doi.org/10.1007/978-981-13-9539-0_30)

© Springer Nature Singapore Pte Ltd. 2021  
Z. Jamaludin and M. N. Ali Mokhtar (Eds.): SympoSIMM 2019, LNME, p. C1, 2021.  
[https://doi.org/10.1007/978-981-13-9539-0\\_56](https://doi.org/10.1007/978-981-13-9539-0_56)



# Author Index

## A

A. Perumal, Puvanasvaran, 410  
A. Rasid, Zainudin, 436  
Ab Aziz, Nor Azlina, 48  
Ab Rahman, Mohd Hidayat, 230  
Ab Rahman, Tasiransurini, 48  
Ab Rashid, Mohd Zamzuri, 138, 146  
Ab Wahab, N., 333  
Ab. Rashid, Mohd Zamzuri, 436  
Abd Aziz, Nur Afifah, 230  
Abdul Aziz, Izzad Shafiq, 221  
Abdul Aziz, Mohd Sanusi, 387  
Abdul Aziz, Nor Hidayati, 48  
Abdul Hamid, Rahimah, 361  
Abdul Majeed, Anwar P. P., 67, 75, 451  
Abdullah, Lokman, 102, 138, 195, 265, 372, 503  
Abdullah, Muhammad Amirul, 67  
Abdullah, Zulkeflee, 399  
Abu, Aminudin, 436  
Abu Bakar, Mohd Hadzley, 569  
Abu Bakar, Shahriman, 57, 526  
Abu Kassim, Khairil Anwar, 75  
Ahmad, Mohd Nazri, 230  
Akmal, M., 321  
Ali, Md. Asraf, 129  
Ali Mokhtar, Mohd Najib, 399  
Ang, Vernoon, 487  
Ansari, Muhammad Taha, 557  
Arshad, Mohd Rizal, 515  
Asohkumaran, Shakti Kumaran, 580  
Azman, A. S., 456, 466

## B

Bani Hashim, A. Y., 112  
Bani Hashim, Ahmad Yusairi, 102

## C

Cheng, Chun-An, 308  
Chern, Shin-Yuh, 497  
Chew, B. C., 244  
Chew, Tony, 343  
Chew, Wi Kang, 535  
Chiew, Tsung Heng, 102  
Chong, Jia Yuik, 410

## F

Fairul, A. J., 112  
Feroz, F. S., 456, 466

## G

Ghani, Azlinda Abdul, 214

## H

Hafizuddin, H., 244  
Halin, Hafiz, 57  
Hanim, A. R., 475  
Hanim, Abdul Razak, 419  
Haris, Hasri, 57  
Hassan, Mohd Hasnun Arif, 75  
Hazura, Haroon, 419, 475  
Hong, Richard Lee Jiang, 515  
Hornng, Jeng-Haur, 497  
How, Choong Chia, 167

Hussain, Jawad, 129  
Hwa, Samson Chan Kit, 167

**I**

Ibrahim, Ahmad Rafeek, 299  
Ibrahim, Haidi, 12, 32  
Ibrahim, Muhammad Ar Rahim, 67  
Ibrahim, Zunaidi, 526  
Ibrahim, Zuwairie, 48  
Idayu, Noorfa, 387, 399  
Idris, Siti Khadijah, 419, 475  
Imam Fauzi, E. R., 83  
Ismail, Mohd Muzafar, 353  
Izamshah, Raja, 321, 361

**J**

Jafar, Fairul Azni, 569  
Jamaludin, Zamberi, 102, 176, 186, 195, 372  
Jamil, Azrul Haniedy, 299  
Jamlos, Mohd Aminudin, 21  
Jamri, Aisyah, 569  
Jiang, Qiong-Mao, 497  
Junid, Ramli, 353

**K**

Kaharudin, Khairil Ezwan, 419, 475  
Kamaludin, K. N., 265  
Kamarudin, Najwa, 343  
Kamarul Bahrin, F. F., 83  
Kasim, Mohd Shahir, 288, 361, 387  
Khairuddin, Mohd Ismail, 451  
Khairunizam, Wan, 3, 21, 57, 91, 526  
Koo, Yeong Chin, 157, 515

**L**

Lam, Chee Kiang, 129  
Lee, M. Y., 456, 466  
Lin, Jin-Long, 497  
Ling, Lee Hui, 91  
Liu, Wei-Lun, 497

**M**

Mahendra Kumar, Jothi Letchumy, 451  
Mahmud, Ahmad Syauqi, 21  
Mahyuddin, Muhammad Nasiruddin, 157, 167, 299, 515, 557  
Maidin, Nurul Ain, 230  
Mamat, Normaisharah, 146  
Maslan, M. N., 112, 265, 372, 503  
Maslan, Mohd Nazmin, 138  
Mat Ali, M., 265, 503  
Mat Ali, Mahasan, 138

Mat Seman, Norhidayah, 186  
Mat Yusoff, A. S., 3  
Md Ali, Mohd Amran, 387, 399  
Md. Taha, Aina Qistina, 32  
Minhat, Mohamad, 176, 186  
Mohamad, Mohd Saberi, 48  
Mohamad, Noraiham, 343, 353  
Mohamed Saiful Firdaus, Hussin, 230  
Mohd Halmy, Nor Amylia, 167  
Mohd Hanid, Mohd Hazwan, 288  
Mohd Nawawi, Mohd Al Hafiz, 21, 280, 288  
Mohd Noor, Nor Safira Elaina, 12  
Mohd Razman, Mohd Azraai, 67, 75, 451  
Mohd Saad, Nurzallia, 343  
Mohd Sobri, Nur Fasihah, 557  
Mohd Zain, Anis Suhaila, 419  
Muhammad, Badaruddin, 48  
Muhammad, M. N., 112  
Munawarah, Sharifah, 146  
Murugappan, Murugappan, 526  
Musa, Rabi'u Muazu, 67, 75  
Mustafa, Wan Azani, 3, 21, 57, 91, 207, 214, 221, 280, 288, 526

**N**

Naaamandadin, Nurul Akmam, 207, 214, 221  
Najib, A. M., 83, 112  
Napiah, Z. A. M., 475  
Narayanan, Thinakaran, 353  
Nasir, N. Syuhada, 333  
Noor, C. Basri, 91  
Noorazizi, Mohd Samsuddin, 138, 265, 503  
Nor, Farizan Md, 569  
Norddin, Nurbahirah, 343

**O**

Omar, Mohammad Iqbal, 526  
Osman, Mohd Hairizal, 230  
Othman, Intan Sharida, 353  
Othman, Muhammad Azri, 176  
Othman, Nur Liyana, 280  
Othman, Nurul Syazwani, 214, 280

**P**

Panneerselvam, Vivekanandan, 252

**R**

Radzuan, Nurul Qastalani, 75  
Rafan, Nur Aidawaty, 102, 195  
Rahiman, M. H. F., 487  
Rahim, R. A., 487  
Rahmad, Suhazri Amrin, 48

Raja Abdullah, Raja Izamshah, 288, 387  
 Ramli, Azlan, 321  
 Ramli, Muhammad Arif Aiman, 580  
 Razak, Jeefferie Abd, 343, 353  
 Razak, Muhammad Aiman, 436  
 Razlan, Z. M., 57  
 Razlan, Zuradzman Mohamad, 526  
 Rohani, Mohamad Nur Khairul Hafizi, 3  
 Roslan, Ameer Farhan, 419, 475  
 Roslan, Shairatul Akma, 146

**S**

Saharudin, Ahmad Izdihar, 207  
 Salehuddin, Fauziyah, 419, 475  
 Salleh, Mohd Shukor, 399  
 Sam, M. F. M., 244  
 Santiagoo, Rangunathan, 207, 214, 221, 280  
 Santuso, K., 372  
 Sasahara, H., 333  
 Shahrman, A. B., 91  
 Shaikh Salim, Sheikh Ahmad Zaki, 146, 436  
 Shamshol Ali, Nur Ayunni, 195  
 Shapiee, Muhammad Nur Aiman Bin, 67  
 Sivaraos, 399  
 Subramaniam, S. K., 456, 466  
 Sulaiman, Mohd Amri, 387  
 Sulaiman, Nur Najwa Izzati, 436  
 Sundaraj, Kenneth, 129  
 Syarifah, S. Diny, 91  
 Syed Idrus, Syed Zulkarnain, 3, 21  
 Syed Mohamed, M. S., 265, 503  
 Syed Mohamed, Mohd Syafiq, 138

**T**

Talib, Irsa, 129  
 Tee, Lau Kok, 343  
 Tong, Timothy, 299  
 Tong, Weng Sun, 102  
 Turan, Faiz Mohd, 252

**W**

Wahid, Mohammad Khalid, 230  
 Wan Md Hatta, Wan Nur Izzati, 569  
 Wan Muhamad, Wan Nur Amirah, 361  
 Wei, Chin-Chung, 308

**Y**

Yakub, Fitri, 146, 436  
 Yean, Choong Wen, 526  
 Yusof, Ahmad Anas, 580  
 Yusof, Y. F., 244

**Z**

Zain, A. S. M., 475  
 Zainal, Mustaffa, 214  
 Zainudin, N. D., 83  
 Zainun, Firdaus, 167  
 Zakaria, Muhammad Aizzat, 451, 535  
 Zamri, R., 265, 372, 503  
 Zamri, Ruzaidi, 138  
 Zheng, Bong Siao, 526  
 Zunaidi, I., 57, 91  
 Zuradzman, M. R., 91